

# The anatomy of electroweak symmetry breaking Tome I: The Higgs boson in the Standard Model

Abdelhak Djouadi\*

*Laboratoire de Physique Théorique d'Orsay, UMR8627–CNRS, Université Paris-Sud, Bât. 210, F-91405 Orsay Cedex, France  
Laboratoire de Physique Mathématique et Théorique, UMR5825–CNRS, Université de Montpellier II, F-34095 Montpellier Cedex 5, France*

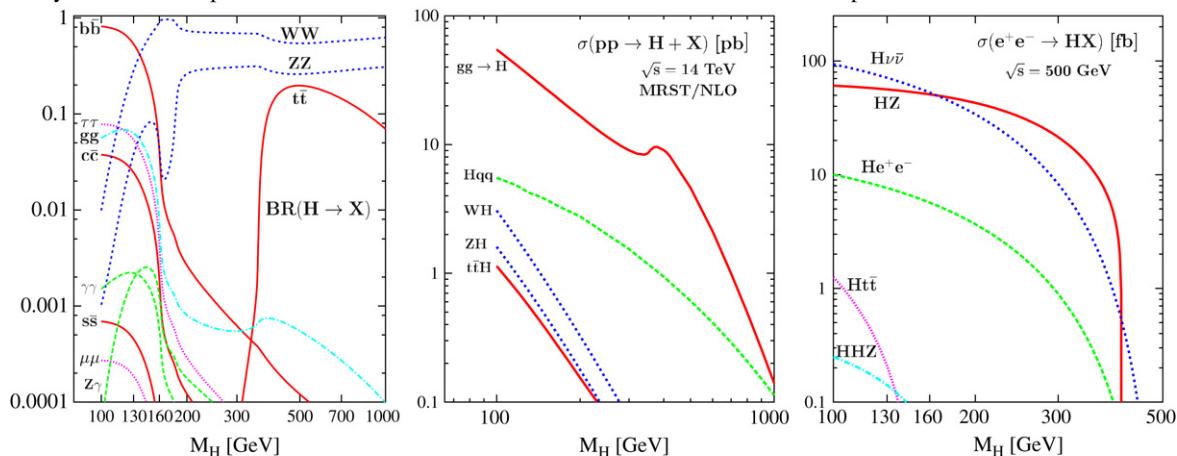
Accepted 7 October 2007

Available online 22 November 2007

editor: J.A. Bagger

## Abstract

This review is devoted to the study of the mechanism of electroweak symmetry breaking and this first part focuses on the Higgs particle of the Standard Model. The fundamental properties of the Higgs boson are reviewed and its decay modes and production mechanisms at hadron colliders and at future lepton colliders are described in detail.



The decay branching ratios of the Standard Model Higgs boson and its production cross sections in the main channels at the LHC and at a 500 GeV  $e^+e^-$  collider.

© 2008 Published by Elsevier B.V.

PACS: 12.15.-y; 14.80.Bn

\* Corresponding address: Laboratoire de Physique Théorique d'Orsay, UMR8627–CNRS, Université Paris-Sud, Bât. 210, F-91405 Orsay Cedex, France.

E-mail address: [Abdelhak.Djouadi@cern.ch](mailto:Abdelhak.Djouadi@cern.ch).

## Contents

0.	Preamble.....	4
0.1.	A short praise of the Standard Model.....	4
0.2.	Probing electroweak symmetry breaking: A brief survey of recent developments.....	4
0.3.	Objectives and limitations of the review.....	6
0.4.	Synopsis of the review.....	6
1.	The Higgs particle in the SM.....	8
1.1.	The SM of the strong and electroweak interactions.....	8
1.1.1.	The SM before electroweak symmetry breaking.....	8
1.1.2.	The Higgs mechanism in the SM.....	10
1.1.3.	The SM Higgs particle and the Goldstone bosons.....	12
1.1.4.	The SM interactions and parameters.....	15
1.2.	Precision tests, radiative corrections and Higgs effects.....	17
1.2.1.	Observables in Z boson decays.....	18
1.2.2.	The electroweak radiative corrections.....	20
1.2.3.	Approximating the radiative corrections.....	22
1.2.4.	The electroweak precision data.....	23
1.3.	Experimental constraints on the Higgs boson mass.....	25
1.3.1.	Constraints from high-precision data.....	25
1.3.2.	Constraints from direct searches.....	26
1.4.	Theoretical constraints on the Higgs boson mass.....	30
1.4.1.	Constraints from unitarity.....	30
1.4.2.	Constraints from perturbativity in processes involving the Higgs boson.....	32
1.4.3.	Triviality and stability bounds.....	33
1.4.4.	The fine-tuning constraint.....	36
2.	Decays of the SM Higgs boson.....	38
2.1.	Decays to quarks and leptons.....	39
2.1.1.	The Born approximation.....	39
2.1.2.	Decays into light quarks and QCD corrections.....	40
2.1.3.	The case of the top quark.....	41
2.1.4.	Distinction between scalar and pseudoscalar Higgs bosons.....	43
2.2.	Decays into electroweak gauge bosons.....	46
2.2.1.	Two-body decays.....	46
2.2.2.	Three-body decays.....	46
2.2.3.	Four-body decays.....	47
2.2.4.	CP-properties and comparison with the CP-odd case.....	47
2.3.	Loop induced decays into $\gamma\gamma$ , $\gamma Z$ and $gg$ .....	49
2.3.1.	Decays into two photons.....	51
2.3.2.	Decays into a photon and a Z boson.....	54
2.3.3.	Decays into gluons.....	55
2.4.	The electroweak corrections and QCD improvements.....	57
2.4.1.	The low-energy theorem.....	58
2.4.2.	EW corrections to decays into fermions and massive gauge bosons.....	59
2.4.3.	NNLO QCD and EW corrections to the loop induced decays.....	62
2.4.4.	Summary of the corrections to hadronic Higgs decays.....	65
2.5.	The total decay width and the Higgs branching ratios.....	66
3.	Higgs production at hadron colliders.....	69
3.1.	Higgs bosons at hadron machines.....	69
3.1.1.	Generalities about hadron colliders.....	69
3.1.2.	Higgs production at hadron machines.....	70
3.1.3.	The higher-order corrections and the $K$ -factors.....	71
3.1.4.	The scale dependence.....	72
3.1.5.	The parton distribution functions.....	73
3.2.	The associated production with W/Z bosons.....	74
3.2.1.	The differential and total cross sections at LO.....	74
3.2.2.	The QCD radiative corrections.....	76

3.2.3.	The electroweak radiative corrections.....	79
3.2.4.	The total cross section and the PDF uncertainties .....	80
3.3.	The vector boson fusion processes .....	81
3.3.1.	The differential and total cross sections at LO .....	81
3.3.2.	The cross section at NLO .....	84
3.3.3.	Kinematics of the process .....	85
3.3.4.	Dependence on the scale and on the PDFs at NLO.....	88
3.3.5.	The effective longitudinal vector boson approximation.....	89
3.4.	The gluon–gluon fusion mechanism .....	91
3.4.1.	The production cross section at LO.....	91
3.4.2.	The cross section at NLO .....	93
3.4.3.	The cross section beyond NLO in the heavy top quark limit.....	96
3.4.4.	The distributions and Higgs + n jet production .....	100
3.5.	Associated Higgs production with heavy quarks .....	103
3.5.1.	The cross sections at the tree level .....	103
3.5.2.	The ttH cross section at NLO .....	105
3.5.3.	The case of the bbH process.....	108
3.5.4.	Associated Higgs production with a single top quark .....	109
3.6.	The higher-order processes.....	111
3.6.1.	Higgs boson pair production .....	111
3.6.2.	Higgs production in association with gauge bosons.....	114
3.6.3.	More on higher-order processes.....	116
3.6.4.	Diffraction Higgs boson production .....	117
3.7.	Detecting and studying the Higgs boson .....	119
3.7.1.	Summary of the production cross sections .....	119
3.7.2.	Higgs signals and backgrounds at the Tevatron and the LHC.....	121
3.7.3.	Discovery expectations at the Tevatron and the LHC.....	126
3.7.4.	Determination of the Higgs properties at the LHC .....	128
3.7.5.	Higher luminosities and higher energies .....	133
4.	Higgs production at lepton colliders .....	135
4.1.	Lepton colliders and the physics of the Higgs boson.....	135
4.1.1.	Generalities about $e^+e^-$ colliders .....	135
4.1.2.	The photon colliders .....	136
4.1.3.	Future muon colliders .....	139
4.1.4.	Higgs production processes in lepton collisions.....	140
4.2.	The dominant production processes in $e^+e^-$ collisions .....	141
4.2.1.	The Higgs–strahlung mechanism.....	141
4.2.2.	The WW fusion process .....	145
4.2.3.	The electroweak radiative corrections.....	147
4.3.	The subleading production processes in $e^+e^-$ collisions .....	149
4.3.1.	The ZZ fusion mechanism .....	149
4.3.2.	Associated production with heavy fermion pairs.....	152
4.3.3.	Higgs boson pair production .....	155
4.3.4.	Other subleading processes in $e^+e^-$ collisions.....	158
4.4.	Higgs studies in $e^+e^-$ collisions.....	161
4.4.1.	Higgs boson signals .....	162
4.4.2.	Precision measurements for a light Higgs boson.....	166
4.4.3.	Combined measurements and the determination of the couplings .....	173
4.4.4.	Measurements at higher and lower energies .....	174
4.5.	Higgs production in $\gamma\gamma$ collisions.....	177
4.5.1.	Higgs boson production as an $s$ -channel resonance .....	177
4.5.2.	Measuring the CP-properties of the Higgs boson .....	181
4.5.3.	Other Higgs production mechanisms.....	184
4.6.	Higgs production at muon colliders .....	186
4.6.1.	Higgs production in the $s$ -channel .....	186
4.6.2.	Determination of the properties of a light Higgs boson.....	189

4.6.3. Study of the CP-properties of the Higgs boson .....	193
5. Summary .....	194
Acknowledgments .....	196
References .....	196

## 0. Preamble

### 0.1. A short praise of the Standard Model

The end of the last millennium witnessed the triumph of the Standard Model (SM) of the electroweak and strong interactions of elementary particles [1,2]. The electroweak theory, proposed by Glashow, Salam and Weinberg [1] to describe the electromagnetic [3] and weak [4] interactions between quarks and leptons, is based on the gauge symmetry group  $SU(2)_L \times U(1)_Y$  of weak left-handed isospin and hypercharge. Combined with Quantum Chromodynamics (QCD) [2], the theory of the strong interactions between the colored quarks based on the symmetry group  $SU(3)_C$ , the model provides a unified framework to describe these three forces of Nature. The theory is perturbative at sufficiently high energies [2] and renormalizable [5], and thus describes these interactions at the quantum level.

A cornerstone of the SM is the mechanism of spontaneous electroweak symmetry breaking (EWSB) proposed forty years ago by Higgs, Brout, Englert, Guralnik, Hagen and Kibble [6] to generate the weak vector boson masses in a way that is minimal and, as was shown later, respects the requirements of renormalizability [5] and unitarity [7]. An  $SU(2)$  doublet of complex scalar fields is introduced and its neutral component develops a non-zero vacuum expectation value. As a consequence, the electroweak  $SU(2)_L \times U(1)_Y$  symmetry is spontaneously broken to the electromagnetic  $U(1)_Q$  symmetry. Three of the four degrees of freedom of the doublet scalar field are absorbed by the  $W^\pm$  and  $Z$  weak vector bosons to form their longitudinal polarizations and to acquire masses. The fermion masses are generated through a Yukawa interaction with the same scalar field and its conjugate field. The remaining degree of freedom corresponds to a scalar particle, the Higgs boson. The discovery of this new type of matter particle is unanimously considered to be of profound importance.

The high-precision measurements of the last decade [8,9] carried out at LEP, SLC, Tevatron and elsewhere have provided a decisive test of the Standard Model and firmly established that it provides the correct effective description of the strong and electroweak interactions at the present energies. These tests, performed at the per mille level accuracy, have probed the quantum corrections and the structure of the  $SU(3)_C \times SU(2)_L \times U(1)_Y$  local symmetry. The couplings of quarks and leptons to the electroweak gauge bosons have been measured precisely and agree with those predicted by the model. The trilinear couplings among electroweak vector bosons have also been measured and agree with those dictated by the  $SU(2)_L \times U(1)_Y$  gauge symmetry. The  $SU(3)_C$  gauge symmetric description of the strong interactions has also been thoroughly tested at LEP and elsewhere. The only sector of the model which has not yet been probed in a satisfactory way is the scalar sector. The missing and most important ingredient of the model, the Higgs particle, has not been observed [9,10] and only indirect constraints on its mass have been inferred from the high-precision data [8].

### 0.2. Probing electroweak symmetry breaking: A brief survey of recent developments

The SM of the electroweak interactions, including the EWSB mechanism for generating particle masses, had been proposed in the mid-sixties; however, it was only in the mid-seventies, most probably after the proof by 't Hooft and Veltman that it developed into a renormalizable theory [5] and the discovery of the weak neutral current in the Gargamelle experiment [11], that all its facets began to be investigated thoroughly. After the discovery of the  $W^\pm$  and  $Z$  bosons at CERN [12], probing the electroweak symmetry breaking mechanism became a dominant theme of elementary particle physics. The relic of this mechanism, the Higgs particle, became the Holy Grail of high-energy collider physics and *l'objet de tous nos desirs*. Finding this particle and studying its fundamental properties will be the major goal of the next generation of high-energy machines [and of the upgraded Tevatron, if enough luminosity is collected]: the CERN Large Hadron Collider (LHC), which will start operation in a few years, and the next high-energy and high-luminosity electron–positron linear collider, which hopefully will allow very detailed studies of the EWSB mechanism in a decade.



In the seventies and eighties, an impressive amount of theoretical knowledge was amassed on EWSB and on the expected properties of the Higgs boson(s), both within the framework of the SM and of its [supersymmetric and non-supersymmetric] extensions. At the end of the eighties, the basic properties of the Higgs particles had been discussed and their principal decay modes and main production mechanisms at hadron and lepton colliders explored. This monumental endeavor was nicely and extensively reviewed in a celebrated book, *The Higgs Hunter's Guide* [13] by Gunion, Haber, Kane and Dawson. The constraints from the experimental data available at that time and the prospects for discovering the Higgs particle(s) at the upcoming high-energy experiments, the LEP, the SLC, the late SSC and the LHC, as well as possible higher-energy  $e^+e^-$  colliders, were analyzed and summarized. The review indeed guided theoretical and phenomenological studies as well as experimental searches performed over the last fifteen years.

Meanwhile, several major developments took place. The LEP experiment, for which the search for the Higgs boson was a central objective, was completed with mixed results. On the one hand, LEP played a key role in establishing the SM as the effective theory of the strong and electroweak forces at presently accessible energies. On the other hand, it unfortunately failed to find the Higgs particle or any other new particle which could play a similar role. Nevertheless, this negative search led to a very strong limit on the mass of the SM-like Higgs boson,  $M_H \gtrsim 114.4$  GeV [10]. This unambiguously ruled out a broad low Higgs mass region, and in particular the range  $M_H \lesssim 5$  GeV, which was rather difficult to explore<sup>1</sup> before the advent of LEP1 and its very clean experimental environment. The mass range  $M_H \lesssim 100$  GeV would have been extremely difficult to probe at very high-energy hadron colliders such as the LHC. At approximately the same period, the top quark was at last discovered at the Tevatron [14]. The determination of its mass entailed that all the parameters of the Standard Model, except the Higgs boson mass, were then known,<sup>2</sup> implying that the profile of the Higgs boson will be uniquely determined once its mass is fixed.

Other major developments occurred in the planning and design of the high-energy colliders. The project of the Superconducting Super Collider has been unfortunately terminated and the energy and luminosity parameters of the LHC became firmly established.<sup>3</sup> Furthermore, the option of upgrading the Tevatron by raising the c.m. energy and, more importantly, the luminosity to a value which allows for Higgs searches in the mass range  $M_H \lesssim 2M_Z$  was not yet considered. In addition, the path toward future high-energy electron–positron colliders became more precise. The feasibility of the next generation machines, that is,  $e^+e^-$  linear colliders operating in the energy range from  $M_Z$  up to 1 TeV with very high luminosities has been demonstrated [as in the case of the TESLA machine] and a consensus on the technology of the future International Linear Collider (ILC) has recently emerged. The designs for the next generation machines running at energies in the multi-TeV range [such as the CLIC machine at CERN] also made rapid developments. Added to this, the option of turning future linear colliders into high-energy and high-luminosity  $\gamma\gamma$  colliders by using Compton back-scattering of laser light off the high-energy electron beams and the possibility of high-energy muon colliders have been seriously discussed only in the last decade.

In parallel to these experimental and technological developments, a huge amount of effort has been devoted to the detailed study of the decay and production properties of the Higgs particle at these colliders. On the theoretical side, advances in computer technology allowed one to perform almost automatically very complicated calculations for loop diagrams and multi-particle processes and enabled extremely precise predictions. In particular, the next-to-leading-order radiative corrections to Higgs production in all the important processes at hadron and  $e^+e^-$  colliders were calculated.<sup>4</sup> The radiative corrections to the cross sections for some production processes, such as Higgs–strahlung

<sup>1</sup> This is mainly due to the hadronic uncertainties which occur for such a small Higgs mass. Almost an entire chapter of Ref. [13] was devoted to this mass range; see pp. 32–56 and 94–129.

<sup>2</sup> Another important outcome is due to the heaviness of the top quark [15]: the search of the Higgs boson would have been extremely more difficult at hadron colliders if the top quark mass were smaller than  $M_W$ , a possibility for which many analyses were devoted in the past and which is now ruled out. As a by-product of the large  $m_t$  value, the cross sections for some Higgs production channels at both hadron and  $e^+e^-$  machines became rather large, thus increasing the chances for the discovery and/or study of the particle.

<sup>3</sup> The SSC was a project for a hadron machine with a center of mass energy of  $\sqrt{s} = 40$  TeV and a yearly integrated luminosity of  $10 \text{ fb}^{-1}$  on which most of the emphasis for Higgs searches at hadron colliders was put in Ref. [13]. Of course these studies can be and actually have been adapted to the case of the LHC. Note that in the late eighties, the c.m. energy and the luminosity of the LHC were expected to be  $\sqrt{s} = 17$  TeV and  $\mathcal{L} = 10^{33} \text{ cm}^{-2} \text{ s}^{-1}$ , respectively, and the discovery range for the SM Higgs boson was considered to be rather limited,  $2M_W \lesssim M_H \lesssim 300$  GeV [13].

<sup>4</sup> This started in the very late eighties and early nineties, when the one-loop QCD corrections to associated Higgs production with  $W/Z$  bosons and the  $WW/ZZ$  and gluon–gluon fusion mechanisms at hadron colliders and the electroweak corrections to the Higgs–strahlung production mechanism at  $e^+e^-$  colliders have been derived, and continued until very recently when the QCD corrections to associated Higgs production with heavy quarks at hadron colliders and the electroweak corrections to all the remaining important Higgs production processes at lepton colliders have been completed.

and gluon–gluon fusion at hadron colliders, have been calculated up to next-to-next-to-leading-order accuracy for the strong interaction part and at next-to-leading order for the electroweak part, a development which occurred only over the last few years. A vast literature on the higher-order effects in Higgs boson decays has also appeared in the last fifteen years and some decay modes have been also investigated to next-to-next-to-leading-order accuracy and, in some cases, even beyond. Moreover, thorough theoretical studies of the various distributions in Higgs production and decays and new techniques for the determination of the fundamental properties of the Higgs particle [a vast subject which was only very briefly touched upon in Ref. [13] for instance] have been recently carried out.

Finally, a plethora of analyses of the various Higgs signals and backgrounds, many detailed parton-level analyses and Monte Carlo simulations taking into account the experimental environment [which is now more or less established, at least for the Tevatron and the LHC and possibly for the first stage of the  $e^+e^-$  linear collider, the ILC] have been performed to assess to what extent the Higgs particle can be observed and its properties studied in given processes at the various machines.

### 0.3. Objectives and limitations of the review

On the experimental front, with the LEP experiment completed, we await the accumulation of sufficient data from the upgraded Tevatron and the launch of the LHC which will start operation in 2007. At this point, we believe that it is useful to collect and summarize the large amount of work carried out over the last fifteen years in preparation for the challenges ahead. This review is an attempt to respond to this need. The review is structured in three parts. In this first part, we will concentrate on the Higgs boson of the Standard Model, summarize the present experimental and theoretical information on the Higgs sector, analyze the decay modes of the Higgs bosons including all the relevant and important higher-order effects, and discuss the production properties of the Higgs boson and its detection strategies at the various hadron and lepton machines presently under discussion. We will try to be as extensive and comprehensive as possible.

However, because the subject is vast and the number of studies related to it is huge,<sup>5</sup> it is almost an impossible task to review all its aspects. In addition, one needs to cover many different topics and each of them could have [and, actually, often does have] its own review. Therefore, in many instances, one will have to face different [sometimes Cornelian] choices. The ones made in this review will be, of course, largely determined by the taste of the author, his specialization and his own prejudice. I therefore apologize in advance if some important aspects are overlooked and/or some injustice to possibly relevant analyses is made. Complementary material on the foundations of the SM and the Higgs mechanism, which will only be briefly sketched here, can be found in standard textbooks [17] or in general reviews [18,19] and an account of the various calculations, theoretical studies and phenomenological analyses mentioned above can be found in many specialized reviews; see Refs. [20–24] for some examples. For the physics of the Higgs particle at the various colliders, in particular for the discussion of the Higgs signals and their respective backgrounds, as well as for the detection techniques, we will simply summarize the progress so far. For this very important issue, we refer for additional and more detailed information to specialized reviews and, above all, to the proceedings which describe the huge collective efforts at the various workshops devoted to the subject. Many of these studies and reviews will be referenced in due time.

### 0.4. Synopsis of the review

The first part of this review (Tome I) on the electroweak symmetry breaking mechanism is exclusively devoted to the SM Higgs particle. The discussion of the Higgs sector of the Minimal Supersymmetric extension of the SM is given in an accompanying report [25]. In our view, the SM incorporates an elementary Higgs boson with a mass below 1 TeV and, thus, the very heavy or the no-Higgs scenarios will not be discussed here.

The first chapter is devoted to the description of the Higgs sector of the SM. After briefly recalling the basic ingredients of the model and its input parameters, including an introduction to the electroweak symmetry breaking mechanism and to the basic properties of the Higgs boson, we discuss the high-precision tests of the SM and introduce

<sup>5</sup> Simply by typing “find title Higgs” in the search field of the Spire database, one obtains more than 6.700 entries. Since this number does not include all the articles dealing with the EWSB mechanism and not explicitly mentioning the name of Prof. Higgs in the title, the total number of articles written on the EWSB mechanism in the SM and its various extensions may, thus, well exceed the level of 10.000.

the formalism which allows a description of the radiative corrections which involve the contribution of the only unknown parameter of the theory, the Higgs boson mass  $M_H$  or, alternatively, its self-coupling. This formalism will be needed when we discuss the radiative corrections to Higgs decay and production modes. We then summarize the indirect experimental constraints on  $M_H$  from the high-precision measurements and the constraints derived from direct Higgs searches at past and present colliders. We close this chapter by discussing some interesting constraints on the Higgs mass that can be derived from theoretical considerations on the energy range in which the SM is valid before perturbation theory breaks down and new phenomena emerge. The bounds on  $M_H$  from unitarity in scattering amplitudes, perturbativity of the Higgs self-coupling, stability of the electroweak vacuum and fine tuning in the radiative corrections in the Higgs sector, are analyzed.

In the second chapter, we explore the decays of the SM Higgs particle. We consider all decay modes which lead to potentially observable branching fractions: decays into quarks and leptons, decays into weak massive vector bosons and loop induced decays into gluons and photons. We discuss not only the dominant two-body decays, but also higher-order decays, which can be very important in some cases. We pay particular attention to the radiative corrections and, especially, to the next-to-leading-order QCD corrections to the hadronic Higgs decays which turn out to be quite large. The higher-order QCD corrections [beyond NLO] and the important electroweak radiative corrections to all decay modes are briefly summarized. The expected branching ratios of the Higgs particle, including the uncertainties which affect them, are given. Whenever possible, we compare the various decay properties of the SM Higgs boson, with its distinctive spin and parity  $J^{PC} = 0^{++}$  quantum numbers, to those of hypothetical pseudoscalar Higgs bosons with  $J^{PC} = 0^{+-}$  which are predicted in many extensions of the SM Higgs sector. This will highlight the unique prediction for the properties of the SM Higgs particle [the more general case of anomalous Higgs couplings will be discussed in the third part of this review].

The third chapter is devoted to the production of the Higgs particle at hadron machines. We consider both the  $p\bar{p}$  Tevatron collider with a center of mass energy of  $\sqrt{s} = 1.96$  TeV and the  $pp$  Large Hadron Collider (LHC) with a center of mass energy of  $\sqrt{s} = 14$  TeV. All the dominant production processes, namely the associated production with  $W/Z$  bosons, the weak vector boson fusion processes, the gluon–gluon fusion mechanism and the associated Higgs production with heavy top and bottom quarks, are discussed in detail. In particular, we analyze not only the total production cross sections, but also the differential distributions and we pay special attention to three important aspects: the QCD radiative corrections or the  $K$ -factors [and the electroweak corrections when important] which are large in many cases, their dependence on the renormalization and factorization scales which measures the reliability of the theoretical predictions, and the choices of different sets of parton distribution functions. We also discuss other production processes such as Higgs pair production, production with a single top quark, production in association with two gauge bosons or with one gauge boson and two quarks as well as diffractive Higgs production. These channels are not considered as Higgs discovery modes, but they might provide additional interesting information. We then summarize the main Higgs signals in the various detection channels at the Tevatron and the LHC and the expectations for observing them experimentally. At the end of this chapter, we briefly discuss the possible ways of determining some of the properties of the Higgs particle at the LHC: its mass and total decay width, its spin and parity quantum numbers and its couplings to fermions and gauge bosons. A brief summary of the benefits that one can expect from raising the luminosity and energy of hadron colliders (the so-called SLHC and VLHC options) is given.

In the fourth chapter, we explore the production of the SM Higgs boson at future lepton colliders. We mostly focus on future  $e^+e^-$  colliders in the energy range  $\sqrt{s} = 350$ – $1000$  GeV as planned for the ILC but we also discuss the physics of EWSB at multi-TeV machines [such as CLIC] or by revisiting the  $Z$  boson pole [the GigaZ option], as well as at the  $\gamma\gamma$  option of the linear collider and at future muon colliders. In the case of  $e^+e^-$  machines, we analyze in detail the main production mechanisms, the Higgs–strahlung and the  $WW$  boson fusion processes, as well as some “subleading” but extremely important processes for determining the profile of the Higgs boson such as associated production with top quark pairs and Higgs pair production. Since  $e^+e^-$  colliders are known to be high-precision machines, the theoretical predictions need to be rather accurate and we summarize the work done on the radiative corrections to these processes [which have been completed only recently] and to various distributions which allows one to test the fundamental nature of the Higgs particle. The expectation for Higgs production at the various possible center of mass energies and the potential of these machines to probe the electroweak symmetry breaking mechanism in all its facets and to check the SM predictions for the fundamental Higgs properties such as the total width, the spin and parity quantum numbers, the couplings to the other SM particles [in particular, the important coupling to the top quark] and the Higgs self-coupling [which allows the reconstruction of the scalar potential which generates

EWSB] are summarized. Higgs production at  $\gamma\gamma$  and at muon colliders are discussed in the two last sections, with some emphasis on two points which are rather difficult to explore in  $e^+e^-$  collisions, namely, the determination of the Higgs spin–parity quantum numbers and the total decay width.

Since the primary goal of this review is to provide the necessary material to discuss Higgs decays and production at present and future colliders, we present the analytical expressions of the partial decay widths, the production cross sections and some important distributions, including the higher-order corrections or effects, when they are simple enough to be displayed. We analyze in detail the main Higgs decay and production channels and also discuss some channels which are not yet established but which can be useful and with further effort might prove to be experimentally accessible. We also present summary and updated plots as well as illustrative numerical examples [which can be used as a normalization in future phenomenological and experimental studies] for the total Higgs decay width and branching ratios, as well as for the cross sections of the main production mechanisms at the Tevatron, the LHC and future  $e^+e^-$  colliders at various center of mass energies. In these updated analyses, we have endeavored to include all currently available information. For collider Higgs phenomenology, in particular for the discussion of the Higgs signals and backgrounds, we simply summarize, as previously mentioned, the main points and refer to the literature for additional details and complementary discussions.

## 1. The Higgs particle in the SM

### 1.1. The SM of the strong and electroweak interactions

In this section, we present a brief introduction to the Standard Model of the strong and electroweak interactions and to the mechanism of electroweak symmetry breaking. This will allow us to set the stage and to fix the notation which will be used later on. For more detailed discussions, we refer the reader to standard textbooks [17] or reviews [18].

#### 1.1.1. The SM before electroweak symmetry breaking

As discussed in the preamble, the Glashow–Weinberg–Salam electroweak theory [1] which describes the electromagnetic and weak interactions between quarks and leptons, is a Yang–Mills theory [26] based on the symmetry group  $SU(2)_L \times U(1)_Y$ . Combined with the  $SU(3)_C$  based QCD gauge theory [2] which describes the strong interactions between quarks, it provides a unified framework to describe these three forces of Nature: the Standard Model (SM).<sup>6</sup> The model, before introducing the electroweak symmetry breaking mechanism to be discussed later, has two kinds of fields.

• There are first the matter fields, that is, the three generations of left-handed and right-handed chiral quarks and leptons,  $f_{L,R} = \frac{1}{2}(1 \mp \gamma_5)f$ . The left-handed fermions are in weak isodoublets, while the right-handed fermions are in weak isosinglets<sup>7</sup>

$$\begin{aligned}
 L_1 &= \begin{pmatrix} \nu_e \\ e^- \end{pmatrix}_L, & e_{R1} &= e_R^-, & Q_1 &= \begin{pmatrix} u \\ d \end{pmatrix}_L, & u_{R1} &= u_R, d_{R1} = d_R \\
 I_f^{3L,3R} &= \pm \frac{1}{2}, 0 : & L_2 &= \begin{pmatrix} \nu_\mu \\ \mu^- \end{pmatrix}_L, & e_{R2} &= \mu_R^-, & Q_2 &= \begin{pmatrix} c \\ s \end{pmatrix}_L, & u_{R2} &= c_R, d_{R2} = s_R \\
 & & L_3 &= \begin{pmatrix} \nu_\tau \\ \tau^- \end{pmatrix}_L, & e_{R3} &= \tau_R^-, & Q_3 &= \begin{pmatrix} t \\ b \end{pmatrix}_L, & u_{R3} &= t_R, d_{R3} = b_R.
 \end{aligned} \tag{1.1}$$

The fermion hypercharge, defined in terms of the third component of the weak isospin  $I_f^3$  and the electric charge  $Q_f$  in units of the proton charge  $+e$ , is given by ( $i = 1, 2, 3$ )

$$Y_f = 2Q_f - 2I_f^3 \Rightarrow Y_{L_i} = -1, \quad Y_{e_{R_i}} = -2, \quad Y_{Q_i} = \frac{1}{3}, \quad Y_{u_{R_i}} = \frac{4}{3}, \quad Y_{d_{R_i}} = -\frac{2}{3}. \tag{1.2}$$

<sup>6</sup> Very often, the electroweak sector of the theory is also referred to as the SM; in this review we will use this name for both options.

<sup>7</sup> Throughout this review, we will assume that the neutrinos, which do not play any role here, are massless and appear only with their left-handed components.

Moreover, the quarks are triplets under the  $SU(3)_C$  group, while leptons are color singlets. This leads to the relation

$$\sum_f Y_f = \sum_f Q_f = 0 \quad (1.3)$$

which ensures the cancellation of chiral anomalies [27] within each generation, thus, preserving [28] the renormalizability of the electroweak theory [5].

• Then, there are the gauge fields corresponding to the spin-one bosons that mediate the interactions. In the electroweak sector, we have the field  $B_\mu$  which corresponds to the generator  $Y$  of the  $U(1)_Y$  group and the three fields  $W_\mu^{1,2,3}$  which correspond to the generators  $T^a$  [with  $a = 1, 2, 3$ ] of the  $SU(2)_L$  group; these generators are in fact equivalent to half of the non-commuting  $2 \times 2$  Pauli matrices

$$T^a = \frac{1}{2}\tau^a; \quad \tau_1 = \begin{pmatrix} 0 & 1 \\ 1 & 0 \end{pmatrix}, \quad \tau_2 = \begin{pmatrix} 0 & -i \\ i & 0 \end{pmatrix}, \quad \tau_3 = \begin{pmatrix} 1 & 0 \\ 0 & -1 \end{pmatrix} \quad (1.4)$$

with the commutation relations between these generators given by

$$[T^a, T^b] = i\epsilon^{abc}T_c \quad \text{and} \quad [Y, Y] = 0 \quad (1.5)$$

where  $\epsilon^{abc}$  is the antisymmetric tensor. In the strong interaction sector, there is an octet of gluon fields  $G_\mu^{1,\dots,8}$  which correspond to the eight generators of the  $SU(3)_C$  group [equivalent to half of the eight  $3 \times 3$  anticommuting Gell-Mann matrices] and which obey the relations

$$[T^a, T^b] = if^{abc}T_c \quad \text{with} \quad \text{Tr}[T^a T^b] = \frac{1}{2}\delta_{ab} \quad (1.6)$$

where the tensor  $f^{abc}$  is for the structure constants of the  $SU(3)_C$  group and where we have used the same notation as for the generators of  $SU(2)$ . The field strengths are given by

$$\begin{aligned} G_{\mu\nu}^a &= \partial_\mu G_\nu^a - \partial_\nu G_\mu^a + g_s f^{abc} G_\mu^b G_\nu^c \\ W_{\mu\nu}^a &= \partial_\mu W_\nu^a - \partial_\nu W_\mu^a + g_2 \epsilon^{abc} W_\mu^b W_\nu^c \\ B_{\mu\nu} &= \partial_\mu B_\nu - \partial_\nu B_\mu \end{aligned} \quad (1.7)$$

where  $g_s$ ,  $g_2$  and  $g_1$  are, respectively, the coupling constants of  $SU(3)_C$ ,  $SU(2)_L$  and  $U(1)_Y$ . Because of the non-abelian nature of the  $SU(2)$  and  $SU(3)$  groups, there are self-interactions between their gauge fields,  $V_\mu \equiv W_\mu$  or  $G_\mu$ , leading to triple and quartic gauge boson couplings. The matter fields  $\psi$  are minimally coupled to the gauge fields through the covariant derivative  $D_\mu$  which, in the case of quarks, is defined as

$$D_\mu \psi = \left( \partial_\mu - ig_s T_a G_\mu^a - ig_2 T_a W_\mu^a - ig_1 \frac{Y_q}{2} B_\mu \right) \psi \quad (1.8)$$

leading to unique couplings between fermion and gauge fields of the form  $g_i \bar{\psi} V_\mu \gamma^\mu \psi$ .

The SM Lagrangian, without mass terms for fermions and gauge bosons is then given by

$$\begin{aligned} \mathcal{L}_{\text{SM}} &= -\frac{1}{4} G_{\mu\nu}^a G_a^{\mu\nu} - \frac{1}{4} W_{\mu\nu}^a W_a^{\mu\nu} - \frac{1}{4} B_{\mu\nu} B^{\mu\nu} \\ &\quad + \bar{L}_i i D_\mu \gamma^\mu L_i + \bar{e}_{Ri} i D_\mu \gamma^\mu e_{Ri} + \bar{Q}_i i D_\mu \gamma^\mu Q_i + \bar{u}_{Ri} i D_\mu \gamma^\mu u_{Ri} + \bar{d}_{Ri} i D_\mu \gamma^\mu d_{Ri}. \end{aligned} \quad (1.9)$$

This Lagrangian is invariant under local  $SU(3)_C \times SU(2)_L \times U(1)_Y$  gauge transformations for fermion and gauge fields. In the case of the electroweak sector, for instance, one has

$$\begin{aligned} L(x) &\rightarrow L'(x) = e^{i\alpha_a(x)T^a + i\beta(x)Y} L(x), & R(x) &\rightarrow R'(x) = e^{i\beta(x)Y} R(x) \\ \vec{W}_\mu(x) &\rightarrow \vec{W}_\mu(x) - \frac{1}{g_2} \partial_\mu \vec{\alpha}(x) - \vec{\alpha}(x) \times \vec{W}_\mu(x), & B_\mu(x) &\rightarrow B_\mu(x) - \frac{1}{g_1} \partial_\mu \beta(x). \end{aligned} \quad (1.10)$$

Up until now, the gauge fields and the fermion fields have been kept massless. In the case of strong interactions, the gluons are indeed massless particles while mass terms of the form  $-m_q \bar{\psi} \psi$  can be generated for the colored quarks

[and for the leptons] in an SU(3) gauge invariant way. In the case of the electroweak sector, the situation is more problematic:

– If we add mass terms,  $\frac{1}{2}M_V^2 W_\mu W^\mu$ , for the gauge bosons [since experimentally, they have been proved to be massive, the weak interaction being of short distance], this will violate local SU(2)  $\times$  U(1) gauge invariance. This statement can be visualized by taking the example of QED where the photon is massless because of the U(1)<sub>Q</sub> local symmetry

$$\frac{1}{2}M_A^2 A_\mu A^\mu \rightarrow \frac{1}{2}M_A^2 \left( A_\mu - \frac{1}{e}\partial_\mu \alpha \right) \left( A^\mu - \frac{1}{e}\partial^\mu \alpha \right) \neq \frac{1}{2}M_A^2 A_\mu A^\mu. \quad (1.11)$$

– In addition, if we include explicitly a mass term  $-m_f \bar{\psi}_f \psi_f$  for each SM fermion  $f$  in the Lagrangian, we would have for the electron for instance

$$-m_e \bar{e}e = -m_e \bar{e} \left( \frac{1}{2}(1 - \gamma_5) + \frac{1}{2}(1 + \gamma_5) \right) e = -m_e (\bar{e}_R e_L + \bar{e}_L e_R) \quad (1.12)$$

which is manifestly non-invariant under the isospin symmetry transformations discussed above, since  $e_L$  is a member of an SU(2)<sub>L</sub> doublet while  $e_R$  is a member of a singlet.

Thus, the incorporation by brute force of mass terms for gauge bosons and for fermions leads to a manifest breakdown of the local SU(2)<sub>L</sub>  $\times$  U(1)<sub>Y</sub> gauge invariance. Therefore, apparently, either we have to give up the fact that  $M_Z \sim 90$  GeV and  $m_e \sim 0.5$  MeV for instance, or give up the principle of exact or unbroken gauge symmetry.

The question, which has been asked already in the sixties, is therefore the following: is there a [possibly nice] way to generate the gauge boson and the fermion masses without violating SU(2)  $\times$  U(1) gauge invariance? The answer is yes: the Higgs–Brout–Englert–Guralnik–Hagen–Kibble mechanism of spontaneous symmetry breaking [6] or the Higgs mechanism for short. By introducing a scalar field which develops a vacuum expectation value, a massless gauge boson (with two degrees of freedom) will absorb a would-be-Goldstone boson [29] (with one degree of freedom) to acquire a longitudinal component and hence, a mass. For fermions, the masses can also be generated by coupling them to the scalar field in a gauge invariant way.

The Higgs mechanism will be briefly sketched in the following subsection and applied to the SM case; more details can be found in standard textbooks and reviews [17,18].

### 1.1.2. The Higgs mechanism in the SM

In the non-abelian case of the SM, we need to generate masses for the three gauge bosons  $W^\pm$  and  $Z$  but the photon should remain massless and QED must retain an exact symmetry. Therefore, we need at least 3 degrees of freedom for the scalar fields. The simplest choice is a complex SU(2) doublet of scalar fields  $\phi$

$$\Phi = \begin{pmatrix} \phi^+ \\ \phi^0 \end{pmatrix}, \quad Y_\phi = +1. \quad (1.13)$$

To the SM Lagrangian discussed in the previous subsection, but where we ignore the strong interaction part and include for simplicity only the first family

$$\mathcal{L}_{\text{SM}} = -\frac{1}{4}W_{\mu\nu}^a W_a^{\mu\nu} - \frac{1}{4}B_{\mu\nu} B^{\mu\nu} + \bar{L}iD_\mu \gamma^\mu L + \bar{e}_R iD_\mu \gamma^\mu e_R \dots \quad (1.14)$$

we need to add the invariant terms of the scalar field part

$$\mathcal{L}_S = (D^\mu \Phi)^\dagger (D_\mu \Phi) - V(\Phi), \quad V(\Phi) = \mu^2 \Phi^\dagger \Phi + \lambda (\Phi^\dagger \Phi)^2. \quad (1.15)$$

If the mass term  $\mu^2$  is positive, the potential  $V(\Phi)$  is also positive if the self-coupling  $\lambda$  is positive [which is needed to make the potential bounded from below], and the minimum of the potential is obtained for  $\langle 0|\phi|0\rangle \equiv \phi_0 = 0$  as shown in the left-hand side of Fig. 1.1;  $\mathcal{L}$  is then simply the Lagrangian of a spin-zero particle of mass  $\mu$ .



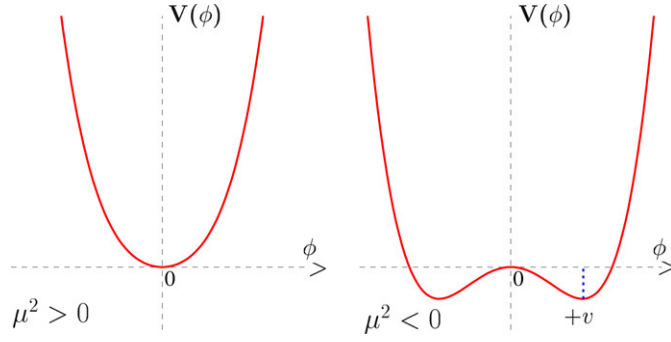


Fig. 1.1. The potential  $V$  of the scalar field  $\phi$  in the case  $\mu^2 > 0$  (left) and  $\mu^2 < 0$  (right).

In turn, for  $\mu^2 < 0$ , the neutral component of the doublet field  $\Phi$  will develop a vacuum expectation value [the vev should not be in the charged direction to preserve  $U(1)_{\text{QED}}$ ]

$$\langle \Phi \rangle_0 \equiv \langle 0 | \Phi | 0 \rangle = \begin{pmatrix} 0 \\ v \\ \sqrt{2} \end{pmatrix} \quad \text{with } v = \left( -\frac{\mu^2}{\lambda} \right)^{1/2}. \quad (1.16)$$

One can then make the following exercise:

- write the field  $\Phi$  in terms of four fields  $\theta_{1,2,3}(x)$  and  $H(x)$  at first order:

$$\Phi(x) = \begin{pmatrix} \theta_2 + i\theta_1 \\ \frac{1}{\sqrt{2}}(v + H) - i\theta_3 \end{pmatrix} = e^{i\theta_a(x)\tau^a(x)/v} \begin{pmatrix} 0 \\ \frac{1}{\sqrt{2}}(v + H(x)) \end{pmatrix} \quad (1.17)$$

- make a gauge transformation on this field to move to the unitary gauge in which only physical particles are left in the Lagrangian

$$\Phi(x) \rightarrow e^{-i\theta_a(x)\tau^a(x)} \Phi(x) = \frac{1}{\sqrt{2}} \begin{pmatrix} 0 \\ v + H(x) \end{pmatrix} \quad (1.18)$$

- then fully expand the term  $|(D_\mu \Phi)|^2$  of the Lagrangian, to obtain  $\mathcal{L}_S$ :

$$|(D_\mu \Phi)|^2 = \frac{1}{2}(\partial_\mu H)^2 + \frac{1}{8}g_2^2(v + H)^2|W_\mu^1 + iW_\mu^2|^2 + \frac{1}{8}(v + H)^2|g_2 W_\mu^3 - g_1 B_\mu|^2$$

- define the new fields  $W_\mu^\pm$  and  $Z_\mu$  [ $A_\mu$  is the field orthogonal to  $Z_\mu$ ]:

$$W^\pm = \frac{1}{\sqrt{2}}(W_\mu^1 \mp iW_\mu^2), \quad Z_\mu = \frac{g_2 W_\mu^3 - g_1 B_\mu}{\sqrt{g_2^2 + g_1^2}}, \quad A_\mu = \frac{g_2 W_\mu^3 + g_1 B_\mu}{\sqrt{g_2^2 + g_1^2}} \quad (1.19)$$

- and pick up the terms which are bilinear in the fields  $W^\pm$ ,  $Z$ ,  $A$ :

$$M_W^2 W_\mu^+ W^{-\mu} + \frac{1}{2}M_Z^2 Z_\mu Z^\mu + \frac{1}{2}M_A^2 A_\mu A^\mu. \quad (1.20)$$

The  $W$  and  $Z$  bosons have acquired masses, while the photon is still massless

$$M_W = \frac{1}{2}vg_2, \quad M_Z = \frac{1}{2}v\sqrt{g_2^2 + g_1^2}, \quad M_A = 0. \quad (1.21)$$

Thus, we have achieved (half of) our goal: by spontaneously breaking the symmetry  $SU(2)_L \times U(1)_Y \rightarrow U(1)_Q$ , three Goldstone bosons have been absorbed by the  $W^\pm$  and  $Z$  bosons to form their longitudinal components and to get their masses. Since the  $U(1)_Q$  symmetry is still unbroken, the photon which is its generator, remains massless as it should be.

In fact, we can also generate the fermion masses using the same scalar field  $\tilde{\Phi}$ , with hypercharge  $Y = 1$ , and the isodoublet  $\tilde{\Phi} = i\tau_2 \Phi^*$ , which has hypercharge  $Y = -1$ . For any fermion generation, we introduce the  $SU(2)_L \times U(1)_Y$  invariant Yukawa Lagrangian

$$\mathcal{L}_F = -\lambda_e \bar{L} \Phi e_R - \lambda_d \bar{Q} \Phi d_R - \lambda_u \bar{Q} \tilde{\Phi} u_R + h.c. \quad (1.22)$$

Taking for instance the case of the electron, one obtains

$$\begin{aligned} \mathcal{L}_F &= -\frac{1}{\sqrt{2}} \lambda_e (\bar{\nu}_e, \bar{e}_L) \begin{pmatrix} 0 \\ v + H \end{pmatrix} e_R + \dots \\ &= -\frac{1}{\sqrt{2}} \lambda_e (v + H) \bar{e}_L e_R + \dots \end{aligned} \quad (1.23)$$

The constant term in front of  $\bar{f}_L f_R$  (and h.c.) is identified with the fermion mass

$$m_e = \frac{\lambda_e v}{\sqrt{2}}, \quad m_u = \frac{\lambda_u v}{\sqrt{2}}, \quad m_d = \frac{\lambda_d v}{\sqrt{2}}. \quad (1.24)$$

Thus, with the same isodoublet  $\Phi$  of scalar fields, we have generated the masses of both the weak vector bosons  $W^\pm$ ,  $Z$  and the fermions, while preserving the  $SU(2) \times U(1)$  gauge symmetry, which is now spontaneously broken or hidden. The electromagnetic  $U(1)_Q$  symmetry, as well as the  $SU(3)$  color symmetry, remains unbroken. The Standard Model refers, in fact, to  $SU(3) \times SU(2) \times U(1)$  gauge invariance when combined with the electroweak symmetry breaking mechanism. Very often, the electroweak sector of the theory is also referred to as the SM; in this review we will use this name for both options.

### 1.1.3. The SM Higgs particle and the Goldstone bosons

Let us now come to the Higgs boson itself. The kinetic part of the Higgs field,  $\frac{1}{2}(\partial_\mu H)^2$ , comes from the term involving the covariant derivative  $|D_\mu \Phi|^2$ , while the mass and self-interaction parts, come from the scalar potential  $V(\Phi) = \mu^2 \Phi^\dagger \Phi + \lambda(\Phi^\dagger \Phi)^2$ . Performing the substitution,  $\Phi = \frac{1}{\sqrt{2}} \begin{pmatrix} 0 \\ v + H \end{pmatrix}$ , and using the relation  $v^2 = -\mu^2/\lambda$ , one finds that the Lagrangian containing the Higgs field  $H$  is given by

$$\mathcal{L}_H = \frac{1}{2}(\partial^\mu H)^2 - \lambda v^2 H^2 - \lambda v H^3 - \frac{\lambda}{4} H^4. \quad (1.25)$$

From this Lagrangian, one can see that the Higgs boson mass simply reads

$$M_H^2 = 2\lambda v^2 = -2\mu^2 \quad (1.26)$$

and the Feynman rules<sup>8</sup> for the Higgs self-interaction vertices are given by

$$g_{H^3} = (3!)i\lambda v = 3i\frac{M_H^2}{v}, \quad g_{H^4} = (4!)i\frac{\lambda}{4} = 3i\frac{M_H^2}{v^2}. \quad (1.27)$$

As for the Higgs boson couplings to gauge bosons and fermions, they were almost derived previously, when the masses of these particles were calculated. Indeed, from the Lagrangian describing the gauge boson and fermion masses

$$\mathcal{L}_{M_V} \sim M_V^2 \left(1 + \frac{H}{v}\right)^2, \quad \mathcal{L}_{m_f} \sim -m_f \left(1 + \frac{H}{v}\right) \quad (1.28)$$

one obtains also the Higgs boson couplings to gauge bosons and fermions

$$g_{Hff} = i\frac{m_f}{v}, \quad g_{HVV} = -2i\frac{M_V^2}{v}, \quad g_{HHVV} = -2i\frac{M_V^2}{v^2}. \quad (1.29)$$

<sup>8</sup> The Feynman rule for these vertices are obtained by multiplying the term involving the interaction by a factor  $i$ . One includes also a factor  $n!$  where  $n$  is the number of identical particles in the vertex.

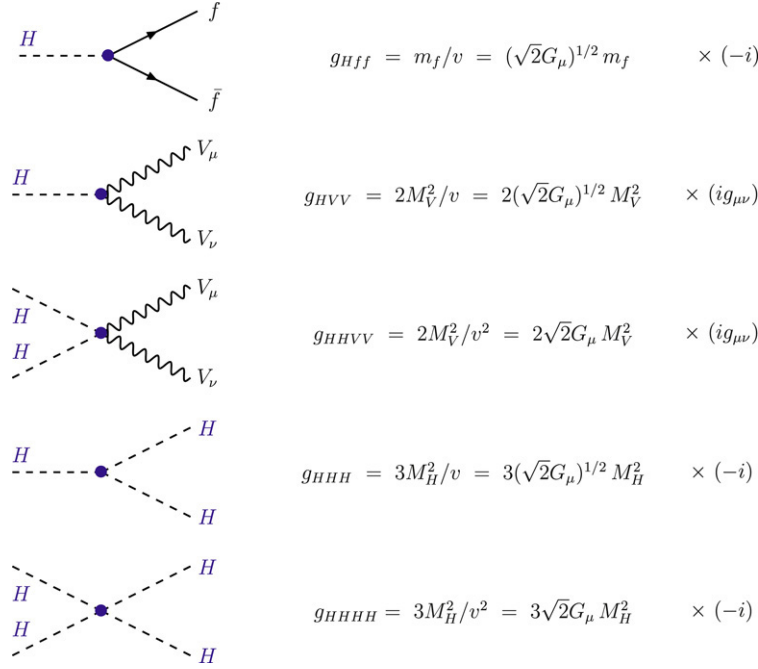


Fig. 1.2. The Higgs boson couplings to fermions and gauge bosons and the Higgs self-couplings in the SM. The normalization factors of the Feynman rules are also displayed.

This form of the Higgs couplings ensures the unitarity of the theory [7] as will be seen later. The vacuum expectation value  $v$  is fixed in terms of the  $W$  boson mass  $M_W$  or the Fermi constant  $G_\mu$  determined from muon decay

$$M_W = \frac{1}{2}g_2v = \left(\frac{\sqrt{2}g^2}{8G_\mu}\right)^{1/2} \Rightarrow v = \frac{1}{(\sqrt{2}G_\mu)^{1/2}} \simeq 246 \text{ GeV}. \quad (1.30)$$

We will see in the course of this review that it will be appropriate to use the Fermi coupling constant  $G_\mu$  to describe the couplings of the Higgs boson, as some higher-order effects are effectively absorbed in this way. The Higgs couplings to fermions, massive gauge bosons as well as the self-couplings, are given in Fig. 1.2 using both  $v$  and  $G_\mu$ . This general form of the couplings will be useful when discussing the Higgs properties in extensions of the SM.

Note that the propagator of the Higgs boson is simply given, in momentum space, by

$$\Delta_{HH}(q^2) = \frac{i}{q^2 - M_H^2 + i\epsilon}. \quad (1.31)$$

Finally, let us make a few comments on the Goldstone bosons. In the unitary gauge, the physical spectrum of the SM is clear: besides the fermions and the massless photon [and gluons], we have the massive  $V = W^\pm$  and  $Z$  bosons and the Goldstones do not appear. The propagators of the vector bosons in this gauge are given by

$$\Delta_{VV}^{\mu\nu}(q) = \frac{-i}{q^2 - M_V^2 + i\epsilon} \left[ g^{\mu\nu} - \frac{q^\mu q^\nu}{M_V^2} \right]. \quad (1.32)$$

The first term,  $\propto g^{\mu\nu}$ , corresponds to the propagation of the transverse component of the  $V$  boson [the propagator of the photon is simply  $-ig^{\mu\nu}/q^2$ ], while the second term,  $\propto q^\mu q^\nu$ , corresponds to the propagation of the longitudinal component which, as can be seen, does not vanish  $\propto 1/q^2$  at high energies. These terms lead to very complicated cancellations in the invariant amplitudes involving the exchange of  $V$  bosons at high energies and, even worse, make the renormalization program very difficult to carry out, as the latter usually makes use of four-momentum power counting analyses of the loop diagrams. It is more convenient to work in  $R_\xi$  gauges where gauge fixing terms are

added to the SM Lagrangian [30]

$$\mathcal{L}_{\text{GF}} = \frac{-1}{2\xi} \left[ 2(\partial^\mu W_\mu^+ - i\xi M_W w^+)(\partial^\mu W_\mu^- - i\xi M_W w^-) + (\partial^\mu Z_\mu - i\xi M_Z w^0)^2 + (\partial^\mu A_\mu)^2 \right] \quad (1.33)$$

$w^0 \equiv G^0$  and  $w^\pm \equiv G^\pm$  being the neutral and charged Goldstone bosons and where different choices of  $\xi$  correspond to different renormalizable gauges. In this case, the propagators of the massive gauge bosons are given by

$$\Delta_{VV}^{\mu\nu}(q) = \frac{-i}{q^2 - M_V^2 + i\epsilon} \left[ g^{\mu\nu} + (\xi - 1) \frac{q^\mu q^\nu}{q^2 - \xi M_V^2} \right] \quad (1.34)$$

which in the unitary gauge,  $\xi = \infty$ , reduces to the expression Eq. (1.32). Usually, one uses the 't Hooft–Feynman gauge  $\xi = 1$ , where the  $q^\mu q^\nu$  term is absent, to simplify the calculations; another popular choice is the Landau gauge,  $\xi = 0$ . In renormalizable  $R_\xi$  gauges, the propagators of the Goldstone bosons are given by

$$\Delta_{w^0/w^\pm w^\pm}(q^2) = \frac{i}{q^2 - \xi M_{Z/W}^2 + i\epsilon} \quad (1.35)$$

and as can be seen, in the unitary gauge  $\xi = \infty$ , the Goldstone bosons do not propagate and decouple from the theory as they should, while in the Landau gauge they are massless and do not interact with the Higgs particle. In the 't Hooft–Feynman gauge, the Goldstone bosons are part of the spectrum and have “masses”  $\propto M_V$ . Any dependence on  $\xi$  should however be absent from physical matrix elements squared, as the theory must be gauge invariant.

Note that the couplings of the Goldstone bosons to fermions are, as in the case of the Higgs boson, proportional to the fermion masses

$$g_{G^0 ff} = -2I_f^3 \frac{m_f}{v}, \quad g_{G^\pm ud} = \frac{-i}{\sqrt{2}v} V_{ud} [m_d(1 - \gamma_5) - m_u(1 + \gamma_5)] \quad (1.36)$$

where  $V_{ud}$  is the CKM matrix element for quarks and which, in the case of leptons [where one has to set  $m_d = m_\ell$  and  $m_u = 0$  in the equation above], is equal to unity. The couplings of the Goldstones to gauge bosons are simply those of scalar spin-zero particles.

The longitudinal components of the  $W$  and  $Z$  bosons give rise to interesting features which occur at high energies and that we shortly describe below. In the gauge boson rest frame, one can define the transverse and longitudinal polarization four vectors as

$$\epsilon_{T_1}^\mu = (0, 1, 0, 0), \quad \epsilon_{T_2}^\mu = (0, 0, 1, 0), \quad \epsilon_L^\mu = (0, 0, 0, 1). \quad (1.37)$$

For a four-momentum  $p^\mu = (E, 0, 0, |\vec{p}|)$ , after a boost along the  $z$  direction, the transverse polarizations remain the same while the longitudinal polarization becomes

$$\epsilon_L^\mu = \left( \frac{|\vec{p}|}{M_V}, 0, 0, \frac{E}{M_V} \right) \xrightarrow{E \gg M_V} \frac{p_\mu}{M_V}. \quad (1.38)$$

Since this polarization is proportional to the gauge boson momentum, at very high energies, the longitudinal amplitudes will dominate in the scattering of gauge bosons.

In fact, there is a theorem, called the Electroweak Equivalence Theorem [31–33], which states that at very high energies, the longitudinal massive vector bosons can be replaced by the Goldstone bosons. In addition, in many processes such as vector boson scattering, the vector bosons themselves can be replaced by their longitudinal components. The amplitude for the scattering of  $n$  gauge bosons in the initial state to  $n'$  gauge bosons in the final state is simply the amplitude for the scattering of the corresponding Goldstone bosons

$$\begin{aligned} A(V^1 \dots V^n \rightarrow V^1 \dots V^{n'}) &\sim A(V_L^1 \dots V_L^n \rightarrow V_L^1 \dots V_L^{n'}) \\ &\sim A(w^1 \dots w^n \rightarrow w^1 \dots w^{n'}). \end{aligned} \quad (1.39)$$

Thus, in this limit, one can simply replace in the SM scalar potential, the  $W$  and  $Z$  bosons by their corresponding Goldstone bosons  $w^\pm$ ,  $w_0$ , leading to

$$V = \frac{M_H^2}{2v}(H^2 + w_0^2 + 2w^+w^-)H + \frac{M_H^2}{8v^2}(H^2 + w_0^2 + 2w^+w^-)^2 \quad (1.40)$$

and use this potential to calculate the amplitudes for the processes involving weak vector bosons. The calculations are then extremely simple, since one has to deal only with interactions among scalar particles.

#### 1.1.4. The SM interactions and parameters

In this subsection, we briefly list the basic parameters of the SM which will be needed in our forthcoming discussions and give their experimental values.

**1.1.4.1. The fine structure constant.** The QED fine structure constant defined in the classical Thomson limit  $q^2 \sim 0$  of Compton scattering, is one of the best measured quantities in Nature,  $\alpha(0) \equiv e^2/(4\pi) \simeq 1/137$ . However, the physics which is studied at present colliders is at scales of the order of 100 GeV and the running between  $q^2 \sim 0$  and this scale must be taken into account. The running  $\Delta\alpha(q^2)$  is defined as the difference between the [transverse components of the] vacuum polarization functions of the photon  $\Pi_{\gamma\gamma}$  at the two scales. Since QED is a vectorial theory, all heavy particles decouple from the photon two-point function [34] and only the light fermions, have to be taken into account in the running.

At the scale  $M_Z$ , the contributions of the  $e$ ,  $\mu$  and  $\tau$  leptons to  $\Delta\alpha$  simply read  $\Delta\alpha^{\text{lept}}(M_Z^2) \simeq 0.0315$  [35]. The contribution of light quarks can be derived via dispersion relations using experimental  $e^+e^- \rightarrow \text{hadrons}$  data in the problematic low-energy range where QCD is non-perturbative and perturbative QCD for the high-energy range [36, 37]. Taking into account all available information, one obtains for the hadronic contribution [37]

$$\Delta\alpha^{\text{had}}(M_Z^2) = 0.02761 \pm 0.00036. \quad (1.41)$$

The latest world average value for the electromagnetic coupling  $\alpha$  at the scale  $M_Z$  is therefore

$$\alpha^{-1}(M_Z^2) = 128.951 \pm 0.027. \quad (1.42)$$

**1.1.4.2. The Fermi coupling constant.** Another quantity in particle physics which is very precisely measured is the muon decay lifetime, which is directly related to the Fermi coupling constant in the effective four-point Fermi interaction [38] and which leads to the precise value

$$G_\mu = (1.16637 \pm 0.00001) \cdot 10^{-5} \text{ GeV}^{-2}. \quad (1.43)$$

In the SM, the decay occurs through gauge interactions mediated by  $W$  boson exchange and therefore, one obtains a relation between the  $W$ ,  $Z$  masses, the QED constant  $\alpha$  and  $G_\mu$

$$\frac{G_\mu}{\sqrt{2}} = \frac{g_2}{2\sqrt{2}} \cdot \frac{1}{M_W^2} \cdot \frac{g_2}{2\sqrt{2}} = \frac{\pi\alpha}{2M_W^2 s_W^2} = \frac{\pi\alpha}{2M_W^2(1 - M_W^2/M_Z^2)}. \quad (1.44)$$

**1.1.4.3. The strong coupling constant.** The strong coupling constant has been precisely determined in various experiments in  $e^+e^-$  collisions; see Refs. [9,39]. The most reliable results have been obtained at LEP and the world average value is given by [9]

$$\alpha_s = 0.1172 \pm 0.002 \quad (1.45)$$

which corresponds to a QCD scale for 5 light flavors  $\Lambda_{\text{QCD}}^5 = 216_{-24}^{+25} \text{ MeV}$ . Using this value of  $\Lambda$ , one can determine  $\alpha_s$  at any energy scale  $\mu$  up to three-loop order in QCD [40]

$$\alpha_s(\mu) = \frac{4\pi}{\beta_0 \ell_\mu} \left[ 1 - \frac{2\beta_1}{\beta_0^2} \frac{\log \ell_\mu}{\ell_\mu} + \frac{4\beta_1^2}{\beta_0^4 \ell_\mu^2} \left( \left( \log \ell_\mu - \frac{1}{2} \right)^2 + \frac{\beta_2 \beta_0}{8\beta_1^2} - \frac{5}{4} \right) \right] \quad (1.46)$$

Table 1.1

The pole quark masses and the mass values in the  $\overline{\text{MS}}$  scheme for the running masses at the scale  $m_Q$  and at a scale  $\mu = 100 \text{ GeV}$ ;  $\alpha_s(M_Z) = 0.1172$

$Q$	$m_Q$	$\overline{m}_Q(m_Q)$	$\overline{m}_Q(100 \text{ GeV})$
$c$	1.64 GeV	1.23 GeV	0.63 GeV
$b$	4.88 GeV	4.25 GeV	2.95 GeV

with  $\ell_\mu \equiv \log(\mu^2/\Lambda^2)$  and the  $\beta_i$  coefficients given by

$$\beta_0 = 11 - \frac{2}{3}N_f, \quad \beta_1 = 51 - \frac{19}{3}N_f, \quad \beta_2 = 2857 - \frac{5033}{9}N_f + \frac{325}{27}N_f^2 \quad (1.47)$$

with  $N_f$  being the number of quarks with a mass smaller than the energy scale  $\mu$ .

**1.1.4.4. The fermion masses.** The top quark has been produced at the Tevatron in the Drell–Yan process  $p\bar{p} \rightarrow t\bar{t}$  [41–46]. Combining CDF and DØ results, the latest average value for the top quark mass is<sup>9</sup> [16]

$$m_t = 171.4 \pm 2.1 \text{ GeV}. \quad (1.48)$$

Besides the top quark mass, the masses of the bottom and charm quarks [and to a lesser extent the mass of the strange quark] are essential ingredients in Higgs physics. From many measurements, one obtains the following values for the pole or physical masses  $m_Q$  [47]

$$m_b = 4.88 \pm 0.07 \text{ GeV}, \quad m_c = 1.64 \pm 0.07 \text{ GeV}. \quad (1.49)$$

However, the masses which are needed in this context are in general not the pole quark masses but the running quark masses at a high scale corresponding to the Higgs mass. In the modified minimal subtraction or  $\overline{\text{MS}}$  scheme, the relation between the pole masses and the running masses at the scale of the pole mass,  $\overline{m}_Q(m_Q)$ , can be expressed as [48]

$$\begin{aligned} \overline{m}_Q(m_Q) = m_Q \left[ 1 - \frac{4}{3} \frac{\alpha_s(m_Q)}{\pi} + (1.0414N_f - 14.3323) \frac{\alpha_s^2(m_Q)}{\pi^2} \right. \\ \left. + (-0.65269N_f^2 + 26.9239N_f - 198.7068) \frac{\alpha_s^3(m_Q)}{\pi^2} \right] \end{aligned} \quad (1.50)$$

where  $\alpha_s$  is the  $\overline{\text{MS}}$  strong coupling constant evaluated at the scale of the pole mass  $\mu = m_Q$ . The evolution of  $\overline{m}_Q$  from  $m_Q$  upward to a renormalization scale  $\mu$  is given by  $\overline{m}_Q(\mu) = \overline{m}_Q(m_Q) c[\alpha_s(\mu)/\pi]/c[\alpha_s(m_Q)/\pi]$  with the function  $c$  known up to three-loop order [49,50]. Using as starting points the values of the  $b, c$ -quark pole masses given previously and for  $\alpha_s(M_Z) = 0.1172$ , the  $\overline{\text{MS}}$  running  $b, c$  quark masses at the scale  $m_Q$  and  $\mu = 100 \text{ GeV}$  are displayed in Table 1.1. As can be seen, the values of the running  $b, c$  masses at the scale  $\mu \sim 100 \text{ GeV}$  are, respectively,  $\sim 1.5$  and  $\sim 2$  times smaller than the pole masses.

Note that for the top quark mass, the  $\overline{\text{MS}}$  values are only slightly different from the pole value. The strange quark mass will play only a minor role in Higgs physics and whenever it appears, we use the value  $\overline{m}_s(1 \text{ GeV}) = 0.2 \text{ GeV}$ .

The masses of the charged leptons are given by

$$m_\tau = 1.777 \text{ GeV}, \quad m_\mu = 0.1056 \text{ GeV}, \quad m_e = 0.511 \text{ MeV} \quad (1.51)$$

with the electron being too light to play any role in Higgs physics. The approximation of massless neutrinos will also have no impact on our discussion.

**1.1.4.5. The gauge boson masses and interactions.** The  $Z$  boson mass has been very accurately measured at LEP1 [8]

$$M_Z = 91.1875 \pm 0.0021 \text{ GeV} \quad (1.52)$$

<sup>9</sup> During the preparation of this review, the average mass value was  $m_t = 178.0 \pm 4.3 \text{ GeV}$ . Thus, several plots will be illustrated for this particular value; the summary plots will, however, be updated to take into account the new determination.



and, averaging the LEP2 [51] and Tevatron [52] measurements, one has for the  $W$  mass

$$M_W = 80.396 \pm 0.029 \text{ GeV}. \quad (1.53)$$

In terms of the electric charge  $Q_f$  of the fermion  $f$  and with  $I_f^3 = \pm \frac{1}{2}$  the left-handed weak isospin of the fermion and the weak mixing angle  $s_W^2 = 1 - c_W^2 \equiv \sin^2 \theta_W$ , one can write the vector and axial-vector couplings of the fermion  $f$  to the  $Z$  boson

$$v_f = \frac{\hat{v}_f}{4s_W c_W} = \frac{2I_f^3 - 4Q_f s_W^2}{4s_W c_W}, \quad a_f = \frac{\hat{a}_f}{4s_W c_W} = \frac{2I_f^3}{4s_W c_W} \quad (1.54)$$

where we also defined the reduced  $Zf\bar{f}$  couplings  $\hat{v}_f, \hat{a}_f$ . In the case of the  $W$  boson, its vector and axial-vector couplings to fermions are simply

$$v_f = a_f = \frac{1}{2\sqrt{2}s_W} = \frac{\hat{a}_f}{4s_W} = \frac{\hat{v}_f}{4s_W}. \quad (1.55)$$

These results are only valid in the one-family approximation. While the extension to three families is straightforward for the neutral currents [54], one needs to include CKM mixing [53] in the charged current case.

*1.1.4.6. The weak mixing angle.* The equations for the field rotation which lead to the physical gauge bosons, Eq. (1.19), define the electroweak mixing angle,  $\sin \theta_W = g_1/\sqrt{g_1^2 + g_2^2} = e/g_2$ , which can be written in terms of the  $W$  and  $Z$  boson masses as

$$\sin^2 \theta_W \equiv s_W^2 = 1 - c_W^2 = 1 - \frac{M_W^2}{M_Z^2}. \quad (1.56)$$

From a combination of the precision measurements at LEP1, one obtains the world average value for this angle [8]

$$\sin^2 \theta_{\text{eff}}^{\text{lep}} = 0.23150 \pm 0.00016. \quad (1.57)$$

Note that the relative strength of the charged and neutral currents,  $J_Z^\mu J_{\mu Z} / J^{\mu+} J_\mu^-$  can be measured by the parameter  $\rho$  [55] which, using previous formulas, is given by

$$\rho = \frac{M_W^2}{c_W^2 M_Z^2} \quad (1.58)$$

and is equal to unity in the SM, Eq. (1.56). This is a direct consequence of the choice of the representation of the Higgs field responsible of the breaking of the electroweak symmetry. In a model which makes use of an arbitrary number of Higgs multiplets  $\Phi_i$  with isospin  $I_i$ , third component  $I_i^3$  and vacuum expectation values  $v_i$ , one obtains for this parameter

$$\rho = \frac{\sum_i [I_i(I_i + 1) - (I_i^3)^2] v_i^2}{2 \sum_i (I_i^3)^2 v_i^2} \quad (1.59)$$

which is also unity for an arbitrary number of doublet [as well as singlet] fields. This is due to the fact that in this case, the model has a custodial  $SU(2)$  global symmetry. In the SM, this symmetry is broken at the loop level when fermions of the same doublets have different masses and by the hypercharge group. The radiative corrections to this parameter will be discussed in some detail in the next section.

This completes the list of SM parameters and interactions that we will use throughout this review.

## 1.2. Precision tests, radiative corrections and Higgs effects

Except for the Higgs mass, all the parameters of the SM, the three gauge coupling constants, the masses of the weak vector bosons and fermions as well as the quark mixing angles, have been determined experimentally as seen

in the previous section. Using these parameters, one can in principle calculate any physical observable and compare the result with experiment. Because the electroweak constants and the strong coupling constant at high energies are small enough, the first order of the perturbative expansion, the tree level or Born term, is in general sufficient to give relatively good results for most of these observables. However, to have a more accurate description, one has to calculate the complicated higher-order terms of the perturbative series, the so-called radiative corrections. The renormalizability of the theory insures that these higher-order terms are finite once various formally divergent counterterms are added by fixing a finite set of renormalization conditions. The theory allows, thus, the prediction of any measurable with a high degree of accuracy.

Very precise experiments, which allow a sensitivity to these quantum corrections, have been made in the last fifteen years. The  $e^+e^-$  colliders LEP and SLC, which started operation in the late 80s, have collected an enormous amount of electroweak precision data. Measurements at the  $Z$ -pole [where the production cross section is extremely large, allowing the collection of more than ten million events at LEP1] of the  $Z$  boson partial and total decay widths, polarization and forward–backward asymmetries were made at the amazing accuracy of one percent to one per mille [8]. The  $W$  boson properties have been also determined at the  $p\bar{p}$  collider Tevatron with a c.m. energy of  $\sqrt{s} = 1.8$  TeV [52] and at LEP2 with a c.m. energy up to  $\sqrt{s} = 209$  GeV [51] with a constant increase in accuracy. Many other high-precision measurements have been performed at much lower energies.

At the same time, a large theoretical effort has been devoted to the calculation of the radiative corrections to the electroweak observables, to match the accuracies which have been or which could be reached experimentally [56–59]. The availability of both highly accurate measurements and theoretical predictions, at the level of 0.1% precision and better, provides stringent tests of the SM. These high-precision electroweak data are a unique tool in the search for indirect effects, through possible small deviations of the experimental results from the theoretical predictions of the minimal SM, and constitute an excellent probe of its still untested scalar sector, as well as a probe of New Physics beyond the SM.

In this section, after summarizing some high-precision observables in the SM, we will describe the formalism needed to incorporate the radiative corrections and how the dominant part of the latter can be approximated. This will allow one to set the notation which will be used later and the framework which will be necessary to discuss the searches for the virtual effects of the Higgs bosons in electroweak observables, and to incorporate the important higher-order corrections in Higgs boson decay and production.

### 1.2.1. Observables in $Z$ boson decays

A large variety of precision tests can be performed in  $e^+e^-$  experiments with center of mass energies near the  $Z$ -resonance in the process  $e^+e^- \rightarrow f\bar{f}$  which is mediated by the exchange of a photon and a  $Z$  boson [56]. The differential cross section is a binomial in  $\cos\theta$ , where  $\theta$  is the angle between the electron and the final fermion  $f$ . For  $\sqrt{s} \simeq M_Z$ , the  $Z$  boson exchange largely dominates and, integrating over the entire range of the angle  $\theta$ , one obtains the total peak cross section

$$\sigma_0(e^+e^- \rightarrow Z \rightarrow f\bar{f}) \equiv \int_{-1}^{+1} \frac{d\sigma}{d\cos\theta} = \frac{12\pi}{M_Z^2} \times \frac{\Gamma_e \Gamma_f}{\Gamma_Z^2} \quad (1.60)$$

with the partial  $Z$  boson decay widths into massless fermion pairs given by

$$\Gamma_f \equiv \Gamma(Z \rightarrow f\bar{f}) = \frac{2\alpha}{3} N_c M_Z (v_f^2 + a_f^2). \quad (1.61)$$

Convenient measurable quantities which have been considered at LEP1 and SLC are, in this context, the ratio of  $Z$  boson partial widths  $R_f = \Gamma(Z \rightarrow f\bar{f})/\Gamma(Z \rightarrow \text{hadrons})$ .

If one integrates asymmetrically and normalizes to the total cross section, one obtains the forward–backward asymmetry for the decay of a  $Z$  boson into a fermion pair

$$A_{FB}^f \equiv \left[ \int_0^{+1} \frac{d\sigma}{d\cos\theta} - \int_{-1}^0 \frac{d\sigma}{d\cos\theta} \right] \times \sigma_0^{-1} \stackrel{\sqrt{s}=M_Z}{=} \frac{3}{4} A_e A_f \quad (1.62)$$

where the combinations  $A_f$  are given, in terms of the vector and axial-vector couplings of the fermion  $f$  to the  $Z$  boson, by

$$A_f = \frac{2a_f v_f}{v_f^2 + a_f^2} \equiv \frac{2\hat{a}_f \hat{v}_f}{\hat{v}_f^2 + \hat{a}_f^2}. \quad (1.63)$$

Note that if the initial  $e^-$  beams are longitudinally polarized, one can construct left–right asymmetries and left–right forward–backward asymmetries which can be written as

$$A_{LR}^f = A_e, \quad A_{LR,FB}^f = \frac{3}{4} A_f. \quad (1.64)$$

In particular  $A_{LR}^f$  [which is the same for all  $f \neq e$ ] and  $A_{\text{pol}}^\tau$  are very sensitive to the precise value of  $\sin^2 \theta_W$ , being proportional to the factor  $\hat{v}_e \equiv 1 - 4s_W^2 \sim 0$  for  $s_W^2 \sim 1/4$ .

The tree-level expressions discussed above give results at the one percent level and hold in most cases, except in the case of  $b$ -quark final states where mass effects,  $\mathcal{O}(4m_b^2/M_Z^2) \sim 0.01$ , have to be taken into account, and in the production of  $e^+e^-$  final states where the complicated  $t$ -channel gauge boson exchange contributions have to be included [this process is particularly important since it allows one to determine the absolute luminosity at  $e^+e^-$  colliders]. However, for a very precise description of the  $Z$  properties, one needs to include the one-loop radiative corrections and possibly some important higher-order effects. These radiative corrections fall into three categories:

(a) QCD corrections to final states quarks, where gluons are exchanged or emitted in the final state. For massless quarks the correction factors are

$$K_{Z \rightarrow q\bar{q}}^{\text{QCD}} = 1 + \frac{\alpha_s}{\pi} + 1.41 \left( \frac{\alpha_s}{\pi} \right)^2 \quad (1.65)$$

for the partial decay widths  $Z \rightarrow q\bar{q}$  or total cross section  $\Gamma_q \propto \sigma(e^+e^- \rightarrow q\bar{q})$ , and

$$K_{A_{FB}^q}^{\text{QCD}} = 1 - \frac{\alpha_s}{\pi} \quad (1.66)$$

for the forward–backward quark asymmetries. In fact these QCD factors are known to exist at  $\mathcal{O}(\alpha_s^3)$  for  $\Gamma_q$  and at  $\mathcal{O}(\alpha_s^2)$  for  $A_{FB}^q$ ; in the case of  $b$ -quarks one can include the mass effects at  $\mathcal{O}(\alpha_s)$  which are also known; see Ref. [57] for a detailed discussion.

(b) Pure electromagnetic corrections. These consist of initial and final state corrections where photons are exchanged in the  $Zf\bar{f}$  vertices or emitted in the initial or final states. For final state corrections, it is sufficient to include the small

$$K_{Z \rightarrow f\bar{f}}^{\text{EM}} = 1 + \frac{3}{4} Q_f^2 \frac{\alpha}{\pi}, \quad K_{A_{FB}^f}^{\text{EM}} = 1 - \frac{3}{4} Q_f^2 \frac{\alpha}{\pi} \quad (1.67)$$

correction factors, while for initial state corrections, in particular the photon radiation (ISR), one can use the standard approach of structure function where the corrections can be exponentiated. This is performed by convoluting the Born cross section with a radiator function  $G(s')$  for the full accessible c.m. energies  $s' = xs$  after photon radiation

$$\sigma^{\text{ISR}}(s) = \int_{x_0}^1 dx G(xs) \sigma_{\text{Born}}(xs), \quad G(xs) = \beta(1-x)^{\beta-1} \delta_{V+S}(x) + \delta_H(x) \quad (1.68)$$

where  $x_0$  is the minimum energy of the final state,  $x_0 = 4m_f^2/s$  for  $e^+e^- \rightarrow f\bar{f}$ , and  $G(x)$  is the radiator function, which is written in an exponentiated form to resum the infrared sensitive and large corrections. In the previous equation,  $\beta = \alpha/\pi \times [\log s/m_e^2 - 1]$  and  $\delta_{V+S}$ ,  $\delta_H$  contain, respectively, the virtual plus soft-photon contributions, and the hard-photon contributions, which are polynomials in  $\log(s/m_e^2)$ . Their expressions, as well as many details on ISR, FSR and their interference can be found in the reviews of Refs. [56]. Note that all these corrections do not involve any other physics than well-known QED.

(c) Electroweak corrections. They involve non-photon “direct” vertex and box corrections which are in general rather small [except in a few cases to be discussed later] as well as the “oblique”  $\gamma$ ,  $W$  and  $Z$  boson self-energy corrections and the  $\gamma$ – $Z$  mixing, which give the bulk of the contributions [56,59]. In particular, the top quark [which was not yet discovered at the time LEP1 and SLC started] and the Higgs boson will enter the electroweak observables

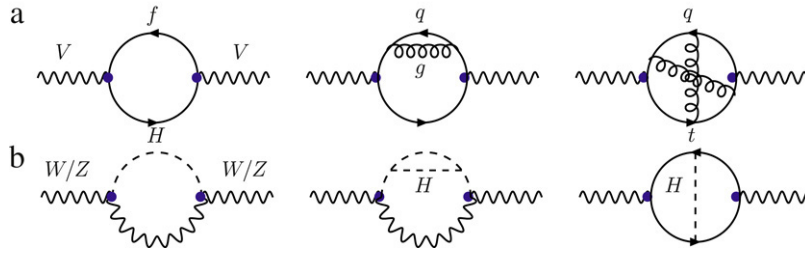


Fig. 1.3. Generic Feynman diagrams for the main electroweak radiative corrections: fermionic (a) and Higgs (b) contributions to the two-point functions of the  $V = W/Z$  bosons.

through their contributions to the  $W$  and  $Z$  boson self-energies. These electroweak corrections are discussed in some detail in the next subsection.

### 1.2.2. The electroweak radiative corrections

The electroweak radiative corrections can be cast into three main categories; Fig. 1.3:

- (a) The fermionic corrections to the gauge boson self-energies. They can be divided into the light fermion  $f \neq t$  contributions and the contribution of the heavy top quark  $f = t$ . For the contributions of quarks, one has to include the important corrections stemming from strong interactions.
- (b) The contributions of the Higgs particle to the  $W$  and  $Z$  boson self-energies both at the one-loop level and at the two level when e.g. the heavy top quark is involved.

There are also vertex corrections to the  $Z$  decays into fermions, in particular into  $b\bar{b}$  pairs, and vertex plus box contributions to muon decay [in which the bosonic contribution is not gauge invariant by itself and should be combined with the self-energy corrections] as well as negligible direct box corrections. However, these corrections do not involve a significant Higgs contribution and will not be discussed here.

The contribution of the light fermions to the vector boson self-energies can be essentially mapped into the running of the QED coupling constant which, as discussed in the previous section, is defined as the difference between the vacuum polarization function of the photon evaluated at low energies and at the scale  $M_Z$ ,  $\Delta\alpha(M_Z^2) = \Pi_{\gamma\gamma}(0) - \Pi_{\gamma\gamma}(M_Z^2) = 0.0590 \pm 0.00036$ . Therefore, the only remaining fermionic contribution to the two-point functions is the one due to the top quark on which, besides the effects of the Higgs boson, we will mainly concentrate by studying two important quantities,  $\Delta\rho$ ,  $\Delta r$ .

**1.2.2.1. The effective mixing angle and the  $\rho$  parameter.** The effective weak mixing angle can be defined in the Born approximation in terms of the  $W$  and  $Z$  boson masses,<sup>10</sup> Eq. (1.56). To include higher orders, one has to renormalize the  $V$  boson masses  $M_V^2 \rightarrow M_V^2 - \Pi_{VV}(M_V^2)$  where  $\Pi_{VV}$  is the real part of the transverse component of the self-energy of  $V$  at the scale  $M_V$ . One obtains an effective mixing angle [56,59]

$$\bar{s}_W^2 = 1 - \frac{M_W^2}{M_Z^2} + c_W^2 \left( \frac{\Pi_{WW}(M_W^2)}{M_W^2} - \frac{\Pi_{ZZ}(M_Z^2)}{M_Z^2} \right) \sim 1 - \frac{M_W^2}{M_Z^2} + c_W^2 \Delta\rho. \quad (1.69)$$

This is in fact the correction to the  $\rho$  parameter [55] which *historically* was used to measure the strength of the ratio of the neutral current to the charged current at zero-momentum transfer in deep-inelastic neutrino–nucleon scattering, Eq. (1.58). In the SM, as already mentioned, because of a global or custodial  $SU(2)_R$  symmetry of the Higgs Lagrangian [which survives the spontaneous breaking of the EW symmetry], this parameter is equal to unity. However, it receives higher-order corrections usually parametrized by

$$\rho = \frac{1}{1 - \Delta\rho}, \quad \Delta\rho = \frac{\Pi_{WW}(0)}{M_W^2} - \frac{\Pi_{ZZ}(0)}{M_Z^2}. \quad (1.70)$$

<sup>10</sup> When higher-order corrections are included, different definitions of  $\bar{s}_W^2$  lead to different values. For instance,  $\bar{s}_W^2$  as defined above is different from the effective leptonic  $\bar{s}_W^2|_{\text{eff}}^{\text{lept}}$  defined in terms of  $a_e$  and  $v_e$ .

The main contribution to this parameter is due to the  $(t, b)$  weak isodoublet. Indeed, the large mass splitting between the top and bottom quark masses breaks the custodial  $SU(2)_R$  symmetry and generates a contribution which grows as the top mass squared<sup>11</sup> [60]. Including the dominant higher-order QCD and electroweak corrections, one finds

$$\Delta\rho = 3x_t \left[ 1 + (\Delta\rho)^{\text{QCD}} + (\Delta\rho)^{\text{EW}} \right] \quad (1.71)$$

$$x_t = \frac{g_{Htt}^2}{(4\pi)^2} = \frac{G_\mu m_t^2}{8\sqrt{2}\pi^2} \sim 0.3\%. \quad (1.72)$$

The higher-order QCD corrections are known at two-loop [61] and three-loop [62] orders; with  $\alpha_s$  defined at the scale  $\mu = m_t$  with 6 flavors, they are given by

$$(\Delta\rho)^{\text{QCD}} = -\frac{2}{3} \frac{\alpha_s}{\pi} \left( \frac{\pi^2}{3} + 1 \right) - 14.59 \left( \frac{\alpha_s}{\pi} \right)^2. \quad (1.73)$$

There are also two-loop electroweak corrections stemming from fermion loops. In particular, there is a correction where a Higgs or a Goldstone boson is exchanged in loops containing top quarks and which grows as  $G_\mu^2 m_t^4$  and  $G_\mu^2 m_t^2 M_Z^2$ . In the limit where the Higgs boson mass is much smaller than  $m_t$ , the leading piece gives a tiny correction [63]

$$(\Delta\rho)^{\text{EW}} \simeq (19 - 2\pi^2)x_t \sim -x_t. \quad (1.74)$$

However, for the more realistic case of a finite Higgs mass, the correction can be much larger [64]; in addition, the subleading  $\mathcal{O}(G_\mu^2 m_t^2 M_Z^2)$  are also significant [65]. Recently, the full fermionic contributions to  $\Delta\rho$  and to  $\sin^2 \theta_W$  have been derived at the two-loop level [66]. Other higher-order corrections, such as the mixed QED–QCD contributions and the three-loop QCD corrections, are also available [67].

The Higgs boson will also contribute to the  $\rho$  parameter [68]. Using the definition of Eq. (1.70), the dependence of the  $\rho$  parameter on the Higgs mass at one loop is

$$(\Delta\rho)^{1\text{-Higgs}} = -\frac{3G_\mu M_W^2}{8\sqrt{2}\pi^2} f\left(\frac{M_H^2}{M_Z^2}\right), \quad f(x) = x \left[ \frac{\ln c_W^2 - \ln x}{c_W^2 - x} + \frac{\ln x}{c_W^2(1-x)} \right]. \quad (1.75)$$

This contribution vanishes in the limit  $s_W^2 \rightarrow 0$  or  $M_W \rightarrow M_Z$ , i.e. when the hypercharge group is switched off. For a very light Higgs boson the correction also vanishes

$$(\Delta\rho)^{1\text{-Higgs}} \rightarrow 0 \quad \text{for } M_H \ll M_W \quad (1.76)$$

while for a heavy Higgs boson, the contribution is approximately given by

$$(\Delta\rho)^{1\text{-Higgs}} \sim -\frac{3G_\mu M_W^2}{8\sqrt{2}\pi^2} \frac{s_W^2}{c_W^2} \log \frac{M_H^2}{M_W^2} \quad \text{for } M_H \gg M_W. \quad (1.77)$$

This contribution has only a logarithmic dependence in the Higgs boson mass. This has to be contrasted with the general case, where the contribution of two particles with a large mass splitting grows with the mass of the heaviest particle [as in the case of the top/bottom weak isodoublet] and thus, can be very large. This logarithmic dependence is due to what is called the “Veltman screening theorem” [68,69] which tells us that the quadratic corrections  $\propto M_H^2$  appear only at the two-loop level, and are therefore screened or damped by an extra power of the electroweak coupling squared.

The two-loop Higgs corrections to the  $\rho$  parameter stemming from the exchange of the Higgs particles [and the Goldstone bosons] are known in the large Higgs mass limit since quite some time [70], but recently the three-loop

<sup>11</sup> Because  $m_t$  is large, the contributions are approximately the same at the scale  $q^2 \sim 0$  or  $q^2 \sim M_V^2$ ; in addition the light fermion contributions to  $\Pi_{WW}$  and  $\Pi_{ZZ}$  almost cancel in the difference,  $\sim \log M_W/M_Z$ . This is the reason why one can approximate the correction to  $s_W^2$  in Eq. (1.69) by the one in Eq. (1.70).

contribution has been also calculated [71]. The sum of the two contributions reads for  $M_H \gg M_W$

$$(\Delta\rho)^{2+3\text{-Higgs}} \sim 0.15 \left( \frac{G_\mu M_W^2}{2\sqrt{2}\pi^2} \right)^2 \frac{s_W^2}{c_W^2} \frac{M_H^2}{M_W^2} - 1.73 \left( \frac{G_\mu M_W^2}{2\sqrt{2}\pi^2} \right)^4 \frac{s_W^2}{c_W^2} \frac{M_H^4}{M_W^4}. \quad (1.78)$$

Both the two- and three-loop corrections are extremely small for reasonable values of  $M_H$ . However, for  $M_H \sim 400$  GeV, the two corrections become of the same size,  $\mathcal{O}(10^{-5})$ , but with opposite signs and cancel each other. For  $M_H \sim 1.2$  TeV, the three-loop correction is comparable with the one-loop contribution and has the same sign.

Nevertheless, for a relatively light Higgs boson and except when it comes to very high-precision tests, one can neglect these Higgs boson corrections to the  $\rho$  parameter, and keep only the QCD and leading electroweak corrected top quark contribution. This  $\Delta\rho$  correction will be the largest contribution to the electroweak corrections after  $\Delta\alpha(M_Z^2)$  since, for  $m_t \sim 180$  GeV, it is at the level of  $\sim 1\%$ .

*1.2.2.2. Muon decay and the radiative corrections to the W boson mass.* As previously discussed, the  $W$  boson mass is related to  $\alpha$ ,  $G_\mu$  and  $M_Z$ , Eq. (1.44). Including the radiative corrections, one obtains the celebrated relation [72]

$$M_W^2 \left( 1 - \frac{M_W^2}{M_Z^2} \right) = \frac{\pi\alpha}{\sqrt{2}G_\mu} (1 + \Delta r). \quad (1.79)$$

The  $\Delta r$  correction can be decomposed into three main components and can be written as [56]

$$1 + \Delta r = \frac{1}{(1 - \Delta\alpha)(1 + \frac{c_W^2}{s_W^2}\Delta\rho) - (\Delta r)_{\text{rem}}} \quad (1.80)$$

where the  $\Delta\alpha$  and  $\Delta\rho$  contributions have been discussed previously and  $(\Delta r)_{\text{rem}}$  collects the remaining non-leading contributions [56]. At one loop, the Higgs boson has a contribution to  $(\Delta r)$  that is also only logarithmically dependent on  $M_H$ , as in the case of  $\Delta\rho$ . For a heavy Higgs,  $M_H \gg M_W$ , it reads [72,73]

$$(\Delta r)_{\text{rem}}^{1\text{-Higgs}} \simeq \frac{G_\mu M_W^2}{8\sqrt{2}\pi^2} \frac{11}{3} \left( \log \frac{M_H^2}{M_W^2} - \frac{5}{6} \right). \quad (1.81)$$

Again, the quadratic correction  $\propto M_H^2$  appears only at the two-loop level.

The complete two-loop bosonic corrections to  $\Delta r$  have been calculated recently [74] including the full  $M_H$  dependence and were found to be very small: a few times  $\times 10^{-5}$  for  $M_H$  values in the range between 100 GeV and 1 TeV. There are also two-loop electroweak corrections stemming from fermions; the main contribution is in fact contained in  $\Delta\rho$  but there is an extra piece contributing to  $(\Delta r)_{\text{rem}}$  which, however, is small [65]. Hence, the theoretical knowledge of the  $W$  mass is rather precise, being approximately the same as that for the electroweak mixing angle.

### 1.2.3. Approximating the radiative corrections

The evaluation of the complete set of the previously discussed radiative corrections is a very complicated task, in particular when initial and final state photonic corrections or processes which need some special treatment, such as Bhabha  $e^+e^- \rightarrow e^+e^-$  scattering, are involved. This can be performed only with the help of very sophisticated programs which fortunately exist [57]. However, in most practical purposes, in particular when effects of New Physics are analyzed, it is sufficient to probe some quantities where the most important radiative correctives are expected to occur. This is the case, for instance, of the  $\Delta r$  and  $\bar{s}_W^2$  observables. Here, we will shortly describe the improved Born approximation which will have some application later.

One can express electroweak observables in the Born approximation in terms of the QED constant  $\alpha$ , but to be accurate, one should use the running  $\alpha$  defined at the scale where the considered process takes place,  $M_Z$  or higher energies. Since the running of  $\alpha$  between the two latter scales is rather small, one can make the substitution  $\alpha(0) \rightarrow \alpha(M_Z^2) = \alpha(0)/(1 - \Delta\alpha)$  for scales larger than  $M_Z$ . The  $\Delta\alpha$  corrections should in principle cancel the light fermion contributions in the two-point functions when the radiative corrections to the observables are calculated.



This is in fact effectively done by using the Fermi decay constant in the tree-level expressions of the observables,  $\alpha(0) \rightarrow \alpha(M_Z^2) = (\sqrt{2}G_\mu/\pi)M_W^2 s_W^2$ , which implicitly includes the  $\Delta\alpha$  contribution. Since  $\Delta\alpha$  is rather large being at the level of 6% [and which for  $2 \rightarrow 2$  (3) processes that are proportional to  $\alpha^2$  ( $\alpha^3$ ), leads to contributions of the order of 12% (18%)], this gives a more accurate description of the observable, already at the tree level. This procedure is called the naive improved Born approximation (naive IBA) [75].

The IBA is said to be naive because there are still residual contributions from  $\Delta\rho$  and  $(\Delta r)_{\text{rem}}$  and additional contributions to  $\bar{s}_W^2$  which, despite the fact that they are smaller than  $\Delta\alpha$ , should be taken into account. The dominant top quark contribution which is contained in the  $\Delta\rho$  piece given in Eq. (1.71) can be simply included by performing the shift

$$\alpha \rightarrow \frac{\sqrt{2}G_\mu}{\pi} M_W^2 \left(1 - \frac{M_W^2}{M_Z^2}\right) (1 + \Delta r)^{-1}, \quad \Delta r \simeq \Delta\alpha(M_Z^2) - 3\Delta\rho. \quad (1.82)$$

In the context of  $Z$  physics, the IBA may be sufficient in many purposes and can be implemented in the electroweak observables by simply performing the following substitutions:

- (i) replace the electromagnetic couplings of fermions by

$$Q_f e \rightarrow Q_f \sqrt{4\pi\alpha/[1 - \Delta\alpha(M_Z^2)]^{-1}} \quad (1.83)$$

- (ii) replace the Born couplings of the fermion to the  $Z$  boson by

$$v_f \rightarrow (\sqrt{2}G_\mu M_Z^2 \rho)^{1/2} \hat{v}_f, \quad a_f \rightarrow (\sqrt{2}G_\mu M_Z^2 \rho)^{1/2} \hat{a}_f \quad (1.84)$$

- (iii) replace everywhere  $s_W^2$ , in particular in the vector couplings  $\hat{v}_f = 2I_3^f - 4Q_f s_W^2$ , by the effective electroweak mixing angle for leptons

$$s_W^2 \rightarrow \bar{s}_W^2 \equiv \sin^2 \theta_{\text{eff}}^{\text{lept}} = \frac{1}{2} \left[ 1 - \sqrt{1 - \frac{4\pi\alpha(0)}{\sqrt{2}M_Z^2 G_\mu} \frac{1}{\rho(1 - \Delta\alpha)}} \right]. \quad (1.85)$$

The remaining non-universal electroweak corrections are small and can be safely neglected in most cases [except for  $b$ -quark final states where one can easily include large top quark mass corrections to the  $Zb\bar{b}$  vertex], but obviously not when probing the small Higgs boson effects. Of course, this IBA needs to be supplemented by the important QCD corrections to hadronic processes and QED corrections, in particular ISR corrections, whenever needed. The IBA will be very often used when discussing Higgs boson production and decay.

#### 1.2.4. The electroweak precision data

Besides  $\alpha(M_Z)$ ,  $G_\mu$  and  $M_Z$  which are used as the basic input parameters, there is an impressive list of electroweak observables which have been measured with a very good accuracy and which can be predicted in the SM with an equally good precision. These are:

- Observables from the  $Z$  lineshape at LEP1: the  $Z$  boson total width  $\Gamma_Z$ , the peak hadronic cross section  $\sigma_{\text{had}}^0$ , the partial decay widths of the  $Z$  boson into leptons and  $c$ ,  $b$ -quarks normalized to the hadronic  $Z$  decay width,  $R_{\ell,c,b}$ , the forward–backward asymmetries  $A_{FB}^f$  for leptons and heavy  $c$ ,  $b$ -quarks, as well as the  $\tau$  polarization asymmetry  $A_{\text{pol}}^\tau$ ; the asymmetries provide a determination of  $\sin^2 \theta_W$  as measured from leptons and hadrons.

- The longitudinal polarization asymmetry  $A_{LR}^f$  which has been measured at the SLC and which gives the best individual measurement of  $\sin^2 \theta_W$ , as well as the left–right forward–backward asymmetries for the heavy  $b$ ,  $c$  quarks,  $A_{LR,FB}^{b,c}$ .

- The mass of the  $W$  boson  $M_W$  which is precisely measured at LEP2 and at the Tevatron equation (1.53) as well as the total decay width  $\Gamma_W$ .

- In addition there are high-precision measurements at low energies: (i) the  $\nu_\mu$ - and  $\bar{\nu}_\mu$ -nucleon deep-inelastic scattering cross sections, the ratios of which measure the  $Z$ -fermion couplings and (ii) the parity violation in the Cesium and Thallium atoms which provide the weak charge  $Q_W$  that quantifies the  $Z$ -nucleus coupling; both can be turned into a determination of the electroweak mixing angle.

Table 1.2

Summary of electroweak precision measurements at LEP1, LEP2, SLC and the Tevatron; from Ref. [8]

	Measurement	Fit	$ \text{O}^{\text{meas}} - \text{O}^{\text{fit}} /\sigma^{\text{meas}}$
			0 1 2 3
$\Delta\alpha_{\text{had}}^{(5)}(m_Z)$	$0.02758 \pm 0.00035$	0.02766	
$m_Z$ [GeV]	$91.1875 \pm 0.0021$	91.1874	
$\Gamma_Z$ [GeV]	$2.4952 \pm 0.0023$	2.4957	
$\sigma_{\text{had}}^0$ [nb]	$41.540 \pm 0.037$	41.477	
$R_l$	$20.767 \pm 0.025$	20.744	
$A_{\text{fb}}^{0,l}$	$0.01714 \pm 0.00095$	0.01640	
$A_l(P_\tau)$	$0.1465 \pm 0.0032$	0.1479	
$R_b$	$0.21629 \pm 0.00066$	0.21585	
$R_c$	$0.1721 \pm 0.0030$	0.1722	
$A_{\text{fb}}^{0,b}$	$0.0992 \pm 0.0016$	0.1037	
$A_{\text{fb}}^{0,c}$	$0.0707 \pm 0.0035$	0.0741	
$A_b$	$0.923 \pm 0.020$	0.935	
$A_c$	$0.670 \pm 0.027$	0.668	
$A_l(\text{SLD})$	$0.1513 \pm 0.0021$	0.1479	
$\sin^2\theta_{\text{eff}}^{\text{lept}}(Q_{\text{fb}})$	$0.2324 \pm 0.0012$	0.2314	
$m_W$ [GeV]	$80.392 \pm 0.029$	80.371	
$\Gamma_W$ [GeV]	$2.147 \pm 0.060$	2.091	
$m_t$ [GeV]	$171.4 \pm 2.1$	171.7	

The SM fit results, which have been derived including all radiative corrections, and the standard deviations are also shown.

In addition one has to include as inputs, the measurement  $m_t$  at the Tevatron,  $\alpha_s$  at LEP and elsewhere, as well as the value of  $\Delta\alpha_{\text{had}}(M_Z^2)$  as measured in low-energy  $e^+e^-$  collisions and in  $\tau$ -lepton decays at LEP1. The experimental values of some of the electroweak observables mentioned above [as they were in summer 2006] are displayed in Table 1.2 together with the associated errors. Also shown are the theoretical predictions of the SM [for the best fit of  $M_H$  to be discussed later] that have been obtained by including all known radiative corrections with the central values of the previous parameters.

As can be seen from Table 1.2, the theoretical predictions are in remarkable agreement with the experimental data, the pulls being smaller than 2 standard deviations in all cases, except for  $A_{\text{FB}}^b$  where the deviation is at the  $2.5\sigma$  level. In particular, the number of light neutrino flavors is measured and agrees with the SM expectation  $N_\nu = 3$  at the  $2\sigma$  level and the effective weak mixing angle is measured with a very high accuracy from lepton asymmetries and partial widths and from hadronic asymmetries, Eq. (1.57). Note also, that the cross sections for the pair production of gauge bosons, which for the  $e^+e^- \rightarrow W^+W^-$  process depend on the triple self-coupling among the  $W$  and the  $V = \gamma, Z$  bosons and on the  $W\psi\psi$ -coupling equation (1.55), have been rather accurately measured at LEP2 and at the Tevatron and shown to agree with the SM expectation.

In summary, the electroweak precision data have provided a decisive test of the SM. These tests have been performed at the per mille level and have probed the quantum corrections of the  $\text{SU}(2)_L \times \text{U}(1)_Y$  theory. The couplings of quarks and leptons to the electroweak gauge bosons have been measured precisely and found to be those predicted by the gauge symmetry. The trilinear couplings among electroweak gauge bosons have been also measured and found to be those dictated by the gauge symmetry. If, in addition, one recalls that the  $\text{SU}(3)_C$  gauge symmetry description of the strong interactions has been thoroughly tested at LEP1 and elsewhere, one concludes that the SM based on the  $\text{SU}(3)_C \times \text{SU}(2)_L \times \text{U}(1)_Y$  gauge symmetry has been firmly established as the theory of the strong and electroweak

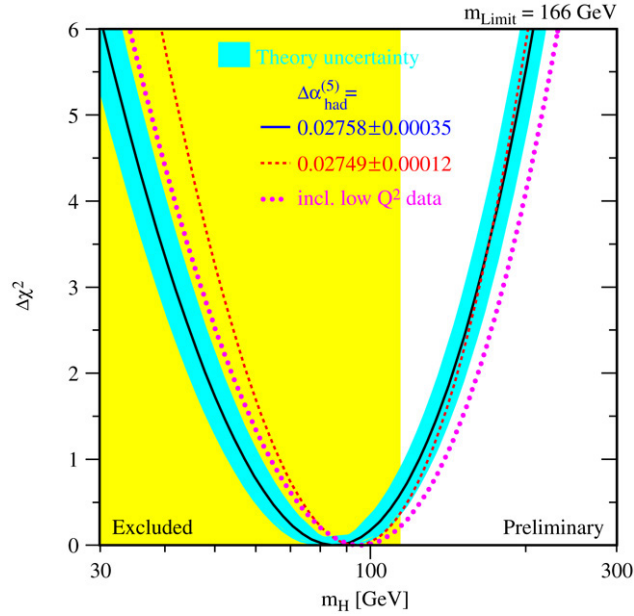


Fig. 1.4. The  $\Delta\chi^2$  of the fit to the electroweak precision data as a function of  $M_H$ . The solid line results when all data are included and the blue/shaded band is the estimated theoretical error from unknown higher-order corrections. The effects of including the low  $Q^2$  data and the use of a different value for  $\Delta\alpha_{\text{had}}$  are also shown; from Ref. [8].

interactions at the present energies. The only missing ingredient of the model is the Higgs particle, which has not yet been observed directly. However, indirect constraints on this particle can be obtained from the high-precision data as we will discuss now.

### 1.3. Experimental constraints on the Higgs boson mass

Since the Higgs particle contributes to the radiative corrections to the high-precision electroweak observables discussed previously, there are constraints on its mass which, as discussed in Section 1.1, is the only yet unknown free parameter in the SM. There are also constraints from direct searches of the Higgs boson at colliders and in particular at LEP. These indirect and direct constraints on  $M_H$  will be summarized in this section.

#### 1.3.1. Constraints from high-precision data

The electroweak precision measurements allow rather stringent constraints on the Higgs boson mass in the SM. Taking into account all the precision data of Table 1.2 in a combined fit, one can determine the constraint summarized in Fig. 1.4 which shows the  $\Delta\chi^2$  of the fit to all measurements as a function of  $M_H$ , with the uncertainties on  $\Delta\alpha_{\text{had}}$ ,  $\alpha(M_Z)$ ,  $\alpha_s(M_Z)$ ,  $m_t$  as well as on  $M_Z$  included [8]. One then obtains the value of the SM Higgs boson mass

$$M_H = 85^{+39}_{-28} \text{ GeV} \quad (1.86)$$

leading to a 95% Confidence Level (CL) upper limit in the SM

$$M_H < 166 \text{ GeV}. \quad (1.87)$$

These values are relatively stable when the low-energy data are included in the fit, or when a slightly different value for  $\Delta\alpha_{\text{had}}^{(5)}$  is used. The area to the left to the vertical band which is very close to the minimum of the fit, shows the exclusion limit  $M_H > 114.4$  GeV from direct searches at LEP2 to which we will turn our attention shortly.

It thus appears that the high-precision data, when confronted with the predictions of the SM after the radiative corrections have been incorporated, lead to stringent constraints on the Higgs sector of the SM. The data strongly disfavor a heavy Higgs boson with a mass  $M_H \gtrsim 700$  GeV for which the perturbation theory breaks down anyway, as will be seen in the next section. They clearly favor a light Higgs boson,  $M_H \lesssim 166$  GeV, which is very encouraging for the next generation of high-energy experiments.

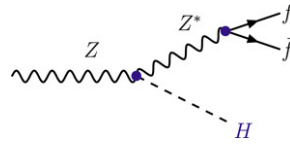


Fig. 1.5. The main production mechanism for Higgs bosons in Z decays at LEP1.

However, there are two caveats to this statement, a theoretical and an experimental one. The most constraining observables, besides  $M_W$ , are the leptonic asymmetries led by  $A_{LR}$ , on the one hand, and the hadronic asymmetries led by  $A_{FB}^b$ , on the other hand. However, while the former set favors a light Higgs, as is also the case of  $M_W$ , the hadronic asymmetries favor a heavier one. Because of the  $3\sigma$  difference of the value of  $\sin^2 \theta_W$  as measured in the two sets of observables, it is only if one averages all measurements that one obtains the central value  $M_H \sim 100$  GeV. In fact, because of this  $\sim 3\sigma$  deviation, the SM fit is rather poor [76]. It can be improved if one assumes New Physics effects which appear only in the  $Zb\bar{b}$  coupling. However, it is very difficult to induce new effects in  $A_{FB}^b$  without spoiling the agreement of  $R_b$  with the data. On the other hand, if one assumes that the discrepancy in  $A_{FB}^b$  is due to some systematical errors underestimated by the experiments and remove this quantity from the global fit, one obtains a central value of  $M_H$  which is even lower than the mass bound obtained from direct Higgs searches at LEP2 and hence, increasing the tension between the central value of the fit and the bound from direct Higgs searches.

The bound on the Higgs mass, Eq. (1.87), is quite strong and there have been many speculations on how it can be relaxed or evaded. To do so, one has to introduce New Physics contributions which are of the same order as the one due to a heavy Higgs boson, and which conspire with the latter so as to mimic the effect of a light SM Higgs particle. This has to be done without spoiling the rest of the agreement of the SM with the high-precision data. A way to look at these new contributions is to parametrize the Higgs sector by an effective Lagrangian in which higher-dimensional operators [77,78] are added. These operators should respect the  $SU(2)_L \times U(1)_Y$  gauge symmetry, as well as some other constraints. In this approach, one or a few higher-dimensional operators which are damped by powers of the new scale  $\Lambda$ , produce corrections that counteract the one of a heavy Higgs boson, in such a way that the net result is compatible with the SM for  $M_H \sim 100$  GeV. To produce such a conspiracy, the scale  $\Lambda$  should range between 2 and 10 TeV, depending on the nature of the operator or the combination of operators which generates the effect [79].

However, this approach does not tell anything about the New Physics which is behind the effective Lagrangian, and it is not actually clear whether it is possible to produce such a set of conspiring operators in a well-motivated and consistent theoretical model. One therefore prefers to consider specific and preferably well-motivated models. In general, because of decoupling, models which contain an elementary Higgs particle generate only small radiative corrections even if they involve a large number of new particles. This is typically the case of supersymmetric extensions of the SM. In contrast, models where the Higgs boson is composite or strongly interacting can generate large effects. However, in most cases the new contributions add to the effect of a heavy Higgs boson, leading to a stronger disagreement with the precision data. This is, for instance, the case of early versions of Technicolor models which have been ruled out in the beginning of the nineties [80]. Nevertheless, there are still models of New Physics that are weakly interacting and which induce corrections that are large enough, and with the adequate sign, to accommodate a heavy Higgs boson. In Ref. [81], large classes of models have been considered and their effects on the radiative corrections have been analyzed. The conclusion of the study is that indeed, models with a heavy Higgs boson exist, but they always need some conspiracy to produce the required effect and more importantly, in most cases they predict new degrees of freedom which should be sufficiently light enough to be observed at the next generation of colliders.

### 1.3.2. Constraints from direct searches

**1.3.2.1. Searches at LEP1.** The Higgs boson has been searched for at the LEP experiment, first at energies near the Z boson resonance,  $\sqrt{s} \simeq M_Z$ . In this case, two channels allow the probe of the Higgs boson [82]. The dominant production mode is the Bjorken process [83], where the Z boson decays into a real Higgs boson and an off-shell Z boson which goes into two light fermions,  $Z \rightarrow HZ^* \rightarrow Hf\bar{f}$ ; the Feynman diagram is shown in Fig. 1.5.

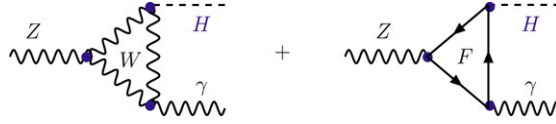
Fig. 1.6. Feynman diagrams for the one-loop induced decay mode  $Z \rightarrow H\gamma$  in the SM.

Table 1.3

The number of events for Higgs production at LEP1 per  $10^7 Z$  bosons

$M_H$ (GeV)	10	20	30	40	50	60	70
$Z \rightarrow H\mu^+\mu^-$	750	290	120	46	15.6	3.7	0.6
$Z \rightarrow H\gamma$	20.4	18.4	15.3	11.6	7.8	4.4	1.8

The partial decay width  $\Gamma(Z \rightarrow Hf\bar{f})$ , when normalized to the  $Z \rightarrow f\bar{f}$  decay width where the fermion  $f \neq t$  is considered to be massless, is given by [84]

$$\text{BR}(Z \rightarrow Hf\bar{f}) \equiv \frac{\Gamma(Z \rightarrow Hf\bar{f})}{\Gamma(Z \rightarrow f\bar{f})} = \frac{G_\mu M_Z^2}{2\sqrt{2}\pi^2} \int_{2a}^{1+a^2} dx \Gamma_0(x) \quad (1.88)$$

with the variable appearing in the integration bounds being  $a = M_H/M_Z$  and  $x$  is the reduced energy of the Higgs boson  $x = 2E_H/M_Z$ . The function in the integrand reads

$$\Gamma_0(x) = \frac{\sqrt{x^2 - 4a^2}}{(x - a^2)^2 + \gamma^2} \left( 1 - x + \frac{x^2}{12} + \frac{2a^2}{3} \right) \quad (1.89)$$

where  $\gamma = \Gamma_Z/M_Z$  is the reduced total decay width of the  $Z$  boson. Neglecting the  $Z$  width in  $\Gamma_0$ , the integration over the variable  $x$  leads to a relatively simple analytical result [13]

$$\begin{aligned} \text{BR}(Z \rightarrow Hf\bar{f}) = \frac{G_\mu M_Z^2}{2\sqrt{2}\pi^2} & \left[ \frac{3a(a^4 - 8a^2 + 20)}{\sqrt{4 - a^2}} \arccos\left(\frac{1}{2}a(3 - a^2)\right) \right. \\ & \left. - 3(a^4 - 6a^2 + 4) \ln a - \frac{1}{2}(1 - a^2)(2a^4 - 13a^2 + 47) \right]. \end{aligned} \quad (1.90)$$

This branching ratio follows that of the  $Z$  decay into a given fermionic final state. For instance,  $\text{BR}(Z \rightarrow H\mu^+\mu^-)$  for muons and  $\text{BR}(Z \rightarrow H\nu\bar{\nu})$  when summing over the three neutrino species are, respectively, 3% and 18% of the total Higgs sample.

The Higgs boson can also be produced in the decay  $Z \rightarrow H\gamma$  [85,86] which occurs through triangular loops built up by heavy fermions and the  $W$  boson; Fig. 1.6. The partial decay width, including only the dominant top quark and  $W$  contributions, reads

$$\Gamma(Z \rightarrow H\gamma) = \frac{\alpha G_\mu^2 M_W^2}{48\pi^4} M_Z^3 \left( 1 - \frac{M_H^2}{M_Z^2} \right)^3 |A_t + A_W|^2. \quad (1.91)$$

The complete expressions of the form factors  $A_t$  and  $A_W$  will be given later, when the reverse decay  $H \rightarrow Z\gamma$  will be discussed in detail. In the case of interest here, i.e. for  $M_H \lesssim M_W$ , one can approximate the top quark form factors by its value in the vanishing  $M_H$  limit,  $A_t = N_c Q_t \hat{v}_t / (3c_W) \sim 0.3$ , but for the  $W$  form factor, a good approximation in the Higgs boson mass range relevant at LEP1, is given by  $A_W \simeq -4.6 + 0.3M_H^2/M_W^2$  [86].

The two contributions interfere destructively, but the  $W$  contribution is largely dominating. Table 1.3 shows the number of produced Higgs particles per  $10^7 Z$  bosons, in both the  $Z \rightarrow H\gamma$  and  $Z \rightarrow H\mu^+\mu^-$  processes. As can be seen, the number of produced  $H$  bosons is much larger in the Bjorken process for small Higgs masses but the loop decay process becomes more important for masses around  $M_H \sim 60$  GeV. However, in this case, only a handful of events can be observed.

As will be discussed in great detail in the next chapter, the Higgs boson in the mass range relevant at LEP1 [and also LEP2], decays dominantly into hadrons [mostly  $b\bar{b}$  final states for  $M_H \gtrsim 10$  GeV], and less than  $\sim 8\%$  of the

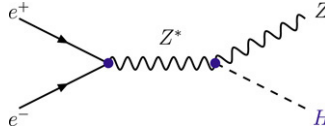


Fig. 1.7. The production mechanism for SM Higgs bosons in  $e^+e^-$  collisions at LEP2.

time into  $\tau$ -lepton pairs. Thus, not to be swamped by the large  $e^+e^- \rightarrow$  hadron background, the Higgs boson has been searched for at LEP1 in the two topologies  $Z \rightarrow (H \rightarrow \text{hadrons})(Z^* \rightarrow \nu\bar{\nu})$  leading to a final state consisting of two acoplanar jets and missing energy and  $Z \rightarrow (H \rightarrow \text{hadrons})(Z^* \rightarrow e^+e^-, \mu^+\mu^-)$  with two energetic leptons isolated from the hadronic system. The absence of any Higgs boson signal by the four collaborations at LEP1 [87], allowed one to set the 95% Confidence-Level limit of  $M_H \gtrsim 65.2$  GeV on the SM Higgs boson mass [88].

Before the advent of LEP1, the low Higgs mass range,  $M_H \lesssim 5$  GeV, was very difficult to explore. Indeed, the main probes were, for Higgs masses below 20 MeV, Nuclear Physics experiments which are very sensitive to the theoretically uncertain Higgs–nucleon couplings and for larger masses, rare meson [from pions to heavy  $B$  mesons] decays which were plagued by various theoretical and experimental uncertainties.<sup>12</sup> On the  $Z$ -resonance, this low mass range can be easily probed by considering the clean final state  $Z \rightarrow Z^*H \rightarrow \mu^+\mu^-H$ : since the invariant mass of the system recoiling against the lepton pair is simply the Higgs boson mass, the precise knowledge of the c.m. energy and the accurate measurement of the invariant mass and energy of the leptons allow an excellent resolution on  $M_H$ . This process therefore definitely rules out any Higgs boson with a mass below  $\sim 60$  GeV, independently of its decay modes, provided that its coupling to the  $Z$  boson is as predicted in the SM.

**1.3.2.2. Searches at LEP2.** The search for Higgs bosons has been extended at LEP2 with c.m. energies up to  $\sqrt{s} = 209$  GeV. In this energy regime, the dominant production process is Higgs–strahlung [32,84,89–91] where the  $e^+e^-$  pair goes into an off-shell  $Z$  boson which then splits into a Higgs particle and a real  $Z$  boson,  $e^+e^- \rightarrow Z^* \rightarrow HZ$ ; see the diagram of Fig. 1.7. The cross section for the  $WW$  fusion process, to be discussed later, is very small at these energies [92]; however, it is not completely negligible and is included to set the final Higgs mass limit at LEP2.

The production cross section for this Higgs–strahlung process [which will be discussed in more detail later] is given by

$$\sigma(e^+e^- \rightarrow ZH) = \frac{G_\mu^2 M_Z^4}{96\pi s} [1 + (1 - 4s_W^2)^2] \lambda^{1/2} \frac{\lambda + 12M_Z^2/s}{(1 - M_Z^2/s)^2}. \quad (1.92)$$

At LEP2 and for the maximal c.m. energy reached,  $\sqrt{s}_{\text{max}} \sim 209$  GeV, it is shown in Fig. 1.8 as a function of  $M_H$ . At  $M_H \sim 115$  GeV, that of  $\mathcal{O}(100)$  fb which, for the integrated luminosity that has been collected,  $\int \mathcal{L} \sim 0.1 \text{ fb}^{-1}$ , corresponds to ten events. For  $M_H^{\text{max}} \sim \sqrt{s} - M_Z \sim 117$  GeV, the  $2 \rightarrow 2$  cross section vanishes, being suppressed by the phase-space factor  $\lambda^{1/2}$ .

The searches by the LEP collaborations have been made in several topologies:  $e^+e^- \rightarrow (H \rightarrow b\bar{b})(Z^* \rightarrow \nu\bar{\nu})$  and  $e^+e^- \rightarrow (H \rightarrow b\bar{b})(Z^* \rightarrow \ell^+\ell^-)$  as at LEP1, as well as  $e^+e^- \rightarrow (H \rightarrow \tau^+\tau^-)(Z^* \rightarrow b\bar{b})$  and  $e^+e^- \rightarrow (H \rightarrow b\bar{b})(Z^* \rightarrow \tau^+\tau^-)$ . Combining the results of the four LEP collaborations, no significant excess above the expected SM background has been seen, and the exclusion limit [10]

$$M_H > 114.4 \text{ GeV} \quad (1.93)$$

has been established at the 95% CL from the non-observation of a signal, as shown in Fig. 1.9 (left). This upper limit, in the absence of additional events with respect to SM predictions, was expected to be  $M_H > 115.3$  GeV. The reason for the discrepancy is that there is a  $1.7\sigma$  excess [compared to the value  $2.9\sigma$  reported at the end of 2000] of events for a Higgs boson mass in the vicinity of  $M_H = 116$  GeV [10]. But this excess is not significant enough, since we need a  $5\sigma$  signal to be sure that we have indeed discovered the Higgs boson.

<sup>12</sup> For a very detailed discussion of the SM Higgs boson searches in this low mass range, see Chapter 3.1 of *The Higgs Hunter's Guide* [13], pages 91–130.



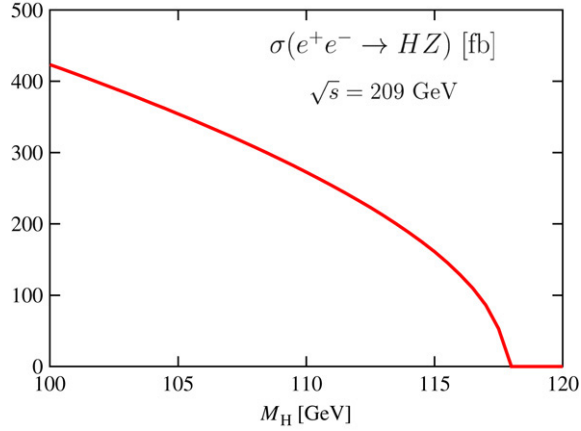


Fig. 1.8. Production cross section for the SM Higgs boson at LEP2 [in femtobarns] for a center of mass energy  $\sqrt{s} = 209$  GeV as a function of the Higgs boson mass.

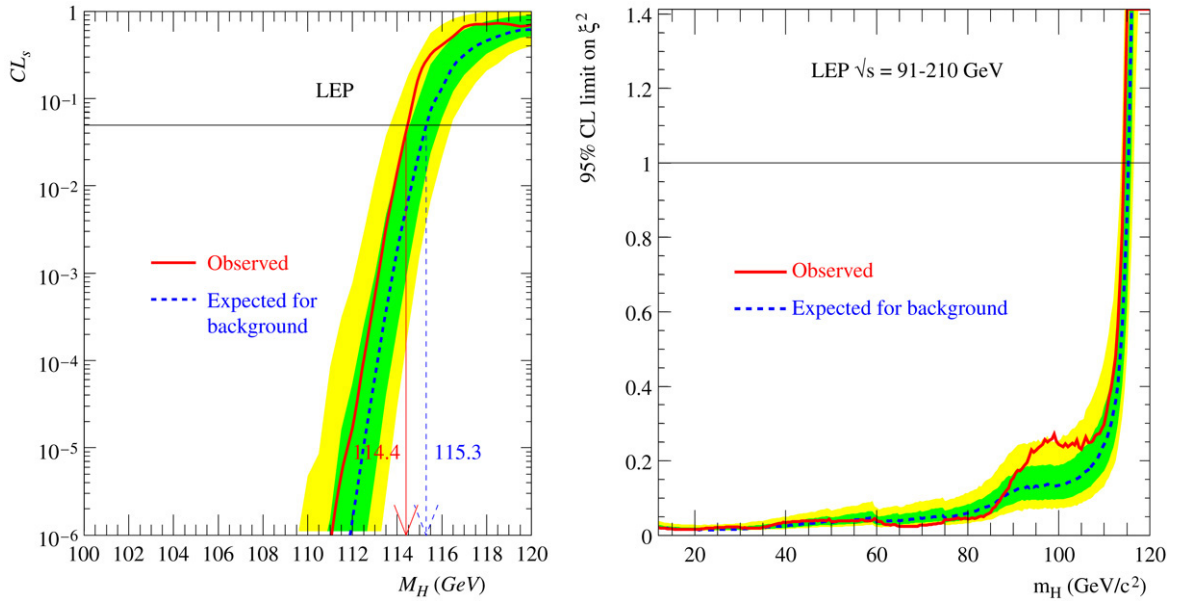
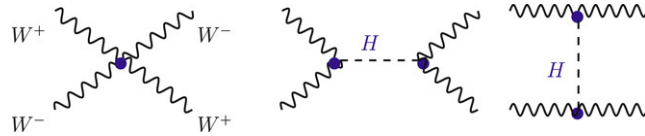


Fig. 1.9. Left: Confidence Level  $CL_s$  for the signal + background hypothesis in Higgs production at LEP2. The solid/red line is for the observation, the dashed line is the median background expectation, the dark-grey/green and light-grey/yellow shaded bands around the median expected line correspond to the 68% and 95% simulated probability bands. The intersection of the horizontal line at  $CL_s = 0.05$  with the observed curve defines the 95% CL lower bound for  $M_H$ ; from Ref. [10]. Right: The upper bound on the coupling  $\xi^2 = (g_{HZZ}/g_{HZZ}^{\text{SM}})^2$  as a function of the Higgs mass. The solid line represents the observed limit while the dark (light) shaded band is for the 68% (95%) probability band; from Ref. [10].

Higgs bosons with SM couplings to the Z boson have been searched for in various decay modes, such as invisible [93] and flavor blind hadronic decays [94] by considering the recoil of the Z boson in the process  $e^+e^- \rightarrow H(Z^* \rightarrow \ell^+\ell^-)$  for instance; Higgs masses close to the  $M_H \sim 114$  GeV bound have been ruled out. The bound  $M_H \gtrsim 114.4$  GeV can be evaded only if the Higgs boson has non-standard couplings to the Z boson. Indeed a smaller value of the  $g_{HZZ}$  coupling compared to the SM prediction would suppress the  $e^+e^- \rightarrow HZ$  cross section which is directly proportional to  $g_{HZZ}^2$ . The 95% CL bound on the Higgs boson mass as a function of its coupling relative to the SM value,  $\xi = g_{HZZ}/g_{HZZ}^{\text{SM}}$  is shown in Fig. 1.9 (right). For masses below  $M_H \lesssim 80$  GeV, Higgs bosons with couplings to the Z boson having an order of magnitude smaller than that in the SM have thus also been ruled out [10].

Fig. 1.10. Some Feynman diagrams for the scattering of  $W$  bosons at high energy.

#### 1.4. Theoretical constraints on the Higgs boson mass

In addition to the experimental constraints on the Higgs boson mass discussed previously, there are interesting theoretical constraints which can be derived from assumptions on the energy range in which the SM is valid before perturbation theory breaks down and new phenomena should emerge. These include constraints from unitarity in scattering amplitudes, perturbativity of the Higgs self-coupling, stability of the electroweak vacuum and fine tuning. These constraints are summarized in this section.

##### 1.4.1. Constraints from unitarity

One of the main arguments to abandon the old Fermi theory for the weak interaction was that it violates unitarity at energies close to the Fermi scale. Indeed, taking for instance the reaction  $\nu_\mu e \rightarrow \nu_e \mu$  [which, in principle, proceeds through the  $t$ -channel exchange of a  $W$  boson and has only the  $J = 1$  partial wave], the cross section at a high-energy  $\sqrt{s}$  behaves like  $\sigma \sim G_\mu^{-1/2} s$ . However, unitarity requires that the cross section should be bounded by  $s^{-1}$  and for energies above  $\sqrt{s} \sim G_\mu^{-1/2} \sim 300$  GeV, the cross section will violate unitarity. This particular problem was cured in the intermediate massive vector boson theory [in which the  $W$  mass is included by hand] but in other processes, such as  $\nu\bar{\nu} \rightarrow W^+W^-$  through the  $t$ -channel  $e$  exchange, the amplitude had also a bad high-energy behavior which called for the introduction of the neutral  $Z$  boson to be exchanged in the  $s$ -channel to cancel it. In fact, if one demands that there is no such process which violates unitarity, one would end up with just the renormalizable Lagrangian of the SM discussed in Section 1.1; see Ref. [7].

However, there is still a potential problem in the SM, but at much higher energies than the Fermi scale. As discussed in Section 1.1.3, the interactions of  $W_L$ ,  $Z_L$  grow with their momenta and in processes involving these states, it would eventually lead to cross sections that increase with the energy which would then violate unitarity at some stage. We briefly discuss this aspect, taking as an example the scattering process  $W^+W^- \rightarrow W^+W^-$  at high energies [31,68,95]; for a detailed discussion, see Ref. [96] for instance. Some contributing Feynman diagrams to this process are displayed in Fig. 1.10; there are also additional diagrams involving the  $s$ - and  $t$ -channel exchanges of  $\gamma$  and  $Z$  bosons.

To derive the amplitude for the scattering of  $W$  bosons in the high-energy limit  $s \gg M_W^2$  and for heavy Higgs bosons, one recalls that in this regime one can concentrate on longitudinal  $W$  bosons which are equivalent to the would-be-Goldstone bosons. One can then use the potential of Eq. (1.40) which gives the  $w^0$ ,  $w^\pm$  interactions and write in a very simple way the three individual amplitudes for the scattering of the  $W_L$  bosons

$$A(w^+w^- \rightarrow w^+w^-) = - \left[ 2 \frac{M_H^2}{v^2} + \left( \frac{M_H^2}{v} \right)^2 \frac{1}{s - M_H^2} + \left( \frac{M_H^2}{v} \right)^2 \frac{1}{t - M_H^2} \right] \quad (1.94)$$

where  $s, t$  are the Mandelstam variables.

These amplitudes will lead to cross sections  $\sigma(W^+W^- \rightarrow W^+W^-) \simeq \sigma(w^+w^- \rightarrow w^+w^-)$  which could violate their unitarity bounds. To see this explicitly, one can decompose the scattering amplitude  $A$  into partial waves  $a_\ell$  of orbital angular momentum  $\ell$  and use the optical theorem which tells us also that the cross section is proportional to the imaginary part of the amplitude in the forward direction. One has then the identity

$$\sigma = \frac{1}{s} \text{Im}[A(\theta = 0)] = \frac{16\pi}{s} \sum_{\ell=0}^{\infty} (2\ell + 1) |a_\ell|^2. \quad (1.95)$$

This leads to the unitary conditions [97]

$$|a_\ell|^2 = \text{Im}(a_\ell) \Rightarrow [\text{Re}(a_\ell)]^2 + [\text{Im}(a_\ell) - \frac{1}{2}]^2 = \frac{1}{4} \quad (1.96)$$

which is simply the equation of a circle of radius  $\frac{1}{2}$  and center  $(0, \frac{1}{2})$  in the plane  $[\text{Re}(a_\ell), \text{Im}(a_\ell)]$ . The real part lies between  $-\frac{1}{2}$  and  $\frac{1}{2}$ , leading to the unitarity condition  $|\text{Re}(a_\ell)| < \frac{1}{2}$ .

If one takes the  $J = 0$  partial wave for the amplitude  $A(w^+w^- \rightarrow w^+w^-)$

$$a_0 = \frac{1}{16\pi s} \int_s^0 dt |A| = -\frac{M_H^2}{16\pi v^2} \left[ 2 + \frac{M_H^2}{s - M_H^2} - \frac{M_H^2}{s} \log \left( 1 + \frac{s}{M_H^2} \right) \right] \quad (1.97)$$

and assumes the Higgs boson mass to be much smaller than  $\sqrt{s}$ , which leads to

$$a_0 \xrightarrow{s \gg M_H^2} -\frac{M_H^2}{8\pi v^2}. \quad (1.98)$$

From the requirement of the unitarity condition above, one obtains the upper bound [32]

$$M_H \lesssim 870 \text{ GeV}. \quad (1.99)$$

In fact the scattering channel  $W_L^+ W_L^-$  considered above can be coupled with other channels:  $Z_L Z_L$ ,  $HH$  and  $Z_L H$  [for a recent discussion, see Ref. [98] e.g.]. In addition to the four neutral particle initial states, one can also consider the two charged channels  $W_L^+ H$  and  $W_L^+ Z_L$  which, because of charge conservation, are not coupled to the neutral ones. The scattering amplitude is then given by a  $6 \times 6$  matrix which is diagonal by block: a  $4 \times 4$  block for the neutral channels and a  $2 \times 2$  block for the charged channels. The requirement that the largest eigenvalues of  $a_0$ , respects the unitarity constraint yields [99]

$$M_H \lesssim 710 \text{ GeV}. \quad (1.100)$$

Thus, in the SM, if the Higgs boson mass exceeds values of  $\mathcal{O}(700 \text{ GeV})$ , unitarity will be violated unless new phenomena appear and restore it. There is, however, a caveat to this conclusion. The analysis above has been performed only at tree level and since the Higgs boson self-coupling becomes strong for large masses,  $\lambda = M_H^2/(2v^2)$ , the radiative corrections can be very large and, eventually, render the theory non-perturbative; this tree-level result would be then lost. Thus, to apply the previous argument to set a bound on the Higgs boson mass, one has to assume that the SM remains perturbative and that higher-order corrections are not large. The unitarity argument should therefore more properly be called, the tree-level unitarity or perturbative unitarity argument.

In fact, the unitarity argument is more rigorous and robust in the opposite limit [31] where one assumes the Higgs boson mass to be much larger than  $\sqrt{s}$  [which in turn, is much larger than  $M_W$ ]. In this case, the unitarity constraint writes, if one takes into account only the  $W_L^+ W_L^- \rightarrow W_L^+ W_L^-$  channel,

$$a_0 \xrightarrow{s \ll M_H^2} -\frac{s}{32\pi v^2} \quad (1.101)$$

and is valid to all orders in the Higgs self-coupling and which receives only small corrections from the gauge couplings. With the unitarity condition  $|\text{Re}(a_0)| < \frac{1}{2}$ , one then obtains

$$\sqrt{s} \lesssim 1.7 \text{ TeV}. \quad (1.102)$$

Again, a more stringent bound is obtained by considering all the coupled channels above

$$\sqrt{s} \lesssim 1.2 \text{ TeV}. \quad (1.103)$$

This means that if the Higgs boson is too heavy [or, equivalently, not existing at all], some New Physics beyond the SM should manifest itself at energies in the TeV range to restore unitarity in the scattering amplitudes of longitudinal gauge bosons.

Therefore, from the requirement that the tree-level contributions to the partial waves of scattering processes involving gauge and Higgs bosons should not exceed the unitarity bound, one concludes that either: (i) some New Physics, which plays a role similar to that of the Higgs particle should appear in the TeV range to cancel this breakdown, or (ii) the unitarity breakdown is canceled by high-order terms which signal the failure of perturbation theory and the loss of the predictive power of the SM.

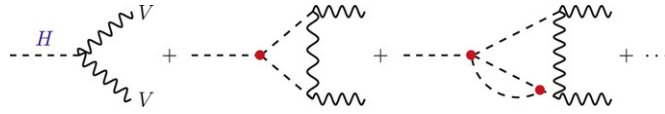


Fig. 1.11. Generic diagrams for the one- and two-loop corrections to Higgs boson decays.

#### 1.4.2. Constraints from perturbativity in processes involving the Higgs boson

It is a known fact that for large values of the Higgs boson mass, perturbation theory is jeopardized in the SM. This occurs for instance in the decays of the Higgs boson into massive gauge bosons, which will be discussed later in detail. Using the equivalence theorem and the Lagrangian equation (1.40), one can write immediately the partial decay width of the Higgs boson into two longitudinal Z bosons [or W bosons]

$$\Gamma(H \rightarrow ZZ) \sim \Gamma(H \rightarrow w_0 w_0) = \left( \frac{1}{2M_H} \right) \left( \frac{2! M_H^2}{2v} \right)^2 \frac{1}{2} \left( \frac{1}{8\pi} \right) \rightarrow \frac{M_H^3}{32\pi v^2} \quad (1.104)$$

where the first parenthesis is for the flux factor, the second for the amplitude squared, the factor  $\frac{1}{2}$  is for the two identical final particles, and the last parenthesis is for the phase-space factor. For the decay  $H \rightarrow WW$ , one simply needs to remove the statistical factor to account for both  $W^\pm$  states,  $\Gamma(H \rightarrow W^+W^-) \simeq 2\Gamma(H \rightarrow ZZ)$ . The behavior,  $\Gamma_H \propto M_H^3$ , compared to  $\Gamma_H \propto M_H$  for decays into fermions for instance, is due to the longitudinal components that grow with the energy [which is  $M_H$  in this context].

Let us have a brief look at these decays when higher-order radiative corrections, involving the Higgs boson and therefore the quartic coupling  $\lambda$ , are taken into account. Including the one-loop and two-loop radiative corrections, with some generic Feynman diagrams shown in Fig. 1.11, the partial Higgs decay width into gauge bosons is given by [99,100]

$$\Gamma_{\text{tot}} \simeq \Gamma_{\text{Born}} \left[ 1 + 3\hat{\lambda} + 62\hat{\lambda}^2 + \mathcal{O}(\hat{\lambda}^3) \right] \quad (1.105)$$

with  $\hat{\lambda} = \lambda/(16\pi^2)$ . If the Higgs boson mass is very large,  $M_H \sim \mathcal{O}(10 \text{ TeV})$ , the one-loop term becomes close to the Born term,  $3\hat{\lambda} \sim 1$ , and the perturbative series is therefore not convergent. Even worse, already for a Higgs boson mass in the TeV range,  $M_H \sim \mathcal{O}(1 \text{ TeV})$ , the two-loop contribution becomes as important as the one-loop contribution,  $3\hat{\lambda} \sim 62\hat{\lambda}^2$ . Hence, for perturbation theory to hold,  $M_H$  should be smaller than about 1 TeV.

In addition, the partial decay widths become extremely large for a very heavy Higgs particle. Indeed, taking into account only W and Z decay modes, the total width is

$$\Gamma(H \rightarrow WW + ZZ) \sim 500 \text{ GeV} (M_H/1 \text{ TeV})^3 \quad (1.106)$$

and for a mass  $M_H \sim 1.3 \text{ TeV}$ , the total decay width becomes comparable to the mass: the Higgs boson is then “obese” and cannot be considered as a “true” resonance anymore.

The same exercise can be made in the case of the Higgs decays into fermions. Including the one- and two-loop corrections involving the quartic interaction, one obtains [68,101]

$$\Gamma_{\text{tot}} \simeq \Gamma_{\text{Born}} \left[ 1 + 2\hat{\lambda} - 32\hat{\lambda}^2 + \mathcal{O}(\hat{\lambda}^3) \right]. \quad (1.107)$$

Qualitatively, the situation is the same as that for the decays into gauge bosons, although the breakdown of perturbation theory is delayed because of the smaller coefficients of the one- and two-loop corrections. These features will be discussed in the chapter on Higgs decays.

The jeopardy of perturbation theory at large Higgs masses can also be seen in the scattering of longitudinal gauge bosons from which we have previously derived the upper bound on  $M_H$  from perturbative unitarity. In the case of the  $W_L^+ W_L^- \rightarrow W_L^+ W_L^-$  scattering, the radiative corrections have been calculated at one and two loops in Refs. [102, 103] where it has been found that at high energy, the amplitude depends on the considered energy, contrary to what was occurring in the tree-level case discussed previously. However, applying Renormalization Group methods, one can absorb the logarithmic energy dependence by defining a running self-coupling  $\lambda$  at the energy scale  $\sqrt{s}$  [see next subsection]. At two-loop order, one then finds for the  $W_L^+ W_L^- \rightarrow W_L^+ W_L^-$  scattering cross section at very high

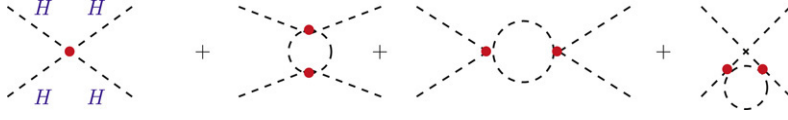


Fig. 1.12. Typical Feynman diagrams for the tree level and one-loop Higgs self-coupling.

energies [103]

$$\sigma(W_L^+ W_L^- \rightarrow W_L^+ W_L^-) \sim \frac{1}{s} \hat{\lambda}(s) \left(1 - 48.64 \hat{\lambda} + 333.21 \hat{\lambda}^2\right). \quad (1.108)$$

Here, the coefficients of the corrections are much larger than that in Higgs decays and in fact, the one-loop correction becomes of order unity already for  $\lambda(s)$  values close to 3.

Using various criteria, such as the scheme and scale dependence of the amplitudes, to estimate at which stage the breakdown of perturbation theory occurs [104] and a comparison with non-perturbative calculations on the lattice [97], one arrives at the conclusion that the perturbation theory is lost for Higgs boson masses above  $M_H \sim 700$  GeV. This result is remarkably close to what has been obtained by simply using the [somewhat naive] perturbative unitarity argument.

#### 1.4.3. Triviality and stability bounds

As seen in previous discussions, because of quantum corrections, the couplings as well as the masses which appear in the SM Lagrangian, depend on the considered energy. This is also the case for the quartic Higgs coupling which will be monotonically increasing with the energy scale  $|Q|$ . This leads to non-trivial constraints on this coupling and, hence, on the Higgs boson mass, that we summarize in this subsection.

**1.4.3.1. The triviality bound.** Let us have a look at the one-loop radiative corrections to the Higgs boson quartic coupling, taking into account for the present moment only the contributions of the Higgs boson itself. The Feynman diagrams for the tree level and the one-loop corrections to the Higgs boson self-coupling are depicted in Fig. 1.12.

The variation of the quartic Higgs coupling with the energy scale  $Q$  is described by the Renormalization Group Equation (RGE) [105]

$$\frac{d}{dQ^2} \lambda(Q^2) = \frac{3}{4\pi^2} \lambda^2(Q^2) + \text{higher orders}. \quad (1.109)$$

The solution of this equation, choosing the natural reference energy point to be the electroweak symmetry breaking scale,  $Q_0 = v$ , reads at one loop

$$\lambda(Q^2) = \lambda(v^2) \left[ 1 - \frac{3}{4\pi^2} \lambda(v^2) \log \frac{Q^2}{v^2} \right]^{-1}. \quad (1.110)$$

The quartic couplings vary logarithmically with the squared energy  $Q^2$ . If the energy is much smaller than the electroweak breaking scale,  $Q^2 \ll v^2$ , the quartic coupling becomes extremely small and eventually vanishes,  $\lambda(Q^2) \sim \lambda(v^2)/\log(\infty) \rightarrow 0_+$ . It is said that the theory is trivial, i.e. non-interacting since the coupling is zero [106].

In the opposite limit, when the energy is much higher than weak scale,  $Q^2 \gg v^2$ , the quartic coupling grows and eventually becomes infinite,  $\lambda(Q^2) \sim \lambda(v^2)/(1 - 1) \gg 1$ . The point, called the Landau pole, where the coupling becomes infinite is at the energy

$$\Lambda_C = v \exp \left( \frac{4\pi^2}{3\lambda} \right) = v \exp \left( \frac{4\pi^2 v^2}{M_H^2} \right). \quad (1.111)$$

The general triviality argument [97,107] states that the scalar sector of the SM is a  $\phi^4$ -theory, and for these theories to remain perturbative at all scales one needs to have a coupling  $\lambda = 0$  [which in the SM, means that the Higgs boson is massless], thus rendering the theory trivial, i.e. non-interacting. However, one can view this argument in a different way: one can use the RGE for the quartic Higgs self-coupling to establish the energy domain in which the SM is valid,



Fig. 1.13. Diagrams for the one-loop contributions of fermions and gauge bosons to  $\lambda$ .

i.e. the energy cut-off  $\Lambda_C$  below which the self-coupling  $\lambda$  remains finite. In this case, and as can be seen from the previous equation, if  $\Lambda_C$  is large, the Higgs mass should be small to avoid the Landau pole; for instance for the value  $\Lambda_C \sim 10^{16}$  GeV, one needs a rather light Higgs boson,  $M_H \lesssim 200$  GeV. In turn, if the cut-off  $\Lambda_C$  is small, the Higgs boson mass can be rather large and for  $\Lambda_C \sim 10^3$  GeV for instance, the Higgs mass is allowed to be of the order of 1 TeV.

In particular, if the cut-off is set at the Higgs boson mass itself,  $\Lambda_C = M_H$ , the requirement that the quartic coupling remains finite implies that  $M_H \lesssim 700$  GeV. But again, there is a caveat in this argument: when  $\lambda$  is too large, one cannot use the perturbation theory anymore and this constraint is lost. However, from simulations of gauge theories on the lattice, where the non-perturbative effects are properly taken into account, it turns out that one obtains the rigorous bound  $M_H < 640$  GeV [108], which is in remarkable agreement with the bound obtained by naively using the perturbation theory.

**1.4.3.2. The stability bound.** In the preceding discussion, only the contribution of the Higgs boson itself has been included in the running of the quartic coupling  $\lambda$ . This is justified in the regime where  $\lambda$  is rather large. However, to be complete, one needs to also include the contributions from fermions and gauge bosons in the running. Since the Higgs boson couplings are proportional to the particle masses, only the contribution of top quarks and massive gauge bosons need to be considered. Some generic Feynman diagrams for these additional contributions are depicted in Fig. 1.13.

The one-loop RGE for the quartic coupling, including the fermion and gauge boson contributions, becomes [105]

$$\frac{d\lambda}{d\log Q^2} \simeq \frac{1}{16\pi^2} \left[ 12\lambda^2 + 6\lambda\lambda_t^2 - 3\lambda_t^4 - \frac{3}{2}\lambda(3g_2^2 + g_1^2) + \frac{3}{16}(2g_2^4 + (g_2^2 + g_1^2)^2) \right] \quad (1.112)$$

where the top quark Yukawa coupling is given by  $\lambda_t = \sqrt{2}m_t/v$ . The first effect of this extension is that for not too large  $\lambda$  values, the additional contributions will slightly alter the triviality bounds. In particular, the scale at which the New Physics should appear will depend on the precise value of the top quark mass.

However, it is for small values of the quartic couplings that the additional contributions can have a large impact and give some new information. Indeed, for  $\lambda \ll \lambda_t, g_1, g_2$ , the solution of the RGE, taking again the weak scale as the reference point, is given by

$$\lambda(Q^2) = \lambda(v^2) + \frac{1}{16\pi^2} \left[ -12\frac{m_t^4}{v^4} + \frac{3}{16}(2g_2^4 + (g_2^2 + g_1^2)^2) \right] \log \frac{Q^2}{v^2}. \quad (1.113)$$

If the coupling  $\lambda$  is too small, the top quark contribution can be dominant and could drive it to a negative value  $\lambda(Q^2) < 0$ , leading to a scalar potential  $V(Q^2) < V(v)$ . The vacuum is not stable anymore since it has no minimum. The stability argument [109–111] tells us that to have a scalar potential which is bounded from below and, therefore, to keep  $\lambda(Q^2) > 0$ , the Higgs boson mass should be larger than the value

$$M_H^2 > \frac{v^2}{8\pi^2} \left[ -12\frac{m_t^4}{v^4} + \frac{3}{16}(2g_2^4 + (g_2^2 + g_1^2)^2) \right] \log \frac{Q^2}{v^2}. \quad (1.114)$$

This puts a strong constraint on the Higgs boson mass, which depends on the value of the cut-off  $\Lambda_C$ . For relatively low and very high values for this cut-off, one obtains

$$\begin{aligned} \Lambda_C \sim 10^3 \text{ GeV} &\Rightarrow M_H \gtrsim 70 \text{ GeV} \\ \Lambda_C \sim 10^{16} \text{ GeV} &\Rightarrow M_H \gtrsim 130 \text{ GeV}. \end{aligned} \quad (1.115)$$

Note, however, that the stability bound on the New Physics scale can be relaxed if the vacuum is metastable as discussed in Ref. [112]. Indeed, the SM effective potential can have a minimum which is deeper than the standard



electroweak minimum if the decay of the latter into the former, via thermal fluctuations in the hot universe or quantum fluctuations at zero temperature, is suppressed. In this case, a lower bound on the Higgs mass follows from the requirement that no transition between the two vacua occurs and we always remain in the electroweak minimum. The obtained bound on  $M_H$  is in general much weaker than that in the case of absolute stability of the vacuum and even disappears if the cut-off of the theory is at the TeV scale.<sup>13</sup>

In fact, in Ref. [113], it has been advocated that the SM scalar potential, besides the usual minimum with  $v = 246$  GeV, could have another minimum with a vev close to the Planck scale. Imposing the condition that our vacuum is metastable, allows one to predict the top quark and Higgs boson masses to be  $m_t = 173$  GeV and  $M_H = 122$  GeV with small errors; see Ref [113] for more details.

Finally, let us note that in Ref. [114], it has been shown using Wilsonian Renormalization Group equations that this instability, which would have generated a convex effective potential contradicting general theorems, is only apparent and is simply due to an extrapolation of the potential to regions in which it is not valid. Imposing the convexity of the effective potential allows one to derive a lower bound on the Higgs mass as a function of the cut-off  $\Lambda_C$  which is very close to the usual stability bound. As a by-product of the analysis, the possibility of a metastable vacuum is ruled out.

**1.4.3.3. Higher-order effects and combined triviality and stability bounds.** Thus, the positivity and the finiteness of the self-coupling  $\lambda$  impose, respectively, a lower bound  $M_H \gtrsim 70$  GeV and an upper bound  $M_H \lesssim 1$  TeV, on the SM Higgs boson mass if the cut-off is set to  $\mathcal{O}(1 \text{ TeV})$ . These bounds are only approximative and to have more precise ones, some refinements must, however, be included [110,115,116].

Since the  $\beta$  functions of all SM couplings have been calculated up to two loops, they can be included in the analysis. For the scalar sector for instance, one has at this order

$$\frac{d\lambda}{d \log Q^2} \equiv \beta_\lambda = 24 \frac{\lambda^2}{(16\pi^2)} - 312 \frac{\lambda^3}{(16\pi^2)^2}. \quad (1.116)$$

While, at one loop, the  $\lambda(\mu)$  coupling monotonically increases with the scale  $\mu$  until it becomes infinite when reaching the Landau pole at the scale  $\Lambda_C$ , at the two-loop level, it approaches an ultraviolet fixed point corresponding to  $\beta_\lambda = 0$ . From the previous equation at the two loop, the resulting fixed-point value is  $\lambda_{\text{FP}} = 16\pi^2 \times 24/312 \simeq 12.1$  [however, top contributions cannot be neglected and they modify the behavior of this fixed point.]

To obtain the upper bound on  $M_H$ , we need to choose the cut-off value for  $\lambda$ . Since  $\lambda_{\text{FP}}$  is large and the perturbation theory is lost even before reaching this value, one can choose a value smaller than  $\lambda_{\text{FP}}$  as being this cut-off. An estimate of the stability of the bound can be made by varying the cut-off value for instance between  $\lambda_{\text{FP}}/4$  and  $\lambda_{\text{FP}}/2$ , which leads to two-loop corrections which are about, respectively, 25% and 50%, of the one-loop result. Therefore, one can consider the first value as leading to a well-behaved perturbative series and the second value as being at the limit where the perturbation theory is valid.

For the stability bound, one simply requires that the coupling remains positive at the cut-off scale,  $\lambda(\Lambda_C) > 0$ . For an accurate determination of the bound, this requirement has to be made at two-loop order including matching conditions, i.e. the precise relation between the physical gauge boson and top quark masses and their corresponding couplings.

Including the theoretical uncertainties by a variation of the cut-off  $\Lambda_C$  from  $\lambda_{\text{FP}}/2$  to  $\lambda_{\text{FP}}/4$  using the matching conditions for the top quark and Higgs boson masses, and the experimental errors mainly on  $\alpha_s = 0.118 \pm 0.002$  and  $m_t = 175 \pm 6$  GeV, one obtains [116] the modern version of the Roman plot shown in Fig. 1.14 for the stability [lower band] and triviality [upper band] constraints, which gives the allowed range of  $M_H$  as a function of the scale of New Physics  $\Lambda_C$  [between the bands]. The widths of the bands corresponds to the various experimental and theoretical errors. As can be seen, if the New Physics scale  $\Lambda_C$  is at the TeV scale, the Higgs boson mass is allowed to be in the range

$$50 \text{ GeV} \lesssim M_H \lesssim 800 \text{ GeV} \quad (1.117)$$

<sup>13</sup> Note that the first argument, i.e. thermal fluctuations, relies on several cosmological assumptions such as that the universe went through a phase of very high temperature, which has been indirectly tested so far only for temperatures of the order of a few MeV. The second argument, quantum tunneling, where the only cosmological input is the knowledge of the age of the universe which should be larger than the lifetime of the instability of the vacuum, gives less severe bounds; see Ref. [111] for instance.



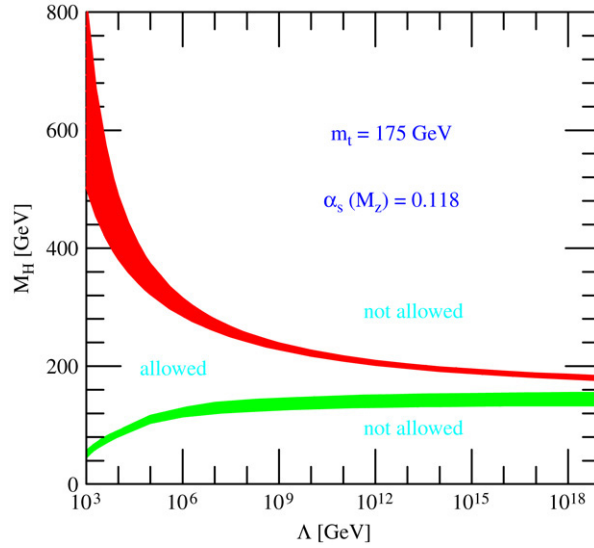


Fig. 1.14. The triviality (upper) bound and the vacuum stability (lower) bound on the Higgs boson mass as functions of the New Physics or cut-off scale  $\Lambda$  for a top quark mass  $m_t = 175 \pm 6$  GeV and  $\alpha_s(M_Z) = 0.118 \pm 0.002$ ; the allowed region lies between the bands and the colored/shaded bands illustrate the impact of various uncertainties. From Ref. [116].

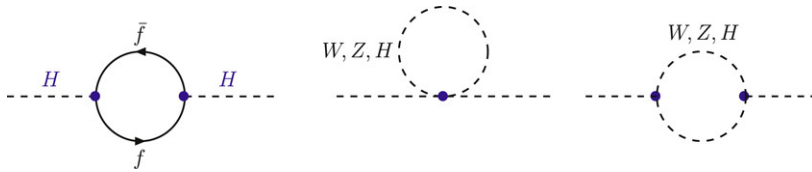


Fig. 1.15. Feynman diagrams for the one-loop corrections to the SM Higgs boson mass.

while, requiring the SM to be valid up to the Grand Unification scale,  $\Lambda_{\text{GUT}} \sim 10^{16}$  GeV, the Higgs boson mass should lie in the range

$$130 \text{ GeV} \lesssim M_H \lesssim 180 \text{ GeV}. \quad (1.118)$$

#### 1.4.4. The fine-tuning constraint

Finally, a last theoretical constraint comes from the fine-tuning problem originating from the radiative corrections to the Higgs boson mass. The Feynman diagrams contributing to the one-loop radiative corrections are depicted in Fig. 1.15 and involve Higgs boson, massive gauge boson and fermion loops.

Cutting off the loop integral momenta at a scale  $\Lambda$ , and keeping only the dominant contribution in this scale, one obtains

$$M_H^2 = (M_H^0)^2 + \frac{3\Lambda^2}{8\pi^2 v^2} \left[ M_H^2 + 2M_W^2 + M_Z^2 - 4m_t^2 \right] \quad (1.119)$$

where  $M_H^0$  is the bare mass contained in the unrenormalized Lagrangian and where we retained only the contribution of the top heavy quark for the fermion loops. This is a completely new situation in the SM: we have a quadratic divergence rather than the usual logarithmic ones. If the cut-off  $\Lambda$  is very large, for instance of the order of the Grand Unification scale  $\sim 10^{16}$  GeV, one needs a very fine arrangement of 16 digits between the bare Higgs mass and the radiative corrections to have a physical Higgs boson mass in the range of the electroweak symmetry breaking scale,

$M_H \sim 100$  GeV to 1 TeV, as is required for the consistency of the SM. This is the naturalness of the fine-tuning problem.<sup>14</sup>

However, following Veltman [117], one can note that by choosing the Higgs mass to be

$$M_H^2 = 4m_t^2 - 2M_W^2 - M_Z^2 \sim (320 \text{ GeV})^2 \quad (1.120)$$

the quadratic divergences can be canceled and this would be even a prediction for the Higgs boson mass. But the condition above was given only at the one-loop level and at higher orders, the general form of the correction to the Higgs mass squared reads [118,119]

$$\Lambda^2 \sum_{n=0}^{\infty} c_n(\lambda_i) \log^n(\Lambda/Q) \quad (1.121)$$

where  $(16\pi^2)c_0 = (3/2v^2)(M_H^2 + 2M_W^2 + M_Z^2 - 4m_t^2)^2$  and the remaining coefficients  $c_n$  can be calculated recursively from the requirement that  $M_H^2$  should not depend on the renormalization scale  $Q$ . For instance, for the two-loop coefficient, one finds [118]

$$\begin{aligned} (16\pi^2)^2 c_1 = & \lambda(114\lambda - 54g_2^2 - 18g_1^2 + 72\lambda_t)^2 + \lambda_t^2(27g_2^2 + 17g_1^2 + 96g_s^2 - 90\lambda_t^2) \\ & - \frac{15}{2}g_2^4 + \frac{25}{2}g_1^4 + \frac{9}{2}g_1^2g_2^2. \end{aligned} \quad (1.122)$$

The higher-order coefficients have more powers of  $1/(16\pi^2)$  and should therefore be more and more suppressed. The Veltman condition requires that the fine cancellation occurs to all perturbative orders, i.e. for any value of  $n$ . Given the fact that the various  $c_n$  terms of the perturbative series are independent, there is obviously no solution for  $M_H$ .

A priori, one can then conclude that the Veltman condition is not useful and cannot solve the fine-tuning problem. However, as it has been discussed in Refs. [120,121], this is only true if the scale of New Physics is extremely large. For scales not much larger than the electroweak scale, one does not need very large cancellations. For instance, at the one-loop level, the fine-tuning problem appears only if  $\Lambda \gtrsim 4\pi v \sim 2$  TeV. If the Veltman solution is by chance satisfied, then the scale  $\Lambda$  can be pushed at the two-loop level to a much higher value,  $\Lambda^2 \log \Lambda \gtrsim (16\pi^2)^2 v^2$ , that is, for  $\Lambda \sim 15$  TeV. If again the Veltman conjecture is satisfied, then the three-loop quadratic divergences start to be problematic only at a scale  $\Lambda \gtrsim 50$  TeV. One can thus have almost no, or only a small amount of fine tuning, up to rather high scales.

For such a scale, one simply needs to manage such that  $\sum_{n=0}^1 c_n(\lambda_i) \log^n(\Lambda/M_H) = 0$  at two loop. It appears that first, such a solution exists and second, that the predicted  $M_H$  value becomes cut-off dependent. As mentioned previously, this prediction assumes exact cancellation and this is not required for rather low scales  $\Lambda$ . Following again Ref. [120], a more adequate condition would be

$$\sum_{n=0}^1 c_n(\lambda_i) \log^n(\Lambda/M_H) \lesssim v^2/\Lambda^2 \quad (1.123)$$

and if it is satisfied, the fine tuning might be acceptable. But, as is well known, there is a problem with the definition of the amount of fine tuning, that is largely a subjective matter. Following again Ref. [120], one can define it as the sensitivity of the electroweak scale to the cut-off  $\Lambda$ ,  $\Delta M_W^2(\Lambda)/M_W^2$ . This leads then to the measure

$$\Delta_{\text{FT}} = \left| \frac{\Delta M_W^2}{M_W^2} \right| = \left| \frac{\Delta M_H^2}{M_H^2} \right| = \frac{2\Lambda^2}{M_H^2} \left| \sum_n c_n \log^n(\Lambda/M_H) \right|. \quad (1.124)$$

For a given value of  $\Delta_{\text{FT}}$ , the weak scale is fine-tuned to one part in  $\Delta_{\text{FT}}$ : the larger than unity is the value of  $\Delta_{\text{FT}}$ , the more fine tuning we have and there is no fine tuning if  $\Delta_{\text{FT}} \leq 1$ . One can see from the previous equation that the fine tuning is large not only when  $\Lambda$  increases but also when the Higgs boson is light.

<sup>14</sup> Note, however that the SM is a renormalizable theory and this cancellation can occur in a mathematically consistent way by choosing a similarly divergent counterterm. Nevertheless, one would like to give a physical meaning to this scale  $\Lambda$  and view it as the scale up to which the SM is valid.

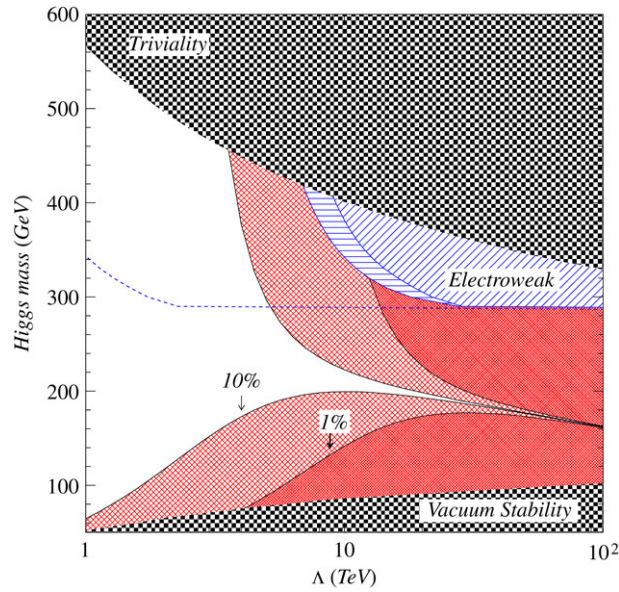


Fig. 1.16. The contours for the fine-tuning parameter  $\Delta_{\text{FT}}$  in the plane  $(M_H, \Lambda)$ . The dark (light) hatched region marked “1%” (“10%”) represents fine tunings of greater than 1 part in 100 (10). The constraints from triviality, stability and electroweak precision data are also shown. The empty region is consistent with all constraints and has  $\Delta_{\text{FT}}$  less than 10%. From Ref. [120].

The Higgs boson mass is shown in Fig. 1.16 as a function of the maximal value of the cut-off scale  $\Lambda$ . Also shown, are the regions not allowed by the triviality and stability bounds on  $M_H$ , as well as the (“electroweak”) area ruled out by high-precision measurements.<sup>15</sup> The regions of fine tuning less than 10 and 100 are given, respectively, by the light and dark hatched regions. The white region corresponds to the one where all constraints are fulfilled and where the Veltman condition is approximately satisfied.

For low values of the scale,  $\Lambda \lesssim 1$  TeV, there is no fine-tuning problem for any reasonable Higgs boson mass value. But as  $\Lambda$  increases, the range of Higgs masses where the fine tuning is smaller than 10% or 1% becomes narrow. For instance, with  $\Lambda \sim 3$  TeV, the Higgs boson mass must be above  $\sim 150$  GeV while with  $\Lambda \sim 10$  TeV, only a narrow range around  $M_H \sim 200$  GeV for  $\Delta_{\text{FT}} = 10$ , sometimes called the Veltman throat, is allowed. For even higher scales, only the line with  $M_H \sim 200$  GeV, where the Veltman condition is approximately satisfied, survives.

Thus, one can obtain a very useful information by considering the fine-tuning problem in the SM at scales of a few tens of TeV. In the vicinity of these scales, a Higgs boson with a mass  $M_H \sim 200$  GeV can still allow for an acceptable amount of fine tuning.

## 2. Decays of the SM Higgs boson

In the Standard Model, once the Higgs mass is fixed, the profile of the Higgs particle is uniquely determined. The Higgs couplings to gauge bosons and fermions are directly proportional to the masses of the particles and the Higgs boson will have the tendency to decay into the heaviest ones allowed by phase space. Since the pole masses of the gauge bosons and fermions are known [the electron and light quark masses are too small to be relevant]

$$\begin{aligned} M_Z &= 91.187 \text{ GeV}, & M_W &= 80.425 \text{ GeV}, & m_\tau &= 1.777 \text{ GeV}, & m_\mu &= 0.106 \text{ GeV}, \\ m_t &= 171.4 \pm 2 \text{ GeV}, & m_b &= 4.88 \pm 0.07 \text{ GeV}, & m_c &= 1.64 \pm 0.07 \text{ GeV}, \end{aligned} \quad (2.1)$$

all the partial widths for the Higgs decays into these particles can be predicted.

<sup>15</sup> More details on how these constraints have been obtained can be found in Ref. [120].

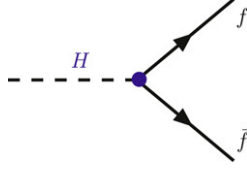


Fig. 2.1. The Feynman diagram for the Higgs boson decays into fermions.

The decay widths into massive gauge bosons  $V = W, Z$  are directly proportional to the  $HVV$  couplings, which in the SM are given in terms of the fields by

$$\mathcal{L}(HVV) = \left(\sqrt{2}G_\mu\right)^{1/2} M_V^2 H V^\mu V_\mu. \quad (2.2)$$

These are S-wave couplings and even so under parity and charge conjugation, corresponding to the  $J^{\text{PC}} = 0^{++}$  assignment of the Higgs spin and parity quantum numbers. The decay widths into fermions are proportional to the  $Hf\bar{f}$  couplings which are of the scalar type

$$g_{H\bar{f}f} \propto \frac{m_f}{v} = (\sqrt{2}G_\mu)^{1/2} m_f. \quad (2.3)$$

In this section, we will discuss all the decay modes of the SM Higgs boson: decays into quarks and leptons, into real or virtual gauge bosons and loop induced decays into photons [including  $Z\gamma$  final states] and gluons, and summarize the important QCD and electroweak radiative corrections to these processes.

The  $J^{\text{PC}} = 0^{++}$  quantum numbers of the SM Higgs particle lead also to unique predictions for the angular and energy distributions of the partial decay widths. Whenever possible, we will confront these properties with those of an hypothetical CP-odd Higgs particle,<sup>16</sup> that we will denote by  $A$ , and which is predicted in many extensions of the SM. In this case, the Higgs coupling to vector gauge bosons is a P-wave coupling corresponding to the  $J^{\text{PC}} = 0^{+-}$  assignment and, if CP symmetry is conserved, does not occur at the tree level and is only induced by higher loop effects. With  $\eta$  being a dimensionless factor, the effective point-like coupling can be written as

$$\mathcal{L}(AVV) = \frac{1}{4}\eta \left(\sqrt{2}G_\mu\right)^{1/2} M_V^2 A V^{\mu\nu} \tilde{V}_{\mu\nu}, \quad \tilde{V}^{\mu\nu} = \epsilon^{\mu\nu\rho\sigma} V_{\rho\sigma}. \quad (2.4)$$

In the presence of fermions, the couplings of the  $A$  boson are of the pseudoscalar type

$$g_{A\bar{f}f} \propto \frac{m_f}{v} \gamma_5 = (\sqrt{2}G_\mu)^{1/2} m_f \gamma_5. \quad (2.5)$$

## 2.1. Decays to quarks and leptons

### 2.1.1. The Born approximation

In the Born approximation, the partial width of the Higgs boson decays into fermion pairs, Fig. 2.1, is given by [89, 126]

$$\Gamma_{\text{Born}}(H \rightarrow f\bar{f}) = \frac{G_\mu N_c}{4\sqrt{2}\pi} M_H m_f^2 \beta_f^3 \quad (2.6)$$

with  $\beta = (1 - 4m_f^2/M_H^2)^{1/2}$  being the velocity of the fermions in the final state and  $N_c$  the color factor  $N_c = 3$  (1) for quarks (leptons). In the lepton case, only decays into  $\tau^+\tau^-$  pairs and, to a much lesser extent, decays into muon pairs are relevant.

The partial decay widths exhibit a strong suppression near threshold,  $\Gamma(H \rightarrow f\bar{f}) \sim \beta_f^3 \rightarrow 0$  for  $M_H \simeq 2m_f$ . This is typical for the decay of a Higgs particle with a scalar coupling equation (2.3). If the Higgs boson were a

<sup>16</sup> The decays of the Higgs bosons [77,78] in the general case of anomalous Higgs couplings have been discussed in Refs. [122–124] and more details will be given in Ref. [125].

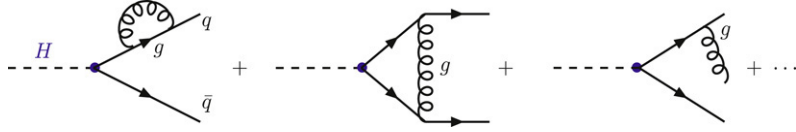


Fig. 2.2. Generic diagrams for the one-loop QCD corrections to Higgs decays into quarks.

pseudoscalar  $A$  boson with couplings given in Eq. (2.5), the partial decay width would have been suppressed only by a factor  $\beta_f$  [127]

$$\Gamma_{\text{Born}}(A \rightarrow f \bar{f}) = \frac{G_\mu N_c}{4\sqrt{2}\pi} M_H m_f^2 \beta_f. \quad (2.7)$$

More generally, and to anticipate the discussions that we will have on the Higgs CP-properties, for a  $\Phi$  boson with mixed CP-even and CP-odd couplings  $g_{\Phi \bar{f} f} \propto a + ib\gamma_5$ , the differential rate for the fermionic decay  $\Phi(p_+) \rightarrow f(p, s) \bar{f}(\bar{p}, \bar{s})$  where  $s$  and  $\bar{s}$  denote the polarization vectors of the fermions and the four momenta are such that  $p_\pm = p \pm \bar{p}$ , is given by [see Ref. [128] for instance]

$$\begin{aligned} \frac{d\Gamma}{d\Omega}(s, \bar{s}) = & \frac{\beta_f}{64\pi^2 M_\Phi} \left[ (|a|^2 + |b|^2) \left( \frac{1}{2} M_\Phi^2 - m_f^2 + m_f^2 s \cdot \bar{s} \right) \right. \\ & + (|a|^2 - |b|^2) \left( p_+ \cdot s p_+ \cdot \bar{s} - \frac{1}{2} M_\Phi^2 s \cdot \bar{s} + m_f^2 s \cdot \bar{s} - m_f^2 \right) \\ & \left. - \text{Re}(ab^*) \epsilon_{\mu\nu\rho\sigma} p_+^\mu p_-^\nu s^\rho \bar{s}^\sigma - 2\text{Im}(ab^*) m_f p_+ \cdot (s + \bar{s}) \right]. \end{aligned} \quad (2.8)$$

The terms proportional to  $\text{Re}(ab^*)$  and  $\text{Im}(ab^*)$  represent the CP-violating part of the couplings. Averaging over the polarizations of the two fermions, these two terms disappear and we are left with the two contributions  $\propto \frac{1}{2}|a|^2(M_\Phi^2 - 2m_f^2 - 2m_f^2)$  and  $\propto \frac{1}{2}|b|^2(M_\Phi^2 - 2m_f^2 + 2m_f^2)$  which reproduce the  $\beta_f^3$  and  $\beta_f$  threshold behaviors of the pure CP-even ( $b = 0$ ) and CP-odd ( $a = 0$ ) states noted above.

### 2.1.2. Decays into light quarks and QCD corrections

In the case of the hadronic decays of the Higgs boson, the QCD corrections turn out to be quite large and, therefore, must be included. At the one-loop level, the Feynman diagrams for the corrections are shown in Fig. 2.2: one has to include gluon exchange [which multiplies the Born term] and the emission of a gluon in the final state [which has to be squared and added to the former]. In the limit where  $M_H$  is much larger than the quark masses,  $M_H \gg 2m_f$ , one obtains for the next-to-leading-order (NLO) decay width [the quark mass is kept only in the Yukawa coupling and in the leading logarithmic term] [129,130]

$$\Gamma_{\text{NLO}}(H \rightarrow q \bar{q}) \simeq \frac{3G_\mu}{4\sqrt{2}\pi} M_H m_q^2 \left[ 1 + \frac{4}{3} \frac{\alpha_s}{\pi} \left( \frac{9}{4} + \frac{3}{2} \log \frac{m_q^2}{M_H^2} \right) \right]. \quad (2.9)$$

As can be seen, there is a large logarithmic  $\log(m_q/M_H)$  contribution which, for very light quarks, might render the partial decay width very small and even drive it to negative values [a definitely not physical situation]. However, these large logarithms can be absorbed in the redefinition of the quark masses: by using the running quark masses in the  $\overline{\text{MS}}$  scheme at the scale of the Higgs mass, as discussed in Section 1.1.4, these logarithms are summed to all orders in the strong interaction coupling constant [129].

Including the  $\mathcal{O}(\alpha_s^2)$  [49] and  $\mathcal{O}(\alpha_s^3)$  [131] QCD radiative corrections, the partial Higgs decay widths into light quarks can be then written as

$$\Gamma(H \rightarrow q \bar{q}) = \frac{3G_\mu}{4\sqrt{2}\pi} M_H \bar{m}_q^2(M_H) \left[ 1 + \Delta_{qq} + \Delta_H^2 \right] \quad (2.10)$$

with the running quark mass  $\bar{m}_q(M_H)$  and the strong coupling constant  $\bar{\alpha}_s \equiv \alpha_s(M_H^2)$  both defined at the scale  $M_H$ . In the  $\overline{\text{MS}}$  renormalization scheme, with  $N_f$  the number of light quark flavors, one has for the QCD correction factor

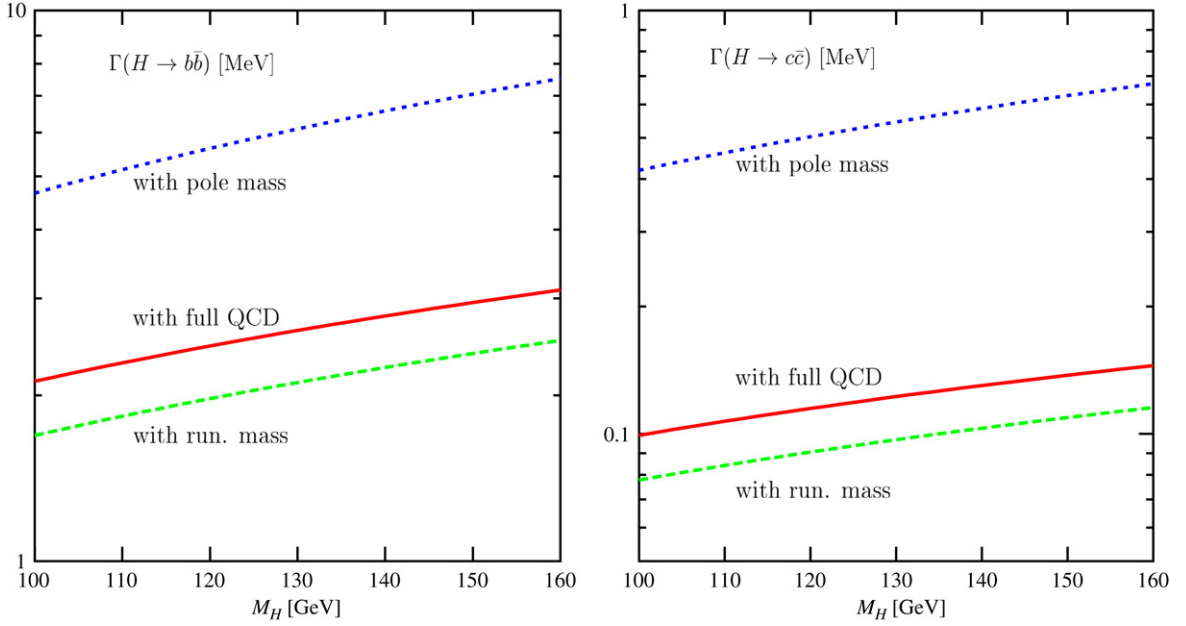


Fig. 2.3. The partial widths for the decays  $H \rightarrow b\bar{b}$  (left) and  $H \rightarrow c\bar{c}$  (right) as functions of  $M_H$ . They are shown in the Born approximation (dotted lines), including only the running quark masses (dashed lines) and with the full set of QCD corrections (solid lines). The input pole masses are  $m_b = 4.88$  GeV and  $m_c = 1.64$  GeV and the running strong coupling constant is taken at the scale of the Higgs mass and is normalized to  $\alpha_s(M_Z) = 0.1172$ .

$\Delta_{qq}$

$$\Delta_{qq} = 5.67 \frac{\bar{\alpha}_s}{\pi} + (35.94 - 1.36N_f) \frac{\bar{\alpha}_s^2}{\pi^2} + (164.14 - 25.77N_f + 0.26N_f^2) \frac{\bar{\alpha}_s^3}{\pi^3}. \quad (2.11)$$

Since the values of the running  $b$ - and  $c$ -quark masses at the scale  $\mu \sim M_H = 100$  GeV are typically, respectively, a factor  $\sim 1.5$  and a factor of  $\sim 2$  smaller than the pole masses, the partial decay widths are suppressed by large factors compared to the case where the pole masses are used. This is shown in Fig. 2.3 where  $\Gamma(H \rightarrow b\bar{b})$  and  $\Gamma(H \rightarrow c\bar{c})$  are displayed as functions of the Higgs mass  $M_H$  in the Born approximation, using only the running quark masses and with the full set of QCD corrections implemented. Note that the latter increases the partial widths by approximately 20%.

The additional correction at  $\mathcal{O}(\alpha_s^2)$  involves logarithms of the masses of the light quarks and the heavy top quark and is given by [132]

$$\Delta_H^2 = \frac{\bar{\alpha}_s^2}{\pi^2} \left( 1.57 - \frac{2}{3} \log \frac{M_H^2}{m_t^2} + \frac{1}{9} \log^2 \frac{\bar{m}_q^2}{M_H^2} \right). \quad (2.12)$$

Because of chiral symmetry, all this discussion holds true if the Higgs particle were a pseudoscalar boson; the only exception is that the correction  $\Delta_H^2$  would be different, since it involves the quark masses which break the symmetry.

### 2.1.3. The case of the top quark

For Higgs bosons decaying into top quarks, the QCD corrections do not lead to large logarithms since  $m_t$  is comparable to  $M_H$ . However, these corrections can be sizable, in particular near the threshold  $M_H \sim 2m_t$ . At next-to-leading order, they are given by

$$\Gamma(H \rightarrow t\bar{t}) = \frac{3G_\mu}{4\sqrt{2}\pi} M_H m_t^2 \beta_t^3 \left[ 1 + \frac{4}{3} \frac{\alpha_s}{\pi} \Delta_H^t(\beta_t) \right]. \quad (2.13)$$

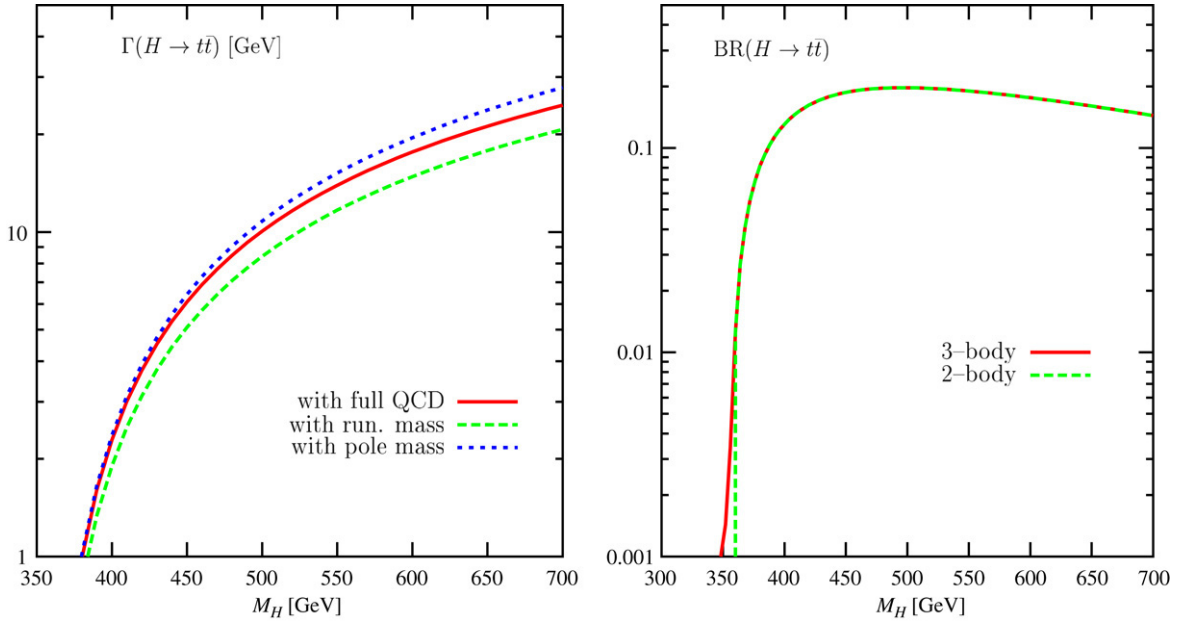


Fig. 2.4. The partial width for the decay  $H \rightarrow t\bar{t}$  as a function of  $M_H$ . In the left figure, it is shown in the Born approximation (dotted line), with the running top mass (dashed lines) and with the full set of QCD corrections (solid lines). In the right figure the partial width is shown with (solid line) and without (dashed line) the inclusion of the three-body decay. The inputs are  $m_t = 178$  GeV and  $\alpha_s(M_Z) = 0.1172$ .

Using the Spence function defined by  $\text{Li}_2(x) = -\int_0^x dy y^{-1} \log(1-y)$ , the QCD correction factor in the massive case reads [129,130,133]

$$\Delta_H^t(\beta) = \frac{1}{\beta} A(\beta) + \frac{1}{16\beta^3} (3 + 34\beta^2 - 13\beta^4) \log \frac{1+\beta}{1-\beta} + \frac{3}{8\beta^2} (7\beta^2 - 1) \quad (2.14)$$

with

$$A(\beta) = (1 + \beta^2) \left[ 4\text{Li}_2\left(\frac{1-\beta}{1+\beta}\right) + 2\text{Li}_2\left(-\frac{1-\beta}{1+\beta}\right) - 3 \log \frac{1+\beta}{1-\beta} \log \frac{2}{1+\beta} - 2 \log \frac{1+\beta}{1-\beta} \log \beta \right] - 3\beta \log \frac{4}{1-\beta^2} - 4\beta \log \beta. \quad (2.15)$$

Part of the full massive two-loop corrections, i.e. corrections of  $\mathcal{O}(N_f \alpha_s^2)$  which are expected to provide the largest contribution, have been computed some time ago [134] and the full two-loop corrections have been derived slightly after [135].

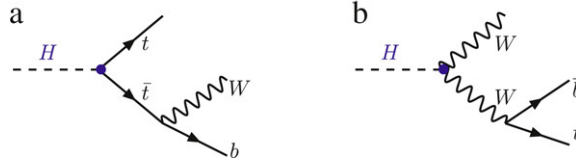
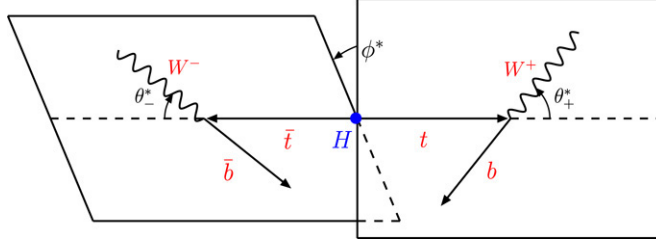
The left-hand side of Fig. 2.4 shows the partial  $H \rightarrow t\bar{t}$  decay width in the Born approximation, with the running top quark mass and including the full set of one-loop QCD corrections. As can be seen, and contrary to the  $b\bar{b}$  and  $c\bar{c}$  cases, the corrections are rather moderate in this case.

Another special feature in the case of top quarks is that the three-body decays  $H \rightarrow t\bar{t}^* \rightarrow t\bar{b}W^-$  into on-shell and off-shell top states are possible [136–138], see Fig. 2.5. These three-body decays reach the percent level slightly below the  $2m_t$  threshold, when compared to the two-body decay as shown in the right-hand side of Fig. 2.4. A smooth transition from below to the above threshold occurs when the top quark width is included.

Taking into account only the diagram of Fig. 2.5(a) where the top quark is off-shell and which provides the dominant contribution [the virtuality of the  $W$  boson in the other diagram is too large, thus strongly suppressing the contribution], the differential partial width or Dalitz density for this decay can be written as

$$\frac{d\Gamma}{dx_1 dx_2}(H \rightarrow t\bar{t}^* \rightarrow t\bar{b}W^-) = \frac{3G_\mu^2}{32\pi^3} M_H^3 m_t^2 \frac{\Gamma_H^t}{y_1^2 + \gamma_t \kappa_t} \quad (2.16)$$



Fig. 2.5. Diagrams for the three-body decays of the Higgs boson into  $tbW$  final statesFig. 2.6. The definition of the polar angles  $\theta_{\pm}^*$  and the azimuthal angle  $\phi^*$  for the sequential decay  $H \rightarrow t\bar{t} \rightarrow (bW^+)(\bar{b}W^-)$ . The polar angles are defined in the  $t, \bar{t}$  rest frames, with respect to the  $t$  flight direction. The angle  $\phi^*$  remains the same after the boost along the  $t\bar{t}$  directions.

with the reduced energies  $x_{1,2} = 2E_{t,b}/M_H$ , the scaling variables  $y_{1,2} = 1 - x_{1,2}$ ,  $\kappa_i = M_i^2/M_H^2$  and the reduced decay width of the virtual top quark  $\gamma_t = \Gamma_t^2/M_H^2$ . The squared amplitude is given by [137]

$$\Gamma_H^t = y_1^2(1 - y_1 - y_2 + \kappa_W - 5\kappa_t) + 2\kappa_W(y_1y_2 - \kappa_W - 2\kappa_t y_1 + 4\kappa_t \kappa_W) - \kappa_t y_1 y_2 + \kappa_t(1 - 4\kappa_t)(2y_1 + \kappa_W + \kappa_t). \quad (2.17)$$

The differential decay width has to be integrated over the allowed range of the  $x_1, x_2$  variables. The boundary condition is

$$\left| \frac{2(1 - x_1 - x_2 + \kappa_t + \kappa_b - \kappa_W) + x_1 x_2}{\sqrt{x_1^2 - 4\kappa_t} \sqrt{x_2^2 - 4\kappa_b}} \right| \leq 1. \quad (2.18)$$

The additional diagram leading to the same final state, with the Higgs boson decaying into two  $W$  bosons with one of them being off-shell and decaying into  $t\bar{b}$  final states,  $H \rightarrow WW^* \rightarrow t\bar{b}W$ , gives very small contributions and can be safely neglected.

#### 2.1.4. Distinction between scalar and pseudoscalar Higgs bosons

The distinction between a scalar and a pseudoscalar Higgs particle can be made by investigating the angular correlations in the decays into heavy fermions [139–144]. In the processes  $H/A \rightarrow t\bar{t} \rightarrow (W^+b)(W^-\bar{b})$ , denoting the spin vector of the  $t$  and  $\bar{t}$  states in their respective rest frames by  $s$  and  $\bar{s}$ , and orienting the  $z$  axis along the  $t$  flight direction, the spin dependence is different in the two cases; from Eq. (2.8) one obtains [140]

$$\Gamma(H/A \rightarrow t\bar{t}) \propto 1 - s_z \bar{s}_z \pm s_{\perp} \bar{s}_{\perp}. \quad (2.19)$$

Denoting by  $\theta_{\pm}^*$  the polar angle between the  $W^{\pm}$  bosons and the  $t$ -quark in the  $W^{\pm}$  rest frames and by  $\phi^*$  the relative azimuthal angle between the decay planes of the two  $W$  bosons, Fig. 2.6, and using the abbreviations  $c_{\theta_{\pm}^*} = \cos \theta_{\pm}^*$  etc., the angular distributions of the  $W^{\pm}$  bosons in the decays of scalar and pseudoscalar Higgs particles are given by [141,145]

$$\frac{d\Gamma(H/A \rightarrow W^+W^-b\bar{b})}{\Gamma_{H/A} dc_{\theta_{+}^*} dc_{\theta_{-}^*} d\phi^*} = \frac{1}{8\pi} \left[ 1 + \left( \frac{m_t^2 - 2M_W^2}{m_t^2 + 2M_W^2} \right)^2 (c_{\theta_{+}^*} c_{\theta_{-}^*} \mp s_{\theta_{+}^*} s_{\theta_{-}^*} c\phi^*) \right]. \quad (2.20)$$

[The QCD corrections to the angular distributions can be found in Ref. [146] for instance]. If the Higgs boson mass is precisely known, the Higgs rest frame can be reconstructed. Because the boost of the Higgs boson to quarks

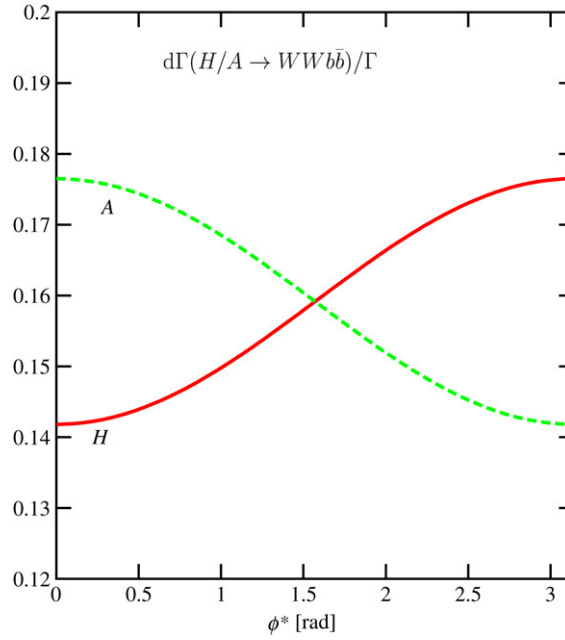


Fig. 2.7. Distribution of the decays  $H/A \rightarrow t\bar{t} \rightarrow b\bar{b}W^+W^-$  in the azimuthal angle  $\phi^*$ .

is not too large and the mass ratio between daughter-to-parent particles in the decay is significant, the kinematical reconstruction of the full event should not be very difficult.

If the integral over the polar angles is performed, one obtains a simple asymmetry in the azimuthal angle which projects out the parity of the Higgs boson [140,141]

$$\frac{1}{\Gamma_{H/A}} \frac{d\Gamma(H/A \rightarrow W^+W^-b\bar{b})}{d\phi^*} = \frac{1}{2\pi} \left[ 1 \mp \frac{\pi^2}{16} \left( \frac{m_t^2 - 2M_W^2}{m_t^2 + 2M_W^2} \right)^2 c\phi^* \right] \quad (2.21)$$

allowing one to determine the azimuthal angle up to a two-fold ambiguity. The distribution of the decays  $H/A \rightarrow t\bar{t} \rightarrow b\bar{b}W^+W^-$  as a function of the azimuthal angle is shown in Fig. 2.7. One sees that the separation between the scalar and pseudoscalar cases can clearly be made.

One can perform the same study when integrating over the  $b$ -quark directions and consider the  $W$  bosons decaying into leptons  $W^\pm \rightarrow \ell^\pm \nu_e$ . The angular distribution is still given by Eq. (2.20) but with  $\theta_\pm^*$  denoting this time the polar angles between the charged leptons and the top quarks in the rest frame of the latter, and with the mass factor  $(m_t^2 - 2M_W^2)^2/(m_t^2 + 2M_W^2)^2$  omitted.

CP-quantum number studies of the Higgs particles can also be performed for smaller Higgs masses, in the decays into light fermions. In the case of  $b\bar{b}$  final state decays [which are dominant for relatively light Higgs bosons], it is unfortunately very difficult, because of depolarization effects, to extract the spin information of the bottom quark. A much cleaner channel is provided by the Higgs decays into  $\tau^+\tau^-$  pairs [141,147,148], although the rates are suppressed by an order of magnitude compared to the  $b\bar{b}$  case. A possible channel would be the decays  $H/A \rightarrow \tau^+\tau^- \rightarrow \pi^+\bar{\nu}_\tau\pi^-\nu_\tau$ .

Defining again the polar angles  $\theta_\pm^*$  as those giving the  $\pi^\pm$  and  $\tau^\mp$  directions and the azimuthal angle  $\phi^*$  as the angle between the decay planes of  $\tau^\pm$ , the angular distribution will be as in the case of  $H/A \rightarrow t\bar{t} \rightarrow WWb\bar{b}$  with  $W^\pm \rightarrow \ell^\pm \nu_e$  [141]

$$\frac{1}{\Gamma_{H/A}} \frac{d\Gamma(H/A \rightarrow \pi^+\bar{\nu}_\tau\pi^-\nu_\tau)}{dc_{\theta_+^*}dc_{\theta_-^*}d\phi^*} = \frac{1}{8\pi} \left[ 1 + c_{\theta_+^*}c_{\theta_-^*} \mp s_{\theta_+^*}s_{\theta_-^*}c\phi^* \right] \quad (2.22)$$

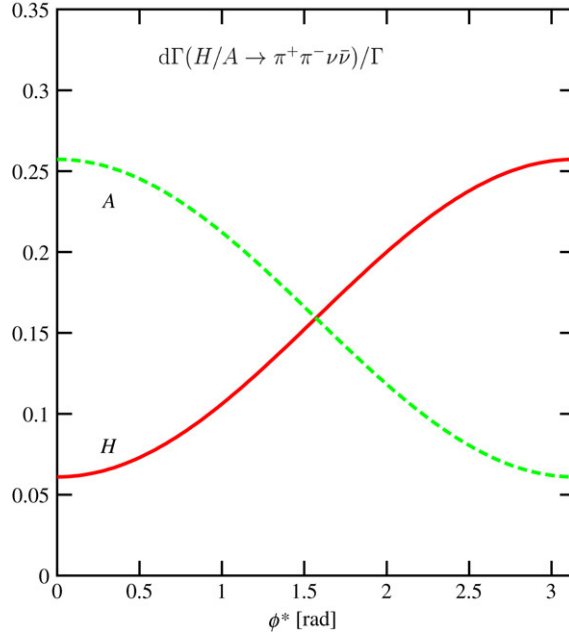


Fig. 2.8. Distribution of the decays  $H/A \rightarrow \tau^+\tau^- \rightarrow \pi^+\bar{\nu}_\tau\pi^-\nu_\tau$  in the azimuthal angle  $\phi^*$ .

leading, once the polar angles are integrated out, to an asymmetry in the azimuthal angle

$$\frac{d\Gamma_{H/A}}{\Gamma_{H/A}d\phi^*} = \frac{1}{2\pi} \left[ 1 \mp \frac{\pi^2}{16} c_{\phi^*} \right]. \quad (2.23)$$

The asymmetry is shown in Fig. 2.8 and the distinction between the scalar and pseudoscalar cases is even easier than in the case of top quarks in Fig. 2.7, since the suppression factor  $(m_t^2 - 2M_W^2)^2/(m_t^2 + 2M_W^2)^2$  is absent.

An observable which is sensitive to the Higgs parity is the angle  $\delta$  between the pions in the rest frame of the Higgs boson [141,145,147,148]

$$16\vec{\pi}^+ \cdot \vec{\pi}^- = M_H^2 \left[ (1 + \beta_\tau \beta_\pi c_{\theta_\pi^*})^2 - 16 \frac{m_\pi^2}{M_H^2} \right]^{\frac{1}{2}} \left[ (1 - \beta_\tau \beta_\pi c_{\theta_\pi^*})^2 - 16 \frac{m_\pi^2}{M_H^2} \right]^{\frac{1}{2}} \cos \delta \quad (2.24)$$

where  $\beta_\tau = (1 - 4m_\tau^2/M_H^2)^{1/2}$  and  $\beta_\pi = (m_\tau^2 - m_\pi^2)/(m_\tau^2 + m_\pi^2)$  are the rest frame boosts of, respectively, the Higgs to the  $\tau$ -lepton and the  $\tau$ -lepton to the pions. The azimuthal angle  $\phi^*$  can be then written in terms of the angles  $\theta_\pm^*$  and  $\delta$  and, integrating over the polar angles, one obtains for the distributions a rather complicated function of  $\delta$ . However, for  $\delta = \pi$ , the distributions are rather simple and very different for  $0^{++}$  and  $0^{+-}$  states. For a scalar Higgs boson decay, it reaches its maximum for  $\delta = \pi$

$$\frac{1}{\Gamma_H} \frac{d\Gamma(H)}{d\cos\delta} \simeq \frac{2}{15} \frac{5 + \beta_\tau^2}{1 - \beta_\tau^2} \quad (2.25)$$

while for a pseudoscalar Higgs boson, it peaks at a small value of  $\pi - \delta$  for  $m_\pi \sim 0$

$$\frac{1}{\Gamma_A} \frac{d\Gamma(A)}{d\cos\delta} \simeq (1 + \cos\delta) \frac{1}{20} \frac{5 + 10\beta_\tau^2 + \beta_\tau^4}{(1 - \beta_\tau^2)^2}. \quad (2.26)$$

The analysis for Higgs decays into multi-pion final states, such as  $H/A \rightarrow \tau^+\tau^- \rightarrow \rho^+\bar{\nu}_\tau\rho^-\nu_\tau \rightarrow \pi^+\pi^0\bar{\nu}_\tau\pi^-\pi^0\nu_\tau$  follows the same line if the hadron system is treated as a single particle; see Refs. [141,148] for more details.

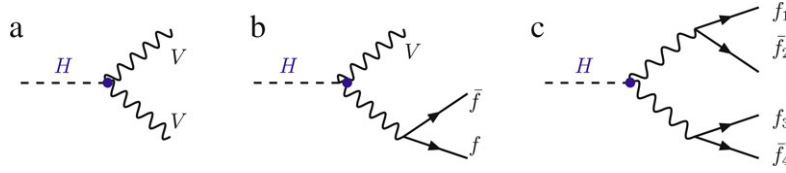


Fig. 2.9. Diagrams for the Higgs boson decays into real and/or virtual gauge bosons.

## 2.2. Decays into electroweak gauge bosons

### 2.2.1. Two-body decays

Above the  $WW$  and  $ZZ$  kinematical thresholds, the Higgs boson will decay mainly into pairs of massive gauge bosons; Fig. 2.9(a). The decay widths are directly proportional to the  $HVV$  couplings given in Eq. (2.2) which, as discussed in the beginning of this chapter, correspond to the  $J^{PC} = 0^{++}$  assignment of the SM Higgs boson spin and parity quantum numbers. These are S-wave couplings,  $\sim \vec{\epsilon}_1 \cdot \vec{\epsilon}_2$  in the laboratory frame, and linear in  $\sin \theta$ , with  $\theta$  being the angle between the Higgs and one of the vector bosons.

The partial width for a Higgs boson decaying into two real gauge bosons,  $H \rightarrow VV$  with  $V = W$  or  $Z$ , is given by [32,126]

$$\Gamma(H \rightarrow VV) = \frac{G_\mu M_H^3}{16\sqrt{2}\pi} \delta_V \sqrt{1-4x}(1-4x+12x^2), \quad x = \frac{M_V^2}{M_H^2} \quad (2.27)$$

with  $\delta_W = 2$  and  $\delta_Z = 1$ . For large enough Higgs boson masses, when the phase-space factors can be ignored, the decay width into  $WW$  bosons is two times larger than the decay width into  $ZZ$  bosons and the branching ratios for the decays would be, respectively, 2/3 and 1/3 if no other decay channel is kinematically open.

For large Higgs masses, the vector bosons are longitudinally polarized [140]

$$\frac{\Gamma_L}{\Gamma_L + \Gamma_T} = \frac{1-4x+4x^2}{1-4x+12x^2} \xrightarrow{M_H \gg M_V} 1 \quad (2.28)$$

while the  $L, T$ -polarization states are democratically populated near the threshold, at  $x = 1/4$ . Since the longitudinal wave functions are linear in the energy, the width grows as the third power of the Higgs mass,  $\Gamma(H \rightarrow VV) \propto M_H^3$ . As discussed in Section 1.4.1, a heavy Higgs boson would be obese since its total decay width becomes comparable to its mass

$$\Gamma(H \rightarrow WW + ZZ) \sim 0.5 \text{ TeV} [M_H / 1 \text{ TeV}]^3 \quad (2.29)$$

and behaves hardly as a resonance.

### 2.2.2. Three-body decays

Below the  $WW/ZZ$  kinematical thresholds, the Higgs boson modes decay into gauge bosons, with one of them being off-shell, Fig. 2.9(b), are also important. For instance, from  $M_H \gtrsim 130 \text{ GeV}$ , the Higgs boson decay into  $WW$  pairs with one off-shell  $W$  boson, starts to dominate over the  $H \rightarrow b\bar{b}$  mode. This is due to the fact that in these three-body decays, although suppressed by an additional power of the electroweak coupling squared compared to the dominant  $H \rightarrow b\bar{b}$  case and by the virtuality of the intermediate vector boson state, there is a compensation since the Higgs couplings to  $W$  bosons are much larger than the Higgs–Yukawa coupling to  $b$ -quarks.

The partial width for the decay  $H \rightarrow VV^* \rightarrow Vf\bar{f}$ , the charges of the vector bosons  $V$  summed over and assuming massless fermions, is given by [149]

$$\Gamma(H \rightarrow VV^*) = \frac{9G_\mu^2 M_V^4}{16\pi^3} M_H \delta'_V R_T(x) \quad (2.30)$$

with  $\delta'_W = 1$ ,  $\delta'_Z = \frac{7}{12} - \frac{10}{9} \sin^2 \theta_W + \frac{40}{9} \sin^4 \theta_W$  and

$$R_T(x) = \frac{3(1-8x+20x^2)}{(4x-1)^{1/2}} \arccos\left(\frac{3x-1}{2x^{3/2}}\right) - \frac{1-x}{2x}(2-13x+47x^2) - \frac{3}{2}(1-6x+4x^2) \log x. \quad (2.31)$$

The invariant mass ( $M_*$ ) spectrum of the off-shell vector boson peaks close to the kinematical maximum corresponding to zero momentum of the on-shell and off-shell final state bosons

$$\frac{d\Gamma(H \rightarrow VV^*)}{dM_*^2} = \frac{3G_\mu^2 M_V^4}{16\pi^3 M_H} \delta_V \frac{\beta_V (M_H^4 \beta_V^2 + 12M_V^2 M_*^2)}{(M_*^2 - M_V^2)^2 + M_V^2 \Gamma_V^2} \quad (2.32)$$

with  $\beta_V^2 = [1 - (M_V + M_*)^2/M_H^2][1 - (M_V - M_*)^2/M_H^2]$ . Since both  $V$  and  $V^*$  preferentially have small momenta, the transverse and longitudinal polarization states are populated with almost equal probabilities. Neglecting the widths of the vector bosons,  $\Gamma_V$ , one finds after summing over all  $M_*$  values

$$\frac{\Gamma_L}{\Gamma_L + \Gamma_T} = \frac{R_L(M_V^2/M_H^2)}{R_T(M_V^2/M_H^2)} \quad (2.33)$$

where  $R_T$  is given in Eq. (2.31) and  $R_L$  reads [140]

$$R_L(x) = \frac{3 - 16x + 20x^2}{(4x - 1)^{1/2}} \arccos\left(\frac{3x - 1}{2x^{3/2}}\right) - \frac{1 - x}{2x} (2 - 13x + 15x^2) - \frac{1}{2} (3 - 10x + 4x^2) \log x. \quad (2.34)$$

[Note that for heavy Higgs bosons, the three-body modes  $H \rightarrow W^+W^-Z$  and  $H \rightarrow t\bar{t}Z$  have been considered [136, 150]; they lead to marginal branching ratios.]

### 2.2.3. Four-body decays

In fact, even Higgs decays into two off-shell gauge bosons, Fig. 2.9(c), can be relevant [151,152]; see also Ref. [124]. The branching ratios for the latter reach the percent level for Higgs masses above about 100 (110) GeV for both  $W$  ( $Z$ ) boson pairs off-shell. For higher masses, it is sufficient to allow for one off-shell gauge boson only. The decay width can be cast into the compact form [151]

$$\Gamma(H \rightarrow V^*V^*) = \frac{1}{\pi^2} \int_0^{M_H^2} \frac{dq_1^2 M_V \Gamma_V}{(q_1^2 - M_V^2)^2 + M_V^2 \Gamma_V^2} \int_0^{(M_H - q_1)^2} \frac{dq_2^2 M_V \Gamma_V}{(q_2^2 - M_V^2)^2 + M_V^2 \Gamma_V^2} \Gamma_0 \quad (2.35)$$

with  $q_1^2, q_2^2$  being the squared invariant masses of the virtual gauge bosons,  $M_V$  and  $\Gamma_V$  their masses and total decay widths, and in terms of  $\lambda(x, y; z) = (1 - x/z - y/z)^2 - 4xy/z^2$  with  $\delta_V = 2(1)$  for  $V = W(Z)$ , the matrix element squared  $\Gamma_0$  is

$$\Gamma_0 = \frac{G_\mu M_H^3}{16\sqrt{2}\pi} \delta_V \sqrt{\lambda(q_1^2, q_2^2; M_H^2)} \left[ \lambda(q_1^2, q_2^2; M_H^2) + \frac{12q_1^2 q_2^2}{M_H^4} \right]. \quad (2.36)$$

Taking into account the total decay width of the vector bosons in the denominators of Eq. (2.35), this expression for the four-body decay mode can be in fact used to reproduce the partial widths of the two-body and three-body decay modes, once the thresholds are crossed. Fig. 2.10 shows the branching ratios for the decays  $H \rightarrow WW$  and  $H \rightarrow ZZ$  in the three cases of two-body, three-body and four-body modes.

### 2.2.4. CP-properties and comparison with the CP-odd case

Let us now confront the angular distributions of the final state fermions in the decay processes  $H/A \rightarrow VV^* \rightarrow (f_1 \bar{f}_2)(f_3 \bar{f}_4)$ , which are different for a CP-even Higgs particle and a CP-odd Higgs particle [140,153–155]. Denoting the polar and azimuthal angles of the fermions  $f_1, f_3$  in the rest frames of the vector bosons by  $(\theta_1, 0)$  and  $(\theta_3, \phi_3)$  [see Fig. 2.11 for the conventions and definitions], the angular distribution is given by [140]

$$\begin{aligned} \frac{d\Gamma(H \rightarrow VV)}{dc_{\theta_1} dc_{\theta_3} d\phi_3} &\sim s_{\theta_1}^2 s_{\theta_3}^2 + \frac{1}{2\gamma_1 \gamma_3 (1 + \beta_1 \beta_3)} s_{2\theta_1} s_{2\theta_3} c_{\phi_3} \\ &+ \frac{1}{2\gamma_1^2 \gamma_3^2 (1 + \beta_1 \beta_3)^2} \left[ (1 + c_{\theta_1}^2) (1 + c_{\theta_3}^2) + s_{\theta_1}^2 s_{\theta_3}^2 c_{2\phi_3} \right] \\ &- \frac{4A_{f_1} A_{f_3}}{\gamma_1 \gamma_3 (1 + \beta_1 \beta_3)} \left[ s_{\theta_1} s_{\theta_3} c_{\phi_3} + \frac{1}{\gamma_1 \gamma_3 (1 + \beta_1 \beta_3)} c_{\theta_1} c_{\theta_3} \right] \end{aligned} \quad (2.37)$$

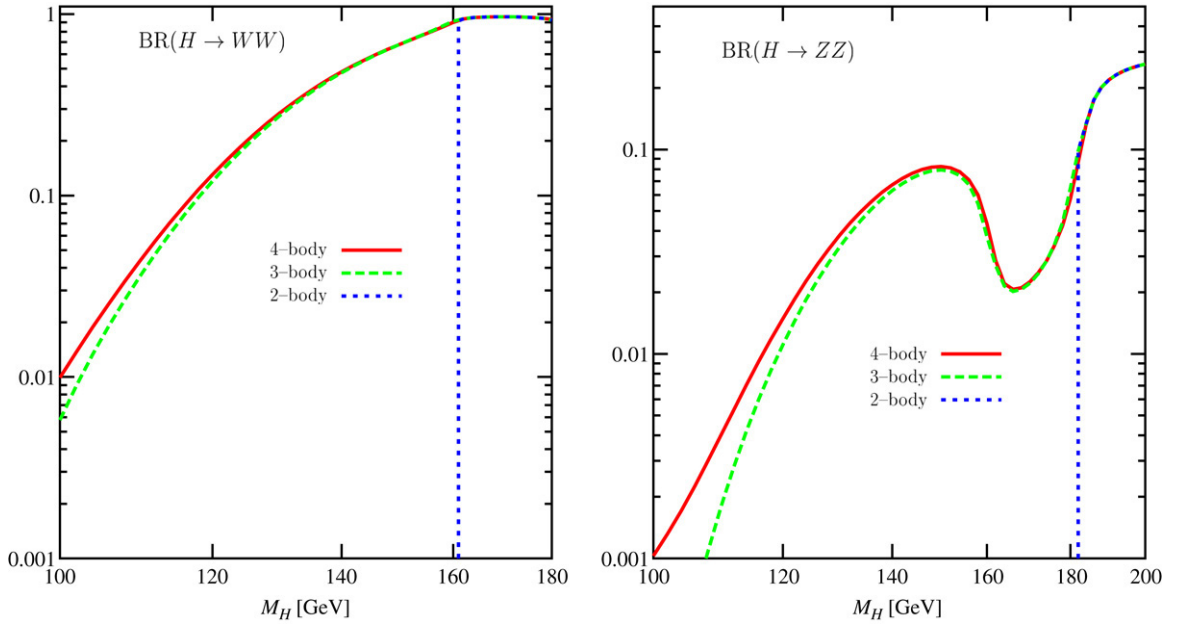


Fig. 2.10. The branching ratios for the decays  $H \rightarrow W^+W^-$  (left) and  $ZZ$  (right) as functions of  $M_H$  at the two- (dotted), three- (dashed) and four-body (solid) levels.

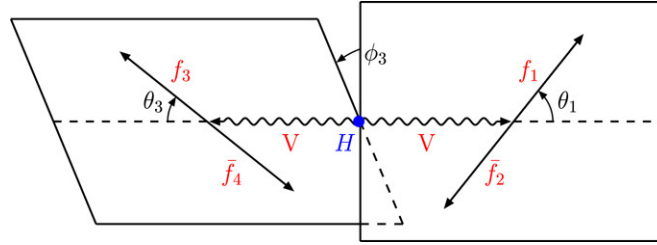


Fig. 2.11. The definition of the polar angles  $\theta_{1,3}$  and the azimuthal angle  $\phi_3$  for the sequential decay  $H \rightarrow VV \rightarrow (f_1 \bar{f}_2)(f_3 \bar{f}_4)$  in the rest frame of the Higgs particle.

where the combination of  $Vf\bar{f}$  couplings is  $A_f = 2\hat{v}_f\hat{a}_f/(\hat{v}_f^2 + \hat{a}_f^2)$ ; for  $V = W$ , the weak charges are as usual  $\hat{v}_f = \hat{a}_f = \sqrt{2}$  while for  $V = Z$ ,  $\hat{v}_f = 2I_f^3 - 4Q_f \sin^2 \theta_W$  and  $\hat{a}_f = 2I_f^3$ .  $\beta_i, \gamma_i = (1 - \beta_i^2)^{-1/2}$  are the velocities and  $\gamma$  factors of the [on/off-shell] vector bosons and  $s_\theta \equiv \sin \theta$ , etc. The dependence on the azimuthal angle between the decay planes disappears for large Higgs masses,  $\sim 1/\gamma$ , a consequence of the asymptotic longitudinal  $V$ -polarization. After integrating out the polar angles, we are left with [140]

$$\frac{d\Gamma(H \rightarrow VV)}{d\phi_3} \sim 1 + a_1 c\phi_3 + a_2 c2\phi_3$$

$$a_1 = -\frac{9\pi^2}{32} \frac{\gamma_1 \gamma_3 (1 + \beta_1 \beta_3)}{\gamma_1^2 \gamma_3^2 (1 + \beta_1 \beta_3)^2 + 2} A_{f_1} A_{f_3}, \quad a_2 = \frac{1}{2} \frac{1}{\gamma_1^2 \gamma_3^2 (1 + \beta_1 \beta_3)^2 + 2} \quad (2.38)$$

where the coefficient  $a_1$  measures the P-odd amplitude.

These are unique predictions for the SM Higgs boson with  $J^{\text{PC}} = 0^{++}$  quantum numbers. One can again confront these predictions with what is expected in the case of a  $J^{\text{PC}} = 0^{+-}$  CP-odd Higgs boson.<sup>17</sup> The AVV coupling has been defined in Eq. (2.4), and reduces to  $(\vec{\epsilon}_1 \times \vec{\epsilon}_2) \cdot (\vec{p}_1 - \vec{p}_2)$  in the laboratory frame. The CP-odd angular distributions

<sup>17</sup> The more general case where both CP-even and CP-odd couplings are present can be found in Ref. [156].

in the decays  $A \rightarrow VV \rightarrow (f_1 \bar{f}_2)(f_3 \bar{f}_4)$  are given by [140]

$$\frac{d\Gamma(A \rightarrow VV)}{dc_{\theta_1} dc_{\theta_3} d\phi_3} \sim 1 + c_{\theta_1}^2 c_{\theta_3}^2 - \frac{1}{2} s_{\theta_1}^2 s_{\theta_3}^2 - \frac{1}{2} s_{\theta_1}^2 s_{\theta_3}^2 c_{2\phi_3} - 2A_{f_1} A_{f_3} c_{\theta_1} c_{\theta_3} \quad (2.39)$$

and simply reduces, after integrating over the polar angles, to

$$\frac{d\Gamma(A \rightarrow VV)}{d\phi_3} \sim 1 - \frac{1}{4} c_{2\phi_3}. \quad (2.40)$$

The normalization follows from the total and differential decay widths. Since the  $A$  boson does not decay into longitudinal gauge bosons, the partial width for the two-body decay is

$$\Gamma(A \rightarrow VV) = \frac{G_\mu M_H^3}{16\pi^3 M_A} \delta_V \eta^2 (8x^2) \sqrt{1-4x} \quad (2.41)$$

while for the three-body decay, one has

$$\Gamma(A \rightarrow VV^*) = \frac{3G_\mu^2 M_V^6}{8\pi^3 M_A} \delta'_V \eta^2 R_A \left( \frac{M_V^2}{M_A^2} \right) \quad (2.42)$$

with

$$R_A(x) = (1-7x)(4x-1)^{1/2} \arccos\left(\frac{3x-1}{2x^{3/2}}\right) - \frac{1-x}{6}(17-64x-x^2) + \frac{1}{2}(1-9x+6x^2) \log x. \quad (2.43)$$

The invariant mass spectrum of the off-shell vector bosons reads

$$\frac{d\Gamma(A \rightarrow VV^*)}{dM_*^2} = \frac{3G_\mu^2 M_V^6}{8\pi^3 M_A} \delta'_V \eta^2 \frac{M_*^2 \beta_V^3}{(M_*^2 - M_V^2)^2 + M_V^2 \Gamma_V^2}. \quad (2.44)$$

The fraction of the decay of the Higgs bosons into longitudinal vector bosons [which is zero in the CP-odd Higgs case] and the distributions with respect to the invariant mass of the off-shell gauge boson in the decays  $H/A \rightarrow Z^* Z$  for  $M_{H/A} = 150$  GeV are shown in Fig. 2.12. The mass and momentum distributions of the decay width are determined by the P-wave decay characteristics and the transverse polarization of the gauge bosons. The dependence on the azimuthal angle is shown in Fig. 2.13 for the decays  $H/A \rightarrow ZZ \rightarrow 4\mu$  and  $H/A \rightarrow WW \rightarrow 4f$  with  $M_{H/A} = 300$  GeV. Again, the difference between the CP-even and CP-odd cases is noticeable. In the case of  $H \rightarrow ZZ$  decays, the variation with the azimuthal angle is small since the factor in front of  $\cos \phi_3$  is tiny,  $a_1 \propto v_e^2 \ll 1$  [while  $v_f = \sqrt{2}$  for  $W$  bosons]; the coefficient of  $\cos 2\phi_3$  drops like  $1/\gamma^4$  in the scalar case.

### 2.3. Loop induced decays into $\gamma\gamma$ , $\gamma Z$ and $gg$

Since gluons and photons are massless particles, they do not couple to the Higgs boson directly. Nevertheless, the  $Hgg$  and  $H\gamma\gamma$  vertices, as well as the  $HZ\gamma$  coupling, can be generated at the quantum level with loops involving massive [and colored or charged] particles which couple to the Higgs boson. The  $H\gamma\gamma$  and  $HZ\gamma$  couplings are mediated by  $W$  boson and charged fermions loops, while the  $Hgg$  coupling is mediated only by quark loops; Fig. 2.14. For fermions, only the heavy top quark and, to a lesser extent, the bottom quark contribute substantially for Higgs boson masses  $M_H \gtrsim 100$  GeV.

For masses much larger than the Higgs boson mass, these virtual particles do not decouple since their couplings to the Higgs boson grow with the masses, thus compensating the loop mass suppression. These decays are thus extremely interesting since their strength is sensitive to scales far beyond the Higgs boson mass and can be used as a possible probe for new charged and/or colored particles whose masses are generated by the Higgs mechanism and which are too heavy to be produced directly.

Unfortunately, because of the suppression by the additional electroweak or strong coupling constants, these loop decays are important only for Higgs masses below  $\sim 130$  GeV when the total Higgs decay width is rather small. However, these partial widths will be very important when we will discuss the Higgs production at hadron and photon



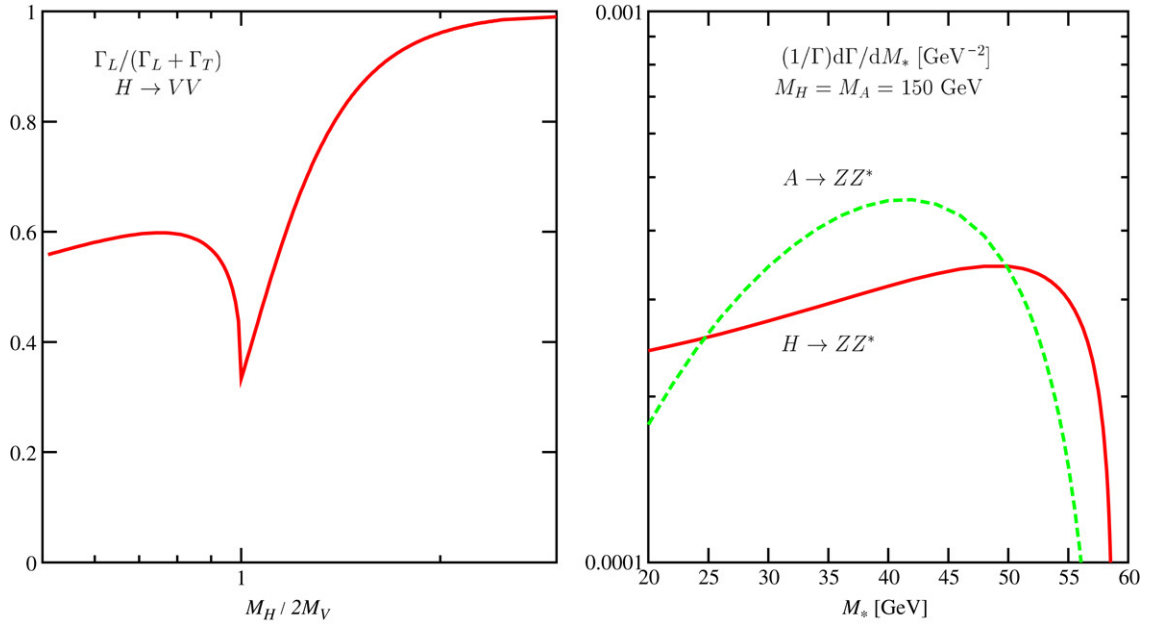


Fig. 2.12. The decay width of the Higgs boson into longitudinal gauge bosons as a function of the ratio  $M_H/2M_V$  (left) and the distribution with respect to the invariant mass of the off-shell gauge boson in the decays  $H/A \rightarrow ZZ^*$  for  $M_H = M_A = 150$  GeV (right).

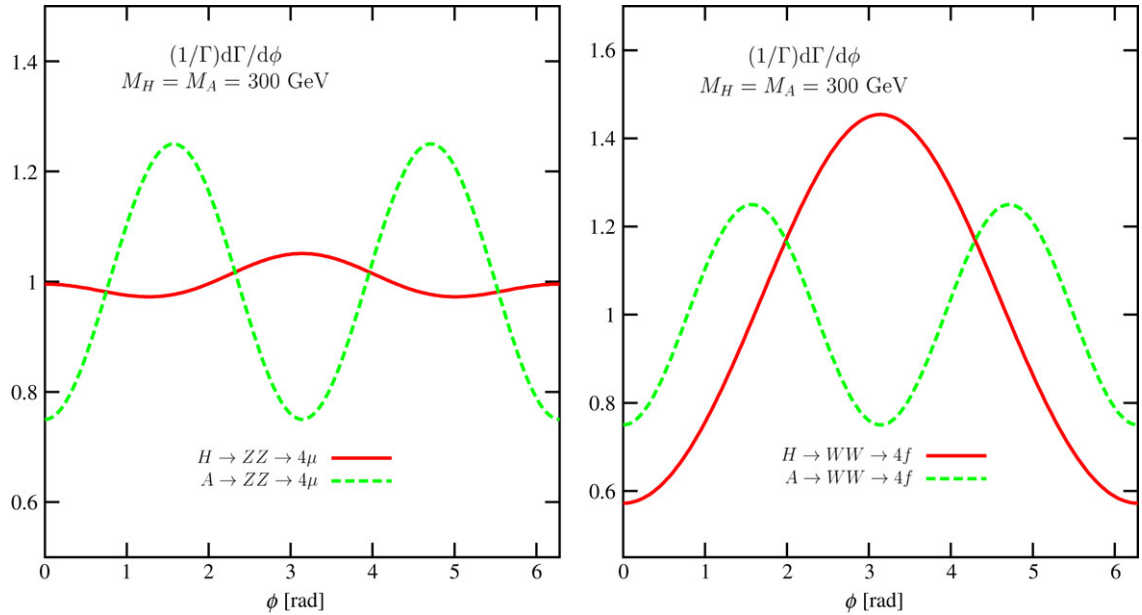


Fig. 2.13. The azimuthal dependence in the decays  $H/A \rightarrow ZZ \rightarrow 4\mu^\pm$  (left) and  $H/A \rightarrow WW \rightarrow 4f$  for CP-even and CP-odd Higgs bosons with masses  $M_H = M_A = 300$  GeV.

colliders, where the cross sections will be directly proportional to, respectively, the gluonic and photonic partial decay widths. Since the entire Higgs boson mass range can be probed in these production processes, we will also discuss the amplitudes for heavy Higgs bosons.

In this section, we first analyze the decays widths both at leading order (LO) and then including the next-to-leading-order (NLO) QCD corrections. The discussion of the LO electroweak corrections and the higher-order QCD corrections will be postponed to the next section.

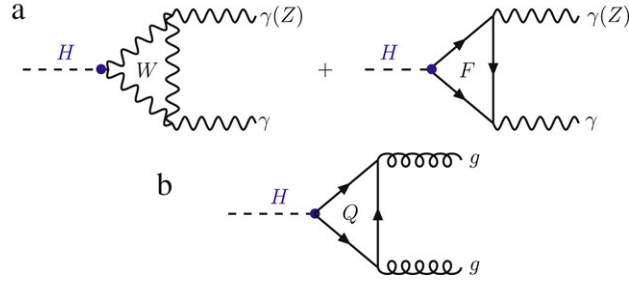


Fig. 2.14. Loop induced Higgs boson decays into (a) two photons ( $Z\gamma$ ) and (b) two gluons.

### 2.3.1. Decays into two photons

**2.3.1.1. The partial width at leading order.** The decay of the SM Higgs boson into two photons is mediated by  $W$  boson and heavy charged fermion loops. The partial decay width can be cast into the form [89,157–159]

$$\Gamma(H \rightarrow \gamma\gamma) = \frac{G_\mu \alpha^2 M_H^3}{128\sqrt{2}\pi^3} \left| \sum_f N_c Q_f^2 A_{1/2}^H(\tau_f) + A_1^H(\tau_W) \right|^2 \quad (2.45)$$

with the form factors for spin- $\frac{1}{2}$  and spin-1 particles given by

$$\begin{aligned} A_{1/2}^H(\tau) &= 2[\tau + (\tau - 1)f(\tau)]\tau^{-2} \\ A_1^H(\tau) &= -[2\tau^2 + 3\tau + 3(2\tau - 1)f(\tau)]\tau^{-2} \end{aligned} \quad (2.46)$$

and the function  $f(\tau)$  defined as

$$f(\tau) = \begin{cases} \arcsin^2 \sqrt{\tau} & \tau \leq 1 \\ -\frac{1}{4} \left[ \log \frac{1 + \sqrt{1 - \tau^{-1}}}{1 - \sqrt{1 - \tau^{-1}}} - i\pi \right]^2 & \tau > 1. \end{cases} \quad (2.47)$$

The parameters  $\tau_i = M_H^2/4M_i^2$  with  $i = f, W$  are defined by the corresponding masses of the heavy loop particles. The electromagnetic constant in the coupling should be taken at the scale  $q^2 = 0$  since the final state photons are real.

Since the  $Hf\bar{f}$  coupling is proportional to  $m_f$ , the contribution of light fermions is negligible so that in the SM with three families, only the top quark and the  $W$  boson effectively contribute to the  $\gamma\gamma$  width. If the Higgs boson mass is smaller than the  $WW$  and  $f\bar{f}$  pair thresholds, the amplitudes are real and above the thresholds they are complex; Fig. 2.15. Below thresholds, the  $W$  amplitude is always dominant, falling from  $A_1^H = -7$  for very small Higgs masses to  $A_1^H = -5 - 3\pi^2/4$  at the  $WW$  threshold; for large Higgs masses the  $W$  amplitude approaches  $A_1^H \rightarrow -2$ . The fermionic contributions increase from  $A_{1/2}^H = 4/3$  for small  $\tau_f$  values to  $A_{1/2}^H \sim 2$  at the  $2m_f$  threshold; far above the fermion threshold, the amplitude vanishes linearly in  $\tau_f$  modulo logarithmic coefficients,

$$\begin{aligned} M_H^2 \gg 4m_f^2 : A_{1/2}^H(\tau_f) &\rightarrow -[\log(4\tau_f) - i\pi]^2/(2\tau_f) \\ M_H^2 \ll 4m_f^2 : A_{1/2}^H(\tau_f) &\rightarrow 4/3. \end{aligned} \quad (2.48)$$

In Fig. 2.16, we display the partial decay width  $\Gamma(H \rightarrow \gamma\gamma)$ . The width varies rapidly from a few KeV for  $M_H \sim 100$  GeV to  $\sim 100$  KeV for  $M_H \sim 300$  GeV as a consequence of the growth  $\propto M_H^3$ . The contribution of the  $W$  boson loop interferes destructively with the quark loop and for Higgs masses of about 650 GeV, the two contributions nearly cancel each other. The contribution of the  $b$ -loop is negligible, while the  $t$ -quark contribution with  $m_t \rightarrow \infty$  is a good approximation for Higgs masses below the  $2m_t$  threshold.

**2.3.1.2. The NLO QCD corrections.** The QCD corrections to the quark amplitude in the decay  $H \rightarrow \gamma\gamma$  consist only of two-loop virtual corrections and the corresponding counterterms; some generic diagrams are shown in Fig. 2.17.

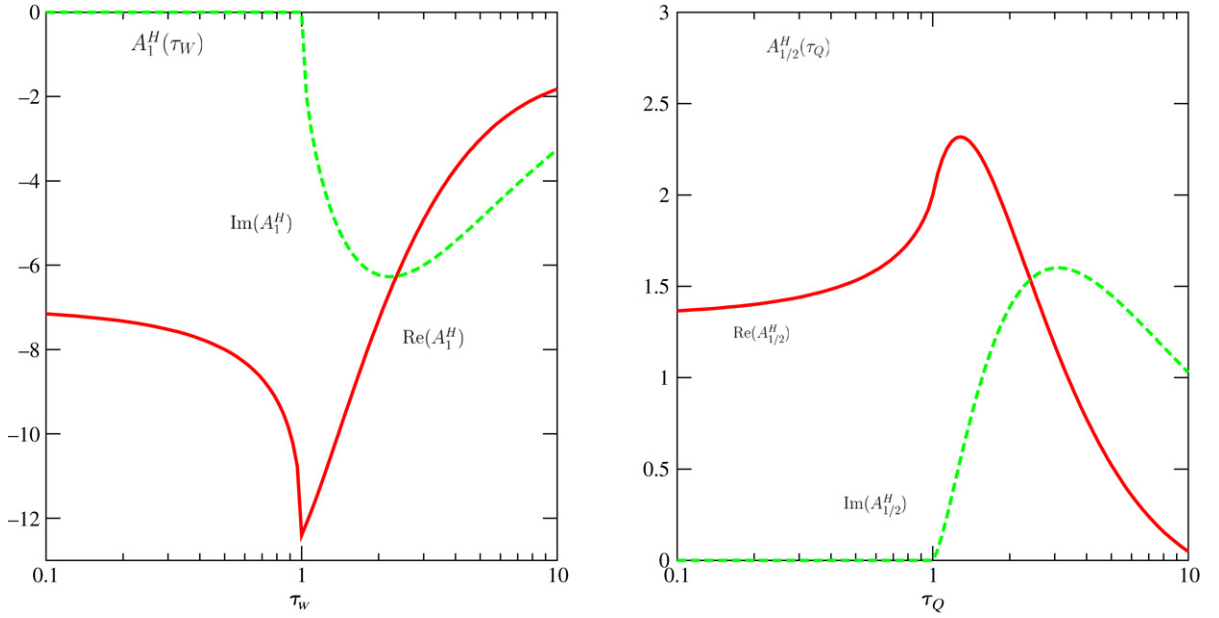


Fig. 2.15. Real and imaginary parts of the  $W$  boson (left) and heavy fermion (right) amplitudes in the decay  $H \rightarrow \gamma\gamma$  as functions of the mass ratios  $\tau_i = M_H^2/4M_i^2$ .

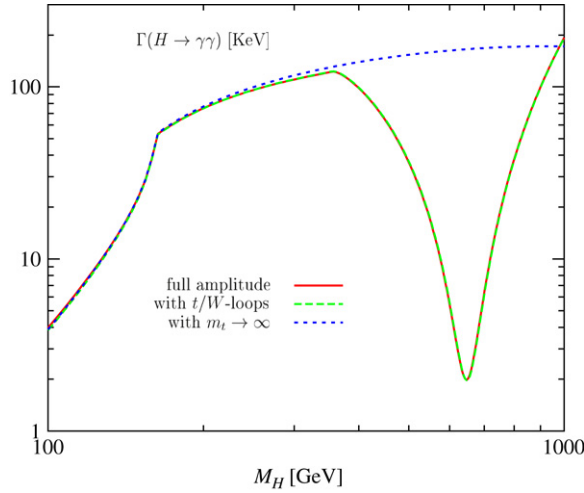
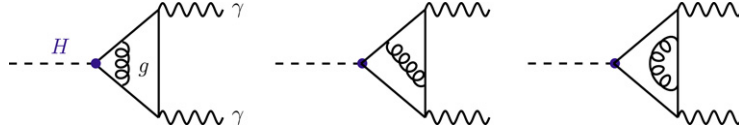
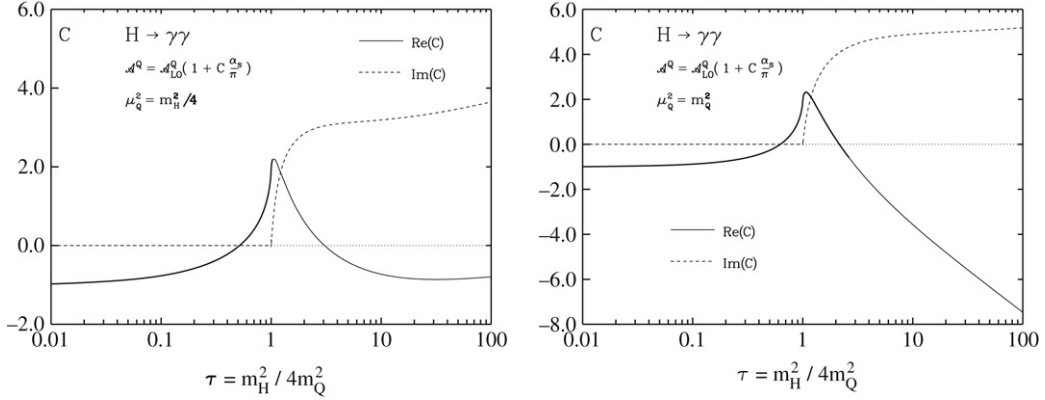


Fig. 2.16. The partial width for the decay  $H \rightarrow \gamma\gamma$  as a function of  $M_H$  with the  $W$  and all third generation fermion contributions (solid) and with  $W$  and only the top quark contribution (dashed) and with the  $W$  and  $t$ -quark contributions for  $m_t \rightarrow \infty$  (dotted lines).

There are no real corrections since the decay  $H \rightarrow \gamma\gamma + g$  does not occur due to color conservation. The calculation can be done in the on-shell scheme, in which the quark mass  $m_Q$  is defined as the pole of the propagator and the quark wave function is renormalized with a renormalization constant  $Z_2^{1/2}$  such that the residue at the pole is equal to unity. The photon-quark vertex is renormalized at zero-momentum transfer and the standard QED Ward identity renders the corresponding renormalization factor equal to the one of the wave function. Since in the SM the fermion masses are generated by the interaction with the Higgs field, the renormalization factor  $Z_{HQQ}$  associated with the Higgs-quark vertex is fixed unambiguously by the renormalization factors  $Z_m$  for the mass and  $Z_2$  for the wave function. From the bare Lagrangian [the subscript 0 stands for bare quantities]

$$\mathcal{L}_0 = -m_0 \bar{Q}_0 Q_0 \frac{H}{v} = -m_Q \bar{Q} Q \frac{H}{v} + Z_{HQQ} m_Q \bar{Q} Q \frac{H}{v} \quad (2.49)$$

Fig. 2.17. QCD corrections to the quark amplitude for the  $H \rightarrow \gamma\gamma$  decay.Fig. 2.18. The QCD correction factor to the real and imaginary parts of the quark amplitude  $A_{1/2}^H$  in the  $H \rightarrow \gamma\gamma$  decay as a function of  $\tau_Q = M_H^2/4m_Q^2$ . The scale at which the correction is evaluated is  $\mu_Q = \frac{1}{2}M_H$  (left) and  $\mu_Q = m_Q$  (right).

one finds  $Z_{HQQ} = 1 - Z_2 Z_m$  [129,130]. Thus, in contrast to the photon–fermion vertex, the scalar  $HQQ$  vertex is renormalized at zero-momentum transfer by a finite amount  $\gamma_m$  after subtracting  $Z_{HQQ}$  due to the lack of a corresponding Ward identity.

The two-loop amplitudes for the  $H \rightarrow \gamma\gamma$  decay have been calculated in Refs. [160–162]. In the general massive case, the five-dimensional Feynman parameter integrals have been reduced analytically down to one-dimensional integrals over polylogarithms which were evaluated numerically [161]. Very recently [162], these integrals have been derived analytically. The QCD corrections of the quark contribution to the two-photon Higgs decay amplitude can be parametrized as

$$A_{1/2}^H(\tau_Q) = A_{1/2}^H(\tau_Q)|_{\text{LO}} \left[ 1 + \frac{\alpha_s}{\pi} C_H(\tau_Q) \right]. \quad (2.50)$$

In principle, the scale in  $\alpha_s$  is arbitrary to this order although, in practice, it should be chosen to be, typically, of order  $M_H$ . However, the renormalization scale should be defined at  $\mu_Q = \frac{1}{2}M_H$  for two reasons: (i) the  $Q\bar{Q}$  decay threshold is defined at the correct position  $2m_Q(m_Q) = 2m_Q$  and (ii) it turns out a posteriori that all relevant large logarithms are effectively absorbed into the running mass for the entire range of the variable  $\tau$ . Note that near the threshold [163], within a margin of a few GeV, the perturbative analysis is in principle not valid since the formation of a P-wave  $0^{++}$  resonance, interrupted by the rapid quark decay modifies the amplitude in this range. Since  $Q\bar{Q}$  pairs cannot form  $0^{++}$  states at the threshold,  $\text{Im } C_H$  vanishes there and  $\text{Re } C_H$  develops a maximum very close to this threshold.

The real and imaginary parts of the correction factor  $C_H$  are shown in Fig. 2.18 as functions of  $\tau_Q$  with the scale set to  $\mu_Q = \frac{1}{2}M_H$  (left) and  $\mu_Q = m_Q$  (right). In the limit  $m_Q \rightarrow \infty$ , the correction factor can be evaluated analytically and one finds [160]

$$M_H^2/4m_Q^2 \rightarrow 0 : \quad 1 + C_H \frac{\alpha_s}{\pi} \rightarrow 1 - \frac{\alpha_s}{\pi}. \quad (2.51)$$

In the opposite limit  $m_Q(\mu_Q^2) \rightarrow 0$  the leading and subleading logarithms of the correction factor can also be evaluated analytically

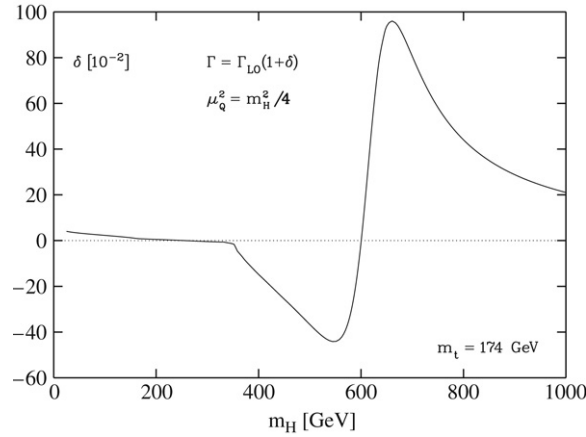


Fig. 2.19. The QCD correction factor for the partial width  $\Gamma(H \rightarrow \gamma\gamma)$  as a function of  $M_H$ . The pole quark masses are  $m_t = 174$  GeV and  $m_b = 5$  GeV and the QCD couplings are normalized at  $\alpha_s(M_Z) = 0.118$ . The renormalization scale is set to  $\mu_Q = \frac{1}{2}M_H$ .

$$m_Q(\mu_Q^2) \rightarrow 0 : \quad \begin{cases} \text{Re } C_H \rightarrow -\frac{1}{18}[\log^2(4\tau) - \pi^2] - \frac{2}{3}\log(4\tau) + 2\log\frac{\mu_Q^2}{m_Q^2} \\ \text{Im } C_H \rightarrow \frac{\pi}{3}\left[\frac{1}{3}\log(4\tau) + 2\right]. \end{cases} \quad (2.52)$$

The QCD correction factor to the partial decay width relative to the lowest-order result,  $\Gamma = \Gamma_{\text{LO}}(1 + \delta)$  is shown in Fig. 2.19 as a function of the Higgs boson mass. The correction is very large slightly above the  $t\bar{t}$  threshold and in the area  $M_H \sim 650$  GeV where the destructive  $W$ - and  $t$ -loop interference makes the decay amplitude nearly vanish.

### 2.3.2. Decays into a photon and a Z boson

Similarly to the  $\gamma\gamma$  case, the  $H \rightarrow Z\gamma$  coupling is built up by the heavy top quark and  $W$  boson loops. The partial decay width is given by [85,86]

$$\Gamma(H \rightarrow Z\gamma) = \frac{G_\mu^2 M_W^2 \alpha M_H^3}{64 \pi^4} \left(1 - \frac{M_Z^2}{M_H^2}\right)^3 \left| \sum_f N_f \frac{Q_f \hat{v}_f}{c_W} A_{1/2}^H(\tau_f, \lambda_f) + A_1^H(\tau_W, \lambda_W) \right|^2 \quad (2.53)$$

with now  $\tau_i = 4M_i^2/M_H^2$ ,  $\lambda_i = 4M_i^2/M_Z^2$  and the form factors

$$A_{1/2}^H(\tau, \lambda) = [I_1(\tau, \lambda) - I_2(\tau, \lambda)] \quad (2.54)$$

$$A_1^H(\tau, \lambda) = c_W \left\{ 4 \left( 3 - \frac{s_W^2}{c_W^2} \right) I_2(\tau, \lambda) + \left[ \left( 1 + \frac{2}{\tau} \right) \frac{s_W^2}{c_W^2} - \left( 5 + \frac{2}{\tau} \right) \right] I_1(\tau, \lambda) \right\}$$

with  $\hat{v}_f = 2I_f^3 - 4Q_f s_W^2$  as usual. The functions  $I_1$  and  $I_2$  are given by

$$\begin{aligned} I_1(\tau, \lambda) &= \frac{\tau\lambda}{2(\tau - \lambda)} + \frac{\tau^2\lambda^2}{2(\tau - \lambda)^2} [f(\tau^{-1}) - f(\lambda^{-1})] + \frac{\tau^2\lambda}{(\tau - \lambda)^2} [g(\tau^{-1}) - g(\lambda^{-1})] \\ I_2(\tau, \lambda) &= -\frac{\tau\lambda}{2(\tau - \lambda)} [f(\tau^{-1}) - f(\lambda^{-1})] \end{aligned} \quad (2.55)$$

where the function  $f(\tau)$  is defined in Eq. (2.47) while the function  $g(\tau)$  can be expressed as

$$g(\tau) = \begin{cases} \sqrt{\tau^{-1} - 1} \arcsin \sqrt{\tau} & \tau \geq 1 \\ \frac{\sqrt{1 - \tau^{-1}}}{2} \left[ \log \frac{1 + \sqrt{1 - \tau^{-1}}}{1 - \sqrt{1 - \tau^{-1}}} - i\pi \right] & \tau < 1. \end{cases} \quad (2.56)$$

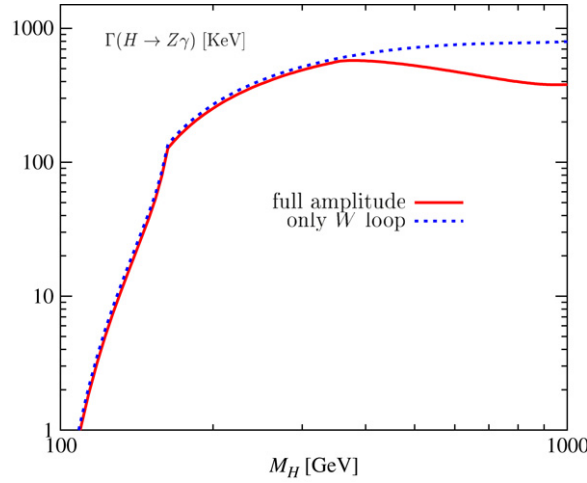


Fig. 2.20. The partial width for the decay  $H \rightarrow Z\gamma$  as a function of  $M_H$  with the full  $W$  boson and top quark contributions (solid line) and with the  $W$  and top quark contributions but with  $m_t \rightarrow \infty$  (dotted line).

Due to charge conjugation invariance, only the vectorial  $Z$  coupling contributes to the fermion loop so that in the limit  $M_H \gg M_Z$ , the  $HZ\gamma$  amplitude reduces to the  $H\gamma\gamma$  amplitude modulo the different  $Z$  and  $\gamma$  couplings to fermions and  $W$  bosons.

The partial width for this decay is shown in Fig. 2.20 as a function of  $M_H$ . As mentioned in Section 1.3.2 where the reverse decay  $Z \rightarrow H\gamma$  was discussed, the  $W$  loop contribution is by far dominating. Below the  $WW$  threshold, where this decay might have a visible branching ratio, it can be approximated by  $A_1^H \simeq -4.6 + 0.3M_H^2/M_W^2$ . The top quark contribution interferes destructively with the  $W$  loop but is very small; for low Higgs boson masses it can be approximated by  $A_{1/2}^H = N_c Q_t \hat{v}_t / (3c_W) \sim 0.3$ . The partial decay width, varies from a few KeV for  $M_H \sim 120$  GeV to  $\sim 100$  KeV for  $M_H \sim 2M_W$ .

The QCD corrections to the quark loop, calculated in Ref. [164], are rather small in the interesting mass range,  $M_H \lesssim 2M_W$ . In the heavy top quark limit, which can be used here, the correction factor for the top quark amplitude is exactly as that in the  $H \rightarrow \gamma\gamma$  case

$$A_{1/2}^H(\tau_t, \lambda_t) \rightarrow A_{1/2}^H(\tau_t, \lambda_t) \times \left[ 1 - \frac{\alpha_s}{\pi} \right] \quad \text{for } M_H^2 \ll 4m_t^2. \quad (2.57)$$

### 2.3.3. Decays into gluons

**2.3.3.1. The partial width at leading order.** The decay of the Higgs boson into two gluons is mediated by loops involving heavy quarks, with the main contribution coming from top quarks and a small contribution from bottom quarks. At the one-loop (leading) order, the partial decay width reads [165,166]

$$\Gamma(H \rightarrow gg) = \frac{G_\mu \alpha_s^2 M_H^3}{36\sqrt{2}\pi^3} \left| \frac{3}{4} \sum_Q A_{1/2}^H(\tau_Q) \right|^2. \quad (2.58)$$

The parameter  $\tau_Q = M_H^2/4m_Q^2$  is defined by the pole mass  $m_Q$  of the heavy quark. The form factor  $A_{1/2}^H(\tau_Q)$ , similar to the  $H \rightarrow \gamma\gamma$  case, is given in Eq. (2.46) and is again normalized such that for  $m_Q \gg M_H$ , it reaches  $\frac{4}{3}$ , while it approaches zero in the chiral limit  $m_Q \rightarrow 0$ . When crossing the quark threshold,  $M_H = 2m_Q$ , the amplitude develops an imaginary part.

The gluonic decay width is shown as a function of the Higgs mass in Fig. 2.21 in the exact case where top and bottom quark loops, with  $m_t = 178$  GeV and  $m_b = 5$  GeV, are included (solid line), when only the top quark contribution is included (dashed line) and when the top quark mass is sent to infinity (dotted line). As can be seen, keeping only the top quark contribution is a good approximation, better than 10% even for  $M_H \sim 100$  GeV, and below the  $M_H = 2m_t$  threshold, the heavy top quark approximation is quite reliable.

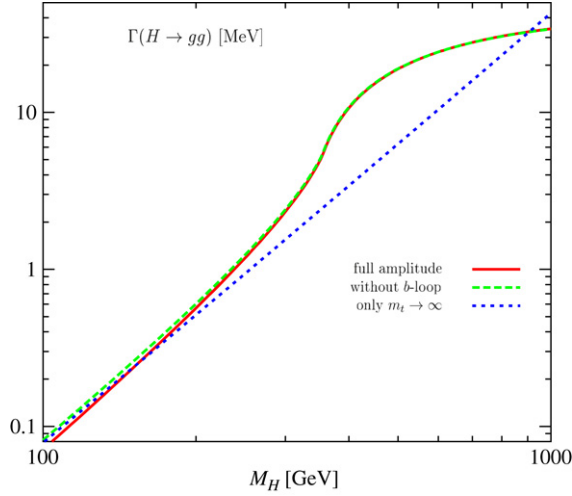


Fig. 2.21. The partial width for the decay  $H \rightarrow gg$  as a function of the Higgs boson mass with the top and bottom quark contributions included (solid line), with only the top quark contribution included (dashed line) and in the limit of infinite top quark mass (dotted line).

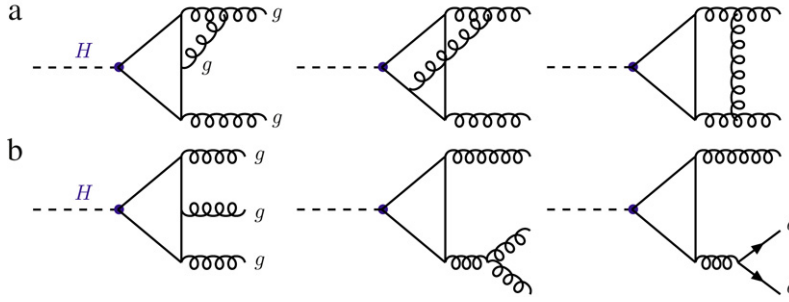


Fig. 2.22. Typical Feynman diagrams for the QCD corrections to the process  $H \rightarrow gg$  at NLO: (a) virtual corrections not present in the decay  $H \rightarrow \gamma\gamma$  and (b) real corrections.

**2.3.3.2. The QCD corrections at NLO.** To incorporate the QCD corrections into the gluonic Higgs boson decay width, one needs to consider not only virtual corrections where the gluons are attached to the quark lines, as in the case of the  $H \rightarrow \gamma\gamma$  decay at NLO, but also corrections involving the triple and quartic gluon vertices; Fig. 2.22(a). These corrections are finite in ultraviolet [since the complementary virtual corrections involved in the  $H \rightarrow \gamma\gamma$  amplitude are also finite] once the proper counterterms associated with the renormalization of the QCD coupling [ $Z_g - 1 = (Z_1 - 1) - \frac{3}{2}(Z_3 - 1)$ ] have been added;  $\alpha_s$  can be defined in the  $\overline{\text{MS}}$  scheme with five active quark flavors and the heavy top quark decoupled. However, there are left-over infrared and collinear singularities which are canceled only if the real corrections with three gluon and a gluon plus a quark–antiquark pair final states  $H \rightarrow gg + g$  and  $g + q\bar{q}$  are added, Fig. 2.22(b). The  $q\bar{q}$  final states will be assumed to be massless and, as a consequence of chiral symmetry, there is no interference of the amplitude for  $H \rightarrow g + q\bar{q}$  and the one  $H \rightarrow q\bar{q}^* \rightarrow q\bar{q}g$  in which the Higgs boson couples directly to quarks [this interference will be discussed in more detail later].

The calculation of the NLO QCD correction in the full massive case has been performed in Ref. [161] where the rather complicated analytical expressions can be found. The total correction can be cast into the form

$$\Gamma(H \rightarrow gg(g), gq\bar{q}) = \Gamma_{\text{LO}}(H \rightarrow gg) \left[ 1 + E_H(\tau_Q) \frac{\alpha_s}{\pi} \right] \quad (2.59)$$

and one obtains for the correction factor

$$E_H(\tau_Q) = \frac{95}{4} - \frac{7}{6}N_f + \frac{33 - 2N_f}{6} \log \frac{\mu^2}{M_H^2} + \Delta E_H(\tau_Q) \quad (2.60)$$



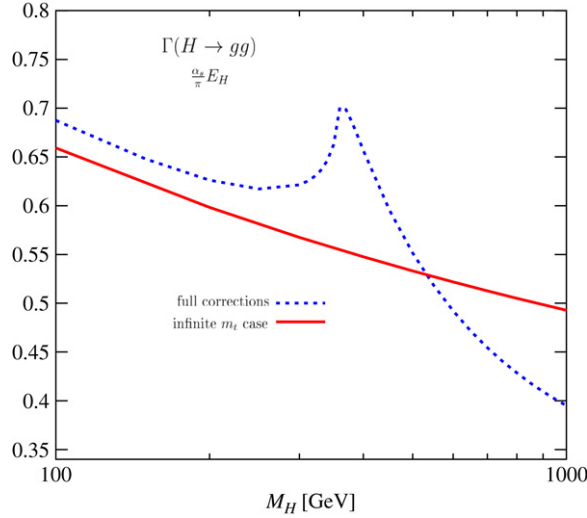


Fig. 2.23. The QCD correction factor for the partial width  $\Gamma(H \rightarrow gg)$  as a function of the Higgs boson mass in the full massive case with  $m_t = 178$  GeV (dotted line) and in the heavy top quark limit (solid line). The strong coupling constant is  $\alpha_s(M_Z) = 0.118$ .

where  $\mu$  is the renormalization point and defines the scale of  $\alpha_s$ . The first three terms survive in the limit of large loop masses while  $\Delta E_H$  vanishes in this limit [167–170].

The QCD radiative corrections turn out to be quite important, nearly doubling the gluonic partial decay width; Fig. 2.23. In the mass range  $M_H \lesssim 2M_W$ , assuming  $N_f = 5$  light quarks and a scale  $\mu = M_H$ , the leading-order term is corrected by a factor

$$K = 1 + \frac{215}{12} \frac{\alpha_s^{N_f=5}(M_H)}{\pi} \quad (2.61)$$

leading to an increase of the partial width by  $\sim 70\%$ . Near the  $t\bar{t}$  threshold, when the  $Hgg$  form factor develops an imaginary part, the correction is also at the level of 70%. It decreases slowly with the Higgs mass to reach 40% at  $M_H \sim 1$  TeV. Also shown in Fig. 2.23 are the QCD corrections in the heavy top quark limit, but where the LO amplitude includes the full  $m_t$  dependence. As can be seen, this procedure approximates quite well the full result in the mass range  $M_H \lesssim 300$  GeV, the difference being less than ten percent.

Since  $b$ -quarks, and eventually  $c$ -quarks, can in principle be tagged experimentally, it is physically meaningful to include gluon splitting  $g^* \rightarrow b\bar{b} (c\bar{c})$  in  $H \rightarrow gg^* \rightarrow gb\bar{b} (c\bar{c})$  decays to the inclusive decay probabilities  $\Gamma(H \rightarrow b\bar{b} + \dots)$  etc. [161,171]. The contribution of the  $b, c$ -quark final states in  $H \rightarrow g + q\bar{q}$  reads

$$-\frac{7}{3} + \frac{1}{3} \left[ \log \frac{M_H^2}{m_b^2} + \log \frac{M_H^2}{m_c^2} \right]. \quad (2.62)$$

Separating this contribution generates large logarithms, which can be effectively absorbed by redefining the number of active flavors in the gluonic decay mode, i.e. by evaluating  $\alpha_s$  with  $N_f = 3$  when both the charm and bottom quark contributions are subtracted. The contributions of the subtracted flavors have then to be added to the corresponding heavy quark decay modes discussed in Section 2.1 [some details will be given in the next section].

#### 2.4. The electroweak corrections and QCD improvements

In this section, we discuss the electroweak radiative corrections and the higher-order QCD corrections to the Higgs decay modes. Some of these corrections have been reviewed in Refs. [20] and [22,23] for, respectively, the electroweak and higher-order QCD parts.

The electroweak radiative corrections to the decays of Higgs bosons into fermions and gauge bosons can be classified in three categories:

- (i) The fermionic corrections, which can be separated into the loop contributions of the light fermions and those due to the heavy top quark: Most of the former corrections are involved in the running of  $\alpha$  and can be readily taken into account by using the improved Born approximation discussed in Section 1.2.4. For the top quark correction, a universal part is due to the renormalization of the Higgs wave function and  $v$  and appears for all fermion species and for gauge bosons. These corrections are in general the dominant electroweak corrections for a SM Higgs boson with a mass  $M_H \lesssim 2m_t$ .
- (ii) Corrections due to the Higgs boson itself that are proportional to the Higgs self-coupling  $\lambda$ : These corrections are important only when  $M_H \gg M_W$ , when the coupling  $\lambda$  becomes sizable. We have seen in Section 1.4.1 that for  $M_H \sim \mathcal{O}(1 \text{ TeV})$ , they can be so large that perturbation theory breaks down.
- (iii) The electromagnetic and the remaining weak corrections which do not depend on  $\lambda$  and which are not quadratic in the top quark mass: These corrections are process dependent and, in general, they lead to small contributions, except in very special cases such as the  $H \rightarrow t\bar{t}$  decay where the heavy top quark limit cannot be applied.

Collecting all these electroweak contributions, the correction factor for a given Higgs decay channel  $H \rightarrow XX$  [also including the decay  $H \rightarrow Z\gamma$ ], can be then written as

$$K_{H \rightarrow XX}^{\text{EW}} = 1 + \delta_{HXX}^t + \delta_{HXX}^\lambda + \delta_{HXX}^e + \delta_{HXX}^w. \quad (2.63)$$

The present knowledge of the electroweak radiative corrections to the SM Higgs decays is as follows. The complete one-loop calculations of the  $H \rightarrow f\bar{f}$  and  $H \rightarrow VV$  decays have been carried out in the massive cases in Refs. [172,173] and [172,174], respectively. The knowledge of the partial widths for these decays has been improved by considering higher-order corrections either in  $\alpha_s$  or in the dominant electroweak coupling  $G_\mu m_t^2$ . The two-loop  $\mathcal{O}(\alpha_s G_\mu m_t^2)$  heavy top corrections to the light-fermion and bottom Yukawa couplings have been calculated in Refs. [175–177], respectively, and those to the  $HVV$  couplings in Ref. [178]. The three-loop  $\mathcal{O}(\alpha_s^2 G_\mu m_t^2)$  corrections may be found in Ref. [179] for the  $H \rightarrow \ell^+ \ell^-$  and  $H \rightarrow VV$  decays and in Ref. [180] for the decay  $H \rightarrow q\bar{q}$ , including the  $b\bar{b}$  case. The two-loop  $\mathcal{O}(G_\mu^2 m_t^4)$  pure electroweak corrections for the  $H \rightarrow f\bar{f}$  and  $H \rightarrow VV$  decays have been derived in Ref. [181]. The radiative corrections due to the Higgs self-couplings have been calculated at one and two loops in Refs. [99,100] for decays into massive gauge bosons and in Refs. [99,101] for decays into fermions.

As for the loop induced Higgs boson vertices, the leading two-loop electroweak corrections, which are of  $\mathcal{O}(G_\mu m_t^2)$  relative to the one-loop results, have been calculated in Refs. [182] for the  $Hgg$  coupling and in Refs. [181,183] for the  $H\gamma\gamma$  and  $HZ\gamma$  couplings. Recently, the two-loop electroweak corrections induced by light fermion loops have been calculated for the  $H \rightarrow \gamma\gamma$  and  $H \rightarrow gg$  decays [184,185]. Furthermore, still in the heavy top quark limit, the NNLO QCD corrections to the decays  $H \rightarrow \gamma\gamma$  [186] and  $H \rightarrow gg$  [187] have been evaluated. Other corrections [188–190] are also available and will be discussed.

The dominant heavy top quark corrections, including the two-loop order in  $G_\mu m_t^2$  and in  $\alpha_s$ , as well as the NNLO QCD corrections to the loop induced decays, can be derived using a low-energy theorem in which the top quark has been integrated out by sending its mass to infinity. The results can nevertheless be extrapolated to Higgs boson masses up to the  $M_H \sim 2m_t$  threshold in principle. In the following, we first discuss this low-energy theorem and its applications for SM Higgs boson decays.

#### 2.4.1. The low-energy theorem

In the case of the top quark loop contributions to the interactions of a light Higgs boson with  $M_H \ll 2m_t$ , a rather simple and efficient way of deriving the corrections is to construct an effective Lagrangian where the top quark is integrated out. This can be done by considering the limit of a massless Higgs boson or, equivalently, of a very heavy top quark and using a low-energy theorem proposed in Refs. [89,157,191] and extended to higher orders in Refs. [161,192]. The low-energy theorem relates the amplitudes of two processes which differ only by the emission of a Higgs boson with vanishing momentum. Indeed, if one recalls the discussion in Section 1.1.3, the coupling of a Higgs boson to a fermion with a mass  $m_i$  is generated by simply performing the substitution

$$m_i^0 \rightarrow m_i^0(1 + H^0/v^0) \quad (2.64)$$

in the bare Lagrangian [the index 0 stands for bare quantities], where the Higgs boson is a constant field. This implies the following relation between two matrix elements with and without the attachment of a Higgs field with zero-

momentum  $p_H$

$$\lim_{p_H \rightarrow 0} \mathcal{M}(X \rightarrow Y + H) = \frac{1}{v_0} m_i^0 \frac{\partial}{\partial m_i^0} \mathcal{M}(X \rightarrow Y). \quad (2.65)$$

However, in higher orders, there is a subtlety in the use of this relation: when renormalizing the  $Hf\bar{f}$  interaction, the counterterm for the Higgs fermion–Yukawa coupling is not the  $Hf\bar{f}$  vertex with a subtraction at zero-momentum transfer,  $\Gamma_{Hf\bar{f}}(q^2 = 0)$  [which is implicitly used in the low-energy theorem] but, rather, is determined by the counterterms for the fermion mass  $Z_m$  and wave function  $Z_2$  as discussed previously. This has to be corrected for and, in fact, this can be done by replacing the differentiation with respect to the bare mass with a differentiation with respect to the renormalized mass, which gives rise to a finite contribution which is simply the anomalous mass dimension of the fermion

$$m_0 \frac{\partial}{\partial m_0} = \frac{m}{1 + \gamma_m} \frac{\partial}{\partial m} \quad (2.66)$$

which relates the bare mass  $m_0$  and the renormalized mass  $m$ ,  $d \log m_0 = (1 + \gamma_m) d \log m$ .

It is well known that this low-energy theorem can be exploited to derive the  $H\gamma\gamma$  coupling in lowest order [157, 191], but the theorem is also valid if radiative QCD corrections are included [161, 192]. The contribution of a heavy quark to the vacuum polarization of the photon at zero-momentum transfer is given in dimensional regularization, with  $n = 4 - \epsilon$  being the number of space dimensions, by

$$\Pi = -Q_Q^2 \frac{\alpha}{\pi} \Gamma(\epsilon) \left( \frac{4\pi\mu^2}{m_Q^2} \right)^\epsilon \left[ 1 + \frac{\alpha_s}{2\pi} \Gamma(1 + \epsilon) \left( \frac{4\pi\mu^2}{m_Q^2} \right)^\epsilon + \mathcal{O}(\epsilon) \right] \quad (2.67)$$

so that  $m_Q(\partial \Pi / \partial m_Q) = 2Q_Q^2 \frac{\alpha}{\pi} (1 + \frac{\alpha_s}{\pi})$ . From the anomalous quark mass dimension to lowest order,  $\gamma_m = 2\alpha_s/\pi$ , one immediately obtains the correction  $C_H$  of the  $H\gamma\gamma$  coupling in agreement with what has been discussed in the previous section, Section 2.3.1,

$$M_H^2/4m_Q^2 \rightarrow 0: \quad 1 + C_H \frac{\alpha_s}{\pi} \rightarrow \frac{1 + \alpha_s/\pi}{1 + 2\alpha_s/\pi} = 1 - \frac{\alpha_s}{\pi}. \quad (2.68)$$

The same result can also be derived by exploiting well-known results on the anomaly in the trace of the energy–momentum tensor [193]

$$\Theta_{\mu\mu} = (1 + \gamma_m) m_0 \bar{Q}_0 Q_0 + \frac{1}{4} \frac{\beta_\alpha}{\alpha} F_{\mu\nu} F_{\mu\nu} \quad (2.69)$$

with  $\beta_\alpha$  denoting the mixed QED/QCD  $\beta$  function defined by  $\partial \alpha(\mu^2) / \partial \log \mu = \beta_\alpha$ . Since the matrix element  $\langle \gamma\gamma | \Theta_{\mu\mu} | 0 \rangle$  vanishes at zero-momentum transfer, the coupling of the two-photon state to the Higgs source  $(m_0/v) \bar{Q}_0 Q_0$  is simply given by the effective Lagrangian

$$\mathcal{L}(H\gamma\gamma) = \frac{H}{v} F^{\mu\nu} F_{\mu\nu} \frac{1}{4} \frac{\beta_\alpha^Q}{\alpha} \frac{1}{1 + \gamma_m} \quad (2.70)$$

including only the heavy quark contribution to the QED/QCD  $\beta$  function. With  $\beta_\alpha^Q = 2Q_Q^2 \alpha^2 / \pi (1 + \alpha_s/\pi)$  and  $\gamma_m = 2\alpha_s/\pi$ , one recovers again the previous result for the QCD correction to the  $H\gamma\gamma$  coupling.

## 2.4.2. EW corrections to decays into fermions and massive gauge bosons

### 2.4.2.1. Heavy top quark corrections.

If one only wishes to extract the leading correction to the Higgs couplings due to a heavy top quark, one may work in the framework of a Yukawa Lagrangian where it couples only to the Higgs boson and to the longitudinal components of the gauge bosons, a situation which corresponds to the gaugeless limit of the SM; of course, the interactions due to light quarks and gluons have to be kept in mind when considering the QCD corrections.

The bare Lagrangian describing the interactions of the Higgs boson with fermions and vector bosons

$$\mathcal{L} = \frac{H_0}{v_0} \left( - \sum_f m_{f0} \bar{f}_0 f_0 + 2M_{W0}^2 W_{0\mu}^\dagger W_0^\mu + M_{Z0}^2 Z_{0\mu}^\dagger Z_0^\mu \right) \quad (2.71)$$

contains the overall factor  $H_0/v_0$ , which undergoes a finite renormalization. Working in the on-shell scheme, where  $G_\mu$  and the physical  $W$  boson mass are used as inputs, and performing the renormalization of all the fields and couplings that are involved, one obtains a universal electroweak correction which appears in the Higgs boson couplings to all particles

$$\begin{aligned} \frac{H_0}{v_0} &\rightarrow (\sqrt{2}G_\mu)^{1/2} H \left( 1 - \frac{\Delta M_W^2}{M_W^2} \right)^{-1/2} [1 + \text{Re } \Pi'_{HH}(M_H^2)]^{-1/2} \\ &\rightarrow (\sqrt{2}G_\mu)^{1/2} H(1 + \delta_u). \end{aligned} \quad (2.72)$$

In the heavy top quark limit, one sets the momentum transfer to zero in the boson propagators, since  $m_t \gg M_W$  and  $M_H$ , and extracts the leading components which grow as  $m_t^2$ . Including the QCD corrections up to  $\mathcal{O}(\alpha_s^2)$  and electroweak corrections to  $\mathcal{O}(G_\mu m_t^2)$  to this terms, one obtains results similar to what has been obtained for  $\Delta\rho$  at this order, Eq. (1.71), with the Higgs boson mass set to zero in the corrections  $(\Delta\rho)^{\text{EW}}$ . Using the abbreviations  $x_t = G_\mu m_t^2 / (8\sqrt{2}\pi^2)$  and  $a_s = \alpha_s^{N_f=6}(m_t)/\pi$ , the end result for the contribution  $\delta_u$  will then be [175,176]

$$\delta_u = x_t \left[ \frac{7}{2} + 3 \left( \frac{149}{8} - \pi^2 \right) x_t - \left( 3 + \frac{\pi^2}{3} \right) a_s - 56.7 a_s^2 \right]. \quad (2.73)$$

For the Higgs boson couplings to leptons, this is in fact the only heavy top quark correction which is involved, unless one moves to higher orders in the electroweak coupling. For the couplings to light quarks  $q \neq b, t$  the same correction  $\delta_u$  appears, except from the small  $\mathcal{O}(x_t a_s^2)$  term which is different. However, in the case of the bottom quarks as well as for the massive gauge bosons, there are extra contributions due to the exchange of the top quark in the vertices. As previously mentioned, to derive these additional terms, one can use again the low-energy theorem with the additional information provided by the knowledge of the particle self-energies. In the case of  $b$ -quarks, one obtains the non-universal correction from the Lagrangian

$$\mathcal{L}(Hb\bar{b}) = -m_b \bar{b} b \frac{H^0}{v_0} (1 + \delta_{Hbb}^{\text{non-univ}}) = -m_b \bar{b} b \frac{H^0}{v_0} \left( 1 - \frac{m_{t0} \partial \Sigma_{bb}}{\partial m_{t0}} \right) \quad (2.74)$$

where  $\Sigma_b$  is the two-point function of the  $b$ -quark, which receives contributions from the top quark when exchanged together with a  $W$  boson in the propagator loop. The non-universal correction in this case is obtained to be [177]

$$\delta_{Hbb}^{\text{non-univ}} = -3x_t \left( 1 - \frac{1}{3} a_s - 11.2 a_s^2 \right). \quad (2.75)$$

Combining this with the universal corrections,  $\delta_u \sim \frac{7}{2} x_t$ , leads to a large cancellation which gives a rather small total correction,  $\delta_b = \frac{1}{2} x_t$ , at the one-loop level.

In the case of the massive gauge bosons, besides the correction  $\delta_u$ , one should also include a non-universal vertex correction, which is different for  $W$  and  $Z$  bosons at higher orders. Again, using the knowledge on the  $W$  and  $Z$  boson two-point functions and setting their momentum transfer to zero, the non-universal correction is obtained from the differentiation with respect to the top mass of the bare  $M_V^2 V_\mu V^\mu$  interaction

$$\delta_{HVV} = (1 + \delta_u) \left( 1 - \frac{m_t^2 \partial}{\partial m_t^2} \right) \frac{\Pi_{VV}(0)}{M_V^2}. \quad (2.76)$$

One then obtains for the total heavy top quark correction at the same order as for the correction  $\delta_u$  [178]

$$\delta_w = x_t \left[ -\frac{5}{2} + \left( \frac{39}{8} - 3\pi^2 \right) x_t + \left( 9 - \frac{\pi^2}{3} \right) a_s + 27.0 a_s^2 \right]$$

$$\delta_z = x_t \left[ -\frac{5}{2} + \left( \frac{177}{8} + 3\pi^2 \right) x_t + \left( 15 - \frac{\pi^2}{3} \right) a_s + 17.1 a_s^2 \right]. \quad (2.77)$$

Adding up all the previous results, one finds for the heavy top correction factor  $\delta_{HXX}^t$  in Eq. (2.63), for the fermionic and bosonic decay widths of the Higgs boson [in which the  $HXX$  coupling appears squared]

$$\delta_{HXX}^t = (1 + \delta_x)^2 - 1. \quad (2.78)$$

**2.4.2.2. The remaining electroweak corrections.** In the case of light fermions, the electromagnetic corrections are simply given by [173]

$$\delta_{Hff}^e = \frac{3}{2} \frac{\alpha}{\pi} Q_f^2 \left( \frac{3}{2} - \log \frac{M_H^2}{m_f^2} \right). \quad (2.79)$$

For quark final states, the large logarithms  $\log M_H^2/m_q^2$  can be absorbed in the running quark masses analogously to the QCD corrections. In this case, the electromagnetic correction, supplemented by the NLO QCD correction, reads [188]

$$\delta_{Hqq}^e = 4.2 Q_q^2 \frac{\bar{\alpha}(M_H)}{\pi} \left[ 1 + 5.2 \frac{\alpha_s}{\pi} \right]. \quad (2.80)$$

The remaining weak corrections can be approximated by [the reduced vector and axial couplings  $\hat{v}_f$  and  $\hat{a}_f$  have been defined previously] [20]

$$\delta_{Hff}^w = \frac{G_\mu M_Z^2}{8\sqrt{2}\pi^2} \left[ c_W^2 \left( -5 + \frac{3}{s_W^2} \log c_W^2 \right) - \frac{6\hat{v}_f^2 - \hat{a}_f^2}{2} \right]. \quad (2.81)$$

In the case of Higgs decays into massive gauge bosons, the electromagnetic corrections for  $H \rightarrow ZZ$  are absent, while the vertex corrections and the real-photon emission in the decay  $H \rightarrow W^+W^-$  do not form a gauge invariant and meaningful set, and must be combined with the photonic contributions to the self-energies [174]. The remaining electroweak corrections [except for the ones involving the self-coupling  $\lambda$ ] are in general small.

For Higgs boson decay into top quarks, since  $m_t$  cannot be set to zero or infinity anymore, the situation is more complicated. The electromagnetic corrections with virtual photon exchange and real-photon emission [the running of  $\alpha$  is again taken care of by using the IBA with  $G_\mu$  as input] are the same as the QCD corrections discussed in Section 2.1.3 if the strong coupling  $\alpha_s$  is replaced by the proper electromagnetic factor

$$\delta_{Htt}^e = \frac{3}{4} Q_t^2 \frac{\alpha}{\pi} \Delta_H^t(\beta_t). \quad (2.82)$$

Because of the Coulomb singularity, these corrections are large near threshold,  $M_H \sim 2m_t$ , but are small far above threshold leading to a correction less than 1%.

For the electroweak corrections, which are interesting since they involve the Higgs contributions [and if  $M_H \sim 2m_t$  mixing between the Higgs boson and the spin-zero  $t\bar{t}$  bound state would occur], the expression is rather complicated since  $m_t \neq 0$  [173]. However a simple interpolating formula can be obtained, which approximates the full result to the level of 1% even in the threshold region. In terms of  $h_t = M_H^2/4m_t^2$  and  $\ell_t = \log M_H/m_t$ , one has [20]

$$\delta_{Htt}^w = \frac{G_\mu m_t^2}{2\sqrt{2}\pi^2} \left( 1 + \frac{5}{2h_t} \right) \ell_t (\ell_t - 2) + 1.059h_t + 3.477 + \frac{0.272}{h_t} - \frac{1.296}{h_t^2} - \frac{0.182}{h_t^3}. \quad (2.83)$$

Numerically, this correction is extremely small near the threshold and increases monotonically to reach the level of  $\sim 15\%$  for  $M_H \sim 1$  TeV.

**2.4.2.3. Higgs self-coupling corrections.** Finally, one has to include the corrections due to the triple and quartic Higgs boson couplings. In the regime where the Higgs boson mass is large, one obtains at two-loop order in the on-shell

scheme [100,101]

$$\begin{aligned}\delta_{Hff}^\lambda &= (13 - 2\sqrt{3}\pi) \left( \frac{\lambda}{16\pi^2} \right) - 32.66 \left( \frac{\lambda}{16\pi^2} \right)^2 \\ \delta_{HVV}^\lambda &= \left( 19 - 6\sqrt{3}\pi - \frac{5\pi^2}{3} \right) \left( \frac{\lambda}{16\pi^2} \right) + 62.0 \left( \frac{\lambda}{16\pi^2} \right)^2.\end{aligned}\quad (2.84)$$

Numerically, the result as a function of the Higgs boson mass is

$$\begin{aligned}\delta_{Hff}^\lambda &= 0.11 (M_H/1 \text{ TeV})^2 - 0.09 (M_H/1 \text{ TeV})^2 \\ \delta_{HVV}^\lambda &= 0.15 (M_H/1 \text{ TeV})^2 + 0.17 (M_H/1 \text{ TeV})^2.\end{aligned}\quad (2.85)$$

As discussed in Section 1.4.1, if the Higgs boson mass is very large,  $M_H \sim \mathcal{O}(10 \text{ TeV})$ , the one-loop terms of these expansions become close to the Born terms and the perturbative series does not converge. In fact, already for a Higgs boson mass close to  $M_H \sim 1 \text{ TeV}$ , the two-loop contributions become as important as the one-loop contributions. Hence, for the perturbation theory to hold,  $M_H$  should be smaller than about one TeV. In this mass regime, however, the total correction  $\delta_{HVV}^\lambda$  is moderate, being at the level of  $\delta_{HVV}^\lambda \sim 20\%$  for  $M_H \sim 1 \text{ TeV}$ . In the case of fermionic decays, the total correction is even smaller,  $\delta_{Hff}^\lambda \simeq 2\%$  for  $M_H \simeq 1 \text{ TeV}$ , because of the accidental cancellation of the one-loop and two-loop contributions.

#### 2.4.3. NNLO QCD and EW corrections to the loop induced decays

**2.4.3.1. The NNLO QCD corrections.** One can use the low-energy theorem discussed in Section 2.4.1 to derive the higher-order QCD corrections to the  $H\gamma\gamma$  and  $Hgg$  couplings in the heavy top quark limit. In the case of the  $H\gamma\gamma$  operator, the QED/QCD  $\beta$  function and the anomalous mass dimension  $\gamma_m$  are known for four loops. The contribution of the top quark to the  $H\gamma\gamma$  coupling at  $\mathcal{O}(\alpha_s^2)$ , with  $N_f = 6$  flavors and a renormalization scale  $\mu$ , is found to be [186]

$$\mathcal{L}_{\text{eff}}(H\gamma\gamma) = \frac{Q_t^2 \alpha}{2\pi} (\sqrt{2} G_F)^{1/2} \left[ 1 - \frac{\alpha_s}{\pi} - \left( \frac{31}{4} + \frac{7}{4} \log \frac{\mu^2}{m_t^2} \right) \left( \frac{\alpha_s}{\pi} \right)^2 \right] F_{\mu\nu} F_{\mu\nu} H. \quad (2.86)$$

In the case of the  $Hgg$  operator in the heavy top quark limit

$$\mathcal{L}_{\text{eff}}(Hgg) = \frac{H}{v} G_{\mu\nu}^a G^{a\mu\nu} C_g \quad (2.87)$$

the QCD correction can be again expressed in terms of the heavy quark contribution  $\beta_Q(\alpha_s)$  to the QCD  $\beta$  function and to the anomalous quark mass dimension  $\gamma_m$  as

$$\mathcal{L}_{\text{eff}}(Hgg) = -\frac{\alpha_s}{4} \frac{H}{v} G_{\mu\nu}^a G^{a\mu\nu} \frac{\beta_Q(\alpha_s)}{\alpha_s^2} \frac{1}{1 + \gamma_m(\alpha_s)} \quad (2.88)$$

which is valid at two loops [at three loops, some subtleties appear and are discussed in Ref. [22] for instance]. At  $\mathcal{O}(\alpha_s^2)$ , the anomalous quark mass dimension is given by [194]

$$\gamma_m(\alpha_s) = 2 \frac{\alpha_s}{\pi} + \left( \frac{101}{12} - \frac{5}{18} (N_f + 1) \right) \left( \frac{\alpha_s}{\pi} \right)^2 \quad (2.89)$$

while the QCD  $\beta$  function at NNLO in the  $\overline{\text{MS}}$  scheme is given by [40]

$$\beta_Q(\alpha_s) = \frac{\alpha_s^2}{3\pi} \left[ 1 + \frac{19}{4} \frac{\alpha_s}{\pi} + \frac{7387 - 325N_f}{288} \left( \frac{\alpha_s}{\pi} \right)^2 \right]. \quad (2.90)$$

From these expressions and taking care of the fact that the  $\overline{\text{MS}}$  strong coupling  $\alpha_s$  of the effective theory should include only the  $N_f = 5$  light flavors [see again Ref. [22] for details], one arrives, using a consistent  $\alpha_s$  expansion at

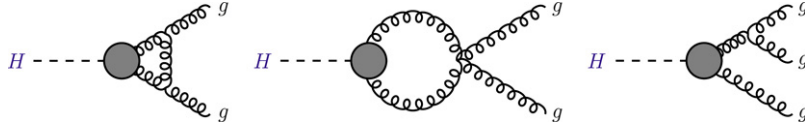


Fig. 2.24. Effective diagrams contributing to the  $Hgg$  interaction in the limit where the top quark is heavy and has been integrated out. The blob represents the effective  $Hgg$  coupling.

the final result for the coefficient function  $C_g$  at NNLO with a scale taken to be  $\mu = m_t$ , to [180]

$$C_g = -\frac{\alpha_s}{12\pi} \left[ 1 + \frac{11}{4} \frac{\alpha_s}{\pi} + \frac{2777 - 201N_f}{288} \left( \frac{\alpha_s}{\pi} \right)^2 + \dots \right]. \quad (2.91)$$

However, contrary to the two-photon case,  $\mathcal{L}_{\text{eff}}(Hgg)$  does not describe the  $Hgg$  interaction in total: it accounts only for the interactions mediated by the heavy quarks directly but it does not include the interactions of the light fields. It must be added to the light-quark and gluon parts of the basic QCD Lagrangian, i.e. the effective coupling has to be inserted into the blobs of the effective diagrams shown in Fig. 2.24 for the interaction of the Higgs boson with gluons and massless quarks.

For instance, for the Higgs decay into gluons at NLO, one adds to the contribution to the effective  $Hgg$  coupling squared  $(1 + \frac{11}{4} \frac{\alpha_s}{\pi})^2$ , the gluon and light quarks contributions from the pure gluonic virtual corrections and the real correction from  $H \rightarrow ggg$  and  $H \rightarrow gq\bar{q}$  with  $N_f$  light quarks,  $(\frac{73}{4} - \frac{7N_f}{6})$ , leading to the total contribution for  $\mu^2 = M_H^2$

$$\frac{11}{2} \frac{\alpha_s}{\pi} + \left( \frac{73}{4} - \frac{7N_f}{6} \right) \frac{\alpha_s}{\pi} = \left( \frac{95}{4} - \frac{7N_f}{6} \right) \frac{\alpha_s}{\pi} \quad (2.92)$$

which was given in Eq. (2.60) for the gluonic Higgs partial width at NLO.

At NNLO, the calculation has also been done for the interaction of the Higgs boson with the light fields and this will be discussed later when we will address the question of Higgs production in the  $gg \rightarrow H$  fusion mechanism. Here, we simply give the final result for the correction factor for the partial  $H \rightarrow gg$  decay width at NNLO, for a number of light flavors  $N_f = 5$  and with a scale  $\mu = M_H$ , which reads [187]

$$K_{H \rightarrow gg}^{\text{QCD}} = 1 + \frac{215}{12} \frac{\alpha_s(M_H)}{\pi} + \frac{\alpha_s^2(M_H)}{\pi^2} \left( 156.8 - 5.7 \log \frac{m_t^2}{M_H^2} \right). \quad (2.93)$$

The three-loop correction amounts to  $\sim 20\%$  of the [one-loop] Born term and  $\sim 30\%$  of the two-loop term, therefore showing a good convergence behavior of the perturbative series.

**2.4.3.2. Electroweak and self-coupling corrections.** We now turn to the dominant electroweak corrections to the Higgs boson loop induced decays, those which are proportional to  $G_\mu m_t^2$ . Again, one can use a variant of the low-energy theorem discussed previously to calculate the two-loop  $\mathcal{O}(G_\mu m_t^2)$  correction to the  $Hgg$  coupling [157,191]. The obtained effective  $Hgg$  coupling at this order is given by

$$\mathcal{L}(Hgg) = (\sqrt{2}G_\mu)^{1/2} \frac{\alpha_s}{12\pi} H G_{\mu\nu} G^{\mu\nu} (1 + \delta_1 + \delta_2 + \delta_3). \quad (2.94)$$

Here,  $\delta_1$  is the contribution of the top quark to the QCD  $\beta$  function at  $\mathcal{O}(\alpha_s G_\mu m_t^2)$ , which can be evaluated by considering the two-loop diagrams where Higgs and Goldstone bosons are exchanged in the heavy quark loop

$$\frac{\beta(\alpha_s)}{g_s} = \frac{\alpha_s}{6\pi} (1 + \delta_1) \Rightarrow \delta_1 = -12 \frac{G_\mu m_t^2}{8\sqrt{2}\pi^2}. \quad (2.95)$$

The term  $\delta_2$  is simply the contribution of the anomalous quark mass dimension

$$\delta_2 = (Z_2^Q - 1) - \frac{\delta m_Q}{m_Q} + \Gamma_{HQ\bar{Q}}(q^2 = 0) = 6 \frac{G_\mu m_t^2}{8\sqrt{2}\pi^2}. \quad (2.96)$$



Finally,  $\delta_3$  represents the renormalization of the Higgs wave function and vev

$$\delta_3 = -\frac{1}{2} \left[ \frac{\Pi_{WW}(0)}{M_W^2} + \frac{\partial \Pi_{HH}(M_H^2 = 0)}{\partial M_H^2} \right] = 7 \frac{G_\mu m_t^2}{8\sqrt{2}\pi^2}. \quad (2.97)$$

Due to the large cancellation between the three components,  $\delta_1 = -12$ ,  $\delta_2 = +6$  and  $\delta_3 = 7$  in units of  $\frac{1}{2}x_t = G_\mu m_t^2/(16\sqrt{2}\pi^2)$ , the total correction factor at this order is rather small. The  $\mathcal{O}(G_\mu m_t^2)$  correction to the NLO QCD term has also been also calculated [189] and the total correction factor for the gluonic decay width is then

$$\delta_{Hgg}^t = x_t \left( 1 + 30.3 \frac{\alpha_s}{\pi} \right). \quad (2.98)$$

For  $m_t \sim 180$  GeV, the total factor is very small being at the level of 0.5%. Recently, these top quark corrections to the  $H \rightarrow gg$  decays have been calculated exactly in the mass range  $M_H \lesssim 2M_W$  [185]. The numerical result turned out to be quite different from the one obtained in the infinite top mass limit, even for a low mass Higgs boson. However, the correction factor is still rather small.

The electromagnetic corrections to the  $Hgg$  amplitude can be straightforwardly adapted from those of the NLO QCD corrections to the  $H\gamma\gamma$  coupling. Indeed, the only contributions which are involved are those in which a photon is exchanged in the internal quark lines. One then obtains, after the appropriate change of the QCD and electric charge factors

$$\delta_{Hgg}^e = -\frac{3}{4} Q_t^2 \frac{\alpha}{\pi} = -\frac{1}{3} \frac{\alpha}{\pi} \quad (2.99)$$

a correction which is extremely small, being at the per mille level.

In the case of the  $H\gamma\gamma$  coupling, while the correction to the fermionic loop can be carried out along the same lines as in the case of the  $Hgg$  coupling, for the  $W$  boson loop several subtleties arise. First, the application of the low-energy theorem is restricted to the mass range  $M_H \lesssim 160$  GeV in this case. A second complication is due to the fact that when considering the leading  $m_t$  correction, owing to QED-like Ward identities, there is no  $\mathcal{O}(G_\mu^2 m_t^4)$  correction [as one notices from the  $Hgg$  case] and the largest correction scales only quadratically with the top mass. In the calculation of this  $\mathcal{O}(G_\mu^2 m_t^2)$  correction, one cannot simply use the gaugeless limit of the SM since the contributions involving virtual  $W$  bosons cannot be neglected. In fact, after integrating out the heavy fermion contribution, one has two-dimensional four operators which produce  $\mathcal{O}(G_\mu^2 m_t^2)$  corrections to the  $H\gamma\gamma$  amplitude

$$\mathcal{L}(H\gamma\gamma) = (\sqrt{2}G_\mu)^{1/2} H \left( c_1 F_{\mu\nu} F^{\mu\nu} + c_2 M_W^2 W_\mu^\dagger W^\mu + \dots \right) \quad (2.100)$$

with the dots standing for the contribution of higher-order operators. While the coefficient  $c_2$  has been previously derived, one needs to perform an explicit two-loop calculation to derive the coefficient  $c_1$ . This can be done again by considering only diagrams involving, along with top quarks, virtual Goldstone bosons minimally coupled to photons. Once the relevant contribution to the photon self-energy has been calculated, one can use the low-energy theorem to relate it to the  $H\gamma\gamma$  amplitude in the kinematical regime where  $M_H \lesssim 2M_W \lesssim 2m_t$ . The calculation has been performed in Ref. [183] and the obtained correction factor can be attributed to the  $W$  amplitude and written as

$$A_1^H(\tau_W) \rightarrow A_1^H(\tau_W)(1 - 2.9x_t). \quad (2.101)$$

The total correction decreases the  $H \rightarrow \gamma\gamma$  decay width by approximately 2.5% and, thus, fully cancels the positive  $\mathcal{O}(\alpha_s/\pi)$  QCD correction in the heavy top limit.

In the loop induced decays, there are also corrections due to the light fermions,  $f \neq t$ . At the one-loop level, these contributions are suppressed by their couplings to the Higgs boson and are thus negligible. However, at the two-loop level, one can avoid this suppression by coupling them to the  $W$  and  $Z$  bosons which are then directly attached to the Higgs boson. These corrections have been calculated only recently [184].

In the case of the  $H \rightarrow gg$  decay, the light quark contributions generate a correction to the partial decay width that is positive and increases from  $\sim 4.5\%$  at  $M_H \sim 115$  GeV to  $\sim 9\%$  at  $M_H \sim 2M_W$  [the correction varies from 4.5% to 7.5% in this mass range, if the heavy top contribution is included]. Above this value, the correction decreases sharply and remains below  $-2\%$  for  $M_H \lesssim 2m_t$ . In the case of the  $H \rightarrow \gamma\gamma$  decay, below the  $2M_W$  threshold, the

light fermion contribution leads to a correction of the same size as the QCD correction, i.e.  $\sim 1\%$ , but with opposite sign. Above the  $2M_W$  threshold, the corrections are larger and lead to a suppression of the decay width by a few percent.

Finally, one has to include the Higgs self-coupling corrections which appear only in the bosonic contribution to the  $H\gamma\gamma$  amplitude at two loops. The calculation can be done using the equivalence theorem where the  $W$  boson is replaced by its corresponding Goldstone boson which can be taken as massless [but only at the end of the calculation, since it serves as an infrared cut-off in intermediate steps]. In this limit one obtains [190]

$$\delta_{H\gamma\gamma}^\lambda = -12.1 \frac{\lambda^2}{16\pi^2}. \quad (2.102)$$

The correction is small for  $M_H \lesssim 500$  GeV, but is significant for values  $M_H \sim 650$  GeV where the amplitude almost vanishes because of the  $t$  and  $W$  negative interference. For  $M_H \sim 1$  TeV, the correction becomes large and decreases the partial width by approximately  $-30\%$ .

#### 2.4.4. Summary of the corrections to hadronic Higgs decays

Let us finally reconsider the QCD corrections to the hadronic Higgs boson decays in the light of all the corrections that have been discussed previously. As already mentioned, at higher orders, the Higgs decays into gluons and light quarks are mixed and already at the next-to-leading order, the two decays  $H \rightarrow gg^* \rightarrow g\bar{q}q$  and  $H \rightarrow \bar{q}^*q \rightarrow g\bar{q}q$  lead to the same final states. The two decays cannot therefore be considered separately at higher orders. The present knowledge of the higher-order QCD corrections [and the leading electroweak corrections] to the full decay  $H \rightarrow \text{hadrons}$  has been discussed in detail in Ref. [23]. In this subsection, we will simply give the full result for the hadronic Higgs decay width that one obtains for  $M_H \lesssim 2M_W$  by including all the corrections which are known up to  $\mathcal{O}(\alpha_s^3)$ ,  $\mathcal{O}(\alpha\alpha_s)$ ,  $\mathcal{O}(G_\mu m_t^2 \alpha_s^2)$  and  $\mathcal{O}(\lambda^2)$ .

Writing the interaction Lagrangian of the Higgs boson with quarks and gluons as

$$\mathcal{L}_{\text{had}} = \sqrt{2}G_\mu H [m_q \bar{q}q C_q + G_{\mu\nu}^a G_a^{\mu\nu} C_g] \quad (2.103)$$

the decay width of the Higgs boson, summing the gluonic and light-quark decays and working in the approximation of an infinitely heavy top quark, can be written as [23]

$$\begin{aligned} \Gamma(H \rightarrow \text{hadrons}) = & \sum_q A_{q\bar{q}} K_{H \rightarrow q\bar{q}}^{\text{EW}} \left[ (1 + \Delta_{qq}) (C_q)^2 + \Delta_{qg} C_g C_q + \delta_q^{\text{me}} \right] \\ & + A_{gg} K_{H \rightarrow gg}^{\text{EW}} \left[ \Delta_{gg} (C_g)^2 + \delta_g^{\text{me}} \right] \end{aligned} \quad (2.104)$$

where the tree level  $q\bar{q}$  and  $gg$  squared amplitudes are given by

$$A_{q\bar{q}} = \frac{3G_\mu M_H}{4\sqrt{2}\pi} \bar{m}_q^2 (M_H^2), \quad A_{gg} = \frac{4G_\mu M_H^3}{\sqrt{2}\pi} \quad (2.105)$$

and the coefficients of the operators appearing in the Lagrangian, by

$$\begin{aligned} C_g = & -\frac{1}{12} \frac{\alpha_s}{\pi} \left[ 1 + \left( \frac{11}{4} - \frac{1}{6} \ell_t \right) \frac{\alpha_s}{\pi} + \left( 9.35 - 0.7N_f + (0.33N_f - 0.52\ell_t) + 0.028\ell_t^2 \right) \left( \frac{\alpha_s}{\pi} \right)^2 \right] \\ C_q = & 1 + \left( \frac{5}{18} - \frac{1}{3} \ell_t \right) \left( \frac{\alpha_s}{\pi} \right)^2 + \left( 1.35 + 0.25N_f - 2.9\ell_t + (0.056N_f - 0.8)\ell_t^2 \right) \left( \frac{\alpha_s}{\pi} \right)^3 \end{aligned} \quad (2.106)$$

with  $\alpha_s \equiv \alpha_s^5(M_H^2)$  defined at the scale  $M_H$  with  $N_f = 5$  light quarks and  $\ell_t = \log(M_H^2/m_t^2)$ . The various terms appearing in equation Eq. (2.104), are as follows:

- $\Delta_{qq}$  is the pure QCD corrections to the decays into quarks Eq. (2.11) up to  $\mathcal{O}(\alpha_s^3)$ , supplemented by the contributions of order  $\alpha$  and the mixed QCD/QED contribution at  $\mathcal{O}(\alpha\alpha_s)$  Eq. (2.80)

$$\Delta_{qq} = \frac{\alpha_s}{\pi} \left[ \frac{17}{3} + (35.94 - 1.36N_f) \frac{\alpha_s}{\pi} + (164.14 - 25.77N_f + 0.26N_f^2) \left( \frac{\alpha_s}{\pi} \right)^2 \right] + \frac{\alpha(M_H)}{\pi} Q_q^2 \left[ 4.25 + 11.71 \frac{\alpha_s}{\pi} \right]. \quad (2.107)$$

- $\Delta_{gg}$  is the QCD correction to the gluonic decay mode due to the light quark and gluon fields

$$\Delta_{gg} = 1 + (18.25 - 1.17N_f) \frac{\alpha_s}{\pi} + (243 - 39.4N_f + 0.9N_f^2) \left( \frac{\alpha_s}{\pi} \right)^2. \quad (2.108)$$

- $\Delta_{gq}$  is the mixed contribution in quark and gluon Higgs decays

$$\Delta_{gq} = -\frac{\alpha_s}{\pi} \left[ 30.67 + (524.85 - 20.65N_f) \frac{\alpha_s}{\pi} \right]. \quad (2.109)$$

If one considers final states involving quarks only, one has to subtract from the previous equation the gluonic contribution as discussed previously; at  $\mathcal{O}(\alpha_s)$ , one has for instance

$$\Delta'_{gg} = \frac{\alpha_s}{\pi} \left[ 13.56 - \frac{4}{3} \log^2(m_q^2/M_H^2) + \mathcal{O}\left(\frac{\alpha_s^2}{\pi^2}\right) \right]. \quad (2.110)$$

- $K_{H \rightarrow qq}^{\text{EW}}$  and  $K_{H \rightarrow gg}^{\text{EW}}$  are the sum of the electroweak corrections for the quark and gluonic decays discussed previously [but without the electromagnetic corrections for the former decay since they are included in  $\Delta_{qq}$ ]. Note that in this case,  $\alpha_s$  is defined at the scale  $m_t$ .

• Finally,  $\delta_q^{\text{me}}$  and  $\delta_g^{\text{me}}$  are the remaining contributions that contain the light quark masses and non-leading terms in  $m_t$  in fermionic and gluonic Higgs decays. Since higher-order terms  $\mathcal{O}(M_H^4/m_t^4)$  and  $\mathcal{O}(\bar{m}_b^4/M_H^4)$  are very small for  $M_Z \lesssim M_H \lesssim 2M_W$ , one can simply retain the first terms in the  $M_H^2/m_t^2$  and  $\bar{m}_q^2/M_H^2$  expansions

$$\begin{aligned} \delta_q^{\text{me}} &= \left( \frac{\alpha_s}{\pi} \right)^2 \frac{M_H^2}{m_t^2} \left[ 0.241 - 0.07 \log \frac{M_H^2}{m_t^2} \right] - 6 \frac{\bar{m}_q^2}{M_H^2} \left[ 1 + 6.67 \frac{\alpha_s}{\pi} \right] \\ \delta_g^{\text{me}} &= 0.1167 \frac{M_H^2}{m_t^2} \left( \frac{\alpha_s}{\pi} \right)^2 \left[ 1 + \left( 17.85 - 2 \log \frac{M_H^2}{m_t^2} \right) \frac{\alpha_s}{\pi} \right]. \end{aligned} \quad (2.111)$$

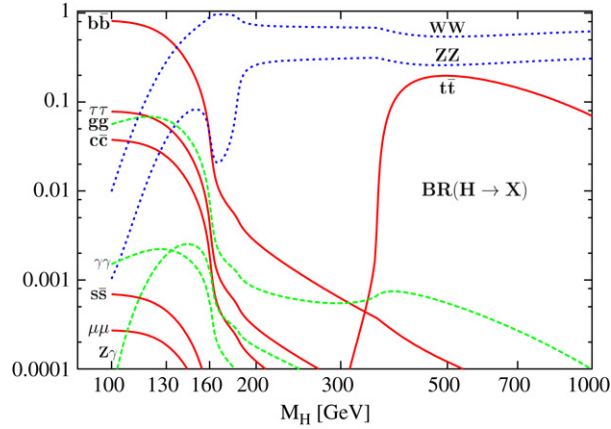
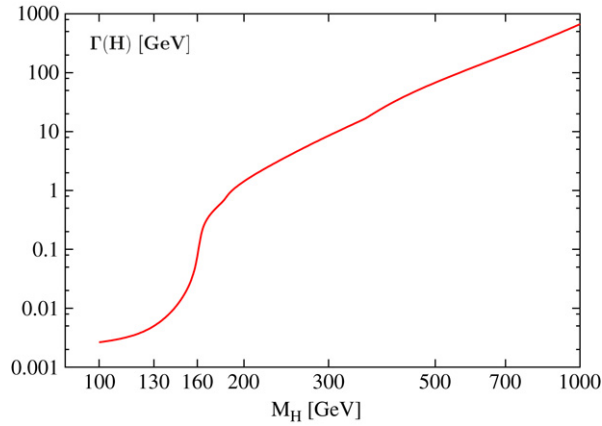
This completes the discussion of the main QCD and electroweak radiative corrections to the hadronic decays of an intermediate mass Higgs boson.

### 2.5. The total decay width and the Higgs branching ratios

The decay branching ratios and the total width of the SM Higgs boson are shown in Figs. 2.25 and 2.26, respectively, as functions of the Higgs mass. They have been obtained using the FORTRAN code HDECAY [195] with the fermion and gauge boson mass inputs of Eq. (2.1) and with the strong coupling constant normalized to  $\alpha_s(M_Z) = 0.1172$ . Included are all decay channels that are kinematically allowed and that have branching ratios larger than  $10^{-4}$ , *y compris* the loop mediated, the three-body  $\bar{t}t^*$  and  $VV^*$  decay modes and the double off-shell decays of the Higgs boson into massive gauge bosons which then decay into four massless fermions. In addition, all relevant two-loop QCD corrections to the decays into quark pairs and to the quark loop mediated decays into gluons [and photons] are incorporated; the smaller leading electroweak radiative corrections are also included. To be as complete as possible, we also present in Table 2.1 the numerical values of the branching ratios and total decay width for selected values of  $M_H$ , as it might be useful to have a normalization as close as possible to the state of the art, to be used in other theoretical or experimental studies.

To discuss the Higgs decays, it is useful to consider three distinct mass ranges:

- the “low mass” range  $110 \text{ GeV} \lesssim M_H \lesssim 130 \text{ GeV}$ ,
- the “intermediate mass” range  $130 \text{ GeV} \lesssim M_H \lesssim 180 \text{ GeV}$ ,
- the “high mass” range  $180 \text{ GeV} \lesssim M_H \lesssim 1 \text{ TeV}$ .

Fig. 2.25. The SM Higgs boson decay branching ratios as functions of  $M_H$ .Fig. 2.26. The SM Higgs boson total decay width as a function of  $M_H$ .

The main features of the branching ratios and total width can be summarized as follows.

In the “low mass” range,  $100 \text{ GeV} \lesssim M_H \lesssim 130 \text{ GeV}$ , the main decay mode of the Higgs boson is by far  $H \rightarrow b\bar{b}$  with a branching ratio of  $\sim 75\%$ – $50\%$  for  $M_H = 115$ – $130 \text{ GeV}$ , followed by the decays into  $\tau^+\tau^-$  and  $c\bar{c}$  pairs with branching ratios of the order of  $\sim 7\%$ – $5\%$  and  $\sim 3\%$ – $2\%$ , respectively. Also of significance is the  $H \rightarrow gg$  decay with a branching fraction of  $\sim 7\%$  for  $M_H \sim 120 \text{ GeV}$ . The  $\gamma\gamma$  and  $Z\gamma$  decays are rare, with branching ratios at the level of a few per mille, while the decays into pairs of muons and strange quarks [where  $\bar{m}_s(1 \text{ GeV}) = 0.2 \text{ GeV}$  is used as input] are at the level of a few times  $10^{-4}$ . The  $H \rightarrow WW^*$  decays, which are below the 1% level for  $M_H \sim 100 \text{ GeV}$ , dramatically increase with  $M_H$  to reach  $\sim 30\%$  at  $M_H \sim 130 \text{ GeV}$ ; for this mass value,  $H \rightarrow ZZ^*$  occurs at the percent level.

In the “intermediate mass” range, the Higgs boson decays mainly into  $WW$  and  $ZZ$  pairs, with one virtual gauge boson below the  $2M_V$  kinematical thresholds. The only other decay mode which survives is the  $b\bar{b}$  decay which has a branching ratio that drops from 50% at  $M_H \sim 130 \text{ GeV}$  to the level of a few percent for  $M_H \sim 2M_W$ . The  $WW$  decay starts to dominate at  $M_H \sim 130 \text{ GeV}$  and becomes gradually overwhelming, in particular for  $2M_W \lesssim M_H \lesssim 2M_Z$  where the  $W$  boson is real [and thus the decay  $H \rightarrow WW$  occurs at the two-body level] while the  $Z$  boson is still virtual, strongly suppressing the  $H \rightarrow ZZ^*$  mode and leading to a  $WW$  branching ratio of almost 100%.

In the “high mass” range,  $M_H \gtrsim 2M_Z$ , the Higgs boson decays exclusively into the massive gauge boson channels with a branching ratio of  $\sim 2/3$  for  $WW$  and  $\sim 1/3$  for  $ZZ$  final states, slightly above the  $ZZ$  threshold. The opening of the  $t\bar{t}$  channel for  $M_H \gtrsim 350 \text{ GeV}$  does not alter significantly this pattern, in particular for high Higgs masses: the  $H \rightarrow t\bar{t}$  branching ratio is at the level of 20% slightly above the  $2m_t$  threshold and starts decreasing for

Table 2.1

The Higgs decay branching ratios and total widths in the SM

$M_H$ (GeV)	BR ( $b\bar{b}$ )	BR ( $\tau\tau$ )	BR ( $\mu\mu$ )	BR ( $s\bar{s}$ )	BR ( $c\bar{c}$ )	BR ( $t\bar{t}$ )
115	0.736	$7.21 \times 10^{-2}$	$2.51 \times 10^{-4}$	$6.23 \times 10^{-4}$	$3.39 \times 10^{-2}$	–
120	0.683	$6.78 \times 10^{-2}$	$2.35 \times 10^{-4}$	$5.79 \times 10^{-4}$	$3.15 \times 10^{-2}$	–
130	0.533	$5.36 \times 10^{-2}$	$1.86 \times 10^{-4}$	$4.51 \times 10^{-4}$	$2.45 \times 10^{-2}$	–
140	0.349	$3.56 \times 10^{-2}$	$1.23 \times 10^{-4}$	$2.95 \times 10^{-4}$	$1.60 \times 10^{-2}$	–
150	0.179	$1.85 \times 10^{-2}$	–	$1.51 \times 10^{-4}$	$8.23 \times 10^{-3}$	–
160	$4.11 \times 10^{-2}$	$4.30 \times 10^{-3}$	–	–	$1.89 \times 10^{-3}$	–
170	$8.64 \times 10^{-3}$	$9.13 \times 10^{-4}$	–	–	$3.97 \times 10^{-4}$	–
180	$5.53 \times 10^{-3}$	$5.90 \times 10^{-4}$	–	–	$2.54 \times 10^{-4}$	–
200	$2.65 \times 10^{-3}$	$2.89 \times 10^{-4}$	–	–	$1.22 \times 10^{-4}$	–
300	$6.21 \times 10^{-4}$	–	–	–	–	–
400	$2.35 \times 10^{-4}$	–	–	–	–	0.157
500	$1.20 \times 10^{-4}$	–	–	–	–	0.199
600	–	–	–	–	–	0.171
700	–	–	–	–	–	0.138
1000	–	–	–	–	–	0.066

$M_H$ (GeV)	BR ( $gg$ )	BR ( $\gamma\gamma$ )	BR ( $Z\gamma$ )	BR ( $WW$ )	BR ( $ZZ$ )	$\Gamma_H$ (GeV)
115	$6.74 \times 10^{-2}$	$2.04 \times 10^{-3}$	$6.75 \times 10^{-4}$	$7.84 \times 10^{-2}$	$8.04 \times 10^{-3}$	$3.27 \times 10^{-3}$
120	$6.84 \times 10^{-2}$	$2.16 \times 10^{-3}$	$1.06 \times 10^{-3}$	0.130	$1.49 \times 10^{-2}$	$3.65 \times 10^{-3}$
130	$6.30 \times 10^{-2}$	$2.21 \times 10^{-3}$	$1.91 \times 10^{-3}$	0.283	$3.80 \times 10^{-2}$	$5.00 \times 10^{-3}$
140	$4.82 \times 10^{-2}$	$1.93 \times 10^{-3}$	$2.47 \times 10^{-3}$	0.480	$6.71 \times 10^{-2}$	$8.11 \times 10^{-3}$
150	$2.87 \times 10^{-2}$	$1.39 \times 10^{-3}$	$2.39 \times 10^{-3}$	0.679	$8.27 \times 10^{-2}$	$1.67 \times 10^{-2}$
160	$7.57 \times 10^{-3}$	$5.54 \times 10^{-4}$	$1.23 \times 10^{-3}$	0.900	$4.36 \times 10^{-1}$	$0.77 \times 10^{-1}$
170	$1.82 \times 10^{-3}$	$1.50 \times 10^{-4}$	$3.97 \times 10^{-4}$	0.965	$2.25 \times 10^{-2}$	0.383
180	$1.32 \times 10^{-3}$	$1.02 \times 10^{-4}$	$2.98 \times 10^{-4}$	0.934	$5.75 \times 10^{-1}$	0.628
200	$8.06 \times 10^{-4}$	–	$1.77 \times 10^{-4}$	0.735	0.261	1.425
300	$5.74 \times 10^{-4}$	–	–	0.691	0.307	8.50
400	$7.36 \times 10^{-4}$	–	–	0.574	0.268	29.54
500	$5.27 \times 10^{-4}$	–	–	0.542	0.260	67.89
600	$3.64 \times 10^{-4}$	–	–	0.558	0.270	122.6
700	$2.53 \times 10^{-4}$	–	–	0.578	0.283	199.9
1000	–	–	–	0.625	0.309	664.3

$M_H \sim 500$  GeV to reach a level below 10% at  $M_H \sim 800$  GeV. The reason is that while the  $H \rightarrow t\bar{t}$  partial decay width grows as  $M_H$ , the partial decay width into (longitudinal) gauge bosons increases as  $M_H^3$ .

Finally, for the total decay width, the Higgs boson is very narrow in the low mass range,  $\Gamma_H < 10$  MeV, but the width becomes rapidly wider for masses larger than 130 GeV, reaching  $\sim 1$  GeV slightly above the  $ZZ$  threshold. For larger Higgs masses,  $M_H \gtrsim 500$  GeV, the Higgs boson becomes obese: its decay width is comparable to its mass because of the longitudinal gauge boson contributions in the decays  $H \rightarrow WW, ZZ$ . For  $M_H \sim 1$  TeV, one has a total decay width of  $\Gamma_H \sim 700$  GeV, resulting in a very broad resonant structure. However, as previously discussed, for this large Higgs mass value, the perturbation theory is jeopardized anyway.

A final word must be devoted to the uncertainties on these Higgs decay branching ratios. As discussed at length in this section, the strong coupling constant  $\alpha_s$  and the quark masses play a prominent role in Higgs physics. However, these parameters are affected by relatively large experimental errors which then translate into sizable uncertainties in the Higgs boson decay branching ratios and in the total decay width.<sup>18</sup> Following Ref. [171], and using the updated values of the quark masses given in Eq. (2.1) and of  $\alpha_s(M_Z) = 0.1172 \pm 0.002$ , we show in Fig. 2.27 the effect of varying the input parameters [but only one at a time] by one standard deviation from their central values.

In the low-to-intermediate mass range where the Higgs decays into light quarks and gluons are significant, these errors are rather large. In particular, the branching ratios for the charm and gluonic decays have uncertainties at the

<sup>18</sup> Thus, contrary to what is sometimes claimed in the literature, these are not “theoretical errors” but mostly a reflection of the poor knowledge of the quark masses and QCD coupling constant.

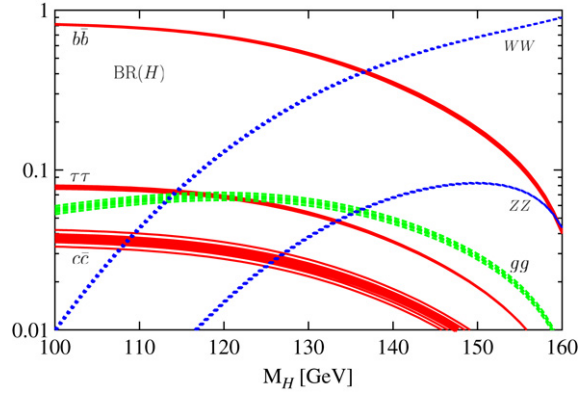


Fig. 2.27. The SM Higgs boson decay branching ratios in the low and intermediate Higgs mass ranges including the uncertainties from the quark masses  $m_t = 178 \pm 4.3$  GeV,  $m_b = 4.88 \pm 0.07$  GeV and  $m_c = 1.64 \pm 0.07$  GeV as well as from  $\alpha_s(M_Z) = 0.1172 \pm 0.002$ .

level of 20% and 10%, respectively. The main reason for these errors is the  $\sim 2\%$  uncertainty in  $\alpha_s$ , which translates into a 4% (6%) error in  $\Gamma(H \rightarrow gg) \propto \alpha_s^2 (\alpha_s^3)$  at the one- (two-) loop level, and in a very strong variation of the charm quark mass,  $m_c(\mu) \sim [\alpha_s(\mu)]^{12/13}$ , at the high scales. The error on  $m_t$  does not affect substantially the  $H \rightarrow gg$  branching ratio since, as already noticed, the heavy top quark limit is a good approximation for these Higgs mass values. The uncertainty on the dominant  $H \rightarrow b\bar{b}$  branching ratio is small since the experimental error on the  $b$ -quark mass is relatively smaller and its running is less important than that in the case of charm quarks; in addition for low Higgs masses,  $\Gamma(H \rightarrow b\bar{b})$  controls the total width and most of the uncertainty cancels in the branching ratio. The error on the  $H \rightarrow \tau^+\tau^-$  branching ratio is simply due to that of  $\Gamma(H \rightarrow b\bar{b})$  in the total Higgs decay width.

[Note that, in the high mass range above the  $t\bar{t}$  threshold, the errors on the top quark mass and the strong coupling constant do not affect significantly the branching fraction of the  $H \rightarrow t\bar{t}$  decay, the error being at the percent level for  $M_H \gtrsim 500$  GeV, and *a fortiori* the branching ratios for  $H \rightarrow WW, ZZ$  which dominate in this Higgs mass range.]

Thus, although the expected hierarchy of the Higgs decay modes is still visible from Fig. 2.27, a more precise measurement of  $\alpha_s$  and the quark masses will be necessary to check completely the predictions of the SM for the Higgs decay branching ratios which, as will be discussed in the next sections, can be measured at the level of a few percent. In turn, if we are confident enough that the observed Higgs is the SM Higgs particle, one can turn the experimental measurement of the branching ratios into a determination of the light quark masses and  $\alpha_s$  at the scale of the Higgs mass, in much the same way as the running  $b$ -quark mass has been determined in  $Z$  decays at LEP1 [47].

### 3. Higgs production at hadron colliders

#### 3.1. Higgs bosons at hadron machines

##### 3.1.1. Generalities about hadron colliders

The  $p\bar{p}$  collider<sup>19</sup> Tevatron at Fermilab is the highest-energy accelerator available today. In the previous Run I, the collider was operating at an energy of  $\sqrt{s} = 1.8$  TeV in the  $p\bar{p}$  center of mass, and from both the CDF and DØ experiments data corresponding to about  $\int \mathcal{L} dt \sim 100 \text{ pb}^{-1}$  of integrated luminosity has been collected.<sup>20</sup> The upgrade with the Main Injector allows the machine to possibly deliver an order of magnitude more instantaneous luminosity. In Run II, it is expected that  $5 \text{ fb}^{-1}$  of data will be collected, with the possibility of increasing the sample to  $10 \text{ fb}^{-1}$  if the machine runs efficiently until the end of the decade [196]; see Ref. [197] for the luminosity delivered by the machine. In Run II, the energy of the machine has been raised from  $\sqrt{s} = 1.8$  TeV to  $\sqrt{s} = 1.96$  TeV which, typically, increased the cross sections for some physics processes by about 30%. The CDF and DØ detectors have also been upgraded, allowing them to make more sensitive searches than before [198,199].

<sup>19</sup> For simplicity, we will use sometimes the notation  $pp$  for both  $pp$  and  $p\bar{p}$  collisions in this review.

<sup>20</sup> Also for simplicity, we will denote by  $\mathcal{L}$  both the instantaneous and integrated luminosities.



The CERN Large Hadron Collider (LHC) under construction is a  $pp$  collider designed to run at an energy  $\sqrt{s} = 14$  TeV in the  $pp$  center of mass and a luminosity of  $\mathcal{L} = 10^{34} \text{ cm}^{-2} \text{ s}^{-1}$  (high-luminosity regime). The first collisions are expected in June 2007 but only with an instantaneous luminosity of  $\mathcal{L} = 10^{33} \text{ cm}^{-2} \text{ s}^{-1}$  (low-luminosity regime); see [200,201]. At the end of the decade, the accumulated integrated luminosity is expected to be  $\mathcal{L} = 30 \text{ fb}^{-1}$ , to be increased to  $100 \text{ fb}^{-1}$  per year when the machine runs at the design luminosity. The hope is to collect at least  $300 \text{ fb}^{-1}$  of data per experiment during the entire LHC operation [200]. There are plans, the so-called SLHC, to operate the LHC at still the same energy  $\sqrt{s} \sim 14$  TeV, i.e. retaining the present magnets and dipoles, but at the luminosity of  $\mathcal{L} = 10^{35} \text{ cm}^{-2} \text{ s}^{-1}$  leading to  $1 \text{ ab}^{-1}$  integrated luminosity per year [202–204]. With new magnets with field strengths of approximately 16 Tesla (which do not currently exist), the energy of the collider could be raised to  $\sqrt{s} = 28$  TeV. Designs for a very large hadron collider (VLHC), with a c.m. of mass energy of the order of 40 TeV to 200 TeV [a revival of the ancient Eloisatron idea, see Ref. [205] for instance], are currently studied [206,207]. The SLHC and VLHC options will only be briefly discussed in this report.

The two general purpose experiments under construction, ATLAS [208,209] and CMS [210,211], have been optimized to cover a large spectrum of possible signatures in the LHC environment [212]. However, the Higgs search, together with Supersymmetry, has been the major guide to define the detector requirements and performances for the experiments, and most of the simulation studies have been performed for these two physics cases.

The total cross section at hadron colliders is extremely large. It is about 100 mb at the LHC, resulting in an interaction rate of  $\approx 10^9$  Hz at the design luminosity. In this hostile environment, the detection of processes with signal-to-total-hadronic-cross-section ratios of about  $10^{-10}$ , as is the case for the production a SM Higgs boson in most channels, will be a difficult experimental challenge [213–221]. The huge QCD-jet backgrounds prevent one from detecting the produced Higgs boson [and any particle in general] in fully hadronic modes. Recalling that when ignoring the light quark and gluon modes, the Higgs decays mostly into  $b\bar{b}$ ,  $\tau\tau$ ,  $WW$ ,  $ZZ$  and  $\gamma\gamma$ ,  $Z\gamma$  final states in the mass range below  $M_H \lesssim 160$  GeV and into  $WW$ ,  $ZZ$  and  $t\bar{t}$  final states above this mass value, the following general requirements have to be met in order to extract a signal in the entire Higgs mass range:

- In the decay  $H \rightarrow WW, ZZ$ , at least one of the  $W/Z$  bosons has to be observed in its leptonic decays which have small branching ratios,  $\text{BR}(W \rightarrow \ell\nu) \simeq 20\%$  with  $\ell = \mu, e$  and  $\text{BR}(Z \rightarrow \ell^+\ell^-) \simeq 6\%$ ; in the latter case the invisible neutrino decays,  $\text{BR}(Z \rightarrow \nu\nu) \simeq 18\%$ , can also be sometimes used to increase the statistics. A very good detection of isolated high transverse momentum muons and electrons and an accurate calorimetry with hermetic coverage to measure the transverse energy of the missing neutrinos are thus required.

- A very high resolution of the photons is necessary to isolate the narrow  $\gamma\gamma$  signal peak in the decay  $H \rightarrow \gamma\gamma$  from the large continuum  $\gamma\gamma$  background. Since the Higgs boson width is small, a few MeV for  $M_H \simeq 120\text{--}140$  GeV, the measured mass peak is entirely dominated by the experimental resolution. Furthermore, the very large number of high transverse momentum  $\pi^0$  decaying into two photons should be rejected efficiently.

- In the dominant Higgs decay mode in the low mass range,  $H \rightarrow b\bar{b}$ , excellent micro-vertex detectors are needed to identify the  $b$ -quark jets with a high efficiency and a high purity.  $\tau$ -lepton identification is also important to detect the decays  $H \rightarrow \tau^+\tau^-$  and the invariant mass of the final state should be reconstructed with a good resolution.

Together with good granularity and hermeticity coverage for jet resolution and missing transverse energy, these requirements are apparently met by the CDF and DØ detectors at Tevatron [199] and are expected to be met by the ATLAS and CMS detectors at LHC.

The most unambiguous signal for a Higgs boson [and for any new particle] is a peak in the invariant mass distribution of its decay products. The narrow mass peak can be discovered without any Monte Carlo simulation for the backgrounds, since the latter can be precisely measured from the side bands. In addition, the discovery can be made even if the signal is rather low and the background large, since the significance is  $\propto S/\sqrt{S+B}$ . This however is not true when it comes to the study of some properties of the Higgs boson, such as its couplings and its spin–parity quantum numbers. In this case, Monte Carlo simulations are needed to determine the cross sections and the various characteristic distributions of the signal and backgrounds. The most precise theoretical predictions are therefore required.

### 3.1.2. Higgs production at hadron machines

In the Standard Model, the main production mechanisms for Higgs particles at hadron colliders make use of the fact that the Higgs boson couples preferentially to the heavy particles, that is the massive  $W$  and  $Z$  vector bosons, the top quark and, to a lesser extent, the bottom quark. The four main production processes, the Feynman diagrams



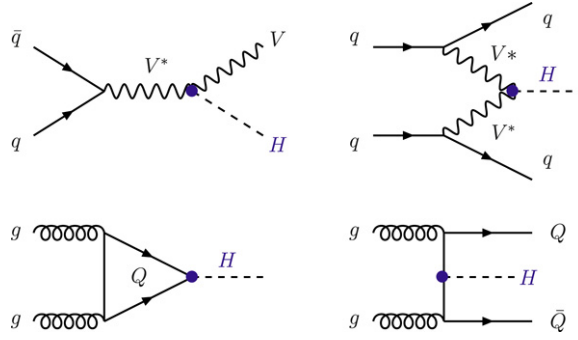


Fig. 3.1. The dominant SM Higgs boson production mechanisms in hadronic collisions.

of which are displayed in Fig. 3.1, are thus: the associated production with  $W/Z$  bosons [222,223], the weak vector boson fusion processes [90,224–227], the gluon–gluon fusion mechanism [166] and the associated Higgs production with heavy top [228,229] or bottom [230,231] quarks:

$$\text{associated production with } W/Z: \quad q\bar{q} \longrightarrow V + H \quad (3.1)$$

$$\text{vector boson fusion:} \quad qq \longrightarrow V^*V^* \longrightarrow qq + H \quad (3.2)$$

$$\text{gluon–gluon fusion:} \quad gg \longrightarrow H \quad (3.3)$$

$$\text{associated production with heavy quarks:} \quad gg, q\bar{q} \longrightarrow Q\bar{Q} + H. \quad (3.4)$$

There are also several mechanisms for the pair production of the Higgs particles

$$\text{Higgs pair production:} \quad pp \longrightarrow HH + X \quad (3.5)$$

and the relevant subprocesses are the  $gg \rightarrow HH$  mechanism, which proceeds through heavy top and bottom quark loops [232,233], the associated double production with massive gauge bosons [234,235],  $q\bar{q} \rightarrow HHV$ , and the vector boson fusion mechanisms  $qq \rightarrow V^*V^* \rightarrow HHqq$  [236,237]; see also Ref. [235]. However, because of the suppression by the additional electroweak couplings, they have much smaller production cross sections than the single Higgs production mechanisms listed above.

Also suppressed are processes where the Higgs is produced in association with one [239,240], two [241,242] or three [243] hard jets in gluon–gluon fusion, the associated Higgs production with gauge boson pairs [244,245], the production with a vector boson and two jets [245–247]. Other production processes exist which have even smaller production cross sections [136,248–253]. Finally, Higgs bosons can also be produced in diffractive processes [254–258]. For the interesting exclusive-central-diffractive processes [256–258], the mechanism is mediated by color singlet exchanges leading to the diffraction of the incoming hadrons and a centrally produced Higgs boson. A mixture of perturbative and non-perturbative aspects of QCD is needed to evaluate the cross sections, leading to uncertainties in the predictions.

In this chapter, we discuss all these processes in detail, analyzing not only the total production cross sections but also the differential distributions and, in particular, the Higgs boson transverse momentum and rapidity distributions. In addition, we pay special attention to three very important points: the QCD radiative corrections or the  $K$ -factors, the residual cross section dependence on the renormalization and factorization scales, and the choices of different sets of parton distributions functions (PDFs) with which one has to convolute the partonic cross sections to obtain the total hadronic cross sections.

### 3.1.3. The higher-order corrections and the $K$ -factors

It is well known that for processes involving strongly interacting particles, as is the case for the ones that we will consider here, the lowest-order (LO) cross sections are affected by large uncertainties arising from higher-order (HO) corrections. If at least the next-to-leading-order (NLO) QCD corrections to these processes are included, the total cross sections can be defined properly and in a reliable way in most cases: the renormalization scale  $\mu_R$  at which one defines the strong coupling constant and the factorization scale  $\mu_F$  at which one performs the matching between the

perturbative calculation of the matrix elements and the non-perturbative part which resides in the parton distribution functions, are fixed and the generally non-negligible radiative corrections are taken into account.

The impact of higher-order QCD corrections is usually quantified by calculating the  $K$ -factor, which is defined as the ratio of the cross section for the process [or its distribution] at HO with the value of  $\alpha_s$  and the PDFs evaluated also at HO, over the cross section [or distribution] at LO with  $\alpha_s$  [for those processes which are QCD processes at LO] and the PDFs consistently also evaluated at LO<sup>21</sup>

$$K = \frac{\sigma_{\text{HO}}(pp \rightarrow H + X)}{\sigma_{\text{LO}}(pp \rightarrow H + X)}. \quad (3.6)$$

All the dominant Higgs production processes which are addressed here will be discussed at least at NLO [259]. At this order, the QCD corrections are known since more than a decade for the associated production with  $W/Z$  bosons [260–262], the vector boson fusion processes [262–265] and the gluon–gluon mechanism [161,168,266,267], while the NLO corrections to the associated production with heavy quarks have been calculated only recently [268–272]. To improve further the theoretical predictions for the cross sections, one can also resum the soft and collinear gluon radiation parts which in general leads to large logarithms and includes the dominant electroweak radiative corrections which however, are much smaller than the QCD corrections, in particular when the improved Born approximation of Section 1.2.4 is used.

The QCD corrections to the transverse momentum and rapidity distributions are also available in the case of vector boson fusion [264,265] and gluon–gluon fusion [273–279]. In the latter case, the resummation of the large logarithms for the  $P_T$  distribution has been performed at next-to-next-to-leading-logarithm (NNLL) accuracy. The QCD corrections to the various distributions in the associated Higgs production with  $t\bar{t}$  are discussed in [268].

In two cases, the associated  $HV$  production [280] and the  $gg \rightarrow H$  fusion mechanism in the approximation where the top quark is very heavy [281–284], the calculation of the production cross sections at NNLO has been performed recently and will be discussed. However, these calculations are not sufficient to obtain a full NNLO prediction: the cross sections must be folded with the NNLO evolved PDFs, which is also necessary. The latter require the calculation of the Altarelli–Parisi splitting functions [285] up to three loops and until very recently the latter were not completely known at this order. Nevertheless, a large number of moments of these functions were available [286] which, when combined with additional information on the behavior at small  $x$ , allowed one to obtain an approximation of the splitting functions at the required order. The NNLO MRST [287] parton distributions followed this approach and have been therefore adopted for NNLO calculations.<sup>22</sup>

### 3.1.4. The scale dependence

The evaluation of the residual theoretical uncertainties in the production cross sections or distributions, due to the not yet calculated higher-order corrections, is generally based on the exploration of the cross section dependence on the renormalization scale  $\mu_R$  and on the factorization scale  $\mu_F$ . Starting from a median scale  $\mu_0$  which, with an educated guess, is considered as the “natural scale” of the process and is expected to absorb the large logarithmic corrections, the current standard convention is to vary the two scales, either collectively or independently [i.e. keeping one scale fixed at the reference value], within

$$\mu_0/a \leq \mu_F, \mu_R \leq a\mu_0. \quad (3.7)$$

The value of the constant  $a$  is in general chosen to be 2 or 3, the latter case being more conservative and will be adopted in most cases. In some situations in which widely different scales are involved in the processes, it is more prudent to use larger values for  $a$ , as will be seen in the case of Higgs production in bottom quark fusion for instance.

<sup>21</sup> Note that if the  $K$ -factor is defined as the ratio of NLO to LO cross sections both evaluated with  $\alpha_s$  and PDFs at NLO, it would be in many cases larger since the value of the strong coupling constant, which appears in both the matrix element squared of the hard process and in the parton distribution functions, is smaller at NLO,  $\alpha_s^{\text{NLO}}(M_Z) \sim 0.12$ , than at LO,  $\alpha_s^{\text{LO}}(M_Z) \sim 0.13$ , thereby decreasing the LO cross section.

<sup>22</sup> The calculation of the  $N_f$  part of the non-singlet structure function in DIS, from which one can extract the corresponding splitting function, is available since some time and has been compared to the approximate result of Ref. [286] and a full agreement has been obtained, giving rise to great confidence that the approximate NNLO PDFs are rather accurate. Recently, the full calculation of the NNLO splitting function has been completed [288] and it alters the NNLO MRST PDFs only by a small amount [289].

Note that the scale dependence at leading order can be studied by defining a kind of  $K$ -factor for the LO cross section,  $K_{\text{LO}}$ , by evaluating the latter at given factorization and renormalization scales  $\mu_F$  and  $\mu_R$ , and normalizing to the LO cross sections evaluated at the median scale  $\mu_0$

$$K_{\text{LO}} = \sigma_{\text{LO}}(\mu_F, \mu_R) / \sigma_{\text{LO}}(\mu_F = \mu_R = \mu_0). \quad (3.8)$$

By varying the scales  $\mu_R$  and  $\mu_F$ , one then obtains an uncertainty band: the narrower the band is, the smaller the higher-order corrections are expected to be. Note that the scale uncertainty should be in principle reduced when higher-order corrections are included, that is, the scale variation should be smaller at NNLO, than at NLO and LO. However, this is not the case all the time, and a counterexample will be discussed later.

One should nevertheless caution that the variation of the cross section with respect to the scale choice is unphysical: it is just a reflexion of the truncation of the perturbative series; if the cross sections are known to all orders, they will not exhibit this dependence. The scale variation is thus, by no means a rigorous way to estimate the theoretical uncertainty. At best, it might only give an indication of the “full” uncertainty. This can be seen in many cases, where for instance the NLO and LO uncertainty bands for some production cross sections do not overlap at all, as will be shown later.

### 3.1.5. The parton distribution functions

Parton distribution functions (PDFs), which describe the momentum distribution of a parton in the proton, play a central role at hadron colliders. A precise knowledge of the PDFs over a wide range of the proton momentum fraction  $x$  carried by the parton and the squared center of mass energy  $Q^2$  at which the process takes place, is mandatory to precisely predict the production cross sections of the various signal and background processes. However, they are plagued by uncertainties, which arise either from the starting distributions obtained from a global fit to the available data from deep-inelastic scattering, Drell–Yan and hadronic data, or from the DGLAP evolution [285,290] to the higher  $Q^2$  relevant to the scattering processes. Together with the effects of unknown perturbative higher-order corrections, these uncertainties dominate the theoretical error on the predictions of the cross sections.

The CTEQ [291] and MRST [292] collaborations, as well as Alekhin [293] and others [294], recently introduced new schemes, which provide the possibility of estimating the intrinsic and spread uncertainties on the prediction of physical observables at hadron colliders. The CTEQ and MRST schemes are based on the Hessian matrix method which enables a characterization of a parton parametrization in the neighborhood of the global  $\chi^2$  minimum fit and gives an access to the uncertainty estimation through a set of PDFs that describe this neighborhood. The corresponding PDFs are constructed as follows: (i) a global fit of the data is performed using the free parameters  $N_{\text{PDF}} = 20$  for CTEQ and  $N_{\text{PDF}} = 15$  for MRST; this provides the nominal PDF (reference set) denoted by  $S_0$  and corresponding to CTEQ6M and MRST2001C, respectively; (ii) the global  $\chi^2$  of the fit is increased by  $\Delta\chi^2 = 100$  for CTEQ and  $\Delta\chi^2 = 50$  for MRST, to obtain the error matrix; (iii) the error matrix is diagonalized to obtain  $N_{\text{PDF}}$  eigenvectors corresponding to  $N_{\text{PDF}}$  independent directions in the parameter space; (iv) for each eigenvector, up and down excursions are performed in the tolerance gap, leading to  $2N_{\text{PDF}}$  sets of new parameters, corresponding to 40 new sets of PDFs for CTEQ and 30 sets for MRST. They are denoted by  $S_i$ , with  $i = 1, 2N_{\text{PDF}}$ .

To build the Alekhin PDFs [293], only light-target deep-inelastic scattering data are used. This PDF set involves 14 parameters, which are fitted simultaneously with  $\alpha_s$  and the structure functions, leading to  $2N_{\text{PDF}} = 30$  sets of PDFs for the uncertainty estimation. Note that the three PDF sets use different values for  $\alpha_s$ : at NLO, the central sets CTEQ6M, MRST2001C and A02 use, respectively,  $\alpha_s^{\text{NLO}}(M_Z) = 0.118, 0.119$  and  $0.117$ .

The three sets of PDFs discussed above can be used to calculate the uncertainty on a cross section  $\sigma$  in the following way [295]: one first evaluates the cross section with the nominal PDF  $S_0$  to obtain the central value  $\sigma_0$ . One then calculates the cross section with the  $S_i$  PDFs, giving  $2N_{\text{PDF}}$  values  $\sigma_i$ , and defines, for each  $\sigma_i$  value, the deviations  $\sigma_i^{\pm} = |\sigma_i - \sigma_0|$  when  $\sigma_i \gtrless \sigma_0$ . The uncertainties are summed quadratically to calculate  $\Delta\sigma^{\pm} = \sqrt{\sum_i \sigma_i^{\pm 2}}$ . The cross section, including the error, is then given by  $\sigma_0 \left|_{-\Delta\sigma}^{+\Delta\sigma}\right.$ . This procedure will be applied to estimate the uncertainties in the cross sections for SM Higgs production in the four main mechanisms. The spread in the cross section prediction will depend on the considered partons and their  $x$  regime that we will briefly summarize below.

The differences between the PDFs originate from three main sources: (i) the choice of the data used in the global fit, (ii) the theoretical assumptions made for the fit and (iii) the choice of the tolerance used to define the error in the PDFs. Thus, for example, the MRST and CTEQ differences arise from points (ii) and (iii) only, with point (iii) dominating in most cases. The differences between the two approaches [291,292] are explained in detail in Ref. [292], and for

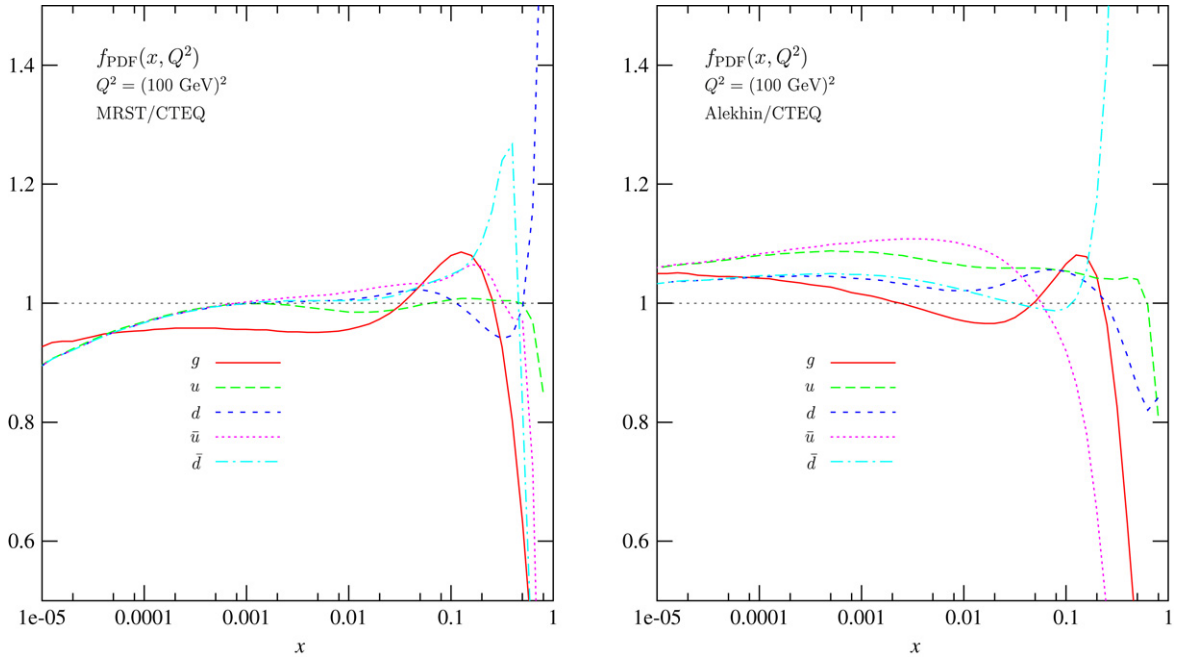


Fig. 3.2. MRST and Alekhin densities for the gluon, up quark/down quark and antiquarks, normalized to the CTEQ6 ones, as functions of  $x$  and for  $Q^2 = (100 \text{ GeV})^2$ ; from Ref. [295].

instance the CTEQ6 high- $x$  gluon is larger than the MRST2001 one. The differences with the Alekhin analysis, which does not use the Tevatron data, are larger.

To be more qualitative, we present in Fig. 3.2, the MRST and Alekhin densities for the gluon and for the up and down quarks and antiquarks, normalized to the CTEQ6 ones, for a wide range of  $x$  values and for a fixed c.m. energy  $Q^2 = (100 \text{ GeV})^2$ . One notices the following main features: (i) the MRST gluon PDF is smaller than the CTEQ one, except for values  $x \sim 0.1$ ; in contrast, the Alekhin gluon PDF is larger than the CTEQ one for all  $x$  values, except for  $x \sim 0.01$  and for very high  $x$ . (ii) The MRST (anti)quark PDFs are practically equal in magnitude and are smaller than the CTEQ ones for low  $x$ , while they are in general slightly larger for higher  $x$ , except for values near unity; in the Alekhin case, all (anti)quark PDFs are larger than the CTEQ ones, except for the  $\bar{u}$  density above  $x \sim 0.05$ . For values,  $x \gtrsim 10^{-4}$ , the differences between the Alekhin and the CTEQ6 PDFs are more pronounced than the differences between the MRST and the CTEQ ones.

As for the CTEQ and MRST parametrizations, three different behaviors of the uncertainty bands according to three  $x$  ranges can be distinguished: decreasing uncertainties at low  $x$ , constant or slightly oscillating ones at intermediate  $x$ , and increasing ones at high  $x$ . The magnitudes of these uncertainties depend on the considered parton and on the c.m. energy  $Q^2$ . In the case of quarks, the three behaviors are observed: the low- $x$  behavior extends up to  $x \sim \text{few } 10^{-3}$ , and the high- $x$  one starts in the neighborhood of  $x = 0.7$ . At high  $Q^2$ , the uncertainties at high- and low- $x$  values exceed a few tens of a percent and in the intermediate regime, they are less than a few percent. In the gluon case and at high  $Q^2$ , the low- $x$  and the intermediate- $x$  bands are not well separated as in the case of quarks; the uncertainty band reaches also the few percent level. The high- $x$  regime starts in the neighborhood of  $x \sim 0.3$ , i.e. earlier than in the case of quarks.

### 3.2. The associated production with W/Z bosons

#### 3.2.1. The differential and total cross sections at LO

It is useful to consider the cross section for the associated production of the Higgs particle with massive gauge bosons, which then decay into two massless fermions, in a completely differential form so that various distributions can be presented and cuts can be imposed on the final decay products. For the Higgs boson, since it is a scalar particle, the incorporation of its decays into a given final state,  $H \rightarrow X$ , is simply done by multiplying the matrix element

squared by the branching ratio  $\text{BR}(H \rightarrow X)$  and generating the final state  $X$  isotropically in the rest frame of the  $H$  boson.

The general form of the matrix element squared for the process

$$q_1(p_1)\bar{q}_2(p_2) \rightarrow V^*(k = p_1 + p_2) \rightarrow V(k_1 = p_3 + p_4)H(k_2) \rightarrow f_3(p_3)\bar{f}_4(p_4)H(k_2) \quad (3.9)$$

where the momenta of the particles are explicitly written, with  $\hat{s} = k^2 = (p_1 + p_2)^2$  being the c.m. energy of the partonic subprocess, can be expressed as

$$\begin{aligned} |\mathcal{M}|^2 = & 2\sqrt{2}N_c^f G_\mu^3 M_V^8 \frac{1}{(k^2 - M_V^2)^2 + \Gamma_V^2 M_V^2} \frac{1}{(k_1^2 - M_V^2)^2 + \Gamma_V^2 M_V^2} \\ & \times \left[ \left( (\hat{v}_{q_1} + \hat{a}_{q_1})^2 (\hat{v}_{f_3} + \hat{a}_{f_3})^2 + (\hat{v}_{q_1} - \hat{a}_{q_1})^2 (\hat{v}_{f_3} - \hat{a}_{f_3})^2 \right) (p_1 \cdot p_4)(p_2 \cdot p_3) \right. \\ & \left. + \left( (\hat{v}_{q_1} + \hat{a}_{q_1})^2 (\hat{v}_{f_3} - \hat{a}_{f_3})^2 + (\hat{v}_{q_1} - \hat{a}_{q_1})^2 (\hat{v}_{f_3} + \hat{a}_{f_3})^2 \right) (p_1 \cdot p_3)(p_2 \cdot p_4) \right] \end{aligned} \quad (3.10)$$

where the reduced fermion couplings to gauge bosons are as usual:  $\hat{a}_f = 2I_f^3$ ,  $\hat{v}_f = 2I_f^3 - 4Q_f s_W^2$  for  $V = Z$  and  $\hat{v}_f = \hat{a}_f = \sqrt{2}$  for  $V = W$ . Averaging over the quark spins and colors, dividing by the flux factor, and integrating over the three-particle phase space, one obtains the total cross section of the subprocess. In the case where the decay products of the final vector boson are ignored, one would have a simple  $2 \rightarrow 2$  subprocess, with an integrated cross section at lowest order given by [222,223]

$$\hat{\sigma}_{\text{LO}}(q\bar{q} \rightarrow VH) = \frac{G_\mu^2 M_V^4}{288\pi\hat{s}} (\hat{v}_q^2 + \hat{a}_q^2) \lambda^{1/2}(M_V^2, M_H^2; \hat{s}) \frac{\lambda(M_V^2, M_H^2; \hat{s}) + 12M_V^2/\hat{s}}{(1 - M_V^2/\hat{s})^2} \quad (3.11)$$

with  $\lambda$  being the usual two-body phase-space function  $\lambda(x, y; z) = (1 - x/z - y/z)^2 - 4xy/z^2$ .

Note that the Higgs and the vector bosons have opposite transverse momenta and the differential partonic distribution with respect to the  $p_T$  is given by

$$\frac{d\hat{\sigma}_{\text{LO}}}{dp_T^2} = \frac{G_\mu^2 M_V^4}{24\pi} \frac{v_q^2 + a_q^2}{(\hat{s} - M_Z^2)^2} \frac{2M_Z^2 + p_T^2}{2(M_Z^2 + M_H^2) - \hat{s}\sqrt{\lambda - 4p_T^2/\hat{s}}}. \quad (3.12)$$

The partonic cross section can be recovered by integrating  $p_T$  in the range  $0 \leq p_T \leq \frac{\sqrt{\hat{s}\lambda}}{2}$ .

In fact, this process can be viewed simply as the Drell–Yan production of a virtual vector boson with  $k^2 \neq M_V^2$ , which then splits into a real vector boson and a Higgs particle. The energy distribution of the full subprocess can be written at leading order as

$$\hat{\sigma}(q\bar{q} \rightarrow HV) = \hat{\sigma}(q\bar{q} \rightarrow V^*) \times \frac{d\Gamma}{dk^2}(V^* \rightarrow HV) \quad (3.13)$$

where, in terms of  $0 \leq k^2 \leq Q^2 = \hat{s}$  and the two-body phase-space function  $\lambda$ , one has

$$\frac{d\Gamma}{dk^2}(V^* \rightarrow HV) = \frac{G_\mu M_V^4}{2\sqrt{2}\pi^2} \frac{\lambda^{1/2}(M_V^2, M_H^2; k^2)}{(k^2 - M_V^2)^2} \left( 1 + \frac{\lambda(M_V^2, M_H^2; k^2)}{12M_V^2/k^2} \right). \quad (3.14)$$

The total production cross section is then obtained by convoluting with the parton densities and summing over the contributing partons

$$\sigma_{\text{LO}}(pp \rightarrow VH) = \int_{\tau_0}^1 d\tau \sum_{q,\bar{q}} \frac{d\mathcal{L}^{q\bar{q}}}{d\tau} \hat{\sigma}_{\text{LO}}(\hat{s} = \tau s) \quad (3.15)$$

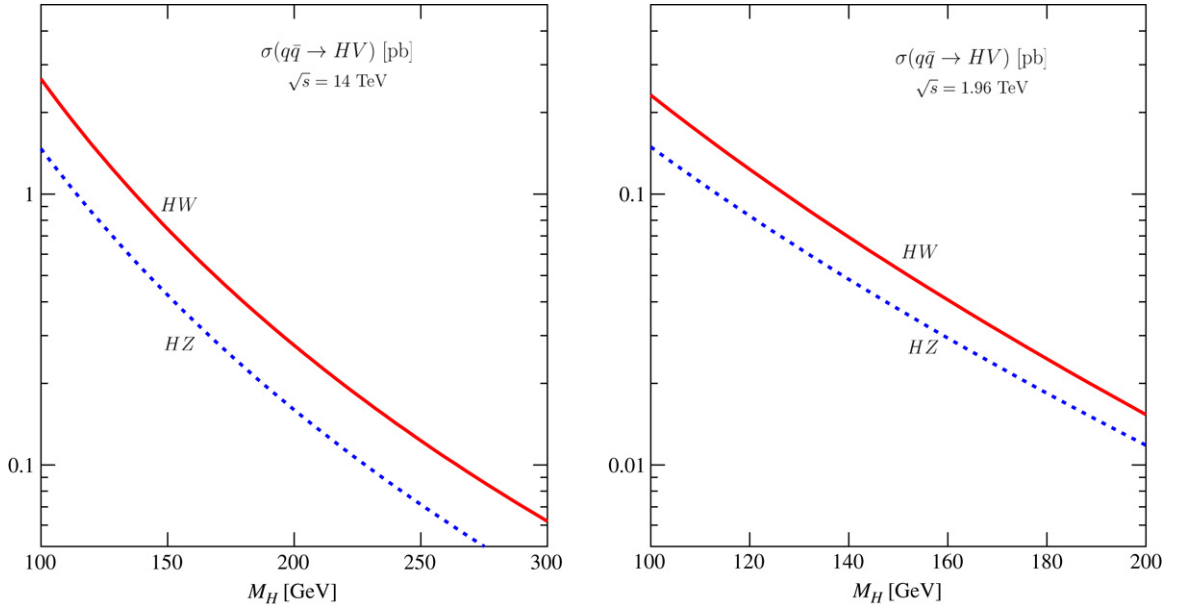


Fig. 3.3. Total production cross sections of Higgs bosons in the strahlung  $q\bar{q} \rightarrow H + W/Z$  processes at leading order at the LHC (left) and at the Tevatron (right). For  $q\bar{q} \rightarrow HW$ , the final states with both  $W^+$  and  $W^-$  have been added. The MRST set of PDFs has been used.

where  $\tau_0 = (M_V + M_H)^2/s$ ,  $s$  being the total hadronic c.m. energy and the parton luminosity is defined in terms of the parton densities  $q_i(x_i, \mu_F^2)$  defined at a factorization scale  $\mu_F$ , by

$$\sum_{q,\bar{q}} \frac{d\mathcal{L}^{q\bar{q}}}{d\tau} = \sum_{q_1,\bar{q}_2} \int_{\tau}^1 \frac{dx}{x} \left[ q_1(x, \mu_F^2) \bar{q}_2(\tau/x, \mu_F^2) \right]. \quad (3.16)$$

The total production cross sections are shown as functions of the Higgs boson mass for the Tevatron and the LHC in both the  $HW^\pm$  and  $HZ$  channels in Fig. 3.3; the MRST parton densities are used. The cross sections for  $W^\pm$  final states are approximately two times larger than the ones for the  $HZ$  final states at both colliders. If, in addition, one requires the gauge bosons to decay into charged leptons  $\ell = \mu + e$ , the charged channel is much more interesting since  $\text{BR}(W^\pm \rightarrow \ell^\pm \nu) \sim 20\%$  while  $\text{BR}(Z \rightarrow \ell^+ \ell^-) \simeq 6\%$ . The various detection channels at the LHC [296–300] and at the Tevatron [301–304] and [300] will be discussed in Section 3.7.

### 3.2.2. The QCD radiative corrections

**3.2.2.1. The NLO corrections.** The factorization of the  $pp \rightarrow HV$  cross section Eq. (3.13) holds in principle at any order of the perturbation theory in the strong interaction and one can thus write

$$\frac{d\hat{\sigma}}{dk^2}(pp \rightarrow HV + X) = \sigma(pp \rightarrow V^* + X) \times \frac{d\Gamma}{dk^2}(V^* \rightarrow HV), \quad (3.17)$$

where  $d\Gamma/dk^2$  is given by Eq. (3.14). Therefore, the QCD corrections to the Higgs–strahlung process, derived at NLO in Refs. [260–262], are simply the corrections to the Drell–Yan process [42,43], as pointed out in Refs. [297,305].

At NLO, the QCD corrections to the Drell–Yan process consist of virtual corrections with gluon exchange in the  $q\bar{q}$  vertex and quark self-energy corrections, which have to be multiplied by the tree-level term, and the emission of an additional gluon, the sum of which has to be squared and added to the corrected tree-level term; see Fig. 3.4.

Including these contributions, and taking into account the virtuality of the vector boson, the LO cross section is modified in the following way

$$\sigma_{\text{NLO}} = \sigma_{\text{LO}} + \Delta\sigma_{q\bar{q}} + \Delta\sigma_{qg} \quad (3.18)$$



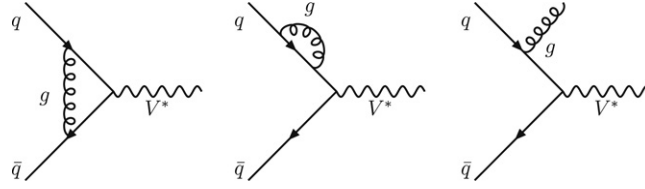
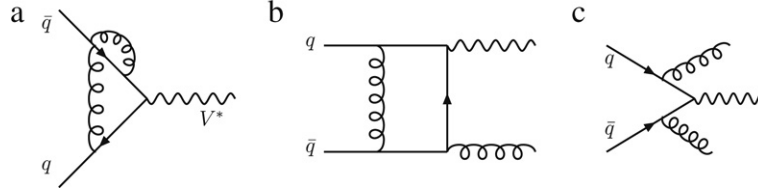


Fig. 3.4. NLO QCD corrections to the vector boson–quark–antiquark vertex.

Fig. 3.5. Diagrams for the NNLO QCD corrections to the process  $q\bar{q} \rightarrow W^*$ .

with

$$\begin{aligned}\Delta\sigma_{q\bar{q}} &= \frac{\alpha_s(\mu_R)}{\pi} \int_{\tau_0}^1 d\tau \sum_q \frac{d\mathcal{L}^{q\bar{q}}}{d\tau} \int_{\tau_0/\tau}^1 dz \hat{\sigma}_{\text{LO}}(\tau z s) \omega_{q\bar{q}}(z) \\ \Delta\sigma_{qg} &= \frac{\alpha_s(\mu_R)}{\pi} \int_{\tau_0}^1 d\tau \sum_{q,\bar{q}} \frac{d\mathcal{L}^{qg}}{d\tau} \int_{\tau_0/\tau}^1 dz \hat{\sigma}_{\text{LO}}(\tau z s) \omega_{qg}(z)\end{aligned}\quad (3.19)$$

with the coefficient functions [42]

$$\begin{aligned}\omega_{q\bar{q}}(z) &= -P_{q\bar{q}}(z) \log \frac{\mu_F^2}{\tau s} + \frac{4}{3} \left[ \left( \frac{\pi^2}{3} - 4 \right) \delta(1-z) + 2(1+z^2) \left( \frac{\log(1-z)}{1-z} \right)_+ \right] \\ \omega_{qg}(z) &= -\frac{1}{2} P_{qg}(z) \log \left( \frac{\mu_F^2}{(1-z)^2 \tau s} \right) + \frac{1}{8} [1 + 6z - 7z^2]\end{aligned}\quad (3.20)$$

where  $\mu_R$  denotes the renormalization scale and  $P_{qq}$ ,  $P_{qg}$  are the well-known Altarelli–Parisi splitting functions which are given by [285,306]

$$\begin{aligned}P_{qq}(z) &= \frac{4}{3} \left[ \frac{1+z^2}{(1-z)_+} + \frac{3}{2} \delta(1-z) \right] \\ P_{qg}(z) &= \frac{1}{2} [z^2 + (1-z)^2].\end{aligned}\quad (3.21)$$

The index  $+$  denotes the usual distribution  $\mathcal{F}_+(z) = \mathcal{F}(z) - \delta(1-z) \int_0^1 dz' \mathcal{F}(z')$ . Note that the cross section depends explicitly on  $\log(\mu_F^2/Q^2)$ ; the scale choice  $\mu_F^2 = Q^2$  therefore avoids the occurrence of these potentially large logarithms. The renormalization scale dependence enters in the argument of  $\alpha_s$  and is rather weak. In most of our discussion, we will set the two scales at the invariant mass of the  $HV$  system  $\mu_F = \mu_R = M_{HV}$ . For this choice, the NLO corrections increase the LO cross section by approximately 30%.

**3.2.2.2. The NNLO corrections.** The NNLO corrections, i.e. the contributions at  $\mathcal{O}(\alpha_s^2)$ , to the Drell–Yan process  $pp \rightarrow V^*$  consist of the following set of corrections besides the one-loop squared terms [see also Fig. 3.5(a)–(c)]: (a) two-loop corrections to  $q\bar{q} \rightarrow V^*$ , which have to be multiplied by the Born term; (b) one-loop corrections to the processes  $qg \rightarrow qV^*$  and  $q\bar{q} \rightarrow gV^*$ , which have to be multiplied by the tree level  $gq$  and  $q\bar{q}$  terms initiated by the diagrams shown in Fig. 3.4; (c) tree-level contributions from  $q\bar{q}$ ,  $qq$ ,  $qg$ ,  $gg \rightarrow V^* + 2$  partons in all possible ways, with the sums of these diagrams for given initial and final states to be squared and added.



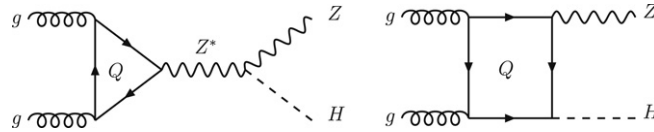


Fig. 3.6. Diagrams for the  $gg \rightarrow HZ$  process, which contributes to  $\mathcal{O}(\alpha_s^2)$ .

These corrections have been calculated a decade ago in Ref. [43] and recently updated [281]. However, these calculations are not sufficient to obtain a full NNLO prediction: in the case of  $pp \rightarrow HZ$  production, because the final state is electrically neutral, two additional sets of corrections need to be considered at  $\mathcal{O}(\alpha_s^2)$  [280].

Indeed, contrary to charged  $W$  bosons, the neutral  $Z$  bosons can be produced via an effective  $Z$  gluon–gluon coupling induced by quark loops. This can occur at the two-loop level in a box + triangle diagram in  $q\bar{q} \rightarrow Z^*$  [to be multiplied by the Born term], or at the one-loop level where vertex diagrams appear for the  $q\bar{q} \rightarrow gZ^*$  and  $qg \rightarrow qZ^*$  processes [to be multiplied by the respective  $\mathcal{O}(\alpha_s)$  tree-level terms]. Because gluons have only vector couplings to quarks and the effective  $Zgg$  coupling must be a color singlet, only the axial-vector part  $a_q = 2I_Q^3$  of the  $Zq\bar{q}$  coupling will contribute as a consequence of Furry’s theorem [307]. Since  $a_q$  differs only by a sign for isospin up- and down-type quarks, their contribution vanishes in the case of quarks that are degenerate in mass. Thus, in the SM, only the top and bottom quarks will contribute to these topologies. These corrections have been evaluated in Refs. [308,309] and have been shown to be extremely small and can be safely neglected.

Another set of diagrams that contribute at  $\mathcal{O}(\alpha_s^2)$  to  $ZH$  and not to  $WH$  production [again because of charge conservation] is the  $gg$  initiated mechanism  $gg \rightarrow HZ$  [310,311]. It is mediated by quark loops [see Fig. 3.6] which enter in two ways. There is first a triangular diagram with  $gg \rightarrow Z^* \rightarrow HZ$ , in which only the top and bottom quark contributions are present, since because of C-invariance, the  $Z$  boson couples only axially to the internal quarks and the contribution of a mass degenerate quark weak isodoublet vanishes. There are also box diagrams where both the  $H$  and  $Z$  bosons are emitted from the internal quark lines and where only the contributions involving heavy quarks which couple strongly to the Higgs boson [the top quark and, to a lesser extent, the bottom quark] are important. It turns out that the two contributing triangle and box amplitudes interfere destructively.

At the LHC, the contribution of this gluon–gluon fusion mechanism to the  $pp \rightarrow HZ$  total production cross section can be substantial. This is due to the fact that the suppression of the cross section by a power  $(\alpha_s/\pi)^2$  is partly compensated by the increased gluon luminosity at high energies. In addition, the tree-level cross section for  $q\bar{q} \rightarrow HZ$  drops for increasing c.m. energy and/or  $M_H$  values, since it is mediated by  $s$ -channel gauge boson exchange. Note that the cross section for this process is negligible at the Tevatron because of the low-gluon luminosity and the reduced phase space.

**3.2.2.3. Numerical results.** The  $K$ -factors, defined as the ratios of the cross sections at higher order with  $\alpha_s$  and the PDFs evaluated also at higher order, relative to the LO-order cross sections with  $\alpha_s$  and the PDFs consistently evaluated also at LO, are shown at NLO and NNLO in Fig. 3.7 in solid black lines for the LHC (left-hand side) and the Tevatron (right-hand side) as functions of the Higgs mass for the process  $pp \rightarrow HW$ . The scales have been fixed to  $\mu_F = \mu_R = M_{HV}$ , where  $M_{HV}$  is the invariant mass of the  $HV$  system, and the MRST sets of PDFs for each perturbative order are used in a consistent manner.

The NLO  $K$ -factor is practically constant at the LHC, increasing only from  $K_{\text{NLO}} = 1.27$  for  $M_H = 110$  GeV to  $K_{\text{NLO}} = 1.29$  for  $M_H = 300$  GeV. The NNLO contributions increase the  $K$ -factor by a mere 1% for the low  $M_H$  value and by 3.5% for the high value. At the Tevatron, the NLO  $K$ -factor is somewhat higher than at the LHC, enhancing the cross section by  $K_{\text{NLO}} = 1.35$  for  $M_H = 110$  GeV and  $K_{\text{NLO}} = 1.3$  for  $M_H = 300$  GeV with a monotonic decrease. The NNLO corrections increase the  $K$ -factor uniformly by about 10%. Thus, these NNLO corrections are more important at the Tevatron than at the LHC.

Because of the slightly different phase space and scale, the  $K$ -factor for  $pp \rightarrow ZH$  is not identical to the  $K$ -factor for  $pp \rightarrow WH$ . However, since  $(M_Z^2 - M_W^2)/\hat{s}$  is small and the dependence of  $d\Gamma$  in Eq. (3.13) on  $k^2$  is not very strong in the range that we are considering, the  $K$ -factors for the two processes are very similar when the contribution of the  $gg \rightarrow HZ$  component to be discussed later is not included.

The bands around the  $K$ -factors in Fig. 3.7 represent the variation of the cross sections when they are evaluated at renormalization and factorization scale values that are independently varied from  $\frac{1}{3}M_{HV} \leq \mu_F(\mu_R) \leq 3M_{HV}$ ,

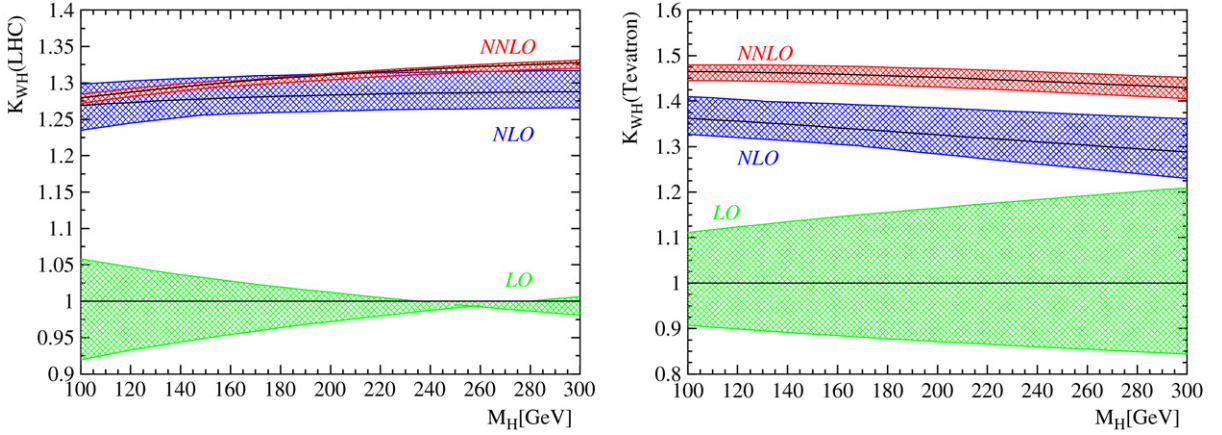


Fig. 3.7. The  $K$ -factors for  $pp \rightarrow HW$  at the LHC (left) and the Tevatron (right) as functions of  $M_H$  at LO, NLO and NNLO (solid black lines). The bands represent the spread of the cross section when the renormalization and factorization scales are varied in the range  $\frac{1}{3}M_{HV} \leq \mu_R(\mu_F) \leq 3M_{HV}$ , the other scale being fixed at  $\mu_F(\mu_R) = M_{HV}$ ; from Ref. [280].

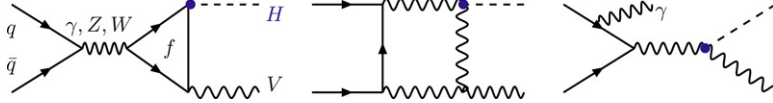


Fig. 3.8. Generic diagrams for the  $\mathcal{O}(\alpha)$  corrections to the  $pp \rightarrow HV$  production process.

while the other is fixed to  $\mu_R(\mu_F) = M_{HV}$ ; the normalization is provided by the production cross section evaluated at scales  $\mu_F = \mu_R = M_{HV}$ . A  $K$ -factor for the LO cross section,  $K_{LO}$ , has also been defined by evaluating the latter at given factorization and renormalization scales and normalizing to the LO cross sections evaluated at the central scale, which, in our case, is given by  $\mu_F = \mu_R = M_{HV}$ . As can be seen, except from the accidental cancellation of the scale dependence of the LO cross section at the LHC for  $M_H \sim 260$  GeV, the decrease of the scale variation is strong when going from LO to NLO and then to NNLO. For  $M_H = 120$  GeV, the uncertainty from the scale choice at the LHC drops from 10% at LO, to 5% at NLO, and to 2% at NNLO. At the Tevatron and for the same Higgs boson mass, the scale uncertainty drops from 20% at LO, to 7% at NLO, and to 3% at NNLO.

If this variation of the cross section with the two scales is taken as an indication of the uncertainties due to the not yet calculated higher-order corrections, one concludes that once the NNLO contributions are included in the prediction, the cross section for the  $pp \rightarrow HV$  process is known at the rather accurate level of a few percent.

### 3.2.3. The electroweak radiative corrections

The associated  $W/Z + H$  process is the only Higgs production mechanism for which the complete calculation of the  $\mathcal{O}(\alpha)$  electroweak corrections has been performed [312]. There are a few hundred Feynman diagrams contributing at the one-loop level, and some generic ones are shown in Fig. 3.8. The radiative corrections can be cast into three categories.

There are first QED corrections in which photons are exchanged in the initial quark–antiquark states and, in order to obtain infrared finite corrections, real-photon bremsstrahlung has to be added. Having done this,  $\mathcal{O}(\alpha)$  corrections due to collinear photon emission and involving logarithms of the initial state quark masses are still present. These mass singularities are absorbed into the PDFs in exactly the same way as in QCD by  $\overline{\text{MS}}$  factorization. This, however, also requires the inclusion of the corresponding  $\mathcal{O}(\alpha)$  corrections into the DGLAP evolution of these distributions and into their fit to experimental data, which has not been performed yet. Nevertheless, an approximate inclusion of these corrections to the DGLAP evolution shows [313] that the impact of these corrections on the quark distributions is well below 1%, at least in the  $x$  range that is relevant at the Tevatron and the LHC. This is also supported by a recent analysis of the MRST collaboration [314] which took into account these effects on the DGLAP equations.

The bulk of the electroweak corrections can be in principle incorporated by using the improved Born approximation discussed in Section 1.2.4. Using the Fermi coupling constant  $G_\mu$  rather than  $\alpha(0)$  as the input in the tree-level cross

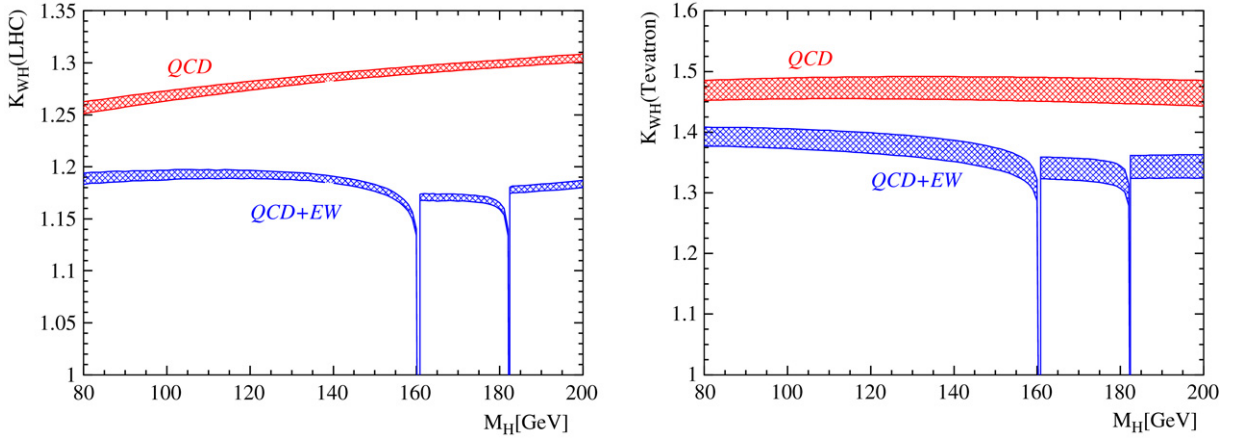


Fig. 3.9.  $K$ -factors for  $WH$  and  $ZH$  production at the LHC (left figure) and the Tevatron (right figure) after including the NNLO QCD and the electroweak  $\mathcal{O}(\alpha)$  corrections [315].

section,  $\pi\alpha \rightarrow \sqrt{2}G_\mu M_W^2(1 - M_W^2/M_Z^2)$ , takes into account the contribution  $\Delta r \simeq \Delta\alpha(M_Z^2) - 3\Delta\rho$ . In this case, the large universal corrections originating from the light fermion contributions to the running of  $\alpha$  [ $2 \times \Delta\alpha(M_Z) \sim 12\%$ , since the cross section is proportional to  $\alpha^2$ ] and those which are quadratic in the top quark [ $2 \times 3\Delta\rho \sim 6\%$ ] are automatically included. One has also to include the contributions that are quadratic in the top mass and which are contained in the  $HVV$  vertex as it was discussed in Section 2.4.2, i.e.  $\delta_{HVV} \sim -5x_t$  with  $x_t = G_\mu^2 m_t^2 / (8\sqrt{2}\pi^2)$  at this order.

Finally, one has to include the bosonic one-loop corrections which involve many self-energy, vertex and box correction diagrams and which have to be calculated by brute force using standard techniques. The calculation of Ref. [312] has been performed in the on-shell renormalization scheme. It turns out that the non-universal bosonic contributions are rather large and negative and, in fact, dominate over the fermionic corrections and even over the photonic initial state corrections.

The fermionic contributions being positive and the bosonic ones negative, there is a partial cancellation of the two contributions and, since the bosonic corrections are more important, the net effect is that the total electroweak corrections decrease the  $q\bar{q} \rightarrow HV$  production cross section at both the Tevatron and the LHC by approximately 5%–10% for Higgs masses in the range 100–200 GeV where the production rates are large enough. This is shown in Fig. 3.9 where we display the  $K$ -factors for  $pp \rightarrow HW$  at the Tevatron and LHC as functions of  $M_H$ , when only NLO + NNLO QCD corrections are included (upper bands) and when the electroweak corrections are also taken into account (lower bands). The thickness of the bands is due to the scale variation as discussed previously. The unphysical singularities in the electroweak corrections at the  $M_H = 2M_W$  and  $2M_Z$  thresholds can be removed by including the finite width of the particles. Note that at the LHC, the electroweak correction is almost the same for  $pp \rightarrow HW$  and  $pp \rightarrow HZ$ , the difference being less than 2%.

### 3.2.4. The total cross section and the PDF uncertainties

In Fig. 3.10, we present the total production cross sections for the processes  $q\bar{q} \rightarrow HW$  and  $HZ$  at the Tevatron and the LHC as functions of  $M_H$ , when both the NNLO QCD and the electroweak corrections are added. In the case of the  $HZ$  process, the contribution of the  $gg \rightarrow ZH$  subprocess to the total cross section is not included, but it is displayed separately in the LHC case. For Higgs masses in the range  $100 \text{ GeV} \lesssim M_H \lesssim 250 \text{ GeV}$  where  $\sigma(q\bar{q} \rightarrow HZ)$  is significant,  $\sigma(gg \rightarrow HZ)$  is at the level of 0.1–0.01 pb and represents about 10% of the total cross section for low  $M_H$  values. The  $gg \rightarrow HZ$  cross section is thus much larger than the contribution of the NNLO correction and, therefore, generates a scale uncertainty that is larger than that in the  $HW$  production case.

Finally, let us discuss the PDF uncertainties in the  $pp \rightarrow HV$  cross sections, following along the same lines introduced in Section 3.1.5. In Fig. 3.11, we show as functions of  $M_H$  and for the LHC and the Tevatron, the central values and the uncertainty band limits of the NLO QCD  $q\bar{q} \rightarrow HW$  cross section for the CTEQ, MRST and Alekhin parametrizations. In the inserts to these figures, we show the spread uncertainties in the predictions for the cross sections, when they are normalized to the prediction of the reference CTEQ6M set.

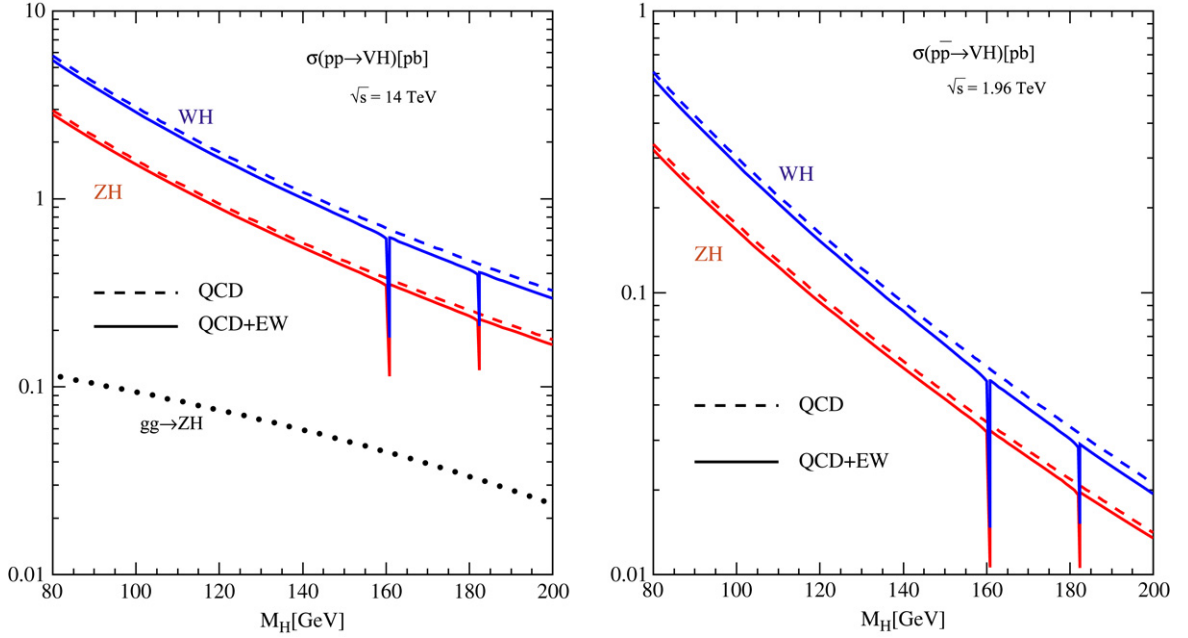


Fig. 3.10. The total production cross sections for  $pp \rightarrow HW$  and  $HZ$  at the LHC (left) and the Tevatron (right) as functions of  $M_H$  when the NNLO QCD and the electroweak corrections are included. The MRST parton densities have been used. The contribution of the  $gg \rightarrow HZ$  process is shown separately in the case of the LHC; from Ref. [315].

At the LHC, the uncertainty band is almost constant and for CTEQ, is of the order of 4% over the Higgs mass range between 100 and 200 GeV. At the Tevatron, the uncertainty band increases with the Higgs mass and exceeds 6% at  $M_H \sim 200$  GeV. The uncertainty in the MRST parametrization is twice smaller. To produce a vector plus a Higgs boson in this mass range, the incoming quarks originate from the intermediate- $x$  regime at the LHC, at Tevatron energies, however, some of the participating quarks originate from the high- $x$  regime, which explains the increasing behavior of the uncertainty bands observed in this case. The different magnitude of the cross section,  $\sim 12\%$  ( $\sim 8\%$ ) larger in the Alekhin case than that for CTEQ at the LHC (Tevatron), is due to the larger quark and antiquark densities of the former parametrization. For this particular PDF set, the difference in the shifts of the central values in the LHC and Tevatron cases is due to the different initial states,  $pp$  [where  $\bar{q}$  comes from the sea] versus  $p\bar{p}$  [where it is valence + sea  $\bar{q}$ ]; see Fig. 3.2.

Note that an additional systematic error of about 5% arises from the  $pp$  luminosity. If one uses the Drell–Yan processes to measure directly the  $q$  and  $\bar{q}$  luminosities at hadron colliders, the errors on the cross sections for associated  $HV$  production when normalized to this rate would lead to a total systematical uncertainty of less than 1% [316]. In this case, the dominant part of the  $K$ -factor will also drop out in the ratio.

### 3.3. The vector boson fusion processes

#### 3.3.1. The differential and total cross sections at LO

The matrix element squared for the massive vector boson fusion process [224–227], in terms of the momenta of the involved particles

$$q_1(p_1)q_2(p_2) \rightarrow V^*(q_1 = p_3 - p_1)V^*(q_2 = p_4 - p_2)q_3(p_3)q_4(p_4) \rightarrow q_3(p_3)q_4(p_4)H(k) \quad (3.22)$$

with  $V = W, Z$ , is given by

$$|\mathcal{M}|^2 = 4\sqrt{2}N_c^f G_\mu^3 M_V^8 \frac{C_+(p_1 \cdot p_2)(p_3 \cdot p_4) + C_-(p_1 \cdot p_4)(p_2 \cdot p_3)}{(q_1^2 - M_V^2)^2(q_2^2 - M_V^2)^2} \quad (3.23)$$

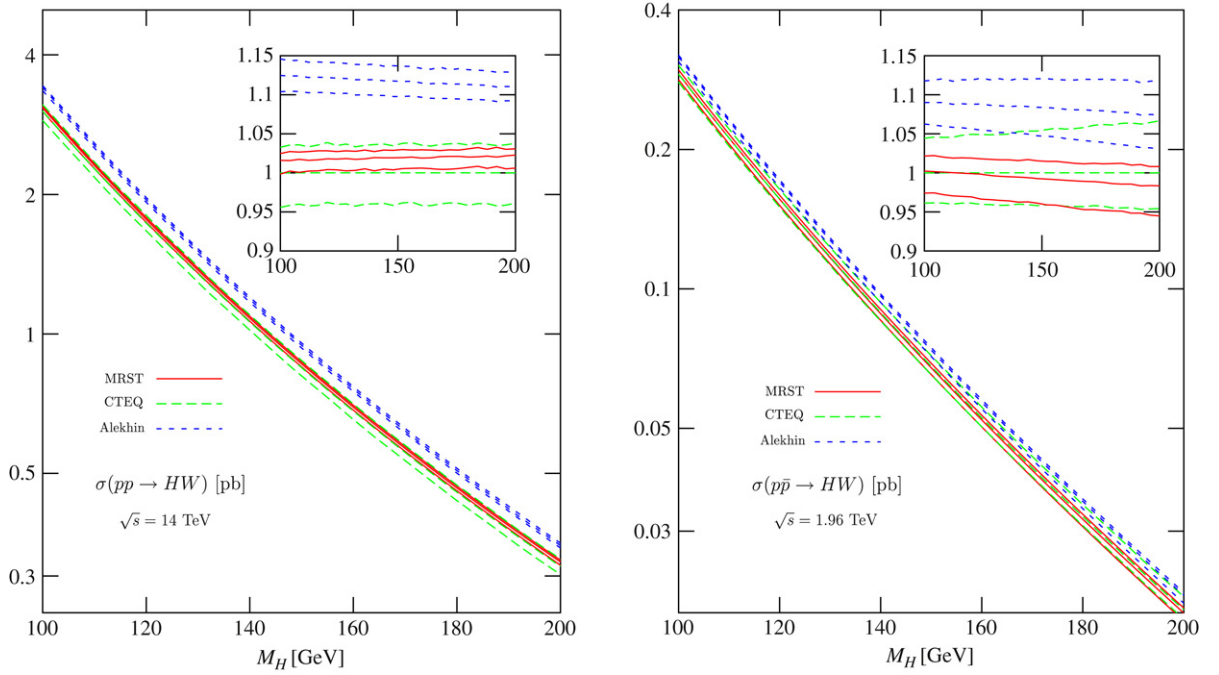


Fig. 3.11. The CTEQ, MRST and Alekhin PDF uncertainty bands for the NLO cross sections for the production of the Higgs boson at the LHC (left) and at the Tevatron (right) in the  $q\bar{q} \rightarrow HW$  process. The inserts show the spread in the predictions; from Ref. [295].

where, in terms of the usual vector and axial-vector couplings of the gauge bosons to fermions  $\hat{a}_f = 2I_f^3$ ,  $\hat{v}_f = 2I_f^3 - 4Q_f s_W^2$  for  $V = Z$  and  $\hat{v}_f = \hat{a}_f = \sqrt{2}$  for  $V = W$ ,  $C_{\pm}$  reads

$$C_{\pm} = (\hat{v}_{q_1}^2 + \hat{a}_{q_1}^2)(\hat{v}_{q_3}^2 + \hat{a}_{q_3}^2) \pm 4\hat{v}_{q_1}\hat{a}_{q_1}\hat{v}_{q_3}\hat{a}_{q_3} \quad (3.24)$$

giving rise to the differential distribution

$$d\hat{\sigma}_{\text{LO}} = \frac{1}{4} \frac{1}{9} \frac{1}{2\hat{s}} \times |\mathcal{M}|^2 \times \frac{1}{(2\pi)^5} \frac{d^3k}{2dE_H} \frac{d^3p_3}{2dE_3} \frac{d^3p_4}{2dE_4} \delta^4(p_1 + p_2 - p_3 - p_4 - k). \quad (3.25)$$

The integration over the variables  $p_3$  and  $p_4$  are conveniently performed in the rest frame of the two quarks  $\vec{p}_3 + \vec{p}_4 = 0$ , and one finds [226,227]

$$\frac{d\hat{\sigma}_{\text{LO}}}{dE_H d\cos\theta} = \frac{G_\mu^3 M_V^8}{9\sqrt{2}\pi^3 \hat{s}} \frac{p_H}{32s_1 s_2 r} [C_+ \mathcal{H}_+ + C_- \mathcal{H}_-] \quad (3.26)$$

with

$$\begin{aligned} \mathcal{H}_+ &= (h_1 + 1)(h_2 + 1) \left[ \frac{2}{h_1^2 - 1} + \frac{2}{h_2^2 - 1} - \frac{6s_\chi^2}{r} + \left( \frac{3t_1 t_2}{r} - c_\chi \right) \frac{\ell}{\sqrt{r}} \right] \\ &\quad - \left[ \frac{2t_1}{h_2 - 1} + \frac{2t_2}{h_1 - 1} + \left( t_1 + t_2 + s_\chi^2 \right) \frac{\ell}{\sqrt{r}} \right] \\ \mathcal{H}_- &= 2(1 - c_\chi) \left[ \frac{2}{h_1^2 - 1} + \frac{2}{h_2^2 - 1} - \frac{6s_\chi^2}{r} + \left( \frac{3t_1 t_2}{r} - c_\chi \right) \frac{\ell}{\sqrt{r}} \right]. \end{aligned} \quad (3.27)$$



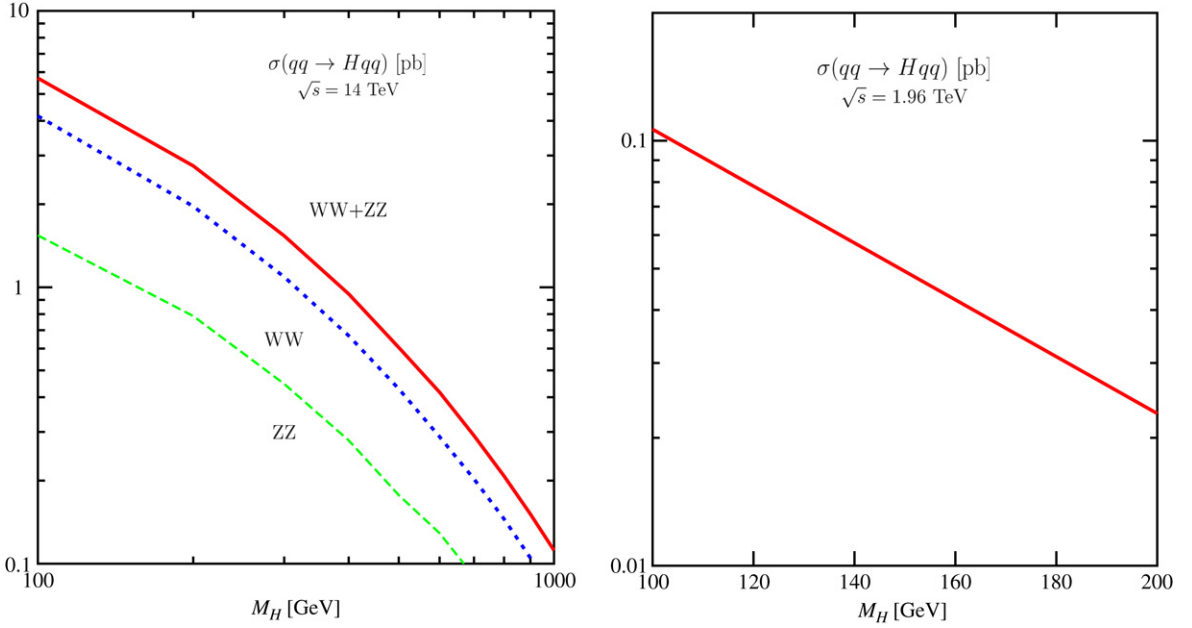


Fig. 3.12. Individual and total cross sections in the vector fusion  $qq \rightarrow V^*V^* \rightarrow Hqq$  processes at leading order at the LHC (left) and total cross section at the Tevatron (right).

In these equations,  $p_H = \sqrt{E_H^2 - M_H^2}$  is the Higgs boson momentum,  $\theta$  is the scattering angle, while  $\epsilon_v = \sqrt{\hat{s}} - E_H$  and  $s_v = \epsilon_v^2 - p_H^2$  are the energy and the invariant mass of the final state quark pair. The other abbreviations are

$$\begin{aligned} s_{1,2} &= \sqrt{\hat{s}}(\epsilon_v \pm p_H \cos \theta), & h_{1,2} &= 1 + 2M_V^2/s_{1,2}, & t_{1,2} &= h_{1,2} + c_\chi h_{2,1} \\ c_\chi &= 1 - \frac{2\hat{s}s_v}{s_1 s_2} = 1 - s_\chi^2, & r &= h_1^2 + h_2^2 + 2c_\chi h_1 h_2 - s_\chi^2, & \ell &= \log \frac{h_1 h_2 + c_\chi + \sqrt{r}}{h_1 h_2 + c_\chi - \sqrt{r}}. \end{aligned} \quad (3.28)$$

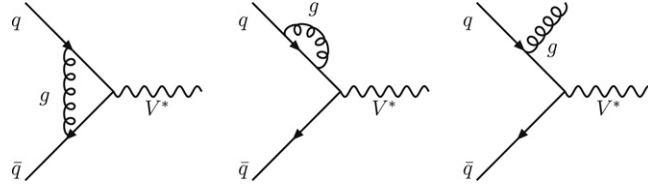
To derive the partonic total cross section,  $\hat{\sigma}_{\text{LO}}(qq \rightarrow qqH)$ , the differential cross section must be integrated over the region

$$-1 < \cos \theta < 1 \quad \text{and} \quad M_H < E_H < \frac{\sqrt{\hat{s}}}{2} \left( 1 + \frac{M_H^2}{\hat{s}} \right). \quad (3.29)$$

Summing over the contributing partons, including both the  $WW$  and  $ZZ$  fusion channels and folding with the parton luminosities, one obtains the total hadronic cross section  $\sigma(pp \rightarrow V^*V^* \rightarrow qqH)$  at LO. The cross sections, using the CTEQ set of parton densities, are shown in Fig. 3.12 as functions of  $M_H$  for  $p\bar{p}$  at the Tevatron and for  $pp$  at the LHC. In the latter case, the separate  $WW$  and  $ZZ$  contributions, as well as their total sum, are displayed; the interference between the  $WW$  and  $ZZ$  contributions is less than 1% and can be neglected.

While they are rather large at the LHC, in particular for Higgs bosons in the mass range  $100 \text{ GeV} \lesssim M_H \lesssim 200 \text{ GeV}$  where they reach the level of a few picobarns, the total cross sections are very small at the Tevatron and they barely reach the level of 0.1 pb even for  $M_H = 100 \text{ GeV}$ . This is due to the fact that the main contribution originates from longitudinal gauge bosons [which as, discussed previously, have interactions which grow with energy], and the partonic cross sections rise logarithmically with the c.m. energy of the subprocess,  $\hat{\sigma} \propto \log \hat{s}/M_V^2$ , giving much larger rates at high energies. In our subsequent discussion, we will therefore consider this process only in the case of the LHC.

Note also that the main contribution to the cross section is due to the  $WW$  fusion channel,  $\sigma(WW \rightarrow H) \sim 3\sigma(ZZ \rightarrow H)$  at the LHC, a consequence of the fact that the  $W$  boson couplings to fermions are larger than those of the  $Z$  boson.

Fig. 3.13. Feynman diagrams for NLO QCD corrections to the  $V^*qq$  vertex.

### 3.3.2. The cross section at NLO

The QCD corrections to the vector boson fusion process,  $qq \rightarrow qqV^*V^* \rightarrow qqH$  consist of the virtual quark self-energy and vertex corrections and the additional gluon emission from the initial and final states,  $qq \rightarrow Hqq + g$ ; the gluon initiated subprocess  $gq \rightarrow Hqq + q$  should also be taken into account. Some generic Feynman diagrams are shown in Fig. 3.13.

Since at the lowest order the incoming/outgoing quarks are in color singlets, at NLO no gluons will be exchanged between the first and the second incoming (outgoing) quark line [this will be no longer true at  $\mathcal{O}(\alpha_s^2)$ ] and, hence, the QCD corrections only consist of the well-known corrections to the structure functions  $F_i(x, M^2)$ . The NLO corrections can therefore be more conveniently calculated in the structure function approach. In this case, the differential LO partonic cross section can be cast into the form [22,262,263]

$$\begin{aligned}
 d\sigma_{\text{LO}} = & \frac{1}{4} \frac{\sqrt{2} G_\mu^3 M_V^8 q_1^2 q_2^2}{[q_1^2 - M_V^2]^2 [q_2^2 - M_V^2]^2} \left\{ F_1(x_1, \mu_F^2) F_1(x_2, \mu_F^2) \left[ 2 + \frac{(q_1 q_2)^2}{q_1^2 q_2^2} \right] \right. \\
 & + \frac{F_1(x_1, \mu_F^2) F_2(x_2, \mu_F^2)}{P_2 q_2} \left[ \frac{(P_2 q_2)^2}{q_2^2} - m_P^2 + \frac{1}{q_1^2} \left( P_2 q_1 - \frac{P_2 q_2}{q_2^2} q_1 q_2 \right)^2 \right] \\
 & + \frac{F_2(x_1, \mu_F^2) F_1(x_2, \mu_F^2)}{P_1 q_1} \left[ \frac{(P_1 q_1)^2}{q_1^2} - m_P^2 + \frac{1}{q_2^2} \left( P_1 q_2 - \frac{P_1 q_1}{q_1^2} q_1 q_2 \right)^2 \right] \\
 & + \frac{F_2(x_1, \mu_F^2) F_2(x_2, \mu_F^2)}{(P_1 q_1)(P_2 q_2)} \left[ P_1 P_2 - \frac{(P_1 q_1)(P_2 q_1)}{q_1^2} - \frac{(P_2 q_2)(P_1 q_2)}{q_2^2} + \frac{(P_1 q_1)(P_2 q_2)(q_1 q_2)}{q_1^2 q_2^2} \right]^2 \\
 & \left. + \frac{F_3(x_1, \mu_F^2) F_3(x_2, \mu_F^2)}{2(P_1 q_1)(P_2 q_2)} [(P_1 P_2)(q_1 q_2) - (P_1 q_2)(P_2 q_1)] \right\} dx_1 dx_2 \frac{d\text{PS}_3}{\hat{s}} \quad (3.30)
 \end{aligned}$$

where  $d\text{PS}_3$  denotes the three-particle phase space,  $m_P$  the proton mass,  $P_{1,2}$  the proton momenta and  $q_{1,2}$  the momenta of the virtual vector bosons  $V^*$ . The functions  $F_i(x, \mu_F^2)$ , with  $i = 1, 2, 3$ , are the usual structure functions from deep-inelastic scattering processes at the factorization scale  $\mu_F$  and read

$$\begin{aligned}
 F_1(x, \mu_F^2) &= \sum_q (\hat{v}_q^2 + \hat{a}_q^2) [q(x, \mu_F^2) + \bar{q}(x, \mu_F^2)] \\
 F_2(x, \mu_F^2) &= 2x \sum_q (\hat{v}_q^2 + \hat{a}_q^2) [q(x, \mu_F^2) + \bar{q}(x, \mu_F^2)] \\
 F_3(x, \mu_F^2) &= 4 \sum_q \hat{v}_q \hat{a}_q [-q(x, \mu_F^2) + \bar{q}(x, \mu_F^2)]. \quad (3.31)
 \end{aligned}$$

The QCD corrections only consist of the well-known corrections to the structure functions  $F_i(x, M^2)$  and the final result for the corrected cross section at  $\mathcal{O}(\alpha_s)$  can be simply obtained from the replacements [22,262,263]

$$F_i(x, \mu_F^2) \rightarrow F_i(x, \mu_F^2) + \Delta F_i(x, \mu_F^2, Q^2) \quad (3.32)$$



$$\begin{aligned} \Delta F_1(x, \mu_F^2, Q^2) = & \frac{\alpha_s(\mu_R)}{\pi} \sum_q (\hat{v}_q^2 + \hat{a}_q^2) \int_x^1 \frac{dy}{y} \left\{ \frac{2}{3} [q(y, \mu_F^2) + \bar{q}(y, \mu_F^2)] \right. \\ & \times \left[ -\frac{3}{4} P_{qq}(z) \log \frac{\mu_F^2 z}{Q^2} + (1+z^2) \mathcal{D}_1(z) - \frac{3}{2} \mathcal{D}_0(z) + 3 - \left( \frac{9}{2} + \frac{\pi^2}{3} \right) \delta(1-z) \right] \\ & \left. + \frac{1}{4} g(y, \mu_F^2) \left[ -2 P_{qg}(z) \log \frac{\mu_F^2 z}{Q^2(1-z)} + 4z(1-z) - 1 \right] \right\} \end{aligned} \quad (3.33)$$

$$\begin{aligned} \Delta F_2(x, \mu_F^2, Q^2) = & 2x \frac{\alpha_s(\mu_R)}{\pi} \sum_q (\hat{v}_q^2 + \hat{a}_q^2) \int_x^1 \frac{dy}{y} \left\{ \frac{2}{3} [q(y, \mu_F^2) + \bar{q}(y, \mu_F^2)] \right. \\ & \times \left[ -\frac{3}{4} P_{qq}(z) \log \frac{\mu_F^2 z}{Q^2} + (1+z^2) \mathcal{D}_1(z) - \frac{3}{2} \mathcal{D}_0(z) + 3 + 2z - \left( \frac{9}{2} + \frac{\pi^2}{3} \right) \delta(1-z) \right] \\ & \left. + \frac{1}{4} g(y, \mu_F^2) \left[ -2 P_{qg}(z) \log \frac{\mu_F^2 z}{Q^2(1-z)} + 8z(1-z) - 1 \right] \right\} \end{aligned} \quad (3.34)$$

$$\begin{aligned} \Delta F_3(x, \mu_F^2, Q^2) = & \frac{\alpha_s(\mu_R)}{\pi} \sum_q 4\hat{v}_q \hat{a}_q \int_x^1 \frac{dy}{y} \left\{ \frac{2}{3} [-q(y, \mu_F^2) + \bar{q}(y, \mu_F^2)] \right. \\ & \times \left[ -\frac{3}{4} P_{qq}(z) \log \frac{\mu_F^2 z}{Q^2} + (1+z^2) \mathcal{D}_1(z) - \frac{3}{2} \mathcal{D}_0(z) + 2 + z - \left( \frac{9}{2} + \frac{\pi^2}{3} \right) \delta(1-z) \right] \left. \right\} \end{aligned} \quad (3.35)$$

where  $z = x/y$  and the Altarelli–Parisi splitting functions  $P_{qq}, P_{qg}$  are as given in Eq. (3.21); the notation  $\mathcal{D}_i(z) = [\log^i(1-z)/(1-z)]_+$  with  $i = 0, 1$  has been introduced before.  $\mu_R$  is the renormalization scale at which  $\alpha_s$  is evaluated and the physical scale  $Q$  is given by  $Q^2 = -q_i^2$  for  $x = x_i$  with  $i = 1, 2$ . These expressions have to be inserted in the LO differential cross section Eq. (3.30) and the full result expanded up to NLO. The typical renormalization and factorization scales are fixed by the corresponding vector boson momentum transfer at each leg,  $\mu_R^2 = \mu_F^2 = -q_i^2$  for  $x = x_i$ .

The correcting  $K$ -factor, again defined as  $K = \sigma_{\text{NLO}}/\sigma_{\text{LO}}$  with  $\alpha_s$  and the PDFs consistently taken at the respective order, where the renormalization and factorization scales are set to  $\mu_R = \mu_F = Q$ , is practically constant at the LHC in the entire Higgs mass range  $100 \lesssim M_H \lesssim 1$  TeV, and increases the LO cross section by about 5%–10%. More details on the  $K$ -factor and the scale dependence at LO and NLO will be given later, after the discussion of the specific kinematics of the vector boson fusion process to which we turn now.

### 3.3.3. Kinematics of the process

Because weak vector boson fusion is a three-body production process and is mediated by  $t$ -channel gauge boson exchange, its kinematics is rather complicated. However, its characteristic distributions play an extremely important role once it comes to the discrimination of the signal from the many large QCD backgrounds. In particular, forward jet tagging [317–319] and central jet-vetoing [319,320] are essential ingredients. We therefore summarize the main features of the various distributions; for more details, see the reviews in Refs. [321,322].

To study the kinematics of the  $pp \rightarrow Hqq$  process, it is more convenient to write the differential partonic cross section, Eq. (3.26), in terms of the transverse momentum and rapidity of the Higgs boson. The latter, in terms of  $p_H, E_H$  and  $\cos \theta$ , are given by

$$E_H = \sqrt{M_H^2 + p_T^2} \text{ch}(y), \quad p_H \cos \theta = \sqrt{M_H^2 + p_T^2} \text{sh}(y). \quad (3.36)$$

The total partonic cross section is obtained by integrating the double differential distribution [which is given in Eq. (3.26) and where the above changes have been performed]

$$\hat{\sigma}_{\text{LO}}(qq \rightarrow Hqq) = \int_{y_-}^{y_+} dy \int_0^{p_T^{\text{max}}} dp_T (2\pi p_T) \frac{d^2 \hat{\sigma}_{\text{LO}}}{dy dp_T} \quad (3.37)$$

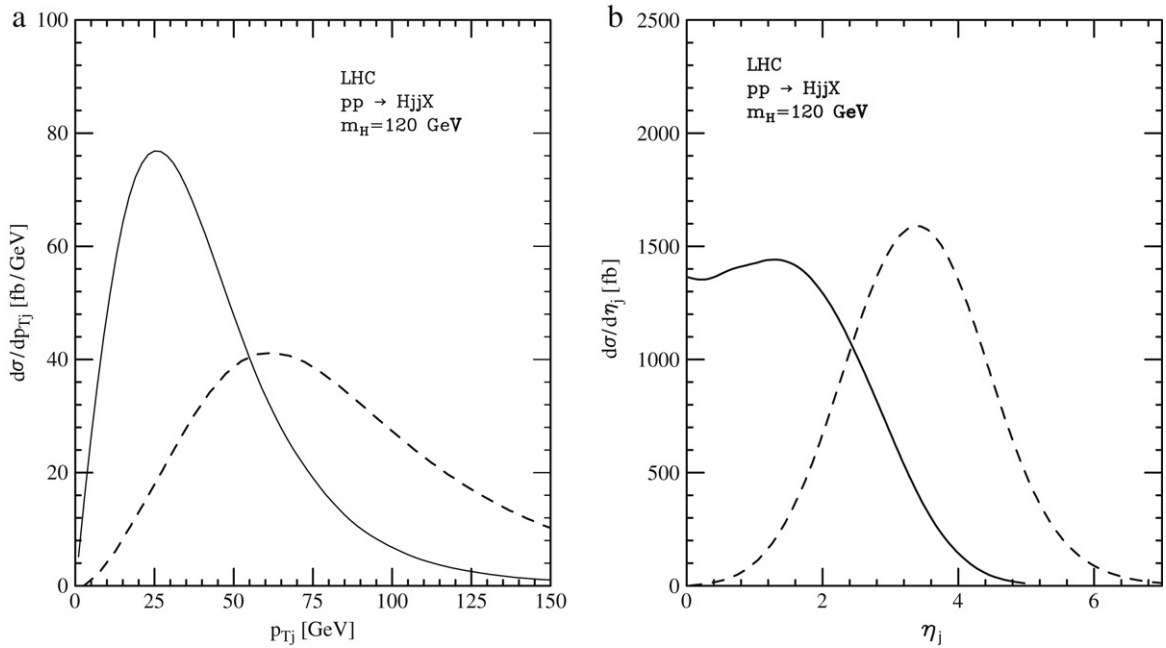


Fig. 3.14. The transverse momentum (left) and pseudorapidity (right) distributions of the two scattered jets in the fusion process  $qq \rightarrow Hqq$  at the LHC with  $M_H = 120$  GeV. Shown are the  $p_T$  distributions for the lowest (solid) and highest (dashed) jets and the  $|\eta|$  distribution for the most central (solid) and most forward (dashed) jets; from Ref. [321].

the integration bounds on the rapidity and the transverse momentum being

$$y_{\pm} = \pm \log \frac{\sqrt{\hat{s}}}{M_H}, \quad p_T^{\max} = \left[ \left( \frac{\hat{s} + M_H^2}{2\sqrt{\hat{s}} \cosh(y)} \right)^2 - M_H^2 \right]^{1/2}. \quad (3.38)$$

Similar to the emission of a Weizsäcker–Williams photon from an energetic electron or positron beam, the intermediate vector bosons in the fusion process tend to carry only a small fraction of the initial parton energies. At the same time, they must have an energy of  $\mathcal{O}(\frac{1}{2}M_H)$  to produce the Higgs boson. Thus, the two quarks in the final state have very large energies, of order 1 TeV at the LHC. In contrast, they have small transverse momenta,  $p_T \sim M_V$ , which are set by the vector boson propagators in the amplitude squared Eq. (3.23),  $1/(q_{1,2}^2 - M_V^2) \lesssim 1/(p_{T3,4}^2 + M_V^2)$ , and which suppress the cross section for  $p_T$  values larger than  $M_V$ . The relatively small transverse momenta and high energies of the final state quarks correspond to rather small scattering angles  $\theta_{3,4}$ . In terms of the pseudorapidity

$$\eta = \frac{1}{2} \log \frac{1 + \cos \theta}{1 - \cos \theta} \quad (3.39)$$

one obtains typically,  $1 \lesssim \eta \lesssim 5$ . This is exemplified in Fig. 3.14 where the transverse momenta and rapidity distributions of the two scattered quarks are shown at the LHC for a Higgs boson mass  $M_H = 120$  GeV. One can see that the rapidity distributions tend to be central, in particular in the case of one of the jets. One also sees that the average transverse momentum of one of the quarks is substantially smaller, a factor of two less, than that for the other quark and that small values,  $p_T \sim 35$  GeV, are possible.

Therefore, requiring that the two scattered jets have a large invariant mass, a sizable  $p_T$  and rapidity distributions which are central, will substantially reduce the backgrounds

$$\text{Cut 1: } m_{q_3, q_4} \gtrsim 1 \text{ TeV}, \quad p_{T_{q_3, q_4}} \gtrsim 20 \text{ GeV}, \quad |\eta_{q_3, q_4}| \lesssim 5. \quad (3.40)$$

Because of the scalar nature of the Higgs boson, its decay  $H \rightarrow X_1 X_2$  is isotropic and can be treated separately from the production process. One can then discuss the kinematics of Higgs production in the vector boson fusion channel, independently of the detection channel. Nevertheless, the Higgs decay products should be observable,

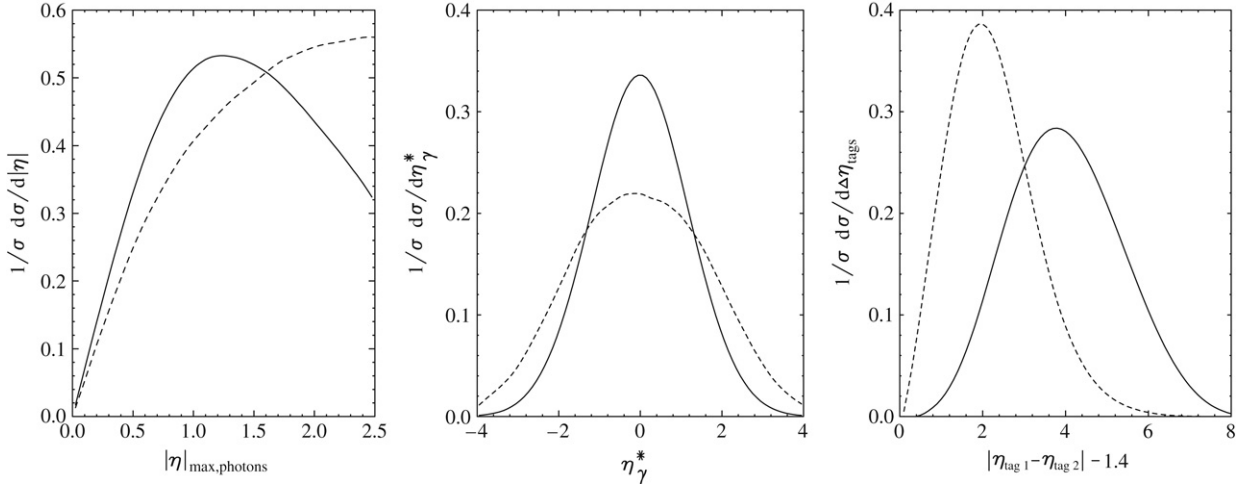


Fig. 3.15. The normalized pseudorapidity distributions of the most forward photon (left), of both photons with respect to the center of the tagging jets (center), and of the two-jet rapidity gap (right) in  $jj\gamma\gamma$  events at the LHC; the solid lines are for the  $H \rightarrow \gamma\gamma$  signal with  $M_H = 120$  GeV and the dotted lines are for the QCD background; from Ref. [322].

i.e. they must have a substantial  $p_T$  and they must be well separated from the jets. The decay products tend to be very central as is exemplified in Fig. 3.15 in the case of the  $H \rightarrow \gamma\gamma$  decay [323], where the normalized pseudorapidity of the most forward photon is shown for  $M_H = 120$  GeV. In contrast, the photons in the irreducible QCD background  $pp \rightarrow jj\gamma\gamma$  are more forward. Thus, a second cut will reduce the background without affecting too much the signal

$$\text{Cut 2: } p_{T_{X1,X2}} \gtrsim 20 \text{ GeV}, \quad |\eta_{X1,X2}| \lesssim 2.5, \quad \Delta R_{qX} \gtrsim 0.7 \quad (3.41)$$

where  $\Delta R_{qX} = \sqrt{(\eta_X - \eta_q)^2 + (\phi_X - \phi_q)^2}$  is the separation between one of the jets and one of the Higgs decay products in the rapidity-azimuthal angle.

In fact, Higgs production takes place in the central region and its decay products will also tend to be central. This is again in contrast to the QCD background which gives a higher rapidity for the  $X$  final states. To visualize more clearly this feature, one can define a shifted rapidity  $\eta_X^*$  which is the rapidity of  $X$  with respect to the center of the two jets,  $\eta_X^* = \eta_X - \frac{1}{2}(\eta_{q3} + \eta_{q4})$ . As shown in the central plot of Fig. 3.15, where the example of  $H \rightarrow \gamma\gamma$  with  $M_H = 120$  GeV is again used, this pseudorapidity is more central in the signal than in the QCD background. One can thus make the additional requirement that the decay products  $X_{1,2}$  fall between the two tagged jets in rapidity, with a minimum separation in  $\eta$ . Typically one can demand that

$$\text{Cut 3: } \eta_{q,\min} + 0.7 \lesssim \eta_{X1,2} \lesssim \eta_{q,\max} - 0.7, \quad \eta_{q3} \cdot \eta_{q4} < 0 \quad (3.42)$$

where it is also required that the two jets are produced in opposite hemispheres and, thus, the product of their pseudorapidities is negative.

In addition, the two forward tagging jets tend to be very well separated in pseudorapidity. This is shown in the right-hand side of Fig. 3.15 in the case of the  $jj\gamma\gamma$  events for both the  $H \rightarrow \gamma\gamma$  signals with again  $M_H = 120$  GeV and the QCD background. Requiring a rapidity gap between the two forward jets, the QCD backgrounds are significantly suppressed

$$\text{Cut 4: } \Delta\eta_{qq} = |\eta_{q3} - \eta_{q4}| \gtrsim 4.4. \quad (3.43)$$

The cuts 1–4 form the basic ingredients to isolate the vector boson fusion signal at the LHC from the various QCD backgrounds. For Higgs masses in the range 100–200 GeV, approximately 30% of the Higgs signal events from the initial sample are left over after these cuts have been imposed; for a detailed discussion see Ref. [322]. Additional and more specialized cuts can be applied for specific Higgs decays, in particular for the  $H \rightarrow \tau^+\tau^-$  [324],  $H \rightarrow W^+W^- \rightarrow \ell\ell\nu\nu$  [325,326], and even  $H \rightarrow \mu^+\mu^-$  [327] or  $b\bar{b}$  [328] final states.

Finally, another important discriminant between the Higgs signal and the backgrounds is the amount of hadronic activity in the central region. Indeed, and as mentioned when studying the QCD corrections, the vector boson fusion

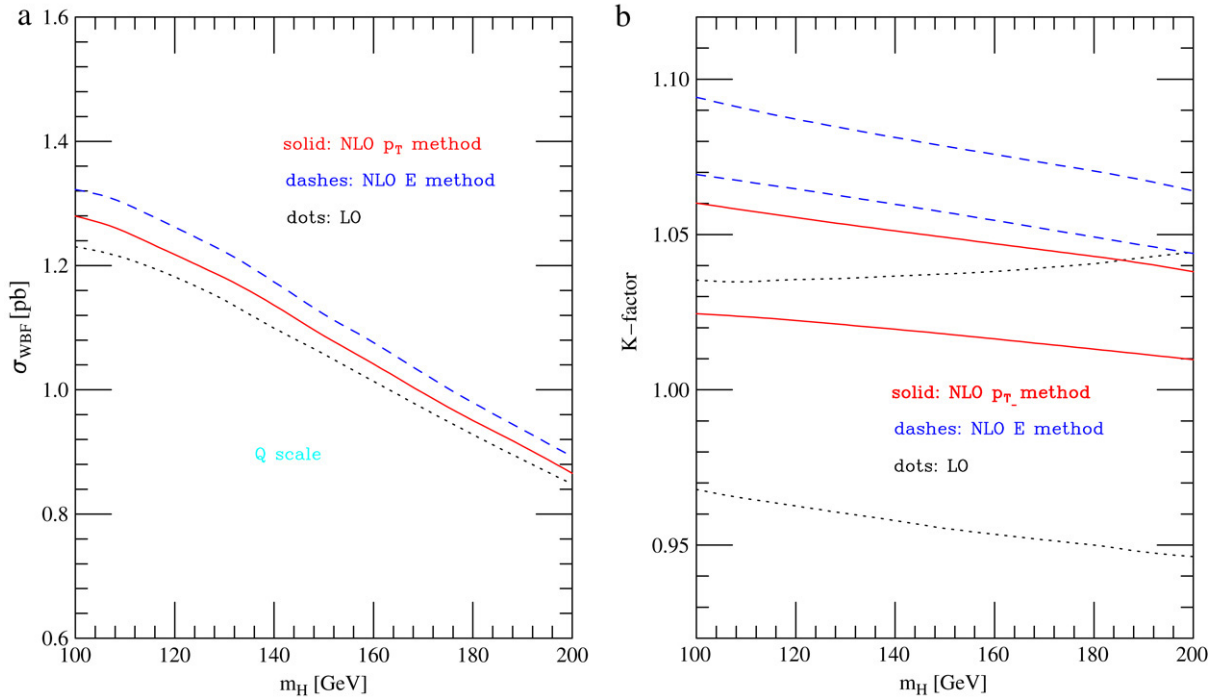


Fig. 3.16. Left: the  $pp \rightarrow Hqq$  cross section at the LHC after cuts as a function of  $M_H$  at LO (dotted line) and NLO with the tagging jets defined in the  $P_T$  (solid line) and  $E$  (dashed line) methods. Right: The scale variation of the LO and NLO cross sections for Higgs production in the  $qq \rightarrow qqH$  fusion process as a function of  $M_H$  at the LHC [264].

process proceeds without color exchange between the scattered quarks, and gluons will be preferentially emitted at rather small angles in the forward and backward directions and not in the central region. This is opposite to the QCD background which proceeds via color exchange of the incident partons and where the gluons are very often in the central region. Therefore vetoing any jet activity in the central region will substantially reduce the backgrounds.

The forward jet tagging and the central jet vetoing techniques have been discussed in numerous papers and have been shown to efficiently allow the isolation of a Higgs production signal in the vector boson fusion process [there are, however, still some experimental issues such as the central jet veto efficiencies and to a lesser extent, the forward jet reconstruction, which need further detailed studies]. Combined with the possibility of having large production rates at the LHC for a Higgs boson in the 100–200 GeV mass range, this process offers therefore a very promising channel not only for the production of the SM Higgs boson but also for the study of its properties.

### 3.3.4. Dependence on the scale and on the PDFs at NLO

Since rather stringent cuts have to be applied to the vector boson fusion process in order to suppress the various backgrounds, one may wonder if the NLO corrections and their residual scale dependence are the same as in the case of the inclusive cross section, i.e. without applying the cuts. This question has been addressed recently [264, 265] by implementing the full one-loop QCD corrections to the  $qq \rightarrow Hqq$  process into a parton-level Monte Carlo program [329]. With cuts similar to those discussed in the previous subsection [see the original reference for the details], the output for the production cross section is shown in Fig. 3.16 for a Higgs boson in the mass range between 100 and 200 GeV.

In the left-hand side of the figure, the cross section is displayed at LO (dotted line) and at NLO for two methods of tagging the forward jets: one chooses the tagging jets as being either the two highest  $P_T$  jets ( $P_T$  method, solid line) or the two highest energy jets ( $E$  method, dashed line). One first notices that with the cuts of Ref. [264], the acceptance is less than  $\sim 25\%$  of the initial cross section, *c.f.* Fig. 3.12. The corrections are modest and, in the chosen Higgs mass range, they are of the order of 3%–5% in the  $P_T$  method and 6%–9% in the  $E$  method, the largest variation being for low Higgs masses.

To illustrate the impact of the choice of the factorization and renormalization scales on the  $qq \rightarrow Hqq$  production cross section at the LHC, we show in the right-hand side of Fig. 3.16 the LO and NLO  $K$ -factors as functions of the Higgs mass when the central value of the scales  $\mu_F = \mu_R = Q_V$  is divided or multiplied by a factor of two,  $\mu_F = \mu_R = \frac{1}{2}Q_V$  and  $2Q_V$  [note that the variation with the renormalization scale  $\mu_R$  is small since  $\alpha_s$  enters only at NLO and the contribution of this order to the total production cross section is tiny]. Again, the  $K$ -factor at leading order is defined as  $K_{LO} = \sigma_{LO}(\mu_F, \mu_R)/\sigma_{LO}(\mu_F = \mu_R = Q_V)$ . As can be seen, the uncertainty on the total cross section that is generated by the scale variation is relatively large at LO, the spread being of the order of  $\Delta\sigma/\sigma \simeq \pm 3\%$  for low Higgs masses and reaching the level of 5% at high Higgs masses. At NLO, the cross section varies only slightly, with a spread smaller than  $\sim 2\%$  for the displayed Higgs mass range. This implies that the vector boson fusion cross section at NLO is well under control and that the higher-order QCD corrections are presumably very small.<sup>23</sup>

Note that the NLO QCD corrections for the  $p_T$  and  $\eta$  distributions in  $pp \rightarrow Hqq$  have also been calculated in this reference. In general, they are of the same size as the corrections to the total cross section,  $\sim 10\%$ , but they can reach larger values depending on the phase-space regions; see Ref. [264] for details.

Turning to the PDF uncertainties in the prediction for the  $qq \rightarrow Hqq$  cross section at NLO, we will follow again the procedure outlined in Section 3.1.5. The central values and the uncertainty band limits of the NLO cross sections are shown for the CTEQ, MRST and Alekhin parametrizations in Fig. 3.17 as functions of  $M_H$  at LHC energies. We also show in the insert to this figure, the spread uncertainties in the predictions when the cross sections are normalized to the values obtained using the reference CTEQ6M set.

In the entire Higgs mass range from 100 GeV to 1 TeV, the incoming quarks involved in this process originate from the intermediate- $x$  regime and the uncertainty band is almost constant, ranging between 3% and 4% in the CTEQ parametrization; as usual, the uncertainty is twice smaller in the MRST case. When using the Alekhin set of PDFs, the behavior is different, because the quark PDF behavior is different, as discussed in the case of the  $q\bar{q} \rightarrow HV$  production channel. The decrease in the central value with higher Higgs masses [which is absent in the  $q\bar{q} \rightarrow HV$  case, since we stopped the  $M_H$  variation at 200 GeV] is due to the fact that we reach here the high- $x$  regime, where the Alekhin  $\bar{u}$  PDF drops steeply; see Fig. 3.2. Thus, as in the case of the  $q\bar{q} \rightarrow HV$  process, the PDF uncertainties are below the 5% level if the Alekhin parametrization is ignored and, therefore, rather small. In view of the small QCD corrections and scale dependence, weak boson fusion can thus also be considered as a rather clean Higgs production process.

### 3.3.5. The effective longitudinal vector boson approximation

Before closing this section, let us reconsider the total  $pp \rightarrow Hqq$  production cross section in the light of the previous discussion. Following Ref. [226] and recalling that the transverse momenta of the scattered quarks are small, one may write the parton four momenta as

$$p_{3/4} = \left( x_{3/4}E + p_{T3/4}^2/(2x_{3/4}E), \vec{p}_{T3/4}, \pm x_{3/4}E \right), \quad p_{1/2} = (E, \vec{0}, \pm E) \quad (3.44)$$

with  $E$  being half of the parton c.m. energy, and neglect terms of the order of  $p_{T3,4}^2/E^2 \ll 1$  in the amplitude squared. One then immediately obtains for the invariants of Eq. (3.23)

$$(p_1 \cdot p_2)(p_3 \cdot p_4) \simeq (p_1 \cdot p_4)(p_2 \cdot p_3) \simeq 4E^4 x_3 x_4 \quad (3.45)$$

leading to an amplitude squared for the process that is simply given by

$$|\mathcal{M}|^2 = \sqrt{2}N_c^f G_\mu^3 M_V^8 \frac{(C_+ + C_-)(x_3 x_4)^3 \hat{s}^2}{(p_{T3}^2 + x_3 M_V^2)^2 (p_{T4}^2 + x_4 M_V^2)^2}. \quad (3.46)$$

<sup>23</sup> The electroweak corrections to this process have not been calculated yet. However, if one uses the IBA discussed in Section 1.2.4, the bulk of these corrections is incorporated and the remaining piece should be rather small. See the discussion in the next chapter, when this process will be considered in  $e^+e^-$  collisions.

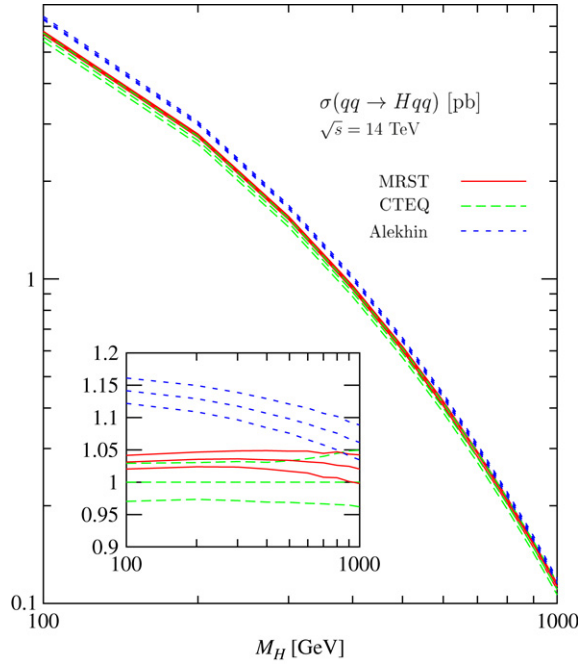


Fig. 3.17. The CTEQ, MRST and Alekhin PDF uncertainty bands for the NLO cross section of the vector boson fusion process  $pp \rightarrow Hqq$  at the LHC. In the insert is shown the spread uncertainty, when the cross sections are normalized to the default CTEQ PDF set; from Ref. [295].

The three-body phase space also simplifies to

$$dPS_3 \simeq \frac{1}{8(2\pi)^5} \frac{dx_3}{x_3} \frac{dx_4}{x_4} d^2\vec{p}_{T3} d^2\vec{p}_{T4} \frac{2}{\hat{s}} \delta \left( (1-x_3)(1-x_4) - \frac{M_H^2}{\hat{s}} \right). \quad (3.47)$$

The integrations on the transverse momenta can therefore be easily done, leading to

$$\int \frac{d^2\vec{p}_{Ti}}{(p_{Ti}^2 + x_i M_V^2)^2} \simeq \pi \int_0^\infty \frac{dp^2}{(p^2 + x_i M_V^2)^2} = \frac{\pi}{x_i M_V^2} \quad (3.48)$$

and, with the help of the delta function, the integrations on  $x_{3,4}$  are straightforward. One finally obtains for the total partonic cross section

$$\hat{\sigma}_{LO}(qq \rightarrow qqH) \simeq \frac{G_\mu^3 M_V^4 N_c}{128\sqrt{2}\pi^3} (C_+ + C_-) \left[ \left( 1 + \frac{M_H^2}{\hat{s}} \right) \log \frac{\hat{s}}{M_H^2} - 2 + 2 \frac{M_H^2}{\hat{s}} \right]. \quad (3.49)$$

This is nothing else than the cross section for Higgs boson production in the effective longitudinal vector boson approximation [31], where one calculates the cross section for the subprocess where the Higgs boson is produced in the fusion of  $V_L V_L$  [which according to the equivalence theorem can be replaced by their corresponding Goldstone bosons] and then folds the result with the  $V_L$  spectra [224,237,330]. Since we will use this approximation in the course of our discussion, we briefly summarize its salient features.

Just as in the Weizsäcker–Williams approximation in the processes  $e^+e^- \rightarrow e^\pm X$ , where the final state  $X$  particle is produced at small angles through the exchange of a photon, and where the bulk of the production rate is described by the cross section  $\hat{\sigma}$  for the subprocess  $\gamma e^\pm \rightarrow X$  folded by the probability of the initial  $e^+e^-$  state to radiate a photon [331]

$$\sigma(e^+e^- \rightarrow e^\pm X) = \int dz P_{\gamma/e^\pm}(z) \hat{\sigma}(\hat{s} = zs), \quad P_{\gamma/e^\pm}(z) = \frac{\alpha}{2\pi} \frac{1 + (1-z)^2}{z} \log \frac{s}{m_e^2} \quad (3.50)$$

where  $\sqrt{s}$  is the total c.m. energy and  $m_e$  the electron mass, the process  $qq \rightarrow qq V^* V^* \rightarrow qq H$  at very high energies can be viewed as originating from the subprocess  $VV \rightarrow H$  with the real vector bosons being radiated from the initial quarks. The only difference with the Weizsäcker–Williams approximation is that the  $W/Z$  bosons are massive and thus have a longitudinal degree of polarization. The distribution functions for the transverse and longitudinal polarizations in this case are given by

$$\begin{aligned} P_{V_{\pm}/q}(z) &= \frac{\alpha}{4\pi} \frac{1}{z} \left[ (v_q \mp a_q)^2 + (v_q \pm a_q)^2 (1-z)^2 \right] \log \frac{\hat{s}}{M_V^2} \\ P_{V_L/q}(z) &= \frac{\alpha}{\pi} \frac{1-z}{z} (v_q^2 + a_q^2). \end{aligned} \quad (3.51)$$

One recovers the photon case in Eq. (3.50) by appropriately replacing the quark weak charge by the electron electric charge,  $v_q \rightarrow 1, a_q \rightarrow 0$ . The  $VV$  luminosity in the process  $VV \rightarrow X$

$$\left. \frac{d\mathcal{L}}{d\tau} \right|_{VV/qq} = \int_{\tau}^1 P_{V/q}(z) P_{V/q}(\tau/z) \frac{dz}{z} \quad (3.52)$$

with  $\tau = M_X^2/\hat{s}$  where  $\hat{s}$  is the  $qq$  c.m. energy, is then given by

$$\begin{aligned} \left. \frac{d\mathcal{L}}{d\tau} \right|_{V_T V_T/qq} &= \frac{\alpha}{8\pi^3} (v_q^2 + a_q^2)^2 \frac{1}{\tau} \log \frac{\hat{s}}{M_V^2} \left[ (2+\tau)^2 \log(1/\tau) - 2(1-\tau)(3+\tau) \right] \\ \left. \frac{d\mathcal{L}}{d\tau} \right|_{V_L V_L/qq} &= \frac{\alpha}{4\pi^3} (v_q^2 + a_q^2)^2 \frac{1}{\tau} \left[ (1+\tau) \log(1/\tau) - 2(1-\tau) \right]. \end{aligned} \quad (3.53)$$

In principle, at high energies, the luminosity for transverse gauge bosons is much larger than that for longitudinal ones because of the  $\log^2(M_V^2/\hat{s})$  term. However, for large masses, the Higgs boson is produced in the subprocess  $VV \rightarrow H$  mainly through the longitudinal components which give rates  $\propto M_H^3$ . The effective cross section in this case is simply given by

$$\sigma_{\text{eff}} = \frac{16\pi^2}{M_H^3} \Gamma(H \rightarrow V_L V_L) \left. \frac{d\mathcal{L}}{d\tau} \right|_{V_L V_L/qq} \quad (3.54)$$

which, when the expression of the luminosity is inserted reproduces the result of Eq. (3.49).

In the case of the partonic process [at the hadronic level, a difference is generated by the parton densities], the contribution of the  $WW$  fusion channel is one order of magnitude larger than the one of the  $ZZ$  channel because of the larger charged current couplings. However, in practice, the effective longitudinal approximation approaches the exact result only by a factor in the range of 2 to 5, depending on the considered c.m. energy and the Higgs mass. For light Higgs bosons, it can be improved by including the transverse vector boson components, see Ref. [332]. This approximation should therefore be used only as an indication of the order of magnitude of the cross sections.

### 3.4. The gluon–gluon fusion mechanism

#### 3.4.1. The production cross section at LO

Higgs production in the gluon–gluon fusion mechanism is mediated by triangular loops of heavy quarks. In the SM, only the top quark and, to a lesser extent, the bottom quark will contribute to the amplitude. The decreasing  $Hgg$  form factor with rising loop mass is counterbalanced by the linear growth of the Higgs coupling with the quark mass. In this section we discuss the analytical features of the process. The relevant phenomenological aspects at the LHC [223,296,333–338] and the Tevatron [339–341] will be presented in Section 3.7.

To lowest order, the partonic cross section can be expressed by the gluonic width of the Higgs boson discussed in Section 2.3.3,

$$\hat{\sigma}_{\text{LO}}(gg \rightarrow H) = \sigma_0^H M_H^2 \delta(\hat{s} - M_H^2) = \frac{\pi^2}{8M_H} \Gamma_{\text{LO}}(H \rightarrow gg) \delta(\hat{s} - M_H^2) \quad (3.55)$$



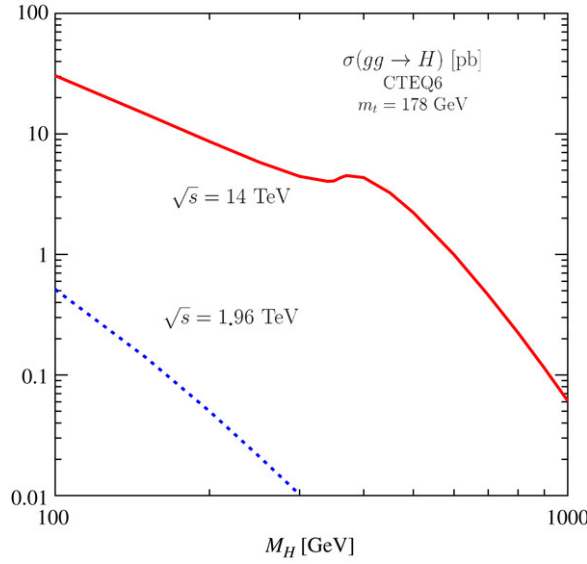


Fig. 3.18. The hadronic production cross section for the  $gg$  fusion process at LO as a function of  $M_H$  at the LHC and the Tevatron. The inputs are  $m_t = 178$  GeV,  $m_b = 4.88$  GeV, the CTEQ set of PDFs has been used and the scales are fixed to  $\mu_R = \mu_F = M_H$ .

where  $\hat{s}$  is the  $gg$  invariant energy squared. Substituting in this LO approximation the Breit–Wigner form of the Higgs boson width, in place of the zero-width  $\delta$  distribution

$$\delta(\hat{s} - M_H^2) \rightarrow \frac{1}{\pi} \frac{\hat{s} \Gamma_H / M_H}{(\hat{s} - M_H^2)^2 + (\hat{s} \Gamma_H / M_H)^2} \quad (3.56)$$

recalling the lowest-order two-gluon decay width of the Higgs boson, one finds for the cross section [166]

$$\sigma_0^H = \frac{G_\mu \alpha_s^2(\mu_R^2)}{288 \sqrt{2} \pi} \left| \frac{3}{4} \sum_q A_{1/2}^H(\tau_Q) \right|^2. \quad (3.57)$$

The form factor  $A_{1/2}^H(\tau_Q)$  with  $\tau_Q = M_H^2/4m_Q^2$  is given in Eq. (2.46) and is normalized such that for  $m_Q \gg M_H$ , it reaches  $\frac{4}{3}$  while it approaches zero in the chiral limit  $m_Q \rightarrow 0$ .

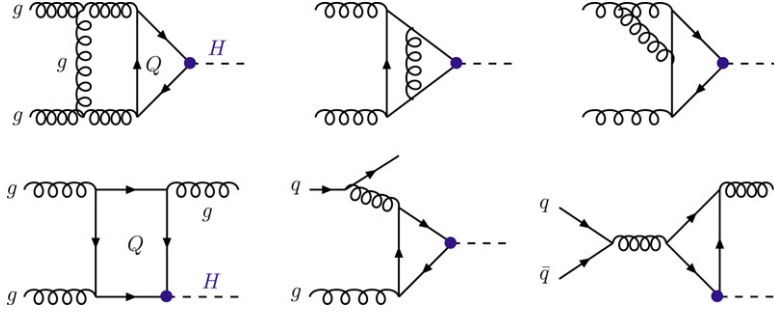
The proton–proton cross section at LO in the narrow-width approximation reads

$$\sigma_{\text{LO}}(pp \rightarrow H) = \sigma_0^H \tau_H \frac{d\mathcal{L}^{gg}}{d\tau_H} \quad \text{with} \quad \frac{d\mathcal{L}^{gg}}{d\tau} = \int_x^1 \frac{dx}{x} g(x, \mu_F^2) g(\tau/x, \mu_F^2) \quad (3.58)$$

where the Drell–Yan variable is defined as usual by  $\tau_H = M_H^2/s$  with  $s$  being the invariant collider energy squared. The expression of the luminosity  $\tau_H d\mathcal{L}^{gg}/d\tau_H$  is only mildly divergent for  $\tau_H \rightarrow 0$ .

The total hadronic cross sections at LO are shown in Fig. 3.18 as functions of the Higgs boson mass for the LHC and the Tevatron energies. We have chosen  $m_t = 178$  GeV,  $m_b = 4.88$  GeV and  $\alpha_s(\mu_Z) = 0.13$  as inputs and used the CTEQ parametrization for the parton densities. For the Tevatron, the cross section is monotonically decreasing with the Higgs boson mass, starting slightly below 1 pb for  $M_H \sim 100$  GeV and reaching  $\sigma \sim 0.01$  pb for  $M_H \sim 300$  GeV. At the LHC, the cross section is two orders of magnitude larger, being at the level of  $\sim 30$  pb for  $M_H \sim 100$  GeV and is still sizable,  $\sigma \sim 1$  pb, for  $M_H \sim 700$  GeV. There is a kink at  $M_H \sim 350$  GeV, i.e. near the  $t\bar{t}$  threshold where the  $Hgg$  amplitude develops an imaginary part.

As discussed in Section 2.3.3, the cross section in the case where the internal quark is assumed to have an infinite mass,  $m_q \rightarrow \infty$ , i.e. when the form factor  $\frac{3}{4}A_{1/2}^H$  is equal to unity, is a rather good approximation for Higgs masses below the  $t\bar{t}$  threshold, and it reproduces the exact result at the level of 10%. For low Higgs masses, the difference is in fact due to the contribution of the bottom quark loop: although the  $b$ -quark mass is small, the form factor  $A_{1/2}^H(\tau_b)$  exhibits a dependence on  $m_b^2/M_H^2 \times \log^2(m_b^2/M_H^2)$  which is not that small. Together with the  $\pi^2$  terms and

Fig. 3.19. Typical diagrams for the virtual and real QCD corrections to  $gg \rightarrow H$ .

the imaginary part, the  $b$ -quark loop generates a non-negligible contribution which interferes destructively with the contribution of the top quark loop. Above the  $t\bar{t}$  threshold,  $M_H \gtrsim 350$  GeV, the approximation of an infinite loop quark mass fails since it cannot reproduce the imaginary part of the form factor.

### 3.4.2. The cross section at NLO

To incorporate the QCD corrections to  $\sigma(pp \rightarrow H + X)$ , one has to consider the processes

$$gg \rightarrow H(g) \quad \text{and} \quad gq \rightarrow Hq, \quad q\bar{q} \rightarrow Hg. \quad (3.59)$$

Characteristic diagrams of the QCD radiative corrections are shown in Fig. 3.19. They involve the virtual corrections to the  $gg \rightarrow H$  subprocess, which modify the LO fusion cross section by a coefficient linear in  $\alpha_s$ , and the radiation of gluons in the final state. In addition, Higgs bosons can be produced in gluon–quark collisions and quark–antiquark annihilation which contribute to the cross section at the same order of  $\alpha_s$ .

The cross sections for the subprocesses  $ij \rightarrow H + X$ ,  $i, j = g, q, \bar{q}$ , can be written as

$$\hat{\sigma}_{ij} = \sigma_0 \left\{ \delta_{ig} \delta_{jg} \left[ 1 + C^H(\tau_Q) \frac{\alpha_s}{\pi} \right] \delta(1 - \hat{\tau}) + D_{ij}^H(\hat{\tau}, \tau_Q) \frac{\alpha_s}{\pi} \Theta(1 - \hat{\tau}) \right\} \quad (3.60)$$

where the new scaling variable  $\hat{\tau}$ , supplementing  $\tau_H = M_H^2/s$  and  $\tau_Q = M_H^2/4m_Q^2$  introduced earlier, is defined at the parton level as  $\hat{\tau} = M_H^2/\hat{s}$ ;  $\Theta$  is the step function.

The coefficients  $C^H(\tau_Q)$  and  $D_{ij}^H(\hat{\tau}, \tau_Q)$  have been determined in Refs. [161,267] for arbitrary Higgs boson and quark masses and the lengthy analytical expressions have been given there [see also Section 2.3.3 for some details on the calculation and on the renormalization scheme]. If all the corrections Eq. (3.60) are added up, ultraviolet and infrared divergences cancel. However collinear singularities are left over and are absorbed into the renormalization of the parton densities [42,306] where the  $\overline{\text{MS}}$  factorization scheme can be adopted.

The final result for the hadronic cross section at NLO can be cast into the form

$$\sigma(pp \rightarrow H + X) = \sigma_0^H \left[ 1 + C^H \frac{\alpha_s}{\pi} \right] \tau_H \frac{d\mathcal{L}^{gg}}{d\tau_H} + \Delta\sigma_{gg}^H + \Delta\sigma_{gq}^H + \Delta\sigma_{q\bar{q}}^H. \quad (3.61)$$

The coefficient  $C^H$  denotes the contributions from the virtual two-loop quark corrections regularized by the infrared singular part of the cross section for real gluon emission. It splits into the infrared term  $\pi^2$ , a term depending on the renormalization scale  $\mu_R$  of the coupling constant, and a piece  $c^H$  which depends on the mass ratio  $\tau_Q$ .

$$C^H = \pi^2 + c^H + \frac{33 - 2N_f}{6} \log \frac{\mu_R^2}{M_H^2} \quad (3.62)$$

with

$$c^H = \text{Re} \sum_Q A_{1/2}^H(\tau_Q) c_Q^H(\tau_Q) / \sum_Q A_{1/2}^H(\tau_Q). \quad (3.63)$$

The (non-singular) contributions from gluon radiation in  $gg$  scattering, from  $gq$  scattering and  $q\bar{q}$  annihilation, depend on the renormalization scale  $\mu_R$  and the factorization scale  $\mu_F$  of the parton densities

$$\begin{aligned}\Delta\sigma_{gg}^H &= \int_{\tau_H}^1 d\tau \frac{d\mathcal{L}^{gg}}{d\tau} \frac{\alpha_s(\mu_R)}{\pi} \sigma_0^H \left\{ -z P_{gg}(z) \log \frac{\mu_F^2}{\tau_S} + d_{gg}^H(z, \tau_Q) \right. \\ &\quad \left. + 12 \left[ \left( \frac{\log(1-z)}{1-z} \right)_+ - z [2 - z(1-z)] \log(1-z) \right] \right\} \\ \Delta\sigma_{gq}^H &= \int_{\tau_H}^1 d\tau \sum_{q,\bar{q}} \frac{d\mathcal{L}^{gq}}{d\tau} \frac{\alpha_s(\mu_R)}{\pi} \sigma_0^H \left\{ \left[ -\frac{1}{2} \log \frac{\mu_F^2}{\tau_S} + \log(1-z) \right] z P_{gq}(z) + d_{gq}^H(z, \tau_Q) \right\} \\ \Delta\sigma_{q\bar{q}}^H &= \int_{\tau_H}^1 d\tau \sum_q \frac{d\mathcal{L}^{q\bar{q}}}{d\tau} \frac{\alpha_s(\mu_R)}{\pi} \sigma_0^H d_{q\bar{q}}^H(z, \tau_Q)\end{aligned}\quad (3.64)$$

with  $z = \tau_H/\tau$  and the standard Altarelli–Parisi splitting functions given by

$$\begin{aligned}P_{gg}(z) &= 6 \left[ \left( \frac{1}{1-z} \right)_+ + \frac{1}{z} - 2 + z(1-z) \right] + \frac{33 - 2N_f}{6} \delta(1-z) \\ P_{gq}(z) &= \frac{4}{3} \frac{1 + (1-z)^2}{z}\end{aligned}\quad (3.65)$$

where  $F_+$  denotes the usual  $+$  distribution such that  $F(\hat{\tau})_+ = F(\hat{\tau}) - \delta(1-\hat{\tau}) \int_0^1 d\hat{\tau}' F(\hat{\tau}')$ .

The coefficients  $d_{gg}^H$ ,  $d_{gq}^H$  and  $d_{q\bar{q}}^H$ , as well as  $c^H$ , have been evaluated for arbitrary quark masses [161,169,267]. In the limit where the Higgs mass is very large compared with the quark mass,  $\tau_Q = M_H^2/4m_Q^2 \gg 1$ , as is the case of the bottom quark contribution, a compact analytic result can be derived, which is valid to leading and subleading logarithmic accuracy

$$\begin{aligned}c^H(\tau_Q) &\rightarrow \frac{5}{36} \left[ \log^2(4\tau_Q) - \pi^2 \right] - \frac{4}{3} \log(4\tau_Q) \\ d_{gg}^H(\hat{\tau}, \tau_Q) &\rightarrow -\frac{2}{5} \log(4\tau_Q) \left[ 7 - 7\hat{\tau} + 5\hat{\tau}^2 \right] - 6 \log(1-\hat{\tau}) \left[ 1 - \hat{\tau} + \hat{\tau}^2 \right] \\ &\quad + 2 \frac{\log \hat{\tau}}{1-\hat{\tau}} \left[ 3 - 6\hat{\tau} - 2\hat{\tau}^2 + 5\hat{\tau}^3 - 6\hat{\tau}^4 \right] \\ d_{gq}^H(\hat{\tau}, \tau_Q) &\rightarrow \frac{2}{3} \left[ \hat{\tau}^2 - \left( 1 + (1-\hat{\tau})^2 \right) \left( \frac{7}{15} \log(4\tau_Q) + \log \left( \frac{1-\hat{\tau}}{\hat{\tau}} \right) \right) \right] \\ d_{q\bar{q}}^H(\hat{\tau}, \tau_Q) &\rightarrow 0.\end{aligned}\quad (3.66)$$

In the limit of large quark masses,  $\tau_Q = M_H^2/4m_Q^2 \ll 1$ , as is the case for the top quark when the Higgs mass is small, one also obtains very simple expressions for the coefficients

$$c^H(\tau_Q) \rightarrow \frac{11}{2}, \quad d_{gg}^H \rightarrow -\frac{11}{2}(1-z)^3, \quad d_{gq}^H \rightarrow -1 + 2z - \frac{1}{3}z^2, \quad d_{q\bar{q}}^H \rightarrow \frac{32}{27}(1-z)^3. \quad (3.67)$$

In this heavy quark case, the corrections of  $\mathcal{O}(M_H^2/m_Q^2)$  in a systematic Taylor expansion have been shown to be very small [170]. In fact, the leading term provides an excellent approximation up to the quark threshold  $M_H \sim 2m_Q$ .

The results for the  $K$ -factors, defined as the ratios  $K_{\text{tot}} = \sigma_{\text{NLO}}/\sigma_{\text{LO}}$ , with the cross section  $\sigma_{\text{NLO}}$  normalized to the LO cross section  $\sigma_{\text{LO}}$ , evaluated consistently for parton densities and an  $\alpha_s$  value at LO, are displayed in Fig. 3.20 as functions of  $M_H$  for the LHC (left) and the Tevatron (right). Again the CTEQ6 parametrization for the structure functions defined in the  $\overline{\text{MS}}$  scheme is used and the top and bottom quark pole masses are fixed to  $m_t = 178$  GeV and  $m_b = 4.88$  GeV. Both the renormalization and the factorization scales have been set to the Higgs mass  $\mu_R = \mu_F = M_H$ .

The  $K$ -factors have been decomposed into their various components:  $K_{\text{virt}}$  accounts for the virtual corrections after regularization [corresponding to the coefficient  $C^H$ ], while  $K_{ij}$  with  $i, j = g, q, \bar{q}$  stand for the real corrections in

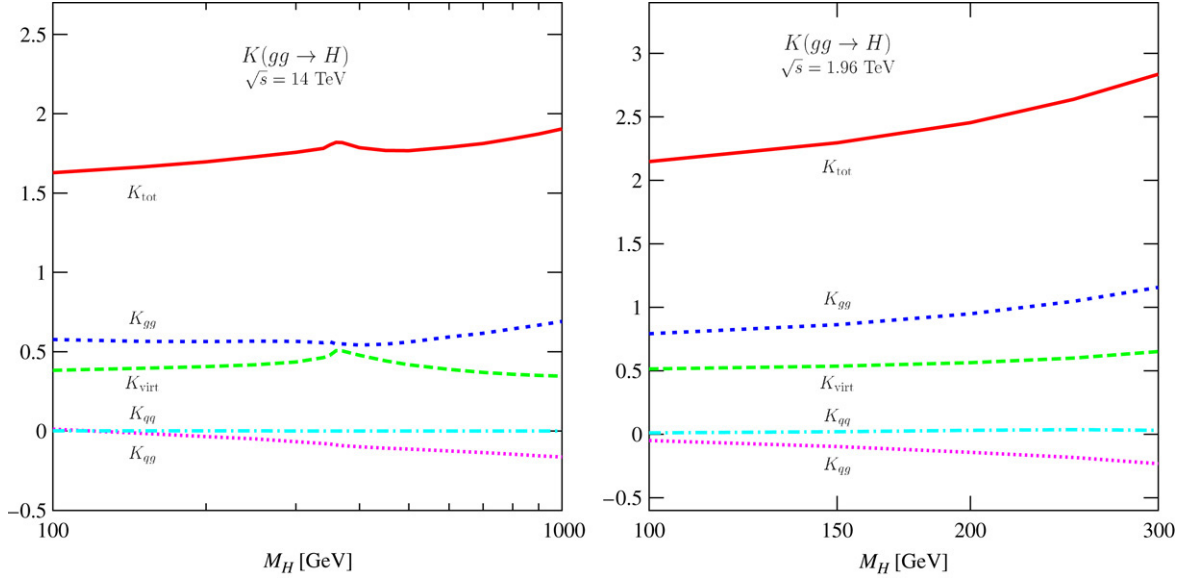


Fig. 3.20. The total  $K$ -factor and its various components,  $K_{\text{virt}}$ ,  $K_{gg}$  and  $K_{q\bar{q}}$ , for Higgs production in the  $gg$  fusion process as functions of  $M_H$  at the LHC (left) and the Tevatron (right). The CTEQ6 parton densities have been adopted and the renormalization and factorization scales are fixed to  $\mu_R = \mu_F = M_H$ ;  $m_t = 178$  GeV and  $m_b = 4.88$  GeV.

the three channels given in Eq. (3.64). One sees that  $K_{\text{virt}}$  and  $K_{gg}$  are rather large, being both of the order of 50%, while  $K_{q\bar{q}}$  and  $K_{qq}$  are tiny, the latter being negative. The total  $K$ -factor is large, increasing the total production cross section by about 60% and 90% for the low and high ranges of the Higgs mass at the LHC and by a factor in the range from 2.2 to 2.8 for  $M_H = 100$ –300 GeV at the Tevatron.

Apart for the small kink in the  $M_H \sim 2m_t$  threshold region,  $K_{\text{tot}}$  is only mildly depending on the Higgs mass. In fact, if one compares the exact numerical results for the cross section at NLO with the approximation of a very heavy top quark, it turns out that multiplying the LO cross section, which includes the full  $m_t$  and  $m_b$  dependence, with the  $K$ -factor taken in the asymptotic limit  $m_t \rightarrow \infty$  and where the  $b$ -quark contribution has been neglected, provides a good approximation

$$\sigma_{\text{NLO}} \simeq K_{\text{tot}}|_{m_t \rightarrow \infty} \times \sigma_{\text{LO}}(\tau_t, \tau_b). \quad (3.68)$$

The difference between this approximation and the exact result is less than 10% even for Higgs boson masses beyond the  $M_H = 2m_t$  threshold and up to  $M_H \sim 700$  GeV [342].

Finally, note that the two-loop electroweak corrections to the  $gg \rightarrow H$  production cross section are the same as the ones discussed previously in Section 2.4.3 for the decay  $H \rightarrow gg$ . While the top quark correction is rather small, being less than one percent [182], the light fermion electroweak contributions [184,185] are much larger in the  $M_H \lesssim 2M_W$  range where they reach the level of 5%–9%; for  $M_H \gtrsim 2M_W$  these corrections become again very small.

**3.4.2.1. Dependence on the PDFs.** The central values and the uncertainty band limits of the NLO cross sections are shown for the CTEQ, MRST and Alekhin parametrizations in Fig. 3.21 for the  $gg \rightarrow H$  process. As usual, in the inserts to these figures, we show the spread uncertainties in the predictions for the cross sections, when normalized to the prediction of the reference CTEQ6M set.

At the LHC, the uncertainty band for the CTEQ set of PDFs decreases from the level of about 5% at  $M_H \sim 100$  GeV, down to the 3% level at  $M_H \sim 300$  GeV. This is because Higgs bosons with relatively small masses are mainly produced by asymmetric low- $x$  and high- $x$  gluons with a low effective c.m. energy. To produce heavier Higgs bosons, a symmetric process in which the participation of intermediate- $x$  gluons with high density is needed, resulting in a smaller uncertainty band. At higher masses,  $M_H \gtrsim 300$  GeV, the participation of high- $x$  gluons becomes more important, and the uncertainty band increases to reach the 10% level at Higgs masses of about 1 TeV. At the Tevatron, because of the smaller c.m. energy, the high- $x$  gluon regime is already reached for low Higgs masses and the uncertainties increase from 5% to 15% for  $M_H$  varying between 100 GeV and 200 GeV. As discussed previously

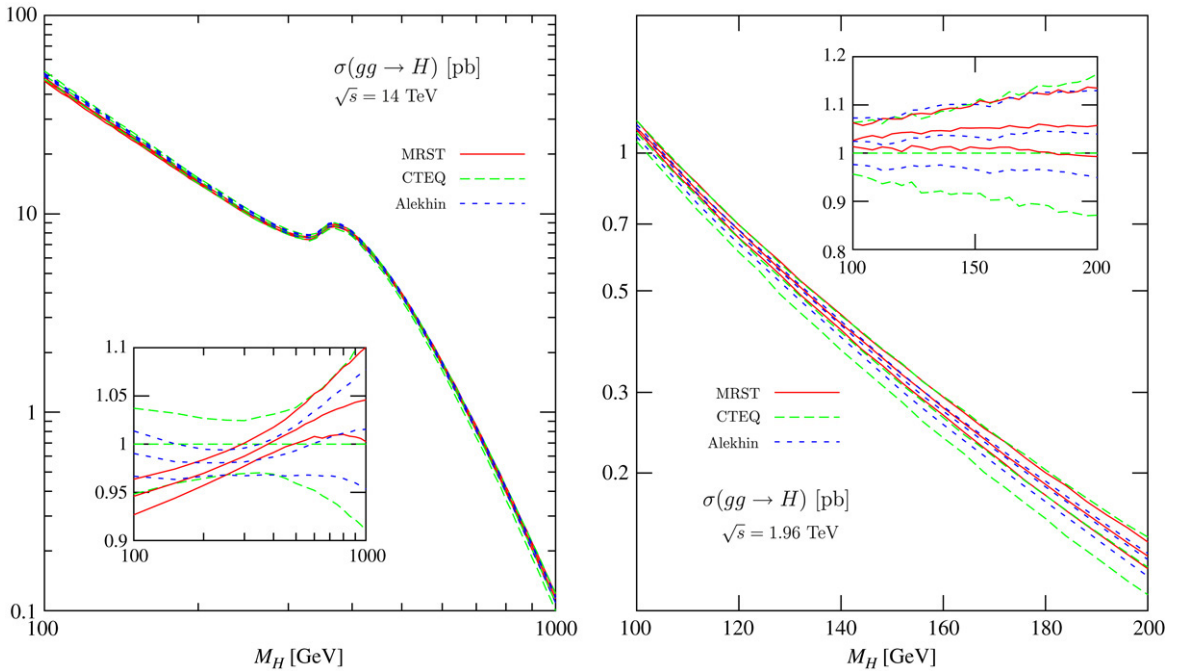


Fig. 3.21. The CTEQ, MRST and Alekhin PDF uncertainty bands for the NLO  $gg \rightarrow H$  cross sections at the LHC (left) and Tevatron (right). The inserts show the spread in the predictions, when the NLO cross sections are normalized to the CTEQ6 reference set [295].

and shown in Fig. 3.2, the MRST gluon PDF is smaller than the CTEQ one for low  $x$  and larger for relatively high  $x$  ( $\sim 0.1$ ); this explains the increasing cross section obtained with MRST compared to the one obtained with CTEQ, for increasing Higgs masses at the LHC. At the Tevatron the gluons are already in the high- $x$  regime.

The variation of the cross section with the renormalization and factorization scales will be discussed later after inclusion of the NNLO corrections to which we turn now.

### 3.4.3. The cross section beyond NLO in the heavy top quark limit

**3.4.3.1. The calculation at NNLO.** Recently, the very complicated three-loop NNLO QCD corrections to the  $gg \rightarrow H$  fusion process have been calculated by three different groups [281–283] in the limit of a very heavy top quark. In this limit, the Feynman diagrams contributing to the process factorize into two pieces: a massive component where the heavy quark has been integrated out and which represents an effective coupling constant which multiplies the  $Hgg$  vertex, and a massless component involving only gluons and light quarks, which describes the short distance effects and where the finite momenta of the particles have to be taken into account. The calculation effectively reduces then to a two-loop calculation with massless particles.

However, many Feynman diagrams, some of which are displayed in Fig. 3.22, have to be evaluated at this order and they can be cast into three categories [which lead to more than one thousand square and interference terms] besides the one-loop squared contribution: (a) two-loop virtual corrections for the process  $gg \rightarrow H$  which have to be multiplied by the effective Born amplitude; (b) one-loop single real emission diagrams for the  $gg \rightarrow Hg$ ,  $gq \rightarrow Hq$  and  $q\bar{q} \rightarrow Hg$  processes, which have to be multiplied by the Born amplitude for the same processes; (c) tree-level double real emission diagrams for the processes  $gg \rightarrow Hgg$ ,  $gg \rightarrow Hq\bar{q}$ ,  $gq \rightarrow Hgq$ ,  $qq \rightarrow Hqq$  and  $q\bar{q} \rightarrow Hq\bar{q}$ , which have to be squared.

This *tour de force* has been made possible thanks to two simplifying features: the possibility of using the low-energy theorem discussed in Section 2.4.1, which allows one to calculate the corrections to the effective  $Hgg$  vertex, and the development of new techniques [343] to evaluate massless three-point functions at the two-loop level in complete analogy to massless three-loop propagator diagrams which are standard and can be done fully automatically.

As already discussed in Section 2.4.3, the NNLO QCD corrected  $Hgg$  effective operator in the heavy quark limit,  $\mathcal{L}_{\text{eff}}(Hgg)$ , can be obtained [22,187,342] by means of the low-energy theorem, Eq. (2.91). This operator does not

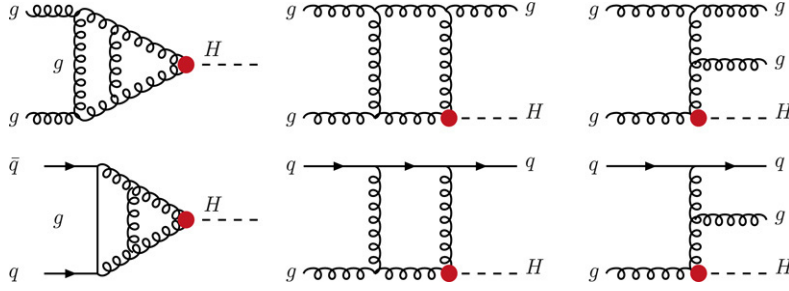


Fig. 3.22. Typical diagrams for the QCD corrections to  $gg \rightarrow H$  at NNLO in the heavy quark limit. • denotes the effective  $Hgg$  vertex where the quark has been integrated out.

describe the  $Hgg$  interaction in total: it accounts only for the interactions mediated by the heavy quarks directly, but it does not include the interactions of the light fields. It must be added to the light-quark and gluon parts of the basic QCD Lagrangian, i.e. the effective coupling has to be inserted into the blobs of the effective two-loop diagrams shown in Fig. 3.22. The NNLO corrections to inclusive Higgs production in  $gg \rightarrow H$  can be cast then into the three categories which have been already encountered when we discussed the NLO case. In terms of the variable  $\hat{\tau}$  defined as  $\hat{\tau} = M_H^2/\hat{s}$ , one has  $\delta$  function terms  $\propto \delta(1 - \hat{\tau})$ , large logarithms of the form  $\log^n(1 - \hat{\tau})/(1 - \hat{\tau})$ , and hard scattering terms that have at most a logarithmic singularity in the limit  $\hat{\tau} \rightarrow 1$

$$\hat{\sigma}_{ij}^{(2)} = a^{(2)}\delta(1 - \hat{\tau}) + \sum_{k=0}^3 b_k^{(2)}\mathcal{D}_k(\hat{\tau}) + \sum_{l=0}^{\infty} \sum_{k=0}^3 c_{lk}^{(2)}(1 - \hat{\tau})^l \ell^k \quad (3.69)$$

where  $\ell_k = \log^k(1 - \hat{\tau})$  and  $\mathcal{D}_k(\hat{\tau})$ , with now  $i = 1, 2, 3$ , are the usual  $+$  distributions defined earlier. The virtual corrections [344], which are of course UV finite when all contributions are added up, and in particular the coefficient function  $C_g$  of the  $Hgg$  effective operator contribute only to the coefficient  $a^{(2)}$  in front of the delta function [344, 345]. The soft corrections to the  $gg \rightarrow H$  cross section, i.e. when the momenta of the final state gluons or quarks tend to zero, contribute to both the  $a^{(2)}$  and  $b^{(2)}$  terms; they have been evaluated in Refs. [346,347] and, when added to the virtual corrections, the infrared divergences cancel out after mass factorization. The combination of the virtual + soft with the collinear terms  $\propto \ell^3$  gives the “soft + subleading” [346] or “soft + virtual + collinear corrections” [347] approximations which include also the contributions to the coefficient  $c_{03}^{(2)}$  which has been evaluated in Ref. [342] using resummation techniques.

The remaining pieces which have to be evaluated at NNLO [281] are then the coefficients  $c_{lk}^{(2)}$  with  $k = 0, \dots, 3$  and  $l \geq 0$  which receive contributions from all subprocesses. One can perform this calculation by making a systematic expansion of the partonic cross section around the soft limit  $\hat{\tau} \sim 1$ , leading to a series in  $(1 - \hat{\tau})^n$  whose coefficients depend on  $\ell^n \equiv \log^n(1 - \hat{\tau})$  with  $n = 0, 1, 2, 3$  at NNLO. However, because the bulk of the cross section is at the threshold  $\hat{\tau} \rightarrow 1$ , the series converges very rapidly and it is sufficient to keep only the contributions of the terms up to order  $(1 - \hat{\tau})^1$ . The convergence can be improved [348] by pulling out a factor  $\hat{\tau}$  before expanding in  $(1 - \hat{\tau})$ . In practice, the expansion to order  $(1 - \hat{\tau})^1$  reproduces the exact result, with all terms up to order  $(1 - \hat{\tau})^{16}$  or equivalently with the exact calculation as performed in Refs. [282,283], with an accuracy of order 1%.

This approach leads to a rather simple analytical result. Summing the soft and hard contributions, one obtains the following partonic cross sections up to NNLO [we display the LO and NLO contributions for completeness] in the various production channels, normalized to  $\sigma_0^H = G_\mu \alpha_s^2 / (288\sqrt{2}\pi)$  introduced before and using  $\ell_H = \log(M_H^2/m_t^2)$  [281]

$$\begin{aligned} \hat{\sigma}_{gg}^{(2)} = & \delta(1 - \hat{\tau}) + \frac{\alpha_s}{\pi} [15.37\delta(1 - \hat{\tau}) + 6 - 24\ell - 9(1 + 4\ell)(1 - \hat{\tau}) + 12\mathcal{D}_1(\hat{\tau})] \\ & + \left(\frac{\alpha_s}{\pi}\right)^2 [87.76\delta(1 - \hat{\tau}) + 5.71\ell_H - 531.134 + 39.92\ell + 185.5\ell^2 + 144\ell^3 \\ & + (632.06 + 632.87\ell - 559.58\ell^2 + 216\ell^3)(1 - \hat{\tau}) \\ & + 222.91\mathcal{D}_0(\hat{\tau}) - 31.71\mathcal{D}_1(\hat{\tau}) - 23\mathcal{D}_2(\hat{\tau}) + 72\mathcal{D}_3(\hat{\tau})] \end{aligned}$$



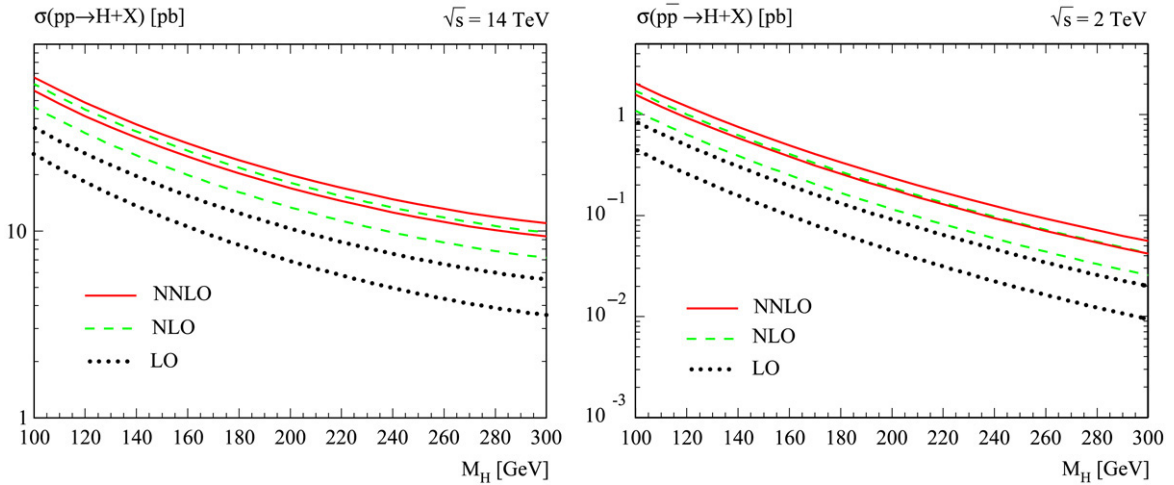


Fig. 3.23. The cross sections for Higgs production in the  $gg \rightarrow H + X$  fusion mechanism at the LHC (left) and Tevatron (right) at LO (dotted), NLO (dashed) and NNLO (solid) for two factorization and renormalization scales:  $\mu_R = \mu_F = \frac{1}{2}M_H$  (upper curves) and  $\mu_R = \mu_F = 2M_H$  (lower curves). The MRST PDFs are used; from Ref. [349].

$$\begin{aligned}\hat{\sigma}_{qg}^{(2)} &= \frac{2}{3} \frac{\alpha_s}{\pi} [1 + 2\ell - (1 - \hat{\tau})] \\ &\quad + \left(\frac{\alpha_s}{\pi}\right)^2 \left[ 29.93 + 6.47\ell + 2.63\ell^2 + 6.79\ell^3(-40.19 + 50.33\ell - 16.5\ell^2)(1 - \hat{\tau}) \right] \\ \hat{\sigma}_{qq}^{(2)} &= \left(\frac{\alpha_s}{\pi}\right)^2 [-0.70 - 1.78\ell + 1.78\ell^2]\end{aligned}\quad (3.70)$$

where the scale dependence has been explicitly suppressed by setting the factorization and renormalization scales to  $\mu_R = \mu_F = M_H$  [the dependence can be reconstructed by requiring the total cross section to be scale invariant] and the number of light quarks has been set to  $N_f = 5$ . The component  $\hat{\sigma}_{q\bar{q}}^{(2)}$  denotes the flavor singlet and non-singlet contributions in both the channels  $qq$  and  $q\bar{q} \rightarrow H + X$ , the contributions of which are equal at order  $(1 - \hat{\tau})$

$$\hat{\sigma}_{qq,S}^{(2)} = \hat{\sigma}_{qq,NS}^{(2)} = \hat{\sigma}_{q\bar{q},S}^{(2)} = \hat{\sigma}_{q\bar{q},NS}^{(2)}. \quad (3.71)$$

**3.4.3.2. The  $K$ -factors and the scale dependence up to NNLO.** The cross sections  $\sigma(pp \rightarrow H + X)$  at the three orders LO, NLO and NNLO, are shown in Fig. 3.23 at the LHC and the Tevatron as functions of the Higgs mass, using the MRST parton distributions which include the approximated NNLO PDFs. The factorization and renormalization scales are set to  $\mu_R = \mu_F = \frac{1}{2}M_H$  (upper curves) and  $\mu_R = \mu_F = 2M_H$  (lower curves). To improve the heavy quark approximation, the LO cross section contains the full top mass dependence where  $m_t = 175$  GeV has been used. Considering first the relative magnitude of the cross sections at the different orders of perturbation theory, one can see that while from LO to NLO, the cross section increases at the LHC by 70% for moderate Higgs boson masses, the increase from NLO to NNLO of about 30%, is more modest. This explicitly shows the nice convergence behavior of the perturbative series. The  $K$ -factors are larger at the Tevatron, since they increase the cross section by a factor of about three at NNLO, the bulk of which is provided by the NLO correction.

When considering the effect of the variation of the renormalization and factorization scales on the cross section, by multiplying and dividing by a factor of two the median scale  $\mu_F = \mu_R = M_H$ , one first sees that globally, the scale dependence is reduced when going from LO, to NLO and then to NNLO. The residual scale dependence at NNLO is 25% at the LHC and 15% at the Tevatron, a factor two and a factor of four smaller than the dependence on the scale choice, at respectively, NLO and LO.

It has been noticed in Refs. [284,349] that at the LHC the dependence on the renormalization and factorization scales have different signs: the cross section increases (decreases) with increasing  $\mu_F$  ( $\mu_R$ ) values when the other scale is fixed, to  $\mu_R(\mu_F) = M_H$  for instance [at the Tevatron the dependence on  $\mu_R$  and  $\mu_F$  is in the same direction]; the decrease with  $\mu_R$  is much stronger. It is thus more appropriate to choose smaller values for the scale than the



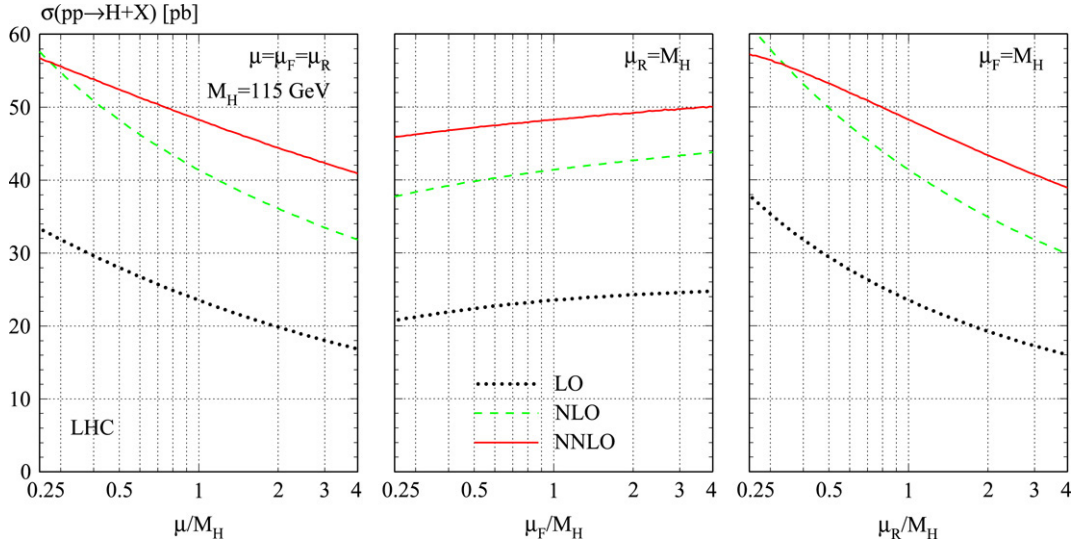


Fig. 3.24. The scale dependence of  $\sigma(gg \rightarrow H)$  at LHC for  $M_H = 115$  GeV: variation of  $\mu \equiv \mu_R = \mu_F$  (left),  $\mu_F$  with  $\mu_R = M_H$  (center) and  $\mu_R$  with  $\mu_F = M_H$  (right); from [349].

standard choice  $\mu_R = \mu_F = M_H$ . This is shown in Fig. 3.24 where the scales are varied within a factor  $\frac{1}{4}$  and 4 with respect to the default scale  $\mu_F = \mu_R = M_H = 115$  GeV, first collectively and then by varying  $\mu_F$  ( $\mu_R$ ) while the other scale is fixed at the default value.

With the choice  $\mu_R = \mu_F = \frac{1}{2}M_H$  e.g., the NLO correction increases while the NNLO correction decreases, with a total cross section which increases compared to the choice  $\mu_R = \mu_F = M_H$ . Therefore, since the difference between the NLO and NNLO contributions is small, the convergence of the perturbative series is improved for  $\mu_R = \mu_F = \frac{1}{2}M_H$ . This choice is supported by the fact that these fixed-order results are in a better agreement with recent estimates of the cross section with a resummation of the dominant corrections which are due the contribution near the threshold  $\hat{\tau} \rightarrow 1$  to which we turn now.

**3.4.3.3. The soft-gluon resummation up to NNLL.** As mentioned when we discussed the necessary ingredients to perform the  $gg \rightarrow H$  calculation at NNLO, the corrections to the cross section, Eq. (3.60), fall into three categories: virtual and soft corrections which generate the  $\delta(1 - \hat{\tau})$  terms and the  $\mathcal{D}_k$  distributions, collinear logarithmic contributions that are controlled by the regular part of the Altarelli–Parisi splitting kernels and the hard scattering terms. The soft-gluon corrections contribute to the most singular terms above and they involve only the  $gg$  initial state which, as already seen at NLO, is the channel where the most important part of the correction originates from.

The soft-gluon contributions in the  $gg \rightarrow H$  process can be resummed up to the next-to-next-to-leading-logarithm (NNLL) order in the heavy top quark limit [284], that is, all large logarithmic terms  $\alpha_s^n \log^m(1 - \hat{\tau})$  in the  $+$  distributions with  $1 \leq m \leq 2n$  in the limit  $\hat{\tau} \rightarrow 1$  can be exponentiated. The resummation relies on the basic factorization theorem for partonic cross sections into soft, collinear and hard parts near the phase-space boundary [350], and can be performed in the Mellin or N-moment space [351] for instance. The formalism and the calculation technique have been presented in detail in Refs. [284,342].

The resummation of the logarithms in the soft-gluon contributions is formally justified only near the thresholds  $\hat{\tau} \rightarrow 1$ . However, it can be used away from the threshold and the expectation is that the soft + virtual corrections, eventually supplemented by the collinear parton radiation (SVC), is a good approximation of the exact result for the cross section. Indeed, owing to the suppression of the gluon densities at large  $x$ , the partonic c.m. energy  $\sqrt{\hat{s}}$  is much smaller than the c.m. energy of the hadron collider,  $s = x_1 x_2 \hat{s}$ , and the dominant value of  $\hat{\tau}$  which appears in the hard scattering terms of the partonic cross section can be close to unity also when  $\sqrt{\hat{s}}$  is not close to  $M_H$  [347,348]. This has been verified both at NLO and NNLO: SVC approximates the exact result quite well, in particular at LHC energies.

The results for the resummed cross sections, in terms of the  $K$ -factors, are shown in Fig. 3.25 for the LHC as functions of  $M_H$ , for the LL, NLL and NNLL approximations (right) and are compared with the fixed-order results

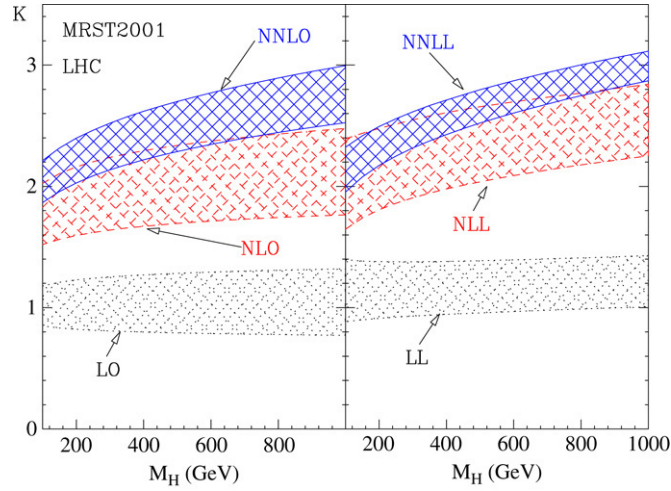


Fig. 3.25. Fixed order (left) and resummed (right)  $K$ -factors for  $gg \rightarrow H + X$  at the LHC as functions of  $M_H$ . The MRST2001 parton distributions have been used; from Ref. [284].

at LO, NLO and NNLO (left). The bands result from a scale variation  $\frac{1}{2}M_H \leq \mu_{F,R} \leq 2M_H$ . One can note that the scale dependence after resummation is smaller than that at fixed order and that, at NNLO, the resummation increases the central value of the cross section by  $\sim 5\%$  in the low Higgs mass range.

### 3.4.4. The distributions and Higgs + $n$ jet production

**3.4.4.1. The transverse momentum and rapidity distributions.** At leading order, the Higgs boson produced in the fusion process  $gg \rightarrow H$  has no transverse momentum. The  $p_T$  of the Higgs boson is generated at higher orders, when additional partons are radiated and balance the Higgs  $p_T$  [239,240,273–276]. The leading order for the Higgs boson transverse momentum and rapidity is therefore part of the NLO for the production cross section, when the processes responsible for them,  $gg \rightarrow Hg$ ,  $gq \rightarrow Hq$  and  $q\bar{q} \rightarrow Hg$ , take place. The  $p_T$  and  $y_H$  distributions have been calculated in the full massive case at LO [239,240] and it was shown that the heavy top quark limit is a reasonably good approximation, provided of course that  $M_H \lesssim 2m_t$ , but more importantly in this case, that  $p_T \lesssim m_t$ , which is typically the case as will be seen shortly. We therefore restrict ourselves to the heavy quark limit and summarize the salient features of these distributions.

Defining the momenta of the initial particles involved in the process  $ij \rightarrow Hk$ , with  $i, j, k = g, q, \bar{q}$ , as  $p_{i,j} = x_{i,j} p_{1,2}$  with  $p_{1,2}$  the incoming hadron momenta, and as  $p_k$  the momentum of the final parton, the differential partonic cross section in terms of the Higgs transverse momentum  $p_T$  and rapidity  $y_H$  can be written in the heavy quark limit as

$$\frac{d^2\hat{\sigma}(ij \rightarrow kH)}{dp_T^2 dy_H} = \frac{G_\mu \alpha_s^3}{576\sqrt{2}\pi^2} \mathcal{H}_{ij \rightarrow kH}(p_T, y_H)$$

$$\mathcal{H}_{gg \rightarrow Hg} = 3 \frac{\hat{s}^4 + \hat{t}^4 + \hat{u}^4 + M_H^8}{\hat{s}^2 \hat{t} \hat{u}}, \quad \mathcal{H}_{gq \rightarrow Hq} = -\frac{4}{3} \frac{\hat{s}^2 + \hat{u}^2}{\hat{s} \hat{t}}, \quad \mathcal{H}_{q\bar{q} \rightarrow Hg} = \frac{32}{9} \frac{\hat{t}^2 + \hat{u}^2}{\hat{s}^2} \quad (3.72)$$

with the Mandelstam variables  $\hat{s}, \hat{t}, \hat{u}$  given in terms of  $y_H$  and the transverse mass squared  $m_T^2 = M_H^2 + p_T^2$  as  $\hat{s} = (p_i + p_j)^2 = (p_k + p_H)^2 = sx_i x_j$  and  $\hat{t}/\hat{u} = (p_{i/j} - p_k)^2 = (p_{j/i} - p_H)^2 = M_H^2 - \sqrt{s} x_j m_T e^{\pm y_H}$ , with  $s$  being the total hadronic c.m. energy. The expressions are singular for  $\hat{t}, \hat{u} \rightarrow 0$  and, in particular,  $\mathcal{H}_{gg \rightarrow Hg}$  is singular in both  $\hat{t}$  and  $\hat{u}$ . The singularities can be regularized by moving to  $n = 4 - 2\epsilon$  space–time dimensions.

To include the NLO corrections to the differential distribution, and similarly to part of the NNLO corrections for the total cross section, one has to calculate: (i) the virtual corrections to Higgs production with a parton, which has to be multiplied by the Born term of the same process, and (ii) the real corrections due to the production of the Higgs boson with two partons, the sum of which has to be squared. In addition, one has to add the corrections to the Altarelli–Parisi splitting functions from the parton densities at NLO.

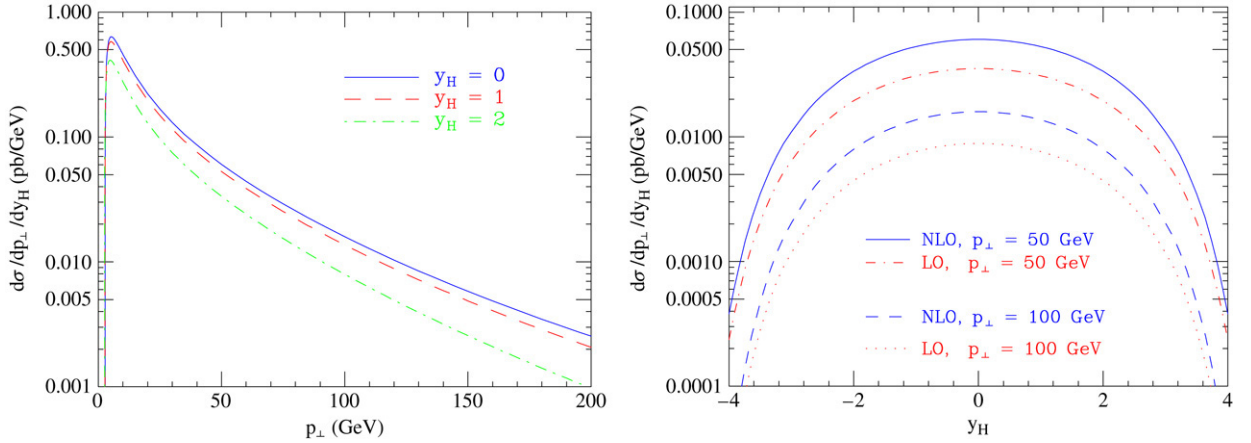


Fig. 3.26. The Higgs transverse momentum dependence at NLO for three values of the rapidity  $y_H = 0, 1, 2$  (left) and the rapidity dependence for two different transverse momenta  $p_T = 50$  and  $100$  GeV at both LO and NLO (right). The CTEQ5 set of PDFs has been used while  $M_H = 120$  GeV and the scales are set to  $\mu_R = \mu_F = m_T$ ; from Ref. [275].

These corrections have been calculated by several groups [274–279], using different methods and different schemes. In all cases, the heavy top quark limit has been used. We summarize below the main results at NLO, concentrating on the case of the LHC where the transverse momentum and rapidity distributions of the Higgs boson are very important ingredients. Unless otherwise stated, the Higgs mass is set to  $M_H = 120$  GeV and the heavy top limit is assumed; the renormalization and factorization scales are set equal and fixed to the transverse Higgs mass,  $\mu_R = \mu_F = m_T = \sqrt{M_H^2 + p_T^2}$ .

The left-hand side of Fig. 3.26 shows the  $p_T$  distribution of the Higgs boson at NLO for several fixed rapidity values. One first notices that the differential distribution decreases with increasing rapidity and with increasing  $p_T$  and that at small values of the latter,  $p_T \rightarrow 0$ , it diverges to  $-\infty$  [while at LO it diverges to  $+\infty$ ]. In the low  $p_T$  regime,  $p_T \lesssim 30$  GeV, the spectrum is unstable due to the occurrence of large logarithms; the perturbative treatment is therefore not reliable and resummation techniques, to be discussed later, are required. Note that at small and moderate  $p_T$ , the cross section is dominated by the gluonic  $gg \rightarrow H + X$  contribution, while for  $p_T$  values beyond 200 GeV the contribution of the  $gq \rightarrow HX$  process becomes comparable; the (anti)quark initiated processes give very small contributions.

The NLO corrections increase the  $p_T$  distribution except for small  $p_T$ . While the increase is very strong for  $p_T$  values below 30 GeV [recall that the distribution at LO was diverging in the opposite direction], it becomes moderate for  $p_T$  values in the range of the applicability of the perturbation theory. The  $K$ -factor, defined as  $K = d\sigma_{\text{NLO}}/d\sigma_{\text{LO}}$ , rises slowly from  $K \sim 1.6$  at  $p_T = 30$  GeV to  $K \sim 1.8$  for  $p_T = 200$  GeV when the total rate becomes too small.

The right-hand side of Fig. 3.26 shows the rapidity dependence of the cross section for fixed values of the transverse momentum,  $p_T = 50$  and  $100$  GeV, at both LO and NLO. As usual, the differential cross section is smaller for higher  $p_T$  values. It is maximal at  $y_H = 0$  and falls off steeply for large rapidity values due to the restriction of the available phase, reaching zero for  $|y_H| \gtrsim 4$ . The NLO corrections increase the distribution: the  $K$ -factor for reasonable  $p_T$  values is at the level  $\sim 1.6$  and is almost independent of the value of the rapidity, except at the boundary of the phase space where it drops slightly.

Thus, the NLO corrections acquire a size of about 60%–80% over the entire perturbative range of  $p_T$  and  $y_H$  values. The variations with the renormalization and factorization scales have also been discussed and found to follow the same trend as that in the production cross section at NLO: a variation from the central value  $\mu_F = \mu_R = m_T$  by a factor of two generates an uncertainty of about 20%. There is also an uncertainty originating from the choice of the PDFs, which is similar to what has been observed for the total cross section and which is thus smaller than the scale uncertainty.

Let us make a final comment on the low  $p_T$  case. As already mentioned, the distribution diverges to  $+\infty$  at LO and to  $-\infty$  at NLO for  $p_T \rightarrow 0$ . This is because in the region  $p_T \ll M_H$ , where the cross section is in fact the largest, the expansion parameter is not  $\alpha_s/\pi$  but rather,  $(\alpha_s/\pi) \log^2(M_H^2/p_T^2)$  which is close to unity and invalidates

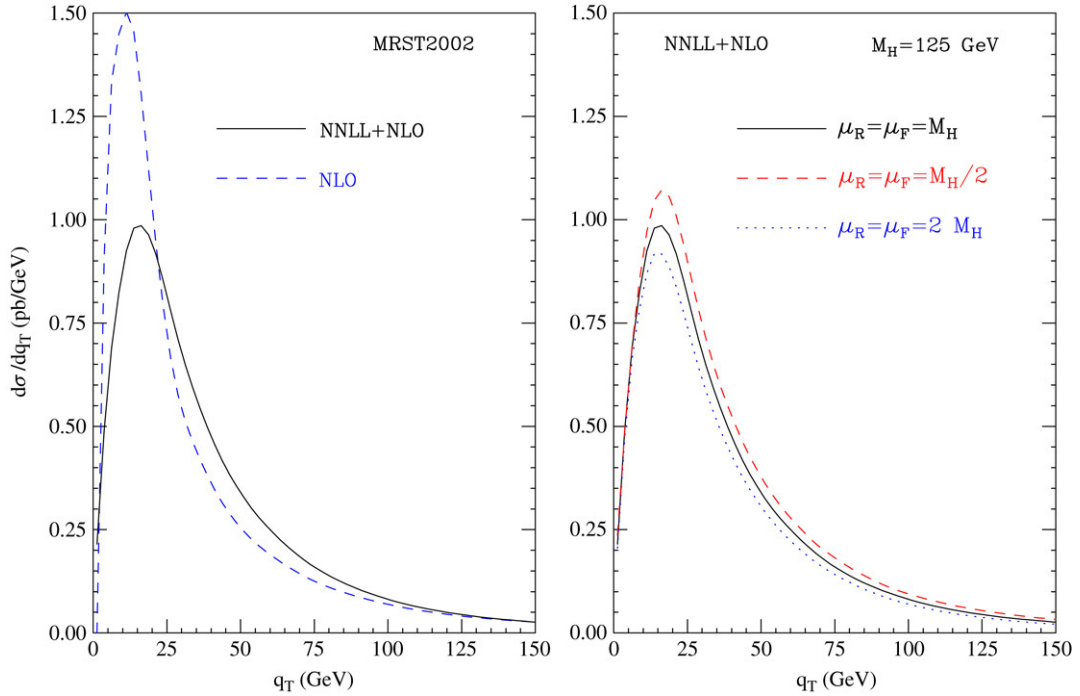


Fig. 3.27. The  $p_T$  distribution in  $gg \rightarrow H$  at the LHC for  $M_H = 125$  GeV: at NLO and NLO + NNLL for scales  $\mu_R = \mu_F = M_H$  (left) and at NLO + NNLL when the scales are collectively varied by a factor of two; from Ref. [276].

the perturbation theory. However, the large logarithms, as singular as  $(1/p_T^2)\alpha_s^n \log^m(M_H^2/p_T^2)$ , with  $1 < m < 2n - 1$ , can be systematically resummed to all orders [352] as in the case of the total cross section, resulting in a well-behaved spectrum for  $p_T \rightarrow 0$ ; see for instance Refs. [275,276] for details.

In the case of the  $gg \rightarrow H$  process, the resummation has been performed at the NNLL level of accuracy. This resummation for the low  $p_T$  region, and the fixed-order calculation at NLO for the high  $p_T$  region, have been consistently matched at intermediate  $p_T$  values to provide a smooth transition. The result for the  $p_T$  distribution is shown in Fig. 3.27 at the LHC for a Higgs mass of  $M_H = 125$  GeV. In the left figure, the NLO and NLO + NNLL approximations are displayed and, as can be seen, the divergent behavior of this distribution is removed by the resummation, the effects of which are relevant up to values  $p_T \sim 100$  GeV. The scale variation is shown in the right figure in the NLO + NNLL case: the spread is at the level of 10% near the peak and increases to 20% for lower  $p_T$  values,  $p_T \sim 100$  GeV.

**3.4.4.2. Higgs boson plus  $n$  jet production.** It has been suggested that Higgs production with one high  $p_T$  jet might have a much smaller background at the LHC, in particular in the decay channel  $H \rightarrow \gamma\gamma$  [353], than the  $gg \rightarrow H$  channel alone. At LO, the process is just the  $gg \rightarrow Hg$ ,  $qg \rightarrow Hq$  and  $q\bar{q} \rightarrow Hg$  processes that we have discussed previously and for which we have displayed the partonic differential cross sections in the heavy top limit, Eq. (3.72). In this limit, the NLO corrections to  $pp \rightarrow H + j$  are those which appear in the  $\mathcal{O}(\alpha_s^2)$  real corrections to the NNLO  $gg \rightarrow H$  cross section.

The Higgs plus two-jet production process is generated by  $q\bar{q}$  scattering mediated by triangles involving top quarks,  $gq$  scattering mediated by boxes and triangles and  $gg$  fusion mediated by triangles up to pentagon diagrams, and is known exactly at LO [242]. This mechanism has been discussed in connection with the vector boson fusion process, since it leads to the same final states, the gluons and the light quarks being indistinguishable, and may act as a background in the study of the former process. Characteristics which discriminate between the processes have been worked out and summarized in Fig. 3.28. The main points have been already discussed in Section 3.3.3: with basic (inclusive) cuts  $p_{Tj} \gtrsim 20$  GeV,  $|\eta_j| < 5$  and  $R_{jj} > 0.6$ , gluon fusion dominates, while the specific additional cuts  $m_{jj} > 0.6$  TeV,  $|\eta_{j1} - \eta_{j2}| > 4.2$  and  $\eta_{j1} \cdot \eta_{j2} < 0$ , select the vector boson fusion (WBF) process [354].

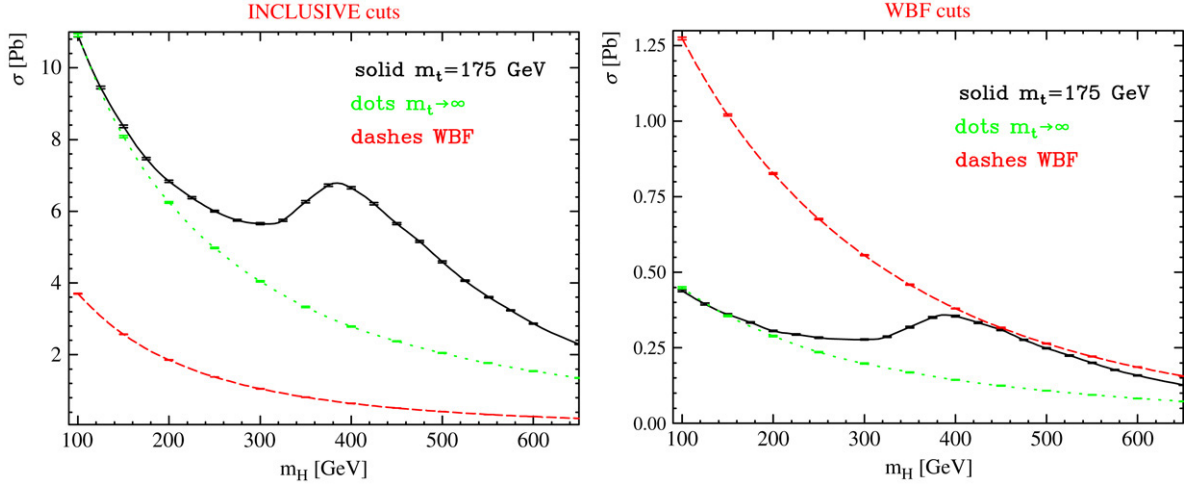


Fig. 3.28. Higgs production with 2 jets at the LHC as a function of  $M_H$ , in gluon fusion with  $m_t = 175$  GeV (solid line) and  $m_t \rightarrow \infty$  (dotted line) and in vector boson fusion (dashed). The left (right) part shows the cross section with the inclusive (WBF) cuts [354].

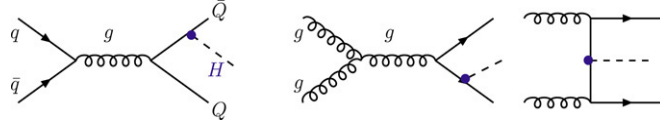


Fig. 3.29. Generic Feynman diagrams for associated Higgs production with heavy quarks in hadronic collisions,  $pp \rightarrow q\bar{q}, gg \rightarrow Q\bar{Q}H$ , at LO.

Recently, associated Higgs production with 3 jets has been calculated in the  $m_t \rightarrow \infty$  limit [243]. This is part of the NLO corrections to the Higgs + two-jet process, which exhibits a strong dependence on the renormalization scale  $\mu_R$  since it is a LO process but of  $\mathcal{O}(\alpha_s^4)$ . The very complicated virtual corrections need to be derived which, when combined with the Higgs + 3 jet real corrections, will hopefully stabilize the scale dependence of the  $H + 2j$  rate.

### 3.5. Associated Higgs production with heavy quarks

#### 3.5.1. The cross sections at the tree level

The process where the Higgs boson is produced in association with heavy quark pairs,  $pp \rightarrow Q\bar{Q}H$  [228,229], with the final state quarks being either the top quark or the bottom quark [in this case, see also Refs. [230,231] for instance], is the most involved of all SM Higgs production mechanisms. At tree level, it originates from  $q\bar{q}$  annihilation into heavy quarks with the Higgs boson emitted from the quarks lines; this is the main source at the Tevatron. At higher energies, when the gluon luminosity becomes important, the process proceeds mainly through gluon fusion, with the Higgs boson emitted from both the external and internal quark lines. A generic set of Feynman diagrams are shown in Fig. 3.29; those which are not shown differ only in the way the Higgs line is attached to the final state quark line and the gluon symmetrization in the last diagram.

Added to the complication that one has to calculate the amplitude of 10 Feynman diagrams and square them, one has to deal with the rather involved phase space with three massive particles in the final state. This is the reason why the complete analytical expression of the cross section is not available in the literature. If only  $q\bar{q}$  annihilation is considered, which is a good approximation in the case of the Tevatron, the matrix element squared in terms of the momenta  $q(\bar{q})$ ,  $p(\bar{p})$  and  $k$  of respectively, the initial light and final heavy quarks (antiquarks) and the Higgs particle, with  $Q^2 = (q + \bar{q})^2 = (p + \bar{p} + k)^2 = \hat{s}$ , is given by [229]

$$|\mathcal{M}_{q\bar{q}}|^2 = \frac{32}{(2k \cdot \bar{p} + M_H^2)(2k \cdot p + M_H^2)} \left\{ Q^2(Q \cdot k)^2 \left[ 1 + \frac{Q^2(4m_Q^2 - M_H^2)}{(2k \cdot \bar{p} + M_H^2)(2k \cdot p + M_H^2)} \right] \right\}$$



$$\begin{aligned}
& + \left( \frac{1}{2} Q^2 m_Q^2 - 2(p \cdot q)(p \cdot \bar{q}) \right) \left[ Q^2 - 4m_Q^2 + M_H^2 + \frac{2k \cdot Q(4m_Q^2 - M_H^2)}{2k \cdot \bar{p} + M_H^2} \right] \\
& + \left( \frac{1}{2} Q^2 m_Q^2 - 2(\bar{p} \cdot q)(\bar{p} \cdot \bar{q}) \right) \left[ Q^2 - 4m_Q^2 + M_H^2 + \frac{2k \cdot Q(4m_Q^2 - M_H^2)}{2k \cdot p + M_H^2} \right] \\
& - (Q^2 + M_H^2 - 4m_Q^2) \left[ 2(p \cdot q)(\bar{p} \cdot \bar{q}) + 2(p \cdot \bar{q})(\bar{p} \cdot q) - Q^2(p \cdot \bar{p}) \right] \Big\} \quad (3.73)
\end{aligned}$$

where the coupling factors,  $g_s^4(\sqrt{2}m_Q^2 G_\mu)$ , with  $g_s^2 = 4\pi\alpha_s$ , have been removed.

For the gluon fusion diagrams, denoting by  $\epsilon_1$  and  $\epsilon_2$  the polarization four vectors of the gluons and by  $g_1$  and  $g_2$  their four momenta, the various amplitudes are given by [the generators  $T^a$  and the SU(3) structure constants  $f^{abc}$  are discussed in Section 1.1.1] [229]

$$\begin{aligned}
\mathcal{M}_{gg}^a &= -T_{ik}^a T_{kj}^b \bar{u}^j(p) \frac{k + \not{p} + m_Q}{2p \cdot k + M_H^2} \not{\epsilon}_2 \frac{-\not{p} + \not{g}_1 + m_Q}{-2g_1 \cdot \bar{p}} \not{\epsilon}_1 v^i(\bar{p}) + \left[ \begin{array}{c} g_1 \leftrightarrow g_2, \epsilon_1 \leftrightarrow \epsilon_2 \\ g_1 \leftrightarrow g_2, \epsilon_1 \leftrightarrow \epsilon_2, p \leftrightarrow \bar{p} \\ p \leftrightarrow \bar{p} \end{array} \right] \\
\mathcal{M}_{gg}^b &= -T_{ik}^a T_{kj}^b \bar{u}^j(p) \not{\epsilon}_2 \frac{\not{p} - \not{g}_2 + m_Q}{-p \cdot g_2} \frac{-\not{p} + \not{g}_1 + m_Q}{-g_1 \cdot \bar{p}} \not{\epsilon}_1 v^i(\bar{p}) + [g_1 \leftrightarrow g_2, \epsilon_1 \leftrightarrow \epsilon_2] \\
\mathcal{M}_{gg}^c &= i f^{abc} T_{ij}^c \bar{u}^j(p) \frac{\not{\epsilon}_1 \not{\epsilon}_2 Q^\lambda}{\hat{s}} \left[ 2g_1^\nu g_2^{\lambda\mu} + (g_2 - g_1)^\lambda g^{\mu\nu} - 2g_2^\mu g^{\nu\lambda} \right] \frac{\not{p} + \not{k} - m_Q}{2k \cdot \bar{p} + M_H^2} v^i(\bar{p}) + [p \leftrightarrow \bar{p}] \quad (3.74)
\end{aligned}$$

where, again, the product of couplings  $g_s^2(\sqrt{2}m_Q^2 G_\mu)^{1/2}$  has been factorized out. The gluon polarization vectors obey the transversality condition  $\epsilon_i \cdot g_i = 0$  and SU(3) gauge invariance can be checked by making the substitutions  $\epsilon_i \rightarrow g_i$ ; one can also use the gauge condition  $\epsilon_1 \cdot g_2 = \epsilon_2 \cdot g_1$  to simplify the calculation. In the amplitude squared, summed over the final quark's color and spin and averaged over the gluon color and polarizations,

$$|\mathcal{M}_{gg}|^2 = \frac{1}{256} \sum_{\text{spin, color}} |\mathcal{M}_{gg}^a + \mathcal{M}_{gg}^b + \mathcal{M}_{gg}^c|^2 \quad (3.75)$$

one has to perform the trace over the  $\gamma$  matrices and the sum over the indices of the QCD Gell-Mann matrices and the  $f^{abc}$  structure functions

$$(T_{ik}^a T_{kj}^b)^2 = 24, \quad (f^{abc} T_{ij}^c)^2 = 12, \quad (T_{ik}^a T_{kj}^b)(f^{abc} T_{ij}^c)^2 = 0. \quad (3.76)$$

The average over the gluon polarizations, since the gluons are massless, should be performed in an axial gauge and, for instance, one can use<sup>24</sup>

$$\sum_{\lambda_i=1}^2 \epsilon_i^\mu(g_i, \lambda_i) \epsilon_i^\nu(g_i, \lambda_i) = -g^{\mu\nu} + \frac{2}{\hat{s}} (g_1^\mu g_2^\nu + g_1^\nu g_2^\mu). \quad (3.77)$$

The obtained expression for the amplitude squared is too long to be reproduced. One then has to integrate over the phase space to obtain the cross section at the partonic level for each subprocess  $ij \rightarrow Q\bar{Q}H$  [with  $ij = q\bar{q}, gg$ ]

$$\hat{\sigma}_{\text{LO}}^{ij} = \frac{1}{2\hat{s}} \frac{\alpha_s^2 G_\mu m_Q^2}{\sqrt{2}\pi^3} \int \frac{d^3 p}{2p_0} \frac{d^3 \bar{p}}{2\bar{p}_0} \frac{d^3 k}{2k_0} \delta^4(Q - p - \bar{p} - k) \left[ \sum |\mathcal{M}_{ij}|^2 \right]. \quad (3.78)$$

These partonic cross sections should then be folded with the quark and gluon luminosities to obtain the full cross section at the hadronic level

$$\sigma_{\text{LO}} = \int \sum_{i,j} \frac{1}{1 + \delta_{ij}} \left( \mathcal{F}_i^p(x_1, \mu_F) \mathcal{F}_j^p(x_2, \mu_F) \hat{\sigma}_{\text{LO}}^{ij}(x_1, x_2, \mu_F) + [1 \leftrightarrow 2] \right) dx_1 dx_2 \quad (3.79)$$

<sup>24</sup> Alternatively, one can use the simpler Feynman gauge for the summation over polarization,  $\sum \epsilon_i^\mu \epsilon_i^\nu = -g^{\mu\nu}$ , but two additional diagrams with ghosts replacing the gluons in the initial state have to be added.

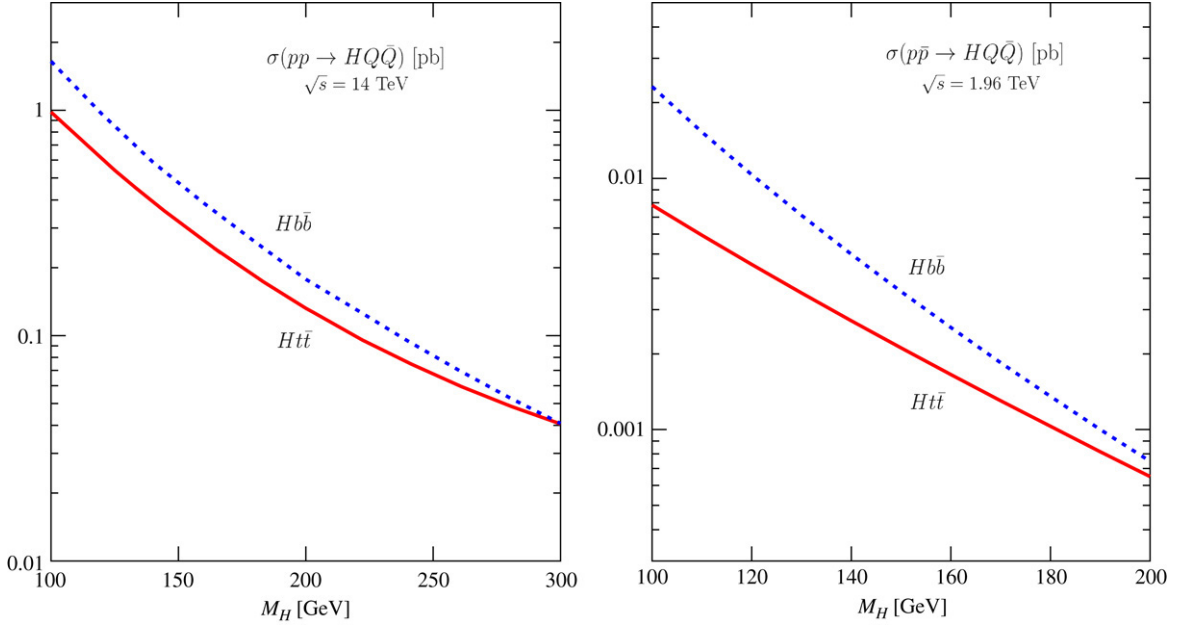


Fig. 3.30. The  $t\bar{t}H$  and  $b\bar{b}H$  production cross sections at the LHC (left) and the Tevatron (right). The pole quark masses in the Yukawa couplings are set to  $m_t = 178$  GeV and  $m_b = 4.88$  GeV and the MRST PDFs are used. The renormalization and factorization scales have been set to  $\mu_{R,F} = m_t + \frac{1}{2}M_H$  for  $pp \rightarrow t\bar{t}H$  and  $\mu_{R,F} = \frac{1}{2}m_b + \frac{1}{4}M_H$  for  $pp \rightarrow b\bar{b}H$ .

where  $\mathcal{F}_i^p$  are the distributions of the parton  $i$  in the proton defined at the factorization scale  $\mu_F$ . The factor  $1/(1+\delta_{ij})$  accounts for the identical gluons in the initial state.

The cross section for associated  $t\bar{t}H$  and  $b\bar{b}H$  production are shown for the Tevatron and LHC energies in Fig. 3.30. The MRST set of parton densities has been used and the renormalization and factorization scales have been identified with  $\mu_R = \mu_F = m_Q + \frac{1}{2}M_H$  and  $\frac{1}{4}M_H$  for the  $t\bar{t}H$  and  $b\bar{b}H$  cases, respectively. The pole masses of the top and bottom quarks have been fixed to  $m_t = 178$  GeV and  $m_b = 4.88$  GeV. As can be seen, the  $p\bar{p} \rightarrow t\bar{t}H$  cross section at the Tevatron is of the order of 5 fb for small Higgs masses,  $M_H \sim 120$  GeV, dropping to a level below 1 fb for  $M_H \sim 180$  GeV, when the phase space becomes too narrow. At the LHC, the cross section is two orders of magnitude larger as a consequence of the higher energy, higher-gluon luminosity and larger phase space. It varies however strongly with  $M_H$ , dropping by more than one order of magnitude when  $M_H$  varies from 120 to 250 GeV. The detection aspects at LHC [355–361] and Tevatron [362] will be discussed in Section 3.7.

Surprisingly, the  $pp \rightarrow b\bar{b}H$  cross sections are slightly larger than the corresponding cross sections for  $pp \rightarrow t\bar{t}H$  at both the Tevatron and the LHC, for small enough Higgs masses. This is a mere consequence of the larger available phase space at the Tevatron and the participation of the low- $x$  gluons in the case of the LHC. The cross sections become comparable at moderate Higgs masses and, eventually, the  $pp \rightarrow t\bar{t}H$  process dominates at higher Higgs masses, but the production rates then become too small.

### 3.5.2. The $t\bar{t}H$ cross section at NLO

**3.5.2.1. The calculation at NLO.** As we have seen just before, it was already rather difficult to calculate the  $pp \rightarrow Q\bar{Q}H$  cross section at LO. At NLO, the task becomes formidable. The computation of these NLO corrections, which was another *tour de force*, has been completed only very recently, by two independent groups [268, 269]. The Feynman diagrams which contribute to the NLO QCD corrections can be divided into four gauge invariant subsets, some representative examples of which are presented in Fig. 3.31: (a) virtual gluonic corrections to the  $q\bar{q}g$  and  $ggg$  vertices as well as to the initial and final quark and gluon self-energies, (b) vertex and box virtual corrections where the Higgs boson is emitted from the internal lines and where a final state gluon is emitted and splits into  $Q\bar{Q}$  pairs, (c) pentagonal  $q\bar{q}$  and  $gg$  initiated diagrams where the Higgs boson is emitted from the heavy quark internal lines, and finally (d) real corrections where an additional gluon is emitted in the final state in all possible ways, and which involve additional  $qg$  and  $\bar{q}g$  scattering diagrams which do not occur at the tree level.



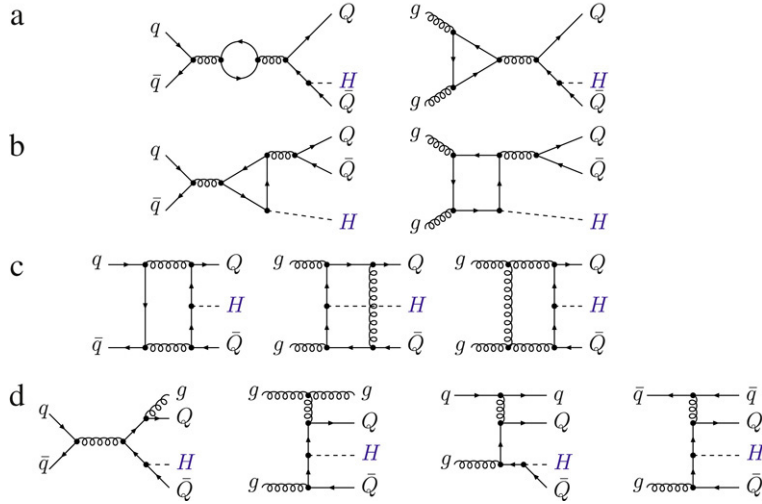


Fig. 3.31. Representative Feynman diagrams for the NLO QCD corrections to  $pp \rightarrow Q\bar{Q}H$ .

Technically speaking, there are two main difficulties which arise when attempting to perform such a calculation. The first one is that the pentagonal one-loop five-point functions [363] are rather difficult to evaluate in  $n$  dimensions since, not to mention the complicated tensorial structure which has to be reduced to known scalar integrals, they involve massive particles and have ultraviolet, soft and collinear singularities which have to be calculated in the dimensional regularization scheme. The second major difficulty is the extraction of the soft and collinear singularities in the real part of the corrections, which involve 4 particles in the final state, with three of them being massive. This leads to severe numerical instabilities which have to be handled with great care [364]. Added to this, a large number of Feynman diagrams and the associated counterterms have to be evaluated.

Several methods have been devised to overcome these problems and a detailed account can be found in the original papers of Refs. [268,269]. In both calculations, the renormalization has been performed in a mixed scheme, where the heavy quark mass is defined on-shell and the running of the  $\overline{\text{MS}}$  strong coupling constant includes only the light quarks and gluons with the heavy quarks decoupled. The factorization has been performed in the  $\overline{\text{MS}}$  scheme where the heavy quark is decoupled from the evolution of the parton densities. The two calculations have been compared against each other and, although the methods which have been used are different, a perfect agreement has been found. In the following, we simply summarize the numerical results which have been obtained in the case of  $pp \rightarrow t\bar{t}H$ .

**3.5.2.2. Numerical results for  $pp \rightarrow t\bar{t}H$ .** In Fig. 3.32, the LO and NLO cross sections for associated Higgs production with top quarks are presented in the case of the Tevatron with a c.m. energy  $\sqrt{s} = 2$  TeV. The CTEQ4M(L) parton distribution functions at NLO (LO) have been used and the top quark mass and the strong coupling constants have been fixed to  $m_t = 174$  GeV and  $\alpha_s^{\text{NLO}}(M_Z) = 0.116$ . The left-hand side of the figure displays the LO and NLO cross sections as functions of the Higgs mass with the renormalization and factorization scales chosen to be  $\mu_R = \mu_F = m_t$  and  $2m_t$ , while the right-hand side displays the variation of the cross sections with the renormalization and factorization scales for a Higgs boson with a mass  $M_H = 120$  GeV.

One can see that over the entire Higgs mass range accessible at the Tevatron, the NLO corrections decrease the production rate. For  $\mu_F = \mu_R = m_t$ , the  $K$ -factor defined as the ratio of the NLO and LO cross sections consistently evaluated at their respective orders, is  $K \sim 0.8$  and is nearly independent of the Higgs mass.<sup>25</sup> However, for a scale choice  $\mu_R = \mu_F = 2m_t$ , the NLO corrections are very small. This suggests a very strong dependence of the cross section on the scale choice and, indeed, as is illustrated in the right-hand side of Fig. 3.32 where the scales are varied from  $m_t$  to  $\sim 3m_t$ , while the NLO cross section is rather stable, the LO cross section changes by 60% in this range. Thus, the NLO corrections are mandatory to stabilize the prediction for the production cross section.

<sup>25</sup> This is one of the few examples of  $K$ -factors below unity. As discussed in Refs. [268,270], the reason lies in the fact that at  $\sqrt{s} = 2$  TeV, the  $t\bar{t}H$  final state is produced in the threshold region, where gluon exchange between the top quarks gives rise to Coulomb singularities  $\propto \alpha_s/\beta_t$ . Since the  $t\bar{t}H$  final state is in a color octet, these corrections are negative and decrease the Born cross section.

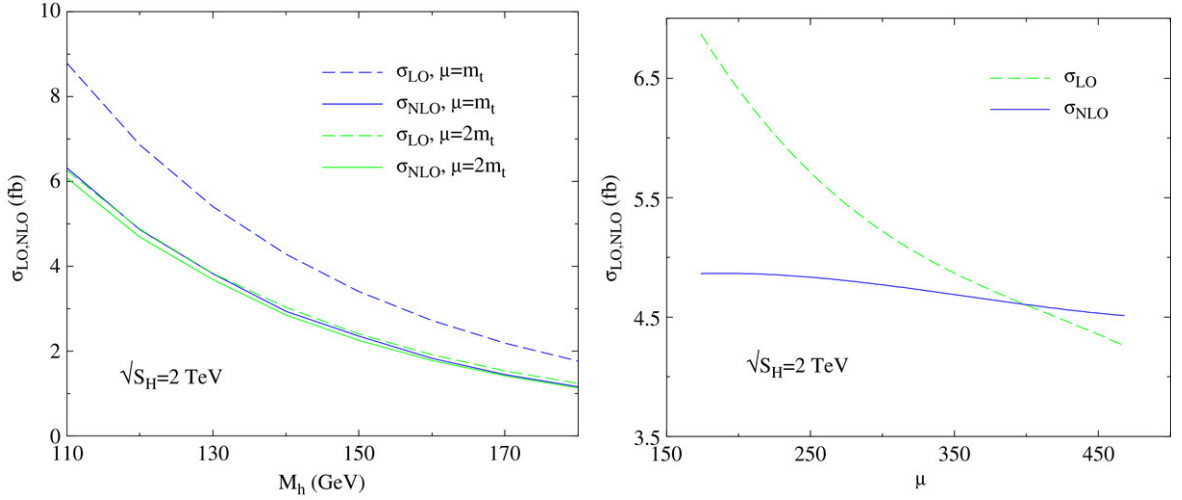


Fig. 3.32. The  $p\bar{p} \rightarrow t\bar{t}H + X$  production cross section at the Tevatron at both LO and NLO, as a function of the Higgs mass with two scale choices (left) and as a function of the scales  $\mu = \mu_R = \mu_F$  for  $M_H = 120$  GeV (right); from Ref. [270].

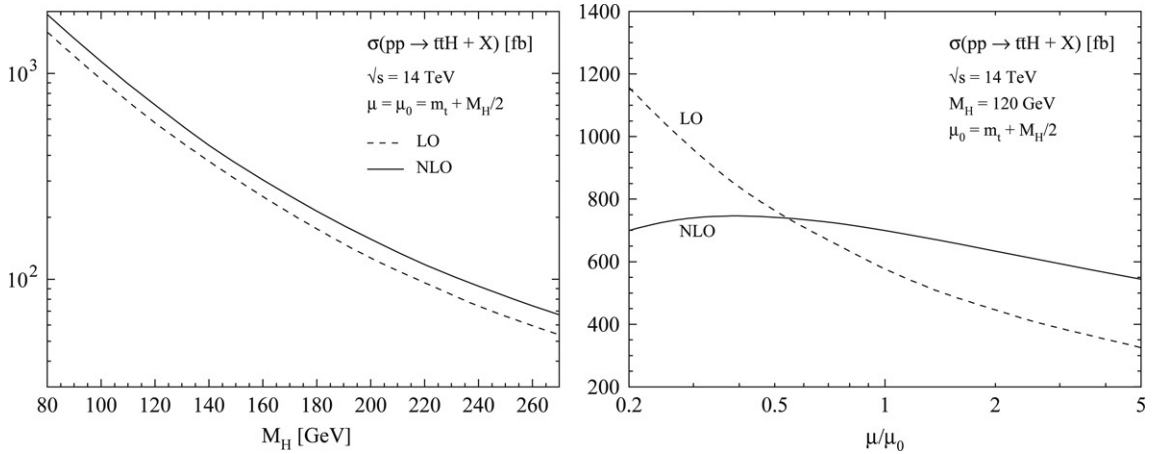


Fig. 3.33. Total cross section for  $pp \rightarrow t\bar{t}H + X$  at the LHC in LO and NLO as a function of  $M_H$  (left) and the variation with the scales for  $M_H = 120$  GeV (right); from Ref. [268].

In the subsequent figures, Figs. 3.33 and 3.34, we present the LO and NLO results for the associated Higgs production with top quarks at the LHC,  $pp \rightarrow t\bar{t}H + X$ , as derived in Ref. [268]. Besides the total hadronic cross sections, the differential distributions in transverse momentum and rapidity of the Higgs boson have been discussed in this case. Here, the MRST sets of parton densities at LO and NLO have been adopted and the renormalization and factorization scales are set to  $\mu_R = \mu_F = \mu_0 = \frac{1}{2}(2m_t + M_H)$  when they are not varied; the top quark mass is also set to the old central value  $m_t = 174$  GeV.

Because the cross section at the LHC is dominated by the  $gg$  fusion process, it receives positive NLO corrections for the central renormalization and factorization scale,  $\mu_0 = m_t + \frac{1}{2}M_H$ , as shown in the left-hand side of Fig. 3.33. For this scale value, a factor  $K \sim 1.2$  is obtained, increasing to  $K \sim 1.4$  when the choice  $\mu_F = \mu_R = 2\mu_0$  is made. As in the case of the Tevatron, these values are nearly independent of the Higgs boson mass in the displayed range. Again, and as is shown in the right-hand side of the figure, the NLO corrections significantly reduce the renormalization and factorization scale dependences and stabilize the theoretical prediction for the cross section at the LHC.

The scale dependences of the rapidity and transverse momentum distributions of the Higgs boson are also significantly reduced at NLO and the shapes of the distributions are practically constant when the scales are varied in a reasonable range. The ratios of the normalized NLO and LO distributions in transverse momentum and rapidity, are

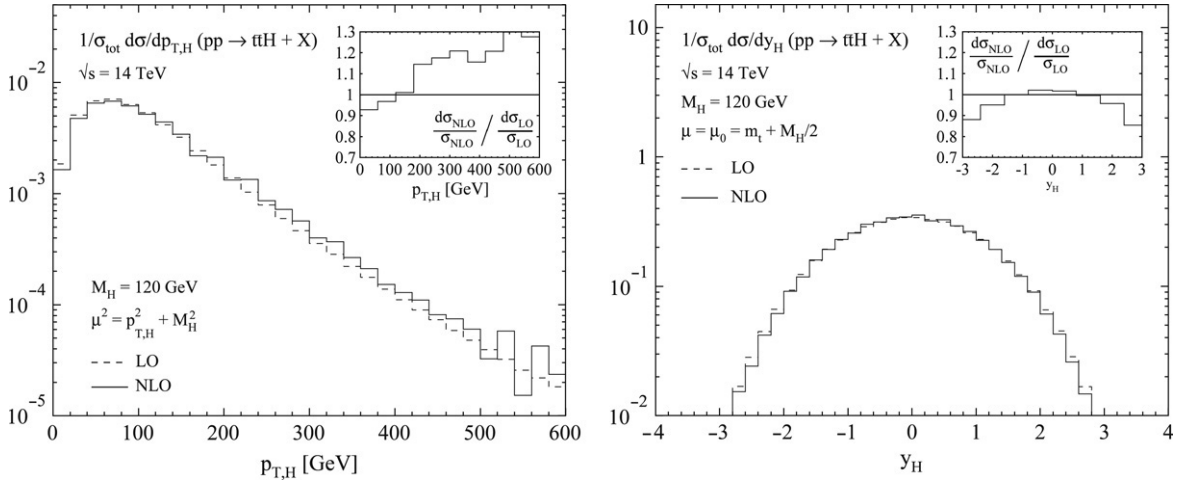


Fig. 3.34. Normalized transverse momentum (left) and rapidity (right) distributions of the Higgs boson in the process  $pp \rightarrow t\bar{t}H + X$  at the LHC in LO and NLO with  $M_H = 120$  GeV. The inserts to the figures show the ratio of the NLO to LO distributions; from Ref. [268].

shown in the inserts of, respectively, the left-hand and right-hand parts of Fig. 3.34 for  $M_H = 120$  GeV. In the former case, the default scale was set to the transverse mass,  $\mu^2 = p_{T,H}^2 + M_H^2$ , which is a more natural choice for large transverse momenta. In this case, the NLO corrections are small for low values of the Higgs transverse momentum,  $p_{T,H} \lesssim m_t$ , but increase with increasing  $p_{T,H}$  values, reaching  $\sim 30\%$  at the boundary of phase space where the cross section is small. In the case of the normalized rapidity distribution, the NLO corrections are also very small in the central region but they become negative and of the order of 10% at the edge of phase space. A conclusion that one can draw from these figures, is that one cannot simply use a constant  $K$ -factor to describe these distributions.

Note that the transverse momentum and rapidity distributions of the top and antitop quarks have been also studied; they are barely affected by the NLO corrections once the scales have been properly chosen; see Ref. [268].

**3.5.2.3. The PDF uncertainties.** Finally, let us discuss the PDF uncertainties in the prediction of the  $pp \rightarrow Ht\bar{t}$  cross section, restricting ourselves to the case of the LHC. The central values and the uncertainty band limits are shown for the CTEQ, MRST and Alekhin parametrizations in Fig. 3.35 as functions of  $M_H$ , using the procedure outlined in Section 3.1.5. We also show in the insert, the spread uncertainties in the predictions when the cross sections are normalized to the values obtained using the CTEQ6M set. Since the NLO corrections have been calculated only recently and the presumably very complicated and slow programs are not yet publicly available, we simply use the program HQQ of Ref. [259] for the LO cross section with scales  $\mu_F = \mu_R = 2m_t + M_H$  that we fold with the NLO PDFs. Although the overall normalization is different when including the NLO correction [one simply has to multiply by the  $K$ -factor which is approximately 1.4 in this case], this procedure should describe the relative effects of the different PDFs at NLO with a rather good approximation.

As discussed above, the process is dominantly generated by gluon–gluon fusion at the LHC and, compared with the process  $gg \rightarrow H$  discussed in Section 3.4 for a fixed Higgs mass, a larger  $Q^2$  is needed for this final state and the initial gluons should therefore have higher  $x$  values. In addition, the quarks that are involved in the subprocess  $q\bar{q} \rightarrow t\bar{t}H$ , which is also contributing, are still in the intermediate regime because of the higher value [ $x \sim 0.7$ ] at which the quark high- $x$  regime starts. This explains why the uncertainty band increases smoothly from 5% to 7% when the  $M_H$  value increases from 100 to 200 GeV.

### 3.5.3. The case of the $b\bar{b}H$ process

As seen in Section 3.5.1, the production cross sections for the associated Higgs production with bottom quarks are not that small, despite the tiny  $Hb\bar{b}$  Yukawa coupling. However, the dominant  $b\bar{b}b\bar{b}$  signal final state for a low mass Higgs boson decaying into  $b\bar{b}$  pairs is rather complicated to be isolated experimentally and suffers from a huge QCD-jet background. This channel is therefore not considered as a discovery channel for the SM Higgs boson at the Tevatron and the LHC. Nevertheless, in extensions of the SM, such as in minimal supersymmetric theories, the Higgs–Yukawa coupling to bottom quarks can be strongly enhanced, leading to large  $b\bar{b}H$  production rates which can

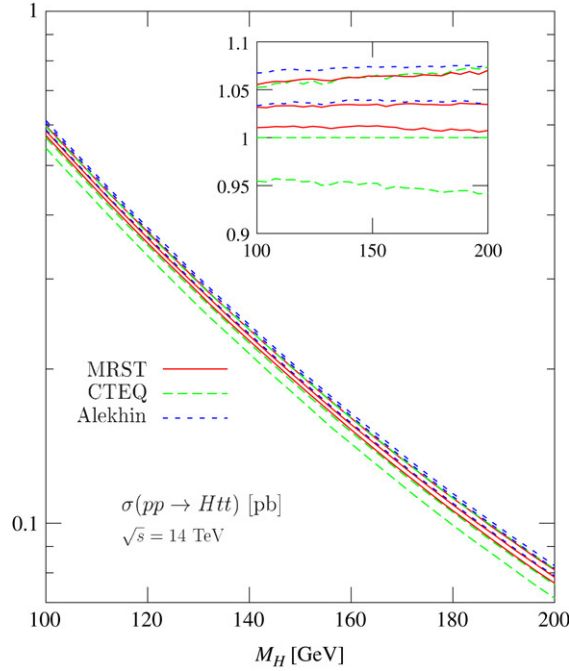


Fig. 3.35. The CTEQ, MRST and Alekhin PDF uncertainty bands for the NLO cross section  $pp \rightarrow t\bar{t}H$  at the LHC; the scales have been fixed to  $\mu_F = \mu_R = 2m_t + M_H$ . The insert shows the spread in the predictions compared to CTE6M; from Ref. [295].

exceed far the cross sections in the  $pp \rightarrow t\bar{t}H$  case, even for high mass Higgs bosons. This channel will be discussed in some detail in the second part of this review [25]. Here, we simply summarize the impact of the NLO corrections, restricting ourselves to the inclusive total rate generated via light quark annihilation and  $gg$  fusion,  $q\bar{q}, gg \rightarrow b\bar{b}H$ .

The calculation of the NLO correction to  $b\bar{b}H$  production follows the same lines as what has been discussed previously for  $pp \rightarrow t\bar{t}H$  and the results have been given in Refs. [271,272]. There is, however, a major difference between the two cases [365]: because of the small  $b$ -quark mass, the cross section  $\sigma(gg \rightarrow b\bar{b}H)$  develops large logarithms,<sup>26</sup>  $\log(Q^2/m_b^2)$ , with the scale  $Q$  being typically of the order of the factorization scale  $Q \sim M_H \gg m_b$ . This leads to large corrections, part of which can be absorbed by choosing a low value for the factorization and renormalization scales,  $\mu_R = \mu_F \sim \frac{1}{4}(M_H + 2m_b)$  [365,366].

The NLO cross sections are shown at Tevatron and LHC energies in Fig. 3.36 as functions of the Higgs mass for this scale choice and compared to the LO cross sections. In both cases, the running  $b$ -quark mass at the scale of the Higgs mass, with the starting pole mass being  $m_b = 4.9$  GeV, has been used for the Yukawa coupling. As can be seen, even with this scale choice, the NLO corrections are large, with  $K$ -factors ranging from 1.6 to 2.6 at the Tevatron and 1.1 to 1.8 at the LHC. The scale variation is still strong even at NLO and further work is needed to improve the theoretical prediction of the  $b\bar{b}H$  production rate.

#### 3.5.4. Associated Higgs production with a single top quark

Since the phase space for  $t\bar{t}H$  production is too penalizing, in particular at the Tevatron, it has been suggested to consider the process where the Higgs boson is produced in association with a single top or antitop quark [367,368]

$$pp/p\bar{p} \rightarrow tH + X. \quad (3.80)$$

The expectation is that the cross section can be comparable to that of the  $t\bar{t}H$  process, similarly to what occurs for top quark production in hadronic collisions where the rate for single top quark is not much smaller than that for top quark pair production, the ratio of the two being of the order of 1/3 [369]. There are three types of contributions to this production channel, as shown in Fig. 3.37 where a few generic Feynman diagrams are presented:

<sup>26</sup> The issue of resumming these large logarithms and stabilizing the scale dependence of the cross section using heavy quark distribution functions has been discussed in Ref. [366].

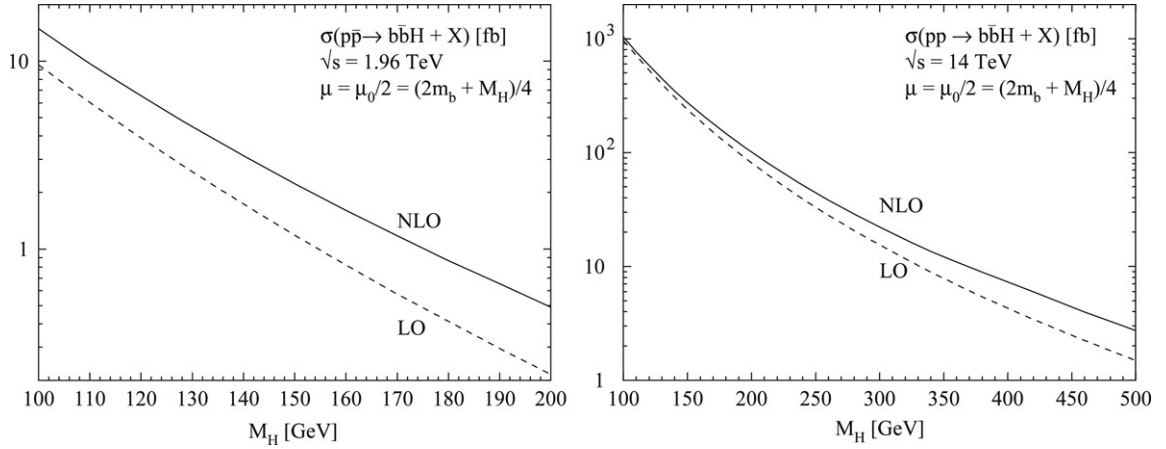


Fig. 3.36. Total inclusive cross sections for  $pp \rightarrow b\bar{b}H + X$  at the Tevatron (left) and the LHC (right) as functions of  $M_H$  with the factorization and renormalization scales set to  $\mu_R = \mu_F \sim \frac{1}{4}(M_H + 2m_b)$ . The running  $b$ -quark mass, with a starting pole value  $m_b = 4.88$  GeV, has been used in the Higgs coupling and the CTEQ6 PDFs are adopted; from [271].

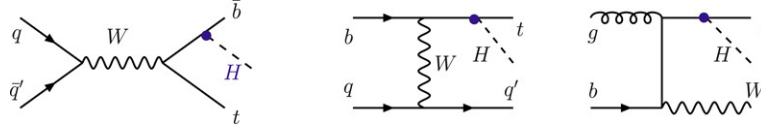


Fig. 3.37. Generic Feynman diagrams for associated Higgs production with a single top quark in hadronic collisions: (a)  $q\bar{q}' \rightarrow \bar{b}tH$ , (b)  $qb \rightarrow q'tH$  and (c)  $gb \rightarrow W^-tH$ .

- (a)  $q\bar{q}'$  annihilation with  $s$ -channel  $W$  boson exchange, which leads to the three-body final state involving a Higgs boson and a  $bt$  pair;
- (b)  $t$ -channel fusion of a light quark and a bottom parton from the proton sea which, through  $W$  exchange, leads to the  $qtH$  final state;
- (c) the scattering of gluons with again bottom partons from the proton sea and which leads to  $tWH$  final states.

In the language of gluon initiated production, the two last processes are in fact the higher-order mechanisms  $gg \rightarrow bH + X$  with four final state particles but with one  $b$ -quark integrated out. Note that in all three channels, the Higgs boson can be radiated not only from the top quark lines but also from the  $W$  boson [as well as from the  $b$ -quark] lines.

These processes have been revisited in Ref. [368] and the production cross sections are shown in Fig. 3.38 for the Tevatron (left) and LHC (right) as functions of the Higgs mass. The rates for the three channels are shown separately and compared with the  $pp \rightarrow t\bar{t}H$  cross section. The renormalization and factorization scales are set to the Higgs mass and the CTEQ5 set of PDFs has been used. Unfortunately, and contrary to the  $t\bar{t}H$  case, the rates for associated Higgs production with a single top quark are in general much smaller than those of  $t\bar{t}H$  production. At the Tevatron, all channels lead to cross sections that are two orders of magnitude smaller. At the LHC, this is also the case for the  $s$ -channel  $q\bar{q}' \rightarrow \bar{b}tH$  and  $WtH$  associated production. However, for low Higgs masses, the  $t$ -channel  $qb \rightarrow q'tH$  cross section is suppressed only by a factor of 10 compared to  $t\bar{t}H$  production and for larger masses,  $M_H \sim 300$  GeV, the two processes have comparable but rather low rates.

Focusing on the latter channel, where for  $M_H \lesssim 150$  GeV approximately  $10^4$  events can be collected at the LHC for  $\mathcal{L} = 100 \text{ fb}^{-1}$  before cuts and efficiency losses are applied, the signals and the various backgrounds have been studied in Ref. [367] for a Higgs boson decaying into two photons and in Ref. [368] where the more copious  $H \rightarrow b\bar{b}$  decays have been considered. The observation of a Higgs boson in the first channel is certainly not possible since the  $\gamma\gamma$  branching ratio is of  $\mathcal{O}(10^{-3})$ . In the configuration where the Higgs boson decays into  $b\bar{b}$  and the top quark into  $Wb \rightarrow \ell\nu b$ , the yield depends on the number of  $b$ -quarks that are to be tagged: for three  $b$ -tags, the background from  $t\bar{t}j$  is overwhelming, while for four  $b$ -tags, several backgrounds with rates that are comparable to the signal

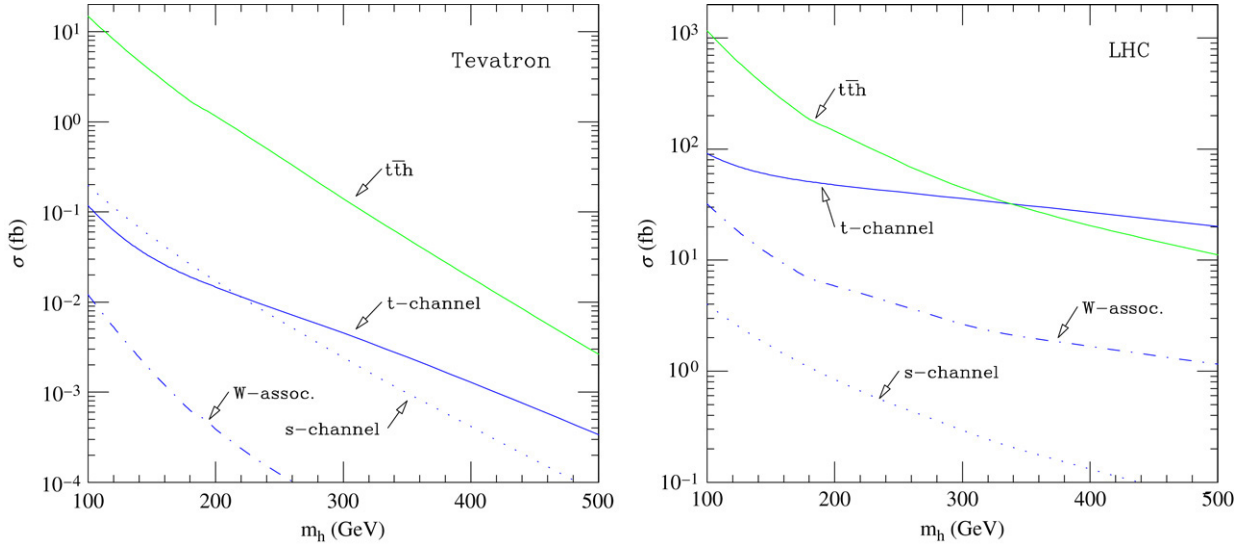


Fig. 3.38. The cross sections for Higgs plus single top production at the Tevatron (left) and at the LHC (right), in the  $t$ -channel,  $s$ -channel and  $W$ -associated processes; for comparison the cross section for  $t\bar{t}H$  is also shown. The CTEQ5L set of PDFs is used and the renormalization and factorization scales are set to  $M_H$ ; from Ref. [368].

are present. The conclusion of Ref. [368] is that a Higgs signal is unlikely to be observed in this channel, except in extensions of the SM where the production cross section can be enhanced.

### 3.6. The higher-order processes

#### 3.6.1. Higgs boson pair production

In hadronic collisions, Higgs particles can be pair produced in three main processes<sup>27</sup>:

- (a) the gluon–gluon fusion mechanism which is mediated by loops of third generation heavy quarks that couple strongly to the Higgs boson [232,233]

$$gg \rightarrow HH \quad (3.81)$$

- (b) double Higgs–strahlung from either a  $W$  or a  $Z$  boson [234,235]

$$q\bar{q} \rightarrow V^* \rightarrow VHH \quad (3.82)$$

- (c) the  $WW/ZZ$  fusion processes which lead to two Higgs particles and two jets [235–237]

$$qq \rightarrow V^*V^*qq \rightarrow HHqq. \quad (3.83)$$

The Feynman diagrams for these processes are shown in Fig. 3.39 and, as can be seen, one of them involves the trilinear Higgs boson coupling,  $\lambda_{HHH} = 3M_H^2/v$ , which can be thus probed in principle. The other diagrams involve the couplings of the Higgs boson to fermions and gauge bosons and are probed in the processes discussed in the previous sections.

We briefly discuss these processes in this subsection, restricting ourselves to the case of the LHC where the phase space is not too penalizing.

**3.6.1.1. The gluon–gluon fusion mechanism.** The large number of gluons in high-energy proton beams implies that the gluon–gluon fusion mechanism is the dominant process for Higgs boson pair production. As for single Higgs production in this mechanism, the coupling between gluons and Higgs bosons is mediated by heavy quark loops. In the SM, the top quark loop is dominating while the bottom quark loop gives a small but non-negligible contribution.

<sup>27</sup> Triple Higgs production, which probes the quadrilinear Higgs coupling, has a too small cross section [370].



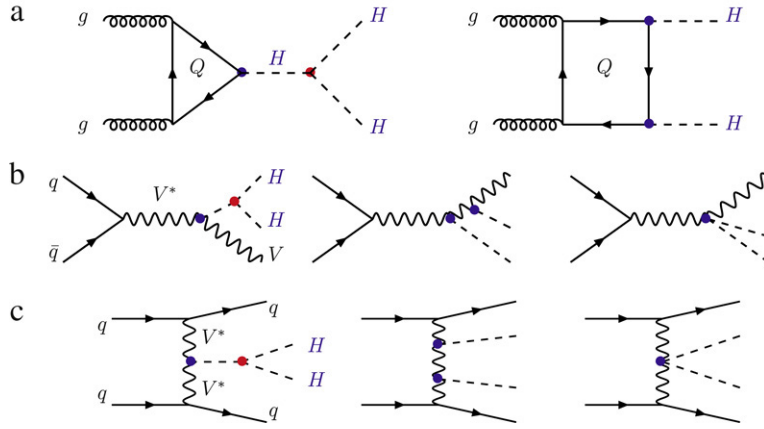


Fig. 3.39. Feynman diagrams for Higgs pair production in hadronic collisions.

In terms of the trilinear Higgs coupling,  $\lambda'_{HHH} = 3M_H^2/M_Z^2$  [note the change in the normalization], the partonic cross section at leading order is given by [233]

$$\hat{\sigma}_{\text{LO}}(gg \rightarrow HH) = \int_{\hat{s}_-}^{\hat{s}_+} d\hat{t} \frac{G_\mu^2 \alpha_s^2(\mu_R)}{256(2\pi)^3} \left\{ \left| \frac{M_Z^2 \lambda'_{HHH}}{\hat{s} - M_H^2} F_T + F_B \right|^2 + |G_B|^2 \right\} \quad (3.84)$$

with the Mandelstam variables for the parton process given by

$$\hat{s} = Q^2, \quad \hat{t}/\hat{u} = -\frac{1}{2} \left[ Q^2 - 2M_H^2 \mp Q^2 \beta_H \cos \theta \right] \quad (3.85)$$

where  $\theta$  is the scattering angle in the partonic c.m. system with invariant mass  $Q$  and, as usual,  $\beta = \sqrt{1 - 4M_H^2/Q^2}$ .  $\mu_R$  is the renormalization scale which, together with the factorization scale, will be identified to  $\hat{s}$  and the integration limits correspond to  $\cos \theta = \pm 1$  and  $\hat{t}_{\pm} = -\frac{1}{2} [Q^2 - 2M_H^2 \mp Q^2 \beta_H]$ . The proton cross section is derived by folding the parton cross section  $\hat{\sigma}(gg \rightarrow HH)$  with the gluon luminosity

$$\sigma(pp \rightarrow HH) = \int_{4M_H^2/s}^1 d\tau \frac{d\mathcal{L}^{gg}}{d\tau} \hat{\sigma}(gg \rightarrow HH; \hat{s} = \tau s). \quad (3.86)$$

The dependence on the quark masses is contained in the triangle and box functions  $F_T$ ,  $F_B$  and  $G_B$ . The expressions of these form factors with the exact dependence on the quark masses can be found in Refs. [232,233]. In the limit where the Higgs boson is much lighter or much heavier than the internal quark  $Q$ , the coefficients take a very simple form [233]

$$\begin{aligned} M_H \ll 4m_Q & \quad F_T \simeq \frac{2}{3}, \quad F_B \simeq -\frac{2}{3}, \quad G_B \simeq 0 \\ M_H \gg 4m_Q & \quad F_T \simeq -\frac{m_Q^2}{\hat{s}} \left[ \log \frac{m_Q^2}{\hat{s}} + i\pi \right], \quad F_B \sim G_B \simeq 0. \end{aligned} \quad (3.87)$$

As one might have expected from single Higgs production, the QCD radiative corrections are particularly important for this production channel and must be included. They have been determined in the heavy quark limit  $M_H^2 \ll 4m_Q^2$ , where one can use the low-energy theorem to determine the effective  $Hgg$  and  $HHgg$  couplings in the triangle and box contributions, when the top quark is integrated out. One can then use these effective couplings to calculate the interaction of the light gluon and quark fields, as discussed previously. The  $K$ -factor was found to be  $K \approx 1.9$  in the Higgs mass range between 100 and 200 GeV [371]. A  $K$ -factor of similar size is generally expected for larger Higgs masses and even beyond the top quark threshold, as it was the case for the  $gg \rightarrow H$  process.



**3.6.1.2. The vector boson fusion and strahlung mechanisms.** At high energies, one expects double Higgs production in the vector boson fusion channel to have a substantial cross section since the longitudinal vector bosons have couplings which grow with energy. The calculation of the full  $2 \rightarrow 4$  process,  $qq \rightarrow qqHH$ , is rather complicated. However, one can use the equivalent longitudinal vector boson approximation in which one calculates the cross section for the  $2 \rightarrow 2$  process

$$V_L V_L \rightarrow HH. \quad (3.88)$$

Taking into account only the dominant longitudinal vector boson contribution, denoting by  $\beta_{V,H}$  the  $V, H$  velocities in the c.m. frame, the production amplitude is given by

$$\begin{aligned} \mathcal{M}_{LL} = \frac{G_\mu \hat{s}}{\sqrt{2}} \left\{ (1 + \beta_V^2) \left[ 1 + \frac{M_Z^2 \lambda'_{HHH}}{(\hat{s} - M_H^2)} \right] \right. \\ \left. + \frac{1}{\beta_V \beta_H} \left[ \frac{(1 - \beta_V^4) + (\beta_V - \beta_H \cos \theta)^2}{\cos \theta - x_V} - \frac{(1 - \beta_V^4) + (\beta_V + \beta_H \cos \theta)^2}{\cos \theta + x_V} \right] \right\} \end{aligned} \quad (3.89)$$

with the variable  $x_V$  defined as  $x_V = (1 - 2M_H^2/\hat{s})/(\beta_V \beta_H)$ ,  $\theta$  the scattering angle in the  $VV$  c.m. frame and  $\hat{s}^{1/2}$  the invariant energy of the  $VV$  pair.

Squaring the amplitude and integrating out the angular dependence, one obtains the cross section for the  $V_L V_L \rightarrow HH$  subprocess,

$$\hat{\sigma}(V_L V_L \rightarrow HH) = \frac{G_\mu^2 M_V^4}{8\pi \hat{s}} \frac{\beta_H}{\beta_V (1 - \beta_V^2)^2} \int_{-1}^1 d\cos \theta |\mathcal{M}_{LL}|^2 \quad (3.90)$$

which then has to be folded with the longitudinal vector boson luminosity spectra Eq. (3.53) to obtain the  $qq \rightarrow HHqq$  cross section, which again has to be convoluted with the parton densities to obtain the full hadronic cross section

$$\sigma(pp \rightarrow HHqq) = \int_{4M_H^2/s}^1 d\tau \frac{d\mathcal{L}^{qq}}{d\tau} \hat{\sigma}(qq \rightarrow HHqq; \hat{s} = \tau s). \quad (3.91)$$

The result obtained in this way is expected to approximate the exact result within about a factor of two for low Higgs masses and very high energies [236,237].

In the case of the double Higgs–strahlung mechanisms,  $q\bar{q} \rightarrow HHV$ , the production cross sections are expected to be rather small. This can be guessed by looking at the cross section for single Higgs–strahlung: for  $M_H \sim 200$  GeV [which in terms of phase space would correspond to the production of two Higgs bosons with a mass of 100 GeV], it is of the order of 30 fb, and there will be still an additional suppression by the electroweak coupling factor in the case of double Higgs–strahlung. The analytical expressions will be given in the next section when this process will be discussed at  $e^+e^-$  colliders, where it is more relevant.

**3.6.1.3. The cross sections at the LHC.** The total cross sections for the pair production of Higgs bosons in the three processes are shown in Fig. 3.40 as functions of the Higgs mass in the range  $M_Z \lesssim M_H \lesssim 2M_Z$ . In the  $gg$  case, the full dependence on the quark mass has been taken into account and the  $K \sim 1.9$  factor has been included. Note that the NLO QCD corrections to the double Higgs production in association with a vector boson and in the vector boson fusion channels, are the same as that for the respective processes for single Higgs production and will increase the cross sections by, respectively,  $\sim 30\%$  and  $\sim 10\%$ ; they have not been included.

As expected, gluon–gluon fusion dominates over the other mechanisms and has a cross section larger than 10 fb for this Higgs mass range. The  $WW/ZZ$  fusion mechanisms are the next important channels, but with cross sections which are one order of magnitude smaller;  $WW$  fusion dominates over  $ZZ$  fusion at a ratio  $WW/ZZ \approx 2.3$ . The cross sections for double Higgs–strahlung are relatively small as it follows from the scaling behavior of the cross sections which drop  $\sim 1/\hat{s}$ . The cross sections for Higgs–strahlung off  $W$  and  $Z$  bosons are combined in the figure and their relative size is close to  $W/Z \approx 1.6$ .

The vertical arrows indicate the sensitivity of the production cross sections to the size of the trilinear Higgs coupling; they correspond to a modification of the coupling  $\lambda'_{HHH}$  by the rescaling coefficient  $\kappa = \frac{1}{2} \rightarrow \frac{3}{2}$ .

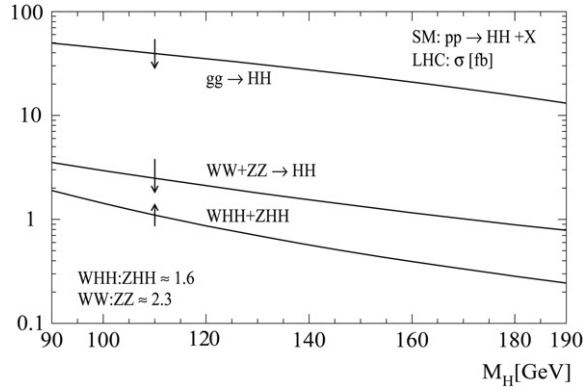


Fig. 3.40. The cross sections for gluon fusion,  $gg \rightarrow HH$ , the  $WW/ZZ$  fusion  $qq \rightarrow qqWW/ZZ \rightarrow HH$  and the double Higgs-strahlung  $q\bar{q} \rightarrow WHH + ZHH$  in the SM as functions of  $M_H$ . The vertical arrows correspond to a variation of the trilinear Higgs coupling from  $\frac{1}{2}$  to  $\frac{3}{2}$  of the SM value,  $\lambda'_{HHH} = 3M_H^2/M_Z^2$ ; from Ref. [235].

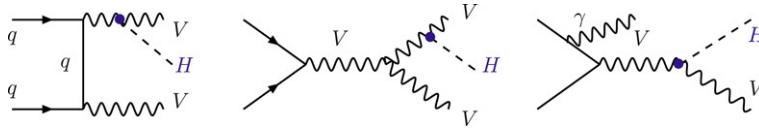


Fig. 3.41. Diagrams for associated Higgs boson production with two gauge bosons.

### 3.6.2. Higgs production in association with gauge bosons

**3.6.2.1. Higgs production in association with gauge boson pairs.** In high-energy collisions, the pair production of massive vector bosons  $pp \rightarrow VV'$ , with  $V, V' = W, Z(\gamma)$ , has a very large cross section. In view of these rates, it is tempting to consider the possibility of emitting an additional Higgs particle from one of the gauge boson lines [244, 245]

$$qq/q\bar{q} \rightarrow W^+W^-H, ZZH, W^\pm ZH \quad \text{and} \quad qq/q\bar{q} \rightarrow \gamma ZH, \gamma W^\pm H. \quad (3.92)$$

The hope is that the suppression by the additional electroweak coupling factor might be compensated by the initially large production rate for gauge bosons. Formally, these processes are of the same order,  $\mathcal{O}(G_\mu^3)$ , as that of Higgs production in the  $WW/ZZ$  fusion mechanisms and the suppression by the phase space should not be too drastic at high enough energies.

As shown in Fig. 3.41, where some generic Feynman diagrams are displayed, the processes proceed through  $s$ -channel gauge boson and/or  $t$ -channel quark exchanges. Strictly speaking, the processes with additional final state photons which have enough large  $p_T$  to be observed, should be viewed as the ISR part of the electroweak corrections to the  $q\bar{q} \rightarrow HV$  processes as discussed in Section 3.2. However, they are interesting since, besides the fact that the final state contains an additional photon which can be tagged, they can have larger rates compared to the parent processes which drop like  $1/\hat{s}$  at high energies. The processes not involving photons are genuine higher-order processes, though at high energies they can also be viewed as a kind of “ $V$  bremsstrahlung” correction to the main mechanisms  $q\bar{q} \rightarrow HV$ .

The cross sections for these processes have been evaluated in Ref. [244] and updated recently [245] using MadGraph [372]. They are shown in Fig. 3.42 for the energy relevant at the LHC as functions of  $M_H$ . For the final states involving photons, the cuts  $p_T^\gamma \geq 10$  GeV and  $|\eta^\gamma| \leq 2.5$  have been applied. The CTEQ6 PDFs have been used and the scales were set at  $\mu_R^2 = \mu_F^2 = \hat{s}$ . The largest cross section is obtained for the  $pp \rightarrow HWW$  process, as anticipated from the fact that the  $WW$  cross section is dominant at the LHC, being at the level of  $\sigma(HWW) \sim 10$  fb for low mass Higgs values and decreases slowly to reach  $\sim 1$  fb for  $M_H \simeq 300$  GeV. Thus, it is larger than that for double Higgs production in the strahlung and fusion processes. The cross sections for the other processes are factors in the range 3–5 smaller but, except for  $\sigma(HWZ)$ , they are above the femtobarn level for  $M_H \lesssim 160$  GeV.

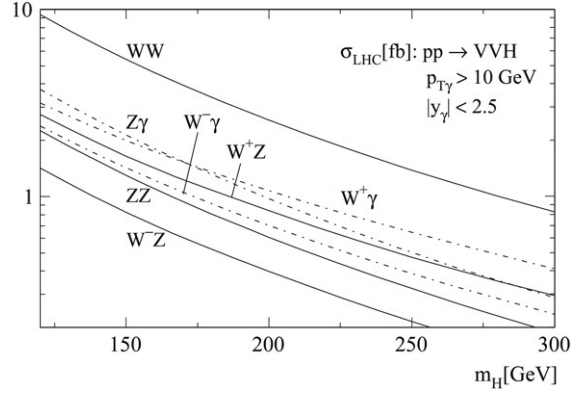


Fig. 3.42. The total cross sections for the associated production of the Higgs boson with a pair of gauge bosons at the LHC,  $pp \rightarrow HVV$ , as functions of  $M_H$ ; from Ref. [245].

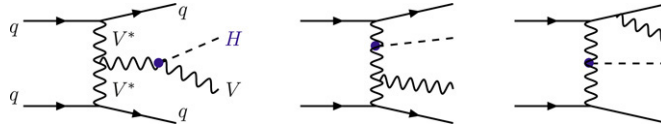


Fig. 3.43. Feynman diagrams for associated  $HVqq$  production in hadronic collisions.

In view of the smallness of the signal cross sections, these processes cannot of course be considered as Higgs discovery channels [in particular since the backgrounds from triple gauge boson production might be large]. However, once Higgs particles have been detected in the dominant detection channels, they could allow for additional tests and measurements, such as the determination of the  $HWW$  coupling from  $pp \rightarrow HWW \rightarrow WWWW$  for instance.

**3.6.2.2. Higgs production in association with a gauge boson and two jets.** Associated Higgs production with a gauge boson and two quarks in hadronic collisions

$$qq \rightarrow HWqq, HZqq, H\gamma qq \quad (3.93)$$

originates from several sources, as shown in Fig. 3.43 where some Feynman diagrams are displayed, with the starting point being the fusion of the vector bosons producing a gauge or a Higgs boson. The production of  $H\gamma qq$  final states occurs only through the  $qq \rightarrow WWqq \rightarrow Hqq$  process, with the photon emitted from the quark or the internal  $W$  lines, which is part of the photonic corrections to the initial mechanism. Note that an additional source might come from the  $pp \rightarrow HV$  process, with the emission of two jets in the final state: this also is part of the NNLO QCD corrections to Higgs-strahlung that we have already discussed.

The cross sections for these processes have been calculated sometime ago [246] both exactly and in the longitudinal  $W$  approximation [for the energy which was relevant for the late SSC] and the output was that the latter approximation gives results which are only about a factor of two different from the exact result. This is similar to Higgs pair production in the vector boson fusion channels  $qq \rightarrow V^*V^* \rightarrow qqHH$ , discussed previously. In fact, for  $pp \rightarrow HZqq$ , the analogy between the two processes is complete since the  $Z$  boson can be treated as a neutral Goldstone boson  $w_0$ , which has exactly the same coupling as the Higgs boson as can be seen from the effective potential equation (1.40). The cross sections are not that small for such higher-order mechanisms: in the case of  $pp \rightarrow HWqq$ , they almost reach the level of 100 fb for Higgs masses in the low range [which is only one order of magnitude smaller than the Higgs-strahlung  $pp \rightarrow HW$  cross section] and decrease only slowly with  $M_H$ .

More recently, a detailed study of the signal for the  $pp \rightarrow HWqq$  process has been performed at the LHC [247], in the channel where the Higgs decays into bottom quarks and the  $W$  boson leptonically. Applying cuts that are similar to those of the vector boson fusion process discussed in Section 3.3.3 and assuming reasonable efficiency for tagging the  $b$ -quarks and resolution for the reconstruction of the  $b\bar{b}$  invariant mass, the various backgrounds [in particular the  $pp \rightarrow tt \rightarrow bbWW$  and the QCD  $Wbbjj$  final states] can be reduced at a level comparable to the signal as shown

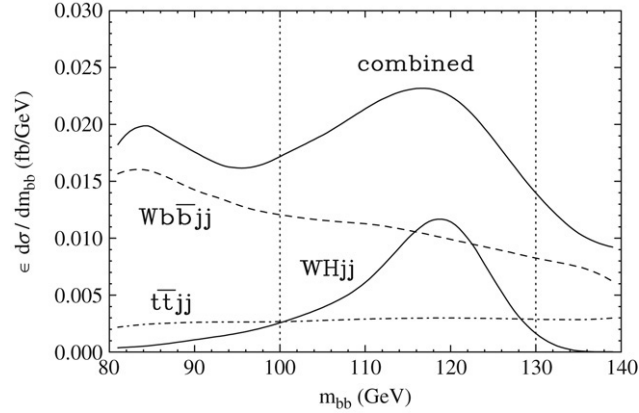


Fig. 3.44. The  $b\bar{b}$  invariant mass distribution of the  $WHjj$  signal for  $M_H = 120$  GeV and the  $Wb\bar{b}jj$ ,  $t\bar{t}jj$  backgrounds after cuts; the combined signal and backgrounds are also shown. The vertical dotted lines denote the mass bin used for calculating the statistical significance of the signal; from Ref. [247].

in Fig. 3.44. This would allow for the extraction of the  $Hb\bar{b}$  Yukawa coupling with a reasonable accuracy if a high luminosity is available.

### 3.6.3. More on higher-order processes

There are several other higher-order processes for Higgs production at hadron colliders, but they lead to extremely small cross sections at the LHC and, *a fortiori*, at the Tevatron. We briefly discuss some of them for completeness.

**3.6.3.1. Higgs production in association with a photon.** Higgs boson and photon final states in hadronic collisions [248] may originate from two main sources. An obvious possibility is the direct production from light quarks,  $qq \rightarrow H\gamma$ , where the Higgs boson is emitted from the quark lines. Because the Yukawa couplings are very tiny, the cross sections are negligible. An exception might be the case of bottom quarks; however, besides the fact that the  $Hb\bar{b}$  Yukawa coupling is still small, there is a suppression from the  $b$  density in the hadron. In fact, the cross section is comparable to the one for charm quark, the suppression of the Yukawa coupling  $m_c/m_b$  being partly compensated by the larger  $c$ -parton density and by the electric charge. For low Higgs masses,  $M_H \sim 100$  GeV, the cross sections are at the femtobarn level at the LHC and one to two orders of magnitude smaller at the Tevatron. Since the dominant contribution is coming from the  $b\bar{b}$  initial state, this process is anyway equivalent to the processes  $b\bar{b} \rightarrow H$  and  $g\gamma \rightarrow b\bar{b}H$  with two undetected  $b$ -quarks, with the radiation of an ISR photon.

Another possibility to generate the Higgs plus photon final state is via loop diagrams in quark–antiquark annihilation [the corresponding process with initial state gluons,  $gg \rightarrow H\gamma$ , is forbidden by Furry’s theorem similar to the  $H \rightarrow \gamma\gamma g$  decay discussed in Section 2.3]. There are triangular diagrams, when the  $q\bar{q}$  state annihilates into a virtual photon or  $Z$  boson in the  $s$ -channel and which involve virtual top quarks and  $W$  bosons and box diagrams with  $W$  bosons and light quarks running in the loop. Since the process is of  $\mathcal{O}(G_\mu^4)$  and because of the suppression by the loop factor, the cross sections are extremely small: at the LHC they are at the level of 0.1 fb and they are much lower at the Tevatron [248].

**3.6.3.2. Loop induced Higgs pair production in  $q\bar{q}$  annihilation.** Similar to the  $gg$  fusion process,  $gg \rightarrow HH$ , which provides the largest cross section for Higgs boson pairs at the LHC, one can produce pairs of Higgs particles in  $q\bar{q}$  annihilation. Because the Higgs couplings to the light quarks are small and since CP-conservation forbids a  $ZHH$  coupling at the tree level, the entire contribution to this process originates from loop diagrams. In fact, as a result of chiral symmetry, only box diagrams involving quarks and massive gauge bosons, from which the Higgs particles are emitted, are present. The process is thus not sensitive to the trilinear Higgs coupling.

This calculation has been performed in Ref. [249] and, as one might have expected, because of the lower luminosity for quarks than for gluons at high energies, the cross sections are much smaller than those of the  $gg \rightarrow HH$  production process. At LHC energies the difference is at least one order of magnitude. At the Tevatron, the cross sections will be

anyway very small because of the reduced phase space. The annihilation of  $q\bar{q}$  states is, thus, not an important process for double Higgs boson production.

**3.6.3.3. Higgs pair production with heavy quarks.** Similar to the double Higgs boson production in the  $WW/ZZ$  fusion processes, one might take advantage of the large Yukawa coupling to top quarks to produce two Higgs bosons emitted from the top quark lines in the process  $gg/q\bar{q} \rightarrow t\bar{t}$ . An interesting feature is that there is a contributing diagram where a Higgs boson is emitted from the top quark lines and then splits into two Higgs bosons. This process is therefore sensitive to the trilinear Higgs coupling and, despite the suppression by the electroweak couplings, one might hope for a compensating enhancement of the cross section due to the presence of the Higgs boson exchange in the  $s$ -channel. The complete calculation for this four massive particle final state is rather complicated<sup>28</sup> and has been performed numerically in Ref. [251]. At the LHC, the cross section is at the level of 1 fb for  $M_H \sim 120$  GeV and, thus, of the same order as that of  $VHH$  production and much smaller than  $gg \rightarrow HH$  production. The large backgrounds make it impossible to extract any signal even with extremely high luminosities [251].

**3.6.3.4. Rare decays of the top quark.** The huge cross section of the process  $gg/q\bar{q} \rightarrow t\bar{t}$  allows the production of  $10^7$  to  $10^8$  top quark pairs per year at the LHC. This large number of events could be used to look for very rare decays of this particle. If the Higgs boson is not too heavy,  $M_H < m_t$ , the decay  $t \rightarrow cH$  can occur through loop diagrams. Starting from the flavor changing transition  $t \rightarrow c$ , which is mediated by loops involving  $W$  bosons and down-type [mainly bottom] quarks, one can attach a Higgs boson either to the external top quark line or to the internal  $W$  boson or  $b$ -quark lines. However, because the decay is suppressed by three powers of the Fermi constant  $G_F$  and by the GIM mechanism, the branching ratio is extremely small  $BR(t \rightarrow cH) \lesssim 10^{-13}$  for  $M_H \gtrsim 100$  GeV [252]. In view of the experimental bound  $M_H \gtrsim 115$  GeV, the parent decay process  $t \rightarrow bWH$  [136,253] is now kinematically closed.

### 3.6.4. Diffractive Higgs boson production

Diffractive processes in (anti)proton collisions are those in which color singlet objects are exchanged between the high-energy initial protons, which allow them to be diffracted [254–256]. This can occur, for instance, when two gluons are exchanged in the  $t$ -channel by the initial protons: this neutralizes the color and allow the two protons to remain intact and continue on their way. Higgs production occurs in the emission from the  $t$ -channel exchanged particles and, in the case of  $t$ -channel gluons, this occurs through the usual  $ggH$  vertex mediated by heavy quark loops. The signature is then two protons which are produced at very large rapidities and a centrally produced Higgs particle

$$p + p \rightarrow p + H + p \quad (3.94)$$

where the  $+$  sign means that there is a large rapidity gap between the particles. In addition, if one tags the initial hadrons [using the so-called roman pot detectors], these diffractive processes can be selected resulting in a very clean signal [the backgrounds will be discussed later]: a Higgs boson in the central region, and nothing else.

There are many models for diffractive Higgs production in the literature, starting from the Bialas–Landshoff exclusive model [254]. They all involve a mixture of perturbative and non-perturbative QCD physics which is not very well understood yet. In the context of Higgs physics, hard-diffractive production in the central region are the most interesting ones. We briefly summarize the main features of some processes for a light Higgs boson decaying mainly into  $b\bar{b}$  pairs, following Refs. [257,258] where a detailed account is given and to which we refer for earlier work. Figure 3.45, taken from Ref. [257], illustrates three processes for double-diffractive Higgs production in hadronic collisions that one can partly discuss in the familiar terms of perturbative QCD. We use the terminology of this reference.

In the central exclusive double-diffractive processes shown in Fig. 3.45(a), the Higgs boson is produced alone and is separated from the outgoing hadrons by large rapidity gaps. If the latter are tagged, the Higgs mass can be determined

<sup>28</sup> One can estimate the order of magnitude of the cross section, by naively treating the heavy top quarks as partons inside the hadron and considering at the partonic level the process of heavy top quark annihilation into two Higgs bosons,  $t\bar{t} \rightarrow HH$ . This calculation has been performed in Ref. [250] some time ago [at the time where the top quark was believed to have a mass of the order of 50 GeV and where the SSC was still expected to operate] and the output was that, even for hadronic c.m. energies of  $\sqrt{s} = 40$  TeV, the “partonic” cross sections folded with luminosities which may be overestimated by a factor of ten, leading to a total rate which is at the level of the cross section for the longitudinal  $W$  boson fusion into two Higgs bosons.

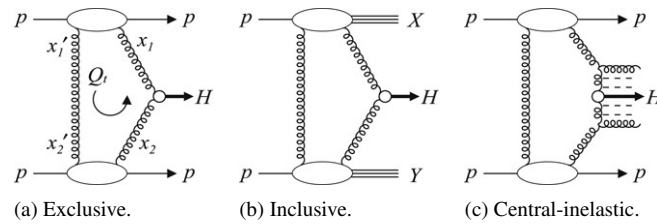


Fig. 3.45. Examples of processes for double-diffractive Higgs production in  $pp$  collisions.

Table 3.1

Higgs boson production cross sections in fb at the Tevatron and the LHC for  $M_H \sim 120$  GeV in the various diffractive models of Fig. 3.45; from Ref. [257]

Model	Exclusive (a)	Inclusive (b)	Central inel. (c)
Tevatron	0.2	1	0.03
LHC	3	40	50

either by measuring the missing mass  $M_{\text{inv}}$  of the system or by reconstructing the  $H \rightarrow b\bar{b}$  decay mass peak  $M_{b\bar{b}}$ ; one can then match the two measurements,  $M_{\text{inv}} = M_{b\bar{b}} = M_H$  which provides a strong kinematical constraint. Moreover, an interesting feature is that in the production vertex, the polarization vectors of the gluons are correlated in a such way that with the resulting effective luminosity, only spin-zero particles with positive parity, i.e. with  $J^{\text{PC}} = 0^{++}$  quantum numbers, can be primarily produced [the cross section for CP-odd states is strongly suppressed]. On the other hand, the background from  $gg \rightarrow b\bar{b}$  for instance is strongly suppressed,  $\hat{\sigma}(gg \rightarrow b\bar{b}) \propto \alpha_s^2 m_b^2 / \hat{s}$ . The Higgs spin and parity quantum numbers can therefore be checked in this process [373] with only an ambiguity with  $2^{++}$  states remaining. Unfortunately, the model predicts rather low Higgs production cross sections: for a Higgs boson with a mass  $M_H \sim 120$  GeV, they are of the order of 0.2 fb at the Tevatron and 3 fb at the LHC; see Table 3.1. The uncertainty in the prediction is also large, a factor of 2 at the LHC for instance.

In central-inelastic production, Fig. 3.45(c), there is an additional radiation accompanying the Higgs boson in the central region, but the latter is still separated from the final hadrons by large rapidity gaps.<sup>29</sup> This leads in general to a much larger Higgs production cross section at the LHC; see Table 3.1 [at the Tevatron all processes have too small cross sections to be useful]. However, the background from  $gg \rightarrow b\bar{b}$  is also very large since there is no more the selection rule for spin-zero particle production and the signal-to-background ratio is then very low. In addition, one cannot use the missing mass technique to measure the Higgs mass [it has been suggested recently [375] to trigger on the remnants to improve the  $S/B$  ratio and to reconstruct the mass]. Nevertheless, besides the fact that these processes are actually the ones which have been experimentally observed, since the CDF dijet data indicate the presence of an additional soft hadronic radiation [376], they need to be considered, first because they are potential backgrounds to the exclusive process, and second because pseudoscalar Higgs bosons can be only produced in these mechanisms.

In inclusive production [according to the terminology of Ref. [257]], Fig. 3.45(b), the previous discussion on the process of Fig. 3.45(c) also applies with the important exception that both incoming protons are allowed to dissociate. This process has not received much attention in the literature as it does not have the advantages of central exclusive diffraction. At the LHC, the production rates [257] are of the same order as in the previous case; Table 3.1.

As mentioned previously, the treatment of diffractive processes involves a mixture of perturbative and non-perturbative aspects of QCD. The rapidity gaps for instance may be associated with the exchange of an effective Pomeron which can be either a QCD Pomeron [which, at lowest order, is a  $gg$  state] or a phenomenological Pomeron fitted from e.g. the HERA data. The non-perturbative aspect in exclusive diffraction arises when one attempts to calculate the survival probabilities  $S^2$  of the rapidity gaps, when secondary particles are produced in the soft rescattering of the spectator partons and populate these gaps. This probability is not universal and depends on the initial energy and the considered final state. A recent estimate gives  $S^2 \sim 0.02$  while diffractive deep-inelastic processes at HERA and diffractive dijet production at the Tevatron suggest, respectively,  $S^2 \sim 1$  and  $\sim 0.1$ . Note that another

<sup>29</sup> In fact, in the terminology of Ref. [374] which is becoming the standard one, it is the process of Fig. 3.45(c) which is called the inclusive-diffractive process.



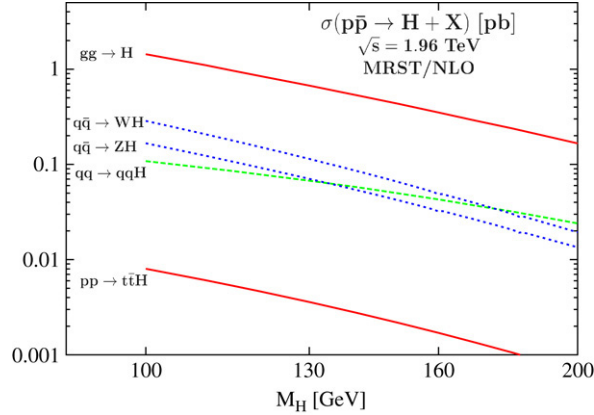


Fig. 3.46. The Higgs boson production cross sections at the Tevatron in the dominant mechanisms as functions of  $M_H$ . They are (almost) at NLO with  $m_t = 178$  GeV and the MRST set of PDFs has been used. The scales are as described in the text.

probability for the gaps to be occupied arises from hard-gluon radiation in  $gg \rightarrow H$  for instance; the latter can be, however, calculated in perturbative QCD.

These non-perturbative aspects generate rather uncertain predictions of the various models and, until recently, the spread in the predictions ranging over several orders of magnitude. A critical comparison of the various predictions has been performed in Ref. [257], where it has been attempted to explain the origin of the large differences. The conclusion was that either different diffractive processes have been considered or important effects, such as higher-order QCD corrections, have been neglected. Many of the models, in particular those which predict large Higgs production rates, are already ruled out by Tevatron data on diffractive dijet production. Besides these theoretical issues, experimental problems such as the possibility of triggering on the events and the integration of the roman pot detectors within the machine, still remain unsolved; see Ref. [258] for instance.

Note that the expectation for the clean exclusive central Higgs production process can be checked at the LHC itself, since the main ingredients which are needed for the calculation of the Higgs signal cross section are involved in the calculation of dijet production with large rapidity gaps,  $pp \rightarrow p + \text{dijet} + p$ . Since the latter can be measured from the side bands, one can improve the prediction of the Higgs cross section. Other checks can be performed [256].

In summary, diffractive processes in hadronic collisions provide an additional means to produce the Higgs boson at the LHC. The double exclusive production process allows a good measurement of the Higgs mass and a check of the SM Higgs spin and parity quantum numbers [besides the selection which favors  $0^{++}$  states, one can also use, for instance, the azimuthal asymmetry of the scattered protons], which are notoriously difficult to verify at hadron colliders, as will be discussed shortly. The production rates are, however, still uncertain and the experimental conditions not yet established. Many studies are being performed and the situation might become more clear in a near future.

### 3.7. Detecting and studying the Higgs boson

#### 3.7.1. Summary of the production cross sections

The cross sections for Higgs boson production in the main channels, Eqs. (3.1)–(3.4), are summarized in Fig. 3.46 at the Tevatron Run II with a c.m. energy  $\sqrt{s} = 1.96$  TeV and in Fig. 3.47 for the LHC with  $\sqrt{s} = 14$  TeV as functions of the Higgs boson mass, an update of Refs. [22,377,378]. They include the full NLO QCD corrections which have been discussed earlier. The MRST sets of parton densities [292] have been used for the cross sections. As inputs, we use the central values for the fermion and gauge boson masses given in Eq. (2.1), in particular we use the updated value  $m_t = 172$  GeV, while the strong coupling constant is chosen to be  $\alpha_s(M_Z) = 0.119$  to match the value that is incorporated in the PDFs at NLO. Again, we will denote sometimes by  $pp$  both  $pp$  and  $p\bar{p}$  reactions and by  $\mathcal{L}$  both  $\mathcal{L}$  and  $\int \mathcal{L} dt$ .

The cross sections Eqs. (3.1)–(3.4) have been calculated using, respectively, the NLO FORTRAN codes V2HV, VV2H, HIGLU and the LO code HQQ of Ref. [259] which are publicly available. A few remarks to explain how these cross sections have been obtained are in order:

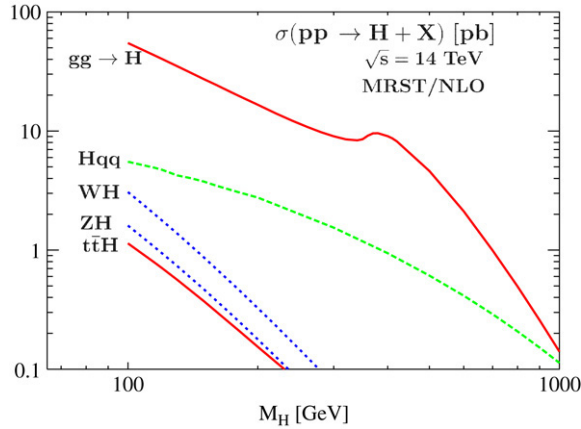


Fig. 3.47. The same as Fig. 3.46 but for the LHC.

– In the  $gg \rightarrow H$  mechanism, we display the NLO cross sections which have been calculated for arbitrary quark masses, since the NNLO calculation is valid only in the heavy top quark limit [although it is expected to be a good approximation for the entire range if the Born amplitude contains the full  $m_t$  dependence]. However, we have set the renormalization and factorization scales at  $\mu_R = \mu_F = \frac{1}{2}M_H$ . As discussed previously, in this way the NLO (NNLO) correction increases (decreases) and the full result approaches the total cross section at NNLO. We have verified that the values that we obtain are in a very good agreement with the NNLO values given for  $M_H \leq 300$  GeV in Ref. [284].

– In the case of the Higgs–strahlung processes,  $pp \rightarrow HW$  and  $pp \rightarrow HZ$ , we incorporate the NLO and NNLO QCD corrections, including the  $gg \rightarrow HZ$  component in the latter production process, as well as the electroweak radiative corrections [where we removed the kinks near the  $2M_V$  thresholds]. For the PDFs, we will use the approximate densities which are included in the MRST2002 set and which approach very closely the exact result.

– For the  $pp \rightarrow t\bar{t}H$  production process, the NLO corrections have become available only recently and the FORTRAN codes for calculating the cross sections at this order are not yet publicly available. We therefore use the LO program HQQ but we choose a scale for which the LO cross sections approach the NLO ones, i.e.  $\mu_R = \mu_F \sim \frac{1}{2}M_H + m_t$ . We then multiply the cross sections by constant  $K$ -factors of 1.2 and 0.8 for the LHC and the Tevatron, respectively, to approach the exact result. We have verified that, for  $m_t = 174$  GeV, the obtained rates are in relatively good agreement with the NLO ones given in Ref. [268].

– The cross section for the vector boson fusion process  $pp \rightarrow Hqq$  has been calculated at NLO with the scales fixed to  $\mu_R = \mu_F = Q_V$ . No kinematical cut has been applied.

In Table 3.2, we display the numerical values of the cross sections for selected values of the Higgs mass that are relevant for the Tevatron and the LHC, as they might serve as useful inputs in other studies. The various SM input parameters are as discussed above.

As can be seen, in the interesting mass range favored by the electroweak precision data,  $100 \lesssim M_H \lesssim 250$  GeV, the dominant production process of the SM Higgs boson at the LHC is by far the gluon–gluon fusion mechanism, the cross section being of the order a few tens of pb. In fact, this process dominates all the way up to Higgs masses of the order of 1 TeV, where the cross section is still sizable,  $\sigma(gg \rightarrow H) \sim 0.1$  pb. It is followed by the  $WW/ZZ$  fusion process which has a cross section of a few pb in the interesting Higgs mass range above and which reaches the level of the  $gg$  fusion cross section for very large  $M_H$  values. The cross sections for the associated production with  $W/Z$  bosons or  $t\bar{t}$  pairs are one to three orders of magnitude smaller than the  $gg$  cross section and these processes are only relevant in the mass range  $M_H \lesssim 250$  GeV. For the luminosities expected at the LHC, a very large sample of Higgs particles can be thus collected before selection cuts are applied.

At the Tevatron, the most relevant production mechanism is the associated production with  $W/Z$  bosons [the  $WH : ZH$  cross section ratio is approximately 1.5 for  $M_H \lesssim 200$  GeV], where the cross section is slightly less than 250 fb for  $M_H \sim 120$  GeV when both processes are summed, leading to 2,500 Higgs events for the maximal luminosity expected at the Tevatron,  $\int \mathcal{L} = 10 \text{ fb}^{-1}$ ; the cross section drops to the level of less than 30 fb for Higgs masses larger than 200 GeV. The  $WW/ZZ$  fusion cross sections are of the same order in the mass range

Table 3.2

Numerical values for SM Higgs production cross sections at the Tevatron (upper part) and the LHC (lower part) in picobarns for selected values of the Higgs mass

$M_H$ (GeV)	$\sigma(HW)$	$\sigma(HZ)$	$\sigma(Hqq)$	$\sigma(gg \rightarrow H)$	$\sigma(Ht\bar{t})$
115	0.178	0.107	0.085	0.97	0.0045
120	0.153	0.093	0.078	0.85	0.0040
130	0.114	0.070	0.067	0.67	0.0031
140	0.086	0.054	0.058	0.54	0.0024
150	0.065	0.042	0.050	0.43	0.0018
160	0.048	0.032	0.043	0.35	0.0015
170	0.039	0.026	0.037	0.29	0.0011
180	0.030	0.020	0.032	0.24	0.0009
200	0.019	0.013	0.024	0.17	0.0006
<hr/>					
115	1.89	1.01	4.93	43.43	0.84
120	1.65	0.89	4.72	40.40	0.74
130	1.28	0.70	4.24	35.18	0.60
140	1.00	0.55	4.01	30.96	0.48
150	0.79	0.44	3.76	27.48	0.39
160	0.62	0.35	3.49	24.60	0.32
170	0.52	0.29	3.26	22.14	0.26
180	0.42	0.24	3.07	20.08	0.22
200	0.30	0.17	2.76	16.79	0.16
300	0.04	0.07	1.54	9.41	–
400	–	–	0.94	9.23	–
500	–	–	0.61	4.43	–
600	–	–	0.41	1.99	–
700	–	–	0.29	0.93	–
800	–	–	0.21	0.46	–
900	–	–	0.15	0.24	–
1000	–	–	0.11	0.13	–

These values have been obtained as in Figs. 3.46 and 3.47 and as explained in the text.

$M_H \lesssim 100$ – $200$  GeV, while the cross sections for associated production with  $t\bar{t}$  pairs are rather low, being less than 10 fb already for  $M_H \sim 115$  GeV. The  $gg$  fusion mechanism has the largest production cross section, reaching the picobarn level for low Higgs masses, but suffers from a very large QCD two-jet background as will be discussed later.

A huge effort, which had already started in the late seventies, has been devoted to the search of suitable signals to detect the Higgs boson at hadron colliders and to suppress the various corresponding backgrounds, which are in general very large. It is an impossible task to present here a detailed account of the large number of theoretical and experimental studies which have been performed in this context. In the next subsection, we simply summarize the Higgs detection channels which have been established since already some time, mostly relying on the report of the Higgs working group in the case of the Tevatron [199] [see [198] for earlier work] and in the case of the LHC,<sup>30</sup> on the ATLAS Technical Design Report [209] and CMS Technical Proposal [210] with some update made in Refs. [215–217] as well as on the joint theoretical and experimental studies which have been performed at the three Les Houches [219–221] and at the 2001 Snowmass [204] Workshops [where some of the references to the original work can be found]; see also Ref. [383]. Some of the important backgrounds will be briefly mentioned and a detailed account can be found in various reviews [44,46,384,385]; see also Ref. [386]. For earlier work, we refer the reader to *The Higgs Hunter's Guide* where the pioneering analyses and a complete set of earlier references can be found.

### 3.7.2. Higgs signals and backgrounds at the Tevatron and the LHC

**3.7.2.1. The  $pp \rightarrow HW/HZ$  channel.** It has been realized a long time ago [223,296] that the associated Higgs production with  $W/Z$  bosons, with the latter decaying into leptons  $\ell = e^\pm, \mu^\pm$ , is a potential channel for detecting

<sup>30</sup> The analyses at the LHC that will be discussed here will be mostly based on Monte Carlo [379,380] simulations which take into account the parametrized [381,382] or full detector response [209,211].

the Higgs particle at high-energy hadron colliders [the LHC and the late SSC]. This has been confirmed later for the LHC in parton-level analyses in the case of the photonic Higgs boson decays [297,298]. Also more recently, it has been shown that this production channel is the most promising detection mode at the Tevatron Run II for a relatively light Higgs boson which decays dominantly into  $b\bar{b}$  pairs [301,302].

In principle, the hadronic decays of the companion vector bosons cannot be used [unless the Higgs boson itself does not decay into hadrons] as they are overwhelmed by the huge irreducible QCD backgrounds. Since the branching fraction  $BR(W \rightarrow \ell\nu) \sim 20\%$  is larger than  $BR(Z \rightarrow \ell\ell) \sim 6\%$ , and the cross section for  $q\bar{q}' \rightarrow WH$  is a factor  $\sim 1.5$  larger than that for  $q\bar{q} \rightarrow ZH$ , the process  $p\bar{p} \rightarrow HW \rightarrow H\ell\nu$  leads to five times more interesting events than the corresponding  $p\bar{p} \rightarrow HZ \rightarrow H\ell\ell$  process. Both channels have to be summed, however, to increase the statistics. In addition, the neutrino decays of the  $Z$  boson which have a substantial rate,  $BR(Z \rightarrow \nu\bar{\nu}) \sim 18\%$ , can also be considered. The final signals depend on the decay modes of the Higgs boson and, thus, on its mass and are summarized below.

- $H \rightarrow b\bar{b}$ : the dominant Higgs decay mode for  $M_H \lesssim 135$  GeV, leads to the final states  $\ell\nu b\bar{b}$ ,  $\ell\ell b\bar{b}$  and  $\nu\bar{\nu} b\bar{b}$  that exhibit distinctive signatures [isolated leptons and/or missing energy] which can be used at the Tevatron where the backgrounds are not too large. The latter mainly originate from the production of vector bosons plus two jets,  $p\bar{p} \rightarrow Vjj$  and in particular  $Wb\bar{b}$  [387,388], vector boson pairs,  $p\bar{p} \rightarrow VV$  [388–390], top quark pairs,  $p\bar{p} \rightarrow t\bar{t}$  [391] and single top quarks  $p\bar{p} \rightarrow t + X$  [369]. These processes are known at least to NLO in QCD.  $b$ -tagging as well as the reconstruction of the  $b\bar{b}$  invariant mass peak are crucial to reject them. Results based on the SHW simulation [392] which gives the average response of the upgraded CDF and DØ detectors in a simple way, show that these processes and, in particular,  $p\bar{p} \rightarrow WH \rightarrow \ell\nu b\bar{b}$ , are viable at the Tevatron [199]. In the case of the  $\nu\bar{\nu} b\bar{b}$  channel, a significant  $b\bar{b}$  background remains [which in Ref. [199] has been assumed to be equal to the sum of the remaining backgrounds]. The separation of the signal and backgrounds was optimized using neural network techniques which lead to an appreciable increase of the signal significance [393,394]. The  $WH \rightarrow \ell\nu b\bar{b}$  channel has been also discussed for the LHC [296,299] but due to the much larger QCD background, it is not considered alone as a clear discovery channel [209,216,395–397]. The significance of the signal is at the level of  $\sim 3\sigma$  for  $M_H = 120$  GeV with  $\mathcal{L} = 30 \text{ fb}^{-1}$  [396] when the  $Wb\bar{b}$  and  $t\bar{t}$  backgrounds have been sufficiently suppressed. This significance can be, however, added to the one from  $p\bar{p} \rightarrow t\bar{t}H$  when it leads to the same final state as will be discussed later.
- $H \rightarrow WW^{(*)}$ : which becomes the dominant Higgs decay mode for  $M_H \gtrsim 135$  GeV has also been considered both at the Tevatron and the LHC [300]. It receives irreducible backgrounds from triple vector boson production,  $pp \rightarrow WW + W/Z$  [398], in addition to those from vector boson and  $t\bar{t}$  pair production. Distinctive signatures are trilepton  $\ell\ell\ell$  events, like-sign dileptons and two jets  $\ell^\pm\ell^\pm jj$  as well as a high- $p_T$ -lepton pair plus missing  $E_T$ . At the Tevatron, the small production cross section, the low luminosity as well as the small branching ratio  $WWW \rightarrow 3\ell \sim 10^{-2}$ , lead to such a situation that only a few trilepton events can be observed even for  $30 \text{ fb}^{-1}$  data; the  $\ell^\pm\nu\ell^\pm\nu jj$  signal is only larger by a factor of three. The rates are thus too small for this channel to be useful. The channel is more promising at the LHC, in particular for a Higgs boson in the mass range  $M_H \sim 160\text{--}180$  GeV, where it decays almost 100% of the time into  $WW$  final states, and where the production cross section is still large. Detailed simulations have shown that a significance  $S/\sqrt{B} \gtrsim 5$  can be obtained in the channel  $pp \rightarrow HW \rightarrow \ell^\pm\nu\ell^\pm\nu jj$  or  $3\ell$  with a high luminosity  $\mathcal{L} = 100 \text{ fb}^{-1}$  [399].
- $H \rightarrow ZZ^{(*)}$ : has a too small branching ratio for  $M_H \lesssim 180$  GeV, when one of the  $Z$  bosons is virtual. Above the  $ZZ$  threshold, the  $HV$  production cross section is very small at the Tevatron. At the LHC, the cross section is still sizable and, once the leptonic branching fractions of the  $Z$  and  $W$  bosons in  $HW$  production have been taken into account, a rate of  $\sim 2 \text{ fb}$  can be obtained for  $M_H \sim 200$  GeV before applying cuts. The few hundred  $\ell\ell\ell\nu jj$  events which could be collected in the high-luminosity regime might allow one to detect the signal. To our knowledge, no simulation has been performed for this channel alone.
- $H \rightarrow \gamma\gamma$ : is a decay mode that is too rare to be useful at the Tevatron but it is the main detection channel at the LHC in the low Higgs mass range for this production process. In fact, it was the first channel in  $HV$  production which has been shown in parton-level analyses to be viable [297,298]. The backgrounds are similar to those which affect the process  $gg \rightarrow H \rightarrow \gamma\gamma(j)$  to be discussed later: the reducible ones are small [400] and the irreducible  $\gamma\gamma\ell\ell + \cancel{E}$  and  $\gamma\gamma\ell\ell$  backgrounds can be suppressed by requiring high- $p_T$  and well-isolated photons and lepton(s). Early analyses have shown that this signal is indeed viable at the LHC for a Higgs boson in the low mass range [209,

210,401] but the signal has a small significance and should be combined with the one from  $pp \rightarrow t\bar{t}H \rightarrow \ell\gamma\gamma + X$  as will be seen shortly. A recent CMS simulation [402] has shown that in one year of LHC at high luminosity, a 5 (4)  $\sigma$  significance can be obtained for the signal if  $M_H \lesssim 135$  (150) GeV.

- $H \rightarrow \tau\tau$ : has a branching ratio of only a few percent for  $M_H \lesssim 135$  GeV and one cannot afford to let the associated gauge bosons to decay leptonically. The  $pp \rightarrow ZH/WH \rightarrow jj\tau\tau$  channel has been considered in a parton-level analysis [303] for the Tevatron with the result that a significant improvement of  $\tau$  identification and a large luminosity might allow one to detect the signal for low mass Higgs bosons if one can trigger on these events. No discussion of this channel has been made in the Tevatron study of Ref. [199] nor at the LHC, though.

**3.7.2.2. The gluon–gluon fusion channel.** This process, having the largest production cross section, has been considered for a long time as being the most efficient one in the search for the Higgs boson at the LHC. However, it appeared quite early that these searches cannot be made in the dominant hadronic  $H \rightarrow b\bar{b}$  and  $H \rightarrow WW/ZZ \rightarrow 4j$  decay channels because of the extremely large QCD-jet backgrounds. The  $H \rightarrow \tau^+\tau^-$  signature in the low Higgs mass range is also very difficult to extract at the LHC [and also at the Tevatron] because of these backgrounds. One then has to rely on rare Higgs decays which provide clean signatures involving photons and/or leptons for which the backgrounds are smaller but far from being negligible.

- $H \rightarrow \gamma\gamma$ : has been proposed rather early [296,333] and is the “silver” detection channel for a Higgs boson with a mass below 150 GeV [403]. The reducible QCD background from jets faking photons is huge and a rejection factor of  $\mathcal{O}(10^6)$  is needed to bring it down to the level of the irreducible one from direct  $q\bar{q} \rightarrow \gamma\gamma + X$  production and the loop induced channel  $gg \rightarrow \gamma\gamma + X$  which provides a 50% contribution. These have been studied in great detail [404] and the state-of-the-art higher-order results are contained in the program DIPHOX [405] which also includes the fragmentation effects. These backgrounds can, in principle, be determined by measuring the two-photon invariant mass distribution  $d\sigma/dM_{\gamma\gamma}$  on both sides of the resonance peak. However, they need to be precisely calculated for the evaluation of the detection significance and also when it comes to measurements of the Higgs properties [386]. A reconstruction efficiency of about 75% can be achieved for a single photon and for  $M_H \sim 130$  GeV, the final signal-to-background ratio is of the order of 1/30 in a window of  $M_{\gamma\gamma} \sim 2$  GeV. However, since the decay is rare, a large amount of luminosity needs to be collected. One could then use, in addition, the  $pp \rightarrow Hj$  signal [353] as the  $gg \rightarrow \gamma\gamma g$  background with a hard jet has been found to be much smaller. In fact, at low luminosities, the combination of all  $H \rightarrow \gamma\gamma$  channels is required: not only the  $pp \rightarrow \gamma\gamma$  and  $pp \rightarrow \gamma\gamma j$  channels but also the channel  $pp \rightarrow \gamma\gamma + \ell$  where the additional lepton comes from the decay of a  $W$  boson in the associated  $HW$  production process discussed previously or in  $t\bar{t}H$  production with  $t \rightarrow bW \rightarrow b\ell\nu$  as will be seen later.
- $H \rightarrow ZZ^{(*)}$ : in the high mass region,  $M_H > 2M_Z$ , the decay  $H \rightarrow ZZ \rightarrow 4\ell$  is the “gold-plated” mode [223, 296,333,334], allowing for Higgs detection up to masses of  $\mathcal{O}(1 \text{ TeV})$  [209,406,407]. The main background is due to continuum  $ZZ$  production which is known rather precisely [389,390] but which can be also directly measured from the side bands of the resonance peak and interpolated to the signal region. For  $M_H \gtrsim 600$  GeV, high enough luminosities are required since  $BR(H \rightarrow ZZ \rightarrow 4\ell) \sim 0.1\%$  is small and the total Higgs width becomes large. To increase the statistics, one can use in addition the  $H \rightarrow ZZ \rightarrow \ell\ell\nu\nu$  decays [335] in which the signal appears as a Jacobian peak in the missing transverse energy spectrum. Additional backgrounds from  $Zj$  events [387], where the  $\cancel{E}_T$  is due to neutrinos from semi-leptonic  $b$  decays for instance, need to be considered [408]. Allowing one of the  $Z$  bosons to be virtual, the discovery reach can be extended down to masses  $M_H \sim 120$  GeV using  $H \rightarrow ZZ^* \rightarrow 4\ell$  decays [409], except in the range  $M_H \sim 2M_W - 2M_Z$  where  $BR(H \rightarrow ZZ^*)$  is too small. In this case, a very sharp peak can be observed in the  $4\ell$  invariant mass distribution. Here, additional backgrounds from  $t\bar{t}$  [391] and  $Zb\bar{b}$  [387] production contribute besides  $ZZ^*$ ,  $Z\gamma^*$  events.
- $H \rightarrow WW^{(*)}$ : leading to  $\ell\ell\nu\nu$  final states turned out to be one of the most promising detection modes of a light Higgs boson at the LHC, i.e. from  $M_H \sim 2M_Z$  down to  $M_H \sim 120$  GeV [410,411], and it is even a potential discovery mode at the Tevatron [339]. Indeed,  $BR(H \rightarrow WW)$  is appreciable if not largely dominating in this mass range and the clean leptonic decays represent 4% of the initial  $WW$  sample. Since the Higgs mass cannot be reconstructed in this process, the signal should be observed from a clear excess of events above backgrounds which need, thus, to be known rather precisely. The most important source is due to  $W$  boson [389] and top quark [391] pair production. The latter can be removed with suitable cuts, while the former one needs, in addition, to take advantage of the characteristic spin correlations in the  $H \rightarrow WW^* \rightarrow \ell\nu\ell\nu$  decays [410,412]: the



azimuthal separation of the charged leptons, for instance, peaks at smaller values for the signal than that for the  $WW$  background. A clear signal has been established at the LHC for Higgs masses down to  $M_H \sim 120$  GeV if enough luminosity is collected [410,411]. At higher Higgs masses, the additional channel  $H \rightarrow WW \rightarrow \ell v j j$ , eventually combined with  $H \rightarrow ZZ \rightarrow \ell \ell j j$  and with the  $H \rightarrow ZZ \rightarrow \ell \ell \nu \bar{\nu}$  channel discussed previously, would extend the discovery reach to masses up to 1 TeV at high luminosities, after reducing the enormous  $t\bar{t}$  and  $W$ +jet backgrounds [413]. At the Tevatron, high  $p_T$  lepton pairs plus missing energy  $\ell \ell \nu \bar{\nu}$  and like-sign dileptons plus jets  $\ell^\pm \ell^\pm j j$  in  $g g \rightarrow H \rightarrow WW^*$ , when combined with similar events in  $p\bar{p} \rightarrow HW/HZ$  associated production, would allow one to detect the Higgs boson at the  $3\sigma$  level for masses up to  $M_H \sim 180$  GeV with  $30 \text{ fb}^{-1}$  data [339].

- $H \rightarrow \tau^+ \tau^-$ : has been proposed long ago [239,336] in associated  $g g \rightarrow H g$  production where the additional jet provides a significant transverse momentum to the  $\tau^+ \tau^-$  system. To our knowledge, the process has not been considered for the LHC in a realistic experimental simulation [at least not in positive terms]; see Ref. [414], however. The process has been discussed for the Tevatron [341] but, again, it needs a better identification of the  $\tau$ -leptons and resolution on the missing  $E_T$  [199].
- $H \rightarrow \mu^+ \mu^-$ : the signal in this very rare decay channel,  $BR(H \rightarrow \mu^+ \mu^-) \sim 10^{-4}$  for  $M_H \sim 115\text{--}140$  GeV, is rather clean but it needs a very large amount of luminosity:  $\mathcal{L} = 300 \text{ fb}^{-1}$  is required for a  $3\sigma$  signal in the Higgs mass range  $M_H \sim 120\text{--}140$  GeV [337] [for lower masses one is still sensitive to the tail of the huge Drell–Yan  $p p \rightarrow \gamma^*/Z \rightarrow \mu^+ \mu^-$  background]. This process is, thus, more appropriate for the SLHC or VLHC.
- $H \rightarrow t\bar{t}$ : suffers from the huge  $t\bar{t}$  continuum background which has to be evaluated in a large mass window as the Higgs total width is large. It has been shown in Refs. [415,416] that the surplus from Higgs events produces a dip-peak structure in the  $g g \rightarrow t\bar{t}$  invariant mass spectrum which could have been observable at the LHC if the Higgs total width were smaller [as in extensions of the SM where the Higgs has reduced couplings to the vector bosons]. This is unfortunate as this process would allow one to probe directly the  $H t\bar{t}$  couplings and to check, for instance, the presence of anomalous interactions and/or CP violation [417,418].

**3.7.2.3. The  $WW/ZZ$  fusion channel.** This channel is not considered as being viable at the Tevatron. In the study of Ref. [199], it has been shown that even with a good resolution on the  $b\bar{b}$  invariant mass,  $\Delta m_{b\bar{b}} = \pm 10$  GeV, the signal to background ratio in the  $p\bar{p} \rightarrow q q b\bar{b}$  channel is of  $\mathcal{O}(10^{-3})$  within a 20 GeV  $m_{b\bar{b}}$  bin. For cleaner decay modes of the Higgs boson, the  $p\bar{p} \rightarrow H q q$  production cross section is too small to be useful: for  $\mathcal{L} \sim 10 \text{ fb}^{-1}$  for instance, only two  $H \rightarrow \gamma\gamma$  events and four dileptons events from  $H \rightarrow \tau^+ \tau^-$  are expected before acceptance cuts are applied.

At the LHC, the cross section is two orders of magnitude larger and the double forward jet tagging as well as the central soft-jet vetoing [the latter still needs more studies to be more firmly established] discussed previously helps in drastically suppressing the various large backgrounds. Applying the specific vector boson fusion cuts discussed in Section 3.3.3, the signal cross section is still large, a few picobarns for Higgs masses in the range  $M_H = 100\text{--}200$  GeV, while the signal-to-background ratio is of order one. In addition, these specific cuts allow one to distinguish between this mechanism and the  $g g \rightarrow H + 2j$  process as discussed in Section 3.4.4 [only  $\sim 10\%$  of the latter is left after cuts]. Adding the fact that it is theoretically rather clean, since the  $K$ -factors, the renormalization and factorization scale dependence as well as the PDF uncertainties are rather small, this process will thus play a key role when it comes to extracting the Higgs couplings to the SM particles at the LHC. For this purpose all possible decay channels of the Higgs boson must be considered.

- $H \rightarrow \tau^+ \tau^-$ : is a promising channel for  $M_H \sim 120\text{--}140$  GeV if enough luminosity,  $\mathcal{L} \sim 30 \text{ fb}^{-1}$ , is available. This has been established first with parton-level analyses [324] which were later confirmed by detector simulations [215, 419,420]. In particular, for  $M_H \sim 125$  GeV, a statistical significance of 2.3, 2.5 and  $\sim 4.5\sigma$  can be achieved in the channels  $q q H \rightarrow q q \tau \tau \rightarrow q q e e / \mu \mu + \cancel{E} + X$ ,  $q q e \mu + \cancel{E} + X$  and  $q q \ell h + \cancel{E} + X$ , respectively, for the luminosity quoted above [419], leading to a combined significance of  $\sim 6\sigma$ . The  $\tau^+ \tau^-$  invariant mass can be determined at the level of 10% which would allow the measurement of the backgrounds [the major ones being QCD and electroweak  $Z j j$  production with  $Z \rightarrow \tau^+ \tau^-$ , in addition to the usual  $V V$  and  $t\bar{t}$  processes] from the side bands.  $\tau$ -polarization effects [421] are useful to discriminate the decays  $H \rightarrow \tau^+ \tau^-$  from the Drell–Yan  $\gamma^*, Z^* \rightarrow \tau^+ \tau^-$  background.
- $H \rightarrow \gamma\gamma$ : as shown in a parton-level analysis [323], this is a rather clean channel with backgrounds which can be measured directly from the data. However, since the decay is rare, the channel needs a high luminosity



and eventually has to be combined with other production processes [such as the  $gg \rightarrow H \rightarrow \gamma\gamma(j)$  and  $pp \rightarrow WH \rightarrow \ell\gamma\gamma$  channel discussed previously] to allow for a significance that is larger than  $5\sigma$  for masses below  $M_H \lesssim 150$  GeV. For instance, in the CMS simulation performed in Ref. [422] and where only the irreducible  $\gamma\gamma jj$  background has been included with an assumed two-photon invariant mass window of  $\pm 3$  GeV, it has been found that a statistical significance of  $3\text{--}5\sigma$  can be obtained in the mass range  $M_H = 115\text{--}140$  GeV with  $\mathcal{L} = 30 \text{ fb}^{-1}$  data.

- $H \rightarrow WW^{(*)}$ : although feasible and competitive [325], this channel might prove to be rather difficult since one cannot reconstruct the Higgs mass peak and, thus, measure the background from the side bands. The most important backgrounds,  $pp \rightarrow t\bar{t} + \text{jets}$  and  $WWjj$  production, need therefore to be known precisely; QCD+EW  $\tau\tau jj$  production [387] can be removed with suitable cuts. Recently, this mode has also been studied experimentally and the prospects are rather good [215,423,424]. In the ATLAS analysis of the  $qqH \rightarrow qq\ell\nu\ell\nu$  channel [215], the signal [with the usual specific vector boson fusion cuts, the contributions of the  $pp \rightarrow WH, ZH$  and  $t\bar{t}H$  processes to this topology are small] and the  $t\bar{t}$  plus zero, one and two-jet backgrounds [the other important background,  $pp \rightarrow \gamma^*/Z + X$  with  $Z \rightarrow \tau^+\tau^-$ , can be rejected by requiring a high  $\ell\ell\nu$  transverse mass] have been studied. It has been shown that a significance larger than  $3\sigma$  can be obtained for a luminosity of  $\mathcal{L} = 10 \text{ fb}^{-1}$  in both the  $e\mu + X$  and  $ee/\mu\mu + X$  channels in the Higgs mass range above  $M_H \sim 130$  GeV, i.e. when  $BR(H \rightarrow WW^*)$  is large enough. Combining these channels with the  $\ell\nu jj$  mode [and with the standard  $\gamma\gamma$  and  $ZZ^*$  channels], one then obtains a  $\sim 5\sigma$  significance for the  $M_H$  and  $\mathcal{L}$  values above [383]. In fact, the  $pp \rightarrow qqH \rightarrow \ell\nu jj$  channel becomes very powerful at higher Higgs masses [215,216,424,425]. With a slightly different optimization of the cuts from that at low Higgs masses, one can arrive at a signal significance that is larger than that  $5\sigma$  in the entire mass range  $M_H \sim 200\text{--}800$  GeV with a luminosity of  $\mathcal{L} = 30 \text{ fb}^{-1}$  [425].
- $H \rightarrow ZZ$ : this channel has also been considered in experimental simulations [425,426], but it cannot be used below the  $M_H = 2M_Z$  threshold as the  $H \rightarrow ZZ^*$  branching ratio is very small in view of the not so large production rate. In addition, since the rates in the  $H \rightarrow ZZ \rightarrow 4\ell$  channel are also very tiny, one has to consider the final states  $\ell\ell\nu\nu$  and  $\ell\ell jj$ . These processes receive large backgrounds, in particular from the process  $Z + 4j$  in the second case where one has  $S/B \sim 1/3$  at  $M_H \sim 300$  GeV, after all cuts have been imposed. In the high Higgs mass range, these channels can be useful, but they need again very high luminosities. For instance, it has been shown in Ref. [425] that a significance of more than  $5\sigma$  can be achieved for the  $qqH \rightarrow \ell^+\ell^-\nu\nu jj$  signal with a luminosity of  $\mathcal{L} = 30 \text{ fb}^{-1}$  in the Higgs mass window  $M_H \sim 500\text{--}800$  GeV.
- $H \rightarrow \mu^+\mu^-$ : again, the signal in this channel is very clean but the branching ratio for the decay is too small. A large amount of luminosity,  $\mathcal{L} = 0.5\text{--}1 \text{ ab}^{-1}$ , is required for a  $3\sigma$  signal in the Higgs mass range below 140 GeV [327]. This signal should be combined with the  $\mu^+\mu^-$  sample obtained from gluon–gluon fusion discussed previously.
- $H \rightarrow b\bar{b}$ : this channel suffers from a huge  $4j$  QCD background which can possibly be measured using the side bands of the  $b\bar{b}$  invariant mass; in addition, it has a major problem with overlapping events. A preliminary parton-level analysis [328] shows that with reasonable assumptions but with a very large luminosity,  $\mathcal{L} = 600 \text{ fb}^{-1}$ , one can obtain a signal-to-square-root-background ratio of  $S/\sqrt{B} \sim 3$  for a mass  $M_H \sim 120$  GeV. However, it is not yet very clear if it is possible to trigger efficiently on this channel [427].

**3.7.2.4. The  $pp \rightarrow t\bar{t}H$  channel.** Finally, Higgs production in association with top quarks has a strongly decreasing cross section with increasing  $M_H$  which makes the process useful only in the low mass range,  $M_H \lesssim 135$  GeV, when the  $\gamma\gamma$  and  $b\bar{b}$  Higgs decays are relatively important [see below, however]. In addition, one needs to have at least one of the  $W$  bosons from  $t \rightarrow bW$  which decays leptonically, to trigger efficiently on the events and suppress the QCD backgrounds. Since the rates are rather low, a large luminosity is required, in particular at the Tevatron.

- $H \rightarrow b\bar{b}$ : associated Higgs production with  $t\bar{t}$  pairs [358] is the only channel in which it has been firmly established that the Higgs decays into  $b\bar{b}$  pair can be extracted from the backgrounds at the LHC [395]. A clear evidence of the  $4b$  tagged jet and lepton signal above the  $W + \text{jets}$  and  $t\bar{t} + jj$  backgrounds [ $b$ -tagging is of course crucial here] can be obtained for  $M_H \lesssim 130$  GeV if enough luminosity,  $\mathcal{L} \gtrsim 100 \text{ fb}^{-1}$ , is collected [428]. A clear reconstruction of the  $H \rightarrow b\bar{b}$  mass peak is difficult because of the combinatorial background from the signal itself and the reconstruction of the top quark decays might be needed. The fully hadronic final state  $pp \rightarrow t\bar{t}H \rightarrow q\bar{q}q\bar{q}b\bar{b}b\bar{b}$  would double the number of  $pp \rightarrow t\bar{t}H$  signal events [429] but one still needs a proper evaluation of the eight jet QCD background. At the Tevatron, the channel is more challenging as the production rate is very small but a signal might be visible if a very high enough luminosity is collected [199,362].

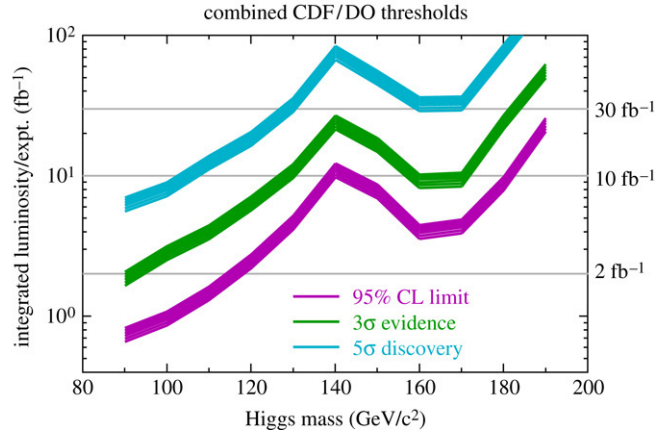


Fig. 3.48. The integrated luminosity required per experiment at the Tevatron, to either exclude a SM Higgs boson at 95% CL or observe it at the  $3\sigma$  or  $5\sigma$  level; from Ref. [199].

- $H \rightarrow \gamma\gamma$ : the decay is too rare for the Tevatron, but it can be detected at the LHC when an additional lepton from the  $t \rightarrow bW$  decay is present [356]. The process, again, gives a narrow mass peak which is visible for  $M_H \lesssim 140$  GeV when the  $pp \rightarrow t\bar{t}H$  production rate and the  $H \rightarrow \gamma\gamma$  branching ratio are sizable enough [356]. With the additional charged lepton, the backgrounds are manageable [357] after suitable cuts [it can also be measured from the side bands], but the statistics have to be added to those obtained in the search of the  $\gamma\gamma$  peak in the three other Higgs production channels  $pp \rightarrow H \rightarrow \gamma\gamma, \gamma\gamma + j$ ,  $pp \rightarrow qqH \rightarrow qq\gamma\gamma$  and  $pp \rightarrow HW \rightarrow \gamma\gamma\ell\nu$  to obtain a significant signal at moderate luminosities.
- $H \rightarrow WW^{(*)}$ : with  $\ell\ell\nu\nu$  final states, has been suggested recently to extend the reach of the  $t\bar{t}H$  process to Higgs masses above  $\sim 140$  GeV [360]. This mode receives very large  $t\bar{t}Wjj$  and  $t\bar{t}\ell\ell + \text{jet}$  backgrounds [and smaller ones from  $t\bar{t}WW$  and  $t\bar{t}t\bar{t}$  final states] which need to be accurately determined as the invariant Higgs mass peak cannot be reconstructed and one would have to rely on a counting of the signal versus the background events. It has been recently shown that a signal can be observed [430] but further investigations are needed to confirm that the backgrounds can be indeed reduced to a low level.
- $H \rightarrow ZZ^*$  has been discussed in Ref. [359] but it has too small rates for  $M_H \lesssim 2M_Z$  if leptonic  $Z$  decays are selected; to our knowledge, no simulation for this channel is available.
- $H \rightarrow \tau\tau$ : this channel has also been discussed [361] in a parton-level analysis. It seems extremely challenging and, again, no detailed experimental simulation has been performed.

### 3.7.3. Discovery expectations at the Tevatron and the LHC

At the Tevatron, the required luminosity to discover or exclude a SM Higgs boson, combining all channels in the processes  $p\bar{p} \rightarrow HV$  and  $gg \rightarrow H$  discussed previously, and the results of both CDF and DØ experiments, are shown in Fig. 3.48 as functions of  $M_H$  [199]. With  $10 \text{ fb}^{-1}$  luminosity per experiment, a  $3\sigma$  evidence for a Higgs boson can be achieved for  $M_H \lesssim 125$  GeV and, in the absence of any signal, a 95% CL exclusion limit can be set up to Higgs masses of order 180 GeV. However, for discovery, only  $30 \text{ fb}^{-1}$  data per experiment will allow one to observe a  $5\sigma$  signal for  $M_H \lesssim 130$  GeV, slightly above the LEP2 Higgs mass bound. Unfortunately, these large luminosities are not expected to be reached in Run II.

At the LHC, the significance of the signals in the various Higgs production and decay channels are shown as functions of  $M_H$  in Figs. 3.49 and 3.50. The ATLAS plot in the left-hand side of Fig. 3.49 shows the significance for an integrated luminosity of  $\mathcal{L} = 100 \text{ fb}^{-1}$  in the “standard” search channels where the vector boson fusion processes are not yet included. The detection in this case relies mostly on the  $gg \rightarrow H$  production mechanism with the decays  $H \rightarrow \gamma\gamma$ ,  $WW^{(*)}$  and  $ZZ^{(*)}$  [where one of the vector bosons is allowed to decay hadronically in the high Higgs mass range], supplemented by the processes  $pp \rightarrow t\bar{t}H$  with  $H \rightarrow \gamma\gamma, b\bar{b}$  and  $pp \rightarrow WH$  with  $H \rightarrow \gamma\gamma$ . As can be seen, the significance is above 10 in the entire Higgs mass range when the various channels are combined. The significance is the smallest in the low mass range,  $M_H \lesssim 130$  GeV, when the  $H \rightarrow VV^*$  decays are not yet dominant. This is exemplified in the right-hand side of the figure where the significance is shown in the mass range

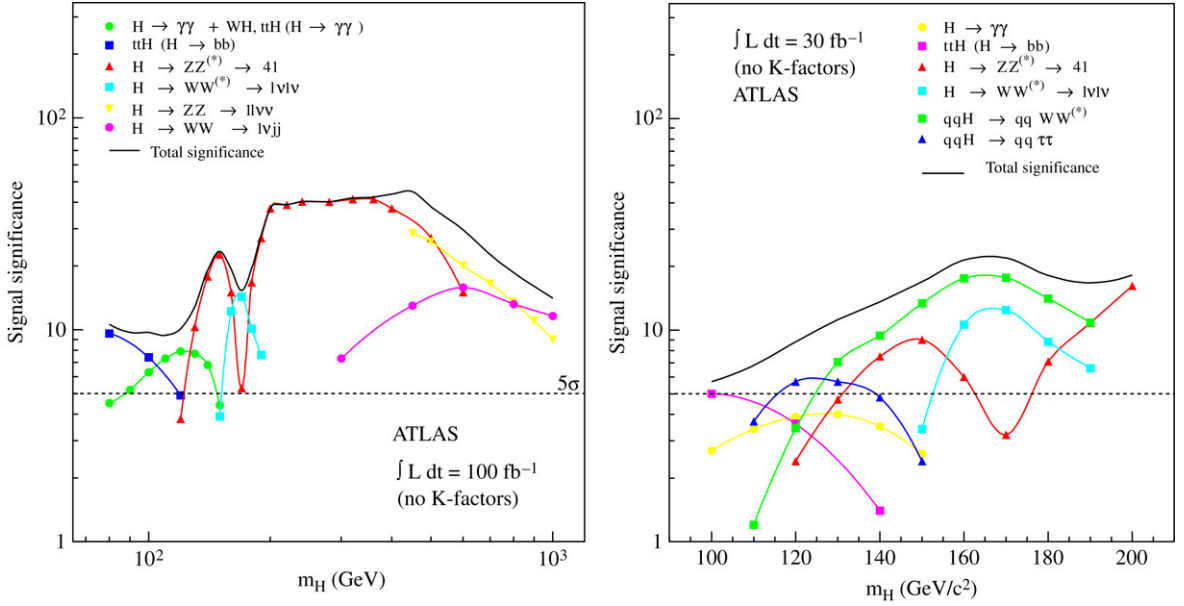


Fig. 3.49. The significance for the SM Higgs boson discovery in various channels in ATLAS as functions of  $M_H$ . Left: the significance for 100 fb<sup>-1</sup> data and with no vector boson fusion channel included and right: for 30 fb<sup>-1</sup> data in the  $M_H \leq 200$  GeV range with the  $qq \rightarrow qqH$  channels included [215].

below  $M_H = 200$  GeV but with the luminosity  $\mathcal{L} = 30$  fb<sup>-1</sup> which is expected at an earlier stage. The updated analysis now includes the vector boson fusion channels with the decays  $H \rightarrow \tau\tau$  and  $H \rightarrow WW^*$  which lead to a substantial increase of the total significance. Note that the  $K$ -factors, which would have significantly increased the signal for the  $gg \rightarrow H$  process that is mostly used at high  $M_H$ , have unfortunately not been included [see the discussion below].

The CMS plot in Fig. 3.50 shows the integrated luminosity that is needed to achieve a 5σ discovery signal in the various detection channels. Here, the vector boson fusion process with all relevant Higgs decays,  $H \rightarrow \gamma\gamma, \tau\tau, WW^{(*)}, ZZ^{(*)}$ , has been included [together with the  $K$ -factors for the  $gg \rightarrow H$  process]. As can be seen, a minimal luminosity of 10 fb<sup>-1</sup> is necessary to cover the low Higgs mass range down to  $M_H \sim 115$  GeV and the high mass range up to  $M_H \sim 800$  GeV when all channels are combined. One can see also that the vector boson fusion channels add value in the entire Higgs mass range. In particular, the  $qq \rightarrow Hqq$  processes with  $H \rightarrow WW, ZZ$  are also very useful in the high Higgs mass range.

Thus, the SM Higgs boson in its entire mass range will be found at the LHC provided that a luminosity larger than  $\int \mathcal{L} = 30$  fb<sup>-1</sup> is collected and the performances of the detectors are as expected. For higher luminosities, this can be done in various and sometimes redundant channels, therefore strengthening the signal and providing great confidence that it is indeed a scalar Higgs boson which has been observed. However, at low luminosities, and in particular in the low Higgs mass range  $M_H \lesssim 135$  GeV, several channels must be combined in order to establish a clear evidence for the Higgs particle. The interesting question which can be asked is this: at which stage will this integrated luminosity be collected?

Before closing this section, let us make a digression about the  $K$ -factors. The inclusion of the higher-order radiative corrections to the Higgs production cross sections and distributions, which is theoretically indispensable to stabilize the scale dependence and to allow for precise predictions as it has been discussed at length in the previous sections, can be also very important in the experimental analyses. Indeed, not only they increase [in general] the size of the discovery signals and, thus, their significance, but they also can change the kinematical properties of the processes under study, leading to different selection efficiencies and, thus, to a different number of collected events. This is particularly the case in the  $gg \rightarrow H$  process where large  $K$ -factors appear and where the Higgs transverse momentum is generated at higher orders, when additional jets which balance this  $p_T$  are produced.

Of course, the  $K$ -factors can be included for the signal only if they are also available for the backgrounds and there are at least two situations in which this holds:

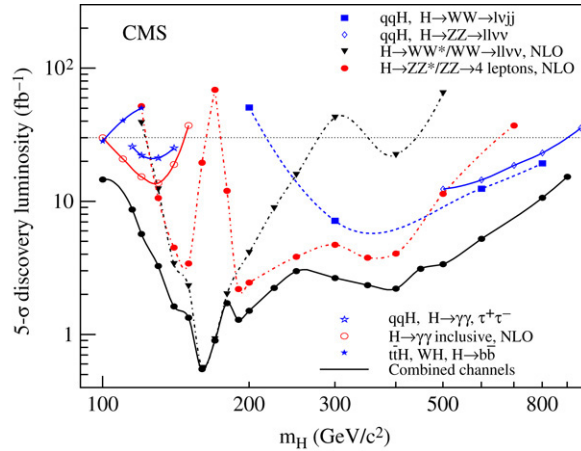


Fig. 3.50. The required integrated luminosity that is needed to achieve a  $5\sigma$  discovery signal in CMS using various detection channels as a function of  $M_H$  [216].

- (i) The signal appears as a narrow peak in an invariant mass distribution and, thus, the corresponding backgrounds can be precisely measured from the side bands and safely extrapolated to the signal region. This is the case of the important  $H \rightarrow \gamma\gamma$  and  $H \rightarrow ZZ^{(*)} \rightarrow 4\ell$  detection channels for instance.
- (ii) When estimates of signal significances are made before having the data or in the case where the invariant Higgs mass peak cannot be reconstructed and one would have to rely on a counting of the number of signal versus background events, the  $K$ -factors can be included if the backgrounds are also known at the same level of accuracy as the signal. This is clearly the case for many background processes such as  $\gamma\gamma$ ,  $WW$ ,  $ZZ$  and  $tt$  production which are known at least to NLO accuracy.

Furthermore, the  $K$ -factors should not only be implemented in the total normalization of the signal and backgrounds, but also in the various kinematical distributions when they are strongly affected by the higher-order corrections.<sup>31</sup> Ideally, this has to be performed at the level of Monte Carlo event generators which are required in practice to obtain a realistic final state with fragmented particles and underlying events. This is not a trivial task and there are many ongoing discussions on this topic; see Ref. [385] as an example. Fortunately, besides the fact that NLO parton-level Monte Carlo programs start to appear [265,278,329], this can be performed in an effective way even in MC event generators [431,432]: differential effective  $K$ -factors can be defined for relevant kinematical variables and used to reweight individual events with reconstructed jets coming from a LO Monte Carlo event generator.<sup>32</sup>

Thus, all  $K$ -factors [which have been determined after a very hard theoretical work] should ultimately be included in the experimental analyses as they allow a more accurate prediction of the discovery potential and often lead to a better cut optimization. Apparently, we are finally heading in this direction.

#### 3.7.4. Determination of the Higgs properties at the LHC

Once a convincing signal for a Higgs boson has been established, the next step would be to determine its properties in all possible details and to establish that the particle is indeed the relic of the electroweak symmetry breaking mechanism and that it has the features that are predicted in the SM, that is: it is a spin-zero particle with  $J^{PC} = 0^{++}$  quantum numbers and that it couples to fermions and gauge boson proportionally to their masses. Ultimately, the

<sup>31</sup> This is not always the case. In Ref. [431], the search sensitivity in the process  $gg \rightarrow H \rightarrow ZZ \rightarrow 4\ell$  has been shown to depend mainly on the signal and background cross sections as well as on the detector performance and the selection cuts and not, for instance, on additional jet activity. A simple scaling of the signal and background rates with their respective  $K$ -factors leads, therefore, to reasonable results. It has been shown that in this particular case, one needs 30%–35% less integrated luminosity to achieve a given signal significance when the  $K$ -factors are included.

<sup>32</sup> For instance, in Ref. [432], the channel  $gg \rightarrow H \rightarrow WW \rightarrow \ell\nu\ell\nu$  has been considered and the higher-order QCD corrections have been taken into account by using this reweighting procedure, allowing the combination of event rates obtained with the PYTHIA event generator with the most up-to-date theoretical predictions for the  $p_T$  spectra of the Higgs signal and the corresponding  $WW$  background. An experimental effective  $K$ -factor of  $\sim 2$  has been obtained in the range  $M_H = 140$ – $180$  GeV, which is only about 15% smaller than the theoretical inclusive  $K$ -factor. This led to a considerable increase of the statistical significance of the Higgs discovery in this specific channel.

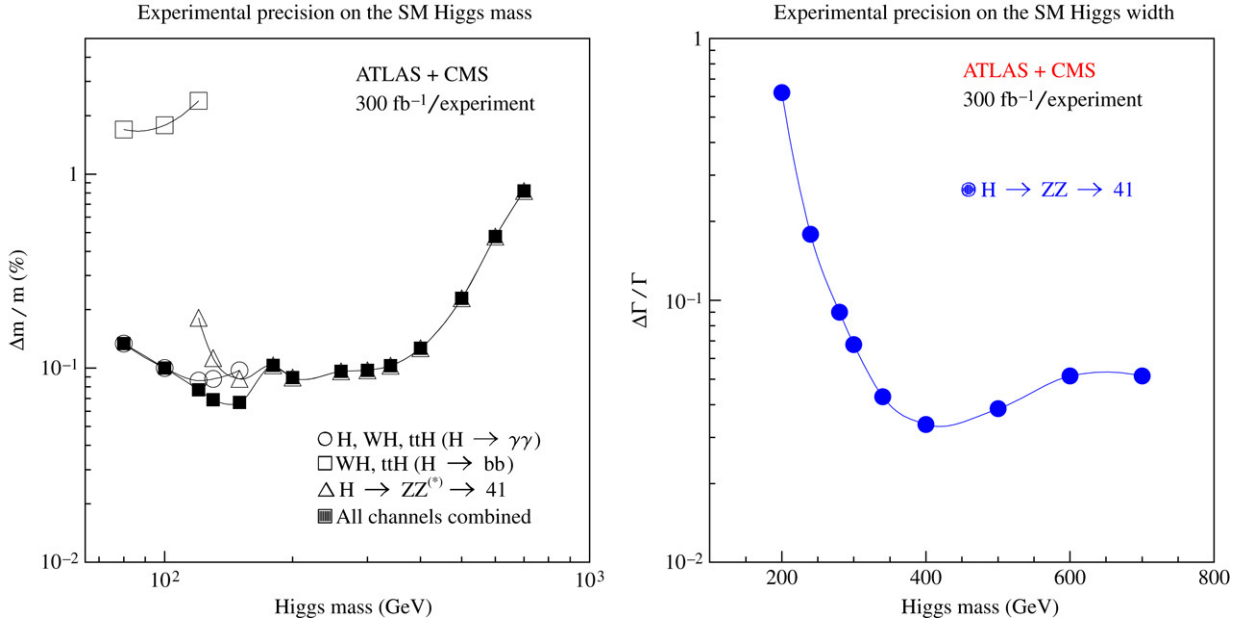


Fig. 3.51. Expected errors on the measurement of the Higgs boson mass (left) and total decay width (right) at the LHC as a function of  $M_H$ , combining both ATLAS and CMS with a luminosity of 300 fb<sup>-1</sup> per experiment; from Ref. [434].

scalar Higgs potential responsible for the symmetry breaking should be reconstructed by precisely measuring the trilinear and quartic Higgs self-couplings. At the LHC, several important measurements can be performed as is briefly summarized below.

**3.7.4.1. The Higgs mass and total decay width.** The Higgs mass can be measured with a very good accuracy [433]. In the range below  $M_H \lesssim 400$  GeV where the total width is not too large, a relative precision of  $\Delta M_H / M_H \sim 0.1\%$  can be achieved in the channel  $H \rightarrow ZZ^{(*)} \rightarrow 4\ell^\pm$  if 300 fb<sup>-1</sup> luminosity is collected by ATLAS and CMS. This is shown in Fig. 3.51 where the relative precision is displayed as a function of  $M_H$  and where the statistical and some systematical errors are included [434].

In the low Higgs mass range, a slight improvement can be obtained by reconstructing the sharp  $H \rightarrow \gamma\gamma$  peak. In the range  $M_H \gtrsim 400$  GeV, the precision starts to deteriorate because of the smaller production rates which increase the statistical error. However a precision of the order of 1% can still be achieved for  $M_H \sim 700$  GeV if theoretical errors, such as width effects, are not taken into account.

Using the same process,  $H \rightarrow ZZ \rightarrow 4\ell^\pm$ , the total decay width of the Higgs boson can be measured for masses above  $M_H \gtrsim 200$  GeV when it is large enough to be resolved experimentally. While the precision is rather poor near this mass value, approximately 60%, it improves to reach the level of  $\sim 5\%$  around  $M_H \sim 400$  GeV and the precision remains almost constant up to a value  $M_H \sim 700$  GeV [433]. This is shown in the right-hand side of Fig. 3.51 where the relative precision on  $\Gamma_H$  is displayed as a function of  $M_H$  with 300 fb<sup>-1</sup> luminosity for the combined ATLAS and CMS experiments [434].

**3.7.4.2. The Higgs spin and parity quantum numbers.** As seen previously, if a high enough luminosity is collected at the LHC, a Higgs boson in the low mass range,  $M_H \lesssim 135$  GeV, will be detected through its  $H \rightarrow \gamma\gamma$  decay mode. This observation will immediately rule out the spin possibility  $J = 1$  by the Yang–Landau theorem, and will fix the charge conjugation to be positive  $C = +$  [435]. This argument cannot be generalized to Higgs production in the  $gg$  fusion mechanism or to Higgs decays into gluons,  $gg \leftrightarrow H$ , since gluons cannot be reasonably distinguished from light quark jets.

For higher Higgs masses when the  $\gamma\gamma$  decay becomes too rare, the observation of the Higgs boson in the decays  $H \rightarrow WW^*, ZZ^*$  provides some information. Indeed, as discussed in Section 2.2, these decays are sensitive to the spin-zero nature of the Higgs boson, if one of the gauge bosons is virtual. The invariant mass ( $M_*$ ) spectrum



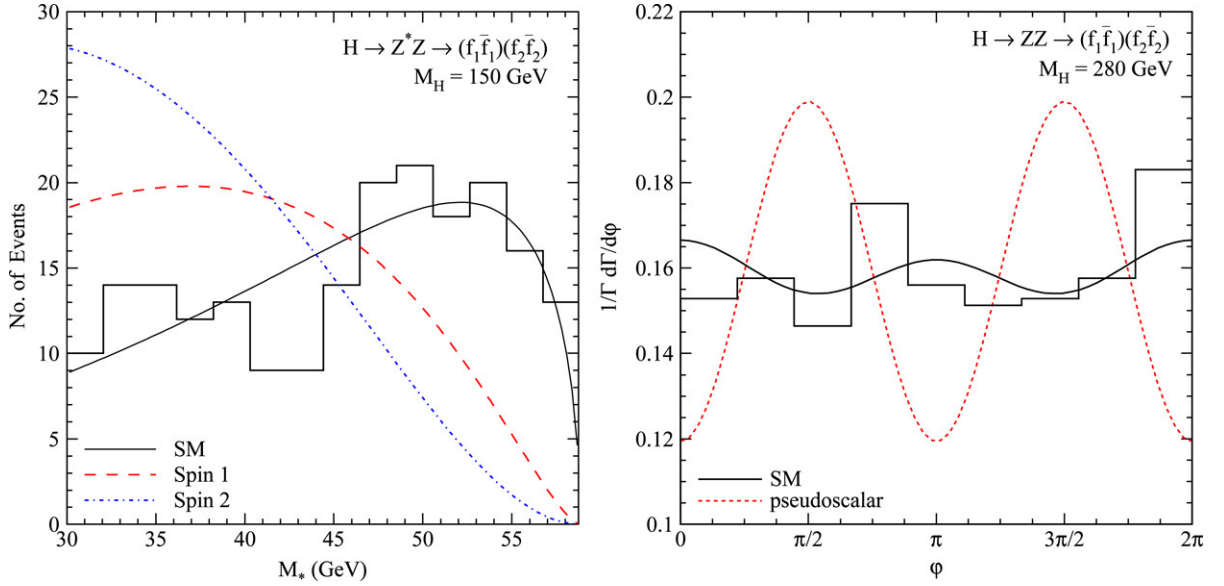


Fig. 3.52. The threshold behavior of the differential distribution  $d\Gamma/dM_*$  for the SM Higgs and two spin examples of  $J = 1$  and  $2$  for  $M_H = 150$  GeV (left) and the azimuthal distributions  $d\Gamma/d\phi$  for the SM and pseudoscalar Higgs bosons for  $M_H = 280$  GeV (right). The histograms have been obtained with  $\int \mathcal{L} dt = 300 \text{ fb}^{-1}$  at the LHC, with efficiencies and cuts included according to an ATLAS simulation of Ref. [436]; from Ref. [155].

of the off-shell gauge boson in  $H \rightarrow VV^*$ , see Eq. (2.32), is proportional to the velocity  $d\Gamma/dM_* \sim \beta \sim \sqrt{(M_H - M_V)^2 - M_*^2}$ , and therefore decreases steeply with  $M_*$  just below the kinematical threshold; see Fig. 2.12. This is characteristic of a spin-zero particle decaying into two-vector bosons, and rules out all spin assignments except for two cases,  $J^P = 1^+$  and  $2^-$ . This is shown in the left-hand side of Fig. 3.52 where the threshold behavior of  $d\Gamma/dM_*$  is displayed for the  $\sim 200$  signal events which are expected for  $M_H = 150$  GeV and  $\mathcal{L} = 300 \text{ fb}^{-1}$  [histogram] and compared with the prediction for the SM Higgs and for two examples of spin-1 and -2 cases [155].

The spin correlations, which are useful to discriminate between the signal  $gg \rightarrow H \rightarrow WW^*$  and  $pp \rightarrow WW$  background [410] for instance, can be used to determine the Higgs boson spin at the LHC. In practice, however, the complete final state must be reconstructed and one has to rely on the decays  $H \rightarrow ZZ^* \rightarrow 4\ell$  which have rather low rates. The two remaining configurations  $J = 1^+$  and  $2^-$  which are not probed, as well as the CP-odd  $0^-$  case, can be discriminated against the Higgs spin by looking at the angular distribution in the decays  $H \rightarrow VV^{(*)} \rightarrow 4f$  given in Eq. (2.38), and experimentally observing a  $\sin^2 \theta_1 \sin^2 \theta_3$  correlation and not observing the  $(1 + \cos^2 \theta_{1,3}) \sin^2 \theta_{3,1}$  correlation [140,155].

In fact, the angular correlations are also sensitive to the parity of the Higgs boson as seen in Section 2.2.4 and can discriminate between the CP-even SM Higgs case and the pseudoscalar Higgs case. In particular, the dependence on the azimuthal angle is very different, as it can be seen from Eq. (2.38) and in Fig. 2.13. The same simulations as that previously carried out [155,436] have been performed for  $M_H = 280$  GeV and the distribution  $d\Gamma/d\phi$  is shown in Fig. 3.52 as a function of the azimuthal angle for the 900 expected events at the LHC for this Higgs mass. A clear discrimination between the CP-even and CP-odd cases can be made in this case.

The Higgs CP-properties and the structure of the  $HVV$  coupling can also be determined in the vector boson fusion process,  $qq \rightarrow qqH$ , by looking at the azimuthal dependence of the two outgoing forward tagging jets [437]. The analysis is independent of the Higgs mass and decay modes but might be difficult because of background problems [242,438].

However, there is a theoretical caveat in this type of analyses [439]: if a Higgs boson is observed with substantial rates in channels where it couples to vector bosons, it is very likely that it is CP-even since the  $VV$  couplings of a pure CP-odd state are generated only through loop corrections. The decisive test of the CP-properties should be therefore to verify that the SM Higgs boson is pure CP-even and rule out the small loop induced CP-odd component. This then becomes a very high-precision test which is very challenging at the LHC.



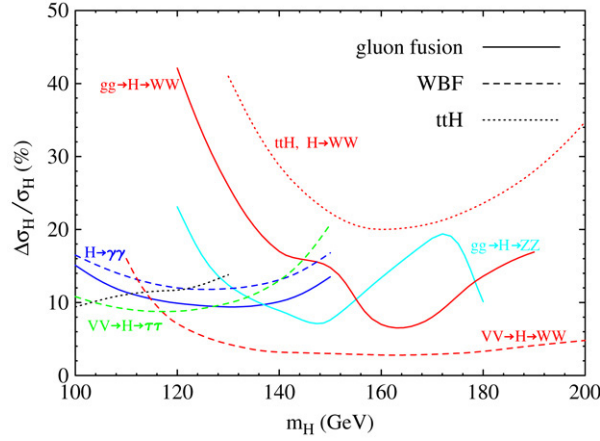


Fig. 3.53. Expected relative errors on the determination of  $\sigma \times \text{BR}$  for various Higgs boson search channels at the LHC with  $200\text{--}300\text{ fb}^{-1}$  data; from Ref. [443]. (For interpretation of the references to colour in this figure legend, the reader is referred to the web version of this article.)

The couplings of the Higgs boson to fermions provide a more democratic probe of its CP nature since in this case, the CP-even and CP-odd components can have the same magnitude. One thus has to look at channels where the Higgs boson is produced and decays through these couplings. Discarding the possibility of  $H \rightarrow b\bar{b}$  and  $\tau^+\tau^-$  decays in the  $gg \rightarrow H$  production channel, which have very large backgrounds, one has to rely on Higgs production in  $pp \rightarrow t\bar{t}H$  with  $H \rightarrow \gamma\gamma$  and eventually  $b\bar{b}$ . Techniques based on the different final state distributions in the production of a scalar or a pseudoscalar Higgs boson have been suggested in Refs. [440,441] to discriminate between the two scenarios or a mixture. However these channels are rather difficult as we have seen previously. With very large luminosities  $\mathcal{L} = 600\text{ fb}^{-1}$  and for a rather light Higgs boson,  $M_H \sim 100\text{ GeV}$ , an equal mixture of CP-even and CP-odd couplings [with a total coupling squared equal to the SM one] can be probed at a few  $\sigma$  levels [441]. But again, this method does not allow one to check precisely the CP-even purity of the SM Higgs boson, at least in this particular channel. Central exclusive-diffractive Higgs production [373,442] might provide the solution; Section 3.6.4.

**3.7.4.3. The measurement of the Higgs couplings at the LHC.** The determination of the Higgs couplings to gauge bosons and fermions is possible at the LHC through the measurement of the cross section times branching ratios,  $\sigma \times \text{BR}$ , given by the event rate in the various search channels [203,443–446]; for earlier analyses see Refs. [208–210]. However, the accuracy in this determination is rather limited because of the small statistics that one obtains after applying the cuts that suppress the large backgrounds which are often plagued with uncertainties, and the various systematical errors such as the common uncertainty in the absolute luminosity. In addition, when one attempts to interpret the measurements, theoretical uncertainties from the limited precision on the parton densities and from the higher-order radiative corrections or scale dependence should be taken into account. Furthermore, the couplings which can be measured will critically depend on the Higgs boson mass. For instance, in the mass range above  $M_H \sim 2M_W$ , only the couplings to gauge bosons can be accessed directly and the  $Ht\bar{t}$  coupling can be probed indirectly.

The cross section times branching ratios which can be measured in various channels at the LHC are shown in Fig. 3.53 for Higgs masses below 200 GeV [443]. The  $gg$  fusion (solid lines), the expectations for weak boson fusion with a parton-level analysis (dashed lines) and the associated  $pp \rightarrow t\bar{t}H$ ,  $H \rightarrow b\bar{b}$  (dotted lines) channels are for a luminosity of  $200\text{ fb}^{-1}$ . The channels  $pp \rightarrow t\bar{t}H \rightarrow t\bar{t}WW^*$  (red-dotted lines) assume a luminosity of  $300\text{ fb}^{-1}$ . In this figure, as well as in the subsequent discussion, only the statistical errors are taken into account. A precision of the order of 10%–20% can be achieved in some channels, while the vector boson fusion process,  $pp \rightarrow Hqq \rightarrow WWqq$ , leads to accuracies of the order of a few percent.

These  $\sigma \times \text{BR}$  can be translated into Higgs partial widths in the various decay channels  $\Gamma_X \equiv \Gamma(H \rightarrow XX)$  [444], which are proportional to the square of the Higgs couplings,  $g_{HXX}^2$ . However, in the case of the vector boson fusion mechanism, which has contributions from  $ZZ \rightarrow H$  and  $WW \rightarrow H$ , the  $HZZ$  and  $HWW$  couplings cannot be disentangled. One then has to assume that they are related by SU(2) symmetry as is the case in the SM [an assumption which can be tested with a 20% accuracy in  $gg \rightarrow H \rightarrow ZZ^*$  versus  $gg \rightarrow H \rightarrow WW^*$  but for large enough  $M_H$ ]. With this assumption, one can perform ratios of partial widths  $\Gamma_{X_i}/\Gamma_{X_j}$ , in which some common theoretical

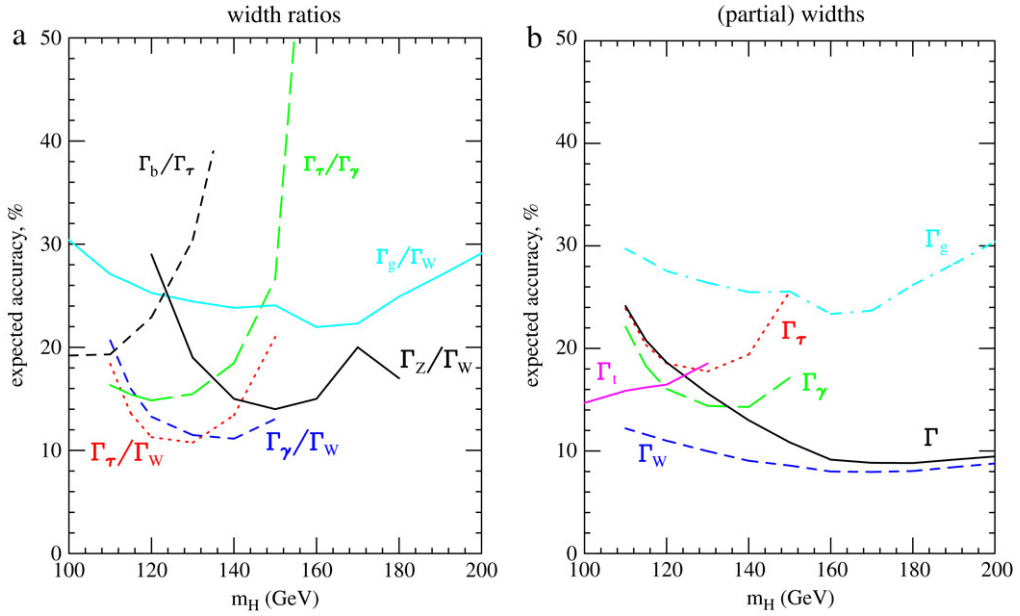


Fig. 3.54. Relative accuracy expected at the LHC with a luminosity of  $200 \text{ fb}^{-1}$  for various ratios of Higgs boson partial widths (left) and the indirect determination of partial and total widths  $\tilde{\Gamma}_i$  and  $\Gamma$  with the assumptions discussed in the text (right); from Ref. [444].

and experimental errors will cancel. This is shown in Fig. 3.54 (left) for a luminosity of  $200 \text{ fb}^{-1}$ , where the relative accuracy on the ratios of  $\sigma \times \text{BR}$  of the production and decay channels discussed above can be formed. Again, measurements at the level of 10%–20% can be made in some cases.

One can indirectly measure the total Higgs width  $\Gamma_H$  and thus derive the absolute values of the partial widths  $\Gamma_X$  by making additional assumptions besides  $g_{HWW}/g_{HZZ}$  universality: (i)  $\Gamma_b/\Gamma_\tau$  is SM-like [with an error of  $\sim 10\%$  corresponding to the uncertainty on the  $b$ -quark mass] since both fermions have the same isospin and (ii) the branching ratio for Higgs decays into unexpected channels is small [in the SM, this error is less than about 3% and corresponds to the missing  $BR(H \rightarrow c\bar{c})$ ] so that  $1 - \Gamma_{X_i}/\Gamma = \epsilon \ll 1$ . The Higgs boson total width  $\Gamma_H$  can be then determined and the partial widths  $\Gamma_X$  as well.

The expected accuracies are shown in the right-hand side of Fig. 3.54. They are at the level of 10%–30% depending on the final states and on  $M_H$ , and translate to an accuracy on the couplings of the order of 5%–15% [444]. Detailed experimental analyses accounting for the backgrounds and for the detector efficiencies, as well as further theoretical studies for the signal and backgrounds, have to be performed to confirm these values.

**3.7.4.4. The Higgs self-coupling.** The trilinear Higgs boson self-coupling  $\lambda_{HHH}$  is too difficult to be measured at the LHC because of the smallness of the  $gg \rightarrow HH$  [and, *a fortiori*, the  $VV \rightarrow HH$  and  $qq \rightarrow HHV$ ] cross sections and the very large backgrounds [447–449]; see also Refs. [450,451] for an earlier and more recent analysis, respectively. A parton-level analysis [448] has been recently performed in the channel  $gg \rightarrow HH \rightarrow (W^+W^-)(W^+W^-) \rightarrow (jj\ell\nu)(jj\ell\nu)$  and  $(jj\ell\nu)(\ell\ell\nu\nu)$  with same sign dileptons, including all the relevant backgrounds which, as one might have expected, are significantly large. At the LHC, the statistical significance of the signals, once most of the backgrounds are removed, is very small, even with an extremely high luminosity. However, it was found that the distribution of the invariant mass of the visible final state particles peaks at much higher values for the backgrounds than for the signal, independently of the value of the trilinear coupling; see the left-hand side of Fig. 3.55.

This observation can be used to set limits on the Higgs self-coupling. For a luminosity of  $300 \text{ fb}^{-1}$  one can check a non-vanishing value of  $\lambda_{HHH}$  at the 95% CL if the Higgs boson mass happens to lie in the range 150–200 GeV. Much more luminosity would be needed to perform a decent measurement; see the right-hand side of Fig. 3.55. For lower Higgs masses,  $M_H \lesssim 140 \text{ GeV}$ , one would have to rely on the dominant decays  $HH \rightarrow 4b$  not to lose too much statistics, but in view of the formidable backgrounds, this process seems to be hopeless at the LHC. The channel  $H \rightarrow b\bar{b}\tau\tau$  is only slightly easier [449].

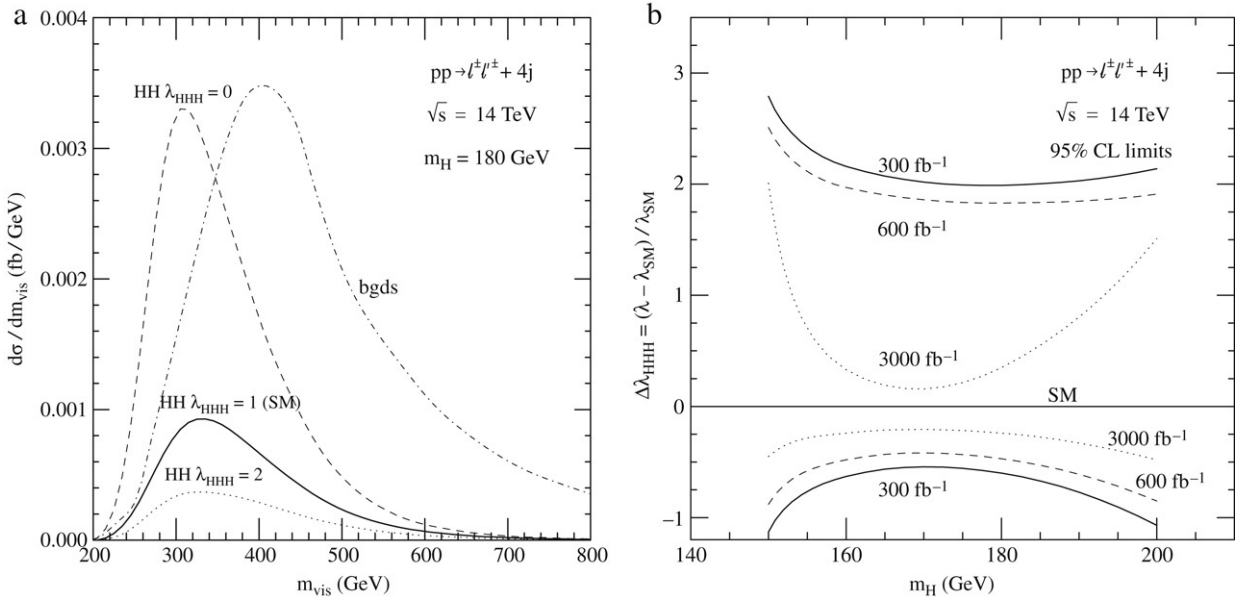


Fig. 3.55. The visible mass distribution of the signal for  $pp \rightarrow \ell^\pm \ell^\pm + 4j$  for  $M_H = 180$  GeV at the LHC for various  $\lambda_{HHH}$  values and for the combined backgrounds (left). Limits achievable at 95% CL for  $\Delta\lambda_{HHH} = (\lambda - \lambda_{SM})/\lambda_{SM}$  in  $pp \rightarrow \ell^\pm \ell^\pm + 4j$  at the LHC for various integrated luminosities (right); from Ref. [448].

### 3.7.5. Higher luminosities and higher energies

Some of the detection signals as well the measurements discussed previously would greatly benefit from an increase of the LHC luminosity. As mentioned in the beginning of this chapter, there are plans to achieve an instantaneous luminosity of  $\mathcal{L} = 10^{35} \text{ cm}^{-2} \text{ s}^{-1}$  at  $\sqrt{s} \simeq 14$  TeV, while retaining the present dipole and magnets. This would allow the collection of  $6 \text{ ab}^{-1}$  for both the ATLAS and CMS experiments after three years of data taking. This SLHC option will allow one to probe rare production and decay processes of the Higgs particle. A brief summary of the interesting physics which can be performed at such a machine in the context of the SM Higgs boson is as follows [202,203]:

- $H \rightarrow \mu^+ \mu^-$ : we have seen that with the present LHC design luminosity, this rare decay can be observed only at the  $3\sigma$  level, even with  $600 \text{ fb}^{-1}$  of data. With  $6 \text{ ab}^{-1}$  data, the process can be observed at the  $5\sigma$  level for  $M_H$  in the range 120–140 GeV and would allow the first measurement of the Higgs coupling to second generation fermions.

- $H \rightarrow Z\gamma$ : this decay has not been mentioned in the previous discussion because it is too rare: if the  $Z$  boson decays leptonically, the branching fraction for this mode is about  $2 \times 10^{-4}$ . With  $6 \text{ ab}^{-1}$  data, the  $gg \rightarrow H \rightarrow Z\gamma \rightarrow \ell\ell\gamma$  process can be observed at the  $\sim 10\sigma$  level for a Higgs boson in the mass range  $M_H = 120$ –150 GeV and would provide complementary information to the  $H \rightarrow \gamma\gamma$  decay channel.

- The measurement of the ratios of Higgs couplings discussed before is mostly statistics limited. Provided that detector performances are not significantly reduced in the high-luminosity environment, these ratios of couplings can be probed at the level of 10% accuracy, and even below in some cases, if the sample of  $6 \text{ ab}^{-1}$  data is collected. This is shown in Fig. 3.56 where the combined ATLAS+CMS accuracies in the direct [with tree-level processes] and indirect measurements [that is, involving the loop induced processes  $gg \rightarrow H$  and  $H \rightarrow \gamma\gamma$  which are indirectly sensitive to the Higgs couplings to the top quark, and in the case of  $H \rightarrow \gamma\gamma$  also to the  $HWW$  coupling] are shown for a luminosity of  $3 \text{ ab}^{-1}$  per experiment and compared to what can be achieved with only  $300 \text{ fb}^{-1}$  data per experiment.

- The most important window that a sample of  $6 \text{ ab}^{-1}$  data could open would be the measurement of the Higgs self-coupling  $\lambda_{HHH}$ . As we have seen previously, this important coupling cannot be probed with the presently planned luminosity. The same parton-level simulation mentioned previously [448] has shown that a signal for the process  $gg \rightarrow HH \rightarrow WWWW \rightarrow \ell^\pm \ell^\pm \nu \nu jjjj$  can be observed with a 5.5 (3.8) significance for  $M_H = 170$  (200) GeV with  $\mathcal{L} = 6 \text{ ab}^{-1}$ , allowing the probe of  $\lambda_{HHH}$ . As can be seen in Fig. 3.55, the trilinear coupling could be measured with a statistical error of about 25% in the Higgs mass window between 160 and 180 GeV in the channel  $pp \rightarrow \ell^\pm \ell^\pm jj$  with  $3 \text{ ab}^{-1}$  data.

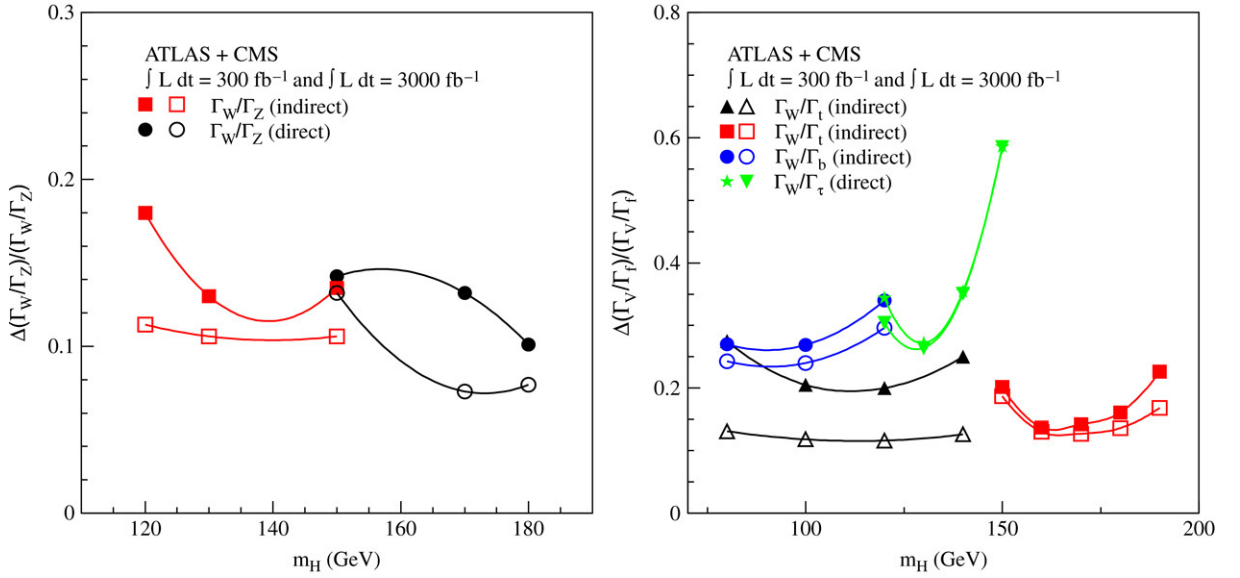


Fig. 3.56. Expected uncertainties on the measured ratios of the Higgs boson widths to final states involving gauge bosons (left) and gauge bosons and fermions (right) as functions of the Higgs mass. The closed (open) symbols are for the two experiments and 3000 (300)  $\text{fb}^{-1}$  data per experiment. Indirect measurements use the loop induced processes  $gg \rightarrow H$  and  $H \rightarrow \gamma\gamma$ ; from Ref. [202].

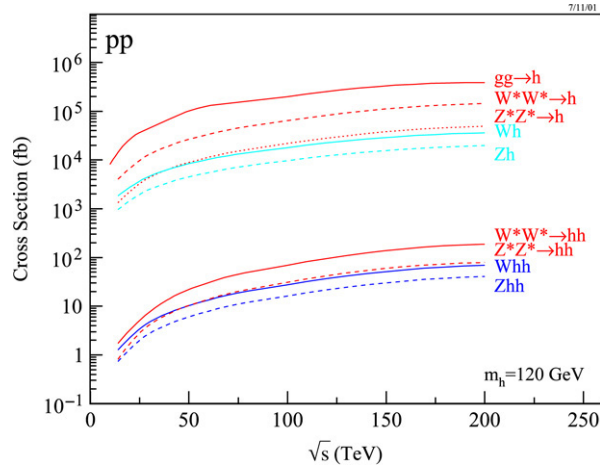


Fig. 3.57. Total cross sections for single and double Higgs boson production in various processes as functions of  $\sqrt{s}$  for  $pp$  collisions and  $M_H = 120$  GeV; from Ref. [203].

The precision of the various measurements discussed above can be improved by increasing the luminosity of the collider but, also, by raising the c.m. energy which leads to an increase of the Higgs boson production rates in most processes. This is explicitly shown in Fig. 3.57, where the cross sections for the various production processes for a single Higgs boson (upper curves) and for Higgs pairs (lower curves) are displayed as functions of  $\sqrt{s}$  for a Higgs mass of 120 GeV. As can be seen, the  $gg \rightarrow H$  cross section for instance increases by almost two orders of magnitude compared to the LHC when the energy of the collider is raised to  $\sqrt{s} = 200$  TeV. The cross sections for Higgs pair production also tremendously increase and for the vector boson fusion processes,  $pp \rightarrow HHqq$ , they reach the level of 0.1 pb at c.m. energies of the order of  $\sqrt{s} = 200$  TeV.

One can then probe the rare decays of the Higgs boson and measure more precisely its couplings to fermions and gauge bosons and its self-coupling, in much the same way as it has been discussed for the SLHC. The accuracies in the determination of some couplings of the SM Higgs boson will for instance start to approach the few percent level.

In fact, with a luminosity of  $100 \text{ fb}^{-1}$ , a VLHC running at  $\sqrt{s} = 50 \text{ TeV}$  will be comparable and in some cases superior to the SLHC. The potential of the two options has been discussed and compared in specific examples in Ref. [203] to which we refer for details. Note, however, that these accuracies cannot compete with those that can be achieved at high-energy  $e^+e^-$  linear colliders [which are expected to operate either before or at the same time] and to which we turn our attention now.

## 4. Higgs production at lepton colliders

### 4.1. Lepton colliders and the physics of the Higgs boson

#### 4.1.1. Generalities about $e^+e^-$ colliders

The  $e^+e^-$  collision [452] is a very simple reaction, with a well-defined initial state and rather simple topologies in the final state. It has a favorable signal to background ratio, leading to a very clean experimental environment which allows one to easily search for new phenomena and to perform very high-precision studies as has been shown at PEP/PETRA/TRISTAN and more recently at SLC and LEP. In particular, the high-precision studies of the properties of the Z boson at LEP1 and SLC, and the determination of the properties of the W boson at LEP2, have laid a very solid base for the Standard Model as was discussed in Section 1.

The physical processes in  $e^+e^-$  collisions are in general mediated by  $s$ -channel photon [for charged particles] and Z boson exchanges with cross sections which scale as the inverse of the center of mass energy squared,  $\sigma \propto 1/s$ , and  $t$ -channel gauge boson or electron/neutrino exchange, with cross sections which may rise like  $\log(s)$ . In these  $t$ -channel processes, only particles which couple directly to the electron are involved at lowest order. The  $s$ -channel exchange is the most interesting process when it takes place: it is democratic, in the sense that it gives approximately the same rates for weakly and strongly interacting matter particles, and for the production of known and new particles, when the energy is high enough.

However, in this channel, the rates are low at high energies and one needs to increase the luminosity to compensate for the  $1/s$  drop of the interesting cross sections. At  $\sqrt{s} \sim 1 \text{ TeV}$ , a luminosity  $\mathcal{L} \sim 10^{34} \text{ cm}^{-2} \text{ s}^{-1}$  is required, which for a run time of  $10^7 \text{ s}$  a year leads to an integrated luminosity of  $\int \mathcal{L} \sim 100 \text{ fb}^{-1}$  per year, to produce  $10^4$  muon pairs as at PEP and PETRA. Such a luminosity is necessary to allow for thorough data analyses, including cuts on the event samples and allowing for acceptance losses in the detectors. At higher energies, the luminosity should be scaled as  $s$  to generate the same number of events.

Because of synchrotron radiation which rises as the fourth power of the c.m. energy in circular machines,  $e^+e^-$  colliders beyond LEP2 must be linear machines [453], a type of accelerator which has been pioneered by the SLC. Two technologies have been proposed for the next linear collider with center of mass energies up to  $\sqrt{s} = 1 \text{ TeV}$  [454]: one based on superconducting acceleration modules at moderate frequency, and another based on warm acceleration structures operating at high radio frequencies. A third and rather new approach [455] is based on a two-beam scheme where high current and low-energy beams create the acceleration field for the high-energy electron–positron beams. This scheme is being followed at CERN and it is hoped that before the end of this decade, the technical concept can be proved; this multi-TeV collider, with presumably some halts at intermediate energies, is thus expected to be a next generation machine.

In the following, we briefly list a few important physics points about the future linear  $e^+e^-$  collider [456–460]:

- One should have the possibility to adjust the c.m. energy of the colliders in order to make detailed studies and, for instance, to maximize the cross section for Higgs boson production in some particular channels or scan the threshold for W boson and top quark pair production, or for some newly produced particles.
- The requirement of a high luminosity is achieved by squeezing the electrons and positrons into bunches of very small transverse size, leading to beamstrahlung which results into beam energy loss and the smearing of the initially sharp  $e^+e^-$  c.m. energy. Since the precise knowledge of the initial state energy is very important for precision studies [in particular in some channels where one would need missing mass techniques], beamstrahlung should be reduced to a very low level, as is already the case in narrow beam designs.
- The longitudinal polarization of the electron [and, to a lesser extent, positron] beam should be easy to obtain as has already been shown at the SLC. Degrees of polarization of the order of 80%–90% and 40%–50% for, respectively, the electron and positron beams are expected. The longitudinal polarization might be important when it comes to



Table 4.1

Main parameters expected for the ILC at the energy  $\sqrt{s} = 500$  GeV; from [453]

Bunch spacing	337 ns
Bunch train length	950 $\mu$ s
Train repetition rate	5 Hz
Beam height at collision	6 nm
Beam width at collision	540 nm
Luminosity	$2 \times 10^{34} \text{ cm}^{-2} \text{ s}^{-1}$
Annihilation rate	$10^5 \text{ ann/s}$
Accelerating gradient	31.5 MV/m
Wall plug efficiency	23%
Site power (500 GeV)	140 MW

making very precise measurements of the properties of Higgs bosons and to suppress some large backgrounds [in particular from  $W$  bosons] to its production signals [461].

- By building a bypass for the transport of the electron and positron bunches, for instance, very high luminosities can also be obtained at energies in the range of 100 GeV. Operating on the  $Z$  boson resonance,  $10^9$   $Z$  bosons can be produced, a sample which is two orders of magnitude larger than the one obtained at LEP1. This GigaZ machine, in particular since longitudinal polarization will be available, could significantly improve the precision tests of the SM which have been performed in the previous decade [462].
- Last but not the least, the linear collider can run in three additional modes. First, one just needs to replace the positron bunches by electron bunches to have an  $e^-e^-$  collider. Then, by illuminating the initial lepton bunches by laser photons, one can convert the original collider into an  $e\gamma$  or  $\gamma\gamma$  collider, with a comparable total center of mass energy and luminosity as the initial lepton collider [463,464]. Higgs particles can be produced as  $s$ -channel resonance at  $\gamma\gamma$  colliders [465,467–469] and this mode will be very useful for addressing problems such as the Higgs boson couplings to photons and its CP-properties. These options, will be also considered in this chapter.

In 2004, the International Technology Recommendation Panel has recommended [453] that the next linear  $e^+e^-$  machine, which should and hopefully will be a joint project, the International Linear Collider (ILC), should be based on superconducting radio-frequency cavities. The machine should, in a first step, run at energies between  $\sqrt{s} = 200$  and 500 GeV with an integrated luminosity of  $500 \text{ fb}^{-1}$  in the four first years, have the possibility of 80% polarized electron beams and two interaction regions with easy switching. In a second phase, the machine should run at an energy of  $\sqrt{s} = 1$  TeV with an integrated luminosity of  $1 \text{ ab}^{-1}$  in four years. As options, the panel recommended that the machine should possibly run in the  $e^-e^-$  mode, have 50% positron polarization, the possibility to operate near the  $M_Z$  and  $2M_W$  thresholds, and the possibility to run in the  $e\gamma$  and  $\gamma\gamma$  modes.

A Global Design Effort (GDE), which is a virtual world laboratory, has been established in 2005 to design, manage the R&D, and make a cost estimate of the machine. It has already proposed some design parameters and, for instance, the main parameters of the beams are summarized in Table 4.1 [453]. The design has not yet been finalised and there are a few parameter sets, such as the bunch charge, the number of bunches, the beam sizes, etc. which can be varied to allow for a flexible operating plan. Note also that only one interaction region is foreseen but the possibility of having two detectors (with the push–pull option) is left. Furthermore, beamstrahlung in such a machine is expected to be small. A detailed Conceptual Design Report for the ILC, which includes a cost estimate, is expected in 2007.

In our study of the physics of the Higgs boson at  $e^+e^-$  linear colliders, we will assume for the numerical analyses three values for the c.m. energy,  $\sqrt{s} = 0.5, 1$  and  $3$  TeV which will correspond to the two phases discussed above and to the subsequent CLIC phase, and an integrated luminosity  $\mathcal{L} \sim 500 \text{ fb}^{-1}$ . We will also consider briefly the GigaZ option and in some detail the option of turning the machine into to a  $\gamma\gamma$  collider, the particularities of which are summarized in the following subsection. Finally, future muon colliders will be discussed in the last section of this chapter.

#### 4.1.2. The photon colliders

The Compton scattering of laser photons with energies  $\omega_0$  in the eV range with high-energy electrons,  $E_e \sim \mathcal{O}(100 \text{ GeV})$ , leads to a tight bunch of back-scattered high-energy photons [463,464]. The kinematics of the process is governed by the dimensionless parameter  $x = 4\omega_0 E_e / m_e^2$ . The fraction of energy carried by the back-scattered



photon,  $y = \omega/E_e$ , is maximal for  $y_{\max} = x/(1+x)$ . The highest energy, compared to the  $e^-$  beam energy is therefore obtained for very large values of the parameter  $x$ . However, to prevent the creation of  $e^+e^-$  pairs in the annihilation of the laser and scattered photons, one demands that  $x \lesssim x_0 = 4.83$ . For this value, the photon collider can have as much as  $\sim 80\%$  of the energy of the original  $e^+e^-$  collider. The scattering angle of the obtained photons is given by  $\theta(y) \simeq m_e(1+x)/E_e \times \sqrt{y_{\max}/y-1}$  and is of the order of a few micro-radians.

The energy spectrum of the back-scattered photon

$$f_c(y) = \sigma_c^{-1} d\sigma_c(y)/dy \quad (4.1)$$

depends on the product of the the mean helicity of the initial electron  $\lambda_e$  and on the degree of circular polarization of the laser photon  $P_\gamma$  with  $-1 \leq 2\lambda_e P_\gamma \leq +1$ . It is defined by the differential Compton cross section [464]

$$\frac{d\sigma_c}{dy} = \frac{\pi\alpha^2}{xm_e^2} [f_0 + 2\lambda_e P_\gamma f_1 + 2\lambda_e P_{\gamma'} f_2 + P_\gamma P_{\gamma'} f_3] \quad (4.2)$$

where the dependence on the polarization of the back-scattered photon  $P_{\gamma'}$  has been retained. In terms of the variable  $r = y/[x(1-y)]$ , the functions  $f_i$  ( $i = 0, \dots, 3$ ) read

$$\begin{aligned} f_0 &= \frac{1}{1-y} + 1 - y - 4r(1-r), & f_1 &= xr(1-2r)(2-y) \\ f_2 &= xr \left[ 1 + (1-y)(1-2r)^2 \right], & f_3 &= (1-2r) \left[ \frac{1}{1-y} + 1 - y \right]. \end{aligned} \quad (4.3)$$

When the polarization of the scattered photon is discarded, the integrated Compton cross section can be cast into the form

$$\begin{aligned} \sigma_c &= \sigma_c^{\text{np}} + 2\lambda_e P_\gamma \sigma_c^{\text{p}} \\ \sigma_c^{\text{np}} &= \frac{\pi\alpha^2}{xm_e^2} \left[ \frac{1}{2} + \frac{8}{x} - \frac{1}{2(1+x)^2} + \left( 1 - \frac{4}{x} - \frac{8}{x^2} \right) \ln(x+1) \right] \\ \sigma_c^{\text{p}} &= \frac{\pi\alpha^2}{xm_e^2} \left[ -\frac{5}{2} + \frac{1}{x+1} - \frac{1}{2(x+1)^2} + \left( 1 + \frac{2}{x} \right) \ln(x+1) \right]. \end{aligned} \quad (4.4)$$

By selecting a given polarization of the initial  $e^-$  and laser beams, one can have different shapes for the energy distribution of the scattered photons: a flat distribution if the electron and the laser have the same polarization, or an almost mono-chromatic distribution peaked at  $y_{\max}$  if they have opposite polarization. The latter scenario is of course very interesting.

Because of the small scattering angle  $\theta$  of the photons, the luminosity of the spectrum depends on the conversion distance, i.e. the distance between the intersecting point of the laser and the electron beam and the interaction point, as well as on the size and shape of the electron beam. A geometrical factor  $\rho = b\theta/a$  takes into account the non-zero conversion distance  $b$  and the radius  $a$  of the assumed round electron beam [typically, the sizes are  $a \sim \mathcal{O}(10^2 \text{ nm})$  and  $b \sim \mathcal{O}(1 \text{ cm})$ ]. If  $\rho$  is much larger than unity, only the photons with high energy can meet at the interaction point, while for  $\rho \ll 1$ , photons with various energies collide and give a rather broad spectrum.

When the Compton back-scattered photons, which we will denote by  $\gamma_1$  and  $\gamma_2$ , are taken as initial states, the cross section for the process  $\gamma\gamma \rightarrow X$  with polarized photons reads

$$d\hat{\sigma}_{\gamma\gamma} = \sum_{i,j=0}^4 \xi_{1i} \xi_{2j} d\hat{\sigma}_{ij} \quad (4.5)$$

in the  $\xi_{1i}$  and  $\xi_{2j}$  photon Stokes parameter basis, with zeroth components such that  $\xi_{10} = \xi_{20} = 1$ . The event rate  $dN$  can be then written as

$$dN = d\mathcal{L} \langle d\hat{\sigma}_{\gamma\gamma} \rangle = d\mathcal{L} \sum_{i,j=0}^3 \langle \xi_{1i} \xi_{2j} \rangle d\hat{\sigma}_{ij} \quad (4.6)$$

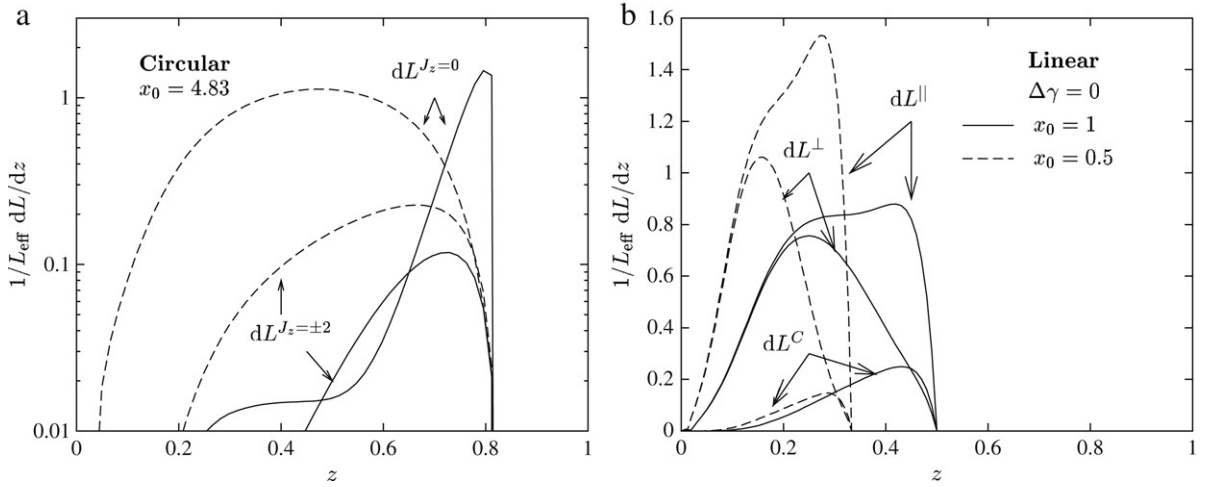


Fig. 4.1. Normalized  $\gamma$  luminosities as functions of  $z = \sqrt{s_{\gamma\gamma}}/\sqrt{s_{e^+e^-}}$  for left: circularly polarized lasers with  $x_0 = 4.83$  and the solid (dashed) lines are for opposite-handed (like-handed) photons and electrons with  $\rho = 3$  (0.6), and right: linearly polarized lasers with  $\Delta\gamma = 0$ ,  $\rho = 0.6$  and  $x_0 = 1$  (0.5) for the solid (dashed) lines. The lasers are assumed to be completely polarized and the electrons 85% longitudinally polarized, and the configurations for both collider arms are the same; from Ref. [469].

where  $d\mathcal{L}$  is the differential  $\gamma\gamma$  luminosity and the average  $\langle\xi_{1i}\xi_{2j}\rangle$  is along the interaction region [only the diagonal terms in the product are relevant in general].

For circularly polarized laser beams, one has for the average Stokes parameters

$$\langle\xi_{12}\xi_{22}\rangle = \xi_{12}\xi_{22}, \quad \langle\xi_{13}\xi_{23}\rangle = -\langle\xi_{11}\xi_{21}\rangle \ll 1 \quad (4.7)$$

so that the event rate can be written in terms of the luminosities corresponding to the  $J_z = 0$  and  $J_z = \pm 2$  scattering channels, as

$$\begin{aligned} dN &= d\mathcal{L}^{J_z=0} d\hat{\sigma}_{J_z=0} + d\mathcal{L}^{J_z=\pm 2} d\hat{\sigma}_{J_z=\pm 2} \\ d\mathcal{L}^{J_z=0} &= \frac{1}{2}d\mathcal{L} (1 + \langle\xi_{12}\xi_{22}\rangle), \quad d\mathcal{L}^{J_z=\pm 2} = \frac{1}{2}d\mathcal{L} (1 - \langle\xi_{12}\xi_{22}\rangle). \end{aligned} \quad (4.8)$$

With this polarization, a broad luminosity spectrum can be achieved by using electrons and laser photons with like-handed helicities and a small value,  $\rho \sim 0.6$ , which leads to low energetic back-scattered photons in the interaction region. In contrast, a sharp spectrum peaking near  $y_{\max}$  can be obtained using opposite-handed electrons and laser photons in a more restrictive interaction region  $\rho \sim 3$ ; see Fig. 4.1 (left). The events in the  $J_z = 0$  ( $J_z = \pm 2$ ) channels can be enhanced (suppressed) by choosing the laser and electron beams so that  $x_0 = 4.83$ , which in addition, maximizes the collider energy.

For linearly polarized laser beams, neglecting  $\rho \neq 0$  effects for simplicity, the average Stokes parameters are

$$\begin{aligned} \langle\xi_{12}\xi_{22}\rangle &\simeq \langle\xi_{12}\rangle\langle\xi_{22}\rangle = 4\lambda_{e^-}\lambda_{e^+}c_1c_2 \\ \langle\xi_{13}\xi_{23} - \xi_{11}\xi_{21}\rangle &\simeq \langle\xi_{13}\rangle\langle\xi_{23}\rangle - \langle\xi_{11}\rangle\langle\xi_{21}\rangle = P_{1t}P_{2t}\ell_1\ell_2 \cos 2(\Delta\gamma) \end{aligned} \quad (4.9)$$

where  $P_{ti}$  are the mean linear laser polarizations while  $c_i$  and  $\ell_i$  are the induced circular and linear polarizations of the back-scattered photons;  $\Delta\gamma$  is the angle between the planes of maximal linear polarization of the two lasers. The circular polarizations  $c_i$  and linear polarizations  $\ell_i$  are large for, respectively, high and low values of the parameter  $x$ , and both increase with  $y$ . The event rate in this case is given by

$$\begin{aligned} dN &= d\mathcal{L}^{\parallel} d\hat{\sigma}_{\parallel} + d\mathcal{L}^{\perp} d\hat{\sigma}_{\perp} + \frac{1}{2}d\mathcal{L}^C (d\hat{\sigma}_{J_z=0} - d\hat{\sigma}_{J_z=2}) \\ d\mathcal{L}^{\parallel} &= \frac{1}{2}d\mathcal{L} (1 + \langle\xi_{13}\xi_{23} - \xi_{11}\xi_{21}\rangle), \quad d\mathcal{L}^{\perp} = \frac{1}{2}d\mathcal{L} (1 - \langle\xi_{13}\xi_{23} - \xi_{11}\xi_{21}\rangle), \quad d\mathcal{L}^C = d\mathcal{L} \langle\xi_{12}\xi_{22}\rangle. \end{aligned} \quad (4.10)$$

For this polarization, one has to make a compromise between having a good separation of the  $\parallel$  and  $\perp$  components, which needs a small value of  $x$ , and having a high energy which needs a larger value since the available energy is proportional to  $x/(x+1)$ .

For more details on the main features of the  $\gamma\gamma$  machines, such as energy, luminosity distributions, polarization, etc., see the reviews given in Refs. [467–469].

#### 4.1.3. Future muon colliders

The concept of  $\mu^+\mu^-$  colliders, although introduced already in the late sixties [470], has been taken very seriously only in the last decade. A Muon Collider Collaboration (MCC) [471,472] has been formed in the US in the mid-nineties to complete the R&D that is required to determine whether a muon collider is technically feasible and, in the case of a positive answer, to propose a design for a First Muon Collider. In the late nineties, the European community joined the project and a study report on the feasibility of a muon collider at CERN has been produced [473]. A three-step scenario for a muon collider is presently foreseen [472,473]:

- (i) A first step would be an intense proton source for producing muons which will be then captured, cooled, accelerated and stored. In the storage ring, they then decay and allow the production of high-intensity and high-quality neutrino beams which could be used to perform detailed studies of neutrino oscillations and neutrino–nucleon scattering, as well as some physics with stopped muons such as the measurement of the muon magnetic and electric dipole moments and the search for some rare  $\mu$  decays.

- (ii) The second step would be a  $\mu^+\mu^-$  collider with a center of mass energy in the range  $\sqrt{s} \sim 100\text{--}200$  GeV. This collider could do the same physics as an  $e^+e^-$  collider and it will be a Higgs factory that would possibly allow one to study in more detail the properties of the Higgs particles that have been produced at the LHC and at the ILC.

- (iii) A final step would be then to operate the muon collider at the maximum possible c.m. energy and to probe the physics of the multi-TeV scale. For instance, energies up to  $\sqrt{s} \sim 7$  TeV could be reached with the facilities that are available at CERN. However, with the present designs [and not to mention the very high luminosities which need to be achieved in this case], the radiation induced by the neutrinos is extremely high for c.m. energies in excess of a few TeV and poses a very serious problem. Major technological developments are therefore required to reach this high-energy step.

In this report, we will be interested only in the second phase of the muon collider, that is, the Higgs factories with c.m. energies  $\sqrt{s} \lesssim 200$  GeV. Compared to an  $e^+e^-$  machine, the main advantages of a muon collider as far as Higgs physics is concerned [474–477], are principally due to the fact that the muon is much heavier than the electron,  $m_\mu/m_e \sim 200$ : the Higgs boson coupling to muons is much larger than the coupling to electrons, yielding significantly larger rates for  $s$ -channel Higgs production at muon colliders,  $\mu^+\mu^- \rightarrow H$  [the production rate in this channel is of course negligible in  $e^+e^-$  collisions].

Another advantage of  $\mu^+\mu^-$  colliders, compared to  $e^+e^-$  colliders, is the very precise knowledge of the beam energy spectrum which would allow for very high-precision analyses of the mass, total width and peak cross section of the produced Higgs resonance. According to the analyses performed in Ref. [472,473], the energy can be tuned with a precision  $\Delta E_b/E_b \sim \times 10^{-6}$  [i.e. 100 keV for  $\sqrt{s} = 100$  GeV] and values ten times smaller seem possible. The small amount of beamstrahlung [which, in  $e^+e^-$  collisions, induces an energy loss of a few percent that is difficult to measure very precisely] and bremsstrahlung [again due to the larger mass of the muon compared to the electron] could lead to a relative beam energy spread or resolution of the order of  $R = \sigma_{E_b}/E_b \sim 10^{-3}$  down to  $R = 3 \times 10^{-5}$  and which could be known with an accuracy of  $\Delta\sigma_{E_b}/E_b \sim 0.5\%$ . Such a small energy spread is very important when performing a scan around the very narrow Higgs resonance,  $\Gamma_H \sim 2$  MeV for  $M_H \sim 100$  GeV. In addition, since synchrotron radiation is also very small, one can still use the available circular machines. The energy calibration can be made by spin precession as the muons that are produced in the weak decays of pions are 100% polarized, leading to a natural longitudinal polarization of approximately 30% which, however, drops to the level of  $\sim 20\%$  due to the handling before injection into the collider. The drawback, compared to  $e^+e^-$  machines, is that it is difficult to maximize this polarization without an important loss in luminosity and that a muon collider cannot be turned into a  $\gamma\gamma$  or  $\mu\gamma$  collider.

Nevertheless, the design of the machine is still at an early stage and many problems remain to be solved [472, 473]. In addition, the delivered luminosity which can be achieved is still uncertain, and it depends strongly on the baseline parameters of the collider; Table 4.2. There is, for instance, a particularly strong dependence on the beam energy resolution. As can be seen from the table, at  $\sqrt{s} = 100$  GeV, the estimates indicate that only

Table 4.2

Possible parameter sets for a  $\mu^+\mu^-$  Higgs factory at  $\sqrt{s} = M_H = 100$  GeV as expected by the MCC [472]; higher-energy machines are also shown for comparison

c.m. energy	3 TeV	400 GeV	100 GeV		
p power (MW)	4	4		4	
$1/\tau_\mu$ (Hz)	32	240		960	
$\mu/\text{bunch}$	$2 \times 10^{12}$	$2 \times 10^{12}$		$2 \times 10^{12}$	
Circumference (m)	6000	1000		350	
$\langle B \rangle$ (T)	5.2	4.7		3	
$n_{\text{turns}}^{\text{effective}}$	785	700		450	
6-D $\epsilon_{6,N} \times 10^{-10}$ ( $\pi \text{m}^3$ )	1.7	1.7		1.7	
$R = \delta p/p$ (%)	0.16	0.14	0.12	0.001	0.003
RMS $\epsilon_T$ ( $\pi$ mm rad)	0.05	0.05	0.085	0.0195	0.29
$\beta^*$ and $\sigma_z$ (cm)	0.3	2.6	4.1	9.4	14.1
$\sigma_r$ ( $\mu\text{m}$ )	3.2	26	86	196	294
Luminosity ( $\text{cm}^2 \text{s}^{-1}$ )	$7 \times 10^{34}$	$10^{33}$	$1.2 \times 10^{32}$	$2.2 \times 10^{31}$	$10^{31}$

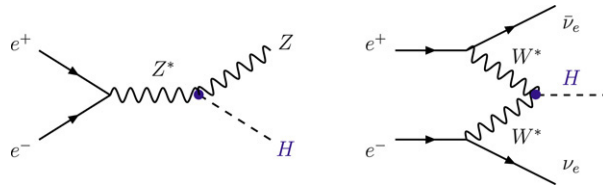


Fig. 4.2. The dominant Higgs production mechanisms in high-energy  $e^+e^-$  collisions.

$\mathcal{L} \sim 10^{31} (10^{32}) \text{ cm}^{-2} \text{ s}^{-1}$  can be obtained for a resolution of  $R = 0.003\%$  (0.1%), leading to an integrated luminosity  $\int \mathcal{L} = 0.1$  (1)  $\text{fb}^{-1}$  per year. The luminosity, however can substantially be increased with energy reaching, for  $R \sim 0.1\%$ , values of the order of  $\mathcal{L} \sim 10^{33} (10^{35}) \text{ cm}^{-2} \text{ s}^{-1}$  for  $\sqrt{s} \sim 0.4$  (3) TeV; see Table 4.2 and the details given in Refs. [472,473].

#### 4.1.4. Higgs production processes in lepton collisions

In  $e^+e^-$  collisions with center of mass energies beyond LEP2, the main production mechanisms for Higgs particles are the Higgs-strahlung process [32,83,89–91] and the  $WW$  fusion mechanism [90,224–227,478,479], depicted in Fig. 4.2,

$$\text{Higgs-strahlung process : } e^+e^- \longrightarrow (Z^*) \longrightarrow Z H \quad (4.11)$$

$$\text{WW fusion process : } e^+e^- \longrightarrow \bar{\nu}\nu (W^*W^*) \longrightarrow \bar{\nu}\nu H. \quad (4.12)$$

There are several other mechanisms in which Higgs bosons can be produced in  $e^+e^-$  collisions: the  $ZZ$  fusion process [224–226,479,480], the radiation off heavy top quarks [481,482] and the double Higgs boson production process either in Higgs-strahlung or  $WW/ZZ$  fusion [236,238,244,483,484]

$$\text{ZZ fusion process : } e^+e^- \longrightarrow e^+e^- (Z^*Z^*) \longrightarrow e^+e^- H \quad (4.13)$$

$$\text{radiation off heavy fermions : } e^+e^- \longrightarrow (\gamma^*, Z^*) \longrightarrow f \bar{f} H \quad (4.14)$$

$$\text{double Higgs production : } e^+e^- \longrightarrow ZHH, \ell\ell HH. \quad (4.15)$$

These are, in principle, higher-order processes in the electroweak coupling with production cross sections much smaller than those of the Higgs-strahlung process and the  $WW$  fusion channel [for  $ZZ$  fusion, only at low energies]. However, with the high luminosity planned for future linear colliders, they can be detected and studied. These processes are extremely interesting since they allow for the determination of some of the fundamental properties of the Higgs particle, such as its self-coupling and its Yukawa coupling to top quarks.

There also other higher-order processes in which Higgs particles can be produced in  $e^+e^-$  collisions, but with even smaller production cross sections than those mentioned previously: associated production with a photon,  $e^+e^- \rightarrow H + \gamma$  [485], loop induced Higgs pair production,  $e^+e^- \rightarrow HH$  [486], associated production with vector bosons,  $e^+e^- \rightarrow VV + H$  [487,488], and associated production with a gauge boson and two fermions,  $e^+e^- \rightarrow VH + f\bar{f}$  [487]. Except possibly for the two latter processes, the cross sections are in general below the femtobarn level and, thus, too small for the processes to be detected at future machines, unless extremely high luminosities are made available.

Higgs particles can be produced as  $s$ -channel resonances [465,466] [among other possibilities which will be also discussed] in the  $\gamma\gamma$  option of future  $e^+e^-$  linear colliders

$$\gamma\gamma \longrightarrow H \quad (4.16)$$

allowing the measurement of the important  $H\gamma\gamma$  coupling. In the  $e\gamma$  option, one can also produce the Higgs boson in the channel  $e\gamma \rightarrow \nu_e W^- H$  [489].

Finally, one can also produce the Higgs boson as an  $s$ -channel resonance at future muon colliders [474,490]

$$\mu^+\mu^- \longrightarrow H. \quad (4.17)$$

In the following sections, we discuss the dominant production processes in some detail and summarize the main features of the subleading processes. We first focus on  $e^+e^-$  linear colliders in the  $e^+e^-$  option, and discuss in more detail the physics potential at the first phase with center of mass energies around  $\sqrt{s} \sim 500$  GeV [491,492]; occasionally, we will comment on the benefits of raising the energy of the machine. The case of the  $\gamma\gamma$  option of the machine, as well as the physics at future muon colliders will be postponed to, respectively, the penultimate and last sections.

Since  $e^+e^-$  colliders are known to be high-precision machines as demonstrated at LEP and SLC, the theoretical predictions have to be rather accurate and thus the radiative corrections to the Higgs production processes have to be taken into account. The one-loop electroweak and QCD radiative corrections to the most important production mechanisms have been completed only recently [493–505] and their main effects will be summarized.

In addition, the main motivation of future  $e^+e^-$  in the sub-TeV energy range is the detailed exploration of the electroweak symmetry breaking mechanism and the thorough study of the fundamental properties of the Higgs particle, in particular the spin and parity quantum numbers. At least in the main processes, we study the energy and the angular dependence of the cross sections as well as the angular correlations of the final decay products, and confront, whenever possible, the predictions for the  $J^{\text{PC}} = 0^{++}$  case of the SM Higgs particle to what would be expected if the Higgs were a pseudoscalar boson with  $J^{\text{PC}} = 0^{+-}$  spin–parity assignments. We also discuss the measurements of the Higgs mass and total decay width, the Higgs couplings to fermions and gauge bosons, and the Higgs self-coupling which allows for the reconstruction of part of the scalar potential that is responsible for the spontaneous breaking of the electroweak symmetry.

Some particular points relevant to this section have been already discussed in the context of hadron colliders or in the section on the decays of the Higgs particle. However, some important features will be rediscussed in the context of lepton colliders, to make the section more complete and self-contained.

## 4.2. The dominant production processes in $e^+e^-$ collisions

### 4.2.1. The Higgs–strahlung mechanism

**4.2.1.1. The production cross section.** The production cross section for the Higgs–strahlung process is given by

$$\sigma(e^+e^- \rightarrow ZH) = \frac{G_\mu^2 M_Z^4}{96\pi s} (\hat{v}_e^2 + \hat{a}_e^2) \lambda^{1/2} \frac{\lambda + 12M_Z^2/s}{(1 - M_Z^2/s)^2} \quad (4.18)$$

where, as usual,  $\hat{a}_e = -1$  and  $\hat{v}_e = -1 + 4s_W^2$  are the  $Z$  charges of the electron and  $\lambda^{1/2}$  the usual two-particle phase-space function

$$\lambda = (1 - M_H^2/s - M_Z^2/s)^2 - 4M_H^2 M_Z^2/s^2. \quad (4.19)$$

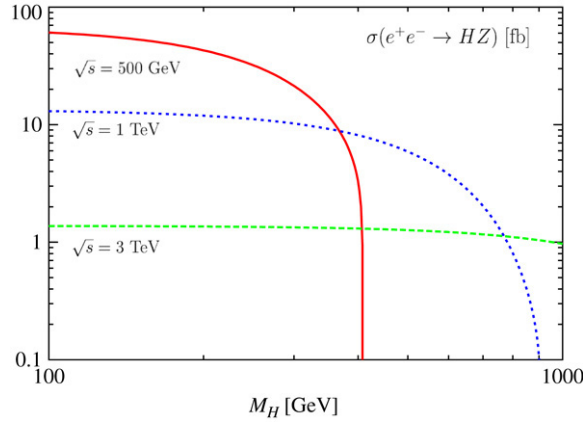


Fig. 4.3. Higgs boson production cross sections in the Higgs–strahlung mechanism in  $e^+e^-$  collisions with c.m. energies  $\sqrt{s} = 0.5, 1$  and  $3$  TeV as functions of  $M_H$ .

The production cross section is shown in Fig. 4.3 as a function of the Higgs mass for the values of the c.m. energy  $\sqrt{s} = 0.5, 1$  and  $3$  TeV. At  $\sqrt{s} = 500$  GeV,  $\sigma(e^+e^- \rightarrow HZ) \sim 50$  fb for  $M_H \sim 150$  GeV, leading to a total of  $\sim 25,000$  Higgs particles that are created at an integrated luminosity of  $\int \mathcal{L} = 500 \text{ fb}^{-1}$ , as expected for future machines. The cross section scales as the inverse of the c.m. energy,  $\sigma \sim 1/s$  and, for moderate Higgs masses, it is larger for smaller c.m. energies. The maximum value of the cross section for a given  $M_H$  value is at  $\sqrt{s} \sim M_Z + \sqrt{2}M_H$ . An energy of the order of  $\sqrt{s} \sim 800$  GeV is needed to cover the entire Higgs boson mass range allowed in the SM,  $M_H \lesssim 700$  GeV.

**4.2.1.2. The energy dependence.** The recoiling  $Z$  boson in the two-body reaction  $e^+e^- \rightarrow ZH$  is mono-energetic,  $E_Z = (s - M_H^2 + M_Z^2)/(2\sqrt{s})$ , and the mass of the Higgs boson can be derived from the energy of the  $Z$  boson,  $M_H^2 = s - 2\sqrt{s}E_Z + M_Z^2$ , if the initial  $e^+$  and  $e^-$  beam energies are sharp.

The excitation curve rises linearly with the phase-space factor  $\lambda^{1/2}$ , which is characteristic to the production of a scalar particle in association with a  $Z$  boson

$$\sigma(e^+e^- \rightarrow HZ) \sim \lambda^{1/2} \sim \sqrt{s - (M_H + M_Z)^2}. \quad (4.20)$$

This behavior for the  $J^{\text{PC}} = 0^{++}$  SM Higgs boson can be compared with the case of a CP-odd Higgs boson  $A$  with  $J^{\text{PC}} = 0^{+-}$  quantum numbers and with couplings given in Section 2. The total production cross section for the process  $e^+e^- \rightarrow ZA$  [140,511]

$$\sigma(e^+e^- \rightarrow ZA) = \eta^2 \frac{G_\mu^2 M_Z^6}{48\pi M_A^4} (\hat{a}_e^2 + \hat{v}_e^2) \frac{\lambda^{3/2}}{(1 - M_Z^2/s)^2} \quad (4.21)$$

has a momentum dependence  $\sim \lambda^{3/2}$  that is characteristically different from the  $ZH$  cross section near threshold. This is illustrated in Fig. 4.4, where the behavior near the production threshold for the assignments  $J^{\text{PC}} = 0^{++}$  and  $0^{+-}$  is shown for a Higgs mass  $M_H = 120$  GeV.

In fact, as discussed in Ref. [512], the linear threshold behavior of the SM Higgs boson rules out not only the quantum number  $J^{\text{P}} = 0^-$  but also  $J^{\text{P}} = 1^-, 2^+$  and higher spin  $3^\pm, \dots$ , which rise with higher powers of  $\lambda$  too. The production of states with the two remaining spin–parity assignments  $J^{\text{P}} = 1^+, 2^-$  can be ruled out using the angular correlations as is discussed hereafter.

**4.2.1.3. The angular distribution.** The angular distribution of the  $Z/H$  bosons in the bremsstrahlung process is also sensitive to the spin of the Higgs particle [513]. The explicit form of the angular distribution, with  $\theta$  being the scattering angle, is given by

$$\frac{d\sigma(e^+e^- \rightarrow ZH)}{d\cos\theta} \sim \lambda^2 \sin^2\theta + 8M_Z^2/s \xrightarrow{s \gg M_Z^2} \frac{3}{4} \sin^2\theta \quad (4.22)$$



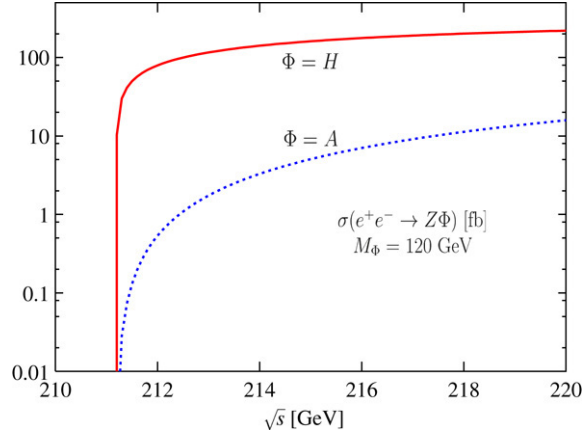


Fig. 4.4. The  $e^+e^- \rightarrow Z\Phi$  cross section energy dependence near the threshold for the two parity cases  $\Phi = H$  and  $\Phi = A$  [with  $\eta = 1$ ] with  $M_\Phi = 120$  GeV.

and approaches the spin-zero distribution asymptotically,  $\propto \sin^2 \theta$ , in accordance with the equivalence theorem which requires that the production amplitude becomes equal to the amplitude where the  $Z$  boson is replaced by the neutral Goldstone boson  $w_0$ . Thus, for high energies, the  $Z$  boson is produced in a state of longitudinal polarization

$$\frac{\sigma_L}{\sigma_L + \sigma_T} = 1 - \frac{8M_Z^2}{12M_Z^2 + \lambda s}. \quad (4.23)$$

Let us again confront the characteristics of a  $J^{PC} = 0^{++}$  state with those of a pseudoscalar Higgs boson  $A$ . In the process  $e^+e^- \rightarrow ZA$ , the angular distribution is given by

$$\frac{d\sigma(e^+e^- \rightarrow ZA)}{d\cos\theta} \sim 1 + \cos^2\theta \quad (4.24)$$

independent of the energy. The  $Z$  boson in the final state is purely transversally polarized, so that the cross section need not be  $\sim \sin^2\theta$  in this case.

If the Higgs particle were a mixture  $\Phi$  of scalar and pseudoscalar bosons, with a coupling to the virtual and real  $Z$  bosons given by

$$g_{ZZ\Phi} \propto g_{\mu\nu} + i\eta M_Z^{-2} \epsilon_{\mu\nu\rho\sigma} p_Z^\sigma p_Z^\rho \quad (4.25)$$

the angular distribution of  $e^+e^- \rightarrow \Phi Z$  would read [ $A_f = 2a_f v_f / (a_f^2 + a_f^2)$  as usual]

$$\frac{d\sigma(e^+e^- \rightarrow Z\Phi)}{d\cos\theta} \sim 1 + \frac{s\lambda^2}{8M_Z^2} \sin^2\theta + \eta A_e \frac{s\lambda}{M_Z^2} \cos\theta + \eta^2 \frac{s^2\lambda^2}{M_Z^4} (1 + \cos^2\theta). \quad (4.26)$$

The presence of the interference term proportional to  $\eta$  is a clear indication of CP-violation in the Higgs sector. One can thus define an observable [514], conveniently written as,

$$\langle O \rangle = 2\text{Re} \left( \frac{\mathcal{M}(e^+e^- \rightarrow ZH) \mathcal{M}^*(e^+e^- \rightarrow ZA)}{|\mathcal{M}(e^+e^- \rightarrow ZH)|^2} \right) \propto \eta A_e \frac{s\lambda}{M_Z^2} \quad (4.27)$$

which quantifies the amount of this CP-violation.

The angular momentum structure specific to Higgs production can also directly be confronted experimentally with one of the processes  $e^+e^- \rightarrow ZZ$  that is distinctly different. Mediated by electron exchange in the  $t$ -channel, the amplitude for this process is built up by many partial waves, peaking in the forward/backward directions. The two angular distributions, together with the angular distribution for the CP-odd Higgs case,  $e^+e^- \rightarrow AZ$ , are compared with each other in Fig. 4.5 which demonstrates the specific character of the SM Higgs production process.

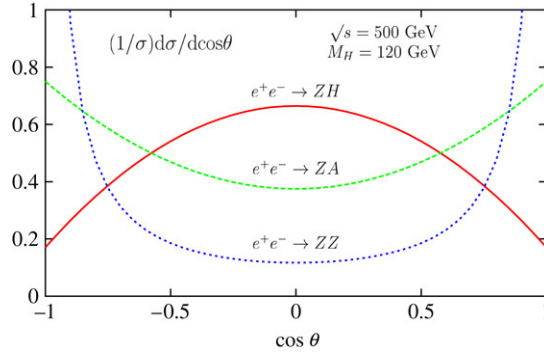


Fig. 4.5. Angular distribution in the process  $e^+e^- \rightarrow HZ$  for  $\sqrt{s} = 500$  GeV and  $M_H = 120$  GeV. The distributions for the CP-odd Higgs and  $e^+e^- \rightarrow ZZ$  cases are also shown.

**4.2.1.4. The angular correlations.** The pattern for the  $Z$  boson polarization in the  $e^+e^- \rightarrow HZ, HA$  and  $ZZ$  processes can be checked [140,511]: while the distribution of the fermions in the  $Z \rightarrow f\bar{f}$  rest frame with respect to the  $Z$  flight direction is given by  $\sin^2 \theta_*$  for longitudinally polarized  $Z$  bosons, it behaves as  $(1 \pm \cos \theta_*)^2$  for transversally polarized states, after averaging over the azimuthal angles. The definitions of the polar angles  $\theta$  and  $\theta_*$  are shown in Fig. 4.6; the azimuthal angle  $\phi_*$  is the angle between the plane of the  $f\bar{f}$  from  $Z$  decays and the Higgs decay products.

Including the azimuthal angles, the final angular correlations may be written for the process  $e^+e^- \rightarrow ZH$  with  $Z \rightarrow f\bar{f}$  as [140]

$$\begin{aligned} \frac{d\sigma(e^+e^- \rightarrow ZH)}{dc_\theta dc_{\theta_*} d\phi_*} &\sim s_\theta^2 s_{\theta_*}^2 - \frac{1}{2\gamma} s_{2\theta} s_{2\theta_*} c\phi_* + \frac{1}{2\gamma^2} [(1 + c_\theta^2)(1 + c_{\theta_*}^2) + s_\theta^2 s_{\theta_*}^2 c2\phi_*] \\ &\quad - 2A_e A_f \frac{1}{\gamma} \left[ s_\theta s_{\theta_*} c\phi_* - \frac{1}{\gamma} c_\theta c_{\theta_*} \right] \end{aligned} \quad (4.28)$$

where  $s_\theta = \sin \theta$  etc.,  $A_f = 2v_f a_f / (v_f^2 + a_f^2)$  and  $\gamma^2 = E^2/M_Z^2 = 1 + \lambda s/4M_Z^2$ . As before,  $\theta$  is the polar  $Z$  angle in the laboratory frame,  $\theta_*$  the polar fermion angle in the  $Z$  rest frame and  $\phi_*$  the corresponding azimuthal angle with respect to the  $e^+e^- \rightarrow ZH$  production plane. After integrating out the polar angles  $\theta$  and  $\theta_*$ , one finds the familiar  $\cos \phi_*$  and  $\cos 2\phi_*$  dependence discussed in Section 2.2.4 associated with P-odd and even amplitudes, respectively

$$\begin{aligned} \frac{d\sigma(e^+e^- \rightarrow ZH)}{d\phi_*} &\sim 1 + a_1 \cos \phi_* + a_2 \cos 2\phi_* \\ a_1 &= -\frac{9\pi^2}{32} A_e A_f \frac{\gamma}{\gamma^2 + 2}, \quad a_2 = \frac{1}{2} \frac{1}{\gamma^2 + 2}. \end{aligned} \quad (4.29)$$

The azimuthal angular dependence disappears for high energies  $\sim 1/\gamma$  as a result of the dominating longitudinal polarization of the  $Z$  boson.

Note again the characteristic difference to the  $0^{+-}$  case,  $e^+e^- \rightarrow ZA \rightarrow f\bar{f}A$  [140,156]

$$\frac{d\sigma(e^+e^- \rightarrow ZA)}{dc_\theta dc_{\theta_*} d\phi_*} \sim 1 + c_\theta^2 c_{\theta_*}^2 - \frac{1}{2} s_\theta^2 s_{\theta_*}^2 - \frac{1}{2} s_\theta^2 s_{\theta_*}^2 c2\phi_* + 2A_e A_f c_\theta c_{\theta_*}. \quad (4.30)$$

This time, the azimuthal dependence is P-even and independent of the energy in contrast to the  $0^{++}$  case; after integrating out the polar  $\theta, \theta_*$  angles, one obtains

$$\frac{d\sigma(e^+e^- \rightarrow ZA)}{d\phi_*} \sim 1 - \frac{1}{4} \cos 2\phi_*. \quad (4.31)$$

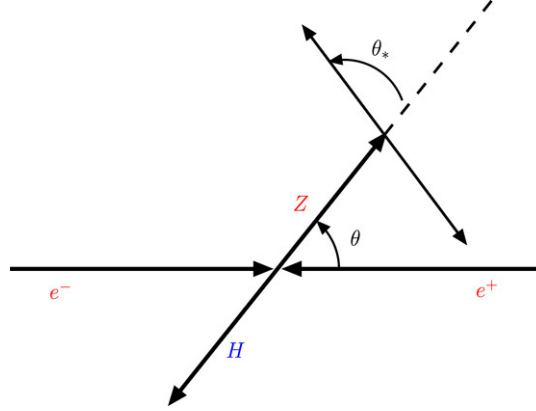


Fig. 4.6. The definitions of the polar angles  $\theta, \theta_*$  in the process  $e^+e^- \rightarrow ZH \rightarrow Hf\bar{f}$ .

The production of the two states with  $J^P = 1^+, 2^-$  quantum numbers, which also leads to a  $\beta$  behavior near the kinematical threshold as in the  $0^+$  case, can be ruled out using the angular correlations as they lead to  $(1 + c_\theta^2)s_{\theta_*}^2$  and  $(1 + c_{\theta_*}^2)s_\theta^2$  distributions which are absent in the SM Higgs case [155].

We can thus conclude that the angular analysis of the Higgs production in  $e^+e^- \rightarrow Z^* \rightarrow ZH$  with  $Z \rightarrow f\bar{f}$ , together with the threshold behavior of the cross section, allows stringent tests of the  $J^{PC} = 0^{++}$  quantum numbers of the Higgs boson in the low and intermediate mass ranges. In the high mass range,  $M_H \gtrsim 2M_W$ , when the Higgs boson decays almost exclusively into two vector bosons, the Higgs spin zero and parity can be checked not only in the production process  $e^+e^- \rightarrow HZ$ , but also in the decay processes  $H \rightarrow VV \rightarrow 4f$  as discussed in Section 2.2.4. The full correlations between the final decay products  $e^+e^- \rightarrow ZH \rightarrow ZVV \rightarrow 6f$  has not been yet worked out explicitly because of the rather complicated six fermion final state.

#### 4.2.2. The WW fusion process

**4.2.2.1. The production cross section.** The  $WW$  fusion process [90,224–227,479] is most important for small values of the ratio  $M_H/\sqrt{s}$ , i.e. high energies where the cross section grows  $\sim M_W^{-2} \log(s/M_H^2)$ . The production cross section, discussed in Section 3.3 at hadron colliders, can be more conveniently written as

$$\sigma = \frac{G_\mu^3 M_V^4}{64\sqrt{2}\pi^3} \int_{\kappa_H}^1 dx \int_x^1 \frac{dy}{[1 + (y-x)/\kappa_V]^2} \left[ (\hat{v}_e^2 + \hat{a}_e^2)^2 f(x, y) + 4\hat{v}_e^2 \hat{a}_e^2 g(x, y) \right] \quad (4.32)$$

$$f(x, y) = \left( \frac{2x}{y^3} - \frac{1+2x}{y^2} + \frac{2+x}{2y} - \frac{1}{2} \right) \left[ \frac{z}{1+z} - \log(1+z) \right] + \frac{x}{y^3} \frac{z^2(1-y)}{1+z}$$

$$g(x, y) = \left( -\frac{x}{y^2} + \frac{2+x}{2y} - \frac{1}{2} \right) \left[ \frac{z}{1+z} - \log(1+z) \right]$$

with  $\kappa_H = M_H^2/s$ ,  $\kappa_V = M_V^2/s$ ,  $z = y(x - \kappa_H)/(\kappa_V x)$  and  $\hat{v}, \hat{a}$  the electron couplings to the massive gauge bosons,  $\hat{v}_e = \hat{a}_e = \sqrt{2}$  for the  $W$  boson. [Note that in the effective longitudinal  $W$  approximation, and as discussed in Section 3.3.5, one obtains a simple result for the cross section of this process, but which is twice larger than the exact result for small Higgs boson masses.]

The production cross section is shown in Fig. 4.7 as a function of  $M_H$  at c.m. energies  $\sqrt{s} = 0.5, 1$  and  $3$  TeV. For Higgs masses in the intermediate range, the cross section is comparable to the one of the Higgs–strahlung process at  $\sqrt{s} = 500$  GeV, leading to  $\sim 25,000$  events for the expected luminosity  $\mathcal{L} = 500 \text{ fb}^{-1}$ , and is larger at higher energies.

**4.2.2.2. The full cross section with the interference with Higgs–strahlung.** The overall cross section that will be observed experimentally for the process  $e^+e^- \rightarrow H + \bar{\nu}\nu$  will not be due to the  $WW$  fusion process only, but part of it will come from the Higgs–strahlung process,  $e^+e^- \rightarrow HZ$ , with the  $Z$  boson decaying into the three types

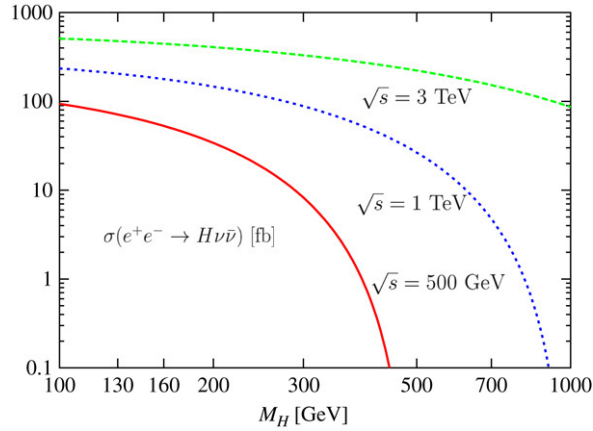


Fig. 4.7. The Higgs production cross section in the  $WW$  fusion mechanism in  $e^+e^-$  collisions with c.m. energies  $\sqrt{s} = 0.5, 1$  and  $3$  TeV as a function of  $M_H$ .

of neutrinos. A compact expression for the full cross section of the Higgs–strahlung and  $WW$  fusion mechanisms, including the interference terms, has been derived in the general case by choosing the energy  $E_H$  and the polar angle  $\theta$  of the Higgs particle as the basic variables in the  $e^+e^-$  c.m. frame. Decomposing the total contribution into three parts, the contributions  $3 \times g_S$  from Higgs–strahlung with  $Z$  decays into three types of neutrinos,  $g_W$  from  $WW$  fusion, and  $g_I$  from the interference term between fusion and Higgs–strahlung for  $\bar{\nu}_e \nu_e$  final states, one has for energies  $\sqrt{s}$  above the  $Z$ -resonance [226,227]

$$\frac{d\sigma(e^+e^- \rightarrow H\bar{\nu}\nu)}{dE_H d\cos\theta} = \frac{G_\mu^3 M_Z^8 p_H}{\sqrt{2}\pi^3 s} (3g_S + g_I + g_W) \quad (4.33)$$

$$g_S = \frac{\hat{v}_e^2 + \hat{a}_e^2}{96} \frac{s s_\nu + s_1 s_2}{(s - M_Z^2)^2 [(s_\nu - M_Z^2)^2 + M_Z^2 \Gamma_Z^2]}, \quad g_W = \frac{c_W^8}{s_1 s_2 r} \mathcal{H}_+$$

$$g_I = \frac{(\hat{v}_e + \hat{a}_e) c_W^4}{8} \frac{s_\nu - M_Z^2}{(s - M_Z^2) [(s_\nu - M_Z^2)^2 + M_Z^2 \Gamma_Z^2]} \mathcal{H}_I \quad (4.34)$$

where all the abbreviated quantities have been defined in Eq. (3.28), the factor  $\mathcal{H}_+$  in Eq. (3.27), while the factor  $\mathcal{H}_I$  for the interference term is given by

$$\mathcal{H}_I = 2 - (h_1 + 1) \log \frac{h_1 + 1}{h_1 - 1} - (h_2 + 1) \log \frac{h_2 + 1}{h_2 - 1} + (h_1 + 1)(h_2 + 1) \frac{\ell}{\sqrt{r}}. \quad (4.35)$$

To derive the total cross section  $\sigma(e^+e^- \rightarrow H\bar{\nu}\nu)$ , the differential cross section must be integrated over  $\theta$  and  $E_H$ , with the boundary conditions given in Eq. (3.29). The two main components and the total cross section for  $e^+e^- \rightarrow H\bar{\nu}\nu$  are displayed in Fig. 4.8 as functions of the c.m. energy for  $M_H = 115$  and  $150$  GeV. One can see that Higgs–strahlung is dominant at lower energies,  $WW$  fusion at higher energies, and the interference term is small except in the cross over regions.

At  $e^+e^-$  colliders, the initial  $e^\pm$  beams can be polarized longitudinally. The Higgs–strahlung and  $WW$  fusion require opposite helicities of the  $e^-$  and  $e^+$  beams. Denoting  $\sigma_{U,L,R}$  the cross sections for unpolarized  $e^-/e^+$ ,  $e_L^-/e_R^+$  and  $e_R^-/e_L^+$ , respectively, one obtains [227]

$$\sigma_U \propto 3g_S + g_I + g_W, \quad \sigma_L \propto 6g_S + 4g_I + 4g_W, \quad \sigma_R \propto 6g_S. \quad (4.36)$$

The cross section for  $WW$  fusion of Higgs particles increases by a factor four, compared with unpolarized beams, if left-handed electrons and right-handed positrons are used. By using right-handed electrons, the  $WW$  fusion mechanism is switched off. The interference term cannot be separated from the  $WW$  fusion cross section.

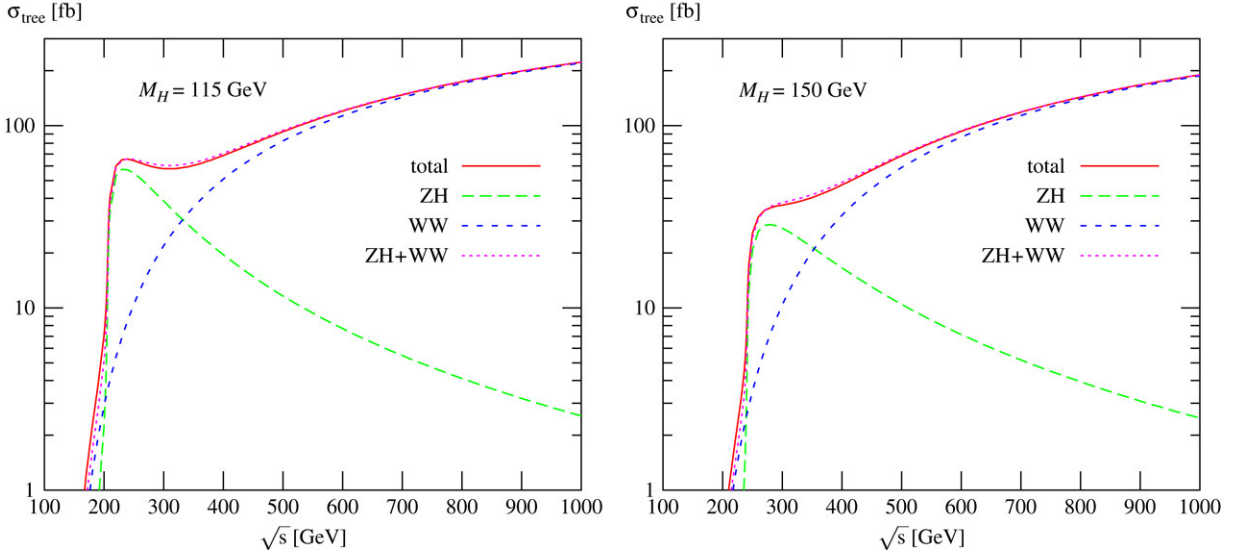


Fig. 4.8. The production cross section for the process  $e^+e^- \rightarrow H\bar{\nu}\nu$  as a function of  $\sqrt{s}$  for  $M_H = 115$  and  $150$  GeV. The three components, i.e. Higgs–strahlung,  $WW$  fusion, their sum, and the total cross section including the interference term, are shown; from Ref. [494].

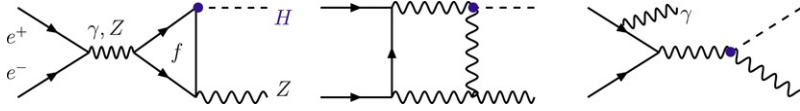


Fig. 4.9. Generic diagrams for the  $\mathcal{O}(\alpha)$  corrections to the process  $e^+e^- \rightarrow HZ$ .

#### 4.2.3. The electroweak radiative corrections

To have a full control on the production cross sections of the Higgs–strahlung and  $WW$  fusion processes, in view of the high-precision tests which can be performed using them, the electroweak radiative corrections must be taken into account. These corrections, consisting of virtual and real corrections with the emission of an additional photon in the final or initial states (ISR), have been completed recently. Note, however, that at high-energy linear colliders, in addition to ISR, one also has to take into account the beam energy spread and beamstrahlung. The latter is machine dependent and will smear out the c.m. energy and the system moves along the beam axes; it must be thus suppressed as strongly as possible in order to allow for high-quality analyses which are often based on kinematical constraints derived from the precise knowledge of the initial beam energies.

**4.2.3.1. The Higgs–strahlung process.** At one-loop order, the radiative corrections to the Higgs–strahlung process consist of self-energy, vertex and box corrections to the tree-level amplitude and the emission of an additional photon in the initial state; Fig. 4.9. The corrections have been calculated some time ago [493] and reanalyzed recently in the context of the full  $e^+e^- \rightarrow H\bar{\nu}\nu$  process [494–496]. Let us summarize the salient features of these corrections.

The photonic corrections to the initial state, that is vertex and self-energy corrections with photon exchange as well as photon radiation (ISR) can be implemented using the structure function approach discussed in Section 1.2.1; see, Eq. (1.68). The fermionic corrections which are contained in the running of the QED constant  $\alpha$  for the light fermions, Eq. (1.42), and the correction to the  $\rho$  parameter for the heavy top quark, Eq. (1.71), can be incorporated by using the improved Born approximation (IBA): starting with the Born cross section defined in terms of the bare electromagnetic coupling  $\alpha(0)$ , one performs the substitution  $\pi\alpha(0) \rightarrow \sqrt{2}G_F M_W^2 (1 - M_W^2/M_Z^2)$  which absorbs the correction  $\Delta r \simeq \Delta\alpha - 3\Delta\rho$ . One also has to include the additional corrections to the  $HZZ$  vertex and in particular the heavy top contributions,  $\delta_{HZZ}^t$  in Eq. (2.77). The largest part of the weak correction is then absorbed into the couplings and the remaining corrections should be in principle rather small [494].

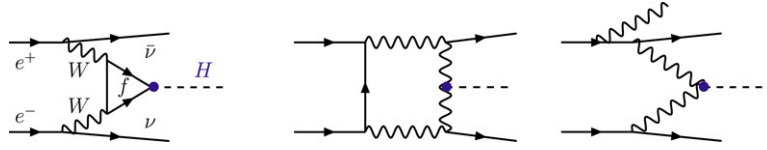


Fig. 4.10. Generic diagrams for the  $\mathcal{O}(\alpha)$  corrections to the  $WW$  fusion process.

The overall correction to the tree-level  $e^+e^- \rightarrow HZ$  amplitude, including an additional term that is logarithmic in the top quark mass, is given by [20]

$$K_{e^+e^- \rightarrow HZ}^t \simeq 1 + \frac{\alpha}{4\pi s_W^2} \frac{1}{g_i} \left[ \frac{1}{8} \left( 6 \frac{c_W}{s_W} + g_i \right) \frac{m_t^2}{M_W^2} + \frac{3 - 2s_W^2}{3c_W s_W} \log \frac{m_t}{M_W} \right]. \quad (4.37)$$

These factors correct in fact the amplitudes with left- and right-handed electrons with couplings  $g_L = (2s_W^2 - 1)/(2s_W c_W)$  and  $g_R = s_W/c_W$ . At low and moderate energies, this approximation is rather good. However, at high energies, it turns out that this expression in the heavy top quark limit does not reproduce exactly the full  $m_t$ -dependent result, as a consequence of the presence of the box contributions which depend both on  $s$  and  $m_t$ .

**4.2.3.2. The  $WW$  fusion process.** Since already at the tree level the  $WW$  fusion mechanism is a three-body final state production process [which was thus not trivial to handle], the calculation of the one-loop radiative corrections is a real challenge. Indeed, not only one has to deal with the numerous diagrams involving self-energy, vertex and box corrections [due to the additional final state, the number of such diagrams is much larger than that for a  $2 \rightarrow 2$  process like Higgs-strahlung], one has to consider in addition one-loop corrections involving pentagonal diagrams which are extremely difficult to handle, and corrections with real-photon emission, leading to four particles in the final state which are rather involved; see Fig. 4.10. To these complications, one has to add the fact that to derive the full corrections to the  $e^+e^- \rightarrow H\nu\bar{\nu}$  final state, both the  $WW$  fusion mechanism and the Higgs-strahlung process with  $Z \rightarrow \nu\bar{\nu}$  have to be considered and added coherently.

The challenge of deriving these corrections has been met by three groups. In Ref. [495], the calculation was performed using GRACE-LOOP [506], an automatic calculation system. In Ref. [496], the results have been obtained as a MAPLE output using the program DIANA [507] without an explicit evaluation. In Ref. [494], the calculation has been performed in two independent ways, using the program FeynArts [508] to generate the Feynman graphs, and using Mathematica to express the amplitudes in terms of standard matrix elements or using the package FormCalc [509] based on Form [510]. We briefly summarize the main results of these calculations, mostly relying on Ref. [494].

The ISR corrections stemming from the radiation of a photon from the initial  $e^+e^-$  states and from the intermediate  $W$  bosons, can again be obtained in the structure function approach either at  $\mathcal{O}(\alpha)$  or including higher-order corrections. The running of the electromagnetic constant due to the light fermion contributions [because the cross section is proportional to  $\alpha^3$ , this leads to a  $\sim 18\%$  change of the cross section] can be included using the IBA discussed previously. Finally, since the  $WW$  fusion cross section gets its main contribution from small momenta  $W$  bosons, the loop corrections are mainly determined by the  $\nu_e e W$  and  $HWW$  vertices at zero-momentum transfer. The correction to the  $\nu_e e W$  vertex is well described by  $\Delta r$  and the  $HWW$  vertex correction is given by  $\delta_{HWW}^t$  in Eq. (2.77). It turns out that these corrections largely cancel the corresponding ones when  $G_\mu$  is used in the tree-level expression of the amplitude and one obtains a small remaining piece [494]

$$K_{e^+e^- \rightarrow H\nu\bar{\nu}}^t = 1 - \frac{5\alpha}{16\pi s_W^2} \frac{m_t^2}{M_W^2} \quad (4.38)$$

which approximates the fermionic contribution to the amplitude quite well. To this correction, one has to add the bosonic contribution for which no simple approximation is possible.

**4.2.3.3. Numerical results.** The final output of the calculation is shown in Fig. 4.11, where the radiative corrections to the Higgs strahlung process [left figure] and the  $WW$  fusion mechanism [right figure], without the small interference terms, are shown as functions of  $\sqrt{s}$  for  $M_H = 150$  GeV. The various components, the fermionic contribution, the bosonic contribution, the initial state radiation at  $\mathcal{O}(\alpha)$  and beyond, are displayed.



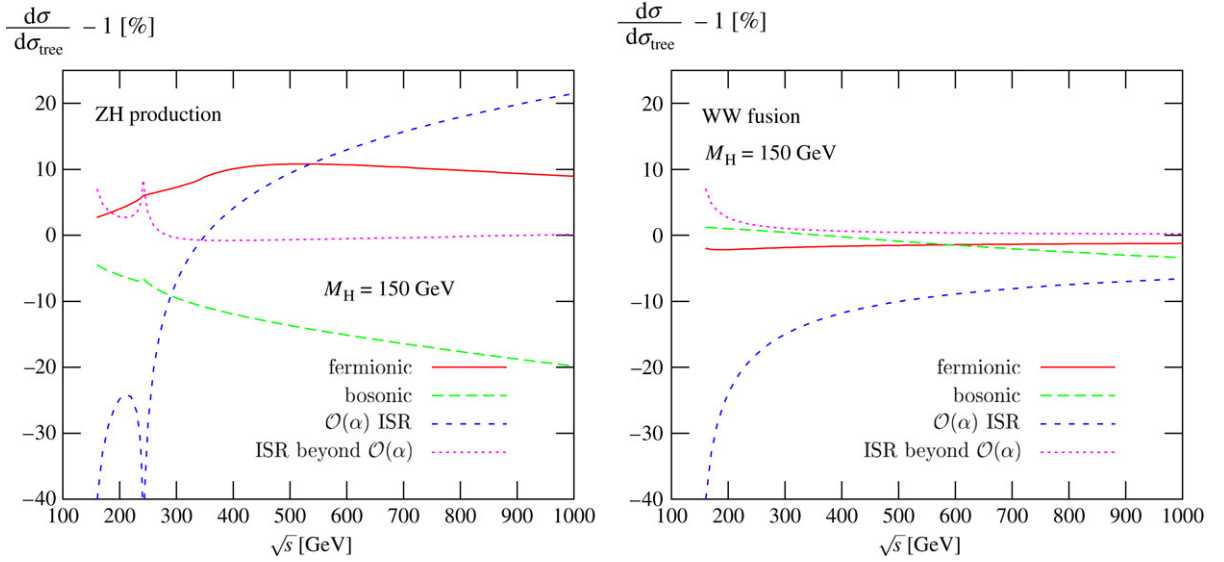


Fig. 4.11. Relative electroweak corrections to the Higgs–strahlung  $e^+e^- \rightarrow HZ$  and to  $WW$  fusion  $e^+e^- \rightarrow H\nu\bar{\nu}$  processes resulting from ISR at  $\mathcal{O}(\alpha)$  and beyond, fermion loops, and non-ISR bosonic corrections as functions of  $\sqrt{s}$  for  $M_H = 150$  GeV; from Ref. [494].

In the case of  $WW$  fusion, the ISR corrections, the bulk of which comes from  $\mathcal{O}(\alpha)$  contributions, are negative for all energies as a consequence of the decrease of the effective c.m. energy which leads to a smaller cross section. The fermionic corrections are negative and small, being at the level of  $-2\%$ , while the bosonic corrections range from  $+1\%$  near the production threshold to  $-3\%$  at high energy. For the Higgs–strahlung process, at high enough energies  $\sqrt{s} \gtrsim 500$  GeV, the fermionic contribution is positive and almost constant,  $+10\%$ , while the bosonic contribution is negative and large, increasing in absolute value with  $\sqrt{s}$ . The largest correction is due to the  $\mathcal{O}(\alpha)$  ISR [the contribution of higher orders is again very small], which increases the cross section by  $20\%$  for  $\sqrt{s} = 1$  TeV.

Adding the channel where the neutrinos are coming from the Higgs–strahlung process and the small interference term, one obtains the total production cross section for the full  $e^+e^- \rightarrow H\nu\bar{\nu}$  process. The relative corrections to the lowest-order cross section for the various components are shown in Fig. 4.12 for  $M_H = 115$  and  $150$  GeV as functions of  $\sqrt{s}$ . Below the threshold, the correction to the  $ZH$  channel are large and negative, reaching  $\sim -20\%$ , rise fastly near threshold, and at  $\sqrt{s} = 1$  TeV reach the level of  $\sim 20$  (10)% for  $M_H = 115$  (150) GeV. The corrections to the  $WW$  fusion channel rise also sharply at the threshold but reach quickly a plateau at a level of  $-10\%$  beyond  $\sqrt{s} = 500$  GeV. The corrections to the complete process follow those of the  $WW$  component at high energy and those of the  $HZ$  process at low energies, a consequence of the relative magnitude of the two processes at tree level. They are always negative, being of order  $-10\%$  at  $\sqrt{s} \gtrsim 350$  GeV.

### 4.3. The subleading production processes in $e^+e^-$ collisions

#### 4.3.1. The $ZZ$ fusion mechanism

The cross section for the  $ZZ$  fusion mechanism,  $e^+e^- \rightarrow e^+e^- (Z^*Z^*) \rightarrow e^+e^- H$ , Fig. 4.13, is given by the same expression in Eq. (4.32) for the  $WW$  fusion mechanism with the vector boson  $V = Z$  having the usual couplings to the electron  $\hat{v}_e = -1 + 4s_W^2$ ,  $\hat{a}_e = -1$ . The total production cross section is about an order of magnitude smaller than the cross section for  $WW$  fusion,  $\sigma(WW \rightarrow H)/\sigma(ZZ \rightarrow H) \sim 16c_W^2 \sim 9$ , a mere consequence of the fact that the neutral current couplings are smaller than the charged current couplings. The lower rate, however, could be at least partly compensated by the clean signature of the  $e^+e^-$  final state. The cross section is shown in Fig. 4.14 as a function of  $M_H$  for the c.m. energies  $\sqrt{s} = 0.5, 1$  and  $3$  TeV. It follows the same trend as the  $WW$  fusion cross section.

Similar to the  $WW$  fusion case, the overall cross section for the process  $e^+e^- \rightarrow H + e^+e^-$  receives contributions  $g_S$  from Higgs–strahlung with  $Z \rightarrow e^+e^-$ ,  $g_{Z\pm}$  from  $ZZ$  fusion, and  $g_I$  from the interference term between fusion

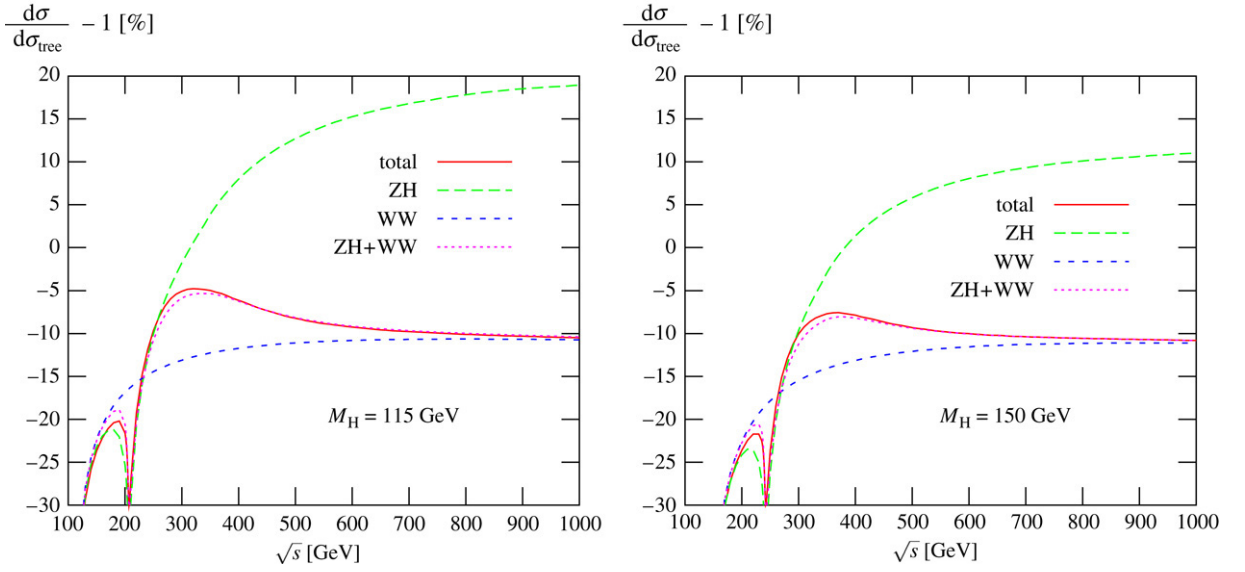


Fig. 4.12. Relative corrections to the complete process  $e^+e^- \rightarrow H\nu\bar{\nu}$  and the contributions of the various components as functions of  $\sqrt{s}$  and for  $M_H = 115$  and  $150$  GeV; from [494].

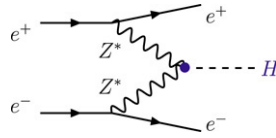


Fig. 4.13. Higgs boson production in the ZZ fusion mechanism in  $e^+e^-$  collisions.

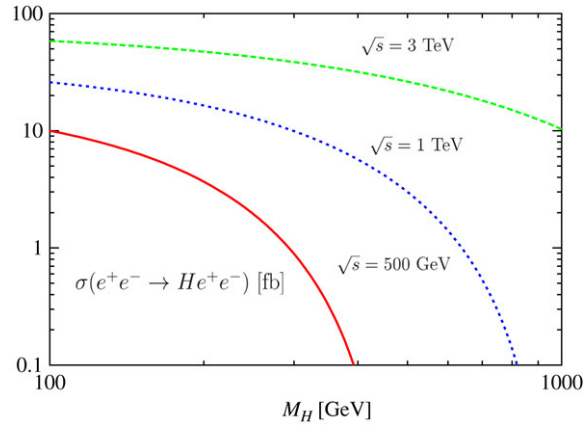


Fig. 4.14. Higgs production cross sections in the ZZ fusion mechanism in  $e^+e^-$  collisions with c.m. energies  $\sqrt{s} = 0.5, 1$  and  $3$  TeV as functions of  $M_H$ .

and Higgs–strahlung [480]

$$\frac{d\sigma(e^+e^- \rightarrow H e^+e^-)}{dE_H d\cos\theta} = \frac{G_\mu^3 M_Z^8 p_H}{\sqrt{2} \pi^3 s} (g_S + g_I + g_{Z+} + g_{Z-}) \quad (4.39)$$

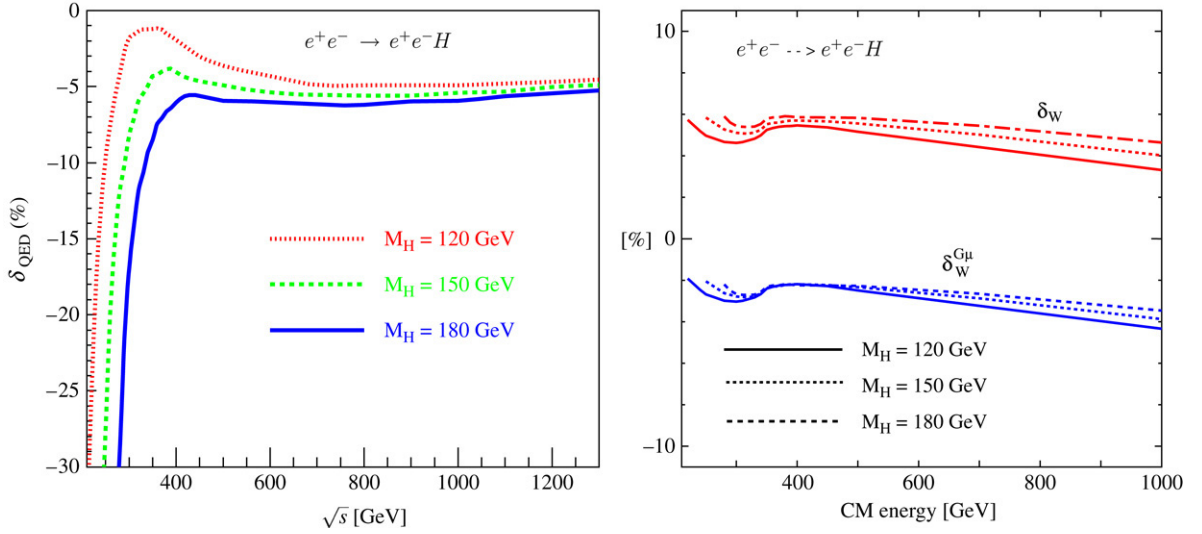


Fig. 4.15. The photonic corrections (left) and the genuine electroweak radiative corrections in the  $G_\mu$  and  $\alpha$  schemes (right) for the process  $e^+e^- \rightarrow He^+e^-$  as functions of the c.m. energy for  $M_H = 120, 150$  and  $180$  GeV; from Ref. [497].

with

$$\begin{aligned}
 g_S &= \frac{(\hat{v}_e^2 + \hat{a}_e^2)^2}{192} \frac{s s_e + s_1 s_2}{(s - M_Z^2)^2 [(s_e - M_Z^2)^2 + M_Z^2 \Gamma_Z^2]} \\
 g_I &= \frac{(\hat{v}_e^2 + \hat{a}_e^2)^2 + 4\hat{v}_e^2 \hat{a}_e^2}{64} \frac{s_e - M_Z^2}{(s - M_Z^2) [(s_e - M_Z^2)^2 + M_Z^2 \Gamma_Z^2]} \mathcal{H}_I \\
 g_{Z+} &= \frac{(\hat{v}_e^2 + \hat{a}_e^2)^2 + 4\hat{v}_e^2 \hat{a}_e^2}{32 s_1 s_2 r} \mathcal{H}_+, \quad g_{Z-} = \frac{(\hat{v}_e^2 - \hat{a}_e^2)^2}{32 s_1 s_2 r} (1 - c_\chi) \mathcal{H}_-
 \end{aligned} \tag{4.40}$$

where the same abbreviations as in the formulas for the  $W$  fusion case, with the appropriate replacements,  $\nu \rightarrow e$  and  $W \rightarrow Z$ , have been used. Again, the three components and the total cross sections follow the same trend as in the case of the  $WW$  fusion process.

The calculation of the one-loop radiative corrections to this process follows the same lines as the one for the companion process  $e^+e^- \rightarrow H\nu\bar{\nu}$ , the only difference being that there are additional diagrams where photons are exchanged between the initial and final state electrons and positrons, and also between the final state  $e^+e^-$  pair. The corrections have been calculated using the GRACE-LOOP [506] system, and the result has recently appeared in Ref. [497]. They are summarized in Fig. 4.15 as functions of  $\sqrt{s}$  for three Higgs mass values.

After subtracting the photonic corrections which decrease the cross section by about 5% for  $\sqrt{s} \gtrsim 350$  GeV, as shown in the left-hand side of the figure, one obtains a rather small electroweak correction: when the tree-level cross section is expressed in terms of  $G_\mu$ , the correction is  $\mathcal{O}(-5\%)$  at  $\sqrt{s} = 350\text{--}500$  GeV and varies very little with energy to reach  $-4\%$  at 1 TeV, as can be seen in the right-hand side of Fig. 4.15. The correction is also almost independent of the Higgs mass in the chosen range,  $M_H \sim 100\text{--}200$  GeV. The correction factor when  $\alpha$  is used as input at the tree level is also shown.

For the process  $e^+e^- \rightarrow He^+e^-$ , the pattern for the polarized and unpolarized cross sections is slightly more complicated than that for the  $WW$  fusion process [480]

$$\begin{aligned}
 \sigma_U &\propto g_S + g_I + g_{Z+} + g_{Z-}, \quad \sigma_{LL} = \sigma_{RR} \propto 2 g_{Z-} \\
 \sigma_{LR/RL} &\propto 2 \frac{(\hat{v}_e \pm \hat{a}_e)^2}{(\hat{v}_e^2 + \hat{a}_e^2)} g_S + 2 \frac{(\hat{v}_e \pm \hat{a}_e)^4}{(\hat{v}_e^2 + \hat{a}_e^2)^2 + 4\hat{v}_e^2 \hat{a}_e^2} (g_I + g_{Z+}).
 \end{aligned}$$

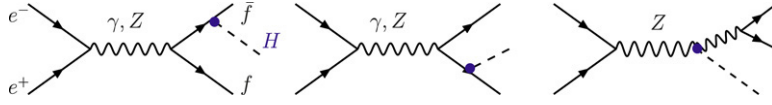


Fig. 4.16. Diagrams for the associated production of Higgs bosons with a fermion pair.

Since  $\hat{v}_e \sim -1 + 4s_W^2 \ll \hat{a}_e$ , the difference between  $\sigma_{RL}$  and  $\sigma_{LR}$  is, however, strongly suppressed and one obtains  $\sigma_{LR} \simeq \sigma_{RL} = 2(g_S + g_I + g_{Z+})$ .

Finally, let us note that in the  $e^-e^-$  option of future high-energy linear colliders, one can produce Higgs bosons in a similar channel [479]

$$e^-e^- \longrightarrow e^-e^-(Z^*Z^*) \longrightarrow e^-e^-H. \quad (4.41)$$

The production cross section [up to some statistical factors due to the identical initial and final states] and the main features of the process are the same as those discussed above for the  $e^+e^-$  option of the machine.

#### 4.3.2. Associated production with heavy fermion pairs

**4.3.2.1. The process at the tree level.** In the SM, the associated production of Higgs bosons with a pair of heavy fermions,  $e^+e^- \rightarrow Hf\bar{f}$  [481,482], proceeds through two set of diagrams: those where the Higgs boson is radiated off the  $f$  and  $\bar{f}$  lines, and a diagram where the Higgs boson is produced in association with a  $Z$  boson which then splits into an  $f\bar{f}$  pair; Fig. 4.16.

Since the fermion and Higgs boson masses must be kept non-zero, the total cross section for these processes is quite involved. However, the Dalitz density, once the angular dependence is integrated out, can be written in a simple and compact form [482]

$$\begin{aligned} \frac{d\sigma(e^+e^- \rightarrow f\bar{f}H)}{dx_1 dx_2} &= \frac{\bar{\alpha}^2 N_c}{12\pi s} \left\{ \left[ Q_e^2 Q_f^2 + \frac{2Q_e Q_f v_e v_f}{1-z} + \frac{(v_e^2 + a_e^2)(v_f^2 + a_f^2)}{(1-z)^2} \right] G_1 \right. \\ &\quad \left. + \frac{v_e^2 + a_e^2}{(1-z)^2} \left[ a_f^2 \sum_{i=2}^6 G_i + v_f^2 (G_4 + G_6) \right] + \frac{Q_e Q_f v_e v_f}{1-z} G_6 \right\} \end{aligned} \quad (4.42)$$

with  $\bar{\alpha} \equiv \alpha(s) \sim 1/128$ ,  $N_c$  the color factor and  $v_e, a_e$  the usual couplings of fermions to the  $Z$  boson, Eq. (1.54).  $z$  is the scaled mass of the  $Z$  boson,  $z = M_Z^2/s$ , and we will use later on the scaled masses  $f = m_f^2/s$  and  $h = M_H^2/s$ .  $x_1 = 2E_f/\sqrt{s}$  and  $x_2 = 2E_{\bar{f}}/\sqrt{s}$  are the reduced energies of the  $f$  and  $\bar{f}$  states; we will also use the Higgs scaled energy,  $x_H = 2E_H/\sqrt{s} = 2 - x_1 - x_2$ , as well as the variables  $x_Z$  and  $x_{12}$  defined by  $x_Z = x_H - 1 - h + z$  and  $x_{12} = (1 - x_1)(1 - x_2)$ . In terms of these variables and the  $g_{Hff} = m_f/v$  and  $g_{HZZ} = 2M_Z/v$  Higgs couplings, the coefficients  $G_i$ , with  $i = 1-6$ , are given by

$$\begin{aligned} G_1 &= \frac{g_{Hff}^2}{x_{12}} \left[ x_H^2 - h \left( \frac{x_H^2}{x_{12}} + 2(x_H - 1 - h) \right) + 2f \left( 4(x_H - h) + \frac{x_H^2}{x_{12}} (4f - h + 2) \right) \right] \\ G_2 &= -2 \frac{g_{Hff}^2}{x_{12}} \left[ x_{12}(1 + x_H) - h(x_{12} + 2x_H + 8f - 2h) + 3fx_H \left( \frac{x_H}{3} + 4 + \frac{x_H}{x_{12}} (4f - h) \right) \right] \\ G_3 &= 2 \frac{g_{HZZ}^2}{x_Z^2} \left[ f(4h - x_H^2 - 12z) + \frac{f}{z} (4h - x_H^2)(x_H - 1 - h + z) \right] \\ G_4 &= 2 \frac{g_{HZZ}^2}{x_Z^2} z [h + x_{12} + 2(1 - x_H) + 4f] \\ G_5 &= -\frac{g_{Hff} g_{HZZ}}{x_{12} x_Z} 4x_H \frac{m_f}{M_Z} \left[ (x_{12} - h)(x_H - 1 - h) + f(12z - 4h + x_H^2) - 3z \left( h - 2 \frac{x_{12}}{x_H} \right) \right] \\ G_6 &= -\frac{g_{Hff} g_{HZZ}}{x_{12} x_Z} 4z \frac{m_f}{M_Z} \left[ x_H(h - 4f - 2) - 2x_{12} + x_H^2 \right]. \end{aligned} \quad (4.43)$$

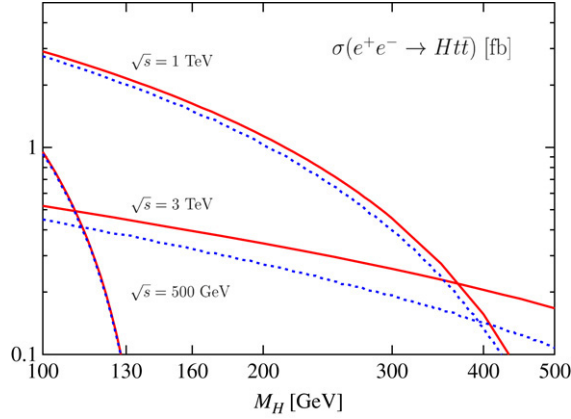


Fig. 4.17. The cross section for the associated production of the Higgs boson with  $t\bar{t}$  pairs in  $e^+e^-$  collisions with c.m. energies  $\sqrt{s} = 0.5, 1$  and  $3$  TeV. The dotted lines represent the instance when only the contributions with the Higgs radiated off the top quark lines are taken into account.

Integrating over the fermion energies, with the boundary conditions similar to that given in Eq. (2.18), one obtains the total production cross section. In the case of  $e^+e^- \rightarrow t\bar{t}H$ , it is shown in Fig. 4.17 as a function of  $M_H$  for three c.m. energy values  $\sqrt{s} = 0.5, 1$  and  $3$  TeV.

While the cross section is in general small for the lowest c.m. energy  $\sqrt{s} = 500$  GeV, it is more important at  $\sqrt{s} = 1$  TeV as a result of the larger available phase space. For  $\sqrt{s} = 3$  TeV, it becomes again smaller as it scales like  $1/s$ . The cross section is at the level of a few to a fraction of a femtobarn, depending on the Higgs mass and the c.m. energy and therefore, this process requires high luminosities. The  $t\bar{t}H$  final state in this associated production mechanism is generated almost exclusively through Higgs-strahlung off top quarks. As shown in Fig. 4.17, the additional contributions from Higgs bosons emitted by the  $Z$  line are very small, amounting, for  $\sqrt{s} \leq 1$  TeV, to only a few percent. In addition, since top quark pair production in  $e^+e^-$  collisions at high energy is known to be dominated by photon exchange, the bulk of the cross section is generated by the  $e^+e^- \rightarrow \gamma^* \rightarrow t\bar{t}H$  subprocess. This process thus allows the determination of the important Yukawa coupling of the Higgs boson to top quarks in an almost unambiguous way.

**4.3.2.2. The radiative corrections.** The QCD corrections to the process  $e^+e^- \rightarrow t\bar{t}H$ , consist of the top vertex and self-energy corrections and the emission of an additional gluon in the final state,  $e^+e^- \rightarrow t\bar{t}H + g$ . The rather involved analytical expression of the cross section at NLO can be found in Refs. [498,499]; see also Refs. [500,501]. The corrections can be interpreted in an easy way and be given analytically in two kinematical regimes [498].

(i) In the case where the invariant  $t\bar{t}$  mass is close to the threshold, the rescattering diagrams generated by the gluon exchange between the two quarks gives rise to a correction that is proportional to  $\alpha_s/\beta_t$ , where  $\beta_t$  is the top quark velocity which vanishes at the threshold in the  $t\bar{t}$  rest frame. The  $K$ -factor in this case is given by [498]

$$K_{e^+e^- \rightarrow t\bar{t}H}^{\text{thresh}} = 1 + 64\alpha_s/(9\pi)\pi m_t \left[ (\sqrt{s} - M_H^2)^2 - 4m_t^2 \right]^{-1/2}. \quad (4.44)$$

This pole is regularized by the vanishing phase space at threshold in the leading-order cross section, once it is integrated over the three-body phase space.

(ii) At high energies, these rescattering corrections become less important. For the dominant component of the  $e^+e^- \rightarrow t\bar{t}H$  process, i.e. Higgs radiation off top quarks, the correction can be crudely estimated in the limit  $s \gg m_t^2 \gg M_H^2$ : the radiation of a low mass Higgs boson can be separated from the top quark production process. The cross section can then be approximated by the product of the probability of producing top quark pairs [which at high energies, is given by the well-known factor  $1 + \alpha_s/\pi$ ] and the probability for the splitting processes  $t \rightarrow t + H$  and  $\bar{t} \rightarrow \bar{t} + H$  [which at this order, gives a factor  $-2\alpha_s$  for each state]. The net result will be then an NLO coefficient factor [498]

$$K_{e^+e^- \rightarrow t\bar{t}H}^{\text{high-en.}} = 1 - 3\alpha_s/\pi \quad (4.45)$$

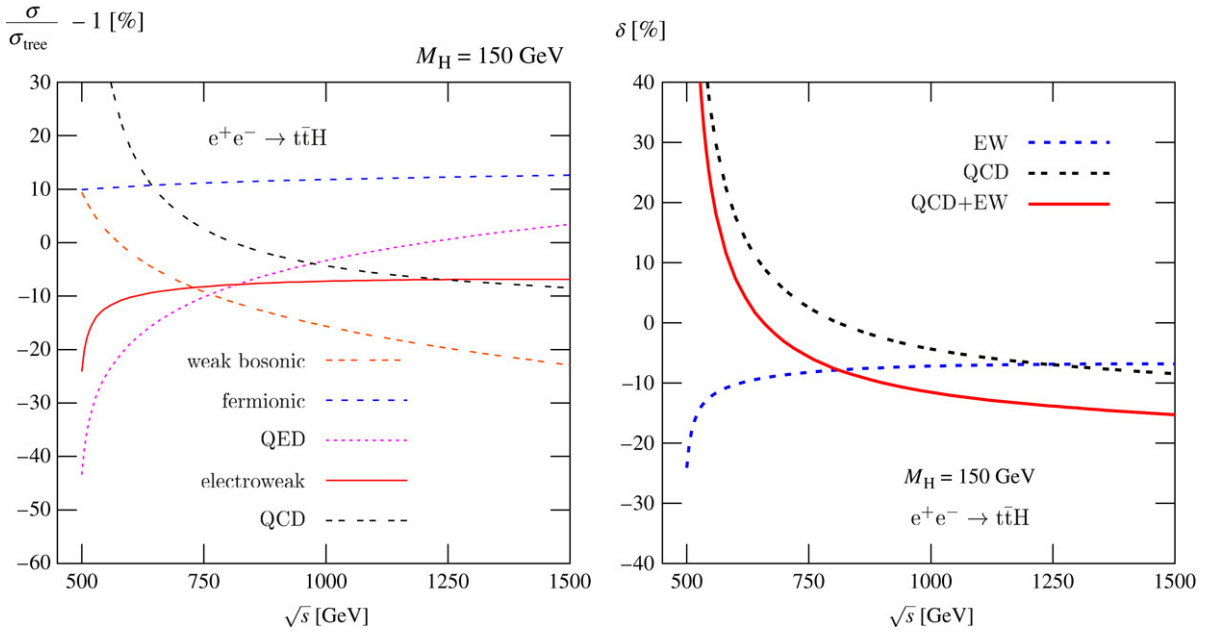


Fig. 4.18. The QCD and the various components and the electroweak radiative corrections (left) and the total QCD and electroweak corrections (right) for the process  $e^+e^- \rightarrow t\bar{t}H + X$  as functions of the c.m. energy for  $M_H = 150$  GeV; from Ref. [500].

leading to a correction factor,  $K \sim 0.9$  at high energies. The QCD correction factor is shown in Fig. 4.18 as a function of the c.m. energy for  $M_H = 150$  GeV.

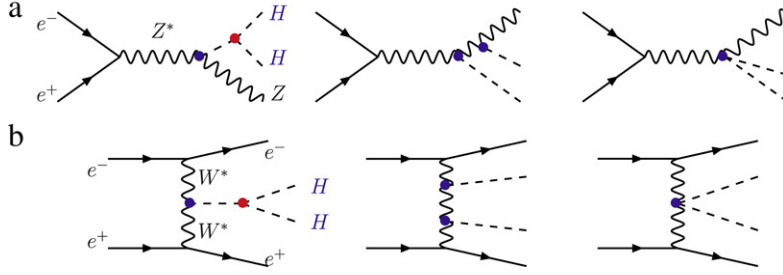
The electroweak corrections have been calculated only recently by two of the groups that evaluated the correction to the  $WW$  fusion process [500,501]. The calculation techniques are the same as those discussed previously. [There is a third calculation performed in Ref. [502] but the results differ from those of the two other calculations at large c.m. energies and at the threshold.] The results are also shown in Fig. 4.18 together with the QCD corrections, as functions of the c.m. energy and for  $M_H = 150$  GeV.

As can be seen, the weak bosonic corrections are at the level of +10% close to the  $2m_t + M_H$  threshold and drop rapidly with increasing energy to reach -20% at  $\sqrt{s} = 1.5$  TeV. The fermionic corrections are approximately +10% over the entire energy range. The QED corrections, which include the full photonic and the higher-order ISR corrections are large and negative near threshold and rise with the energy to reach a few percent at  $\sqrt{s} = 1.5$  TeV. At energies above  $\sqrt{s} \sim 600$  GeV, the fermionic, weak bosonic and QED contributions partly cancel each other, leading to a total electroweak correction that is almost constant and of the order of -10%. This is of the same order as the QCD correction far enough from the production threshold. The total cross section at NLO, in which both the QCD and electroweak corrections are included, is thus 10%–15% smaller than that at tree level for  $\sqrt{s} \gtrsim 750$  GeV; see the right-hand side of Fig. 4.18.

**4.3.2.3. The pseudoscalar case and the Higgs CP-properties.** If the Higgs boson were of pseudoscalar nature, with couplings to fermions as given in Eq. (2.5), the dominant contribution to the cross section of the process  $e^+e^- \rightarrow f\bar{f}A$  would be also due to the Higgs radiation off the heavy fermions that are produced mainly through photon exchange. The expression of the Dalitz density  $d\sigma(e^+e^- \rightarrow f\bar{f}A)/dx_1 dx_2$  will be still as in Eq. (4.43), with the coefficients  $G_1$  and  $G_2$  given by [here  $a = M_A^2/s$ ] [482,515]

$$\begin{aligned}
 G_1 &= \frac{g_{Aff}^2}{x_{12}} \left[ x_A^2 - a \left( \frac{x_A^2}{x_{12}} (1 + 2f) + 2(x_A - 1 - a) \right) \right] \\
 G_2 &= -2 \frac{g_{Aff}^2}{x_{12}} \left[ x_{12}(1 + x_A) - a(x_{12} - 4f + 2x_A - 2a) + f \frac{x_A^2}{x_{12}} (x_{12} - 3a) \right]
 \end{aligned} \tag{4.46}$$



Fig. 4.19. Higgs pair production in the bremsstrahlung and  $WW$  fusion processes.

while the contributions of  $G_3$ – $G_6$  can be neglected [note that, in two-Higgs doublet models, additional contributions to this process might come from other channels]. As can be seen, because the top quark is massive, the Dalitz density is different from the CP-even Higgs case by terms of  $\mathcal{O}(m_t^2/s)$  which, for moderate c.m. energies, are not that small. This feature provides an additional means to discriminate between a scalar and a pseudoscalar Higgs boson and even, to probe CP-violation in the  $t\bar{t}$ -Higgs couplings when both components are present; for a detailed discussion, see Ref. [516].

If one assumes general Higgs couplings to top quarks compared to the SM,  $\mathcal{L}(Ht\bar{t}) = (a + ib\gamma_5)g_{Ht\bar{t}}$  [and also to the  $Z$  boson,  $\mathcal{L}(HZZ) = c g_{HZZ}g_{\mu\nu}$ , when the diagram  $e^+e^- \rightarrow HZ^*$  with  $Z^* \rightarrow t\bar{t}$  is included, since its contribution need not be small relative to the dominant ones in extensions of the SM], one would have a rather involved dependence of the  $e^+e^- \rightarrow t\bar{t}H$  cross section on the phase space. The differential cross section can be written in a general form as  $d\sigma/d\Phi = \sum_i d_i f_i(\Phi)$ , where  $\Phi$  is the final state phase-space configuration and  $d_i$  are combinations of the Higgs coupling parameters  $a, b, c$  [in the SM, only the combinations  $d_i = a^2, ac$  and  $c^2$  will be present with  $a = c = 1$ ]. An optimal technique has been proposed in Ref. [516] for determining the coefficients  $d_i$  of the cross section by using appropriate weighting functions  $w_i(\Phi)$  such that  $\int \omega_i(d\sigma/d\Phi) = d_i$ , with the additional requirement that the statistical error in the extraction of the coefficients is minimized.

#### 4.3.3. Higgs boson pair production

To establish the Higgs mechanism experimentally, once the Higgs particle is discovered, the characteristic self-energy potential of the SM must be reconstructed. This task requires the measurement of the trilinear and quartic self-couplings of the Higgs boson,  $\lambda_{HHH} = 3M_H^2/v$  and  $\lambda_{HHHH} = 3M_H^2/v^2$ . The trilinear Higgs coupling can be measured directly in pair production of Higgs particles in  $e^+e^-$  collisions and several mechanisms can be exploited. Higgs pairs can be produced through double Higgs-strahlung off  $Z$  bosons [238,483,484,517]

$$e^+e^- \rightarrow Z^* \rightarrow ZHH \quad (4.47)$$

and vector boson [mostly  $W$  boson] fusion into two Higgs bosons [236,238,484]

$$e^+e^- \rightarrow V^*V^* \rightarrow \ell\ell HH. \quad (4.48)$$

The Feynman diagrams for the two processes are shown in Fig. 4.19 and, as can be seen, one of them involves the triple Higgs interaction. The other diagrams are generated by the gauge interactions familiar from single Higgs production in the dominant processes.

The complete reconstruction of the SM Higgs potential requires the measurement of the quadrilinear coupling  $\lambda_{HHHH}$  which can be accessed directly only through the production of three Higgs bosons,  $e^+e^- \rightarrow ZHHH$  and  $e^+e^- \rightarrow \bar{\nu}_e\nu_e HHH$ . However, these cross sections are reduced by two to three orders of magnitude compared to the corresponding double Higgs production channels, and are therefore too small to be observed at future  $e^+e^-$  colliders even with the large luminosities which are planned [see Section 4.3.4].

**4.3.3.1. The double Higgs-strahlung.** The differential cross section for the process of double Higgs-strahlung,  $e^+e^- \rightarrow ZHH$ , after the angular dependence is integrated out, can be cast into the form [484]

$$\frac{d\sigma(e^+e^- \rightarrow ZHH)}{dx_1 dx_2} = \frac{G_\mu^3 M_Z^6}{384\sqrt{2}\pi^3 s} \frac{(\hat{a}_e^2 + \hat{v}_e^2)}{(1 - \mu_Z)^2} \mathcal{Z} \quad (4.49)$$

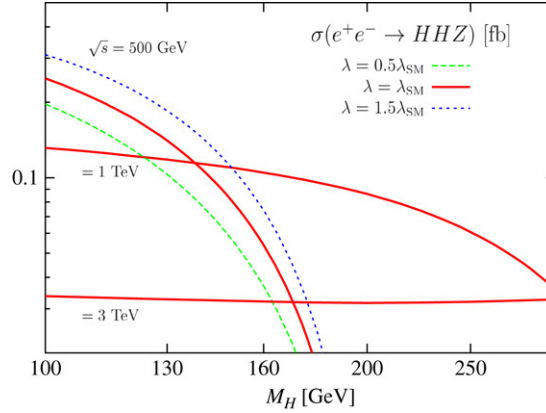


Fig. 4.20. The cross section for double Higgs–strahlung in  $e^+e^-$  collisions,  $e^+e^- \rightarrow HHZ$ , at c.m. energies  $\sqrt{s} = 0.5, 1$  and  $3$  TeV as a function of  $M_H$ . Shown for  $\sqrt{s} = 500$  GeV are the effects of a variation of the trilinear coupling by 50% from its SM value.

where the electron– $Z$  couplings are defined as usual, Eq. (1.54).  $x_{1,2} = 2E_{1,2}/\sqrt{s}$  are the scaled energies of the two Higgs particles,  $x_3 = 2 - x_1 - x_2$  is the scaled energy of the  $Z$  boson, and we define  $y_i = 1 - x_i$ ; the scaled masses are denoted by  $\mu_i = M_i^2/s$ . In terms of these variables, the coefficient  $\mathcal{Z}$  may be written as

$$\mathcal{Z} = \frac{1}{8}a^2 f_0 + \frac{1}{4\mu_Z(y_1 + \mu_H - \mu_Z)} \left[ \frac{f_1}{y_1 + \mu_H - \mu_Z} + \frac{f_2}{y_2 + \mu_H - \mu_Z} + 2\mu_Z a f_3 \right] + \{y_1 \leftrightarrow y_2\}$$

$$\text{with } a = \frac{\lambda'_{HHH}}{y_3 + \mu_Z - \mu_H} + \frac{2}{y_1 + \mu_H - \mu_Z} + \frac{2}{y_2 + \mu_H - \mu_Z} + \frac{1}{\mu_Z}. \quad (4.50)$$

The coefficients  $f_i$  are given by

$$\begin{aligned} f_0 &= \mu_Z[(y_1 + y_2)^2 + 8\mu_Z] \\ f_1 &= (y_1 - 1)^2(\mu_Z - y_1)^2 - 4\mu_H y_1(y_1 + y_1\mu_Z - 4\mu_Z) + \mu_Z(\mu_Z - 4\mu_H)(1 - 4\mu_H) - \mu_Z^2 \\ f_2 &= [\mu_Z(1 + \mu_Z - y_1 - y_2 - 8\mu_H) - (1 + \mu_Z)y_1 y_2](2 + 2\mu_Z - y_1 - y_2) \\ &\quad + y_1 y_2[y_1 y_2 + \mu_Z^2 + 1 + 4\mu_H(1 + \mu_Z)] + 4\mu_H \mu_Z(1 + \mu_Z + 4\mu_H) + \mu_Z^2 \\ f_3 &= y_1(y_1 - 1)(\mu_Z - y_1) - y_2(y_1 + 1)(y_1 + \mu_Z) + 2\mu_Z(\mu_Z + 1 - 4\mu_H). \end{aligned} \quad (4.51)$$

The first term in the coefficient  $a$  includes the scaled trilinear coupling  $\lambda'_{HHH} = 3M_H^2/M_Z^2$ . The other terms are related to sequential Higgs–strahlung and the 4 gauge–Higgs boson coupling; the individual terms can easily be identified by examining the propagators.

The production cross section, which is a binomial in the self-coupling  $\lambda_{HHH}$ , is shown in Fig. 4.20 as a function of the Higgs mass for three c.m. energies  $\sqrt{s} = 0.5, 1$  and  $3$  TeV. It is of the order of a fraction of a femtobarn when it is not too much suppressed by phase space and, because it is mediated by  $s$ -channel gauge boson exchange and scales like  $1/s$ , it is higher at lower energies for moderate Higgs masses. In addition, since the process is mediated by  $Z$  boson exchange, the cross section is doubled if oppositely polarized electron and positron beams are used. The cross section for the  $ZHH$  final state is rather sensitive to the  $\lambda_{HHH}$  coupling: for  $\sqrt{s} = 500$  GeV and  $M_H = 120$  GeV for instance, it varies by about 20% for a 50% variation of the trilinear coupling as shown in the figure.

The one-loop radiative corrections to the double Higgs–strahlung process are also very involved to calculate since, already at the tree level, one has to deal with three massive particles in the final state and, thus, one has to consider pentagonal diagrams and four-body final states at NLO. They have again been calculated recently by two independent groups [503,504], with results that agree reasonably, in particular at low energies. The QED corrections follow the same trend as what has been observed in the case of the  $e^+e^- \rightarrow t\bar{t}H$  process for  $M_H = 150$  GeV: they are very large and negative for c.m. energies near the production threshold,  $\sim -40\%$  at  $\sqrt{s} \sim 400$  GeV, and decrease in absolute value to reach the level of a few percent above  $\sqrt{s} \sim 600$  GeV,  $\sim +5\%$  at  $1.5$  TeV; see the left panel of Fig. 4.21. For the pure weak corrections, when calculated using  $\alpha$  in the Born term, they are rather small not exceeding  $\sim +5\%$  near the threshold and at moderate c.m. energies when the cross section is maximal; see the right panel of Fig. 4.21. At

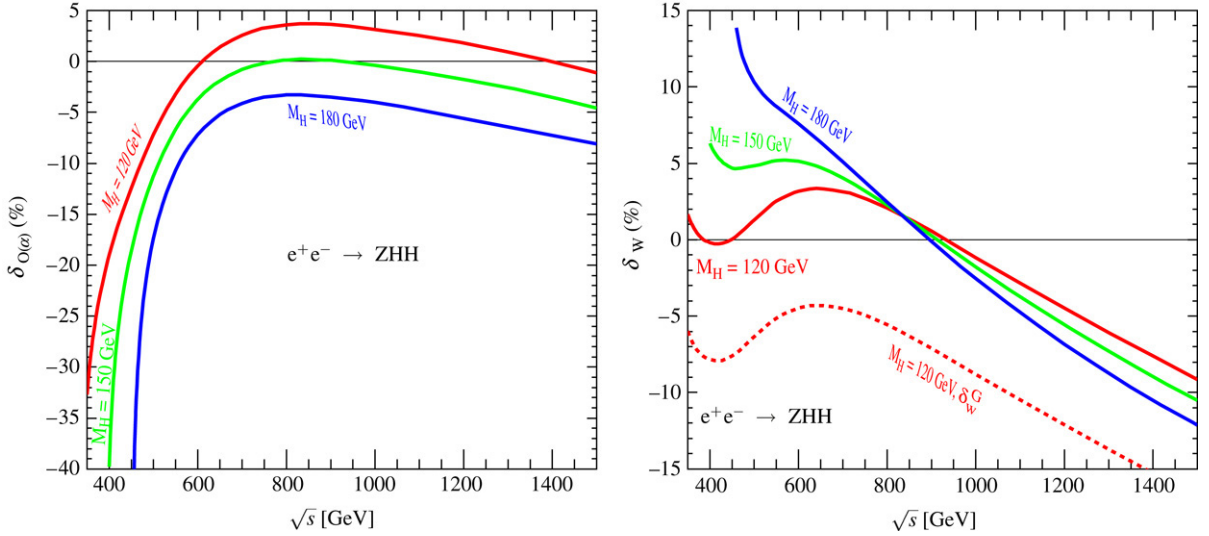


Fig. 4.21. The full  $\mathcal{O}(\alpha)$  relative correction (left panel) and the relative electroweak correction  $\delta_W$  (right panel) as functions of the c.m. energy for  $M_H = 120, 150, 180$  GeV; the genuine weak correction in the IBA is presented for  $M_H = 120$  GeV (dotted line) [503].

higher energies, the weak corrections turn negative and increase in size to reach  $\sim -10\%$  at  $\sqrt{s} = 1.5$  TeV. The weak corrections calculated in the IBA are also shown (dotted lines). As in the case of the  $e^+e^- \rightarrow HZ$  parent process, this approximation fails to reproduce the magnitude of the weak corrections, especially at high energies. The approximate top quark mass correction to the Higgs self-coupling does not also reproduce the bulk of the weak correction.

Note that the correction to the invariant mass distribution of the Higgs pair, which can be a means to isolate the  $HHH$  vertex since the two Higgs bosons originate from the decay of an off-shell scalar particle [518], has also been calculated and found to be small.

**4.3.3.2. The  $WW$  fusion process.** At high energies, double Higgs boson production in the  $WW$  fusion channel,  $e^+e^- \rightarrow \nu\bar{\nu}HH$  [236,238], provides the largest cross section for Higgs bosons in the intermediate mass range, in particular when the initial beams are polarized. [Again, the  $ZZ$  fusion channel has a cross section that is one order of magnitude smaller compared to  $WW$  fusion as a result of the smaller  $Z$  couplings to electrons]. The cross section for this four-particle final state is very involved but it can be roughly estimated in the equivalent  $W$  boson approximation,  $WW \rightarrow HH$ . Taking into account only the dominant longitudinal  $W$  contribution, denoting by  $\beta_{W,H}$  the  $W, H$  boson velocities in the c.m. frame, we define the variable  $x_W = (1 - 2M_H^2/\hat{s})/(\beta_W\beta_H)$  with  $\hat{s}^{1/2}$  as the invariant energy of the  $WW$  pair. The amplitude  $\mathcal{M}_{LL}$  has been given in Eq. (3.90) when this process was discussed at hadron colliders and, integrating out the angular dependence, the corresponding total cross section reads [484,518]

$$\begin{aligned}
 \hat{\sigma}_{LL} = & \frac{G_F^2 M_W^4}{4\pi \hat{s}} \frac{\beta_H}{\beta_W (1 - \beta_W^2)^2} \left\{ (1 + \beta_W^2)^2 \left[ 1 + \frac{\lambda'_{HHH}}{(\hat{s} - M_H^2)/M_Z^2} \right]^2 \right. \\
 & + \frac{16}{(1 + \beta_H^2)^2 - 4\beta_H^2 \beta_W^2} \left[ \beta_H^2 (-\beta_H^2 x_W^2 + 4\beta_W \beta_H x_W - 4\beta_W^2) + (1 + \beta_W^2 - \beta_W^4)^2 \right] \\
 & + \frac{1}{\beta_W^2 \beta_H^2} \left( \ell_W + \frac{2x_W}{x_W^2 - 1} \right) \left[ \beta_H (\beta_H x_W - 4\beta_W) (1 + \beta_W^2 - \beta_W^4 + 3x_W^2 \beta_H^2) \right. \\
 & + \beta_H^2 x_W (1 - \beta_W^4 + 13\beta_W^2) - \frac{1}{x_W} (1 + \beta_W^2 - \beta_W^4)^2 \left. \right] + \frac{2(1 + \beta_W^2)}{\beta_W \beta_H} \left[ 1 + \frac{\lambda_{HHH}}{(\hat{s} - M_H^2)/M_Z^2} \right] \\
 & \times \left. \left[ \ell_W (1 + \beta_W^2 - \beta_W^4 - 2\beta_W \beta_H x_W + \beta_H^2 x_W^2) + 2\beta_H (x_W \beta_H - 2\beta_W) \right] \right\} \quad (4.52)
 \end{aligned}$$

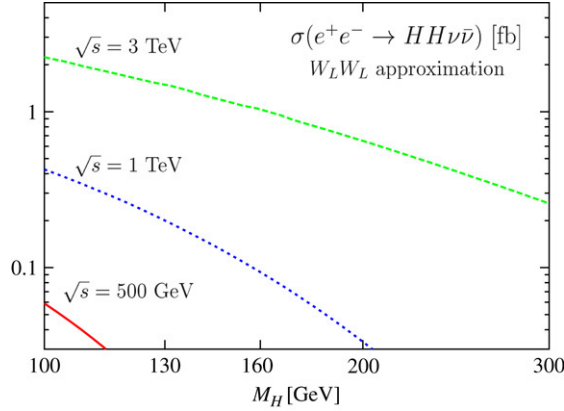


Fig. 4.22. The cross section for the  $W_L W_L \rightarrow HH$  process in  $e^+e^-$  collisions with at c.m. energies  $\sqrt{s} = 0.5, 1$  and  $3$  TeV as a function of  $M_H$ .

with  $\ell_W = \log[(x_W - 1)/(x_W + 1)]$ . After folding the cross section of the subprocess with the longitudinal  $W_L$  spectra given in Eq. (3.51), one obtains the total  $e^+e^-$  cross section in the effective  $W_L W_L$  approximation, which exceeds the exact value of the  $e^+e^- \rightarrow \nu\bar{\nu}HH$  cross section by about a factor in the range 2–5 depending on the collider energy and the Higgs mass.

The cross section is shown in Fig. 4.22 as a function of  $M_H$  for  $\sqrt{s} = 0.5, 1$  and  $3$  TeV. As expected, the fusion cross sections increase with rising energy. Again, there is a significant variation of the cross section with a variation of  $\lambda_{HHH}$ . The transverse components of the  $W$  bosons give rather small contributions through  $W_T W_T \rightarrow HH$  for large Higgs masses. Note that the  $\mathcal{O}(\alpha)$  corrections have been also calculated using GRACE-LOOP and a preliminary result has appeared in Ref. [497]; the corrections are of  $\mathcal{O}(10\%)$ .

#### 4.3.4. Other subleading processes in $e^+e^-$ collisions

Finally, there are other subdominant higher-order Higgs production processes: the associated production with a photon, the loop induced as well as some tree-level higher-order double Higgs production, the associated Higgs production with gauge boson pairs and the associated production with two fermions and a gauge boson. We briefly summarize the main features of these processes for completeness.

**4.3.4.1. Higgs production in association with two gauge bosons.** Similarly to what one observes at hadron colliders, in high-energy  $e^+e^-$  collisions,  $W$  pair production,  $e^+e^- \rightarrow W^+W^-$ , has a very large cross section. This is also the case of  $e^+e^- \rightarrow ZZ$  and  $Z\gamma$  production,<sup>33</sup> which are mediated by  $t$ -channel electron exchange. It is thus tempting to take advantage of these large production rates and consider the emission of an additional Higgs particle from one of the gauge boson lines

$$e^+e^- \rightarrow W^+W^-H, ZZH, Z\gamma H \quad (4.53)$$

as shown in Fig. 4.23. The hope is that the suppression by the additional electroweak factor might be compensated by the initially large production rates.

This turns out to be quite true [245,487,488]: at least for the process  $e^+e^- \rightarrow Z\gamma H$  [where one has to apply a cut on the transverse momentum  $p_T \gtrsim 5$  GeV of the photon] and for the  $e^+e^- \rightarrow W^+W^-H$  mechanism, the cross sections are quite sizable. At  $\sqrt{s} = 800$  GeV and for  $M_H \sim 100$ – $200$  GeV, they are at the level of a few fb as shown in Fig. 4.24. With the expected luminosity  $\mathcal{L} = 500 \text{ fb}^{-1}$ , they could lead to more than 1000 events which are rather clean. For masses  $M_H \sim 300$  GeV, they are still at the level of 1 fb, which is only one order of magnitude smaller than the Higgs–strahlung process at these values of  $M_H$  and  $\sqrt{s}$ . Again, as one might have expected, the production rate for the  $e^+e^- \rightarrow ZZH$  process is an order of magnitude smaller than that of the  $e^+e^- \rightarrow WWH$  process. Note that the cross sections for these processes do not become larger at higher energies.

<sup>33</sup> As noted before, the process with the additional final state photon should be viewed as part of the radiative corrections to the Higgs–strahlung process [the same remark holds for the process  $e^+e^- \rightarrow \nu_e\bar{\nu}_e H\gamma$  to be discussed later, which is part of the QED correction to the  $WW$  fusion

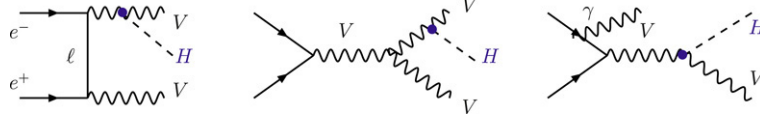
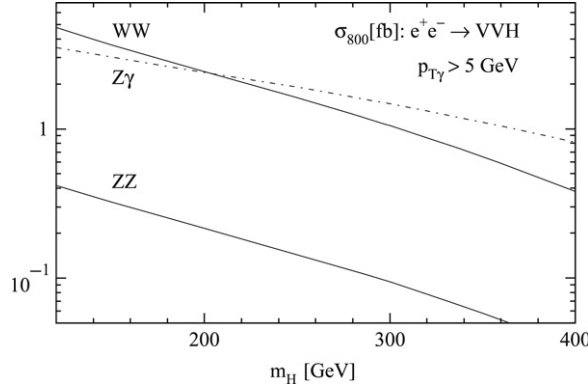
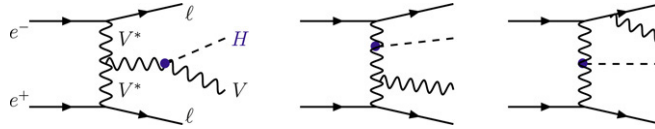


Fig. 4.23. Diagrams for associated Higgs boson production with two gauge bosons.

Fig. 4.24. The cross sections for the associated production of the Higgs boson with a pair of gauge bosons,  $e^+e^- \rightarrow HVV$ , as functions of  $M_H$  at  $\sqrt{s} = 800$  GeV; from [245].Fig. 4.25. Feynman diagrams for the associated production of a Higgs boson with a gauge boson and two leptons in  $e^+e^-$  collisions.

Once the Higgs particle has been detected in the main channels, these processes could be useful: in conjunction with the dominant Higgs-strahlung and  $WW$  fusion processes, they would allow one to test the quartic couplings involving Higgs and gauge bosons and, for instance, to probe directly the  $HZW^+W^-$  and  $H\gamma W^+W^-$  couplings and even, potentially, C-violating  $HZZZ$  and  $H\gamma ZZ$  couplings which are absent in the SM.

**4.3.4.2. Higgs production in association with a gauge boson and two leptons.** Also as in the case of the LHC, Higgs bosons can be produced in association with a gauge boson and two leptons in the fusion processes [245,487]

$$e^+e^- \rightarrow \nu_e e^\pm W^\mp H, \nu_e \bar{\nu}_e \gamma H, \nu_e \bar{\nu}_e ZH \quad (4.54)$$

with some generic Feynman diagrams shown in Fig. 4.25.

Since, as previously discussed, the parent fusion processes  $e^+e^- \rightarrow H\ell\ell$  have rather large production cross sections at high energies, one might hope again that the emission of an additional gauge boson will still lead to a reasonable event rate, similar to the case of double Higgs boson production in the vector boson fusion channels  $e^+e^- \rightarrow HH\ell\ell$  discussed in the preceding section. These processes have been considered in Ref. [487] and are being updated [245]. The cross sections for  $e^+e^- \rightarrow \nu\bar{\nu}ZH$  and  $e^+e^- \rightarrow \nu_e W H$  are shown in Fig. 4.26 as functions of the c.m. energy for  $M_H = 160$  GeV. As can be seen, they follow the general trend of vector boson fusions mechanisms and increase with energy and/or lower Higgs masses. They are quite sizable since, for  $e^+e^- \rightarrow \nu_e e^\pm W^\mp H$ , the cross section reaches almost the level of 10 fb at  $\sqrt{s} \sim 1$  TeV for  $M_H \sim 120$  GeV. The cross section is a factor of  $\sim 5$  smaller in the case of the  $e^+e^- \rightarrow \nu_e \bar{\nu}_e ZH$  mechanism and is even smaller in the case of the  $e^+e^- \rightarrow e^+e^- ZH$  process which is not shown.

mechanism]. However, this process can be discussed on its own since here the photon is required to be detected and the  $e^+e^- \rightarrow HZ\gamma$  process can have a comparable rate than the parent process which scales as  $1/s$  at high energies, as the ISR photon will decrease the effective c.m. energy.

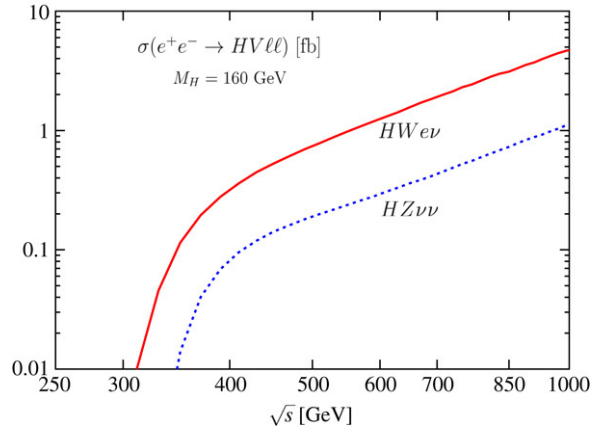


Fig. 4.26. The cross sections for associated production of the Higgs boson with a gauge boson and two leptons,  $e^+e^- \rightarrow HV\ell\ell$ , as functions of  $\sqrt{s}$  for  $M_H = 160$  GeV. They have been obtained using the program WHIZARD [519].

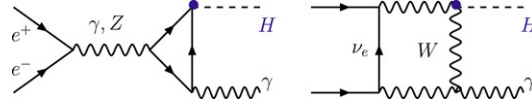


Fig. 4.27. Diagrams for associated Higgs production with a photon in  $e^+e^-$  collisions.

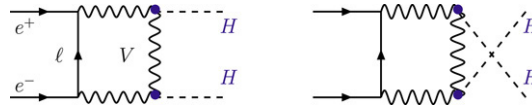


Fig. 4.28. Feynman diagrams for loop induced Higgs pair production.

**4.3.4.3. Higgs production in association with a photon.** In the SM, the process where a Higgs boson is produced in association with a photon,  $e^+e^- \rightarrow H\gamma$  [485], proceeds through  $s$ -channel  $\gamma^*\gamma H$  and  $Z^*\gamma H$  vertex diagrams, but additional  $t$ -channel vertex and box diagrams involving  $W$ /neutrino and  $Z$ /electron exchange also occur; Fig. 4.27. The  $s$ -channel contributions involve the same form factors as that of the effective couplings for the  $H \rightarrow Z\gamma, \gamma\gamma$  decays discussed in Section 2.3, but with one of the two photons and the  $Z$  boson being virtual, with an effective mass  $M_{Z^*} = \sqrt{s}$ .

Since it is a higher-order process in the electroweak coupling, the cross section is rather small,  $\sigma(e^+e^- \rightarrow H\gamma) \sim 0.05$  fb for  $M_H \sim 100\text{--}200$  GeV at  $\sqrt{s} = 500$  GeV. However, since the photon is mono-chromatic, the signal is very clean allowing for a reasonable hope to isolate these events if enough luminosity is collected at future high-energy colliders. Note that the longitudinal polarization of both electron and positron beams will increase the cross sections by about a factor of 4 compared to the unpolarized case. This process would then allow for an alternative way to probe the induced  $H\gamma\gamma$  and  $HZ\gamma$  couplings and, potentially, to probe the heavy particles involved in the loops.

**4.3.4.4. Loop induced double Higgs production.** Due to CP-invariance, the  $ZHH$  coupling is absent in the SM and the process  $e^+e^- \rightarrow Z \rightarrow HH$  does not occur at tree level but only through loop contributions [486]. Because of orbital momentum conservation, the amplitudes for the vertex diagrams with  $s$ -channel  $\gamma$  and  $Z$  bosons giving rise to two  $H$  bosons vanish [only the contribution of the longitudinal component of the  $Z$  boson survives but it is proportional to the electron mass and is thus negligible]. In addition, because of chiral symmetry for  $m_e = 0$ , the diagrams involving the  $He^+e^-$  vertices give zero contributions. The contribution of vertices involving the  $HHVV$  interaction include also contributions that are proportional to  $m_e$  or  $m_{\nu_e}$ . Therefore, in the SM, the process  $e^+e^- \rightarrow HH$  can be generated only through box diagrams involving  $W$ /neutrino and  $Z$ /electron virtual states, Fig. 4.28.

Again, because of the additional electroweak factor, the production cross sections are rather small. Except when approaching the  $M_H = 2M_W$  threshold, where there is a small increase, the cross section is practically constant and



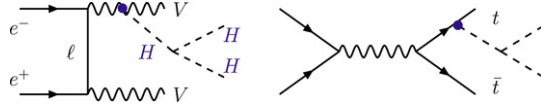


Fig. 4.29. Higher-order double Higgs production processes at the tree level.

amounts to  $\sim 0.2$  fb at  $\sqrt{s} = 500$  GeV for  $M_H \sim 100$ –200 GeV. With left-handed polarization of the electron beam, the cross section is increased by a factor of two, while for left-handed electrons and right-handed positrons, it increases by a factor of four; these simple factors are due to the fact that, as usual the contribution of the box with  $W$  exchange is much larger than that with the  $Z$  exchange. With a very high luminosity, one might hope that the final state can be isolated. A deviation from the SM expectation would signal a breakdown of CP-invariance or the existence of new particles contributing to the loop diagrams.

**4.3.4.5. Higher-order tree-level multi-Higgs production.** Finally, there are also higher-order processes for double Higgs production which occur at the tree level. Besides the  $ZZ$  fusion process  $e^+e^- \rightarrow HH e^+e^-$  which, as mentioned previously, has a cross section that is one order of magnitude smaller than that of the  $WW$  fusion process [for  $M_H \sim 100$  GeV, the  $e^+e^- \rightarrow e^+e^- HH$  cross section barely reaches the level of  $\sim 0.1$  fb even at very high energies,  $\sqrt{s} \sim 2$  TeV], one has the following reactions with  $V = W, Z$  and  $\ell = e, \nu_e$ :

associated double Higgs production with two gauge bosons :  $e^+e^- \rightarrow VVHH$

associated double Higgs production with  $t\bar{t}$  pairs :  $e^+e^- \rightarrow t\bar{t}HH$ . (4.55)

Some Feynman diagrams for these reactions [those which involve the trilinear Higgs interaction] are displayed in Fig. 4.29. The production cross sections for these processes have been calculated in Refs. [520] using the package CompHEP [521] for the automatic evaluation of the full set of amplitudes and, as expected, they are very small. The  $e^+e^- \rightarrow WWHH$  cross section is at the level of 0.03 fb at  $\sqrt{s} \sim 700$  GeV even for a Higgs mass as low as  $M_H \sim 65$  GeV, while the rate for  $e^+e^- \rightarrow ZZHH$  is again one order of magnitude smaller. In the case of the  $e^+e^- \rightarrow t\bar{t}HH$  process [520,522], the cross section is at the level of 6(15) ab at a c.m. energy  $\sqrt{s} = 0.8(1.6)$  TeV for  $M_H \sim 130$  GeV and  $m_t = 175$  GeV. Thus, about 10 of such events could be produced if very high luminosities,  $\mathcal{L} \sim 1 \text{ ab}^{-1}$ , can be collected at these energies.

In the case of triple Higgs production processes, which would allow for the determination of the quartic Higgs coupling, the cross sections are unfortunately too small as mentioned earlier. In the  $e^+e^- \rightarrow ZHHH$  process [484,520], for instance, the signal amplitude squared involving the four-Higgs coupling [as well as the irreducible Higgs-strahlung amplitudes] is suppressed by a factor  $[\lambda_{HHHH}^2/16\pi^2]/[\lambda_{HHH}^2/M_Z^2] \sim 10^{-3}$  relative to  $e^+e^- \rightarrow ZHH$ , not to mention the phase-space suppression due to the additional final-state heavy particle. The cross sections are below the atobarn level:  $\sigma(HHHZ) \sim 0.44$  ab for  $M_H \sim 110$  GeV and  $\sqrt{s} \sim 1$  TeV and are not very sensitive to a variation of the self-coupling:  $\sigma(HHHZ) \sim 0.41$  (0.46) ab when  $\lambda_{HHHH}$  is altered by a factor  $\frac{1}{2}(\frac{3}{2})$  [484]. The fusion process  $e^+e^- \rightarrow HHH\nu\bar{\nu}$  has also a very small cross section,  $\sigma(HHH\nu\bar{\nu}) \sim 0.4$  ab at  $\sqrt{s} = 3$  TeV [523].

#### 4.4. Higgs studies in $e^+e^-$ collisions

In this section, we summarize the precision tests of the SM Higgs sector which can be performed at an  $e^+e^-$  machine operating in the 350–1000 GeV energy range. We also briefly discuss the additional precision studies which can be made by moving to higher energies at CLIC and by revisiting the physics at the  $Z$ -resonance in the GigaZ option. We will almost exclusively rely on the detailed studies which have been performed for the TESLA Technical Design Report [456,462] and on the very recent analyses of the CLIC Physics working group [460], since they involve realistic simulations of the experimental environments.<sup>34</sup> We refer to these two reports for more details and for more references on the original work. We will also mention some updated analyses which appeared during the Linear Collider Workshops held in Amsterdam [530] and Paris [531]. Complementary material can be found in the reports

<sup>34</sup> For the TESLA analyses in particular, the backgrounds, the beamstrahlung and detector response have been taken into account, generally using programs such as CompHEP [521] or WHiZard [519] in addition to the usual Monte Carlo generators [379,524,525], Circe [526] and SIMDET [527] or BRAHMS [528]; see Ref. [529].

Table 4.3

Numerical values for SM Higgs production cross sections [in fb] in  $e^+e^-$  collisions at two center of mass energies  $\sqrt{s} = 500$  GeV (top) and  $\sqrt{s} = 1$  TeV (bottom) for selected values of the Higgs boson mass and  $m_t = 172$  GeV

$M_H$ (GeV)	$\sigma(HZ)$	$\sigma(H\nu_e\bar{\nu}_e)$	$\sigma(He^+e^-)$	$\sigma(Ht\bar{t})$	$\sigma(HHZ)$	$\sigma(HH\nu\bar{\nu})$
115	58.67	81.98	8.77	0.59	0.19	0.03
120	57.91	78.30	8.38	0.43	0.18	0.02
130	56.31	71.28	7.64	0.21	0.14	0.01
140	54.61	64.71	6.95	0.07	0.11	–
150	52.83	58.58	6.30	–	0.08	–
160	50.96	52.88	5.69	–	0.05	–
170	49.03	47.60	5.13	–	0.03	–
180	47.03	42.71	4.60	–	0.02	–
200	42.88	34.03	3.67	–	–	–
300	21.38	8.26	0.89	–	–	–
400	3.24	0.73	0.07	–	–	–
<hr/>						
115	12.90	219.54	24.26	2.30	0.12	0.30
120	12.86	214.58	23.73	2.19	0.12	0.27
130	12.76	204.92	22.70	1.99	0.12	0.21
140	12.66	195.60	21.70	1.81	0.11	0.16
150	12.55	186.63	20.73	1.65	0.11	0.12
160	12.44	178.01	19.80	1.51	0.10	0.10
170	12.32	169.72	18.90	1.37	0.10	0.07
180	12.19	161.76	18.03	1.25	0.10	0.06
200	11.92	146.78	16.40	1.05	0.09	0.03
300	10.22	88.19	9.93	0.43	0.03	–
400	8.13	50.32	5.68	0.16	–	–
500	5.89	26.55	3.00	0.04	–	–
600	3.78	12.41	1.40	–	–	–
700	2.03	4.75	0.53	–	–	–
800	0.81	1.24	0.14	–	–	–

These numbers have been obtained with the program HPROD [533] and no radiative correction nor beamstrahlung is included.

of the American Linear Collider working group [458] and the JLC working group [459], as well as in the detailed reviews given in Refs. [491,532].

#### 4.4.1. Higgs boson signals

As discussed in the previous sections, the main production mechanisms for SM Higgs particles are the Higgs–strahlung process  $e^+e^- \rightarrow ZH$  and the  $WW$  fusion process  $e^+e^- \rightarrow \bar{\nu}_e\nu_e H$ . Subleading production channels are the  $ZZ$  fusion mechanism,  $e^+e^- \rightarrow e^+e^- H$ , the associated production with top quarks  $e^+e^- \rightarrow t\bar{t}H$  and double Higgs production in the strahlung  $e^+e^- \rightarrow HHZ$  and fusion  $e^+e^- \rightarrow \bar{\nu}\nu HH$  processes which, despite the small production rates, are very useful when it comes to the study of the Higgs properties. The other production processes, although some of them have substantial cross sections such as  $e^+e^- \rightarrow HW^+W^-$  and  $\nu_e e^\pm W^\mp H$ , will not [at least in the context of the SM] provide any additional information and we will ignore them in the following discussion.

The cross sections have been given previously, but we summarize them again in Fig. 4.30 for four c.m. energies  $\sqrt{s} = 350$  GeV, 500 GeV, 1 TeV and 3 TeV, as functions of the Higgs mass. They have been obtained with the FORTRAN code HPROD [533]. We should mention that these cross sections do not include the radiative corrections which have been discussed in this chapter [except that we work in the IBA which absorbs some of the electroweak corrections], and no photon ISR nor beamstrahlung effects have been taken into account. However, since these corrections and effects are rather small, except in peculiar regions of the phase space [such as for  $e^+e^- \rightarrow t\bar{t}H$  near threshold and  $e^+e^- \rightarrow HZ$  at  $\sqrt{s} \gg M_H$ ], these numbers approach the exact results to better than 5%–10% depending on the process, and this approximation is sufficient for most of the purposes that one can have before the experiments actually start. In Table 4.3, we display the numerical values of the cross sections for selected values of the Higgs mass at the two different energies  $\sqrt{s} = 500$  GeV and 1 TeV.

As previously mentioned, the Higgs–strahlung cross section scales as  $1/s$  and therefore dominates at low energies, while the one of  $WW$  fusion mechanism rises like  $\log(s/M_H^2)$  and becomes more important at high energies. At

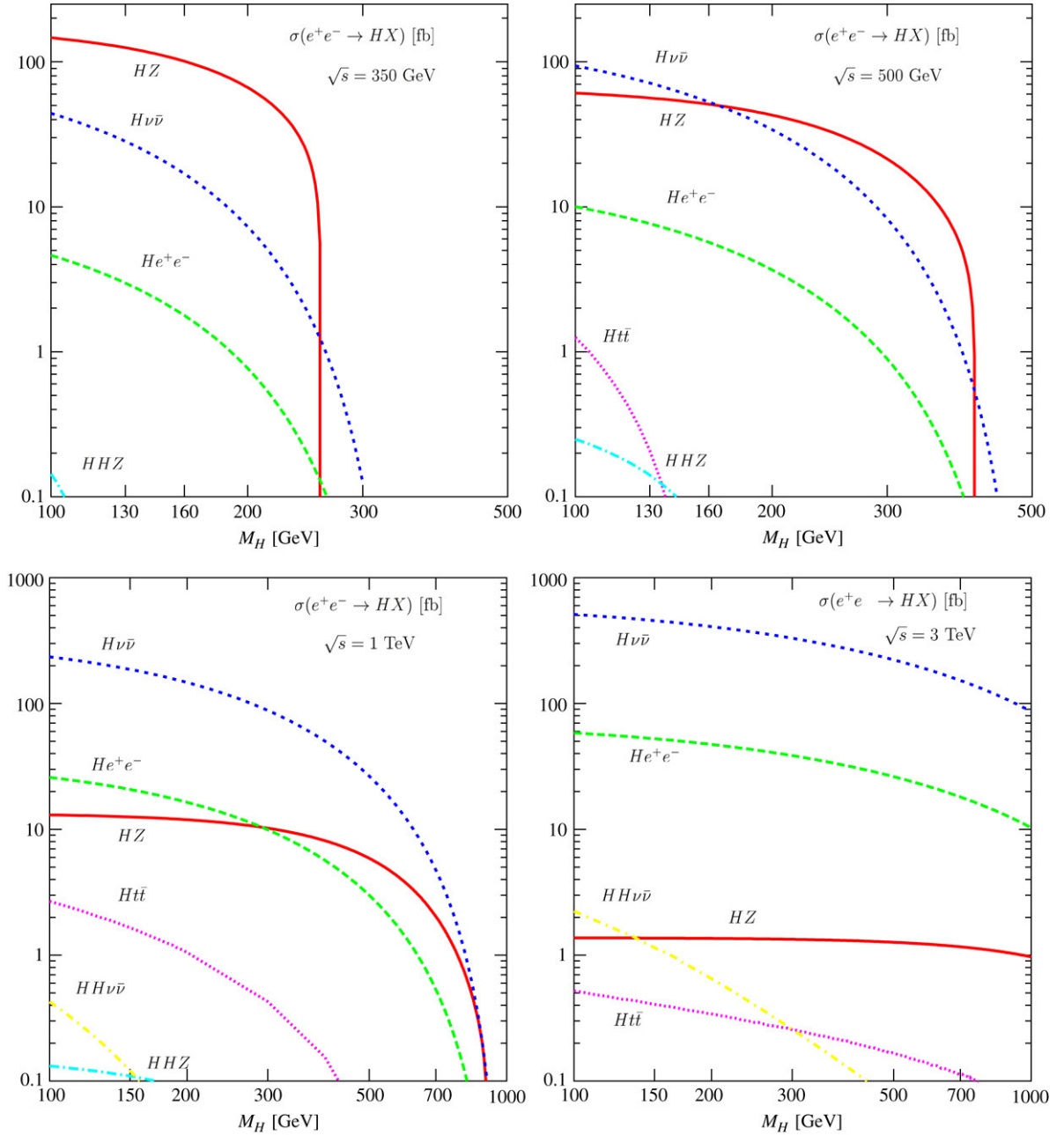


Fig. 4.30. Production cross sections of the SM Higgs boson in  $e^+e^-$  collisions in the dominant and subdominant processes as functions of the Higgs mass for four center of mass energies,  $\sqrt{s} = 350$  GeV, 500 GeV, 1 TeV and 3 TeV. Radiative corrections, initial state radiation and beamstrahlung effects are not included. The cross sections have been obtained with the program HPROD [533].

$\sqrt{s} \sim 500$  GeV, the two processes have approximately the same cross sections,  $\mathcal{O}(50 \text{ fb})$  for the interesting Higgs mass range  $115 \text{ GeV} \lesssim M_H \lesssim 200 \text{ GeV}$ . With an integrated luminosity  $\mathcal{L} \sim 500 \text{ fb}^{-1}$ , as expected at the TESLA machine for instance, approximately 30.000 and 40.000 events can be collected in, respectively, the  $HZ$  and  $\nu\bar{\nu}H$  channels for  $M_H \sim 120$  GeV. This sample is more than enough to observe the Higgs particle and to study its properties in great detail.

In the Higgs-strahlung process, the recoiling Z boson, which can be tagged through its clean  $\ell^+\ell^-$  decays, with  $\ell = e$  or  $\mu$ , but also through decays into quarks which have much larger statistics, is mono-energetic and the Higgs

Table 4.4

Expected number of signal events for  $500 \text{ fb}^{-1}$  for the Higgs–strahlung channel with dilepton final states  $e^+e^- \rightarrow ZH \rightarrow \ell^+\ell^-X$ , at different  $\sqrt{s}$  and  $M_H$  values

$M_H$ (GeV)	350 GeV	500 GeV	1000 GeV
120	4670	2020	377
180	2960	1650	365
250	230	1110	333
Max $M_H$	258	407	730

The last line is for the maximum  $M_H$  value yielding more than 50 signal events in this final state. The numbers for  $\sqrt{s} = 1 \text{ TeV}$  do not include the selection cuts and ISR corrections of [456].

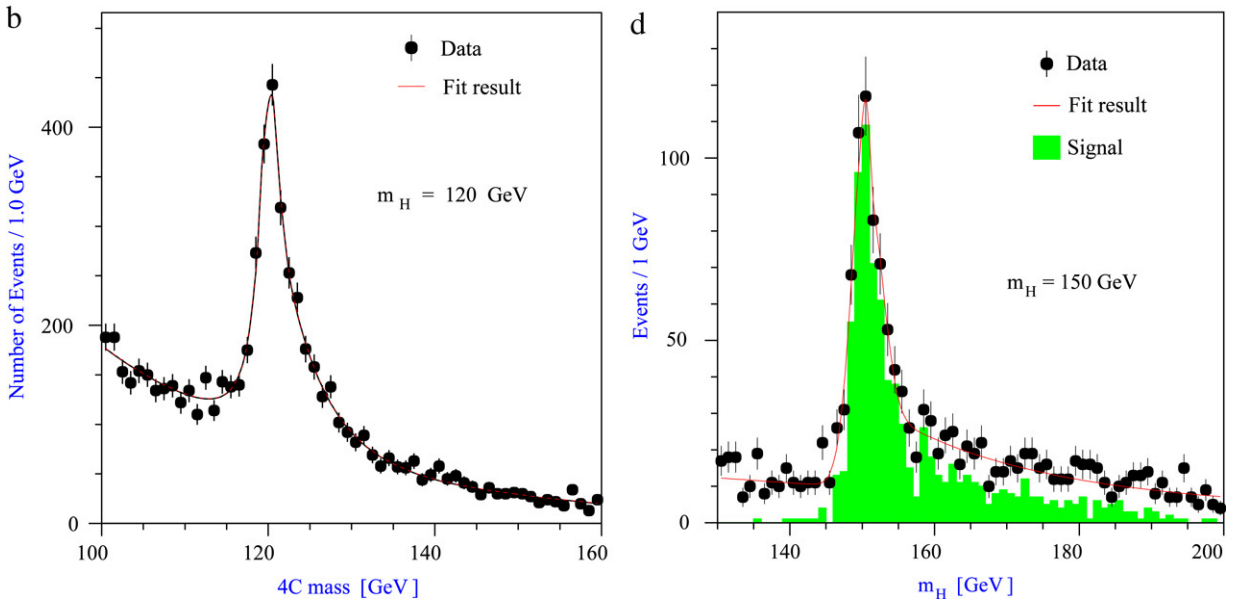


Fig. 4.31. The Higgs mass peak reconstructed in different channels with constrained fits for two values of  $M_H$ , an integrated luminosity of  $500 \text{ fb}^{-1}$  and  $\sqrt{s} = 350 \text{ GeV}$  in  $HZ \rightarrow q\bar{q}\ell^+\ell^-$  at  $M_H = 120 \text{ GeV}$  (left) and  $HZ \rightarrow W^+W^-\ell^+\ell^-$  at  $M_H = 150 \text{ GeV}$  (right); from Ref. [456].

mass can be derived from the energy of the  $Z$  boson since the initial  $e^\pm$  beam energies are sharp when the effect of beamstrahlung is strongly suppressed. Therefore, it will be easy to separate the signal from the backgrounds [534, 535]. In the low mass range,  $M_H \lesssim 140 \text{ GeV}$ , the process leads to  $b\bar{b}q\bar{q}$  and  $b\bar{b}\ell\ell$  final states, with the  $b$ -quarks being efficiently tagged by means of micro-vertex detectors. In the mass range where the decay  $H \rightarrow WW^*$  is dominant, the Higgs boson can be reconstructed by looking at the  $\ell\ell$ +four-jet or six-jet final states, and using the kinematical constraints on the fermion invariant masses which peak at  $M_W$  and  $M_H$ , the backgrounds are efficiently suppressed. Also the  $\ell\ell q\bar{q}\ell\nu$  and  $q\bar{q}q\bar{q}\ell\nu$  channels are easily accessible.

It has been shown in detailed simulations [456] that only a few  $\text{fb}^{-1}$  data are needed to obtain a  $5\sigma$  signal for a Higgs boson with a mass  $M_H \lesssim 150 \text{ GeV}$  at a  $500 \text{ GeV}$  collider, even if it decays invisibly [as could happen in some extensions of the SM]. In fact, for such small masses, it is better to move to lower energies where the Higgs–strahlung cross section is larger. Fig. 4.31 shows the reconstructed Higgs mass peaks in the strahlung process at  $\sqrt{s} = 350 \text{ GeV}$  with a luminosity  $\mathcal{L} = 500 \text{ fb}^{-1}$  for  $M_H = 120 \text{ GeV}$  in the decay  $H \rightarrow q\bar{q}$  and for  $M_H = 150 \text{ GeV}$  in the decay  $H \rightarrow WW^*$ . At this energy and integrated luminosity, Higgs masses up to  $M_H \sim 260 \text{ GeV}$  can be probed in this channel.

Moving to higher energies, Higgs bosons with masses up to  $M_H \sim 400 \text{ GeV}$  can be discovered in the strahlung process at an energy of  $500 \text{ GeV}$  and with a luminosity of  $500 \text{ fb}^{-1}$ . For even higher masses, one needs to increase the c.m. energy of the collider and, as a rule of thumb, Higgs masses up to  $\sim 80\%\sqrt{s}$  can be probed. This means that a  $1 \text{ TeV}$  collider can probe the entire SM Higgs mass range,  $M_H \lesssim 700 \text{ GeV}$ . Table 4.4 shows the maximal

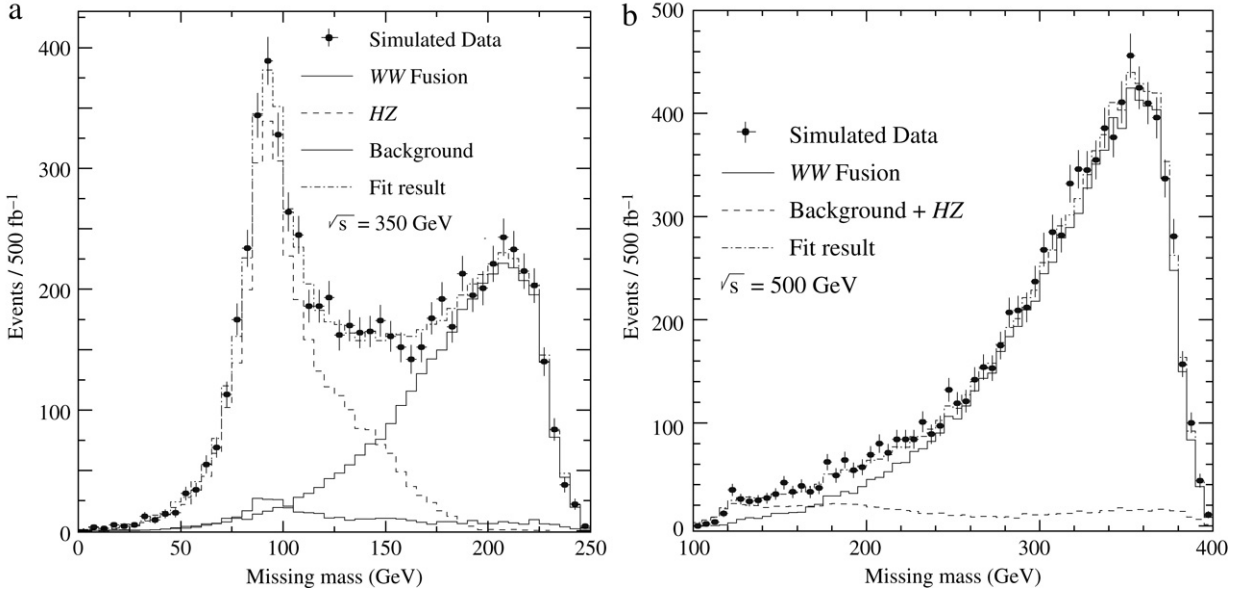


Fig. 4.32. The missing mass distribution in the  $\nu\bar{\nu}b\bar{b}$  final state at  $\sqrt{s} = 350$  GeV (left) and 500 GeV (right) for  $M_H = 120$  GeV in  $WW$  fusion, Higgs–strahlung and the interference, as well as for the background. The  $WW$  fusion contribution is measured from a fit to the shape of this distribution; from Ref. [456].

Higgs mass values which can be reached at various c.m. energies by requiring at least 50 signal events in the process  $e^+e^- \rightarrow HZ \rightarrow H\ell\ell$ .

The  $WW$  fusion mechanism offers a complementary production channel. In the low Higgs mass range where the decay  $H \rightarrow b\bar{b}$  is dominant, flavor tagging plays an important role to suppress the two-jet plus missing energy background. The  $e^+e^- \rightarrow H\bar{\nu}\nu \rightarrow b\bar{b}\bar{\nu}\nu$  final state can be separated from the corresponding one in the Higgs–strahlung process  $e^+e^- \rightarrow HZ \rightarrow b\bar{b}\bar{\nu}\nu$  [536] by exploiting their different characteristics in the  $\nu\bar{\nu}$  invariant mass which are measurable through the missing mass distribution; see Fig. 4.32. The polarization of the electron and positron beams, which allows one to switch on and off the  $WW$  fusion contribution, can be very useful to control the systematic uncertainties.

For larger Higgs boson masses, when the decays  $H \rightarrow WW^{(*)}, ZZ^{(*)}$  are dominant, the main backgrounds are  $WW(Z)$  and  $ZZ(Z)$  production which have large cross sections at high energies and eventually  $t\bar{t}$ , but again, they can be suppressed using kinematical constraints from the reconstruction of the Higgs mass peak. For even higher masses, when the Higgs boson decays into  $t\bar{t}$  final states, the  $e^+e^- \rightarrow t\bar{t}$  and  $t\bar{t}e^+e^-$  backgrounds can be reduced to a manageable level by exploiting the characteristics of the  $\nu\bar{\nu}b\bar{b}WW$  signature.

Turning to the subleading processes, we have seen that the  $ZZ$  fusion mechanism has a cross section that is one order of magnitude smaller than  $WW$  fusion, a result of the comparison of smaller neutral couplings to the charged current couplings. However, the full final state can be reconstructed in this case. At c.m. energies above 1 TeV, the cross section exceeds the one of the Higgs–strahlung process so that  $e^+e^- \rightarrow He^+e^-$  can be used instead for model-independent searches by tagging the  $e^+e^-$  pair and reconstructing the missing mass [531].

The associated production with top quarks has a very small cross section at  $\sqrt{s} = 500$  GeV due to the phase-space suppression but at  $\sqrt{s} = 800$  GeV it can reach the level of a few femtobarns. For  $M_H \lesssim 140$  GeV, the spectacular final state signal,  $W^+W^-b\bar{b}b\bar{b}$ , has large backgrounds which can be suppressed by tagging the  $b$ -quarks and reconstructing the Higgs mass. The statistics are nevertheless very small and one has to resort to a neural network analysis to isolate the signal from the remaining backgrounds. For higher Higgs masses, the final state  $Ht\bar{t} \rightarrow 4Wb\bar{b}$  has also large backgrounds, which are nevertheless manageable using again a neural network.

The cross section for the double Higgs production in the strahlung process is at the level of  $\sim \frac{1}{2}$  fb for a light Higgs at  $\sqrt{s} = 500$  GeV and is smaller at higher energies. The large backgrounds from four and six fermion events can be suppressed for  $M_H \lesssim 140$  GeV by using the characteristic signal of four  $b$ -quarks and a  $Z$  boson, reconstructed in both leptonic and hadronic finally to increase the statistics, and using  $b$ -tagging. For higher Higgs masses, the dominant

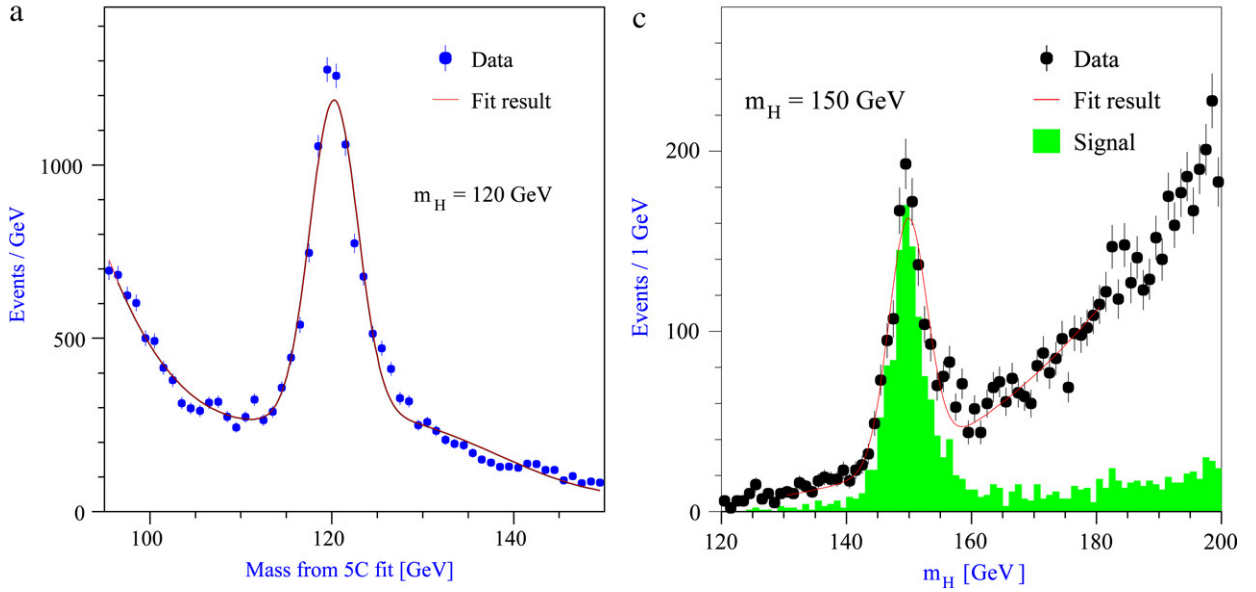


Fig. 4.33. The Higgs mass peak reconstructed in different channels with constrained fits for two values of  $M_H$ , an integrated luminosity of  $500 \text{ fb}^{-1}$  and  $\sqrt{s} = 350 \text{ GeV}$  in  $HZ \rightarrow b\bar{b}q\bar{q}$  at  $M_H = 120 \text{ GeV}$  (left) and  $HZ \rightarrow W^+W^-q\bar{q}$  at  $M_H = 150 \text{ GeV}$  (right); from Ref. [456].

final state is  $Z + 4W$ . In contrast, the cross section for the  $e^+e^- \rightarrow \nu_e\bar{\nu}_e HH$  is extremely small at  $\sqrt{s} = 500 \text{ GeV}$  but reaches the fb level at  $\sqrt{s} = 3 \text{ TeV}$ .

#### 4.4.2. Precision measurements for a light Higgs boson

Once the Higgs boson is found, it will be of great importance to explore all its fundamental properties. This can be done in great detail in the clean environment of  $e^+e^-$  linear colliders: the Higgs boson mass, its spin and parity quantum numbers and its couplings to fermions, massive and massless gauge bosons as well as its trilinear self-couplings can be measured with very good accuracies. The measurements would allow the probe in all its facets the electroweak symmetry breaking mechanism.

**4.4.2.1. The Higgs boson mass.** Many of the properties of the SM Higgs boson can be determined in a model-independent way by exploiting the recoil mass technique in the strahlung process,  $e^+e^- \rightarrow HZ$ . The measurement of the recoil  $e^+e^-$  or  $\mu^+\mu^-$  mass in  $e^+e^- \rightarrow ZH \rightarrow H\ell\ell$ , allows a very good determination of the Higgs mass [537, 538]. At  $\sqrt{s} = 350 \text{ GeV}$  and with a luminosity of  $\mathcal{L} = 500 \text{ fb}^{-1}$ , a precision of  $\Delta M_H \sim 70 \text{ MeV}$  can be reached for a Higgs mass of  $M_H \sim 120 \text{ GeV}$ . The precision can be increased to  $\Delta M_H \sim 40 \text{ MeV}$  by using in addition the hadronic decays of the  $Z$  boson which have more statistics [538]. Accuracies of the order of  $\Delta M_H \sim 80 \text{ MeV}$  can also be reached for  $M_H$  values between 150 and 180 GeV when the Higgs boson decays mostly into gauge bosons [see Ref. [539], however]. The reconstructed Higgs mass peak is shown in Fig. 4.33 at a 350 GeV collider in the two channels  $HZ \rightarrow b\bar{b}q\bar{q}$  for  $M_H = 120 \text{ GeV}$  and  $HZ \rightarrow W^+W^-q\bar{q}$  for  $M_H = 150 \text{ GeV}$ . The obtained accuracy of  $M_H$  is a factor of two better than the one which could be obtained at the LHC.

**4.4.2.2. The Higgs spin and parity.** The determination of the  $J^P = 0^+$  quantum number of the SM Higgs boson can also be performed in the strahlung process. As discussed in Section 4.2.1, the measurement of the rise of the cross section near threshold,  $\sigma(e^+e^- \rightarrow HZ) \propto \lambda^{1/2}$ , rules out  $J^P = 0^-, 1^-, 2^+$  and higher spin  $3^\pm, \dots$ , which rise with higher powers of the velocity  $\lambda^{1/2}$ . A threshold scan with a luminosity of  $20 \text{ fb}^{-1}$  at three center of mass energies is sufficient to distinguish the various behaviors; Fig. 4.34. The production of states with the two remaining  $J^P = 1^+, 2^-$  quantum numbers can be ruled out using the angular correlations of the final state  $e^+e^- \rightarrow HZ \rightarrow 4f$ .

The angular distribution of the  $Z/H$  bosons in the Higgs–strahlung process is also sensitive to the spin zero of the Higgs particle: at high energies, the  $Z$  is longitudinally polarized and the distribution follows the  $\sim \sin^2 \theta$  law which unambiguously characterizes the production of a  $J^P = 0^+$  particle, since in the case of a pseudoscalar Higgs boson,



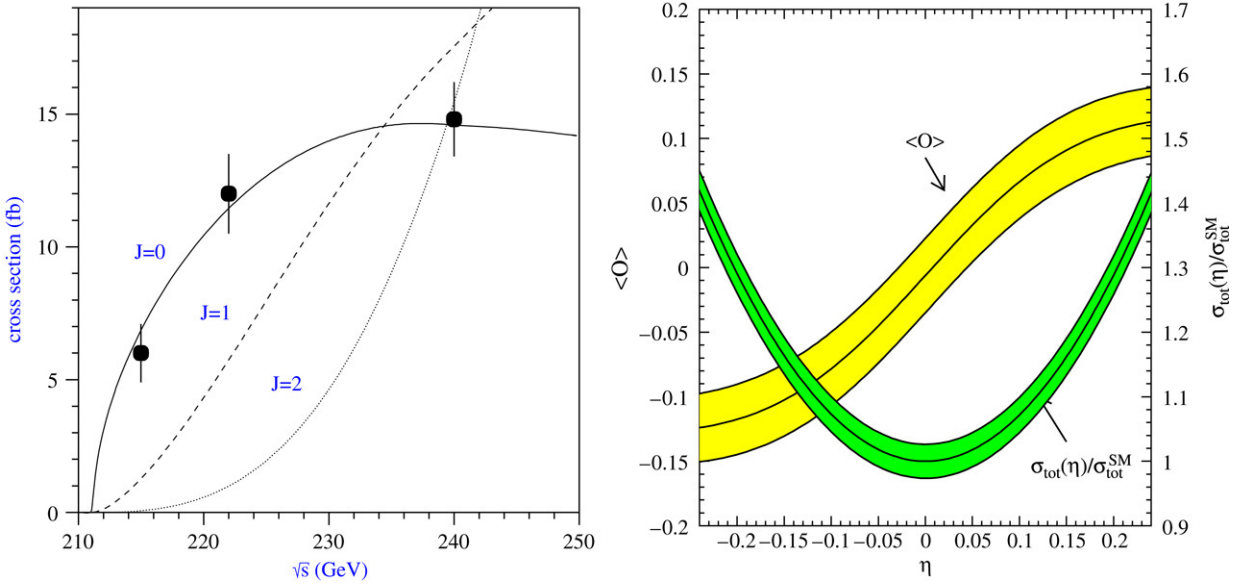


Fig. 4.34. The  $e^+e^- \rightarrow ZH$  cross section energy dependences near threshold for  $M_H = 120$  GeV for spin  $0^+$ ,  $1^-$  and  $2^+$  bosons [540] (left). The dependences of  $\sigma(e^+e^- \rightarrow HZ)$  and the observable  $\langle O \rangle$  defined in Eq. (4.27) on the parameter  $\eta$  with the shaded bands showing the  $1\sigma$  uncertainties at  $\sqrt{s} = 350$  GeV and  $500 \text{ fb}^{-1}$  [541] (right).

the angular distribution would behave as  $1 + \cos^2 \theta$ . Assuming that the Higgs particle is a mixed CP-even and CP-odd state with  $\eta$  parametrizing the mixture, the angular distribution given by Eq. (4.26) can be checked experimentally. This is shown in the right-hand side of Fig. 4.34, where one can see that the parameter  $\eta$  can be measured to a precision of 3%–4%, which is of the typical size of electroweak radiative corrections which, in CP-conserving models, could generate the CP-odd component of the  $ZZ\Phi$  coupling. Note that the Higgs  $J^{PC}$  quantum numbers can also be checked by looking at correlations in the production  $e^+e^- \rightarrow HZ \rightarrow 4f$  or in the decay  $H \rightarrow WW^*, ZZ^* \rightarrow 4f$  processes, just as in the LHC case but with more accuracy at the ILC since one can use the larger hadronic modes of the  $W$  and  $Z$  bosons.

The CP-nature of the Higgs boson would be best tested in the couplings to fermions, where the scalar and pseudoscalar components might have comparable size. Such tests can be performed in the decay channel  $H \rightarrow \tau^+\tau^-$  for  $M_H \lesssim 140$  GeV by studying the spin correlations between the final decay products of the two  $\tau$ -leptons [139, 141]. The acoplanarity angle between the decay planes of the two  $\rho$  mesons produced from  $\tau^+$  and  $\tau^-$ , which can be reconstructed in the Higgs rest frame using the  $\tau$  lifetime information, is a very sensitive probe, allowing a discrimination between CP-even and CP-odd states at the 95% CL for  $M_H = 120$  GeV at the usual energy and luminosity [148]; using the additional information from the  $\tau$  impact parameter significantly improves this determination.

If the observed Higgs boson is a mixture of CP-even and CP-odd states, with a coupling  $g_{\Phi\tau\tau} = g_{H\tau\tau}(\cos\phi + i\sin\phi\gamma_5)$  with  $\phi = 0$  in the SM Higgs case, the angular distributions in the  $\tau^\pm \rightarrow \rho^\pm\nu$  decays allow one to measure the mixing angle with an accuracy of  $\Delta\phi \sim 6^\circ$ . This is shown in Fig. 4.35, which displays the distribution of the acoplanarity angle  $\varphi^*$  between the decay planes of the  $\rho^+$  and  $\rho^-$  in the rest frame of the pair, for several values of the mixing angle  $\phi$ , as a result of a simulation for  $\sqrt{s} = 350$  GeV and  $\mathcal{L} = 1 \text{ ab}^{-1}$ .

For heavier Higgs bosons, when the  $H \rightarrow \tau^+\tau^-$  becomes too small, these studies cannot be performed anymore. A promising channel would be the decay  $H \rightarrow t\bar{t}$  for  $M_H > 2m_t$ , but no realistic simulation of the potential of this channel has been performed. Finally, and as discussed in Section 4.3.2, the differential cross section in associated production with top quarks,  $e^+e^- \rightarrow t\bar{t}H$ , is sensitive to the CP-nature of the Higgs boson, though no analysis has been performed to verify at which extent this information can be experimentally extracted.

**4.4.2.3. The Higgs couplings to gauge bosons.** The fundamental prediction that the Higgs couplings to  $ZZ/WW$  bosons are proportional to the masses of these particles can be easily verified experimentally since these couplings

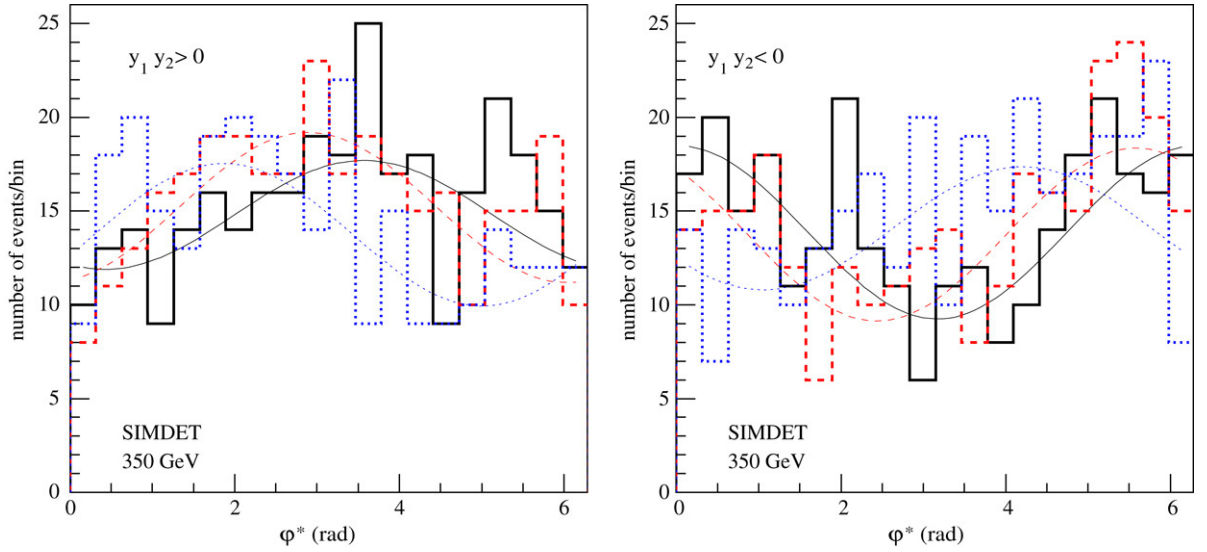


Fig. 4.35. Distribution of the reconstructed acoplanarity angle  $\phi^*$  for  $\phi = 0$  (full histogram),  $\phi = \pi/8$  (dashed) and  $\phi = \pi/4$  (dotted) for  $y_1 y_2 > 0$  (left) and  $y_1 y_2 < 0$  (right) with  $y_{1,2} = (E_{\pi^\pm} - E_{\pi^0})/(E_{\pi^\pm} + E_{\pi^0})$ ; the lines indicate the results of the fits; from [530].

Table 4.5

Relative precision in the determination of the SM Higgs cross sections for  $120 \text{ GeV} \leq M_H \leq 160 \text{ GeV}$  with  $\mathcal{L} = 500 \text{ fb}^{-1}$  at  $\sqrt{s} = 350$  and  $500 \text{ GeV}$ ; from Ref. [456]

Channel	$M_H = 120 \text{ GeV}$	$M_H = 140 \text{ GeV}$	$M_H = 160 \text{ GeV}$
$\sigma(e^+e^- \rightarrow HZ)$	2.5%	2.7%	3.0%
$\sigma(e^+e^- \rightarrow H\nu\bar{\nu})$	2.8%	3.7%	13%

can be directly determined by measuring the production cross sections in the bremsstrahlung and the fusion processes.  $\sigma(e^+e^- \rightarrow HZ \rightarrow H\ell^+\ell^-)$  can be measured by analyzing the recoil mass against the  $Z$  boson and provides a determination of the  $g_{HZZ}$  couplings independently of the decay modes of the Higgs boson. Adding the two lepton channels, one obtains a statistical accuracy of less than 3% at  $\sqrt{s} \sim 350 \text{ GeV}$  and with  $\int \mathcal{L} = 500 \text{ fb}^{-1}$  [537].

The coupling  $g_{HWW}$  for  $M_H \lesssim 2M_W$  can be determined from the measurement of the total cross section of the process  $e^+e^- \rightarrow W^*W^*\nu\bar{\nu} \rightarrow H\nu\bar{\nu}$  which, as discussed previously, can be efficiently separated from the  $e^+e^- \rightarrow HZ \rightarrow H\nu\bar{\nu}$  channel and from the backgrounds, see Fig. 4.32. A precision of also less than 3% can be achieved for  $M_H = 120 \text{ GeV}$ , but at a slightly higher energy,  $\sqrt{s} \sim 500 \text{ GeV}$ , where the production rate is larger [542]. The precision becomes worse for increasing Higgs mass as a result of the falling cross section.

The accuracies which can be achieved are shown in Table 4.5 for three Higgs masses and the precision on the Higgs couplings is half of these errors, since the cross sections scale as  $g_{HVV}^2$ . Thus, a measurement of the Higgs couplings to gauge bosons can be performed at the statistical level of 1%–2% allowing the probe of the quantum corrections.

**4.4.2.4. The Higgs decay branching ratios.** The measurement of the branching ratios of the Higgs boson [543–553] is of utmost importance. For Higgs masses below  $M_H \lesssim 150 \text{ GeV}$  a large variety of branching ratios can be measured at the linear collider, since the  $b\bar{b}$ ,  $c\bar{c}$  and  $g\bar{g}$  final states can be very efficiently disentangled by means of vertex detectors [554]. The  $b\bar{b}$ ,  $c\bar{c}$  and  $\tau^+\tau^-$  fractions allow one to measure the relative couplings of the Higgs boson to these fermions and to check the prediction of the Higgs mechanism that they are indeed proportional to fermion masses. In particular,  $\text{BR}(H \rightarrow \tau^+\tau^-) \sim m_\tau^2/3\bar{m}_b^2$  allows such a test in a rather clean way. The gluonic branching ratio is indirectly sensitive to the  $t\bar{t}H$  Yukawa coupling and would probe the existence of new strongly interacting particles that couple to the Higgs and which are too heavy to be produced directly. The branching ratio of the loop induced  $\gamma\gamma$  and  $Z\gamma$  Higgs decays are also very sensitive to new heavy particles and their measurement is thus very important. The branching ratio of the Higgs decays into  $W$  bosons starts to be significant for  $M_H \gtrsim 120 \text{ GeV}$  and allows one to measure again the  $HWW$  coupling in an independent way. In the mass range  $120 \text{ GeV} \lesssim M_H \lesssim 180$

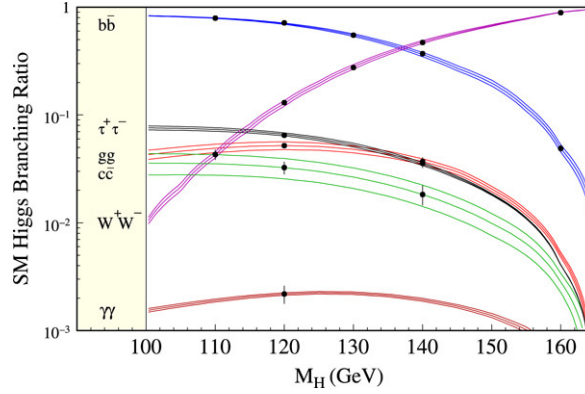


Fig. 4.36. The theoretical predictions [with the bands due to the uncertainties in the measurements of the quark masses and  $\alpha_s$ ] and the experimental accuracy [the points with error bars] for the SM Higgs branching ratios at  $\sqrt{s} = 350$  GeV with  $500 \text{ fb}^{-1}$ ; from Ref. [456].

GeV, the  $H \rightarrow ZZ^*$  fraction is too small to be precisely measured, but for higher masses it is accessible and allows an additional determination of the  $HZZ$  coupling.

There are two methods to measure the Higgs branching ratios: first by measuring the event rate in the Higgs–strahlung process for a given final state configuration and then dividing by the total cross section which is measured from the recoil mass, and second, by selecting a sample of unbiased events in the  $e^+e^- \rightarrow HZ$  recoil mass peak and determining the fraction of events corresponding to a given final state decay. The first case, which is called the indirect method, has been used to study the Higgs branching ratios for the TESLA TDR [456,545] while the second one, called the direct method, appeared only recently [546]. Both methods give rather similar results but, since they are almost independent, these results may be combined to provide a significant improvement of the expected accuracies.

The expected accuracies on the Higgs branching fractions are shown in Fig. 4.36 and in Table 4.6 [the low-energy (LE) numbers at the left] mostly at  $\sqrt{s} = 350$  GeV and with  $500 \text{ fb}^{-1}$  integrated luminosity for  $M_H \leq 160$  GeV. The  $b\bar{b}$ ,  $c\bar{c}$ ,  $\tau^+\tau^-$ ,  $gg$  and  $WW$  branching ratios of the Higgs boson can be measured with a very good accuracy. For the mass value  $M_H = 120$  GeV and using the indirect method, one obtains accuracies of, respectively, 2.4%, 8.3%, 5%, 5.5% and 5.1%. When combined with the direct method measurements labeled LE(D), the errors decrease quite significantly. The uncertainties in the measurements become larger when approaching the  $WW$  threshold: at  $M_H \sim 160$  GeV, only the  $b\bar{b}$ ,  $WW$  and  $ZZ$  fractions are accessible, with still a poor accuracy in the latter case. For  $M_H \sim 200$  GeV, a higher energy  $\sqrt{s} = 500$  GeV is needed to compensate for the falling cross section, and the precision is good only for the  $WW$  and  $ZZ$  channels. For the  $H \rightarrow b\bar{b}$  decays, an energy of 800 GeV and  $1 \text{ ab}^{-1}$  data are required to reach the quoted precision of 17%.

In the low Higgs mass range, even the rare decays into  $\gamma\gamma$  and  $Z\gamma$  final states can be measured with an accuracy of approximately 5%–20% [547,548,550]. The very rare decay into muon pairs is also measurable, though with a rather poor accuracy, by going to high energies and taking advantage of the enhanced production rates in  $e^+e^- \rightarrow H\nu\bar{\nu}$  [551]. A luminosity of  $1 \text{ ab}^{-1}$  is necessary to probe all these rare decay modes of the Higgs boson.

Finally, invisible Higgs decays can also be probed with a very good accuracy, thanks to the missing mass technique. One can also look directly for the characteristic signature of missing energy and momentum. Recent studies show that in the range  $120 \text{ GeV} \lesssim M_H \lesssim 160 \text{ GeV}$ , an accuracy of  $\sim 10\%$  can be obtained on an invisible decay with a branching ratio of 5% and a  $5\sigma$  signal can be seen for a branching ratio as low as 2% [553].

Moving to higher energies,  $\sqrt{s} = 1 \text{ TeV}$ , the larger rate for the  $WW$  fusion process helps to improve the accuracy on the main decay branching ratios and even search for rare decays [as it was the case for  $H \rightarrow \mu^+\mu^-$ ]. In the right-hand side of Table 4.6, the HE numbers stand for measurements performed at this energy and with  $1 \text{ ab}^{-1}$  data, when combined with the respective measurements at low energies [547]. As can be seen the accuracy on some decay branching ratios, in particular  $\text{BR}(H \rightarrow b\bar{b}, \gamma\gamma)$ , can be significantly improved.

**4.4.2.5. The Higgs total decay width.** The total decay width of the Higgs boson, for  $M_H \gtrsim 200$  GeV, is large enough to be accessible directly from the reconstruction of the Higgs boson lineshape. For smaller Higgs masses, the

Table 4.6

Summary of expected precisions on Higgs boson branching ratios from existing studies within the ECFA/DESY workshops (LE) [530] obtained for  $500 \text{ fb}^{-1}$  at  $\sqrt{s} = 350 \text{ GeV}$ , except for  $M_H = 200 \text{ GeV}$  where  $\text{BR}(WW)$  and  $\text{BR}(ZZ)$  are measured at  $\sqrt{s} = 500 \text{ GeV}$  and  $\text{BR}(bb)$  which uses  $1 \text{ ab}^{-1}$  at  $800 \text{ GeV}$ , as in the case of  $\text{BR}(\mu\mu)$

$M_H$ [GeV]	120			140		160		200	
Decay mode	Relative precision (%)								
	LE	LE(D)	HE	LE	HE	LE	HE	LE	HE
$b\bar{b}$	2.4	1.5	1.6	2.6	1.8	6.5	2.0	17.	9.0
$c\bar{c}$	8.3	5.8	–	19.	–				
$\tau\tau$	5.0	4.1	–	8.0	–				
$gg$	5.5	3.6	2.3	14.0	3.5	–	14.6		
$WW$	5.1	2.7	2.0	2.5	1.8	2.1	1.0	3.5	2.5
$ZZ$						16.9	–	9.9	–
$\gamma\gamma$	23	21.	5.4	–	6.2	–	24		
$Z\gamma$				27.	–				
$\mu\mu$	30		–						

LE stands for the measurement with the indirect method, while LE(D) is for the combined measurements of the direct and indirect methods [546]. HE is the combination of the measurements from the direct method with the NLC results obtained for  $1 \text{ ab}^{-1}$  at  $\sqrt{s} = 1 \text{ TeV}$  [547].

Table 4.7

Relative precision in the determination of the SM Higgs decay width with  $\int \mathcal{L} = 500 \text{ fb}^{-1}$  at  $\sqrt{s} = 350 \text{ GeV}$  using the two methods described in the text [456]

Channel	$M_H = 120 \text{ GeV}$	$M_H = 140 \text{ GeV}$	$M_H = 160 \text{ GeV}$
$g_{HWW}$ from $\sigma(e^+e^- \rightarrow H\nu\nu)$	6.1%	4.5%	13.4%
$g_{HWW}$ from $\sigma(e^+e^- \rightarrow HZ)$	5.6%	3.7%	3.6%
$\text{BR}(WW)$ at $\sqrt{s} = 1 \text{ TeV}$	3.4%	3.6%	2.0%

The last line shows the improvement which can be obtained when combining these results with those which can be extracted from measurements at  $\sqrt{s} \sim 1 \text{ TeV}$  with  $\int \mathcal{L} = 1 \text{ ab}^{-1}$  [547].

total decay is less than  $1 \text{ GeV}$  and it cannot be resolved experimentally. However, it can be determined indirectly by exploiting the relation between the total and partial decay widths for some given final states. For instance, in the decay  $H \rightarrow WW^*$ , the total decay width is given by  $\Gamma_H = \Gamma(H \rightarrow WW^*)/\text{BR}(H \rightarrow WW^*)$ . One can then combine the direct measurement of the  $H \rightarrow WW^*$  branching ratio discussed above and use the information on the  $HWW$  coupling from the  $WW$  fusion cross section to determine the partial decay width  $\Gamma(H \rightarrow WW^*)$ . Alternatively, one can exploit the measurement of the  $HZZ$  coupling from the production cross section of the Higgs–strahlung process, since the mass reach is higher than that in  $WW$  fusion, and assume  $\text{SU}(2)$  invariance to relate the two couplings,  $g_{HWW}/g_{HZZ} = 1/\cos\theta_W$ . The accuracy on the total decay width measurement then follows from that of the  $WW$  branching ratio and the  $g_{HWW}$  coupling.

As shown in Table 4.7, in the range  $120 \text{ GeV} \lesssim M_H \lesssim 160 \text{ GeV}$ , an accuracy ranging from 4% to 13% can be achieved on  $\Gamma_H$  if the  $HWW$  coupling is measured in the fusion process. This accuracy greatly improves for higher  $M_H$  values by assuming  $\text{SU}(2)$  universality which allows one to use the  $HWW$  coupling as derived from the strahlung process. If in addition a measurement of  $\text{BR}(H \rightarrow WW)$  is performed at higher energies and combined with the previous values, the accuracy on the total Higgs width will greatly improve for high masses.

Note that the same technique would allow one to extract the total Higgs decay width using the  $\gamma\gamma$  decays of the Higgs boson together with the cross section from  $\gamma\gamma \rightarrow H \rightarrow b\bar{b}$  as measured at a photon collider. This is particularly true since the measurement of  $\text{BR}(\gamma\gamma)$  at  $\sqrt{s} \sim 1 \text{ TeV}$  is rather precise, allowing the total width to be determined with an accuracy of  $\sim 5\%$  with this method for  $M_H = 120\text{--}140 \text{ GeV}$  independently of the  $WW$  measurement.

**4.4.2.6. The Higgs–Yukawa coupling to top quarks.** The Higgs–Yukawa coupling to top quarks, which is the largest coupling in the electroweak SM, is directly accessible in the process where the Higgs is radiated off the top quarks,  $e^+e^- \rightarrow t\bar{t}H$ , since the contribution from the diagram where the Higgs boson is radiated from the  $Z$  line,  $e^+e^- \rightarrow HZ \rightarrow Ht\bar{t}$ , is very small; Fig. 4.17. Because of the limited phase space, this measurement can only be

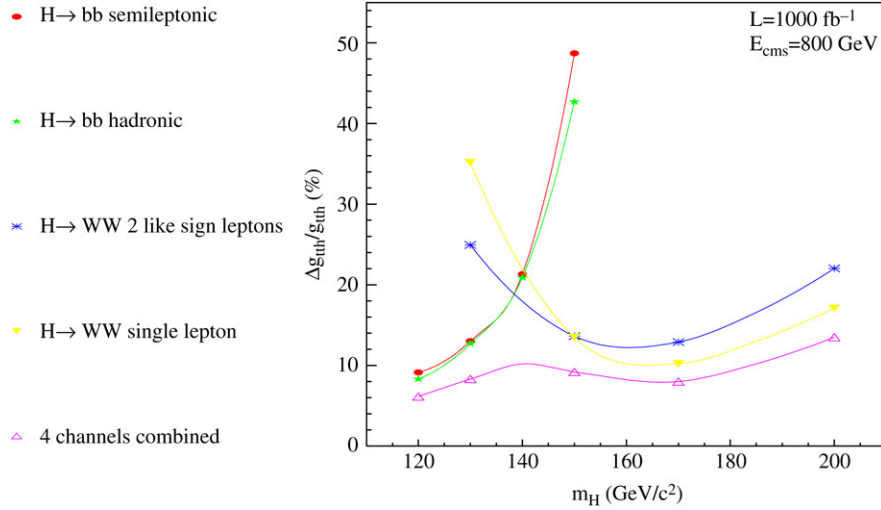


Fig. 4.37. Expected accuracies for the measurement of the  $Ht\bar{t}$  coupling as functions of  $M_H$  in the process  $e^+e^- \rightarrow t\bar{t}H$  for  $\sqrt{s} = 800$  GeV and  $1 \text{ ab}^{-1}$  in various decay channels. A 5% systematical error is assumed on the normalization of the background; from Ref. [555].

performed at high energies  $\sqrt{s} \gtrsim 500$  GeV. For  $M_H \lesssim 140$  GeV, the Yukawa coupling can be measured in the channel  $WWb\bar{b}b\bar{b}$  with the  $W$  bosons decaying both leptonically and hadronically to increase the statistics;  $b$ -tagging is essential in this mass range [555,556]. For higher Higgs masses,  $M_H \gtrsim 140$  GeV, the channels with  $b\bar{b} + 4W$  have to be considered, with again, at least two  $W$  bosons decaying hadronically, leading to 2 leptons plus 6 jets and one lepton plus 8 jets, respectively. The complexities of the final states and the small statistics require a neural network analysis [555].

The expected accuracies on the  $Ht\bar{t}$  Yukawa coupling are shown in Fig. 4.37 from Ref. [555] as functions of the Higgs mass, for  $\sqrt{s} = 800$  GeV and a luminosity of  $1 \text{ ab}^{-1}$ . Assuming a 5% systematical uncertainty on the normalization of the background, accuracies on the  $Ht\bar{t}$  Yukawa coupling of the order of 5% can be achieved for Higgs masses in the low range. A 10% measurement is possible up to Higgs masses of the order of 200 GeV.

For large masses,  $M_H \gtrsim 350$  GeV, the  $Ht\bar{t}$  coupling can be derived by measuring the  $H \rightarrow t\bar{t}$  branching ratio with the Higgs boson produced in the strahlung and  $WW$  fusion processes [557,558]. A detailed simulation, performed for the TESLA TDR in the latter channel, shows that once the  $t\bar{t}$  and  $e^+e^-t\bar{t}$  backgrounds are removed by requiring four light jets and two  $b$  quarks in the final state in addition to the missing energy, an accuracy of the order of 5% (12%) for a Higgs mass of 400 (500) GeV can be achieved on the top quark Yukawa coupling, again at  $\sqrt{s} = 800$  GeV and with  $\mathcal{L} \sim 1 \text{ ab}^{-1}$  data [559].

**4.4.2.7. The trilinear Higgs coupling.** The measurement of the trilinear Higgs self-coupling, which is the first non-trivial probe of the Higgs potential and, probably, the most decisive test of the electroweak symmetry breaking mechanism, is possible in the double Higgs–strahlung process. For Higgs masses in the range  $120 \text{ GeV} \lesssim M_H \lesssim 140 \text{ GeV}$ , one has to rely on the  $b\bar{b}$  decays and the cross section in the  $e^+e^- \rightarrow HHZ \rightarrow b\bar{b}b\bar{b} + \ell^+\ell^-$  or  $q\bar{q}$  channels is rather small, see Fig. 4.20, while the four and six fermion backgrounds are comparatively very large.

The excellent  $b$ -tagging efficiencies and the energy flow which can be achieved at future linear colliders make it possible to overcome the formidable challenge of suppressing the backgrounds, while retaining a significant portion of the signal. Accuracies of about 20% can be obtained on the measurement of the  $e^+e^- \rightarrow HHZ$  cross section in the mass range below 140 GeV; see the left-hand side of Fig. 4.38. Neural network analyses allow one to improve the accuracy of the measurement from 17% to 13% at a Higgs mass  $M_H = 120$  GeV and to obtain a  $6\sigma$  significance for the signal [560]; see also Ref. [561].

Since the sensitivity of the process  $e^+e^- \rightarrow HHZ$  to the trilinear Higgs coupling is diluted by the additional contributions originating from diagrams where the Higgs boson is emitted from the  $Z$  boson lines, only an accuracy of  $\Delta\lambda_{HHH} \sim 22\%$  can be obtained for  $M_H = 120$  GeV at an energy of  $\sqrt{s} \sim 500$  GeV with an integrated luminosity of  $\mathcal{L} \sim 1 \text{ ab}^{-1}$ . The accuracy becomes worse for higher Higgs masses. In particular, for  $M_H \gtrsim 140$  GeV,



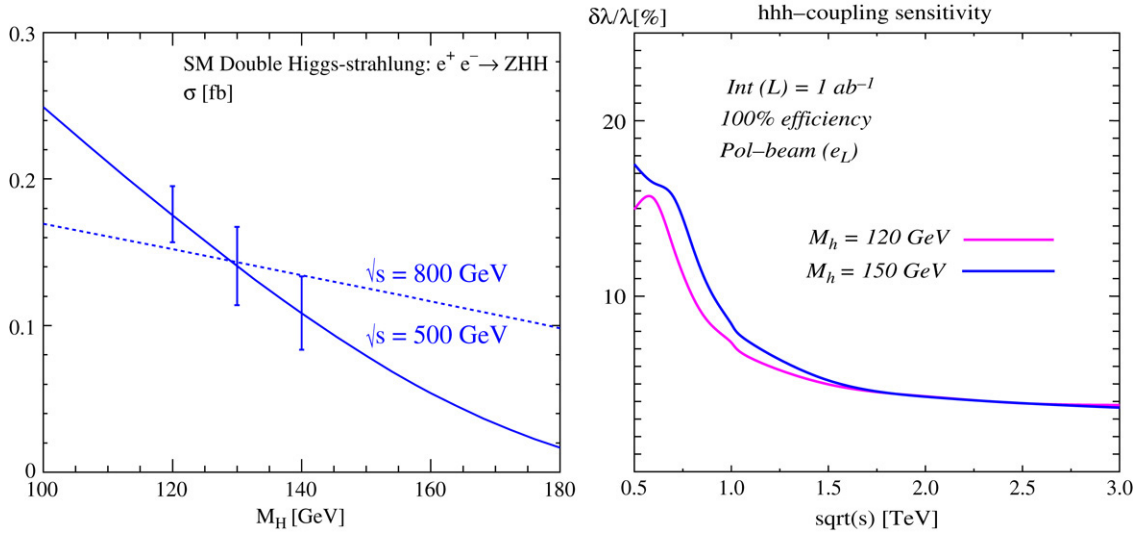


Fig. 4.38. The accuracy in the determination of  $\sigma(e^+e^- \rightarrow HHZ)$  for several Higgs masses at  $\sqrt{s} = 500$  GeV with  $\mathcal{L} = 1 \text{ ab}^{-1}$  (left) [560] and the sensitivity of  $\lambda_{HHH}$  to the c.m. energy for  $\mathcal{L} = 1 \text{ ab}^{-1}$ ,  $P_L(e^-) = 100\%$  and without efficiency corrections (right) [562].

Table 4.8

Expected precision on heavier Higgs lineshape parameters with  $500 \text{ b}^{-1}$  at  $\sqrt{s} = 500$  GeV [530] and on the  $WW/ZZ$  branching ratios with  $1 \text{ ab}^{-1}$  at  $\sqrt{s} = 1$  TeV [547]

$M_H$ (GeV)	$\Delta\sigma$ (%)	$\Delta M_H$ (%)	$\Delta\Gamma_H$ (%)	$\Delta\text{BR}(WW)$ (%)	$\Delta\text{BR}(ZZ)$ (%)
200	3.6	0.11	34	3.5	9.9
240	3.8	0.17	27	5.0	10.8
280	4.4	0.24	23	7.7	16.2
320	6.3	0.36	26	8.6	17.3

the  $H \rightarrow WW^*$  decays must be used, leading to the even more complicated  $4W+2f$  final state topologies. No experimental analysis of this topology has been attempted yet.

Also in this case, one can proceed to higher energy and take advantage of the  $WW$  fusion process  $e^+e^- \rightarrow HH\nu\bar{\nu}$  [562,563] which has a larger cross section, in particular with longitudinally polarized  $e^\pm$  beams. The estimated sensitivity of the trilinear Higgs couplings to  $\sqrt{s}$  is shown in the right-hand side of Fig. 4.38 for  $M_H = 120$  and  $150$  GeV with polarized electron beams and no efficiency loss [562]. It is dominated by Higgs-strahlung at low energy and  $WW$  fusion for  $\sqrt{s} \gtrsim 700$  GeV. A recent simulation at  $\sqrt{s} = 1$  TeV which combines both the  $e^+e^- \rightarrow HHZ$  and  $e^+e^- \rightarrow HH\nu\bar{\nu}$  processes with  $HH \rightarrow 4b$  final states, assuming a 80%  $e_L^-$ -polarization and a luminosity of  $1 \text{ ab}^{-1}$ , shows that an accuracy of  $\Delta\lambda_{HHH}/\lambda_{HHH} \sim 12\%$  may be achieved if the trilinear coupling is SM-like [562]. The relative phase of the coupling and its sign, may be also measured from the interference terms [531,562].

**4.4.2.8. Expectations for a heavier Higgs boson.** Finally, let us make a few remarks about a Higgs boson that is heavier than  $2M_Z$ , which has been recently discussed in Ref. [564]. In this case, all decay channels other than  $H \rightarrow WW, ZZ$  are not accessible experimentally. The only exceptions are the  $b\bar{b}$  decays for masses  $M_H \lesssim 200$  GeV and the  $t\bar{t}$  decays for  $M_H \gtrsim 350$  GeV. However, the Higgs boson mass and its total decay width, as well as the production cross sections which provide the couplings to gauge bosons, can be obtained from the lineshape. Typical accuracies on these parameters are shown in Table 4.8 at a c.m. energy of 500 GeV with  $500 \text{ fb}^{-1}$ . The accuracies of the  $WW$  and  $ZZ$  branching are also shown for the same energy and luminosity [other decay channels have not been discussed yet]. Thus, relatively precise measurements can also be performed for heavier Higgs particles.



Table 4.9

Relative accuracy on Higgs couplings obtained from a global fit

Quantity	$M_H = 120$ GeV	$M_H = 140$ GeV
$\Delta M_H$	$\pm 0.00033$	$\pm 0.0005$
$\Gamma_H$	$\pm 0.061$	$\pm 0.045$
$\Delta CP$	$\pm 0.038$	–
$\lambda_{HHH}$	$\pm 0.22$	$\pm 0.30$
$g_{HWW}$	$\pm 0.012$	$\pm 0.020$
$g_{HZZ}$	$\pm 0.012$	$\pm 0.013$
$g_{Htt}$	$\pm 0.030$	$\pm 0.061$
$g_{Hbb}$	$\pm 0.022$	$\pm 0.022$
$g_{Hcc}$	$\pm 0.037$	$\pm 0.102$
$g_{H\tau\tau}$	$\pm 0.033$	$\pm 0.048$

An integrated luminosity of  $500 \text{ fb}^{-1}$  at  $\sqrt{s} = 500$  GeV is assumed except for the measurement of  $g_{Htt}(\lambda_{HHH})$ , which assumes  $1000 \text{ fb}^{-1}$  at  $\sqrt{s} = 800$  (500) GeV in addition. On top of the table we display the accuracies on the Higgs mass, the total width and its CP-component as obtained at  $\sqrt{s} = 350$  GeV with  $500 \text{ fb}^{-1}$ .

#### 4.4.3. Combined measurements and the determination of the couplings

Once the Higgs production cross sections and the various decay branching ratios have been measured, one can derive the Higgs boson couplings to fermions and gauge bosons. This is a crucial test for the experimental verification that the Higgs mechanism is responsible for the generation of the masses of the particles. Since some of the couplings can be determined in different ways, while other determinations are partially correlated, a global fit to the various observables is highly desirable to extract the Higgs couplings in a model-independent way. Such a fit would optimize the collected information and takes properly into account all the experimental correlations between the various measurements.

A dedicated program called HFITTER [565], based on HDECAY [195] for the calculation of the Higgs decay branching ratios, has been developed for this purpose. It uses as inputs the production cross sections  $\sigma(e^+e^- \rightarrow HZ)$ ,  $\sigma(e^+e^- \rightarrow H\nu\bar{\nu})$  and  $\sigma(e^+e^- \rightarrow t\bar{t}H)$ , and the branching ratios into  $WW$ ,  $\gamma\gamma$ ,  $b\bar{b}$ ,  $c\bar{c}$ ,  $\tau^+\tau^-$  and  $gg$ . It uses the full covariance matrix for the correlated measurements, and the non-correlated measurement of the Higgs self-coupling from  $\sigma(e^+e^- \rightarrow HHZ)$  can be added. The results for the accuracies on the Higgs couplings to fermions, gauge bosons and the self-coupling are displayed in Table 4.9 for  $M_H = 120$  GeV and 140 GeV at a c.m. energy of 500 GeV with a luminosity of  $500 \text{ fb}^{-1}$  [except again for the measurement of  $g_{Htt}$  which has been performed at  $\sqrt{s} = 800$  GeV with a luminosity of  $1 \text{ ab}^{-1}$ ; the same luminosity is also used for the measurement of  $\lambda_{HHH}$ ]. For completeness, we also display the errors on the Higgs boson mass, its total decay width and its CP-even component [ $\Delta CP$  represents the relative deviation from the  $0^{++}$  case], which have been measured at  $\sqrt{s} = 350$  GeV with the same luminosity  $\mathcal{L} = 500 \text{ fb}^{-1}$ .

As can be seen, an  $e^+e^-$  linear collider in the energy range  $\sqrt{s} = 350\text{--}800$  GeV and a high integrated luminosity,  $\mathcal{L} \sim 500 \text{ fb}^{-1}$ , is a very high-precision machine in the context of Higgs physics. This precision would allow the determination of the complete profile of the SM Higgs boson, in particular if its mass is smaller than  $\sim 140$  GeV. It would also allow one to distinguish the SM Higgs particle from a scalar particle occurring in some of its extensions, with a very high level of confidence.

Thus, very precise measurements can be performed at the next linear collider allowing the detailed exploration of the electroweak symmetry breaking mechanism and the determination of the fundamental properties of the Higgs boson in the SM. We have seen in the previous section on hadron colliders that while the SM Higgs boson will undoubtedly be produced at the LHC, the detailed study of its properties will be a difficult task in the rather hostile hadronic environment. Due to the limited signal statistics for some channels, the large backgrounds and various systematic uncertainties, the LHC can provide only some ratios of Higgs couplings [as well as the Higgs mass and the total decay width for  $M_H \gtrsim 200$  GeV, which can be measured rather well]. The measurement of the various absolute couplings can be performed only at an  $e^+e^-$  collider. There is therefore a clear complementarity between the LHC and the linear collider Higgs physics programs.

From the previous discussions, one can single out two physics points for which  $e^+e^-$  colliders have some weakness: the determination of the total width is rather poor [without the  $\gamma\gamma$  option] for low mass Higgs bosons and

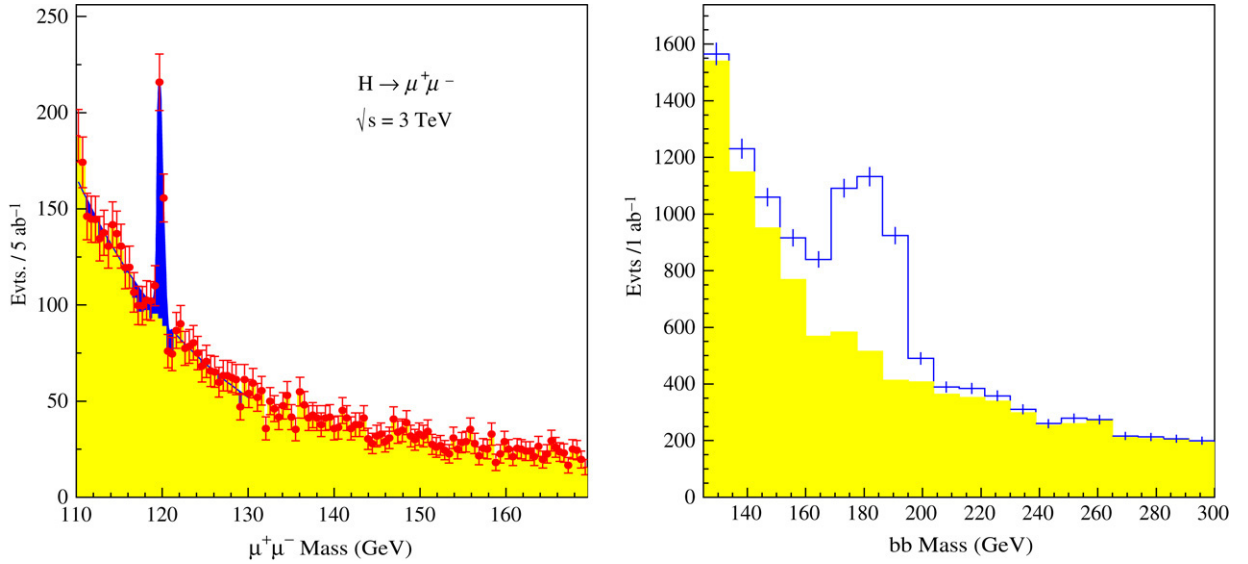


Fig. 4.39. The reconstructed signals for  $e^+e^- \rightarrow \nu\bar{\nu}H \rightarrow \nu\bar{\nu}\mu^+\mu^-$  for  $M_H = 120$  GeV (left) and  $e^+e^- \rightarrow \nu\bar{\nu}H \rightarrow \nu\bar{\nu}b\bar{b}$  for  $M_H = 200$  GeV (right) at CLIC with  $\sqrt{s} = 3$  TeV [523].

the CP-quantum numbers cannot be determined in a very convincing way for  $M_H \gtrsim 140$  GeV when the  $H \rightarrow \tau^+\tau^-$  decay mode becomes too rare. Unambiguous tests of the CP properties of the Higgs boson can be performed at photon colliders in the loop induced process  $\gamma\gamma \rightarrow H$  or at muon colliders in the process  $\mu^+\mu^- \rightarrow H$ , if suitable polarization of the initial beams is available. The measurement of  $\Gamma_H$  can benefit from the precise determination of the Higgs photonic width at  $\gamma\gamma$  colliders. However, it is at the muon collider that extremely good accuracies on  $\Gamma_H$  can be obtained by simply performing a threshold scan around the Higgs resonance produced in  $\mu^+\mu^- \rightarrow H$ . These topics will be addressed in detail in the next section. Before that, we first briefly summarize the benefits of raising and lowering the energy of the  $e^+e^-$  collider.

#### 4.4.4. Measurements at higher and lower energies

**4.4.4.1. Measurements at CLIC.** Some of the previously discussed measurements can significantly benefit from an increase of statistics. This can be obtained not only by increasing the luminosity, but also by raising the energy. Indeed, at the c.m. energies relevant for CLIC,  $\sqrt{s} \sim 3$  TeV, the cross section for the  $WW$  fusion process becomes extremely large. If the luminosity is also scaled with  $s$ , a sample of more than one million Higgs particles can be collected for  $\mathcal{L} = 3$  ab<sup>-1</sup>. Some of the previous measurements could thus be performed with more accuracy and new ones could be made possible. Examples of such measurements at CLIC are as follows [460]:

(i) With  $\mathcal{L} = 3$  ab<sup>-1</sup> at a c.m. energy of 3 TeV, 400  $H \rightarrow \mu^+\mu^-$  events can be collected for  $M_H = 120$  GeV. This sample would allow the measurement of the Higgs couplings to muons to better than 5% [the precision drops to 10% for  $M_H = 150$  GeV due to the smaller branching ratio]. The dimuon signal can be isolated from the important  $WW$ ,  $WW\nu\bar{\nu}$ ,  $ZZ\nu\bar{\nu}$  backgrounds with a statistical significance which is rather large; see the left-hand side of Fig. 4.39. This would be the first precise measurement of the Higgs couplings to second generation fermions since, as seen previously, although the  $Hc\bar{c}$  coupling can be determined with the same accuracy, the associated theoretical uncertainties are rather large.

(ii) The  $H \rightarrow b\bar{b}$  branching ratio becomes very small in the intermediate and high Higgs mass ranges, and at  $\sqrt{s} = 500$  GeV, it cannot be determined to better than 10% for  $M_H \sim 200$  GeV. At  $\sqrt{s} = 3$  TeV, the signal-to-background ratio is very favorable at these masses, as shown in the right-hand side of Fig. 4.39, and the rather large number of events to be collected at CLIC would allow a measurement of the  $Hb\bar{b}$  coupling with an accuracy of 5% for Higgs masses up to about  $M_H = 250$  GeV.

(iii) The trilinear Higgs coupling can be measured in the  $WW$  fusion process,  $e^+e^- \rightarrow \nu\bar{\nu}HH$ , for which the cross section reaches the level of a few fb at energies around 3 TeV. A relative accuracy of  $\sim 10\%$  can be obtained on this

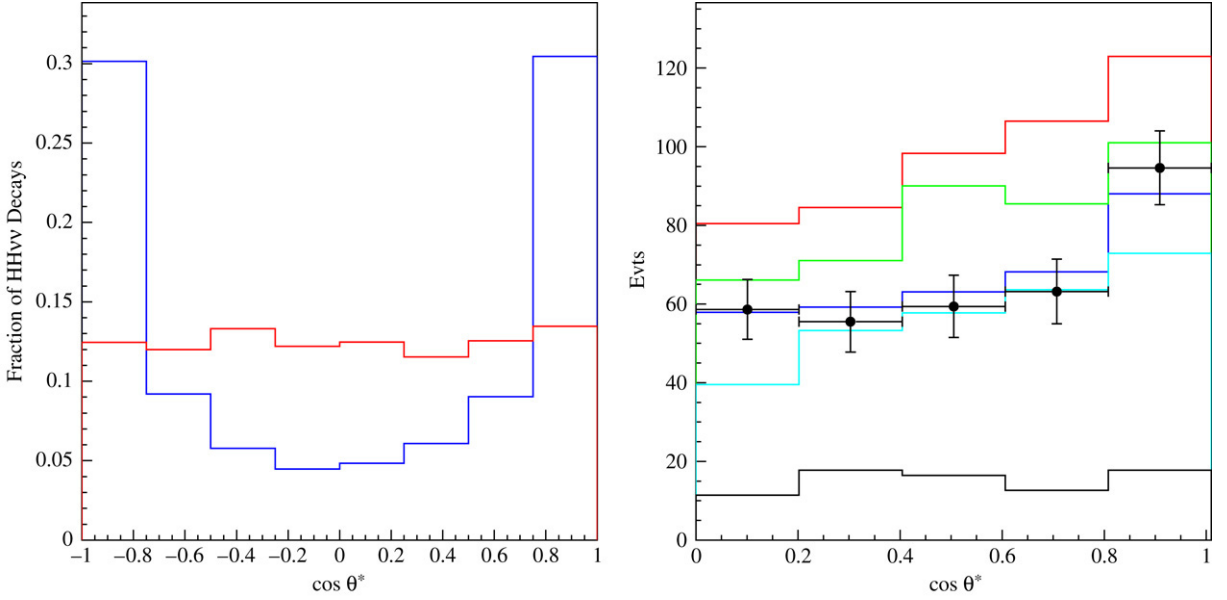


Fig. 4.40. The  $\cos \theta^*$  distribution in the process  $e^+e^- \rightarrow HH\nu\bar{\nu}$  due to the diagram containing the triple Higgs vertex (red/light grey) and other diagrams (blue/dark grey) for  $M_H = 120$  GeV at  $\sqrt{s} = 3$  TeV (left) and the reconstructed  $|\cos \theta^*|$  distribution for  $\lambda_{HHH}/\lambda_{HHH}^{\text{SM}} = 1.25, 1.0, 0.75$  and 0.5 from bottom to top, with the points with error bars showing the expectation for  $5 \text{ ab}^{-1}$  of data (right); from Ref. [523].

coupling for Higgs masses up to 250 GeV. Contrary to what occurs in the process  $e^+e^- \rightarrow HHZ$ , the interference between the diagram involving the self-Higgs coupling and the others, is negative. The sensitivity to  $\lambda_{HHH}$  can be enhanced by studying the angle  $\theta^*$  of the  $H^* \rightarrow HH$  system in its rest frame: because of the scalar nature of the Higgs boson, the  $\cos \theta^*$  distribution is flat for  $H^* \rightarrow HH$  while it is peaked in the forward direction for the other diagrams [518]; see the left-hand side of Fig. 4.40. From a fit of the distribution one can perform a very nice determination of the  $\lambda_{HHH}$  coupling as shown in the right-hand side of Fig. 4.40. Note that the quadrilinear Higgs couplings remains elusive, even at c.m. energies of 5 TeV.

The higher energy of the collider can also be very useful in the case where the Higgs boson is very heavy. For  $M_H \sim 700$  GeV and beyond, the cross sections in the Higgs–strahlung and  $WW$  fusion processes are small at  $\sqrt{s} \sim 1$  TeV [see Fig. 4.30] and do not allow one to perform detailed studies. At CLIC energies,  $\sqrt{s} = 3$  TeV, one has  $\sigma(e^+e^- \rightarrow H\nu\bar{\nu}) \sim 150$  fb which allows for a reasonable sample of Higgs particles to be studied. In addition, the cross section for the  $ZZ$  fusion process is large enough,  $\sigma(e^+e^- \rightarrow He^+e^-) \sim 20$  fb for  $M_H \sim 700$  GeV, to allow for model-independent Higgs searches in much the same way as in the Higgs–strahlung process at low energies, since the forward electron and positron can be tagged, and the mass recoiling against them can be reconstructed. The high energy available at CLIC will also be important to investigate in detail a possible strongly interacting Higgs sector scenario, as will be discussed in another part of this review.

**4.4.4.2. The GigaZ and MegaW options.** The high luminosities available at the next generation of  $e^+e^-$  colliders would allow the collection of more than  $10^9 Z$  bosons in one year by running at energies close to the resonance. The same luminosity would allow the collection of more than  $10^6 W$  boson pairs near the  $WW$  threshold. These samples are two orders of magnitude larger than those obtained at LEP1 and LEP2 and can be used to significantly improve the high-precision tests of the SM which have been performed in the last decade [462].

At GigaZ, using the possibility of polarizing the electron/positron beams, one can measure the longitudinal left–right asymmetry  $A_{LR} = 2a_e v_e / (a_e^2 + v_e^2) \sim 2(1 - 4 \sin^2 \theta_{\text{eff}}^{\text{lep}})$  with a very high statistical accuracy in hadronic and leptonic  $Z$  decays. Using the Blondel scheme [566], the asymmetry can be obtained from the cross sections when the polarization of both the electron and positron beams  $P_{e\pm}$  are used in the various combinations,  $\sigma = \sigma_{\text{unpol}}[1 - P_{e^+}P_{e^-} + A_{LR}(P_{e^+} - P_{e^-})]$ , leading to a systematical error of about  $10^{-4}$ . This corresponds to a

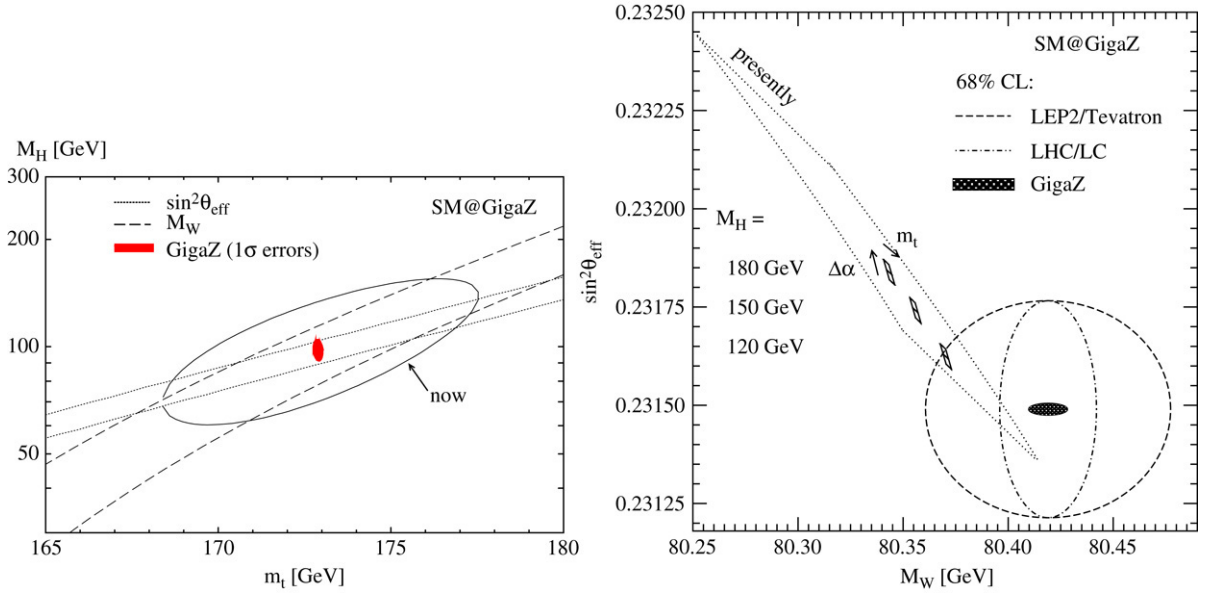


Fig. 4.41. The allowed region in the  $M_H$ - $m_t$  plane after the precision measurements at GigaZ/MegaW compared to the situation in the year 2000 (left) and the theoretical predictions for  $\sin^2 \theta_{\text{eff}}^{\text{lep}}$  and  $M_W$  for three  $M_H$  values compared to the experimental measurements at LEP2/Tevatron, LHC/ILC and after GigaZ/MegaW. The various theoretical and experimental uncertainties are as discussed in the text; from Ref. [567].

measurement of the electroweak mixing angle with a precision

$$\Delta \sin^2 \theta_{\text{eff}}^{\text{lep}} \simeq 1.3 \times 10^{-5} \quad (4.56)$$

which is one order of magnitude more accurate than the presently measured value,  $\sin^2 \theta_{\text{eff}}^{\text{lep}} = 0.2324 \pm 0.00012$ . The measurement of the total and partial Z decay widths and the various polarization and/or forward-backward asymmetries can be significantly improved. In particular, the measurement of the ratio of leptonic to hadronic Z decay widths with an expected accuracy of  $\Delta R_\ell / R_\ell \sim 0.05\%$ , would allow a clean measurement of the strong coupling constant to better than  $\Delta\alpha_s \simeq 0.001$ .

On the other hand, one can perform a scan around the  $W W$  threshold, where the cross section for  $W$  pair production rises quickly,  $\sigma(e^+e^- \rightarrow W^+W^-) \sim \beta$ , allowing an accurate measurement of the  $W$  boson mass. With an integrated luminosity of only  $\mathcal{L} \simeq 100 \text{ fb}^{-1}$  at  $\sqrt{s} \sim 2M_W$  and a six-point scan, the mass can be measured with an accuracy

$$\Delta M_W \simeq 6 \text{ MeV} \quad (4.57)$$

which is six times better than the present measurement,  $M_W = 80.449 \pm 0.034 \text{ GeV}$ , and almost three times the precision which can be reached at the LHC and at the ILC.

Since the top quark mass, which leads to the major part of the theoretical uncertainties in the present high-precision observables, will be measured with an accuracy of  $\Delta m_t \simeq 200 \text{ MeV}$  at the ILC and that  $\alpha_s$  will be known more precisely at this time,  $\Delta\alpha_s \simeq 0.001$ , the only dangerous source of errors from SM inputs will be the hadronic uncertainty in  $\Delta\alpha$ . One might hope that with the low-energy  $e^+e^-$  experiments which will be performed in the future, the error will reduce to  $\Delta\alpha^{\text{had}} \simeq 5 \times 10^{-5}$ . Taking into account also the error  $\Delta M_Z \simeq 2 \text{ MeV}$  on the Z boson mass, which at this level of precision induces an error on  $\sin^2 \theta_{\text{eff}}^{\text{lep}}$  which is of the same size as the experimental error, the future total theoretical uncertainties on the two observables from the various sources are estimated to be [567]

$$\Delta \sin^2 \theta_{\text{eff}}^{\text{lep}} \simeq \pm 3 \times 10^{-5}, \Delta M_W \simeq \pm 3 \text{ MeV}. \quad (4.58)$$

The very small experimental and theoretical errors on these two parameters will allow one to test the SM on much more solid grounds than in the past and to isolate the effects of the Higgs boson in the electroweak radiative corrections with an incredible accuracy. This is exemplified in the left-hand side of Fig. 4.41 where the expected accuracy in the determination of the Higgs mass at GigaZ/MegaW in the plane  $M_H$ - $m_t$ , together with the allowed bands for  $\sin^2 \theta_{\text{eff}}^{\text{lep}}$

and  $M_W$ , are shown. The central values of the various input parameters and the Higgs mass, as well as the area labeled “now”, are for the measurements which were available in the year 2000. One can simply notice the vast improvement which can be made at the GigaZ/MegaW option, where one can indirectly measure the Higgs boson mass with a precision of  $\Delta M_H/M_H \sim 7\%$  [567]. One can also use the direct measurement of the Higgs boson mass at the ILC (and LHC) with  $\Delta M_H \simeq 50$  MeV, to predict the values of  $\sin^2 \theta_{\text{eff}}^{\text{lep}}$  and  $M_W$  and to check the consistency of the SM, as shown in the right-hand side of Fig. 4.41. Because of the high precision which can be reached at GigaZ/MegaW, the improvement compared to the present situation and even after LHC/ILC is again spectacular.

#### 4.5. Higgs production in $\gamma\gamma$ collisions

As discussed in Section 4.1.2, future high-energy  $e^+e^-$  linear colliders can be made to run in the  $e\gamma$  or  $\gamma\gamma$  modes by using Compton back-scattering of laser light off the high-energy electron beams [463,464]. These colliders will have practically the same energy, up to  $\sim 80\%$ , as the original  $e^+e^-$  collider and a luminosity that is somewhat smaller. One of the best motivations for turning to the  $\gamma\gamma$  mode of the linear collider is undoubtedly the study of the properties of the Higgs boson, which can be produced as a resonance in the  $s$ -channel [465–468]. In this context, two main features which are difficult to study in the  $e^+e^-$  mode can be investigated at such colliders: first, the precise measurement of the  $H\gamma\gamma$  coupling [568–572] and second, the determination of the CP-properties of the Higgs boson [141,572–577]. Several other studies can also be made, such as the measurement of the Higgs boson self-coupling and its Yukawa coupling to top quarks, although these studies can be already performed in  $e^+e^-$  collisions [and, in general, in a much cleaner way].

##### 4.5.1. Higgs boson production as an $s$ -channel resonance

The production cross section for the process  $\gamma\gamma \rightarrow X$  with initial state polarized photons, can be written in the helicity basis as

$$d\hat{\sigma}_{\gamma\gamma} = \sum_{i,j,k,l=\pm} \rho_{ik}^1 \rho_{jl}^2 M_{ij} M_{kl}^* d\Gamma \quad (4.59)$$

where  $M_{ij}$  are the invariant scattering amplitudes with photon helicities  $i, j = \pm 1$  and  $d\Gamma$  the phase-space element divided by the incoming flux. Comparing to the cross section written in the Stokes parameter basis, the elements of the photon polarization density matrix are such that  $\rho_{\pm\pm}^i = \frac{1}{2}(1 \pm \xi_{i2})$ ,  $\rho_{+-}^i = \rho_{-+}^{i*} = -\frac{1}{2}(\xi_{i3} - i\xi_{i1})$ . The unpolarized cross section is

$$\begin{aligned} d\hat{\sigma} &= d\hat{\sigma}_{00} = \frac{1}{4} d\Gamma \left( |M_{++}|^2 + |M_{--}|^2 + |M_{+-}|^2 + |M_{-+}|^2 \right) \\ &= \frac{1}{2} (d\hat{\sigma}_{J_Z=0} + d\hat{\sigma}_{J_Z=\pm 2}) = \frac{1}{2} (d\hat{\sigma}_{\parallel} + d\hat{\sigma}_{\perp}) \end{aligned} \quad (4.60)$$

where  $d\hat{\sigma}_{J_Z=0}$  ( $d\hat{\sigma}_{J_Z=\pm 2}$ ) are the cross sections for photons with total helicity  $0(\pm 2)$  and  $d\hat{\sigma}_{\parallel}$  ( $d\hat{\sigma}_{\perp}$ ) is for parallel (orthogonal) linear photon polarizations.

In the case of a spin-zero particle, the production occurs through the  $J_Z = 0$  channel. In terms of the Higgs total decay width  $\Gamma_H$ , the width into two photons  $\Gamma(H \rightarrow \gamma\gamma)$  and into a given final state,  $\Gamma(H \rightarrow X)$ , the cross section for the subprocess  $\gamma\gamma \rightarrow H$  is given by

$$\hat{\sigma}(W) = 8\pi \frac{\Gamma(H \rightarrow \gamma\gamma) \Gamma(H \rightarrow X)}{(W^2 - M_H^2)^2 + M_H^2 \Gamma_H^2} (1 + \lambda_1 \lambda_2) \quad (4.61)$$

where  $W$  is the invariant mass of the  $\gamma\gamma$  system. Using the same photon helicities  $\lambda_1 \lambda_2 = 1$  projects out the  $J_Z = 0$  component and therefore maximizes the Higgs cross section.

For masses below  $M_H \sim 2M_Z$ , the Higgs boson is very narrow with a total decay width  $\Gamma_H \lesssim 1$  GeV and, therefore, the detector resolution should be taken into account. When the Higgs width can be neglected, a rather simple way to obtain the effective signal cross section is to introduce a Gaussian smearing of the  $\gamma\gamma$  invariant mass  $W$  [466]

$$N_{\text{eff}} = \mathcal{L}_{\text{eff}} \frac{d\sigma^{\text{eff}}}{dW}(W) = \int_{M_X}^{y_m \sqrt{s_{e^+e^-}}} dW' \frac{1}{\sqrt{2\pi}\delta} \exp\left(-\frac{(W' - W)^2}{2\delta^2}\right) \frac{d\mathcal{L}}{dW'} \langle \hat{\sigma}(W') \rangle \quad (4.62)$$

and select events within bins of invariant masses  $M_H \pm \Delta$ , where the Higgs mass is assumed to be precisely known already. In the previous expression,  $\mathcal{L}_{\text{eff}}$  and  $y_m \sqrt{s_{e^+e^-}}$  are the effective luminosity and the maximum energy of the  $\gamma\gamma$  collider and  $\delta$  is one sigma of the detector resolution for  $W$ . The cross section for the signal process  $\gamma\gamma \rightarrow H \rightarrow X$  can be written as [for  $\Gamma_H \ll M_H$ ,  $\Gamma_H M_H [(W^2 - M_H^2)^2 + M_H^2 \Gamma_H^2]^{-1} \simeq \frac{\pi}{2M_H} \delta(W - M_H)$ ]

$$\hat{\sigma}_{\text{signal}}(W) = 4\pi^2 \frac{\Gamma(H \rightarrow \gamma\gamma) \text{BR}(H \rightarrow X)}{M_H^2} (1 + \lambda_1 \lambda_2) \delta(W - M_H). \quad (4.63)$$

Inserting this expression in Eq. (4.62), and selecting the events in the bin  $M_H \pm \Delta$ , one has

$$\mathcal{L}_{\text{eff}} \sigma_{\text{signal}}^{\text{eff}}(M_H) = R(\Delta/\delta) \frac{d\mathcal{L}}{dW} \Big|_{W=M_H}^{J_Z=0} 4\pi^2 \frac{\Gamma(H \rightarrow \gamma\gamma) \text{BR}(H \rightarrow X)}{M_H^2} \quad (4.64)$$

with  $R(\Delta/\delta)$  being the Gaussian error function giving the fraction of signal events contained in the bin  $M_H \pm \Delta$  [for instance, for  $\Delta = 2\delta$  one has  $R \simeq 0.95$ ].

The effective background,  $\gamma\gamma \rightarrow X$ , for an effective invariant mass of the two-photon system  $W = M_H$  can be approximated by

$$N_{\text{bckg}}^{\text{eff}}(W) \simeq 2\Delta \frac{d\mathcal{L}}{dW} (d\hat{\sigma}_{\text{bckg}}(W)) \quad (4.65)$$

if one assumes a smooth enough distribution of two-photon invariant masses weighted with luminosity distributions.

To have a large effective cross section for the Higgs boson signal, the  $\gamma\gamma$  energy must be tuned at the peak,  $0.8\sqrt{s_{e^+e^-}} \sim M_H$  for a perfect spectrum, while the luminosity with circularly polarized laser photon and electron beams are chosen so that they have opposite handedness with  $x = 4.83$ . The  $J_Z = 0$  events containing the signal are then enhanced, while the  $J_Z = \pm 2$  events are suppressed [464,578].

The measurement of the  $\Gamma(H \rightarrow \gamma\gamma) \times \text{BR}(H \rightarrow X)$  rate and, thus, the  $H\gamma\gamma$  coupling squared if the branching ratio is known, will follow from Eq. (4.64) if the effective luminosity and the Higgs mass are specified, and from the signal and background rates. The statistical error in the decay width times branching ratio determination is

$$\Delta(\Gamma \times \text{BR})/(\Gamma \times \text{BR}) = (\mathcal{L}_{\text{eff}})^{-1} S^{-1} \sqrt{S + B}. \quad (4.66)$$

**4.5.1.1. Low mass Higgs boson.** In the low mass range,  $M_H \lesssim 130$  GeV, the Higgs boson will mainly decay into  $b\bar{b}$  final states,  $H \rightarrow b\bar{b}$ , and the main source of background is the continuum production of  $b$ - and  $c$ -quark pairs [579], including gluon radiation which leads to fake two-jet events [580]. The total cross section for heavy quark production,  $\gamma\gamma \rightarrow q\bar{q}$ , with a polar cut in the center of mass of the two-photon system  $|\cos \theta| < c$  is given, at the tree level, by

$$\begin{aligned} \hat{\sigma}_{J_Z=0}(W) &= \frac{12\pi\alpha^2 Q_q^4}{W^2} \frac{8m_q^2}{W^2} \left(1 - \frac{2m_q^2}{W^2}\right) \left[ \frac{1}{2} \log \frac{1+c\beta}{1-c\beta} + \frac{c\beta}{1-c^2\beta^2} \right] \\ \hat{\sigma}_{J_Z=2}(W) &= \frac{12\pi\alpha^2 Q_q^4}{W^2} \left[ \frac{1}{2} (5 - \beta^4) \log \frac{1+c\beta}{1-c\beta} - c\beta \left(2 + \frac{(1-\beta^2)(3-\beta^2)}{1-c^2\beta^2}\right) \right] \end{aligned} \quad (4.67)$$

with the quark velocity  $\beta = \sqrt{1 - 4m_q^2/W^2}$  and electric charge  $Q_q$ . One can choose  $c = 0.7$  which helps to eliminate many background events which are peaked in the forward and backward directions, with only a moderate loss of the signal events. In addition, as can be seen, the contribution of the  $J_Z = 0$  channel is proportional to  $m_q^2/W^2$  and is therefore strongly suppressed [579]. Choosing the configuration where  $\lambda_1 \lambda_2 = 1$  helps to suppress the two-jet background, while it maximizes the signal cross section; see e.g. Refs. [464,578].

The background cross sections receive important QCD radiative corrections [580,581], which are particularly large for the  $J_Z = 0$  component to which additional continuum  $q\bar{q}g$  final states contribute [one can select slim two-jet final state configurations to suppress this gluon radiation contribution to the  $J_Z = 0$  amplitude], and also non-negligible electroweak corrections [582]. The radiative corrections to the signal cross section discussed in Section 2.3.1, and the corrections to the interference between the signal and background cross sections [583] have to be taken into account.



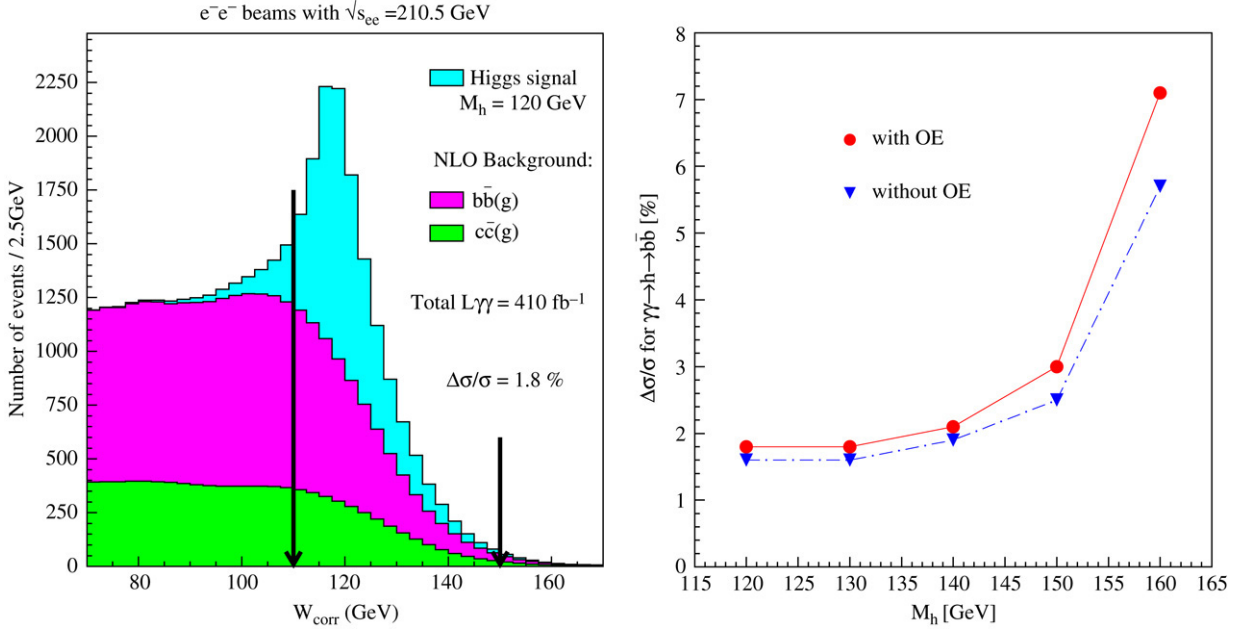


Fig. 4.42. The reconstructed invariant mass distribution of the  $b\bar{b}$  signal and the  $b\bar{b}(g)$  and  $c\bar{c}(g)$  backgrounds for  $M_H = 120$  GeV at the luminosity of  $410 \text{ fb}^{-1}$  (left) and the accuracy of the measurement of the cross section  $\sigma(\gamma\gamma \rightarrow H \rightarrow b\bar{b})$  for various Higgs mass values, with and without the inclusion of the overlaying events (right); from Ref. [569].

In addition, one has to consider low-energy  $\gamma\gamma \rightarrow \text{hadrons}$  processes which contribute to the overlaying events [584]. The overlaying events are peaked in the forward and backward directions and can be suppressed by the angular cut.  $b$ -tagging is of course mandatory and one can take advantage of the fact that the Higgs boson is produced almost at rest so that the total longitudinal momentum of the visible particles is smaller than the total visible energy.

A full simulation, which uses a realistic spectrum for the photon collider and includes the overlaying  $\gamma\gamma \rightarrow \text{hadrons}$  events, as well as a realistic  $b$ -tagging, has been recently performed [569]. The signal and background events have been generated with all the relevant higher-order corrections and including the fragmentation into hadrons, and the expected response of the detector has been taken into account. Cuts such as those discussed above have been applied and the output is shown in Fig. 4.42 where the energy of the original collider,  $\sqrt{s_{ee}} = 210$  GeV leading to a yearly luminosity of  $\mathcal{L}_{\gamma\gamma} = 410 \text{ fb}^{-1}$ , has been optimized for the production of a Higgs boson with a mass  $M_H = 120$  GeV.

The left-hand side of the figure displays the reconstructed invariant mass distribution of the selected  $b\bar{b}$  events, when it is corrected to take into account the effect of the undetected neutrinos. The Higgs boson signal as well as the  $b\bar{b}(g)$  and  $c\bar{c}(g)$  backgrounds including the overlaying events is displayed for  $M_H = 120$  GeV at the luminosity of  $410 \text{ fb}^{-1}$ . The most precise measurement of the  $H \rightarrow \gamma\gamma$  width is obtained in the mass window 110–150 GeV which is indicated. With the assumed luminosity, about 7000 signal events are reconstructed with about 9000 background events surviving the cuts, leading to a signal over background ratio of order one. Therefore, a statistical accuracy of 1.8% can be achieved on the measurement of  $\Gamma(H \rightarrow \gamma\gamma) \times \text{BR}(H \rightarrow b\bar{b})$ . The right-hand side of the figure shows the accuracy of the measurement of  $\Gamma(H \rightarrow \gamma\gamma) \times \text{BR}(H \rightarrow b\bar{b})$  for various Higgs mass values, with and without the inclusion of the overlaying events (OE). Again, this is the result of a full simulation where the energy of the initial collider has been optimized to produce a Higgs boson with a mass  $M_H = 130, 140, 150$  and  $160$  GeV. A precision of 2%–7% can be obtained in the entire Higgs mass range  $M_H = 120$ – $160$  GeV.

From the measurement of the branching ratio of the Higgs decays into bottom quarks which, as seen previously, can be made with an accuracy of 1.5% for  $M_H = 120$  GeV [see Table 4.6], the partial decay width  $\Gamma(H \rightarrow \gamma\gamma)$  can be extracted with a precision of 2.3%. With a precise measurement of the  $H \rightarrow \gamma\gamma$  branching ratio in the  $e^+e^-$  mode of the collider, one can determine the Higgs total width with an accuracy of the order of 10%.

**4.5.1.2. Heavier Higgs bosons.** For masses larger than  $M_H \sim 140$  GeV, the Higgs boson decays predominantly into massive gauge bosons,  $H \rightarrow WW$  and  $H \rightarrow ZZ$ , the branching ratios being  $\sim 2/3$  and  $1/3$ , respectively, for the

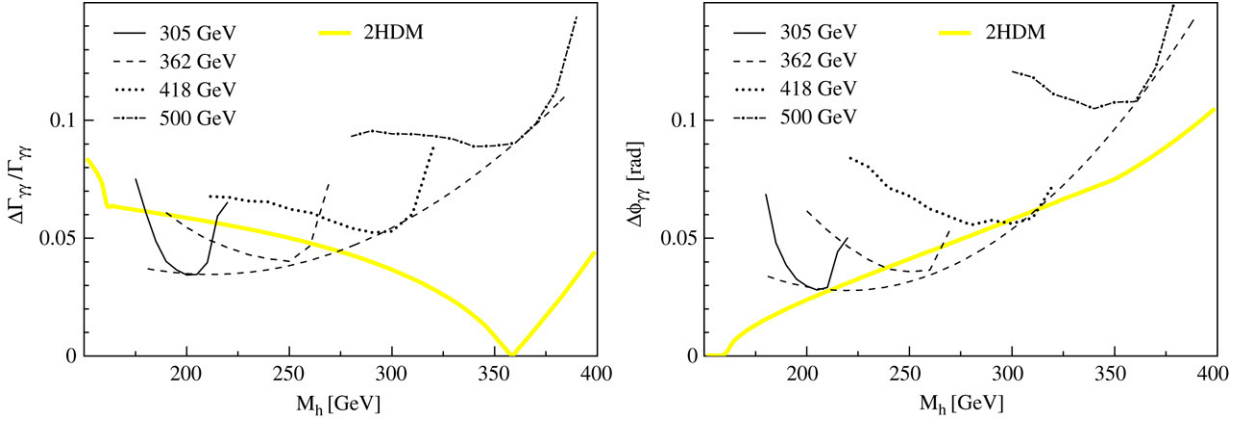


Fig. 4.43. Expected statistical errors in the determination of the Higgs width  $\Gamma_{\gamma\gamma}$  (left) and phase  $\phi_{\gamma\gamma}$  (right) at a photon collider, from the simultaneous fit to the observed  $W^+W^-$  and  $ZZ$  mass spectra. The yellow (thick light) band shows the prediction in a 2HDM [572].

charged and neutral decays for  $M_H$  above the  $ZZ$  threshold. The total Higgs decay width becomes significant, being of the order of  $\Gamma_H \sim 1.5$  (8) GeV for  $M_H = 200$ (300) GeV, and cannot be neglected anymore. However, the total production cross section of such heavy Higgs particles is of the same order as the one discussed previously, once the energy of the  $\gamma\gamma$  collider is tuned to the Higgs boson mass.

The backgrounds for the production of such a Higgs boson at  $\gamma\gamma$  colliders are vector boson production,  $\gamma\gamma \rightarrow W^+W^-$  and  $\gamma\gamma \rightarrow ZZ$ . The former process occurs at the tree level and has an extremely large cross section,  $\sigma(\gamma\gamma \rightarrow W^+W^-) \sim \mathcal{O}(10^2 \text{ pb})$  in both the  $J_Z = 0$  and  $J_Z = \pm 2$  channels [585,586]. This background cannot therefore be very efficiently suppressed by selecting only the  $J_Z = 0$  channel in which the Higgs boson is produced. The only region where the signal and backgrounds have similar rates is for  $M_H \sim 170$  GeV, where the Higgs boson decays almost 100% of the time into  $WW$  bosons, while the background cross sections are not yet too large since they increase with higher photon c.m. energy [571].

In the case of  $ZZ$  boson final states, the background is generated only at the one-loop level [570] since the  $Z$  boson is neutrally charged and does not couple directly to photons. It is therefore much less dangerous than the  $WW$  background: for c.m. energies of the order of  $\sqrt{s_{\gamma\gamma}} \sim 200 - 300$  GeV, the cross section is at the level  $\sigma(\gamma\gamma \rightarrow ZZ) \sim \mathcal{O}(10^2 \text{ fb})$  in the  $J_Z = 0$  channel. Therefore, for  $M_H \gtrsim 180$  GeV where the  $ZZ$  Higgs branching ratio becomes significant, the cross section is dominated by the Higgs boson contribution.

For photons colliding with a total angular momentum  $J_Z = 0$ , the interference between the signal  $\gamma\gamma \rightarrow H \rightarrow VV$  and the background  $\gamma\gamma \rightarrow VV$  must be taken into account. For  $WW$  final states, the interference is very large: for  $M_H \gtrsim 200$  GeV, this term is negative and is larger than the resonant contribution from the Higgs boson, leading to a decrease of the total  $WW$  cross section. For  $ZZ$  production, the interference term is rather small, although it has visible effects, resulting for instance in an asymmetric Higgs resonance. Thus, in addition to the extraction of the  $H\gamma\gamma$  couplings as in the  $H \rightarrow b\bar{b}$  case discussed before, these processes could in principle allow for the determination of the phase of the  $H\gamma\gamma$  amplitude via a measurement of the interference term which is sensitive to it.

A detailed simulation has been also performed in these two channels [572] and the analysis follows along the same lines as what has been previously discussed in the case of  $\gamma\gamma \rightarrow H \rightarrow b\bar{b}$ . The cuts have been optimized to select the final states  $H \rightarrow WW \rightarrow q\bar{q}q\bar{q}$  and  $H \rightarrow ZZ \rightarrow q\bar{q}\ell\ell$ . The center of mass energy of the original electron collider has been tuned to optimize Higgs production: for  $\sqrt{s_{ee}} = 305$ (500) GeV, which is the optimal choice for  $M_H = 200$ (350) GeV, a luminosity of about 600 (1000)  $\text{fb}^{-1}$  can be collected in a photon collider such as the one discussed for TESLA. Once the distributions of the reconstructed invariant masses for  $\gamma\gamma \rightarrow WW$  and  $ZZ$  are obtained experimentally, one can fit the simulated mass distributions with the width  $\Gamma_{\gamma\gamma}$  and the phase  $\phi_{\gamma\gamma}$  as being the only free parameters.

The output is shown in Fig. 4.43 where the statistical accuracies expected for the  $\Gamma_{\gamma\gamma}$  width and the  $\phi_{\gamma\gamma}$  phase are displayed for four examples of Higgs masses  $M_H = 200, 250, 300$  and  $350$  GeV. The solid thick light (yellow) line shows for comparison the prediction in a specific two-Higgs doublet model (2HDM). As can be seen for low Higgs masses,  $M_H \sim 200$  GeV, the width can be measured with a precision  $\Delta\Gamma_{\gamma\gamma} \simeq 3\%$  which is similar to the

accuracy obtained in the case of  $H \rightarrow b\bar{b}$ . For this Higgs mass value, the phase can be measured with an accuracy of  $\Delta\phi_{\gamma\gamma} \sim 35$  mrad. For higher Higgs masses, the uncertainties increase and for  $M_H = 350$  GeV, they are a factor of three larger. Note that the phase is mainly constrained by the  $WW$  process as expected, while the width is more accurately measured in the channel  $ZZ \rightarrow q\bar{q}\ell\ell$  as the background is smaller. Thus, it is only the combination of the two processes which allows one to determine both parameters.

For even heavier Higgs bosons,  $M_H \gtrsim 350$  GeV, the  $H \rightarrow t\bar{t}$  decays can be in principle exploited. However, the branching fraction is not very large,  $\text{BR}(H \rightarrow t\bar{t}) \sim 15\%$  for  $M_H \simeq 400$  GeV, and becomes even smaller for higher masses. The main background process  $\gamma\gamma \rightarrow t\bar{t}$  has a much larger cross section [which is still given by Eq. (4.67)] compared to  $b$ -quark production, first because of the larger charge  $Q_t = +2/3$  with the cross section being proportional to  $Q_q^4$ , and second, because the  $J_Z = 0$  contribution is not suppressed since the top quark mass is of the same order as the effective  $\gamma\gamma$  energy. Furthermore, the total width of the Higgs boson becomes too large,  $\Gamma_H \sim 30$  GeV for the previous mass value, and the particle is not a narrow resonance anymore; because of this large  $\Gamma_H$  value, one has to integrate the continuum background over a rather large bin.

For all these reasons, the process  $\gamma\gamma \rightarrow H \rightarrow t\bar{t}$  is expected to be a rather difficult channel to exploit. However, it can provide some valuable information on the CP-properties of the produced Higgs particle [574–577], a subject to which we turn our attention now.

#### 4.5.2. Measuring the CP-properties of the Higgs boson

**4.5.2.1. Measurements using photon polarization.** The general amplitude for the production of a spin-zero Higgs particle in two-photon collisions,  $\gamma\gamma \rightarrow H$ , can be written in terms of the CP-even and CP-odd components of the  $H\gamma\gamma$  coupling which are proportional to, respectively,  $(\epsilon_1 \cdot \epsilon_2)$  and  $(\epsilon_1 \times \epsilon_2)$ , as

$$M_{\lambda_1\lambda_2} = (\epsilon_1 \cdot \epsilon_2)\mathcal{C}_+ + (\epsilon_1 \times \epsilon_2)\mathcal{C}_- \quad (4.68)$$

where  $\mathcal{C}_+$  ( $\mathcal{C}_-$ ) are the CP-even (odd) contributions to the amplitude. Four independent functions describe the process out of the 16 helicity amplitudes present in the general case

$$\begin{aligned} d\hat{\sigma}_{00} + d\hat{\sigma}_{22} &= \frac{1}{2}d\Gamma \left( |M_{++}|^2 + |M_{--}|^2 \right) = |\mathcal{C}_+|^2 + |\mathcal{C}_-|^2 \\ d\hat{\sigma}_{20} + d\hat{\sigma}_{02} &= \frac{1}{2}d\Gamma \left( |M_{++}|^2 - |M_{--}|^2 \right) = -2\text{Im}(\mathcal{C}_+\mathcal{C}_-^*) \\ d\hat{\sigma}_{31} + d\hat{\sigma}_{13} &= d\Gamma \text{Im}(M_{++}M_{--}^*) = -2\text{Re}(\mathcal{C}_+\mathcal{C}_-^*) \\ d\hat{\sigma}_{33} + d\hat{\sigma}_{11} &= d\Gamma (M_{++}M_{--}^*) = |\mathcal{C}_+|^2 - |\mathcal{C}_-|^2. \end{aligned} \quad (4.69)$$

One can then define the asymmetries [573]

$$\begin{aligned} \mathcal{A}_1 &= \frac{|M_{++}|^2 - |M_{--}|^2}{|M_{++}|^2 + |M_{--}|^2} = -\frac{2\text{Im}(\mathcal{C}_+\mathcal{C}_-^*)}{|\mathcal{C}_+|^2 + |\mathcal{C}_-|^2} \\ \mathcal{A}_2 &= \frac{2\text{Im}(M_{++}M_{--}^*)}{|M_{++}|^2 + |M_{--}|^2} = -\frac{2\text{Re}(\mathcal{C}_+\mathcal{C}_-^*)}{|\mathcal{C}_+|^2 + |\mathcal{C}_-|^2} \\ \mathcal{A}_3 &= \frac{2\text{Re}(M_{++}M_{--}^*)}{|M_{++}|^2 + |M_{--}|^2} = \frac{|\mathcal{C}_+|^2 - |\mathcal{C}_-|^2}{|\mathcal{C}_+|^2 + |\mathcal{C}_-|^2} \end{aligned} \quad (4.70)$$

and write the event rate as  $dN = d\mathcal{L}^{J_Z=0}d\hat{\sigma}$  with

$$d\mathcal{L}^{J_Z=0} = d\mathcal{L} [1 + \langle \xi_{12}\xi_{22} \rangle + \langle \xi_{12} + \xi_{22} \rangle \mathcal{A}_1 + \langle \xi_{13}\xi_{21} + \xi_{11}\xi_{23} \rangle \mathcal{A}_2 + \langle \xi_{13}\xi_{23} - \xi_{11}\xi_{21} \rangle \mathcal{A}_3] \quad (4.71)$$

with the unpolarized cross section given by

$$d\hat{\sigma}_0 = \frac{1}{4}d\Gamma \left( |M_{++}|^2 + |M_{--}|^2 \right). \quad (4.72)$$

If  $\mathcal{A}_1$  and  $\mathcal{A}_2$  are both non-zero, then, CP is violated since the Higgs boson is a mixture of CP-even and CP-odd states. One can thus, by analyzing the spins of the final photons, probe CP-violation. If the Higgs boson is a definite

CP-eigenstate, that is, a pure scalar or pseudoscalar particle, one has  $\mathcal{A}_1 = \mathcal{A}_2 = 0$  and  $\mathcal{A}_3 = \eta_C$  with  $\eta_C = 1(-1)$  for a CP-even (CP-odd) Higgs particle. The luminosity written above simplifies then to

$$d\mathcal{L}^{J_Z=0} = d\mathcal{L}[1 + \langle \xi_{12}\xi_{22} \rangle + \eta_C \langle \xi_{13}\xi_{23} - \xi_{11}\xi_{21} \rangle]. \quad (4.73)$$

In fact, if CP is conserved, one has  $M_{++} = \eta_C M_{--}$  leading to the relation between cross sections with parallel and orthogonal linear polarizations for the photons,  $d\hat{\sigma}_{\parallel} - d\hat{\sigma}_{\perp} = \eta_C \cdot (d\hat{\sigma}_{\parallel} + d\hat{\sigma}_{\perp})$ . This means that only photons with parallel (orthogonal) linear polarizations couple to scalars (pseudoscalars). Note that only if the lasers are linearly polarized it is possible to distinguish between the two CP-quantum numbers since the relevant average for the Stokes parameters,  $\langle \xi_{13}\xi_{23} - \xi_{11}\xi_{21} \rangle$ , is negligible for circularly polarized lasers.

In practice, the asymmetry  $\mathcal{A}_3$  is determined by making two runs and measuring the difference of the event rates for lasers with parallel polarization,  $\Delta\gamma = 0$ , and lasers with perpendicular polarization,  $\Delta\gamma = \frac{\pi}{2}$  [573]

$$\langle \mathcal{A}_3 \rangle = \frac{\sigma^{\text{eff}}(\Delta\gamma = 0) - \sigma^{\text{eff}}(\Delta\gamma = \frac{\pi}{2})}{\sigma^{\text{eff}}(\Delta\gamma = 0) + \sigma^{\text{eff}}(\Delta\gamma = \frac{\pi}{2})} \quad (4.74)$$

where the contamination from the background is taken into account  $\sigma^{\text{eff}} = \sigma_{\text{signal}}^{\text{eff}} + \sigma_{\text{bckg}}^{\text{eff}}$ . In terms of the electron and laser beam polarization, the asymmetry is given by

$$\langle \mathcal{A}_3 \rangle \simeq \frac{\eta_C \sigma_{\text{signal}} P_{1t} P_{2t} \langle \ell_1 \ell_2 \rangle}{\frac{1}{2}(1 + 4\lambda_{e-}\lambda_{e+}\langle c_1 c_2 \rangle)(2\hat{\sigma}^{\text{signal}} + \hat{\sigma}_0^{\text{bckg}}) + \frac{1}{2}(1 - 4\lambda_{e-}\lambda_{e+}\langle c_1 c_2 \rangle)\hat{\sigma}_2^{\text{bckg}}} \quad (4.75)$$

where the effects for  $\rho \neq 0$  have been ignored for simplicity [there is also a generally small contribution to the background in the numerator from the component  $\hat{\sigma}_{\parallel}^{\text{bckg}} - \hat{\sigma}_{\perp}^{\text{bckg}} \propto m_q^4/W^4$ ]. As can be seen, a very important role is played by the linear laser polarization  $P_{it}$ , the average of the induced linear polarizations of the photons [the asymmetry is directly proportional to the product] and by the longitudinal polarizations of the electron beams and the induced circular polarization of the photons.

The statistical significance of the signal is given by

$$N_{\text{SD}}(\mathcal{A}_3) = \frac{|\sigma^{\text{eff}}(\Delta\gamma = 0) - \sigma^{\text{eff}}(\Delta\gamma = \frac{\pi}{2})|}{\sqrt{\sigma^{\text{eff}}(\Delta\gamma = 0) + \sigma^{\text{eff}}(\Delta\gamma = \frac{\pi}{2})}} \times \sqrt{\mathcal{L}^{\text{eff}}}. \quad (4.76)$$

With the machine parameters, polarization and luminosity discussed above, a measurement at the level of 10% can be made, allowing the distinction between the two CP possibilities for the Higgs particle; see Ref. [573] for an analysis where a realistic luminosity spectra and photon polarizations are taken into account.

**4.5.2.2. Measurements using angular distributions.** Another way to test the CP-nature of the produced Higgs particle is to study the angular distributions in its decays. For a relatively heavy Higgs boson,  $M_H \gtrsim 2M_Z$ , this can be done in the final state  $H \rightarrow WW$ ,  $ZZ \rightarrow 4f$  in which, as discussed in Section 2.2.4, the angular correlations between the final state fermions are very different in the case of scalar and pseudoscalar Higgs particles. For instance, the azimuthal dependence on the angle  $\Delta\phi$  between the decay planes of the two vector bosons is characteristically different in the  $0^{++}$  and  $0^{+-}$  cases [140,155]. Another different observable is the correlation

$$\zeta_{VV} = \frac{\sin^2 \theta_1 \sin^2 \theta_3}{(1 + \cos^2 \theta_1)(1 + \cos^2 \theta_3)} \quad (4.77)$$

where  $\theta_1$  and  $\theta_3$  are the polar angles of the two fermions from the  $V \rightarrow f\bar{f}$  decays defined in Fig. 2.11 and which corresponds to the ratio of the angular distributions expected for the decay of a scalar particle and a pseudoscalar particle in the limit  $M_H \gg M_V$ .

A detailed simulation in the decay channels  $H \rightarrow ZZ \rightarrow \ell\ell jj$  and  $H \rightarrow WW \rightarrow 4j$  has been performed [572] along the same lines as that for the measurement of the amplitudes of the  $HVV$  couplings and their phases discussed earlier. The output of this analysis is shown in Fig. 4.44 for the example of a Higgs boson with a mass  $M_H = 200$  GeV, produced in the  $\gamma\gamma$  mode of an  $e^+e^-$  collider with initial energy of  $\sqrt{s_{e^+e^-}} = 305$  GeV and decaying into  $ZZ \rightarrow \ell\ell jj$  final states. The figure shows the number of expected events for a scalar and pseudoscalar Higgs boson and for the

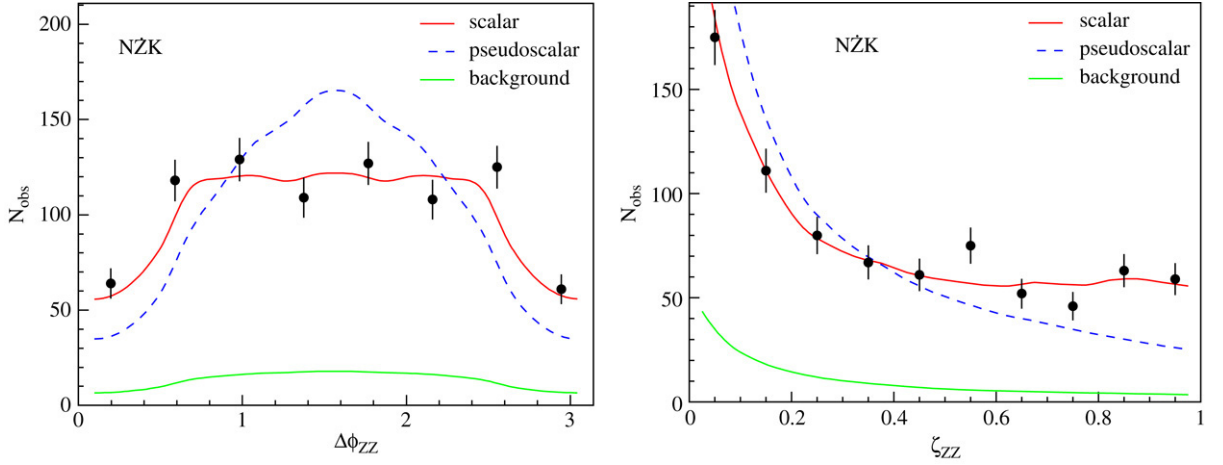


Fig. 4.44. The measurement of the azimuthal angle  $\Delta\phi_{ZZ}$  and the correlation  $\zeta_{ZZ}$  in the process  $\gamma\gamma \rightarrow H \rightarrow ZZ \rightarrow \ell\ell jj$  for  $M_H = 200$  GeV at a photon collider; from [572].

non-resonant SM background, for a variation of the reconstructed azimuthal angle  $\Delta\phi_{ZZ}$  (left) and the correlation  $\zeta_{ZZ}$  (right). The points with error bars indicate the statistical precision of the measurements after a one year running of the photon collider with a luminosity of  $600 \text{ fb}^{-1}$ .

If the  $HVV$  coupling, including CP-violation, is parametrized as  $g_{HVV} = \lambda \cos \Phi$  with  $\lambda = 1$  and  $\Phi = 0$  in the SM, from a combined fit of the  $H \rightarrow WW/ZZ \rightarrow 4f$  events which includes a free variation of the two-photon width and phase one can measure the absolute magnitude of the coupling with a precision  $\Delta\lambda/\lambda = 2\%$  and the CP-violating phase with a precision  $\Delta\Phi = 50 \text{ mrad}$ , in the entire Higgs mass range  $M_H = 200\text{--}350 \text{ GeV}$  [572].

Similar tests can be performed in the decay  $H \rightarrow t\bar{t}$  for a heavier Higgs particle,  $M_H > 350 \text{ GeV}$ . In particular, the interference pattern of the resonant and the continuum amplitudes for the  $\gamma\gamma \rightarrow t\bar{t}$  process allows one to check the parity of the Higgs boson and the presence of CP-violation, by using circularly polarized colliding photons [575]. Indeed, from the  $t\bar{t}$  decay angular distribution one can build four convoluted observables  $\Sigma_{1..4}$

$$\Sigma_i(\sqrt{s}_{\gamma\gamma}) = \int d\sqrt{s}_{\gamma\gamma} \sum_{\lambda_1, \lambda_2} \left( \frac{1}{\mathcal{L}} \frac{d\mathcal{L}^{\lambda_1\lambda_2}}{d\sqrt{s}_{\gamma\gamma}} \right) \left( \frac{3\beta}{32\pi s_{\gamma\gamma}} \int S_{\lambda_1\lambda_2}^i(\theta, \sqrt{s}_{\gamma\gamma}) d\cos\theta \right) \quad (4.78)$$

with  $\theta$  being the polar angle of the  $t$  momentum in the  $\gamma\gamma$  c.m. frame and the first bracket corresponding to the normalized luminosity distribution for each of the photon  $\lambda_1\lambda_2$  helicity combinations. The functions  $S_{\lambda_1\lambda_2}^i$  contain the information on the  $\gamma\gamma \rightarrow t\bar{t}$  helicity amplitudes

$$S_{\lambda_1\lambda_2}^1 = |M_{\lambda_1\lambda_2}^{RR}|^2, \quad S_{\lambda_1\lambda_2}^2 = |M_{\lambda_1\lambda_2}^{LL}|^2, \quad S_{\lambda_1\lambda_2}^{3(4)} = 2\text{Re}(\text{Im}) \left[ M_{\lambda_1\lambda_2}^{RR} M_{\lambda_1\lambda_2}^{LL*} \right]. \quad (4.79)$$

Writing the  $\gamma\gamma \rightarrow t\bar{t}$  amplitudes as sums of the resonant and non-resonant contributions

$$M_{\lambda\lambda}^{\sigma\sigma} = [M_{\lambda\lambda}^{\sigma\sigma}] + \left( \frac{\sqrt{s}_{\gamma\gamma}}{M_H} \right)^3 r_H \cdot i \left[ 1 + \exp \left( 2i \tan^{-1} \frac{s_{\gamma\gamma}^2 - M_H^2}{M_H \Gamma_H} \right) \right] \quad (4.80)$$

the phase of the resonance amplitude is shifted by  $r_H$  which is essentially the phase of the  $\gamma\gamma H$  coupling when neglecting the phase in the  $t\bar{t}H$  vertex. In the left-hand side of Fig. 4.45, the four observables  $\Sigma_{1..4}$  for the production of scalar  $H$  and pseudoscalar  $A$  bosons with  $M_{H,A} = 400 \text{ GeV}$ , are shown for two values of the  $\gamma\gamma H/A$  phase,  $\arg(r_{H,A}) = 0$  and  $\frac{\pi}{4}$ , and one can see that the difference is significant enough to be measured experimentally.

Another possible method to probe the Higgs CP-quantum numbers in  $\gamma\gamma \rightarrow t\bar{t}$  production is to look at the net polarization of the  $t/\bar{t}$ -quarks either with circularly polarized [576] or linearly polarized photons [574]. In the latter case, the top polarization has been analyzed through the decay lepton energy and angular distributions in the decay  $t \rightarrow b\ell\nu$ . The full differential distribution of the decay lepton has been written and, in terms of the initial state  $e^+e^-$



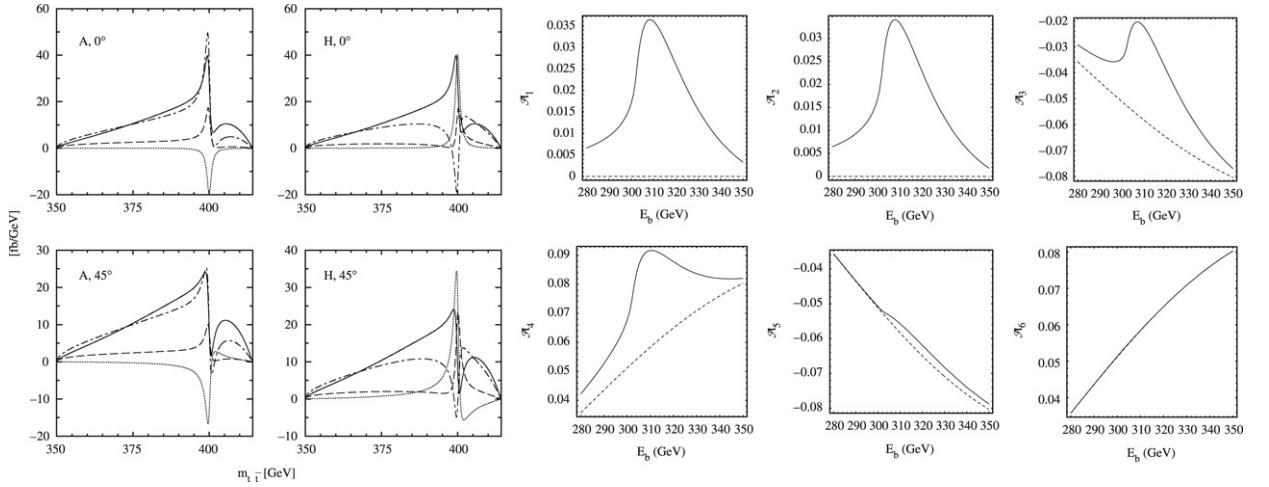


Fig. 4.45. Left: The observables  $\Sigma_1$  (solid),  $\Sigma_2$  (dashed),  $\Sigma_3$  (dotted-dashed) and  $\Sigma_4$  (dotted) for the production of  $H$  and  $A$  bosons for  $\arg(r_{H,A}) = 0$  and  $\frac{\pi}{4}$  with  $x = 4.8$ ,  $P_L = -1.0$  and  $P_e = 0.9$ ; from Ref. [575]. Right: The asymmetries  $\mathcal{A}_{1..6}$  as functions of the  $e^-$  beam energy for continuum  $\gamma\gamma \rightarrow t\bar{t}$  production (dotted line) and when the resonant contribution with  $M_{H,A} = 500$  GeV is included (solid lines); from Ref. [574].

polarizations  $\lambda_{e^+e^-} = \pm 1$  and final charge of the decay lepton  $e_{\ell^\pm} = \pm 1$ , one can obtain four cross sections  $\sigma(\pm, \pm)$  from which one can construct six asymmetries that are sensitive to the Higgs coupling [574]

$$\mathcal{A}_{1/4} = \frac{\sigma(+, \pm) - \sigma(-, -)}{\sigma(+, \pm) + \sigma(-, -)}, \quad \mathcal{A}_{2/3} = \frac{\sigma(+, \mp) - \sigma(-, +)}{\sigma(+, \mp) + \sigma(-, +)}, \quad \mathcal{A}_{5/6} = \frac{\sigma(\pm, +) - \sigma(\pm, -)}{\sigma(\pm, +) + \sigma(\pm, -)}. \quad (4.81)$$

$\mathcal{A}_{5/6}$  are charge asymmetries for a given polarization and vanish for zero angle, which is not the case for the purely CP-violating  $\mathcal{A}_{1/2}$  asymmetries;  $\mathcal{A}_{3/4}$  are the polarization asymmetries for a given lepton charge. Note that the charge asymmetries do not vanish in the case of the SM where only the non-resonant amplitude is taken into account. The sensitivity of the six asymmetries to the  $\gamma\gamma H/A$  coupling and to its possible CP-violating component is exhibited in the right-hand side of Fig. 4.45 for a specific point with  $M_{H,A} = 500$  GeV and a  $\gamma\gamma H/A$  vertex which has both real and imaginary parts, as a function of the electron beam energy. As can be seen, the asymmetries can be large and in most cases different from the asymmetries of the continuum  $\gamma\gamma \rightarrow t\bar{t}$  production.

Finally, for  $M_H \lesssim 140$  GeV, one can also study the CP-nature of the Higgs boson by looking at the polarization of the  $\tau$ -leptons produced in  $\gamma\gamma \rightarrow H \rightarrow \tau^+\tau^-$ . One can again construct polarization asymmetries which probe both the  $H\gamma\gamma$  and  $H\tau\tau$  couplings [587]

#### 4.5.3. Other Higgs production mechanisms

Processes other than Higgs boson production as s-channel resonances have been discussed in the context of  $\gamma\gamma$  colliders: Higgs pair production via loop diagrams [588,589], production in association with vector bosons [518,590,591] and associated Higgs production with top quarks [592]. At  $e\gamma$  colliders, the Higgs boson can also be produced in the reaction  $e\gamma \rightarrow \nu_e W^+ H$  [595,596]. In this section, we briefly summarize the main features of these processes, concentrating only on the magnitude of the cross sections of the subprocesses [i.e. without folding with the photon luminosity spectra].

**4.5.3.1. Higgs pair production:  $\gamma\gamma \rightarrow HH$ .** The pair production of Higgs bosons in  $\gamma\gamma$  collisions is induced by loops of top quarks and  $W$  bosons where two sets of diagrams are involved: (i) s-channel vertex diagrams where the intermediate Higgs particle splits into two and which involves the trilinear Higgs coupling  $\lambda_{HHH}$ ; the contributions of these diagrams are essentially the same as those discussed for  $\gamma\gamma \rightarrow H$ , except that here the Higgs particle is virtual, and (ii) box diagrams involving top quarks and  $W$  bosons, as well as vertex and self-energy diagrams which do not involve the trilinear Higgs coupling but the quartic Higgs–gauge boson interaction.

The cross section has been calculated in Ref. [588] in the SM case; see also Ref. [589]. At small energies,  $\sqrt{s_{\gamma\gamma}} \sim 500$  GeV, it is dominated by the top quark contribution. For photons having the same helicities, it is at



the level of  $\sim 0.5$  fb for  $M_H \sim 100$  GeV, decreases very slowly with  $M_H$  and falls off rapidly when approaching the  $\sqrt{s}_{\gamma\gamma} = 2M_H$  threshold. At higher energies,  $\sqrt{s}_{\gamma\gamma} \gtrsim 1$  TeV, the cross section is dominated by the  $W$  boson loop contribution which, contrary to the case of single Higgs boson, interferes constructively with the top quark contribution for large enough  $M_H$ . While the cross section is smaller than that at 500 GeV for low  $M_H$ , it increases with  $M_H$  almost up to the kinematical boundary, where it reaches values of the order 1(10) fb at  $\sqrt{s}_{\gamma\gamma} \sim 1(2)$  TeV. This is mainly due to the large triple and quartic Higgs couplings to the Goldstone or  $W_L$  bosons which grow as  $M_H^2$ .

For opposite photon helicities, the cross section has the same magnitude as in the same-helicity case for  $M_H \sim 100$  GeV, but because in this case it is dominated by the contributions of transverse  $W$  bosons it falls off more rapidly with increasing  $M_H$  values even for high center of mass energies. At  $\sqrt{s} = 2$  TeV, there is bump for a very heavy Higgs boson.

The sensitivity of the production cross section to the trilinear Higgs coupling  $\lambda_{HHH}$  depends on the relative weight of the diagram with the exchange of the Higgs boson in the  $s$ -channel and the other diagrams [589]. For very heavy Higgs bosons,  $M_H \sim 500$ –800 GeV, the cross section is very sensitive to the coupling  $\lambda_{HHH}$ , in particular near the  $\sqrt{s}_{\gamma\gamma} = 2M_H$  threshold where it is maximal: for  $M_H \sim 700$  GeV, removing the trilinear coupling leads to an increase of the cross section [which is unfortunately rather small, being less than 1 fb] by about 60%. For smaller  $M_H$  values, the sensitivity is much weaker since the cross section at high energies [where it is sizable] is dominated by the box contributions which do not involve  $\lambda_{HHH}$ , while at low energies the rates are too small. Note finally, that a change of the trilinear Higgs coupling does not affect the angular distribution of the Higgs pair production process.

Thus, at very high energies and for rather heavy Higgs bosons, one can possibly probe the trilinear Higgs coupling in the process  $\gamma\gamma \rightarrow HH$ . This is complementary to the  $e^+e^-$  case where the coupling can be best probed for low Higgs boson masses. However, to assess to which extent the coupling can be measured, more detailed analyses are needed.

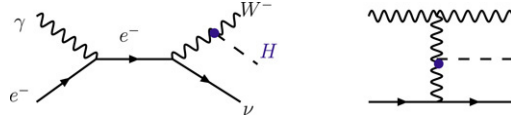
**4.5.3.2. Higgs production in association with top quarks:  $\gamma\gamma \rightarrow t\bar{t}H$ .** The process  $\gamma\gamma \rightarrow t\bar{t}H$  offers an additional opportunity to probe the Yukawa coupling of the Higgs boson to top quarks [592,593]. Contrary to the similar process in the  $e^+e^-$  case, where the Higgs boson can be radiated not only from the top quark lines but also from the  $Z$  line in the Higgs–strahlung-like process  $e^+e^- \rightarrow HZ^* \rightarrow Ht\bar{t}$  [although the contribution of the latter is very tiny as discussed earlier], in associated  $Ht\bar{t}$  production in photon–photon collisions, the Higgs boson is only radiated from the top quark lines and the cross section is directly proportional to the  $Ht\bar{t}$  Yukawa coupling.

As in the case of  $e^+e^-$  collisions, the cross section for  $t\bar{t}H$  production is rather small at  $\sqrt{s}_{\gamma\gamma} \sim 500$  GeV, because of the limited phase space. It increases with energy and for  $M_H \sim 100$  GeV it reaches the level of  $\sigma(\gamma\gamma \rightarrow t\bar{t}H) = \mathcal{O}(1)$  fb at  $\sqrt{s}_{\gamma\gamma} \sim 1$  TeV, where it begins to flatten [this is opposite to the  $e^+e^-$  case, where  $\sigma \propto 1/s$ ]. The cross section drops rapidly with increasing  $M_H$  and at a c.m. energy of 1 TeV it is one order of magnitude smaller for  $M_H \sim 200$  GeV than for  $M_H \sim 100$  GeV.

The  $\gamma\gamma \rightarrow t\bar{t}H$  process can be used as a means to determine the CP-properties of the Higgs boson and to distinguish between scalar and pseudoscalar particles and to probe CP-violation. In addition, associated Higgs production with lighter fermions, such as  $\tau$ -leptons and  $b$ -quarks, which have larger cross sections in extensions of the SM where the Higgs couplings to down-type fermions are enhanced, has been discussed [594].

**4.5.3.3. Higgs production in association with gauge bosons.** As mentioned previously, the  $\gamma\gamma \rightarrow W^+W^-$  production cross section is enormous, being at the level of  $\mathcal{O}(100)$  pb for c.m. energies around  $\sqrt{s}_{\gamma\gamma} \sim 300$ –500 GeV [585], and one could attach one or even two additional Higgs bosons to the  $W$  lines, while still having sizable rates [590]. For a Higgs boson with a mass  $M_H \sim 100$  GeV, the cross section for  $\gamma\gamma \rightarrow W^+W^-H$  is about 20 fb for  $\sqrt{s}_{\gamma\gamma} = 500$  GeV and, therefore, it is at the level of the cross section for the Higgs–strahlung process in  $e^+e^-$  collisions with the same c.m. energy. The cross section quickly rises with energy, to reach the level of 400 fb for  $\sqrt{s}_{\gamma\gamma} = 2$  TeV, i.e. almost two orders of magnitude larger than the Higgs–strahlung cross section which drops like  $1/s$ , and of the same order as the dominant production mechanism,  $e^+e^- \rightarrow H\nu\bar{\nu}$ . Compared to the processes for associated Higgs production with gauge bosons in  $e^+e^-$  collisions discussed previously,  $\sigma(\gamma\gamma \rightarrow W^+W^-H)$  is a factor of three larger than any of the  $e^+e^- \rightarrow HVV$  processes. Note however, that this process does not provide any additional information that could not be obtained in the  $e^+e^-$  option of the machine.

A channel that is, in principle, more interesting is when two Higgs particles are produced in association with the  $W$  boson pair. Indeed, similar to the  $WW$  fusion mechanism  $WW \rightarrow HH$ , this process is sensitive to the trilinear Higgs

Fig. 4.46. Diagrams for Higgs boson production in  $e\gamma$  collisions.

boson coupling since the Higgs particle produced in  $\gamma\gamma \rightarrow WWH$  can split into two Higgs bosons. Unfortunately, the rates are too small to be useful even with very high luminosities [518]: for  $\gamma\gamma$  energies of the order of 1 TeV,  $\sigma(\gamma\gamma \rightarrow W^+W^-HH) \sim 0.02$  fb for  $M_H \sim 100$  GeV, and barely reaches 0.2 fb at  $\sqrt{s}_{\gamma\gamma} \sim 2$  TeV. Finally, note that the Higgs bosons can be also produced in association with a  $Z$  boson in the loop induced process  $\gamma\gamma \rightarrow HZ$  [591] where, in particular, virtual top quarks and  $W$  bosons contribute. The cross sections are, however, rather small: for  $\sqrt{s}_{\gamma\gamma} = 500$  GeV and  $M_H \sim 100$  GeV, they are at the level of 0.1 fb.

**4.5.3.4. Higgs production in  $e\gamma$  collisions.** Finally, let us close this discussion on Higgs physics at the photonic mode of future  $e^+e^-$  linear colliders by considering the other possible option, the  $e\gamma$  mode, that can be obtained by converting only one of the electron beams into a very energetic back-scattered photon. Higgs bosons can be produced in  $e\gamma$  collisions through bremsstrahlung off the  $W$  lines,  $e^-\gamma \rightarrow \nu_e W^- H$  [595,596]; the relevant diagrams are shown in Fig. 4.46.

For a low mass Higgs boson,  $M_H \sim 100$  GeV, the cross section for the subprocess [again without folding with the photon spectrum] is at the level of  $\sim 40$  fb for  $\sqrt{s}_{e\gamma} = 500$  GeV and increases monotonically to reach values of the order of 100 (300) fb for  $\sqrt{s}_{e\gamma} = 1(2)$  TeV; i.e. the rates are comparable to those of the  $WW$  fusion in  $e^+e^-$  collisions at high energies. While the variation of the cross section with the Higgs mass is rather pronounced at low energies [ $\sigma(e\gamma \rightarrow \nu_e WH)$  drops by a factor of two when increasing  $M_H$  from 100 to 150 GeV, as a result of phase-space reduction], it is very mild at higher energies. When convoluting the cross sections with the back-scattered photon flux, they are reduced by about 50% at  $\sqrt{s}_{e\gamma} = 500$  GeV and slightly less at higher energies [596].

The large Higgs production rates in this process could allow one to perform an independent determination of the  $HWW$  couplings [which can be made already in the  $e^+e^- \rightarrow H\nu\bar{\nu}$  production and  $H \rightarrow WW$  decay process if the Higgs is not too heavy] and to probe anomalous contributions. However, the environment of the collision should be well under control to match the accuracy which can be achieved in the clean  $e^+e^-$  mode of the linear collider.

## 4.6. Higgs production at muon colliders

The ability of a future  $\mu^+\mu^-$  collider to investigate the Higgs sector of the SM and its extensions has been discussed in numerous papers; see for instance the detailed reviews of Refs. [472–477]. In this section, we simply summarize the main studies which have been performed in this context, concentrating on the benefits of such a collider compared to  $e^+e^-$  linear colliders for determining the properties of the Higgs particle.

### 4.6.1. Higgs production in the $s$ -channel

**4.6.1.1. Resonant Higgs production at the tree level.** In  $\mu^+\mu^-$  collisions, the resonance production cross section for a Higgs boson decaying into a final state  $X$  is given, in terms of the partial decay widths, by

$$\sigma_H(\sqrt{s}) = \frac{4\pi \Gamma(H \rightarrow \mu^+\mu^-) \Gamma(H \rightarrow X)}{(s - M_H^2)^2 + M_H^2 \Gamma_H^2}. \quad (4.82)$$

In practice, however, one has to include the Gaussian center of mass energy spread  $\sigma_{\sqrt{s}}$ . Assuming a central c.m. energy value  $\sqrt{s}$ , one obtains after convolution [490]

$$\bar{\sigma}_H(\sqrt{s}) = \frac{1}{2\pi\sigma_{\sqrt{s}}} \int \sigma_H(\sqrt{\hat{s}}) \exp\left(-\frac{(\sqrt{\hat{s}} - \sqrt{s})^2}{2\sigma_{\sqrt{s}}^2}\right) d\sqrt{\hat{s}} \quad (4.83)$$

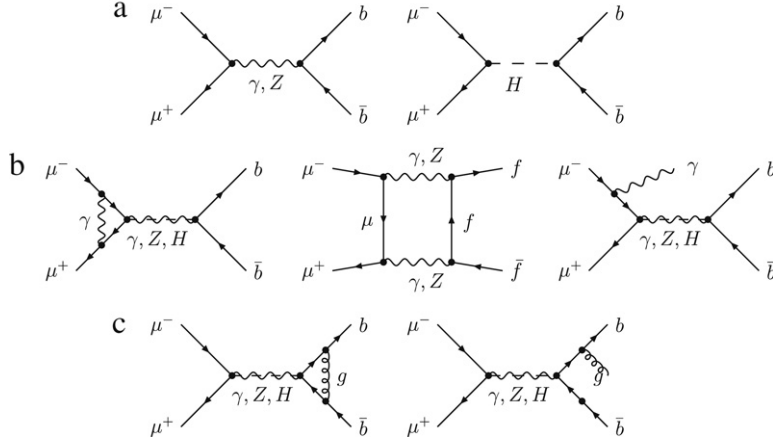


Fig. 4.47. Lowest-order diagrams for  $\mu^-\mu^+ \rightarrow b\bar{b}$  including the continuum and resonant channels (a) as well as the photonic QED (b) and the final state QCD corrections (c).

which, when the energy is tuned to the Higgs boson mass value, gives

$$\bar{\sigma}_H(\sqrt{s} \simeq M_H) = \frac{4\pi}{M_H^2} \frac{\text{BR}(H \rightarrow \mu^+\mu^-)\text{BR}(H \rightarrow X)}{\left[1 + \frac{8}{\pi} \left(\sigma_{\sqrt{s}}/\Gamma_H\right)^2\right]^{1/2}}. \quad (4.84)$$

If the energy spread is much smaller than the Higgs boson total decay width, the effective cross section is simply given by

$$\sigma_{\sqrt{s}} \ll \Gamma_H : \quad \bar{\sigma}_H \simeq \frac{4\pi}{M_H^2} \text{BR}(H \rightarrow \mu^+\mu^-)\text{BR}(H \rightarrow X) \quad (4.85)$$

while in the opposite case, the effective cross section reads

$$\sigma_{\sqrt{s}} \gg \Gamma_H : \quad \bar{\sigma}_H \simeq \frac{4\pi^2}{M_H^2} \Gamma(H \rightarrow \mu^+\mu^-)\text{BR}(H \rightarrow X) \times \frac{1}{2\sqrt{2\pi}\sigma_{\sqrt{s}}}. \quad (4.86)$$

One needs therefore a very small resolution to maximize the Higgs boson production rate.

Recalling that there is a trade between the luminosity delivered by the machine and the energy resolution  $R$  of the muon beams, Section 4.1.3, the production rate can be maximized by choosing  $R$  such that the energy spread  $\sigma_{\sqrt{s}}$  is slightly smaller than the Higgs boson total decay width,  $\sigma_{\sqrt{s}} \lesssim \Gamma_H$ , which in the SM corresponds to  $R = 0.003\%$  for  $M_H \lesssim 120$  GeV. The energy spread can be then more conveniently written as [474]

$$\sigma_{\sqrt{s}} = 0.002 \text{ GeV} \left( \frac{R}{0.003\%} \right) \left( \frac{\sqrt{s}}{100 \text{ GeV}} \right). \quad (4.87)$$

For Higgs bosons in the low mass range,  $M_H \lesssim 130$  GeV, a small resolution  $R = 0.003\%$  would be more advantageous. In the intermediate Higgs mass range,  $130 \text{ GeV} \lesssim M_H \lesssim 160$  GeV, the Higgs boson is broad enough and one can use a resolution  $R = 0.01\%$  without too much loss of production rates. In such a case, the cross sections are functions of the Higgs branching fractions and Higgs masses and practically do not depend on  $R$ ; this is even more true for Higgs bosons in the high mass range,  $M_H \gtrsim 180$  GeV. [See Table 2.1, for the Higgs total width and branching ratios for selected values of  $M_H$ .]

**4.6.1.2.  $\mu^+\mu^- \rightarrow b\bar{b}$  and the radiative corrections.** For a light Higgs boson,  $M_H \lesssim 140$  GeV, the dominant decay is  $H \rightarrow b\bar{b}$  and one has to consider the full process  $\mu^+\mu^- \rightarrow b\bar{b}$  which receives contributions from the resonant  $\mu^+\mu^- \rightarrow H \rightarrow b\bar{b}$  channel and continuum  $\mu^+\mu^- \rightarrow \gamma, Z \rightarrow b\bar{b}$  production; Fig. 4.47(a). The latter is mediated by gauge boson  $s$ -channel exchange and would act as a background.

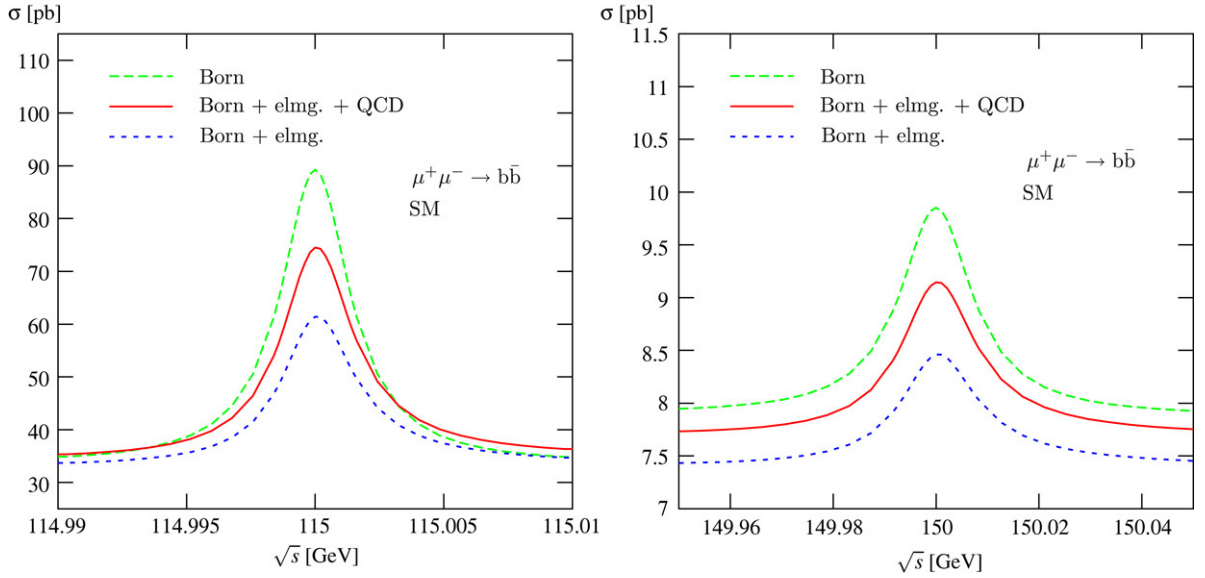


Fig. 4.48. The effective cross section for Higgs production in  $\mu^+\mu^- \rightarrow b\bar{b}$  for  $M_H = 115$  and  $150$  GeV. Shown are the Born cross sections and the cross section with electromagnetic and QCD corrections. No energy resolution has been assumed; from Ref. [597].

The photonic corrections which include the gauge invariant subset of initial and final state virtual corrections and box diagrams involving at least one photon as well as a initial and final state photon radiation, Fig. 4.47(b), and the QCD corrections to the final state with virtual gluon exchange and gluon emission, Fig. 4.47(c), have been calculated in Ref. [597] with a careful treatment of both the  $Z$  and Higgs boson resonances. In the case where no energy resolution is included, the results are shown in Fig. 4.48 for the production of SM Higgs bosons with masses  $M_H = 115$  GeV and  $150$  GeV. The tree-level couplings have been expressed in terms of  $G_\mu$  to encapsulate the leading electroweak correction and the running  $b$ -quark mass has been used in the  $Hb\bar{b}$  coupling to absorb the bulk of the QCD corrections.

For the photonic corrections, the large ISR corrections from the radiative return to the  $Z$ -resonance can be suppressed by requiring that the invariant mass of the hadronic final state, thus including gluon radiation, should not exceed  $10$  GeV compared to the Higgs mass,  $M_{\text{had}} > \sqrt{s} - 10$  GeV. [For continuum production, the main difference between  $e^+e^-$  and  $\mu^+\mu^-$  collisions is due to the different leading logarithmic photonic corrections,  $\log(s/m_\ell^2)$ , which lead to ISR effects that are roughly a factor of two smaller in  $\mu^+\mu^-$  than in  $e^+e^-$  collisions.] With this cut, the photonic corrections which are still dominated by  $\mathcal{O}(\alpha)$  ISR turn negative to be of order  $-5(10)\%$  for  $M_H = 115$  ( $150$ ) GeV for the continuum production and  $\sim -50\%$  for the resonant production, leading to a reduction of the resonance peak compared to the continuum background. The QCD corrections are positive and, as they are larger for the Higgs mediated channel [ $\sim 20\%$  as discussed in Section 2.1.2] compared to  $b\bar{b}$  continuum production [ $\sim \frac{\alpha_s}{\pi} \sim 4\%$ ], they tend to enhance the resonance peak.

When including a beam energy resolution  $R = 0.003\%$ , the relative impact of the radiative correction remains the same. However, the signal peaks are suppressed, in particular for small Higgs masses. For instance, the ratio is  $\sigma_{\sqrt{s}}/\Gamma_H \sim 0.7$  at  $M_H = 115$  GeV, compared to  $\sigma_{\sqrt{s}}/\Gamma_H \sim 0.2$  at  $M_H = 150$  GeV, as can be seen in Fig. 4.49.

**4.6.1.3. Signals and backgrounds in  $\mu^+\mu^- \rightarrow H \rightarrow b\bar{b}, WW, ZZ$ .** In the main Higgs decay channels,  $H \rightarrow b\bar{b}, WW, ZZ$ , the cross sections for the signals and the corresponding SM backgrounds are shown in the left-hand side of Fig. 4.50 as functions of the Higgs mass in the range  $M_H = 80$ – $160$  GeV for an energy resolution  $R = 0.003\%$ . In the right-hand side of the figure, the luminosity that is required to observe the signal at the  $5\sigma$  level is displayed for the same energy resolution. Various cuts have been applied to reject part of the background [ $b$ -tagging, cuts to remove gauge bosons in the forward and backward directions] and are discussed in Ref. [474] from which we borrowed the figure.

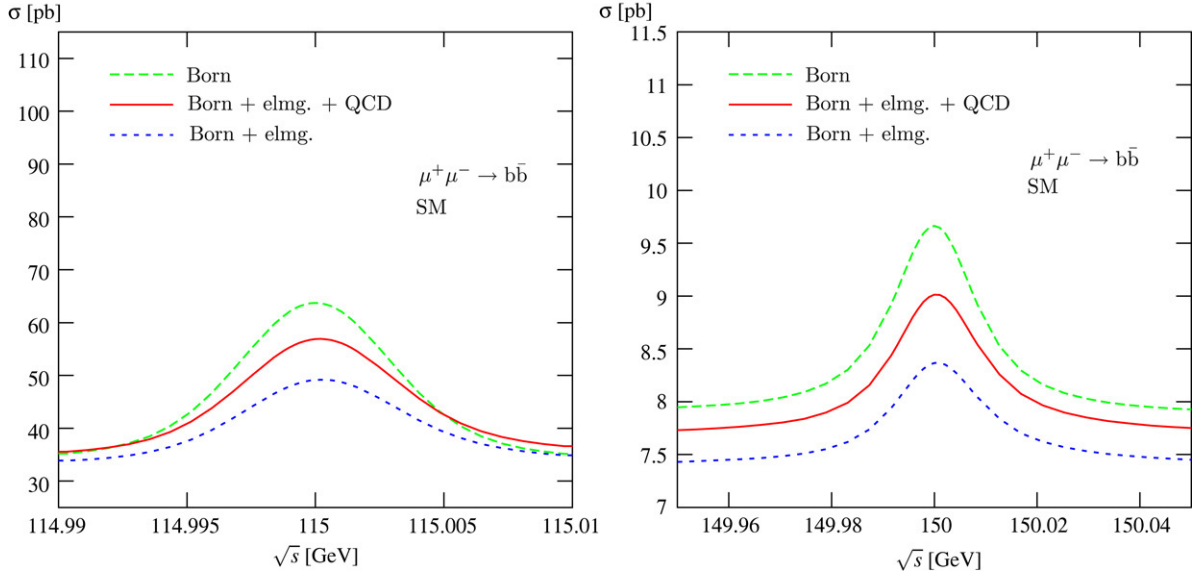


Fig. 4.49. Same as in Fig. 4.48, but with an energy resolution  $R = 0.003\%$ ; from [597].

As can be seen, the  $\mu^+\mu^- \rightarrow H \rightarrow b\bar{b}$  signal rate is rather large for  $M_H \lesssim 140$  GeV, leading to  $\mathcal{O}(10^4)$  events for a luminosity of  $\mathcal{L} = 1 \text{ fb}^{-1}$ . The background from direct  $\mu^+\mu^- \rightarrow \gamma, Z^* \rightarrow b\bar{b}$  production<sup>35</sup> [the light quark-jet background can be removed with  $b$ -tagging] is much larger than the signal for a Higgs boson in the mass range  $M_H \lesssim 115$  GeV which is ruled out by the LEP2 negative searches [in particular, for  $M_H \sim 90$  GeV a huge background from the resonant production  $\mu^+\mu^- \rightarrow Z \rightarrow b\bar{b}$  is present], and is of comparable size as the signal in the mass range  $115 \text{ GeV} \lesssim M_H \lesssim 135$  GeV. For larger masses, the signal event drops dramatically because of the decrease of the  $H \rightarrow b\bar{b}$  branching ratio.

In the case of gauge boson production,  $\mu^+\mu^- \rightarrow WW^*$  and  $ZZ^*$ , the event rates are much smaller than those of the  $b\bar{b}$  final states in the low Higgs mass range, as a result of the tiny branching ratios. For larger masses,  $M_H \sim 140$  GeV, the  $WW$  and  $b\bar{b}$  cross sections become comparable but the absolute rates are rather small; for  $M_H \gtrsim 160$  GeV, the cross sections are below the femtobarn level. The backgrounds from continuum  $\mu^+\mu^- \rightarrow WW^*, ZZ^*$  production [once cuts have been applied to remove for instance the forward and backward events which are rare in the signal where the Higgs boson is centrally produced] do not exceed the signal cross sections for  $M_H \lesssim 150$  GeV. For higher Higgs masses,  $M_H \gtrsim 160$  GeV, when the production of two real gauge bosons opens up kinematically, the backgrounds become much larger than the resonant signal.

For a SM Higgs boson with a mass  $M_H \gtrsim 2M_W$ ,  $s$ -channel production in  $\mu^+\mu^-$  colliders will, anyway, not be very useful since the total width becomes large and the  $H \rightarrow \mu^+\mu^-$  decay branching fraction drops drastically. However, there are extensions of the SM in which Higgs bosons can have relatively large masses but suppressed total widths [this is the case of e.g. pseudoscalar Higgs bosons which do not couple to massive gauge bosons at tree level]. In this case, the production rates are not very suppressed and muon colliders can be valuable tools in determining their properties as will be discussed in another part of this review.

#### 4.6.2. Determination of the properties of a light Higgs boson

In the SM, for Higgs bosons in the mass range  $M_H \lesssim 160$  GeV, important measurements can be performed at the muon collider in the channels  $\mu^+\mu^- \rightarrow H \rightarrow b\bar{b}, WW^*, ZZ^*$ , which have sizable production rates as shown previously, as well as in the channel  $\mu^+\mu^- \rightarrow H \rightarrow \tau^+\tau^-$ . The Higgs mass, its total decay width and the cross section for the various final states, which are sensitive to the branching fractions and thus the Higgs couplings, can be determined.

<sup>35</sup> Since the background is practically constant in the window  $M_H \pm \sigma_{\sqrt{s}}$ , one can measure it below and above the resonance and eventually, subtract it if enough luminosity is available.

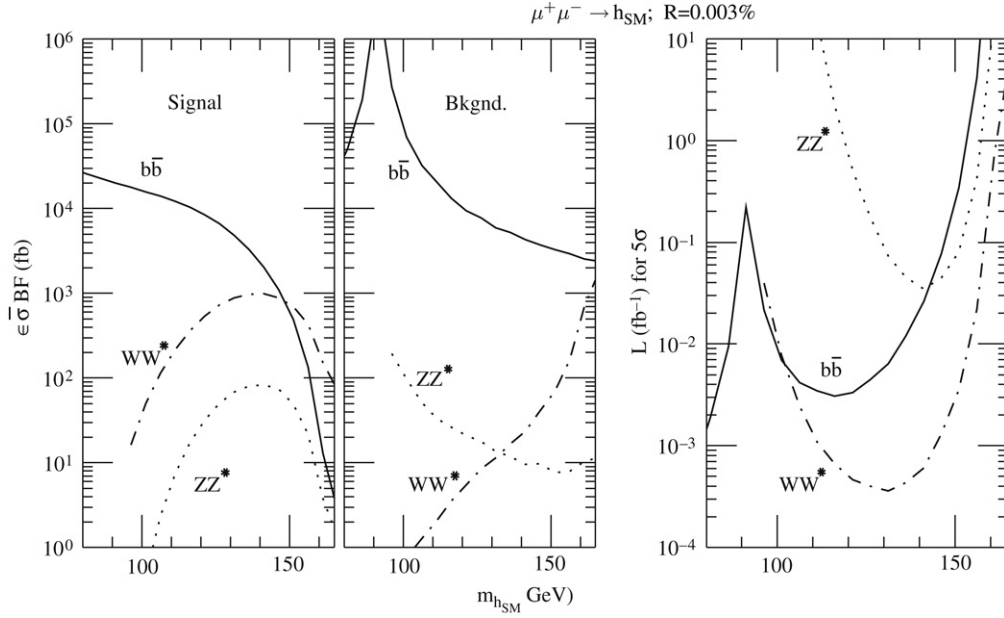


Fig. 4.50. The cross sections for the processes  $\mu^+\mu^- \rightarrow b\bar{b}$ ,  $WW$ ,  $ZZ$  for signals and backgrounds as functions of  $M_H$  for  $R = 0.003\%$  (left) and the luminosity required for a  $5\sigma$  observation of the  $\mu^+\mu^- \rightarrow H \rightarrow b\bar{b}$ ,  $WW$ ,  $ZZ$  signals (right); from Ref. [474].

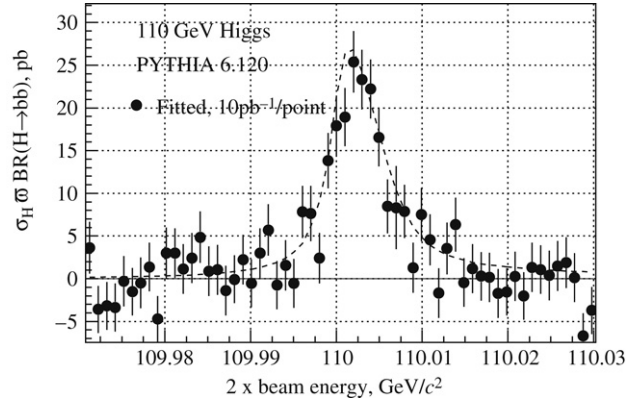


Fig. 4.51. The  $\mu^+\mu^- \rightarrow b\bar{b}$  production cross section as a function of the beam energy for  $M_H = 110 \text{ GeV}$ ; the points corresponding to  $10 \text{ pb}^{-1}$  data are superimposed and no beam energy spread is taken into account; from Ref. [598].

The Higgs mass can be measured by a straightforward scan in the vicinity of  $\sqrt{s} = M_H$ . The approximate values of  $M_H$  would be already known from measurements at  $e^+e^-$  and hadron colliders, or measured at the muon collider by producing first the Higgs boson in the Higgs–strahlung channel,  $\mu^+\mu^- \rightarrow HZ$ . The detection of the signal peak for a Higgs mass  $M_H = 110 \text{ GeV}$  has been performed e.g. in Ref. [598] and the output is summarized in Fig. 4.51 which has been obtained with  $10 \text{ pb}^{-1}$  data, assuming that the beam energy spread is very small. The Monte Carlo generator PYTHIA has been used to generate the  $\mu^+\mu^- \rightarrow H \rightarrow b\bar{b}$  signal and the  $\mu^+\mu^- \rightarrow q\bar{q}(\gamma)$  background events and a crude estimate of detector effects [using a typical LEP detector] has been made. It has been assumed that 80% efficiency for  $b$ -quark tagging can be achieved as expected at the ILC for instance. For such a Higgs mass, one is close the  $Z$  boson resonance and the backgrounds are rather large; they become smaller when one moves to higher Higgs masses, but the Higgs branching ratio  $\text{BR}(H \rightarrow b\bar{b})$  then becomes smaller. In another analysis presented in Ref. [599] but which takes into account the energy spread, it has been shown that a precision of the order of  $\Delta M_H \sim 0.1 \text{ MeV}$  for  $M_H \simeq 115 \text{ GeV}$  can be achieved with  $\sim 30$  data points with a luminosity  $\mathcal{L} = 1.25 \text{ pb}^{-1}$  per point and a resolution  $R = 0.003\%$ .



Since both the Higgs mass  $M_H$  and its total width  $\Gamma_H$  enter the cross section value at the same time, and if one refrains from making any theoretical assumption on the partial decay widths, a model-independent determination of  $\Gamma_H$  is required. This determination can be made [474,600] by noting that if one adjusts the normalization of the theoretical curve of  $\Gamma_H$  at  $\sqrt{s} = M_H$  in such a way that it agrees with the experimental curve, then the wings of the theoretical curve are increased (decreased) if  $\Gamma_H$  is larger (smaller). With precise measurements at a central energy value  $\sqrt{s}$  and at the wings, one can measure  $\Gamma_H$  through the ratio of the cross sections at the central peak and on the wings, in which the partial decay widths cancel out. This method, with a dedicated three-point scan near the threshold, allows one to measure  $M_H$  at the same time with a precision that is expected to be better than the rough scan discussed above, with the same integrated luminosity.

However, for a light Higgs boson which might be very narrow, one could achieve a very small beam energy resolution,  $\sigma_{\sqrt{s}} \ll \Gamma_H$ , only at the cost of a low luminosity. In this case, it has been advocated to operate the collider at the Higgs peak with two different resolutions,  $\sigma_{\sqrt{s}}^{\min} \ll \Gamma_H$  and  $\sigma_{\sqrt{s}}^{\max} \gg \Gamma_H$  and determine the total width from the ratios of the peak cross sections [600]. Using Eqs. (4.85) and (4.86), one obtains

$$\bar{\sigma}_H(\sigma_{\sqrt{s}}^{\min})/\bar{\sigma}_H(\sigma_{\sqrt{s}}^{\max}) = [2\sqrt{2}\sigma_{\sqrt{s}}^{\min}]/[\sqrt{\pi}\Gamma_H]. \quad (4.88)$$

Fig. 4.52(a) shows the results of a Monte Carlo simulation [477] for the determination of the total decay width of the Higgs boson as functions of its mass in the range between 100 and 160 GeV. Also shown in the figure are the spread in the c.m. energy for a resolution of  $R = 0.003\%$  (solid circles) and the spread that is obtained if the resolution  $R$  is varied in such a way that the beam energy spread is always 40% of the Higgs total decay width (open squares). Here, one assumes that any value of the resolution  $R$  can be obtained and that the luminosity scales as  $R^{2/3}$ ; this procedure helps one to optimize the Higgs production rate and, hence, the statistical error on the production cross section.

Fig. 4.52(b) displays the factor which reduces the peak cross section when the Gaussian distribution with a width  $\sigma_{\sqrt{s}}$  is included. This signal reduction factor is given by

$$S_R = \eta A e^{A^2} \left( \sqrt{\pi} - 2 \int_0^A e^{-t^2} dt \right), \quad A = \frac{1}{2\sqrt{2}} \frac{\Gamma_H}{\sigma_{\sqrt{s}}} \quad (4.89)$$

where  $\eta$  is factor which takes into account the effects of ISR. With a fixed resolution,  $R = 0.003\%$  (filled circles), the signal cross section is reduced by approximately a factor of two for low Higgs masses,  $M_H \lesssim 130$  GeV, while for masses close to  $M_H \sim 160$  GeV, the Higgs total width becomes large enough and there is no reduction. For an optimally varying  $R$  value (open squares), the peak cross section is reduced by a constant factor  $S_R \simeq 0.8$ .

The peak cross sections for the processes  $\mu^+\mu^- \rightarrow b\bar{b}$  and  $\mu^+\mu^- \rightarrow WW^{(*)}$  are shown in Fig. 4.52(c) as functions of  $M_H$  under the same conditions as above with an integrated luminosity of  $\mathcal{L} = 100 \text{ pb}^{-1}$ . While the simulation of  $b\bar{b}$  decays is as described previously, the efficiency in the channel  $H \rightarrow WW^*$  is based on a LEP2-type detector with the conservative assumption that the spin information is not used to further reduce the non-resonant  $WW$  background. As can be seen, the  $b\bar{b}$  cross section can be measured with a statistical accuracy of about 10%, while a 20% accuracy can be achieved on the  $WW^*$  cross section for  $M_H = 130\text{--}150$  GeV. The accuracy will improve by a factor of two if the luminosity is increased to  $\mathcal{L} = 400 \text{ pb}^{-1}$ , which corresponds to four years of running, thereby approaching those which can be achieved at the ILC. The accuracy on the production cross section for the  $ZZ$  final state is expected to be worse as  $\text{BR}(H \rightarrow ZZ^*)$  is very small in this mass range.

Once the Higgs mass, total decay width and peak cross sections have been determined, one can measure the partial decay width into muons  $\Gamma(H \rightarrow \mu^+\mu^-)$  and the final state branching ratios  $\text{BR}(H \rightarrow X)$ . From the cross section Eq. (4.86), they appear as the product

$$B(X) = \Gamma(H \rightarrow \mu^+\mu^-) \times \text{BR}(H \rightarrow X). \quad (4.90)$$

These measurements can be then combined with other precision measurements performed at the LHC and/or at  $e^+e^-$  colliders to determine the couplings of the Higgs boson in a model-independent way. For instance, the Higgs partial decay width into muons, if the measurements at the linear collider discussed in the previous section are available, can be determined through [475]

$$\Gamma(H \rightarrow \mu^+\mu^-) = \frac{B(X)}{\text{BR}(H \rightarrow X)_{\text{ILC}}} \quad (4.91)$$

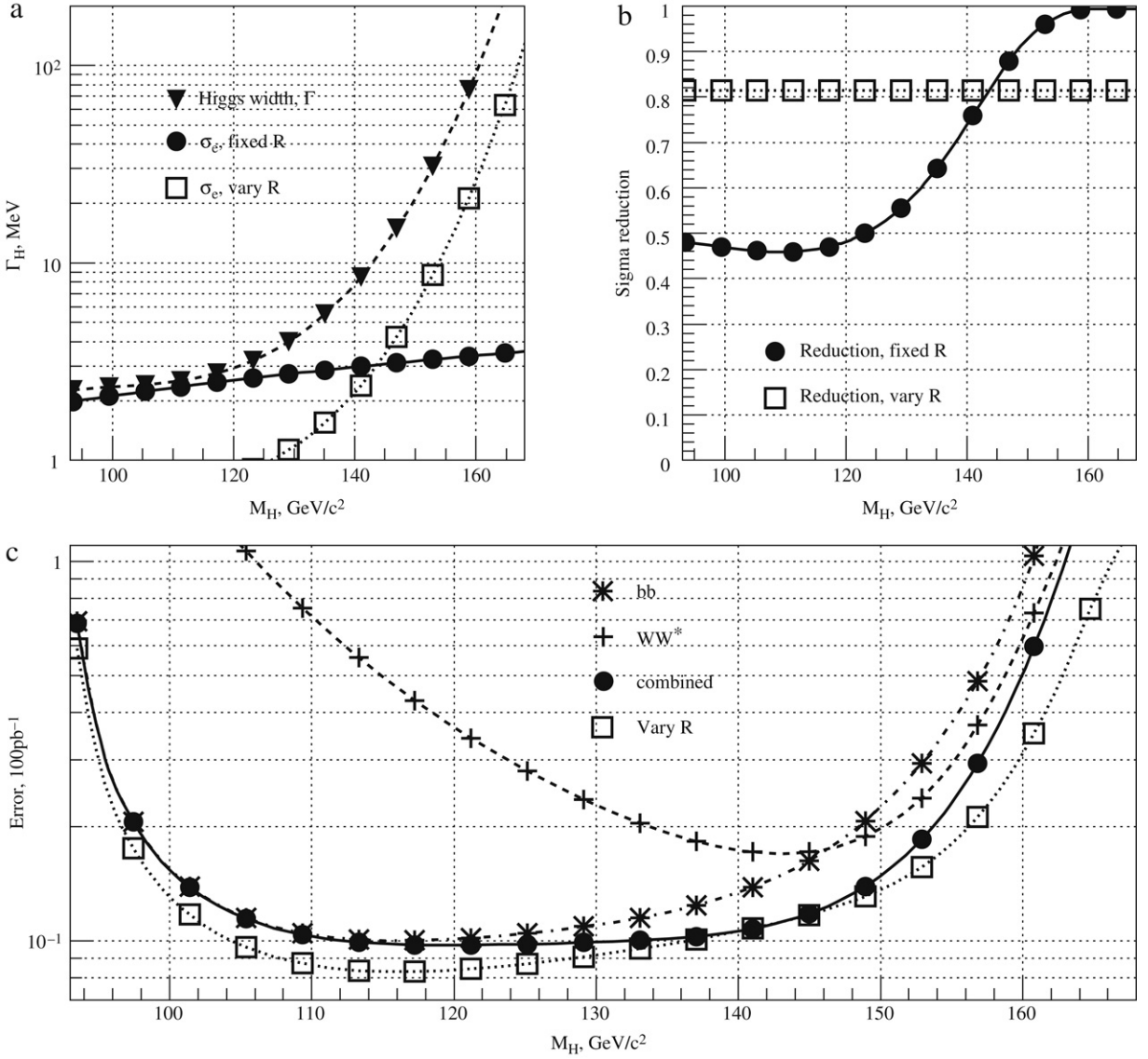


Fig. 4.52. (a): The width of the SM Higgs boson as a function of its mass (triangles), also shown are the effects of a fixed c.m. energy spread for  $R = 0.003\%$  (filled circles) and an optimal varying energy spread (open squares). (b) The cross section suppression factor due to the width of the beams if  $R = 0.003\%$  (filled circles) and for the optimal varying  $R$  (open squares). (c): The fractional error with which the Higgs cross section can be measured in the  $b\bar{b}$  (stars) and  $WW^*$  (crosses) decay modes using  $100 \text{ pb}^{-1}$  data with  $R = 0.003\%$ ; the solid circles show the accuracy with which the peak cross sections can be extracted if the SM branching ratios are assumed and the open squares show the errors obtained in the same running period by optimizing  $R$ . From Ref. [477].

with  $b\bar{b}$  and  $WW^*$  final states for instance, where the branching ratios in the denominator can be measured precisely at the ILC in the low Higgs mass range, or make use of the total decay width measured at muon colliders, via

$$\Gamma(H \rightarrow \mu^+ \mu^-) = \frac{B(X) \times \Gamma_H}{\Gamma(H \rightarrow X)|_{\text{ILC}}} \quad (4.92)$$

for the  $WW^*$  and eventually  $ZZ^*$  final states where the partial widths can be measured at the ILC for large enough Higgs boson masses. The combination of all measurements allow a very precise test of the Higgs couplings to fermions and gauge bosons and, in particular, a precise determination of the Higgs couplings to second generation fermions.

### 4.6.3. Study of the CP-properties of the Higgs boson

**4.6.3.1. Measurements in the decay  $H \rightarrow \tau^+\tau^-$ .** A very interesting process to study at muon colliders is  $\mu^+\mu^- \rightarrow \tau^+\tau^-$  [601,602]. The process proceeds through  $s$ -channel photon and  $Z$  boson exchanges as well as via  $s$ -channel Higgs boson exchange. In the former channels, the production is similar to what occurs in  $e^+e^-$  collisions and, as discussed in Section 1.2, the process has characteristic forward–backward and left–right asymmetries. Assuming that the  $\mu^\pm$  beams have longitudinal polarizations  $P_\pm$  and using Eqs. (1.62) and (1.64) for the cross section and asymmetries, one can write the differential cross section for  $\mu^+\mu^- \rightarrow \gamma, Z^* \rightarrow \tau^+\tau^-$  as

$$\frac{d\sigma_{\gamma,Z}}{d\cos\theta} = \frac{4\pi\alpha^2}{3s} \times \frac{3}{8}\sigma_U \left[ (1 + \cos^2\theta) + \frac{8}{3}\cos\theta A_{FB}^{\text{eff}} \right] \quad (4.93)$$

where  $A_{FB}^{\text{eff}}$  has the usual component  $A_{FB}^\tau$  already discussed, but also a component which includes the information on the longitudinal polarization and  $A_{LR,FB}^\tau$  in Eq. (1.64)

$$A_{FB}^{\text{eff}} = \frac{A_{FB}^\tau + P_{\text{eff}} A_{LR,FB}^\tau}{1 + P_{\text{eff}} A_{LR}^\tau}, \quad P_{\text{eff}} = \frac{P_+ - P_-}{1 - P_+ P_-}. \quad (4.94)$$

The angular distribution has a clear forward–backward asymmetry: it vanishes for  $\theta = \frac{\pi}{2}$  and is large and positive for  $\theta = 0$ . For  $\sqrt{s} = 120$  GeV one has  $A_{FB} \sim 0.7$  and  $A_{LR} = 0.15$  [601].

In the Higgs boson exchange channel, the differential cross section is flat and is simply given, in terms of the effective cross section with  $\sqrt{s} = M_H$ , by

$$\frac{d\sigma}{d\cos\theta} = \frac{1}{2}\bar{\sigma}_H(1 + P_+ P_-). \quad (4.95)$$

Considering this channel as the signal and the  $\gamma, Z$  exchange channel as the background, the enhancement of the signal cross section compared to the background is given by

$$\frac{S}{B} \sim \frac{1 + P_+ P_-}{1 - P_+ P_- + (P_+ - P_-)A_{LR}^\tau}. \quad (4.96)$$

One can therefore use the polarization of the initial beams and the forward–backward asymmetries to enhance the signal-to-background ratio.

One can also distinguish the signal from the background by using the final state polarization of the  $\tau$ -leptons which are very different. We will briefly discuss this point, following Ref. [601] and recalling the discussion of Section 2.1.4 on  $H \rightarrow \tau^+\tau^-$  decays. In the two-body decays of the  $\tau$ -lepton,  $\tau^- \rightarrow \pi^- \nu_\tau, \rho^- \nu_\tau$ , etc., defining  $\theta_i$  as the angle between the momenta of the  $\tau$  lepton and the charged final particle,  $B$  as the branching ratio of the decay and  $P_\tau = \pm 1$  as the  $\tau$ -lepton helicity, the normalized differential decay rate in the  $\tau$  rest frame is simply

$$\frac{1}{\Gamma} \frac{d\Gamma_i}{dc_{\theta_i}} = \frac{B_i}{2} (1 + r_i P_\tau \cos\theta_i) \quad (4.97)$$

with  $r_i = 1$  for decays into pions and  $r_i = -(m_\tau^2 - 2m_i^2)/(m_\tau^2 + 2m_i^2) \simeq 0.45$  for  $i = \rho$ . In the signal,  $\mu^+\mu^- \rightarrow H \rightarrow \tau^+\tau^-$ , the  $\tau^-$  and  $\tau^+$  helicities are correlated as  $P_{\tau^-} = P_{\tau^+} = \pm 1$ , and the spin correlated differential cross section with polarized  $P_\pm$  beams reads

$$\frac{d\sigma_H}{dc_{\theta_i} dc_{\theta_j}} = (1 + P_- P_+) \sigma_H \frac{B_i B_j}{4} [a_i a_j + b_i b_j c_{\theta_i} c_{\theta_j}] \quad (4.98)$$

reaching a maximum (minimum) for  $c_{\theta_i} = c_{\theta_j} (c_{\theta_i} = -c_{\theta_j}) = \pm 1$ , with the significance of the peaks depending on the magnitude of  $r_i$ . In the case of the decay  $\tau^- \rightarrow \rho^- \nu_\tau$ , distinctive peaks in the distribution can be seen for  $c_{\theta_{\rho^-}} = c_{\theta_{\nu_\tau}} = \pm 1$  and  $P_+ = P_- = 25\%$  [601].

In contrast, in the standard channel  $\mu^+\mu^- \rightarrow \gamma, Z^* \rightarrow \tau^+\tau^-$ , the  $\tau$ -leptons are produced with helicities  $P_{\tau^-} = -P_{\tau^+} = \pm 1$  and the number of left-handed and right-handed  $\tau$ -leptons are different because of the polarization

left–right asymmetry. The spin correlated differential distribution in this case is

$$\frac{d\sigma_{\gamma,Z}}{dc_{\theta_i}dc_{\theta_j}} = (1 - P_-P_+)\sigma_{\gamma,Z} (1 + P_{\text{eff}}A_{LR}) \times \frac{1}{4}B_iB_j \left[ (a_ia_j - b_ib_jc_{\theta_i}c_{\theta_j}) + (a_ib_jc_{\theta_j} - a_jb_ic_{\theta_i})A_{LR}^{\text{eff}} \right] \quad (4.99)$$

with

$$A_{LR}^{\text{eff}} = \frac{A_{FB,LR}^{\tau} + P_{\text{eff}}A_{FB}^{\tau}}{1 + P_{\text{eff}}A_{LR}^{\tau}}. \quad (4.100)$$

Again, for the decay  $\tau^- \rightarrow \rho^- \nu_{\tau}$ , the peaks in the distribution for  $\cos \theta_{\rho^-} = -\cos \theta_{\rho^+} = \pm 1$  can be seen for  $P_+ = P_- = 25\%$  [601]. The peaks occur in opposite regions compared to the Higgs signal and the spin correlation in the signal is symmetric, while it is not the case in the background as a consequence of the presence of the term  $A_{LR}^{\text{eff}}$  in Eq. (4.99).

Summing both  $\rho\nu$  and  $\tau\nu$  final states and using  $R = 0.0005\%$ ,  $P_{\pm} = 25\%$  and  $\mathcal{L} = 1 \text{ fb}^{-1}$ , one obtains the statistical error  $\epsilon = \sqrt{S+B}/S$  on the cross section measurement which determines to which extent the  $H\tau^+\tau^-$  coupling can be measured. For  $M_H = 110$  (130) GeV, one has  $\epsilon \simeq 20\%$  (30%) showing that one can observe the resonant  $\mu^+\mu^- \rightarrow H \rightarrow \tau^+\tau^-$  process above the continuum background and therefore possibly measure the  $H\tau^+\tau^-$  coupling and check the Higgs boson spin.

Note that because of depolarization effects, this type of analysis cannot be performed in the decays  $H \rightarrow b\bar{b}$ , while for  $H \rightarrow t\bar{t}$  the rates are too small, the Higgs resonance being very broad as discussed earlier. On the other hand, the CP quantum numbers of a relatively heavier Higgs boson,  $M_H \gtrsim 140$  GeV, can be studied in the decays  $H \rightarrow VV^* \rightarrow 4f$  by looking at angular distributions and correlations as discussed in detail in Section 2.2.4.

**4.6.3.2. CP measurements with transverse polarization.** It is expected that muon colliders will have a natural transverse polarization of the order of 20% for both the  $\mu^+$  and  $\mu^-$  beams. This polarization, if maximized, could also provide an unambiguous test of the CP-quantum numbers of the Higgs boson [144,154,603], similar to the case of  $\gamma\gamma$  colliders previously discussed. Indeed, if one considers a scalar particle with couplings to muons which have both CP-even and CP-odd components,  $\mathcal{L}(H\mu\mu) \propto H\bar{\mu}(a + ib\gamma_5)\mu$ , and assumes that the muon beams are 100% transversally polarized, with  $\phi$  being the angle between the  $\mu^+$  and  $\mu^-$  transverse polarizations, the production cross section of the Higgs boson in the  $s$ -channel reads

$$\sigma(\mu^+\mu^- \rightarrow H) \propto 1 - \frac{a^2 - b^2}{a^2 + b^2} \cos \phi + \frac{2ab}{a^2 + b^2} \sin \phi. \quad (4.101)$$

If the Higgs boson is a mixture of CP-even and CP-odd states, both the  $a_+$  and  $a_-$  components are non-zero and the asymmetry

$$\mathcal{A}_1 = \frac{\sigma(\phi = \frac{\pi}{2}) - \sigma(\phi = -\frac{\pi}{2})}{\sigma(\phi = \frac{\pi}{2}) + \sigma(\phi = -\frac{\pi}{2})} = \frac{2ab}{a^2 + b^2} \quad (4.102)$$

is large if  $a$  and  $b$  have the same magnitude. A non-zero value of this asymmetry would indicate a clear violation of CP symmetry. For a pure CP-eigenstate, one of the coefficients  $a$  or  $b$  is zero and the asymmetry

$$\mathcal{A}_2 = \frac{\sigma(\phi = \pi) - \sigma(\phi = 0)}{\sigma(\phi = \pi) + \sigma(\phi = 0)} = \frac{a^2 - b^2}{a^2 + b^2} \quad (4.103)$$

is either equal to  $+1$  or  $-1$ , if the Higgs boson is, respectively a CP-even state or a CP-odd state. In the ideal world, this is an unambiguous test of the CP-nature of the Higgs boson. However, the transverse polarization will most probably not be maximal and background events will alter the signal and dilute the asymmetries. Thorough studies, including the machine and background aspects must be performed to quantify the extent to which the Higgs boson CP-properties can be measured; see Ref. [154] for such an attempt.

## 5. Summary

The search for Higgs bosons is the main mission of present and future high-energy colliders. The observation of these particles is of major importance for the present understanding of the interactions of the fundamental particles

and the generation of their masses. In fact, despite its numerous successes in explaining the present data, our Standard Model of the electroweak and strong forces will not be completely validated before this particle has been experimentally observed and its predicted fundamental properties have been studied in great detail and verified. This review is devoted to the discussion of the properties of the Higgs bosons and this part deals exclusively with the SM Higgs particle.

The SM makes use of one isodoublet complex scalar field which, after spontaneous electroweak symmetry breaking, generates the weak gauge boson and fermion masses and leads to the existence of one single Higgs particle with the  $J^{\text{PC}} = 0^{++}$  assignment of spin, parity and charge conjugation quantum numbers. The Higgs couplings to fermions and gauge bosons are related to the masses of these particles and the only free parameter of the model is the mass of the Higgs boson itself. There are, however, both experimental and theoretical constraints on this fundamental parameter which have been discussed in detail in the first chapter of this review. From the experimental side, the negative direct searches at LEP led to the lower bound  $M_H \gtrsim 114$  GeV while from the interpretation of high-precision electroweak measurements, one obtains the 95% confidence-level upper bound of  $M_H \lesssim 166$  GeV. From the theoretical side, interesting constraints can be derived from assumptions on the energy range within which the SM is valid before the perturbation theory breaks down and new phenomena would emerge; constraints from perturbativity, unitarity and the triviality of the quartic Higgs self-couplings lead to a coherence limit of  $M_H \lesssim 1$  TeV.

In the SM, once  $M_H$  is fixed, the profile of the Higgs boson is uniquely determined and its decay channels are specified. The particle will have the tendency to decay into the heaviest particles allowed by phase space. For small  $M_H$  values, the fermionic decays into  $b\bar{b}$ ,  $c\bar{c}$ ,  $\tau^+\tau^-$  and the loop decays into  $gg$ ,  $\gamma\gamma$ ,  $Z\gamma$  are the relevant ones, while for higher  $M_H$  values, the decays into a pair of massive gauge bosons, which can be eventually off-shell, are dominant; for even larger masses, Higgs decays into top quark pairs are also relevant. A large theoretical effort has been devoted to the analysis of the partial widths and the branching ratios of these various decays, an effort which has been summarized in the second chapter of this review. The important radiative corrections, in particular those due to strong interactions, the multi-body decays for the decays into gauge bosons for instance and the possibility of verifying the CP-nature of the Higgs boson, have been discussed in great detail.

Hadron colliders will be the instruments which will aid in the discovery of the SM Higgs particle. Several production channels can be used for this purpose and their characteristics have been analyzed in numerous theoretical and experimental studies and have been discussed in great detail in chapter 3. The production rates and the kinematical distributions, including the important radiative corrections, as well as the detection channels in the difficult hadronic environment have been studied. The detailed phenomenological analyses which have been performed at the Tevatron and the LHC have been summarized. At the Tevatron, the low Higgs mass range can be probed if high enough luminosity is collected. Detailed analyses have been performed for the LHC with the conclusion that a  $5\sigma$  discovery is possible with an integrated luminosity of  $30 \text{ fb}^{-1}$  for the entire Higgs mass range, when all production and decay channels are combined. The spin-zero nature of the Higgs boson can be determined and a preliminary probe of its CP-nature can be performed. Furthermore, information on the Higgs couplings to gauge bosons and fermions can be obtained with a higher luminosity; the estimated precision for coupling ratios are typically  $\mathcal{O}(10)\%$  with  $\mathcal{L} = 100 \text{ fb}^{-1}$ . Because of the small production rates and the large backgrounds, the measurement of the Higgs self-coupling is too difficult at the LHC.

The future  $e^+e^-$  linear collider, the ILC, is the ideal instrument – to search for the SM Higgs particle and once it is found – to take the very important challenge of thoroughly exploring all its fundamental properties. The Higgs boson can be produced in various redundant channels. Among the dominant production channels, Higgs–strahlung plays a crucial role as it allows e.g. for the detection of the particle independent of its decay modes, while vector boson fusion is the dominant process at high energies. Associated production with the heavy top quarks and Higgs pair production allow for crucial measurements. These channels have been discussed in detail in the fourth chapter of the review and, again, details on the production rates and the kinematical distributions, including the radiative corrections, as well as on the detection modes have been given. The determination of the Higgs profile can be done at great detail in the clean environment of  $e^+e^-$  linear colliders: the Higgs boson mass, its spin and parity quantum numbers and its couplings to fermions, massive and massless gauge bosons as well as its trilinear self-couplings can be measured with very high accuracies. Additional high-precision measurements can be performed at the GigaZ and  $\gamma\gamma$  options of the collider as well as at possible muon colliders.

We are at last entering the long awaited era of probing the electroweak symmetry breaking mechanism. In a few years from now, the LHC would have observed a Higgs particle and performed a preliminary analysis of its

fundamental properties. Hopefully in a decade, the high-precision measurements which will be performed at the ILC would allow one to probe in all its facets the Higgs mechanism. Whether this mechanism is indeed at work in Nature and whether the Higgs boson is indeed SM-like (and this first part of this review is thus somewhat relevant), only these experiments will tell and we will soon know the answer.

## Acknowledgments

I would first like to thank the many collaborators with whom I shared the pleasure in investigating various aspects of the theme discussed in this review. They are too numerous to be all listed here, but I would like at least to mention Peter Zerwas with whom I started to work on the subject in an intensive way.

I would also like to thank the many colleagues and friends who helped me during the writing of this review and who made important remarks on the preliminary versions of the manuscript and suggestions for improvements: Fawzi Boudjema, Albert de Roeck, Klaus Desch, Michael Dittmar, Manuel Drees, Rohini Godbole, Robert Harlander, Wolfgang Hollik, Karl Jakobs, Sasha Nikitenko, Giacomo Polesello, Francois Richard, Pietro Slavich and Michael Spira. Special thanks go to Manuel Drees and Pietro Slavich for their very careful reading of large parts of the manuscript and for their efficiency in hunting down the many typos, errors and awkwardness contained in the preliminary versions and for their attempt at improving my poor English and fighting against my anarchic way of “distributing commas”. Additional help with English by Martin Bucher and, for the submission of this review to the archives, by Marco Picco are also acknowledged. Finally, I would like to thank Howie Haber for several helpful suggestions and remarks.

I also thank the Djouadi *smala*, my sisters and brothers and their children [at least one of them, Yanis, has already caught the virus of particle physics and I hope that one day he will read this review], who bore my not always joyful mood in the last two years. Their support was crucial for the completion of this review. Finally, I thank the team of *La Bonne Franquette*, where in fact part of this work has been done, for their good couscous and the nice atmosphere, as well as Madjid Belkacem for sharing the drinks with me.

The writing of this review started when I was at CERN as a scientific associate, continued during the six months I spent at the LPTHE of Jussieu, and ended at the LPT d’Orsay. I thank all these institutions for their kind hospitality.

## References

- [1] S. Glashow, Nuclear Phys. 22 (1961) 579;  
S. Weinberg, Phys. Rev. Lett. 19 (1967) 1264;  
A. Salam, in: N. Svartholm (Ed.), Elementary Particle Theory, Almqvist and Wiksells, Stockholm, 1969, p. 367.
- [2] M. Gell-Mann, Phys. Lett. 8 (1964) 214;  
G. Zweig, CERN-Report 8182/TH401 (1964);  
H. Fritzsch, M. Gell-Mann, H. Leutwyler, Phys. Lett. B 47 (1973) 365;  
D. Gross, F. Wilczek, Phys. Rev. Lett. 30 (1973) 1343;  
H.D. Politzer, Phys. Rev. Lett. 30 (1973) 1346;  
G. ’t Hooft, Marseille Conference on Yang–Mills Fields, 1972.
- [3] P.A.M. Dirac, Proc. Roy. Soc. Lond. A 114 (1927) 243;  
P. Jordan, W. Pauli, Z. Phys. 47 (1928) 151;  
W. Heisenberg, W. Pauli, Z. Phys. 56 (1929) 1;  
S. Tomonaga, Progr. Theoret. Phys. 1 (1946) 27;  
J. Schwinger, Phys. Rev. 73 (1948) 416;  
R. Feynman, Phys. Rev. 76 (1949) 749.
- [4] E. Fermi, Nuovo Cim. 11 (1934) 1;  
E. Fermi, Z. Phys. 88 (1934) 161;  
R. Feynman, M. Gell-Mann, Phys. Rev. 109 (1958) 193.
- [5] G. ’t Hooft, Nuclear Phys. B 33 (1971) 173;  
G. ’t Hooft, Nuclear Phys. B 35 (1971) 167;  
G. ’t Hooft, M. Veltman, Nuclear Phys. B 44 (1972) 189.
- [6] P.W. Higgs, Phys. Rev. Lett. 13 (1964) 508;  
P.W. Higgs, Phys. Rev. 145 (1966) 1156;  
F. Englert, R. Brout, Phys. Rev. Lett. 13 (1964) 321;  
G.S. Guralnik, C.R. Hagen, T. Kibble, Phys. Rev. Lett. 13 (1965) 585;  
T. Kibble, Phys. Rev. 155 (1967) 1554.



- [7] Ch. Llewellyn Smith, Phys. Lett. 46B (1973) 233;  
J.S. Bell, Nuclear Phys. B 60 (1973) 427;  
J.M. Cornwall, M.D. Levin, G. Tiktopoulos, Phys. Rev. Lett. 30 (1973) 1268;  
J.M. Cornwall, M.D. Levin, G. Tiktopoulos, Phys. Rev. D 10 (1974) 1145;  
J.M. Cornwall, M.D. Levin, G. Tiktopoulos, Phys. Rev. D 11 (1975) 972 (Erratum).
- [8] The LEP Collaborations (ALEPH, DELPHI, L3 and OPAL), the LEP Electroweak Working Group and the SLD Heavy Flavour Group, A combination of preliminary Electroweak measurements and constraints on the Standard Model. <http://lepewwg.web.cern.ch/LEPEWWG>.
- [9] Particle Data Group, K. Hagiwara, et al., Phys. Rev. D 66 (2002) 010001;  
S. Eidelman, et al., Phys. Lett. B 592 (2004) 1.
- [10] The LEP Collaboration (ALEPH, DELPHI, L3, OPAL, Phys. Lett. B 565 (2003) 61.
- [11] F.J. Hasert, et al., (Gargamelle Coll.), Phys. Lett. B 46 (1973) 121;  
F.J. Hasert, et al., (Gargamelle Coll.), Phys. Lett. B 46 (1973) 138;  
T. Eichten, et al., (Gargamelle Coll.), Phys. Lett. B 46 (1973) 274.
- [12] G. Arnison, et al., (UA1 Coll.), Phys. Lett. B 122 (1983) 103;  
M. Banner, et al., (UA2 Coll.), Phys. Lett. B 122 (1983) 476;  
G. Arnison, et al., (UA1 Coll.), Phys. Lett. B 126 (1983) 398;  
P. Bagnaia, et al., (UA2 Coll.), Phys. Lett. B 129 (1983) 130.
- [13] J. Gunion, H. Haber, G. Kane, S. Dawson, The Higgs Hunter's Guide, Addison–Wesley, Reading, USA, 1990.
- [14] F. Abe, et al., (CDF Collaboration), Phys. Rev. Lett. 74 (1995) 2626;  
S. Abachi, et al., D0 Collaboration, Phys. Rev. Lett. 74 (1995) 2632.
- [15] CDF and DØ Coll. and Tevatron Electroweak Working Group. [hep-ex/0404010](http://hep-ex/0404010).
- [16] CDF and DØ Coll. and Tevatron Electroweak Working Group. [hep-ex/0608032](http://hep-ex/0608032).
- [17] See for instance: I. Aitchison, A. Hey, Gauge Theories in Particle Physics, Adam Hilger, Bristol, UK, 1982;  
C. Quigg, Gauge Theories of the Strong, Weak, and Electromagnetic Interactions, Benjamin-Cummings, Reading, USA, 1983;  
T.P. Cheng, L.F. Li, Gauge theory of Elementary Particle Physics, Oxford Sciences Publications, Clarendon Press, Oxford, 1984;  
F. Halzen, A.D. Martin, Quarks and Leptons: An Introductory Course in Modern Particle Physics, Wiley, New York, USA, 1984;  
C. Itzykson, J.B. Zuber, Quantum Field Theory, Mac Graw Hill Book Co, Singapore, 1985;  
D. Bailin, A. Love, Introduction to Gauge Field Theory, Adam Hilger, Bristol, UK, 1986;  
M.E. Peskin, D.V. Schroeder, An Introduction to Quantum Field Theory, Addison-Wesley, Reading, USA, 1995.
- [18] See for instance E. Abers, B. Lee, Phys. Rep. 9 (1973) 1;  
M.A.B. Beg, A. Sirlin, Phys. Rep. 88 (1982) 1;  
C. Quigg, Introduction to gauge theories of the strong, weak and electromagnetic interactions, Lectures given at “NATO Advanced Study Inst.: Techniques and Concepts of High Energy Physics”, St. Croix, U.S. Virgin Islands, July 1980, published in Virgin Islands Inst. 1980, p. 143;  
R.N. Cahn, Rep. Progr. Phys. 52 (1989) 389;  
M.E. Peskin, Theory of precision electroweak measurements, Lectures given at “17th SLAC Summer Inst.: Physics at the 100 GeV Mass Scale”, Stanford, July 1989, published in SLAC Summer Inst. 1989, pp. 71–126;  
H.E. Haber, Lectures on Electroweak Symmetry Breaking, TASI, Boulder 1990, SCIPP–91–06;  
F.M. Renard, Standardissimo, Annales Phys. (France) 17 (1992) 301;  
G. Altarelli, The standard electroweak theory and its experimental tests, Lectures given at “32nd Internationale Universitätswochen für Kern- und Teilchenphysik”, Schladming, Austria, Feb–Mar 1993, Published in Schladming School 1993, pp. 323–382;  
P. Langacker, Tests of the Standard Model and searches for New Physics, in: Precision tests of the standard electroweak model”, P. Langacker (ed.), [hep-ph/9412361](http://hep-ph/9412361);  
S.F. Novaes, Standard model: An introduction, in: Proceedings of the “10th Jorge Andre Swieca Summer School: Particle and Fields”, Sao Paulo, Brazil, February 1999. [hep-ph/0001283](http://hep-ph/0001283);  
H. Spiesberger, M. Spira, P.M. Zerwas, The standard model: Physical basis and scattering experiments, in: P. Sabatier (Ed.), Scattering, Academic Press, London, 2000, [hep-ph/0011255](http://hep-ph/0011255);  
A. Pich, The Standard Model of Electroweak Interactions, Lectures given at the “2004 European School of High-Energy Physics”, Sant Feliu de Guixol, Spain, June 2004. [hep-ph/0502002](http://hep-ph/0502002).
- [19] See for instance: W.J. Stirling, Higgs Phenomenology, Lectures given at “42nd Scottish Universities Summer School in Physics: High Energy Phenomenology”, St. Andrews (Scotland), August 1993, published in Scottish Summer School, 1993, pp. 0225–270;  
M.E. Peskin, Beyond the Standard Model, Lectures given at the European School of High-Energy Physics, Carry-le-Rouet (France), September 1996. [hep-ph/9705479](http://hep-ph/9705479);  
S. Dawson, Introduction to Electroweak Symmetry Breaking, Lectures given at “ICTP Summer School in High-Energy Physics and Cosmology”, Trieste (Italy), 29 Jun–17 Jul 1998. [hep-ph/9901280](http://hep-ph/9901280);  
M. Spira, P.M. Zerwas, Electroweak symmetry breaking and Higgs Physics, Lectures given at “36th Internationale Universitätswochen fuer Kernphysik und Teilchenphysik: Computing Particle Properties”, Schladming, Austria, March 1997. [hep-ph/9803257](http://hep-ph/9803257);  
C. Quigg, Electroweak Symmetry breaking and the Higgs sector, in: 27th International Meeting on Fundamental Physics, Sierra Nevada, Granada (Spain), February 1999, Acta Phys. Polon. B30 (1999) 2145. [hep-ph/9905369](http://hep-ph/9905369).
- [20] B.A. Kniehl, Phys. Rep. 240 (1994) 211.
- [21] A. Djouadi, Internat. J. Modern Phys. A 10 (1995) 1.

- [22] M. Spira, Fortschr. Phys. 46 (1998) 203.
- [23] M. Steinhauser, Phys. Rep. 364 (2002) 247.
- [24] M. Carena, H.E. Haber, Prog. Part. Nucl. Phys. 50 (2003) 63.
- [25] A. Djouadi, The anatomy of electro-weak symmetry breaking, II: The Higgs bosons in the minimal supersymmetric model. [hep-ph/0503173](#).
- [26] C.N. Yang, R. Mills, Phys. Rev. 96 (1954) 191.
- [27] S.L. Adler, W.A. Bardeen, Phys. Rev. 182 (1969) 1517;  
R. Jackiw, Lectures on Current Algebra and its Applications, Princeton University Press, 1972.
- [28] C. Bouchiat, J. Iliopoulos, Ph. Meyer, Phys. Lett. 38B (1972) 519.
- [29] Y. Nambu, Phys. Rev. Lett. 4 (1960) 380;  
Y. Nambu, G. Jona-Lasinio, Phys. Rev. 122 (1961) 345;  
Y. Nambu, G. Jona-Lasinio, Phys. Rev. 124 (1961) 246;  
J. Goldstone, Nuov. Cim. 19 (1961) 154;  
J. Goldstone, A. Salam, S. Weinberg, Phys. Rev. 127 (1962) 965.
- [30] K. Fujikawa, B.W. Lee, A. Sanda, Phys. Rev. D 6 (1972) 2923;  
Y.P. Yao, Phys. Rev. D 7 (1973) 1647;  
G. 't Hooft in Ref. [5].
- [31] M. Chanowitz, M. Gaillard, Phys. Lett. 142B (1984) 85;  
M. Chanowitz, M. Gaillard, Nuclear Phys. B 261 (1985) 379.
- [32] B.W. Lee, C. Quigg, H.B. Thacker, Phys. Rev. D 16 (1977) 1519.
- [33] C.E. Vayonakis, Lett. Nuovo Cim. 17 (1976) 383;  
H. Weldon, Phys. Lett. 146B (1984) 59;  
G.J. Gounaris, R. Kögerler, H. Neufeld, Phys. Rev. D 34 (1986) 3257;  
Y.P. Yao, C.P. Yuan, Phys. Rev. D 38 (1988) 2237;  
W. Marciano, G. Valencia, S. Willenbrock, Phys. Rev. D 40 (1989) 1725;  
J. Bagger, C. Schmidt, Phys. Rev. D 41 (1990) 264;  
H. Veltman, Phys. Rev. D 41 (1990) 2294.
- [34] T. Appelquist, J. Carazzone, Phys. Rev. D 11 (1975) 2856.
- [35] G. Källén, A. Sabry, K. Dan, Vidensk. Selsk. Mat.-Fys. Medd. 29 (17) (1955);  
M. Steinhauser, Phys. Lett. B 429 (1998) 158.
- [36] M. Davier, A. Köcker, Phys. Lett. B 419 (1998) 419;  
J. Erler, Phys. Rev. D 59 (1999) 054008;  
F. Jegerlehner. [hep-ph/0308117](#);  
K. Hagiwara, A. Martin, D. Nomura, T. Teubner, Phys. Rev. D 69 (2004) 093003.
- [37] H. Burkhardt, B. Pietrzyk, Phys. Lett. B 513 (2001) 46.
- [38] R.E. Behrends, R.J. Finkelstein, A. Sirlin, Phys. Rev. 101 (1956) 866;  
T. Kinoshita, A. Sirlin, Phys. Rev. 113 (1959) 1652;  
T. van Ritbergen, R. Stuart, Phys. Rev. Lett. 82 (1999) 488.
- [39] For reviews, see e.g.: G. Altarelli, A QCD Primer, in: 2001 European School of High-Energy Physics, Beatenberg, Aug–Sep 2001. [hep-ph/0204179](#);  
S. Bethke, J. Phys. G 26 (2000) R27;  
S. Bethke, Nucl. Phys. Proc. Suppl. 121 (2003);  
I. Hinchliffe in Ref. [9].
- [40] O. Tarasov, A. Vladimirov, A. Zharkov, Phys. Lett. B 93 (1980) 429;  
S.A. Larin, J.A.M. Vermaseren, Phys. Lett. B 303 (1993) 334.
- [41] S.D. Drell, T.M. Yan, Phys. Rev. Lett. 25 (1970) 316.
- [42] G. Altarelli, R.K. Ellis, G. Martinelli, Nuclear Phys. B 157 (1979) 461;  
J. Kubar–André, F. Paige, Phys. Rev. D 19 (1979) 221.
- [43] R. Hamberg, W.L. van Neerven, T. Matsuura, Nuclear Phys. B 359 (1991) 343;  
R. Hamberg, W.L. van Neerven, T. Matsuura, Nuclear Phys. B 644 (2002) 403 (Erratum).
- [44] For a detailed review on the top quark see M. Beneke, I. Efthymiopoulos, M.L. Mangano, J. Womersley (conv), et al. Top Quark Physics in the Report of the “1999 CERN Workshop on SM Physics at the LHC”, CERN-TH/2000-100. [hep-ph/0003033](#).
- [45] For theoretically oriented reviews on the top quark properties, see J.H. Kuhn. [hep-ph/9707321](#);  
S. Dawson. [hep-ph/0303191](#).
- [46] For a detailed discussion of electroweak SM processes at LHC, see: R. Haywood, P. Hobson, W. Hollik, Z. Kunszt, (conv.) et al. Report of the Electroweak Working Group at “1999 CERN Workshop on SM Physics at the LHC”. [hep-ph/0003275](#).
- [47] S. Narison, Light and heavy quark masses, flavor breaking of chiral condensates, meson weak leptonic decay constants in QCD. [hep-ph/0202200](#).
- [48] N. Gray, D.J. Broadhurst, W. Grafe, K. Schilcher, Z. Phys. C 48 (1990) 673;  
K.G. Chetyrkin, M. Steinhauser, Phys. Rev. Lett. 83 (1999) 4001;  
K.G. Chetyrkin, M. Steinhauser, Nuclear Phys. B 573 (2000) 617;  
K. Melnikov, T. van Ritbergen, Phys. Lett. B 482 (2000) 99.

- [49] S.G. Gorishny, A.L. Kataev, S.A. Larin, L.R. Surguladze, *Modern Phys. Lett. A* 5 (1990) 2703;  
S.G. Gorishny, A.L. Kataev, S.A. Larin, L.R. Surguladze, *Phys. Rev. D* 43 (1991) 1633.
- [50] K.G. Chetyrkin, *Phys. Lett. B* 404 (1997) 161;  
J.A.M. Vermaseren, S.A. Larin, T. van Ritbergen, *Phys. Lett. B* 405 (1997) 327.
- [51] The LEP2 WW Working Group (U. Parzefall et al.), Note LEPEWWG/TGC/2003–01. See the web site: <http://lepewwg.web.cern.ch/LEPEWWG/tgc>.
- [52] The CDF and DØ collaborations, *Phys. Rev. D* 70 (2004) 092008.
- [53] N. Cabibbo, *Phys. Rev. Lett.* 10 (1963) 531;  
M. Kobayashi, T. Maskawa, *Progr. Theoret. Phys.* 49 (1973) 652.
- [54] S. Glashow, J. Iliopoulos, L. Maiani, *Phys. Rev. D* 2 (1970) 1285.
- [55] D. Ross, M. Veltman, *Nuclear Phys. B* 95 (1975) 135.
- [56] Z Physics at LEP1, Eds. G. Altarelli, R. Kleiss and C. Verzegnassi. CERN Report 89–08 (1989), See this reference for earlier work.
- [57] D. Bardin, W. Hollik, G. Passarino (Eds.), Reports of the Working Group on Precision Calculations for the Z Resonance, CERN Report 95–03, 1995.
- [58] G. Altarelli, T. Sjöstrand, F. Zwirner (Eds.), Physics at LEP2, CERN Report 96–01.
- [59] For a more recent account of high-precision measurements, see W. Hollik, SM Theory, in: Plenary talk at the XXIX ICHEP, Vancouver, Canada, July 1998. [hep-ph/9811313](http://hep-ph/9811313).
- [60] M. Veltman, *Nuclear Phys. B* 123 (1977) 89;  
M.S. Chanowitz, M.A. Furman, I. Hinchliffe, *Phys. Lett. B* 78 (1978) 285.
- [61] A. Djouadi, C. Verzegnassi, *Phys. Lett. B* 195 (1987) 265;  
A. Djouadi, *Nuovo Cim. A* 100 (1988) 357;  
B. Kniehl, *Nuclear Phys. B* 347 (1990) 86;  
F. Halzen, B. Kniehl, *Nuclear Phys. B* 353 (1991) 567;  
A. Djouadi, P. Gambino, *Phys. Rev. D* 49 (1994) 3499.
- [62] L. Avdeev, J. Fleischer, S.M. Mikhailov, O. Tarasov, *Phys. Lett. B* 336 (1994) 560;  
K.G. Chetyrkin, J.H. Kühn, M. Steinhauser, *Phys. Lett. B* 351 (1995) 331.
- [63] J.J. van der Bij, F. Hoogeveen, *Nuclear Phys. B* 283 (1987) 477.
- [64] R. Barbieri, M. Beccaria, P. Ciafaloni, G. Curci, A. Vicere, *Phys. Lett. B* 288 (1992) 95;  
R. Barbieri, M. Beccaria, P. Ciafaloni, G. Curci, A. Vicere, *Nuclear Phys. B* 409 (1993) 105;  
J. Fleischer, F. Jegerlehner, O.V. Tarasov, *Phys. Lett. B* 319 (1993) 249.
- [65] G. Degrandi, P. Gambino, A. Vicini, *Phys. Lett. B* 383 (1996) 219;  
G. Degrandi, P. Gambino, A. Sirlin, *Phys. Lett. B* 394 (1997) 188;  
G. Degrandi, P. Gambino, *Nuclear Phys. B* 567 (2000) 3;  
A. Freitas, W. Hollik, W. Walter, G. Weiglein, *Phys. Lett. B* 495 (2000) 338;  
A. Freitas, W. Hollik, W. Walter, G. Weiglein, *Nuclear Phys. B* 632 (2002) 189;  
M. Awramik, M. Czakon, *Phys. Lett. B* 568 (2003) 48;  
M. Awramik, M. Czakon, A. Freitas, G. Weiglein, *Phys. Rev. D* 69 (2004) 053006.
- [66] M. Awramik, M. Czakon, A. Freitas, G. Weiglein, *Phys. Rev. Lett.* 93 (2004) 201805.
- [67] J. van der Bij, et al., *Phys. Lett. B* 498 (2001) 156;  
M. Faisst, J.H. Kühn, T. Seidensticker, O. Veretin, *Nuclear Phys. B* 665 (2003) 649.
- [68] M. Veltman, *Acta. Phys. Polon. B* 8 (1977) 475.
- [69] T. Appelquist, C. Bernard, *Phys. Rev. D* 22 (1980) 200;  
A. Longhitano, *Nuclear Phys. B* 188 (1981) 118;  
M. Einhorn, J. Wudka, *Phys. Rev. D* 39 (1989) 2758.
- [70] J.J. van der Bij, M. Veltman, *Nuclear Phys. B* 231 (1985) 205.
- [71] R. Boughezal, J.B. Tausk, J.J. van der Bij. [hep-ph/0410216](http://hep-ph/0410216).
- [72] A. Sirlin, *Phys. Rev. D* 22 (1980) 971;  
W. Marciano, A. Sirlin, *Phys. Rev. D* 22 (1980) 2695;  
W. Marciano, A. Sirlin, *Phys. Rev. D* 29 (1984) 945;  
W. Marciano, A. Sirlin, *Nuclear Phys. B* 189 (1981) 442.
- [73] W. Marciano, *Phys. Rev. D* 20 (1979) 274;  
W. Marciano, A. Sirlin, *Phys. Rev. Lett.* 46 (1981) 163;  
W. Marciano, S. Sarantakos, A. Sirlin, *Nuclear Phys. B* 217 (1983) 84.
- [74] M. Awramik, M. Czakon, *Phys. Rev. Lett.* 89 (2002) 241801;  
A. Onishchenko, O. Veretin, *Phys. Lett. B* 551 (2003) 111.
- [75] W. Hollik, *Fortsch. Phys.* 38 (1990) 165.
- [76] For a review, see, M. Chanowitz, published in Zeuthen 2003, Electroweak precision data and the Higgs mass, p. 15–24. [hep-ph/0304199](http://hep-ph/0304199).
- [77] C.J.C. Burges, H.J. Schnitzer, *Nuclear Phys. B* 228 (1983) 464;  
C.N. Leung, S.T. Love, S. Rao, *Z. Phys. C* 31 (1986) 433;  
W. Buchmüller, D. Wyler, *Nuclear Phys. B* 268 (1986) 621;  
K. Hagiwara, S. Ishihara, R. Szalapski, D. Zeppenfeld, *Phys. Lett. B* 283 (1992) 353;  
K. Hagiwara, S. Ishihara, R. Szalapski, D. Zeppenfeld, *Phys. Rev. D* 48 (1993) 2182.

- [78] K. Whisnant, J.M. Yang, B.-L. Young, X. Zhang, Phys. Rev. D 56 (1997) 467;  
G.J. Gounaris, D.T. Papadamou, F.M. Renard, Z. Phys. C 76 (1997) 333;  
J.M. Yang, B.L. Young, Phys. Rev. D 56 (1997) 5907;  
G. Gounaris, G. Tsirigoti, Phys. Rev. D 56 (1997) 3030.
- [79] See for instance R. Barbieri, A. Strumia, Phys. Lett. B 462 (1999) 144;  
L. Hall, C. Kolda, Phys. Lett. B 459 (1999) 213.
- [80] M. Peskin, T. Takeuchi, Phys. Rev. Lett. 65 (1990) 964;  
G. Altarelli, R. Barbieri, F. Caravaglios, Nuclear Phys. B 405 (1993) 3.
- [81] M. Peskin, J. Wells, Phys. Rev. D 64 (2001) 093003.
- [82] P.J. Franzini, P. Taxil, (conv.) et al., Higgs at LEP1 in Ref. [56], Part II, p. 59;  
E.W.N. Glover, J.J. van der Bij, (conv.) et al., Rare Z Decays in Ref. [56], Part II, p. 1.
- [83] J.D. Bjorken, Proc. 1976 SLAC Summer Inst. Part. Phys., SLAC Report 198, 1977, p. 1.
- [84] F.A. Behrends, R. Kleiss, Nuclear Phys. B 260 (1985) 32.
- [85] R.N. Cahn, M.S. Chanowitz, N. Fleishon, Phys. Lett. 82B (1979) 113.
- [86] L. Bergstrom, G. Hulth, Nuclear Phys. B 259 (1985) 137.
- [87] ALEPH Collaboration, D. Buskulic, et al., Phys. Lett. B 384 (1996) 427;  
DELPHI Collaboration, P. Abreu, et al., Nuclear Phys. B 421 (1994) 3;  
L3 Collaboration, M. Acciarri, et al., Phys. Lett. B 385 (1996) 454;  
OPAL Collaboration, G. Alexander, et al., Z. Phys. C 73 (1997) 189.
- [88] J.F. Grivaz, Rapporteur talk given at “International Europhysics Conference on High Energy Physics (HEP 95), Brussels”, 1995;  
Particle Data Group, R.M. Barnett, et al., Phys. Rev. D 54 (1996) 1.
- [89] J. Ellis, M.K. Gaillard, D.V. Nanopoulos, Nuclear Phys. B 106 (1976) 292.
- [90] D.R.T. Jones, S.T. Petcov, Phys. Lett. B 84 (1979) 440.
- [91] B.L. Joffe, V.A. Khoze, Sov. J. Part. Phys. 9 (1978) 50;  
E. Ma, Y. Okada, Phys. Rev. D 20 (1979) 1052;  
J. Finjord, Phys. Scripta 21 (1980) 143.
- [92] M. Carena, P.M. Zerwas, (conv.) et al., Higgs Physics at LEP2 in Ref. [58], Part I, p. 351. [hep-ph/9602250](#).
- [93] The LEP Collaborations (ALEPH, DELPHI, L3 and OPAL). [hep-ex/0107032](#).
- [94] The LEP Collaborations (ALEPH, DELPHI, L3 and OPAL). [hep-ex/0107034](#).
- [95] D.A. Dicus, S. Mathur, Phys. Rev. D 7 (1973) 3111;  
B. Lee, C. Quigg, H. Thacker, Phys. Rev. Lett. 38 (1977) 883;  
H.A. Weldon, Phys. Rev. D 30 (1984) 1547;  
M. Chanowitz, M. Golden, H. Georgi, Phys. Rev. Lett. 57 (1986) 2344;  
M. Chanowitz, M. Golden, H. Georgi, Phys. Rev. D 36 (1987) 1490.
- [96] M.S. Chanowitz, Strong WW scattering at the end of the 90’s: Theory and experimental prospects, published in Zuoz 1998, p. 81. [hep-ph/9812215](#).
- [97] M. Lüscher, P. Weisz, Phys. Lett. B 212 (1988) 472; Nuclear Phys. B 318 (1989) 705.
- [98] A. Arhrib. [hep-ph/0012353](#).
- [99] W. Marciano, S. Willenbrock, Phys. Rev. D 37 (1988) 2509;  
S. Dawson, S. Willenbrock, Phys. Rev. Lett. 62 (1989) 1232.
- [100] L. Durand, B.A. Kniehl, K. Riesselmann, Phys. Rev. D 51 (1995) 5007;  
A. Ghinculov, Nuclear Phys. B 455 (1995) 21;  
A. Frink, B. Kniehl, D. Kreimer, K. Riesselmann, Phys. Rev. D 54 (1996) 4548;  
T. Binoth, A. Ghinculov, J.J. van der Bij, Phys. Rev. D 57 (1998) 1487.
- [101] A. Ghinculov, Phys. Lett. B 337 (1994) 137;  
A. Ghinculov, Phys. Lett. B 346 (1995) 426 (Erratum);  
A. Frink, B. Kniehl, K. Riesselmann, Phys. Rev. Lett. 72 (1994) 2534;  
A. Frink, B. Kniehl, K. Riesselmann, Phys. Rev. Lett. 74 (1995) 1699 (Erratum);  
V. Borodulin, G. Jikia, Phys. Lett. B 391 (1997) 434.
- [102] S. Dawson, S. Willenbrock, Phys. Rev. D 40 (1989) 2880.
- [103] L. Durand, P. Maher, K. Riesselmann, Phys. Rev. D 48 (1993) 1084;  
K. Riesselmann, Phys. Rev. D 53 (1996) 6226;  
U. Nierste, K. Riesselmann, Phys. Rev. D 53 (1996) 6638.
- [104] K. Riesselmann, S. Willenbrock, Phys. Rev. D 55 (1997) 311.
- [105] T. Cheng, E. Eichten, L. Li, Phys. Rev. D 9 (1974) 2259;  
B. Pendleton, G. Ross, Phys. Lett. B 98 (1981) 291;  
C. Hill, Phys. Rev. D 24 (1981) 691;  
J. Bagger, S. Dimopoulos, E. Masso, Nuclear Phys. B 253 (1985) 397;  
M. Beg, C. Panagiotakopoulos, A. Sirlin, Phys. Rev. Lett. 52 (1984) 883;  
M. Duncan, R. Philippe, M. Sher, Phys. Lett. B 153 (1985) 165;  
K. Babu, E. Ma, Phys. Rev. Lett. 55 (1985) 3005.
- [106] K.G. Wilson, J. Kogut, Phys. Rep. 12 (1974) 75.

- [107] N. Cabibbo, L. Maiani, G. Parisi, R. Petronzio, Nuclear Phys. B 158 (1979) 295;  
R. Dashen, H. Neuberger, Phys. Rev. Lett. 50 (1983) 1897;  
D. Callaway, Nuclear Phys. B 233 (1984) 189;  
P. Hasenfratz, J. Nager, Z. Phys. C 37 (1988);  
J. Kuti, L. Lin, Y. Shen, Phys. Rev. Lett. 61 (1988) 678;  
R. Chivukula, E. Simmons, Phys. Lett. B 388 (1996) 788.
- [108] A. Hasenfratz, in: M. Creutz (Ed.), Quantum Fields on the Computer, World Scientific, Singapore, 1992, p. 125;  
M. Göckeler, H. Kastrup, T. Neuhaus, F. Zimmermann, Nuclear Phys. B 405 (1993) 555.
- [109] M. Lindner, M. Sher, H.W. Zaglauer, Phys. Lett. 228B (1989) 139;  
M. Sher, Phys. Lett. B 317 (1993) 159;  
M. Sher, Phys. Lett. B 331 (1994) 448;  
G. Altarelli, I. Isidori, Phys. Lett. B 337 (1994) 141;  
J.A. Casas, J.R. Espinosa, M. Quiros, Phys. Lett. B 342 (1995) 171;  
J. Espinosa, M. Quiros, Phys. Lett. B 353 (1995) 257.
- [110] M. Sher, Phys. Rep. 179 (1989) 273.
- [111] G. Isidori, G. Ridolfi, A. Strumia, Nuclear Phys. B 609 (2001) 387.
- [112] G. Anderson, Phys. Lett. B 243 (1990) 265;  
P. Arnold, S. Vokos, Phys. Rev. D 44 (1991) 3620;  
J.R. Espinosa, M. Quiros, Phys. Lett. B 353 (1995) 257.
- [113] C. Froggat, H. Nielsen, Y. Takanishi, Phys. Rev. D 64 (2001) 113014.
- [114] E. Branchina, H. Faivre, Phys. Rev. D 72 (2005) 065017.
- [115] M. Lindner, Z. Phys. C 31 (1986) 295;  
B. Grzadowski, M. Lindner, Phys. Lett. B 178 (1986) 81.
- [116] T. Hambye, K. Riessellmann, Phys. Rev. D 55 (1997) 7255.
- [117] M. Veltman, Acta Phys. Polon. B 12 (1981) 437.
- [118] M. Einhorn, D. Jones, Phys. Rev. D 46 (1992) 5206.
- [119] I. Jack, D.R.T. Jones, Nuclear Phys. B 342 (1990) 127;  
R. Decker, J. Pestieau, Modern Phys. Lett. A 4 (1989) 2733;  
M. Capdequi-Peyranère, J. Montero, G. Moulataka, Phys. Lett. B 260 (1991) 138;  
P. Osland, T. Wu, Phys. Lett. B 291 (1992) 315;  
M. Chaichian, R. Gonzalez-Felipe, K. Huitu, Phys. Lett. B 363 (1995) 101;  
A. Andrianov, N. Romanenko, Phys. Lett. B 343 (1995) 295.
- [120] C.F. Kolda, H. Murayama, JHEP 0007 (2000) 035.
- [121] J.A. Casas, J.R. Espinosa, I. Hidalgo, JHEP 0411 (2004) 057.
- [122] K. Hagiwara, R. Szalapski, D. Zeppenfeld, Phys. Lett. B 318 (1993) 155;  
J.M. Hernandez, M.A. Perez, J.J. Toscano, Phys. Rev. D 51 (1995) 2044.
- [123] G.J. Gounaris, F.M. Renard, Phys. Rev. D 59 (1999) 113015.
- [124] J. Romao, S. Andringa, Eur. Phys. J. C 7 (1999) 631.
- [125] A. Djouadi, R. Godbole, S. Rindani, R. Singh, Review article for Internat. J. Modern Phys. (in preparation).
- [126] L. Resnick, M.K. Sundaresan, P.J.S. Watson, Phys. Rev. D 8 (1973) 172.
- [127] J.F. Gunion, H.E. Haber, Nuclear Phys. B 272 (1986) 1.
- [128] T. Arens, U. Gieseler, L.M. Sehgal, Phys. Lett. B 339 (1994) 127.
- [129] E. Braaten, J.P. Leveille, Phys. Rev. D 22 (1980) 715;  
N. Sakai, Phys. Rev. D 22 (1980) 2220;  
T. Inami, T. Kubota, Nuclear Phys. B 179 (1981) 171;  
S.G. Gorishny, A.L. Kataev, S.A. Larin, Sov. J. Nucl. Phys. 40 (1984) 329.
- [130] M. Drees, K. Hikasa, Phys. Rev. D 41 (1990) 1547;  
M. Drees, K. Hikasa, Phys. Lett. B 240 (1990) 455;  
M. Drees, K. Hikasa, Phys. Lett. B 262 (1991) 497 (Erratum).
- [131] K.G. Chetyrkin, Phys. Lett. B 390 (1997) 309;  
K.G. Chetyrkin, M. Steinhauser, Phys. Lett. B 408 (1997) 320.
- [132] K.G. Chetyrkin, A. Kwiatkowski, Nuclear Phys. B 461 (1996) 3;  
S.A. Larin, T. van Ritbergen, J.A.M. Vermaseren, Phys. Lett. B 362 (1995) 134.
- [133] A. Djouadi, P. Gambino, Phys. Rev. D 51 (1995) 218.
- [134] K. Melnikov, Phys. Rev. D 53 (1996) 5020.
- [135] R. Harlander, M. Steinhauser, Phys. Rev. D 56 (1997) 3980.
- [136] R. Decker, M. Nowakowski, A. Pilaftsis, Z. Phys. C 57 (1993) 339;  
R. Decker, M. Nowakowski, A. Pilaftsis, Modern Phys. Lett. A 6 (1991) 3491;  
R. Decker, M. Nowakowski, A. Pilaftsis, Modern Phys. Lett. A 7 (1992) 819 (Erratum).
- [137] A. Djouadi, J. Kalinowski, P.M. Zerwas, Z. Phys. C 70 (1996) 435.
- [138] S. Moretti, W. Stirling, Phys. Lett. B 347 (1995) 291;  
S. Moretti, W. Stirling, Phys. Lett. B 366 (1996) 451 (Erratum).

- [139] J.R. Dell'Aquila, C.A. Nelson, Nuclear Phys. B 320 (1989) 61;  
J.R. Dell'Aquila, C.A. Nelson, Nuclear Phys. B 320 (1989) 86;  
C.A. Nelson, Phys. Rev. D 41 (1990) 2805;  
S. Weinberg, Phys. Rev. D 42 (1990) 860;  
B.K. Bullock, K. Hagiwara, A.D. Martin, Phys. Lett. B 273 (1991) 501;  
S. Barr, A. Zee, Phys. Rev. Lett. 65 (1990) 21;  
J. Gunion, R. Vega, Phys. Lett. B 251 (1990) 157;  
D. Chang, W.Y. Keung, T.C. Yuan, Phys. Lett. B 251 (1990) 608;  
D. Chang, W.Y. Keung, T.C. Yuan, Phys. Rev. D 43 (1991) R14;  
R. Leigh, S. Paban, R. Xu, Nuclear Phys. B 352 (1991) 45;  
A. Skjold, P. Osland, Phys. Lett. B 311 (1993) 261;  
W. Bernreuther, P. Overmann, Z. Phys. C 61 (1994) 599;  
W. Bernreuther, P. Overmann, Z. Phys. C 72 (1996) 461;  
X.G. He, J.P. Ma, B. McKellar, Phys. Rev. D 49 (1994) 4548;  
X.G. He, J.P. Ma, B. McKellar, Modern Phys. Lett. A 9 (1994) 205;  
W.N. Cottingham, I.B. Whittingham, Phys. Rev. D 52 (1995) 539.
- [140] V. Barger, K. Cheung, A. Djouadi, B. Kniehl, P. Zerwas, Phys. Rev. D 49 (1994) 79.
- [141] M. Kramer, J.H. Kuhn, M.L. Stong, P.M. Zerwas, Z. Phys. C 64 (1994) 21.
- [142] D. Chang, W.Y. Keung, I. Phillips, Phys. Rev. D 48 (1993) 3225.
- [143] H. Pois, T. Weiler, T.C. Yuan, Phys. Rev. D 47 (1993) 3886;  
D. Chang, W.Y. Keung, Phys. Lett. B 305 (1993) 261.
- [144] B. Grzadkowski, J.F. Gunion, Phys. Lett. B 350 (1995) 218.
- [145] J.H. Kuhn, F. Wagner, Nuclear Phys. B 236 (1984) 16.
- [146] W. Bernreuther, A. Brandenburg, M. Flesch, Phys. Rev. D 56 (1997) 90.
- [147] Z. Was, M. Worek, Acta Phys. Polon. B 33 (2002) 1875;  
M. Worek, Acta Phys. Polon. B 34 (2003) 4549;  
G.R. Bower, T. Pierzchala, Z. Was, M. Worek, Phys. Lett. B 543 (2002) 227.
- [148] K. Desch, Z. Was, M. Worek, Eur. Phys. J. C 29 (2003) 491;  
K. Desch, A. Imhof, Z. Was, M. Worek, Phys. Lett. B 579 (2004) 157.
- [149] G. Pocsik, T. Torma, Z. Phys. C 6 (1980) 1;  
T.G. Rizzo, Phys. Rev. D 22 (1980) 722;  
W.-Y. Keung, W.J. Marciano, Phys. Rev. D 30 (1984) 248.
- [150] D.A. Dicus, S. Willenbrock, T. Imbo, W.K. Keung, T. Rizzo, Phys. Rev. D 34 (1986) 2157;  
T.G. Rizzo, Phys. Rev. D 31 (1985) 2366;  
P. Langacker, J. Liu, Phys. Rev. D 46 (1992) 5069.
- [151] A. Grau, G. Panchieri, R.J.N. Phillips, Phys. Lett. B 251 (1990) 293.
- [152] R.N. Cahn, Rep. Prog. Phys. 52 (1989) 389;  
B. Kniehl, Phys. Lett. B 244 (1990) 537;  
E. Gross, B. Kniehl, G. Wolf, Z. Phys. C 63 (1994) 417;  
E. Gross, B. Kniehl, G. Wolf, Z. Phys. C 66 (1995) 321 (Erratum);  
D.J. Summers, Phys. Rev. D 53 (1996) 6374.
- [153] J.R. Dell'Aquila, C.A. Nelson, Phys. Rev. D 33 (1986) 80;  
M. Duncan, G. Kane, W. Repko, Nuclear Phys. B 272 (1986) 517;  
C.A. Nelson, Phys. Rev. D 37 (1988) 1220;  
D. Chang, W.Y. Keung, I. Phillips, Phys. Lett. B 305 (1993) 261;  
B. Grzadkowski, Phys. Lett. B 305 (1993) 384;  
A. Soni, R.M. Xu, Phys. Rev. D 48 (1993) 5259;  
T. Arens, L.M. Sehgal, Z. Phys. C 66 (1995) 89.
- [154] B. Grzadkowski, J.F. Gunion, J. Pliszka, Nuclear Phys. B 583 (2000) 49.
- [155] S. Choi, D. Miller, M. Muhlleitner, P. Zerwas, Phys. Lett. B 553 (2003) 61.
- [156] A. Djouadi, B. Kniehl, Correlations in Higgs production and decay as a probe of CP-violation in the scalar sector, in: Proceedings of Workshop on " $e^+e^-$  Collisions", Report DESY-93-123C.
- [157] A.I. Vainshtein, M.B. Voloshin, V.I. Zakharov, M.A. Shifman, Sov. J. Nucl. Phys. 30 (1979) 711.
- [158] L. Okun, Leptons and Quarks, Ed. North Holland, Amsterdam, 1982.
- [159] M. Gavela, G. Girardi, C. Malleville, P. Sorba, Nuclear Phys. B 193 (1981) 257.
- [160] H. Zheng, D. Wu, Phys. Rev. D 42 (1990) 3760;  
A. Djouadi, M. Spira, J. van der Bij, P.M. Zerwas, Phys. Lett. B 257 (1991) 187;  
S. Dawson, R.P. Kauffman, Phys. Rev. D 47 (1993) 1264;  
K. Melnikov, O. Yakovlev, Phys. Lett. B 312 (1993) 179;  
A. Djouadi, M. Spira, P.M. Zerwas, Phys. Lett. B 311 (1993) 255;  
M. Inoue, R. Najima, T. Oka, J. Saito, Modern Phys. Lett. A 9 (1994) 1189;  
J. Fleischer, O.V. Tarasov, Z. Phys. C 64 (1994) 413.



- [161] M. Spira, A. Djouadi, D. Graudenz, P.M. Zerwas, Nuclear Phys. B 453 (1995) 17.
- [162] J. Fleischer, O.V. Tarasov, V.O. Tarasov, Phys. Lett. B 584 (2004) 294.
- [163] K. Melnikov, M. Spira, O. Yakovlev, Z. Phys. C 64 (1994) 401.
- [164] M. Spira, A. Djouadi, P.M. Zerwas, Phys. Lett. B 276 (1992) 350.
- [165] F. Wilczek, Phys. Rev. Lett. 39 (1977) 1304;  
J. Ellis, M. Gaillard, D. Nanopoulos, C. Sachrajda, Phys. Lett. 83B (1979) 339;  
T. Rizzo, Phys. Rev. D 22 (1980) 178.
- [166] H. Georgi, S. Glashow, M. Machacek, D. Nanopoulos, Phys. Rev. Lett. 40 (1978) 692.
- [167] T. Inami, T. Kubota, Y. Okada, Z. Phys. C 18 (1983) 69.
- [168] A. Djouadi, M. Spira, P.M. Zerwas, Phys. Lett. B 264 (1991) 440.
- [169] M. Spira, A. Djouadi, D. Graudenz, P.M. Zerwas, Phys. Lett. B 318 (1993) 347.
- [170] S. Dawson, R.P. Kauffman, Phys. Rev. D 49 (1994) 2298.
- [171] A. Djouadi, M. Spira, P.M. Zerwas, Z. Phys. C 70 (1996) 427.
- [172] M.S. Chanowitz, M.A. Furman, I. Hinchliffe, Phys. Lett. 78B (1978) 285; Nuclear Phys. B 153 (1979) 402;  
J. Fleischer, F. Jegerlehner, Phys. Rev. D 23 (1981) 2001;  
F. Jegerlehner, in: B.W. Lynn, J.F. Wheeler (Eds.), Workshop on Radiative Corrections in  $SU(2)_L \times U(1)$ , Trieste, Italy, June 1983, World Scientific, Singapore, 1984, p. 237;  
Z. Hioki, Phys. Lett. B 224 (1989) 417;  
Z. Hioki, Phys. Lett. B 228 (1989) 560 (Erratum).
- [173] B.A. Kniehl, Nuclear Phys. B 376 (1992) 3;  
D.Yu. Bardin, B.M. Vilenskiĭ, P.Kh. Khristova, Sov. J. Nucl. Phys. 53 (1991) 152;  
A. Dabelstein, W. Hollik, Z. Phys. C 53 (1992) 507.
- [174] S. Dawson, S. Willenbrock, Phys. Lett. B 211 (1988) 200;  
B.A. Kniehl, Nuclear Phys. B 352 (1991) 1;  
B.A. Kniehl, Nuclear Phys. B 357 (1991) 439;  
D.Yu. Bardin, B.M. Vilenskiĭ, P.Kh. Khristova, preprint JINR-P2-91-140.
- [175] B.A. Kniehl, A. Sirlin, Phys. Lett. B 318 (1993) 367;  
B.A. Kniehl, Phys. Rev. D 50 (1994) 3314.
- [176] A. Djouadi, P. Gambino, Phys. Rev. D 49 (1994) 4705.
- [177] B.A. Kniehl, M. Spira, Nuclear Phys. B 432 (1994) 39;  
A. Kwiatkowski, M. Steinhauser, Phys. Lett. B 338 (1994) 66; B342 (1995) 455 (Erratum).
- [178] B.A. Kniehl, M. Spira, Nuclear Phys. B 443 (1995) 37;  
B.A. Kniehl, Phys. Rev. D 53 (1996) 6477.
- [179] B.A. Kniehl, M. Steinhauser, Nuclear Phys. B 454 (1995) 485;  
B.A. Kniehl, M. Steinhauser, Phys. Lett. B 365 (1996) 297.
- [180] K.G. Chetyrkin, B.A. Kniehl, M. Steinhauser, Phys. Rev. Lett. 78 (1997) 594;  
K.G. Chetyrkin, B.A. Kniehl, M. Steinhauser, Nuclear Phys. B 490 (1997) 19.
- [181] A. Djouadi, P. Gambino, B. Kniehl, Nuclear Phys. B 523 (1998) 17.
- [182] A. Djouadi, P. Gambino, Phys. Rev. Lett. 73 (1994) 2528.
- [183] F. Fugle, B. Kniehl, M. Steinhauser, Nuclear Phys. B 702 (2004) 333.
- [184] U. Aglietti, R. Bonciani, G. Degrossi, A. Vicini, Phys. Lett. B 595 (2004) 432.
- [185] G. Degrossi, F. Maltoni, Phys. Lett. B 600 (2004) 255.
- [186] M. Steinhauser, Proceedings of the Ringberg Workshop on “The Higgs Puzzle”. [hep-ph/9612395](http://hep-ph/9612395).
- [187] K.G. Chetyrkin, B.A. Kniehl, M. Steinhauser, Phys. Rev. Lett. 79 (1997) 353;  
K.G. Chetyrkin, B.A. Kniehl, M. Steinhauser, Nuclear Phys. B 510 (1998) 61.
- [188] A.L. Kataev, JETP Lett. 66 (1997) 327;  
A.L. Kataev, V. Kim. [hep-ph/93042428](http://hep-ph/93042428).
- [189] M. Steinhauser, Phys. Rev. D 59 (1999) 054005.
- [190] J.K. Korner, K. Melnikov, O. Yakovlev, Phys. Rev. D 53 (1996) 3737.
- [191] M.A. Shifman, A.I. Vainshteĭn, V.I. Zakharov, Phys. Lett. 78B (1978) 443;  
A.I. Vainshteĭn, V.I. Zakharov, M.A. Shifman, Sov. Phys. Usp. 23 (1980) 429;  
M.B. Voloshin, Sov. J. Nucl. Phys. 44 (1986) 478.
- [192] B. Kniehl, M. Spira, Z. Phys. C 69 (1995) 77;  
W. Kilian, Z. Phys. C 69 (1995) 89.
- [193] S.L. Adler, J.C. Collins, A. Duncan, Phys. Rev. D 15 (1977) 1712.
- [194] O. Tarasov, preprint JINR P2-82-900, 1982 (unpublished).
- [195] A. Djouadi, J. Kalinowski, M. Spira, Comput. Phys. Commun. 108 (1998) 56.
- [196] P. Garbincius, 2004 Moriond Conference on Electroweak Interactions. [hep-ph/0406013](http://hep-ph/0406013).
- [197] The web site: <http://www.fnal.gov/pub/now/tevum.html>.

- [198] U. Heintz, S. Kuhlmann, S. Willenbrock, Report of the TeV2000 Study Group, D. Amidei and R. Brock (Eds.), Fermilab-PUB-96-082, pp. 120–156;  
W.M. Yao, Proceedings of the 1996 DPF/DPB Summer Study on High Energy Physics, in: D.G. Cassel et al. (Eds.), Snowmass, June 25–July 12, 1996, pp. 619–621;  
D. Amidei, et al. The TEV33 Committee Report, February, 1996; J. Womersly, DØ Note 003227, April, 1997.
- [199] M. Carena, J. Conway, H. Haber, J. Hobbs, (conv.) et al., Report of the Higgs Working Group for “RUN II at the Tevatron”. [hep-ph/0010338](http://hep-ph/0010338).
- [200] See the review talk given by J. Engelen in Ref. [201].
- [201] Proceedings of the Conference “Physics at LHC” in Vienna, 13–17 July 2004. See the web site: [wwwhep.phy.oeaw.ac.at/phlhc04/](http://wwwhep.phy.oeaw.ac.at/phlhc04/).
- [202] F. Gianotti, M. Mangano et, T. Virdee, (conv.) et al., Physics potential and experimental challenges of the LHC luminosity upgrade. [hep-ph/0204087](http://hep-ph/0204087).
- [203] U. Baur, et al., Report of the Working Group, Physics at future colliders, in APS/DPF/DPB Snowmass study in Ref. [204]. [hep-ph/0201227](http://hep-ph/0201227).
- [204] Proceedings of the APS/DPF/DPB Summer Study on the Future of Particle Physics, Snowmass 2001, Colorado. See the web site, <http://snowmass2001.org/>.
- [205] Proceedings of the LaThuile Workshop on Physics at Future Accelerators, La Thuile 1987, Yelllow Report CERN–87–07, 2 Volumes.
- [206] VLHC Design Study Group, Design Study for a Staged Very Large Hadron Collider, FERMILAB-TM-2149, June 2001.
- [207] S. Peggs, The Hadron Colliders WG Report in Snowmass 2001 [204].
- [208] ATLAS Collaboration, Technical Proposal, CERN/LHCC/94-43.
- [209] ATLAS Collaboration, Detector and Physics Performance Technical Design Report, vols. 1, 2, CERN–LHCC–99–14 and CERN–LHCC–99–15.
- [210] CMS Collaboration, Technical Proposal, CERN–LHCC–94–38.
- [211] CMS Collaboration, ECAL Project Technical Design Report, CERN/LHCC/97-33 and The compact muon solenoid: The muon Technical Design Report, CERN/LHCC/97-32.
- [212] See the talks given by M. Nessi (ATLAS) and A. Ball (CMS) in Ref. [201].
- [213] G. Jarlskog, D. Rein (Eds.), Proceedings of the Large Hadron Collider Workshop, Aachen 1990, CERN Report 90–10.
- [214] D. Froidevaux, Z. Kunszt, J. Stirling, (conv.) et al., Report of the SM Higgs Working Group in the proceedings of Ref. [213], vol. II. See also the Rapporteurs talks by G. Altarelli, D. Denegri, Report of the SM Higgs Working Group in the proceedings of Ref. [213], vol. I.
- [215] S. Asai, et al., (ATLAS Collaboration), Eur. Phys. J. C 32S2 (2004) 19.
- [216] S. Abdullin, et al. (CMS Collaboration), CMS Note 2003/33.
- [217] G. Branson, et al., (CMS and ATLAS Coll.), Eur. Phys. J. Direct C 4 (2002) N1.
- [218] P. Sphicas, Talk at the conference “Physics at LHC” in Ref. [201];  
D. Froidevaux, Talk given at the final meeting of the European Network “Physics at Colliders”, Montpellier, 26–27 September 2004.
- [219] A. Djouadi, R. Kinnunen, E. Richter-Was, H.U. Martyn (conv.), et al., Report of the Higgs Working Group, in: Proceedings of the Les Houches Workshop on “Physics at TeV Colliders”, 1999. [hep-ph/0002258](http://hep-ph/0002258).
- [220] D. Cavalli, A. Djouadi, K. Jakobs, A. Nikitenko, M. Spira, C.E.M. Wagner, W.-M. Yao (conv.), et al., Report of the Higgs Working Group, in: Proceedings of the Les Houches Workshop on “Physics at TeV Colliders”, 2001. [hep-ph/0203056](http://hep-ph/0203056).
- [221] K.A. Assamagan, M. Narain, A. Nikitenko, M. Spira, D. Zeppenfeld, (conv.) et al., Report of the Higgs Working Group, in: Proceedings of the Les Houches Workshop on “Physics at TeV Colliders”. [hep-ph/0406152](http://hep-ph/0406152), 2003.
- [222] S.L. Glashow, D. Nanopoulos, A. Yildiz, Phys. Rev. D 18 (1978) 1724;  
J. Finjord, G. Girardi, P. Sorba, Phys. Lett. B 89 (1979) 99.
- [223] E. Eichten, I. Hinchliffe, K. Lane, C. Quigg, Rev. Modern Phys. 56 (1984) 579.
- [224] R.N. Cahn, S. Dawson, Phys. Lett. 136B (1984) 196;  
R.N. Cahn, S. Dawson, Phys. Lett. B 138 (1984) 464 (Erratum).
- [225] D. Dicus, S. Willenbrock, Phys. Rev. D 32 (1985) 1642.
- [226] G. Altarelli, B. Mele, F. Pitoli, Nuclear Phys. B 287 (1987) 205.
- [227] W. Kilian, M. Kramer, P.M. Zerwas, Phys. Lett. B 373 (1996) 135.
- [228] R. Raitio, W.W. Wada, Phys. Rev. D 19 (1979) 941;  
Z. Kunszt, Nuclear Phys. B 247 (1984) 339;  
A.S. Bagdasaryan, et al., Sov. J. Nucl. Phys. 46 (1987) 315.
- [229] J. Ng, P. Zakarauskas, Phys. Rev. D 29 (1984) 876.
- [230] R.M. Barnett, H.E. Haber, D.E. Soper, Nuclear Phys. B 306 (1988) 697;  
F.I. Olness, W.-K. Tung, Nuclear Phys. B 308 (1988) 813.
- [231] D.A. Dicus, S. Willenbrock, Phys. Rev. D 39 (1989) 751.
- [232] E.N. Glover, J. van der Bij, Nuclear Phys. B 309 (1988) 282;  
D.A. Dicus, C. Kao, S. Willenbrock, Phys. Lett. B 203 (1988) 457;  
G. Jikia, Nuclear Phys. B 412 (1994) 57.
- [233] T. Plehn, M. Spira, P.M. Zerwas, Nuclear Phys. B 479 (1996) 46.
- [234] V. Barger, T. Han, R. Phillips, Phys. Rev. D 38 (1988) 2766.
- [235] A. Djouadi, W. Kilian, M. Mühlleitner, P. Zerwas, Eur. Phys. J. C 10 (1999) 45.
- [236] W.Y. Keung, Modern Phys. Lett. A 2 (1987) 765;  
O. Eboli, G. Marques, S. Novaes, A. Natale, Phys. Lett. B 197 (1987) 269;  
D. Dicus, K. Kallianpur, S. Willenbrock, Phys. Lett. B 200 (1988) 187;  
K. Kallianpur, Phys. Lett. B 215 (1988) 392;  
A. Dobrovolskaya, V. Novikov, Z. Phys. C 52 (1991) 427.

- [237] A. Abbassabadi, W. Repko, D. Dicus, R. Vega, Phys. Rev. D 38 (1988) 2770.
- [238] V. Barger, T. Han, Modern Phys. Lett. A 5 (1990) 667.
- [239] R.K. Ellis, I. Hinchliffe, M. Soldate, J.J. van der Bij, Nuclear Phys. B 297 (1988) 221.
- [240] U. Baur, E. Glover, Nuclear Phys. B 339 (1990) 38;  
C. Kao, Phys. Lett. B 328 (1994) 420.
- [241] S. Dawson, R. Kauffman, Phys. Rev. Lett. 68 (1992) 2273;  
R.P. Kauffman, S.V. Desai, D. Risal, Phys. Rev. D 55 (1997) 4005; Phys. Rev. D 59 (1999) 057504.
- [242] V. Del Duca, W. Kilgore, C. Oleari, C. Schmidt, D. Zeppenfeld, Phys. Rev. Lett. 87 (2001) 122001;  
V. Del Duca, W. Kilgore, C. Oleari, C. Schmidt, D. Zeppenfeld, Nuclear Phys. B 616 (2001) 307.
- [243] V. Del Duca, A. Frizzo, F. Maltoni, JHEP 0405 (2004) 064.
- [244] K. Cheung, Phys. Rev. D 49 (1994) 6224.
- [245] A. Djouadi, W. Kilian, T. Plehn, (in preparation).
- [246] A. Abbassabadi, W. Repko, D. Dicus, R. Vega, Phys. Lett. B 213 (1988) 386.
- [247] D. Rainwater, Phys. Lett. B 503 (2001) 320.
- [248] A. Abbassabadi, D. Bowser–Cho, D. Dicus, W. Repko, Phys. Rev. D 58 (1998) 057301;  
A. Abbassabadi, D. Bowser–Cho, D. Dicus, W. Repko, Phys. Rev. D 57 (1998) 550.
- [249] D. Dicus, Z. Phys. C 39 (1988) 583.
- [250] K.J. Kallianpur, Phys. Lett. B 215 (1988) 392.
- [251] C.G. Papadopoulos in Ref. [202].
- [252] B. Mele, S. Petrarca, A. Soddu, Phys. Lett. B 435 (1998) 401;  
G. Eilam, J.L. Hewett, A. Soni, Phys. Rev. D 44 (1991) 1473;  
G. Eilam, J.L. Hewett, A. Soni, Phys. Rev. D 59 (1999) 039901 (Erratum).
- [253] G. Mahlon, S. Parke, Phys. Lett. B 347 (1995) 394.
- [254] A. Bialas, P.V. Landshoff, Phys. Lett. B 256 (1991) 540.
- [255] M. Boonekamp, R. Peschanski, C. Royon, Phys. Rev. Lett. 87 (2001) 251806;  
M. Boonekamp, R. Peschanski, C. Royon, Nuclear Phys. B 669 (2003) 277;  
B.E. Cox, J.R. Forshaw, B. Heinemann, Phys. Lett. B 540 (2002) 263;  
R. Enberg, G. Ingelman, A. Kissavos, N. Timneanu, Phys. Rev. Lett. 89 (2002) 081801;  
J.-R. Cudell, O.F. Hernandez, Nuclear Phys. B 471 (1996) 471;  
E.M. Levin, [hep-ph/9912402](http://hep-ph/9912402).
- [256] V.A. Khoze, A.D. Martin, M.G. Ryskin, Eur. Phys. J. C 23 (2002) 311;  
A. De Roeck, et al., Eur. Phys. J. C 25 (2002) 391;  
A.B. Kaidalov, V.A. Khoze, A.D. Martin, M.G. Ryskin, Eur. Phys. J. C 31 (2003) 387;  
A.B. Kaidalov, V.A. Khoze, A.D. Martin, M.G. Ryskin, Eur. Phys. J. C 33 (2004) 261.
- [257] V.A. Khoze, A.D. Martin, M.G. Ryskin, Eur. Phys. J. C 26 (2002) 229.
- [258] A. De Roeck, V.A. Khoze in Ref. [221].
- [259] The NLO Fortran codes for  $HV$ ,  $Hqq$  and  $gg \rightarrow H$  production and the LO Fortran code for  $Q\bar{Q}H$  production, have been written by M. Spira and can be found at: <http://people.web.psi.ch/spira/>. See also M. Spira, [hep-ph/9510347](http://hep-ph/9510347) for the users manual of the program HIGLU.
- [260] T. Han, S. Willenbrock, Phys. Lett. B 273 (1990) 167.
- [261] H. Baer, B. Bailey, J. Owens, Phys. Rev. D 47 (1993) 2730;  
J. Ohnemus, W. Stirling, Phys. Rev. D 47 (1993) 2722;  
S. Mrenna, C.P. Yuan, Phys. Lett. B 416 (1998) 200.
- [262] A. Djouadi, M. Spira, Phys. Rev. D 62 (2000) 014004.
- [263] T. Han, G. Valencia, S. Willenbrock, Phys. Rev. Lett. 69 (1992) 3274.
- [264] T. Figy, C. Oleari, D. Zeppenfeld, Phys. Rev. D 68 (2003) 073005.
- [265] E.L. Berger, J. Campbell, Phys. Rev. D 70 (2004) 073011.
- [266] S. Dawson, Nuclear Phys. B 359 (1991) 283.
- [267] D. Graudenz, M. Spira, P.M. Zerwas, Phys. Rev. Lett. 70 (1993) 1372;  
M. Spira, Ph.D. Thesis, RWTH Aachen, 1992.
- [268] W. Beenakker, S. Dittmaier, M. Krämer, B. Plümper, M. Spira, P.M. Zerwas, Phys. Rev. Lett. 87 (2001) 201805;  
W. Beenakker, S. Dittmaier, M. Krämer, B. Plümper, M. Spira, P.M. Zerwas, Nuclear Phys. B 653 (2003) 151.
- [269] S. Dawson, L. Orr, L. Reina, D. Wackeroth, Phys. Rev. D 67 (2003) 071503;  
S. Dawson, C. Jackson, L. Orr, L. Reina, D. Wackeroth, Phys. Rev. D 68 (2003) 034022.
- [270] L. Reina, S. Dawson, Phys. Rev. Lett. 87 (2001) 201804;  
L. Reina, S. Dawson, D. Wackeroth, Phys. Rev. D 65 (2002) 053017.
- [271] S. Dittmaier, M. Krämer, M. Spira, Phys. Rev. D 70 (2004) 074010.
- [272] S. Dawson, C. Jackson, L. Reina, D. Wackeroth, Phys. Rev. D 69 (2004) 074027.
- [273] I. Hinchliffe, S.F. Novaes, Phys. Rev. D 38 (1988) 3475;  
S. Catani, E. D’Emilio, L. Trentadue, Phys. Lett. B 211 (1988) 335;  
R.P. Kauffman, Phys. Rev. D 44 (1991) 1415; D45 (1992) 1512;  
C.P. Yuan, Phys. Lett. B 283 (1992) 395;  
C. Balazs, C.P. Yuan, Phys. Lett. B 478 (2000) 192;  
C. Balazs, J. Huston, I. Puljak, Phys. Rev. D 63 (2001) 014021.

- [274] C.R. Schmidt, Phys. Lett. B 413 (1997) 391;  
D. de Florian, M. Grazzini, Z. Kunszt, Phys. Rev. Lett. 82 (1999) 5209;  
D. de Florian, M. Grazzini, Phys. Rev. Lett. 85 (2000) 4678; Nuclear Phys. B 616 (2001) 247;  
S. Catani, D. de Florian, M. Grazzini, Nuclear Phys. B 596 (2001) 299;  
V. Ravindran, J. Smith, W.L. Van Neerven, Nuclear Phys. B 634 (2002) 247;  
E.L. Berger, J.W. Qiu, Phys. Rev. D 67 (2003) 034026;  
A. Kulesza, G. Sterman, W. Vogelsang, Phys. Rev. D 69 (2004) 014012.
- [275] C.J. Glosser, C.R. Schmidt, JHEP 0212 (2002) 016.
- [276] G. Bozzi, S. Catani, D. de Florian, M. Grazzini, Phys. Lett. B 564 (2003) 65.
- [277] C. Anastasiou, L. Dixon, K. Melnikov, Nucl. Phys. Proc. Suppl. 116 (2003) 193.
- [278] C. Anastasiou, K. Melnikov, F. Petriello. [hep-ph/0501130](#).
- [279] V. Ravindran, J. Smith, W.L. Van Neerven, Nucl. Phys. B634 (2002) 247;  
V. Ravindran, J. Smith, W.L. Van Neerven, Modern Phys. Lett. A18 (2003) 1721;  
C. Anastasiou, K. Melnikov, F. Petriello. [hep-ph/0409088](#).
- [280] O. Brein, A. Djouadi, R. Harlander, Phys. Lett. B579 (2004) 149.
- [281] R. Harlander, W. Kilgore, Phys. Rev. Lett. 88 (2002) 201801.
- [282] C. Anastasiou, K. Melnikov, Nuclear Phys. B646 (2002) 220.
- [283] V. Ravindran, J. Smith, W.L. van Neerven, Nuclear Phys. B665 (2003) 325.
- [284] S. Catani, D. de Florian, M. Grazzini, P. Nason, JHEP 0307 (2003) 028.
- [285] G. Altarelli, G. Parisi, Nuclear Phys. B126 (1977) 298.
- [286] S.A. Larin, T. van Ritbergen, J.A.M. Vermaseren, Nuclear Phys. B427 (1994) 41; B492 (1997) 338;  
A. Rétey, J.A.M. Vermaseren, Nuclear Phys. B604 (2001) 281.
- [287] A.D. Martin, R.G. Roberts, W.J. Stirling, R.S. Thorne, Phys. Lett. B531 (2002) 216.
- [288] S. Moch, J.A.M. Vermaseren, A. Vogt, Nuclear Phys. B688 (2004) 101;  
S. Moch, J.A.M. Vermaseren, A. Vogt, Nuclear Phys. B691 (2004) 129.
- [289] R.S. Thorne et al. (MRST Collaboration). [hep-ph/0407311](#).
- [290] V. Gribov, L. Lipatov, Sov. J. Nucl. Phys. 15 (1972) 438;  
Y. Dokshitzer, Sov. Phys. JETP 46 (1977) 641.
- [291] J. Pumplin, D.R. Stump, J. Huston, H.L. Lai, P. Nadolsky, W.K. Tung, (CTEQ Collaboration), JHEP 0207 (2002) 012.
- [292] A.D. Martin, R.G. Roberts, W.J. Stirling, R.S. Thorne, (MRST Collaboration), Eur. Phys. J. C28 (2003) 455.
- [293] S. Alekhin, Phys. Rev. D63 (2001) 094022; Phys. Rev. D68 (2003) 014002.
- [294] W. Giele, S. Keller, D. Kosower. [hep-ph/0104052](#);  
M. Botje, J. Phys. G28 (2002) 779.
- [295] A. Djouadi, S. Ferrag, Phys. Lett. B586 (2004) 345.
- [296] J. Gunion, P. Kalyniak, M. Soldate, P. Galison, Phys. Rev. D34 (1986) 101.
- [297] R. Kleiss, Z. Kunszt, W.J. Stirling, Phys. Lett. B253 (1991) 269.
- [298] Z. Kunszt, Z. Trocsanyi, W.J. Stirling, Phys. Lett. B271 (1991) 247;  
J.F. Gunion, L.H. Orr, Phys. Rev. D46 (1992) 2052;  
J. Ohnemus, W.J. Stirling, Phys. Rev. D47 (1993) 336.
- [299] J. Gunion, P. Kalyniak, M. Soldate, P. Galison, Phys. Rev. Lett. 54 (1985) 1226;  
P. Agrawal, S.D. Ellis, Phys. Lett. B229 (1989) 145;  
P. Agrawal, D. Bowser-Chao, K. Cheung, Phys. Rev. D51 (1995) 6114.
- [300] H. Baer, J.D. Wells, Phys. Rev. D57 (1998) 4446;  
W. Loinaz, J.D. Wells, Phys. Lett. B445 (1998) 178.
- [301] A. Stange, W.J. Marciano, S. Willenbrock, Phys. Rev. D49 (1994) 1354; D50 (1994) 4491.
- [302] J. Gunion, T. Han, Phys. Rev. D51 (1995) 1051.
- [303] S. Mrenna, G.L. Kane. [hep-ph/9406337](#).
- [304] U. Baur, T. Han, N. Kauer, R. Sobey, D. Zeppenfeld, Phys. Rev. D56 (1997) 140.
- [305] J.F. Gunion, G. Kane, et al., Snowmass Summer Study, 1990, pp. 0059–81.
- [306] W. Furmanski, R. Petronzio, Z. Phys. C11 (1982) 293.
- [307] W.H. Furry, Phys. Rev. 51 (1937) 125.
- [308] D.A. Dicus, S.S.D. Willenbrock, Phys. Rev. D34 (1986) 148.
- [309] K. Hikasa, Phys. Rev. D29 (1984) 1939;  
R. Gonsalves, C. Hung, J. Pawlowski, Phys. Rev. D46 (1992) 4930;  
P. Rijken, W. van Neerven, Phys. Rev. D52 (1995) 149.
- [310] V. Barger, et al., Phys. Rev. Lett. 57 (1986) 1672;  
D. Dicus, C. Kao, Phys. Rev. D38 (1988) 1008;  
D. Dicus, C. Kao, Phys. Rev. D42 (1990) 2412 (Erratum).
- [311] B. Kniehl, Phys. Rev. D42 (1990) 2253.
- [312] M.L. Ciccolini, S. Dittmaier, M. Krämer, Phys. Rev. D68 (2003) 073003.
- [313] J. Kripfganz, H. Perl, Z. Phys. C41 (1988) 319;  
H. Spiesberger, Phys. Rev. D52 (1995) 4936.

- [314] W.J. Stirling, Talk given at the Workshop “Electroweak Radiative Corrections to Hadronic Observables at TeV Energies”, Durham, UK, September 2003. In a toy model, it has been shown that these effects amount to  $\mathcal{O}(1\%)$ ;  
See M. Roth, S. Weizierl, Phys. Lett. B590 (2004) 190. Recently, the QED effects have been included in the MRST set of PDFs and the fit remains essentially unchanged;  
See A.D. Martin, R.G. Roberts, W.J. Stirling, R.S. Thorne, Eur. Phys. J. C39 (2005) 155.
- [315] O. Brein, M.L. Ciccolini, S. Dittmaier, A. Djouadi, M. Krämer, R. Harlander, [hep-ph/0402003](#) and in Ref. [221].
- [316] M. Dittmar, F. Pauss, D. Zürcher, Phys. Rev. D56 (1997) 7284.
- [317] R.N. Cahn, S.D. Ellis, R. Kleiss, W.J. Stirling, Phys. Rev. D35 (1987) 1626;  
V. Barger, T. Han, R. Phillips, Phys. Rev. D37 (1988) 2005 D36 (1987) 295;  
R. Kleiss, J. Stirling, Phys. Lett. 200B (1988) 193;  
V. Barger, et al., Phys. Rev. D42 (1990) 3052;  
V. Barger, Phys. Rev. D44 (1991) 1426;  
V. Barger, Phys. Rev. D46 (1992) 2028;  
D. Froidevaux, in Ref. [213], vol. II, p. 444;  
M.H. Seymour, in Ref. [213], vol. II, p. 557;  
U. Baur, E.W.N. Glover, Phys. Lett. B252 (1990) 683.
- [318] D. Dicus, J. Gunion, R. Vega, Phys. Lett. B258 (1991) 475;  
D. Dicus, J. Gunion, L. Orr, R. Vega, Nuclear Phys. B377 (1991) 31.
- [319] V. Barger, R. Phillips, D. Zeppenfeld, Phys. Lett. B346 (1995) 106.
- [320] Y.L. Dokshitzer, S.I. Troian, V.A. Khoze, Sov. J. Nucl. Phys. 46 (1987) 712;  
J.F. Gunion, G. Kane, C.P. Yuan, H. Sadrozinski, A. Seiden, A. Weinstein, Phys. Rev. D40 (1989) 2223;  
J.D. Bjorken, Internat. J. Modern Phys. A7 (1992) 4189;  
J.D. Bjorken, Phys. Rev. D47 (1993) 101;  
K. Iordanidis, D. Zeppenfeld, Phys. Rev. D57 (1998) 3072.
- [321] D. Zeppenfeld, Collider physics, in: Lectures given at TASI98, [hep-ph/9902307](#).
- [322] D. Rainwater, Ph.D Thesis, [hep-ph/9908378](#).
- [323] D. Rainwater, D. Zeppenfeld, JHEP 9712 (1997) 005.
- [324] D. Rainwater, D. Zeppenfeld, K. Hagiwara, Phys. Rev. D59 (1999) 014037;  
T. Plehn, D. Rainwater, D. Zeppenfeld, Phys. Rev. D61 (2000) 093005; Phys. Lett. B454 (1999) 297.
- [325] D. Rainwater, D. Zeppenfeld, Phys. Rev. D60 (1999) 113004;  
N. Kauer, T. Plehn, D. Rainwater, D. Zeppenfeld, Phys. Lett. B503 (2001) 113.
- [326] For an early analysis, See: R. Kleiss, J. Stirling, Phys. Lett. 200B (1988) 193.
- [327] T. Plehn, D. Rainwater, Phys. Lett. B520 (2001) 108.
- [328] M.L. Mangano, M. Moretti, F. Piccinini, R. Pittau, A.D. Polosa, Phys. Lett. B556 (2003) 50.
- [329] J. Campbell, K. Ellis, “MCFM — Monte Carlo for FeMtobarn processes”, See the web site: <http://mcfm.fnal.gov/>.
- [330] G. Kane, W. Repko, W. Rolnick, Phys. Lett. B148 (1984) 367;  
R. Cahn, Nuclear Phys. B255 (1985) 341;  
J. Gunion, J. Kalinowski, A. Tofighi-Niaki, Phys. Rev. Lett. 57 (1986) 2351;  
J. Gunion, A. Tofighi-Niaki, Phys. Rev. D36 (1987) 2671;  
M. Bento, C.H. Llewellyn Smith, Nuclear Phys. B289 (1987) 36.
- [331] C. von Weizsäcker, Z. Phys. 88 (1934) 612;  
E. Williams, Phys. Rev. 45 (1934) 729;  
S. Brodsky, T. Kinoshita, H. Terezawa, Phys. Rev. D4 (1971) 1532.
- [332] S. Dawson, Nuclear Phys. B249 (1985) 42;  
J. Lindfors, Z. Phys. C28 (1985) 427;  
P. Johnson, F. Olness, W.K. Tung, Phys. Rev. D36 (1987) 291;  
R. Godbole, S. Rindani, Phys. Lett. 190B (1987) 192;  
R. Godbole, S. Rindani, Z. Phys. C36 (1987) 295;  
I. Kuss, H. Spiesberger, Phys. Rev. D53 (1996) 6078.
- [333] J. Gunion, G. Kane, J. Wudka, Nuclear Phys. B299 (1988) 231.
- [334] J. Stirling, R. Kleiss, S.D. Ellis, Phys. Lett. 163B (1985) 261;  
J. Gunion, Z. Kunst, M. Soldate, Phys. Lett. 163B (1985) 389;  
J. Gunion, M. Soldate, Phys. Rev. D34 (1986) 826;  
E. Glover, J. Ohnemus, S. Willenbrock, Phys. Rev. D37 (1988) 3193;  
V. Barger, G. Bhattacharya, T. Han, B. Kniehl, Phys. Rev. D43 (1991) 779.
- [335] R. Cahn, M. Chanowitz, Phys. Rev. Lett. 56 (1986) 1327.
- [336] M. Chaichian, I. Liede, J. Lindfors, D.P. Roy, Phys. Lett. B198 (1987) 416;  
D. Atwood, et al., in: R. Donaldson, M. Gilchrist (Eds.), Proceedings of the “1987 Berkeley Workshop”, World Scin., 1988, p. 20.
- [337] T. Han, B. McElrath, Phys. Lett. B528 (2002) 81.
- [338] For a discussion of the  $\mu^+\mu^-$  channel in extensions of the SM, See: V. Barger, C. Kao, Phys. Lett. B424 (1998) 69;  
S. Dawson, D. Dicus, C. Kao, Phys. Lett. B545 (2002) 132;  
E. Boos, A. Djouadi, A. Nikitenko, Phys. Lett. B578 (2004) 384.



- [339] T. Han, R.-J. Zhang, Phys. Rev. Lett. 82 (1999) 25;  
T. Han, A.S. Turcot, R.-J. Zhang, Phys. Rev. D59 (1999) 093001.
- [340] For an earlier study of  $H \rightarrow WW^*$  and for higher Tevatron energies, see Ref. [302].
- [341] A. Belyaev, T. Han, R. Rosenfeld, JHEP 0307 (2003) 021.
- [342] M. Krämer, E. Laenen, M. Spira, Nuclear Phys. B511 (1998) 523.
- [343] P.A. Baikov, V.A. Smirnov, Phys. Lett. B477 (2000) 367.
- [344] R. Harlander, Phys. Lett. B492 (2000) 74.
- [345] See also for earlier work R. Harlander, M. Steinhauser, Prog. Part. Nucl. Phys. 43 (1999) 167.
- [346] R. Harlander, W. Kilgore, Phys. Rev. D64 (2001) 013015.
- [347] S. Catani, D. de Florian, M. Grazzini, JHEP 05 (2001) 025.
- [348] S. Catani, D. de Florian, M. Grazzini, JHEP 0201 (2002) 015.
- [349] R. Harlander, W. Kilgore, [hep-ph/0211380](https://arxiv.org/abs/hep-ph/0211380).
- [350] J.C. Collins, D.E. Soper, G. Sterman, in: A.H. Mueller (Ed.), Perturbative Quantum Chromodynamics, World Scientific, Singapore, 1989.
- [351] G. Sterman, Nuclear Phys. B281 (1987) 310;  
S. Catani, L. Trentadue, Nuclear Phys. B327 (1989) 323.
- [352] G. Parisi, R. Petronzio, Nuclear Phys. B154 (1979) 427;  
G. Curci, M. Greco, Y. Srivastava, Nuclear Phys. B159 (1979) 451;  
J. Kodaira, L. Trentadue, Phys. Lett. B112 (1982) 66;  
J.C. Collins, D.E. Soper, Nuclear Phys. B193 (1981) 381;  
Y.L. Dokshitzer, D. Diakonov, S.I. Troian, Phys. Rep. 58 (1980) 269;  
J.C. Collins, D.E. Soper, G. Sterman, Nuclear Phys. B250 (1985) 199.
- [353] S. Abdullin, M. Dubinin, V. Ilyin, D. Kovalenko, V. Savrin, N. Stepanov, Phys. Lett. B431 (1998) 410.
- [354] V. Del Duca, International Workshop on QCD, Conversano, [hep-ph/0312184](https://arxiv.org/abs/hep-ph/0312184).
- [355] J. Gunion, H. Haber, F. Paige, W.-K. Tung, S. Willenbrock, Nuclear Phys. B294 (1987) 621.
- [356] W.J. Marciano, F.E. Paige, Phys. Rev. Lett. 66 (1991) 2433;  
J.F. Gunion, Phys. Lett. B261 (1991) 510.
- [357] A. Ballestrero, E. Maina, Phys. Lett. B268 (1991) 437;  
D.J. Summers, Phys. Lett. B306 (1993) 129;  
E. Richter-Was, Z. Phys. C61 (1994) 323;  
H.Y. Zhou, Y.P. Kuang, Phys. Rev. D47 (1993) 3680;  
H.Y. Zhou, Y.P. Kuang, Phys. Rev. D53 (1996) 4095;  
M. Dubinin, V. Ilyn, V. Savrin, [hep-ph/9712335](https://arxiv.org/abs/hep-ph/9712335).
- [358] J. Dai, J.F. Gunion, R. Vega, Phys. Rev. Lett. 71 (1993) 2699.
- [359] A. Ballestrero, E. Maina, Phys. Lett. B287 (1992) 231.
- [360] F. Maltoni, D. Rainwater, S. Willenbrock, Phys. Rev. D 66 (2002) 034022.
- [361] A. Belyaev, L. Reina, JHEP 0208 (2002) 041.
- [362] J. Goldstein, C.S. Hill, J. Incandela, S.J. Parke, D. Rainwater, D. Stuart, Phys. Rev. Lett. 86 (2001) 1694.
- [363] D.B. Melrose, Nuovo Cim. 40 (1965) 181;  
W.L. van Neerven, J.A. Vermaseren, Phys. Lett. B137 (1984) 241.
- [364] S. Catani, S. Dittmaier, M. Seymour, Z. Trócsányi, Nuclear Phys. B627 (2002) 189.
- [365] D. Dicus, T. Stelzer, Z. Sullivan, S. Willenbrock, Phys. Rev. D59 (1999) 094016;  
C. Balazs, H.-J. He, C.P. Yuan, Phys. Rev. D60 (1999) 114001;  
M. Spira, Plenary talk at SUSY02, [hep-ph/0211145](https://arxiv.org/abs/hep-ph/0211145);  
T. Plehn, Phys. Rev. D67 (2003) 014018;  
E. Boos, T. Plehn, Phys. Rev. D69 (2004) 094005.
- [366] J. Campbell, R.K. Ellis, F. Maltoni, S. Willenbrock, Phys. Rev. D67 (2003) 095002;  
R. Harlander, W. Kilgore, Phys. Rev. D68 (2003) 013001;  
F. Maltoni, Z. Sullivan, S. Willenbrock, Phys. Rev. D67 (2003) 093005;  
J. Campbell, et al. in Ref. [221].
- [367] J.L. Diaz-Cruz, O.A. Sampayo, Phys. Lett. B276 (1992) 211;  
W.J. Stirling, D.J. Summers, Phys. Lett. B283 (1992) 411;  
A. Ballestrero, E. Maina, Phys. Lett. B299 (1993) 312;  
G. Bordes, B. van Eijk, Phys. Lett. B299 (1993) 315.
- [368] F. Maltoni, K. Paul, T. Stelzer, S. Willenbrock, Phys. Rev. D64 (2001) 094023.
- [369] S.S. Willenbrock, D.A. Dicus, Phys. Rev. D34 (1986) 155;  
C.P. Yuan, Phys. Rev. D41 (1990) 42;  
R.K. Ellis, S. Parke, Phys. Rev. D46 (1992) 3785;  
S. Cortese, R. Petronzio, Phys. Lett. B253 (1991) 494;  
T. Stelzer, S. Willenbrock, Phys. Lett. B357 (1995) 125;  
A.P. Heinson, A.S. Belyaev, E.E. Boos, Phys. Rev. D56 (1997) 3114;  
T. Stelzer, Z. Sullivan, S. Willenbrock, Phys. Rev. D58 (1998) 094021.
- [370] G. Cynolter, E. Lendvai, G. Pocsik, Acta Phys. Polon. B31 (2000) 1749.



- [371] S. Dawson, S. Dittmaier, M. Spira, Phys. Rev. D58 (1998) 115012.
- [372] T. Stelzer, W.F. Long, Comput. Phys. Commun. 81 (1994) 357;  
F. Maltoni, T. Stelzer, JHEP 0302 (2003) 027.
- [373] V.A. Khoze, A.D. Martin, M.G. Ryskin, Eur. Phys. J. C23 (2002) 311;  
V.A. Khoze, A.D. Martin, M.G. Ryskin, Eur. Phys. J. C34 (2004) 327;  
B.E. Cow, et al., Phys. Rev. D68 (2003) 075004.
- [374] M. Boonekamp, R. Peschanski, C. Royon, Phys. Lett. B599 (2004) 236. In which a detailed MC analysis of signal, backgrounds and detector effects has been performed for the double exclusive diffraction process and it is shown that  $S/B \sim 1$  can be achieved for  $M_H = 120\text{GeV}$  and a missing mass resolution of 1 GeV.
- [375] M. Boonekamp, R. Peschanski, A. de Roeck, C. Royon, Phys. Lett. B550 (2002) 93.
- [376] T. Affolder, et al., (CDF Collaboration), Phys. Rev. Lett. 84 (2000) 5043.
- [377] Z. Kunszt, J. Stirling, in Ref. [213];  
Z. Kunszt, S. Moretti, W.J. Stirling, Z. Phys. C74 (1997) 479.
- [378] M. Spira, [hep-ph/9711394](#); [hep-ph/9810289](#);  
A. Djouadi, Pramana 60 (2003) 215. [hep-ph/0205248](#); Pramana 62 (2004) 191. [hep-ph/0303097](#);  
Plenary talk given at the conference “Physics at the LHC” in Ref. [201]. [hep-ph/0412238](#).
- [379] T. Sjöstrand, PYTHIA, Comput. Phys. Comm. 82 (1994) 74.
- [380] G. Corcella, et al., HERWIG, JHEP 01 (2001) 010. [hep-ph/0011363](#); [hep-ph/0107071](#); [hep-ph/0201201](#); [hep-ph/0210213](#).
- [381] E. Richter-Was, D. Froidevaux, L. Poggioli, ATLAS Note ATL-PHYS-98-131.
- [382] S. Abdullin, A. Khanov, N. Stepanov, CMS Note-1994/180; for the CMS Simulation Package. See: <http://cmsdoc.cern.ch/cmsim/cmsim.html>.
- [383] After completing this work, we received the paper, *Higgs bosons searches at hadron colliders* by V. Büscher and K. Jakobs (to appear in Modern Phys. Lett. A), where the recent experimental analyses of the various channels for Higgs detection at the Tevatron and the LHC have been reviewed and where complementary material can be found. We thank Karl Jakobs for pointing this review to us.
- [384] S. Catani, M. Dittmar, D. Soper, W.J. Stirling, S. Tapprogge, (conv.) et al., Report of the QCD Working Group at the Workshop “Standard Model physics (and more) at the LHC”, CERN Geneva 1999. [hep-ph/0005025](#).
- [385] See e.g. the proceedings of the SM/QCD working groups at the three Les Houches Workshops: S. Catani et al., [hep-ph/0005114](#);  
W. Giele, et al., [hep-ph/0204316](#);  
M. Dobbs et al., [hep-ph/0403045](#); [hep-ph/0403100](#).
- [386] D. Rainwater, M. Spira, D. Zeppenfeld in Ref. [221].
- [387] R.K. Ellis, S. Veseli, Phys. Rev. D60 (1999) 011501;  
R.K. Ellis, S. Veseli, Nuclear Phys. B511 (1998) 649;  
J.M. Campbell, R.K. Ellis, Phys. Rev. D62 (2000) 114012;  
J.M. Campbell, R.K. Ellis, Phys. Rev. D65 (2002) 113007.
- [388] F. Berends, H. Kuijf, B. Tausk, W. Giele, Nuclear Phys. B357 (1991) 32;  
W. Giele, E. Glover, D. Kosower, Nuclear Phys. B403 (1993) 633;  
C. Balazs, C.-P. Yuan, Phys. Rev. D56 (1997) 5558.
- [389] J. Smith, D. Thomas, W.L. van Neerven, Z. Phys. C44 (1989) 267;  
B. Mele, P. Nason, G. Ridolfi, Nuclear Phys. B357 (1991) 409;  
S. Frixione, P. Nason, G. Ridolfi, Nuclear Phys. B383 (1992) 3;  
J. Ohnemus, J.F. Owens, Phys. Rev. D43 (1991) 3626;  
J. Ohnemus, Phys. Rev. D44 (1991) 1403;  
J. Ohnemus, Phys. Rev. D44 (1991) 3477;  
J. Ohnemus, Phys. Rev. D47 (1992) 940;  
S. Frixione, Nuclear Phys. B410 (1993) 280;  
U. Baur, T. Han, J. Ohnemus, Phys. Rev. D48 (1993) 5140;  
U. Baur, T. Han, J. Ohnemus, Phys. Rev. D51 (1995) 3381;  
U. Baur, T. Han, J. Ohnemus, Phys. Rev. D48 (1996) 1098;  
U. Baur, T. Han, J. Ohnemus, Phys. Rev. D57 (1998) 2823;  
L.J. Dixon, Z. Kunszt, A. Signer, Phys. Rev. D60 (1999) 114037.
- [390] E. Glover, J. van der Bij, Nuclear Phys. B321 (1989) 561; Phys. Lett. B219 (1991) 488;  
E. Richter-Was, Z. Phys. C64 (1994) 227;  
C. Zecher, T. Matsuura, J.J. van der Bij, Z. Phys. C64 (1994) 219;  
D. Kominis, V. Koulovassilopoulos, Phys. Rev. D52 (1995) 2737;  
C. Balazs, C.-P. Yuan, Phys. Rev. D59 (1999) 114007;  
K.L. Adamson, D. de Florian, A. Signer, Phys. Rev. D65 (2002) 094041.
- [391] S. Dawson, P. Nason, R.K. Ellis, Nuclear Phys. B303 (1988) 607;  
S. Dawson, P. Nason, R.K. Ellis, Nuclear Phys. B327 (1989) 49;  
W. Beennakker, H. Kuijf, W. van Neerven, J. Smith, Phys. Rev. D40 (1989) 54;  
For later developments, see the review of S. Frixione, M. Mangano, P. Nason and G. Ridolfi. [hep-ph/9702287](#);  
See also N. Kauer, D. Zeppenfeld, Phys. Rev. D65 (2002) 014021.
- [392] See the site: <http://www.physics.rutgers.edu/~jconway/soft/shw/shw.html>.

- [393] P. Bhat, R. Gilmartin, H. Prosper, Phys. Rev. D62 (2000) 074022.
- [394] For an updated analysis, see: E. Boos et al. in Ref. [221].
- [395] D. Froidevaux, E. Richter-Was, Z. Phys. C67 (1995) 213.
- [396] E. Richter-Was, Acta. Phys. Polon. B31 (2000) 1931 and ATL-PHYS-2000-023.
- [397] B.P. Kersevan, E. Richter-Was, Eur. Phys. J. C25 (2002) 379;  
V. Drollinger, T. Muller, D. Denegri, CMS-Note-2002/006;  
V. Drollinger, Ph.D. Thesis, University of Karlsruhe, 2001.
- [398] M. Golden, S. Sharpe, Nuclear Phys. B261 (1985) 217;  
V. Barger, T. Han, Phys. Lett. B212 (1988) 117.
- [399] V. Cavasinni, D. Costanzo, ATL-PHYS-2000-013;  
K. Jakobs, ATL-PHYS-2000-008.
- [400] M. Dubinin, et al., CMS-NOTE-1997-101.
- [401] M. Dzelalija, Z. Antunovic, D. Denegri, R. Kinnunen, CMS-TN 96-091;  
G. Eynard, Etude de la production associée du boson de Higgs  $WH, t\bar{t}H$  avec  $H \rightarrow \gamma\gamma$  avec le detecteur ATLAS, Ph.D. Thesis, 1997, LAPP–Annecy.
- [402] O. Ravat, M. Lethuillier in Ref. [221].
- [403] L. Fayard, G. Unal, EAGLE internal note PHYS-NO-NO-001, 1992;  
C. Seez, CMS-TN/94-289, 1994;  
D. Froidevaux, F. Gianotti, E. Richter Was, ATLAS Note PHYS-NO-064, 1995;  
F. Gianotti, I. Vichou, ATLAS Note PHYS-NO-078, 1996;  
V. Tisserand, Ph.D. Thesis, 1997, LAL 97-01;  
K. Lassila–Perini, Ph.D. Thesis, 1998, ETH no. 12961;  
M. Wielers, ATL-PHYS-2002-004.
- [404] E.L. Berger, E. Braaten, R.D. Field, Nuclear Phys. B239 (1984) 52;  
P. Aurenche, A. Douiri, R. Baier, M. Fontannaz, D. Schiff, Z. Phys. C29 (1985) 459;  
L. Ametller, E. Gava, N. Paver, D. Treleani, Phys. Rev. D32 (1985) 1699;  
D.A. Dicus, S.S.D. Willenbrock, Phys. Rev. D37 (1988) 1801;  
B. Bailey, J.F. Owens, J. Ohnemus, Phys. Rev. D46 (1992) 2018;  
B. Bailey, J.F. Owens, Phys. Rev. D47 (1993) 2735;  
Z. Bern, L. Dixon, D.A. Kosower, Phys. Rev. Lett. 70 (1993) 2677;  
C. Balazs, E.L. Berger, S. Mrenna, C.-P. Yuan, Phys. Rev. D57 (1998) 6934;  
D. de Florian, Z. Kunszt, Phys. Lett. B460 (1999) 184;  
C. Balazs, P. Nadolsky, C. Schmidt, C.-P. Yuan, Phys. Lett. B489 (2000) 157;  
T. Binoth, J.P. Guillet, E. Pilon, M. Werlen, Phys. Rev. D63 (2001) 114016;  
T. Binoth, [arXiv:hep-ph/0005194](https://arxiv.org/abs/hep-ph/0005194);  
Z. Bern, A. De Freitas, L.J. Dixon, JHEP 0109 (2001) 037;  
C. Anastasiou, E.W.N. Glover, M.E. Tejeda-Yeomans, Nuclear Phys. B629 (2002) 255;  
Z. Bern, L.J. Dixon, C. Schmidt, Phys. Rev. D66 (2002) 074018.
- [405] T. Binoth, J.P. Guillet, E. Pilon, M. Werlen, Eur. Phys. J. C16 (2000) 311.
- [406] J.C. Cholle, et al. ATLAS PHYS-NO-17, 1992;  
L. Poggioli, ATLAS PHYS-NO-066, 1995;  
D. Denegri, R. Kinnunen, G. Roulet, CMS-TN/93-101, 1993;  
I. Iashvili, R. Kinnunen, A. Nikitenko, D. Denegri, CMS TN/95-076;  
D. Bomestar, et al., Note CMS TN-1995/018;  
C. Charlot, A. Nikitenko, I. Puljak, CMS TN/95-101;  
G. Martinez, E. Gross, G. Mikenberg, L. Zivkovic, ATLAS ATL-PHYS-2003-001.
- [407] For recent studies using the new software, see the talks of S. Hassani, T. Lagouri and M. Sani, at the Conference “Physics at LHC” in Ref. [201].
- [408] G. Zuckerman, et al., ATLAS Internal Note PHYS-NO-007, 1992;  
M. Bosman, M. Nessi, ATLAS Note PHYS-NO-050, 1994;  
N. Stepanov, CMS-TN/93-87, 1993.
- [409] Ph. Mine, S. Moreau, I. Puljak, CMS Note 1999/071;  
I. Puljak, Ph.D Thesis, Ecole Polytechnique, 2000.
- [410] M. Dittmar, H. Dreiner, Phys. Rev. D55 (1997) 167;  
M. Dittmar, [hep-ex/9901009](https://arxiv.org/abs/hep-ex/9901009).
- [411] D. Green, et al., J. Phys. G26 (2000) 1751;  
K. Jakobs, Th. Trefzger, ATLAS Note ATL–PHYS–2003–024.
- [412] M.J. Duncan, Phys. Lett. 179B (1986) 393;  
A. Abbasabadi, W.W. Repko, Nuclear Phys. B292 (1987) 461;  
T. Matsuura, J. van der Bij, Z. Phys. C51 (1991) 259;  
M.J. Duncan, M.H. Reno, Phys. Rev. D56 (1997) 3129.

- [413] S. Zmushko, et al. ATLAS Internal Note PHYS-NO-008, 1992;  
S. Abdullin, N. Stepanov, CMS-TN/94-178, 1994.
- [414] E. Richter-Was, T. Szymocha, ATL-PHYS-2004-012;  
S. Mrenna, Talk given at the GDR–Supersymétrie, Lyon 2002.
- [415] D. Dicus, A. Stange, S. Willenbrock, Phys. Lett. B333 (1994) 126.
- [416] For an early study, see K. Gaemers, F. Hoogeveen, Phys. Lett. 146B (1984) 347.
- [417] G. Kane, G.A. Ladinsky, C.P. Yuan, Phys. Rev. D45 (1991) 124;  
C. Schmidt, M. Peskin, Phys. Rev. Lett. 69 (1992) 410;  
W. Bernreuther, A. Brandenburg, Phys. Lett. B314 (1993) 104;  
A. Pilaftsis, M. Nowakowski, Internat. J. Modern Phys. A9 (1994) 1097;  
W. Bernreuther, M. Flesch, P. Haberl, Phys. Rev. D58 (1998) 114031;  
W. Khater, P. Osland, Nuclear Phys. B661 (2003) 209.
- [418] For a review of CP-violation in the top quark sector and a complete set of references, See: D. Atwood, S. Bar-Shalom, G. Eilam, A. Soni, Phys. Rep. 347 (2001) 1.
- [419] G. Azuelos, et al. in Ref. [220].
- [420] M. Klute, ATLAS Note ATL-PHYS-2002-018, 2002;  
G. Azuelos, R. Mazini, ATL-PHYS-2003-004.
- [421] R. Decker, S. Jadach, M. Jezabek, J.H. Kühn, Z. Was, Comput. Phys. Comm. 76 (1993) 361;  
R. Decker, S. Jadach, M. Jezabek, J.H. Kühn, Z. Was, Comput. Phys. Comm. 70 (1992) 69;  
R. Decker, S. Jadach, M. Jezabek, J.H. Kühn, Z. Was, Comput. Phys. Comm. 64 (1991) 275.
- [422] M. Dubinin, CMS–NOTE–2001/022. For an ATLAS analysis, See: K. Cranmer, B. Mellado, W. Quayle and S.L. Wu, ATLAS Note ATL-PHYS-2003-036. [hep-ph/0401088](http://hep-ph/0401088), 2003.
- [423] C. Buttar, K. Jakobs, R. Harper, ATL-PHYS-2002-033;  
N. Akchurin, et al., CMS–NOTE–2002/016;  
K. Cranmer, B. Mellado, W. Quayle, S.L. Wu, ATLAS Notes ATL-PHYS-2003-007 and ATL-PHYS-2003-008. A study has been performed for CMS in N. Akchurin et al., CMS–NOTE–2002/016.
- [424] M. Dittmar, Pramana 55 (2000) 151;  
M. Dittmar, S. Nicollerat, CMS–Note 2001/036.
- [425] H.D. Yildiz, M. Zeyrek, R. Kinnunen, CMS–NOTE–2001/050;  
H.D. Yildiz, Ph.D. Thesis, Ankara, 2002.
- [426] K. Cranmer, B. Mellado, W. Quayle, S.L. Wu, Note ATL-PHYS-2004-005 and in Ref. [221];  
Michael Dührssen, Ph.D. Thesis.
- [427] K. Jacobs, private communications to the authors. We thank Tilman Plehn for pointing this feature to us and for other discussions on the vector boson fusion process.
- [428] E. Richter-Was, M. Sapinski, Acta. Phys. Polon. B30 (1999) 1001;  
V. Drollinger, T. Muller, D. Denegri, CMS-Note-2002/054. [hep-ph/0111312](http://hep-ph/0111312);  
J. Cammin, M. Schumacher, ATL-PHYS-2000-013;  
D. Green, K. Maeshima, R. Vidal, W. Wu, S. Kunori, CMS–NOTE–2001/039.
- [429] D. Benedetti, L. Fano, CMS–NOTE–2002/044.
- [430] J. Leveque, J.B. de Vivie, V. Kostikhine, A. Rozanov, ATL-PHYS-2002-019.
- [431] K. Cranmer, B. Mellado, W. Quayle, S.L. Wu, [hep-ph/0307242](http://hep-ph/0307242).
- [432] G. Davatz, G. Dissertori, M. Dittmar, M. Grazzini, F. Pauss, JHEP 0405 (2004) 009.
- [433] V. Drollinger, A. Sopczak, Eur. Phys. J. direct C3 (2001) N1;  
M. Hohfeld, ATLAS Note ATL-Phys-2001-004.
- [434] F. Gianotti, M. Pepe–Altarelli, Nucl. Phys. Proc. Suppl. 89 (2000) 177.
- [435] L. Landau, Dokl. Akad. Nauk. Ser. Fiz. 60 (1948) 207;  
C.N. Yang, Phys. Rev. 77 (1950) 242;  
N. Kroll, W. Wada, Phys. Rev. 98 (1955) 1355;  
R. Plano, A. Prodel, N. Samios, M. Schwartz, J. Steinberger, Phys. Rev. Lett. 3 (1959) 525.
- [436] C. Buszello, I. Fleck, P. Marquard, J. van der Bij, Eur. Phys. J. C32 (2004) 209.
- [437] T. Plehn, D. Rainwater, D. Zeppenfeld, Phys. Rev. Lett. 88 (2002) 051801.
- [438] K. Odagiri, JHEP 0303 (2003) 009.
- [439] J. Gunion, L. Poggiali, R. van Kooten, C. Kao, P. Rowson, et al., Higgs boson discovery and properties, 1996 DPF/DPB Snowmass study. [hep-ph/9703330](http://hep-ph/9703330).
- [440] J.F. Gunion, X.G. He, Phys. Rev. Lett. 76 (1996) 4468;  
J.F. Gunion, J. Pliska, Phys. Lett. B444 (1998) 136.
- [441] B. Field, Phys. Rev. D66 (2002) 114007.
- [442] J.R. Ellis, J.S. Lee, A. Pilaftsis, [hep-ph/0502251](http://hep-ph/0502251).
- [443] D. Zeppenfeld, R. Kinnunen, A. Nikitenko, E. Richter-Was, Phys. Rev. D62 (2000) 013009 and in Ref. [219].
- [444] M. Dührssen, S. Heinemeyer, H. Logan, D. Rainwater, G. Weiglein, D. Zeppenfeld, Phys. Rev. D70 (2004) 113009 and in Ref. [221].
- [445] M. Dührssen, ATLAS Note PHYS-2003-030 and talk given in Ref. [201].
- [446] J. Conway, et al., The precision Higgs working group of Snowmass 2001 in Ref. [204]. [hep-ph/0203206](http://hep-ph/0203206).

- [447] U. Baur, T. Plehn, D.L. Rainwater, Phys. Rev. D69 (2004) 053004.
- [448] U. Baur, T. Plehn, D.L. Rainwater, Phys. Rev. Lett. 89 (2002) 151801;  
U. Baur, T. Plehn, D.L. Rainwater, Phys. Rev. D67 (2003) 033003.
- [449] U. Baur, T. Plehn, D.L. Rainwater, Phys. Rev. D68 (2003) 033011.
- [450] R. Lafaye, D. Miller, M. Muhlleitner, S. Moretti, [hep-ph/0002238](#) and Ref. [220].
- [451] M. Moretti, M. Moretti, F. Piccinini, R. Pita, A. Polosa, [hep-ph/0410334](#).
- [452] F.M. Renard, Basics of electron–positron collisions, Ed. Frontières, Gif–sur–Yvette, France, 1981;  
P.M. Zerwas, Physics with an  $e^+e^-$  linear collider at high luminosity, in: J.J. Aubert, et al. (Eds.), Particle Physics: Ideas and Recent Developments, Kluwer Academic Publishers, Amsterdam, 1999.
- [453] See the web site: <http://www.interactions.org/linearcollider/>.
- [454] J. Andruskow, et al. R. Brinkmann et al. (Eds.), TESLA Technical Design Report, Part II, The Accelerator, DESY 2001-011, Zeroth Order Design Report for the Next Linear Collider, SLAC Report 474, 1996; 2001 Report on the Next Linear Collider, Fermilab-Conf-01-075-E; N. Akasaka et al., JLC Design Study Group, KEK-Report 97-1.
- [455] R.W. Assmann, et al., A 3-TeV  $e^+e^-$  linear collider based on CLIC technology, Report CERN-2000-008, Ed. G. Guignard.
- [456] J. Aguilar-Saavedra, et al. R. Heuer, D. Miller, F. Richard, P. Zerwas, (Eds.), TESLA TDR Part III, Physics at an  $e^+e^-$  Linear Collider, [hep-ph/0106315](#).
- [457] The LC notes on the ECFA–DESY Workshops used for the TESLA report and after can be found at: <http://www.desy.de/lcnotes>.
- [458] T. Abe, et al., Linear collider physics resource book for snowmass, [hep-ex/0106055-58](#).
- [459] K. Abe, et al., Particle Physics Experiments at JLC, [hep-ph/0109166](#).
- [460] M. Battaglia, A. de Roeck, J. Ellis, and D. Schulte (Eds.), Physics at the CLIC multi-TeV Linear Collider, CERN Report CERN–2004–005, [hep-ph/0412251](#), June 2004.
- [461] See e.g. G. Moortgat-Pick, et al. [hep-ph/0210212](#);  
G. Moortgat-Pick, [hep-ph/0410118](#).
- [462] See section 5.1 of Ref. [456].
- [463] I. Ginzburg, G. Kotkin, V. Telnov, Pisma ZhETF 34 (1981) 514; JETP Lett. 34 (1982) 491;  
I. Ginzburg, G. Kotkin, V. Serbo, V. Telnov, Nucl. Instrum. Methods 205 (1983) 47;  
V. Telnov, Nucl. Instrum. Methods A472 (2001) 43.
- [464] I. Ginzburg, G. Kotkin, S. Panfil, V. Serbo, V. Telnov, Nucl. Instrum. Methods A219 (1984) 5.
- [465] J.F. Gunion, H.E. Haber, Proceedings of the 1990 Snowmass Study, p. 206;  
T. Barklow, Proceedings of the 1990 Snowmass Study, p. 440;  
J.F. Gunion, H.E. Haber, Phys. Rev. D48 (1993) 5109;  
S. Brodsky, P.M. Zerwas, Nucl. Instrum. Methods A355 (1995) 19;  
M. Baillargeon, G. Bélanger, F. Boudjema, Phys. Rev. D51 (1995) 4712;  
A. Djouadi, V. Driesen, W. Hollik, J.I. Illana, Eur. Phys. J. C1 (1998) 149;  
M. Melles, W.J. Stirling, V.A. Khoze, Phys. Rev. D61 (2000) 054015;  
S. Soldner-Rembold, G. Jikia, Nucl. Instrum. Methods A472 (2001) 133.
- [466] D.L. Borden, D.A. Bauer, D.O. Caldwell, Phys. Rev. D48 (1993) 4018.
- [467] B. Badelek, et al. [hep-ph/0108012](#);  
A. de Roeck, [hep-ph/0311138](#);  
E. Boos, et al., Nucl. Instrum. Methods A472 (2001) 100;  
D. Asner, et al. [hep-ph/0308103](#).
- [468] M.M. Velasco, et al.,  $\gamma\gamma$  and  $e\gamma$  Colliders with energies below a TeV, [hep-ex/0111055](#);  
D. Asner, J. Gronberg, J.F. Gunion, Phys. Rev. D67 (2003) 035009.
- [469] J. Illana, [hep-ph/9912467](#).
- [470] G.I. Budker, Proceedings of the “7th Conference on High Energy Accelerators”, Yerevan, 1969 and extract from AIP Conf. Proc. 352, 1996, p. 4;  
A.N. Skrinsky, Proceedings of the “International Seminar on Prospects in High Energy Physics”, Morges, 1971 and extract from AIP Conf. Proc. 352, 1996, p. 6;  
G.I. Budker, A.N. Skrinsky, Sov. Phys. Usp. 21 (1978) 277;  
D. Cline, D. Neuffer, extracts from AIP Conf. Proc., 68, 1980, p. 846 and AIP Conf. Proc. 352, 1996, p. 10.
- [471] The Working Group on  $\mu^+\mu^-$  Collider Feasibility Study, Reports BNL–52503, FNAL Conf–96/092 and LBNL–389446, 1996; S. Geer, R. Raja (Eds.), Proceedings of the Workshop on Physics at the First Muon Collider and at the front end of the Muon Collider, 6–9 Nov 1997, Batavia, IL, USA (AIP Conf. Proc. 435). See also the web site of the Neutrino factory and Muon Collider Collaboration: <http://www.cap.bnl.gov/mumu>.
- [472] C.M. Ankenbrandt, et al., Phys. Rev. ST Accel. Beams 2 (1999) 081001.
- [473] B. Autin, A. Blondel and J. Ellis (conv.) et al., Proceedings of the “Workshop Prospective Study of Muon Storage Rings at CERN”, CERN Report 99–02, 1999.
- [474] V. Barger, M.S. Berger, J.F. Gunion, T. Han, Phys. Rep. 286 (1997) 1.
- [475] J.F. Gunion, [hep-ph/9707379](#).
- [476] V.D. Barger, M. Berger, J.F. Gunion, T. Han, Proc. of the APS/DPF/DPB 2001 Snowmass Study, [hep-ph/0110340](#);  
J. Gunion, [hep-ph/9802258](#).
- [477] C. Blöchliger, et al., Proceedings of the CERN Workshop “Physics Opportunities at  $\mu^+\mu^-$  Higgs Factories”. [hep-ph/0202199](#).

- [478] S. Dawson, J.L. Rosner, Phys. Lett. B 148 (1984) 497.
- [479] K. Hikasa, Phys. Lett. 164B (1985) 385 and (E);  
K. Hikasa, Phys. Lett. 195B (1987) 623.
- [480] W. Kilian, M. Kramer, P.M. Zerwas, [hep-ph/9605437](#).
- [481] K. Gaemers, G. Gounaris, Phys. Lett. B 77 (1978) 379.
- [482] A. Djouadi, J. Kalinowski, P.M. Zerwas, Modern Phys. Lett. A 7 (1992) 1765;  
A. Djouadi, J. Kalinowski, P.M. Zerwas, Z. Phys. C 54 (1992) 255.
- [483] G. Gounaris, D. Schildknecht, F.M. Renard, Phys. Lett. B 83 (1979) 191;  
E.W.N. Glover, A.D. Martin, Phys. Lett. B 226 (1989) 393.
- [484] A. Djouadi, W. Kilian, M.M. Muhlleitner, P.M. Zerwas, Eur. Phys. J. C 10 (1999) 27;  
A. Djouadi, W. Kilian, M.M. Muhlleitner, P.M. Zerwas, [hep-ph/0001169](#).
- [485] A. Barroso, J. Pulido, J.C. Romao, Nuclear Phys. B 267 (1986) 509;  
A. Abbasabadi, D. Bowser-Chao, D.A. Dicus, W. Repko, Phys. Rev. D 52 (1995) 3919;  
A. Djouadi, V. Driesen, W. Hollik, J. Rosiek, Nuclear Phys. B 491 (1997) 68.
- [486] K. Gaemers, F. Hoogeveen, Z. Phys. C 26 (1984) 249;  
A. Djouadi, V. Driesen, C. Junger, Phys. Rev. D 54 (1996) 759.
- [487] V. Barger, T. Han, A. Stange, Phys. Rev. D 42 (1990) 777.
- [488] M. Baillargeon, F. Boudjema, F. Cuypers, E. Gabrielli, B. Mele, Nuclear Phys. B 424 (1994) 343.
- [489] E. Boos, et al., Phys. Lett. B 273 (1991) 173;  
K. Hagiwara, I. Watanabe, P.M. Zerwas, Phys. Lett. 278B (1992) 187.
- [490] V.D. Barger, M.S. Berger, J.F. Gunion, T. Han, Phys. Rev. Lett. 75 (1995) 1462.
- [491] For earlier reviews on  $e^+e^-$  physics, see for instance: S. Dawson, M. Oreglia, [hep-ph/0403015](#);  
J. Gunion, H. Haber, R. Van Kooten, [hep-ph/0301023](#);  
P. Derwent, et al., [hep-ex/0107044](#);  
J. Bagger, et al., [hep-ex/0007022](#);  
E. Accomando, Phys. Rept. 299 (1998) 1;  
P.M. Zerwas, Acta Phys. Polon. B 30 (1999) 1871;  
H. Murayama, M. Peskin, Ann. Rev. Nucl. Part. Sci. 46 (1996) 533;  
P.M. Zerwas, et al., [hep-ph/9605437](#).
- [492] P.M. Zerwas, et al., Proceedings of the ECFA–DESY Workshops  $e^+e^-$  collisions at TeV energies: The physics Potential, DESY-92-123A-B (1991), DESY-92-123C (1993) and DESY-96-123D (1996).
- [493] J. Fleischer, F. Jegerlehner, Nuclear Phys. B 216 (1983) 469;  
B. Kniehl, Z. Phys. C 55 (1992) 605;  
A. Denner, J. Küblbeck, R. Mertig, M. Böhm, Z. Phys. C 56 (1992) 261.
- [494] A. Denner, S. Dittmaier, M. Roth, M.M. Weber, Nuclear Phys. B 660 (2003) 289.
- [495] G. Bélanger, F. Boudjema, J. Fujimoto, T. Ishikawa, T. Kaneko, K. Kato, Y. Shimizu, Phys. Lett. B 559 (2003) 252.
- [496] F. Jegerlehner, O. Tarasov, Nucl. Phys. Proc. Suppl. 116 (2003) 83.
- [497] F. Boudjema, J. Fujimoto, T. Ishikawa, T. Kaneko, K. Kato, Y. Kurihara, Y. Shimizu, Y. Yasui, Phys. Lett. B 600 (2004) 65.
- [498] S. Dittmaier, M. Krämer, Y. Liao, M. Spira, P.M. Zerwas, Phys. Lett. B 478 (2000) 247;  
S. Dittmaier, M. Krämer, Y. Liao, M. Spira, P.M. Zerwas, Phys. Lett. B 441 (1998) 383.
- [499] S. Zhu, [hep-ph/0212273](#);  
For the correction to the dominant channel see also: S. Dawson, L. Reina, Phys. Rev. D 57 (1998) 5851;  
S. Dawson, L. Reina, Phys. Rev. D 59 (1999) 054012.
- [500] G. Bélanger, F. Boudjema, J. Fujimoto, T. Ishikawa, T. Kaneko, K. Kato, Y. Shimizu, Y. Yasui, Phys. Lett. B 571 (2003) 163.
- [501] A. Denner, S. Dittmaier, M. Roth, M.M. Weber, Phys. Lett. B 575 (2003) 290.
- [502] Y. You, W.G. Ma, H. Chen, R.Y. Zhang, Y.B. Sun, H.S. Hou, Phys. Lett. B 571 (2003) 85.
- [503] G. Bélanger, F. Boudjema, J. Fujimoto, T. Ishikawa, T. Kaneko, Y. Kurihara, K. Kato, Y. Shimizu, Phys. Lett. B 576 (2003) 152.
- [504] T. Zhang, W. Ma, H. Chen, Y. Sun, H. Hou, Phys. Lett. B 578 (2004) 349.
- [505] F. Boudjema, et al. as reported by Y. Yasue in the talk given at the ECFA Workshop on  $e^+e^-$  colliders, Durham, September 2004.
- [506] J. Fujimoto, et al., Acta Phys. Polon. B 28 (1997) 945;  
F. Yuasa, et al., Prog. Theor. Phys. Suppl. 138 (2000) 18;  
G. Bélanger, et al. [hep-ph/0308080](#).
- [507] M. Tentyukov, J. Fleischer, Comput. Phys. Commun. 132 (2000) 124.
- [508] J. Küblbeck, M. Böhm, A. Denner, Comput. Phys. Commun. 60 (1990) 165;  
J. Küblbeck, M. Böhm, A. Denner, Comput. Phys. Commun. 64 (1991) 345;  
T. Hahn, Comput. Phys. Commun. 140 (2001) 418.
- [509] T. Hahn, M. Perez-Victoria, Comput. Phys. Commun. 118 (1999) 153.
- [510] J.A.M. Vermaseren, [math-ph/0010025](#).



- [511] K. Hagiwara, M.L. Stong, Z. Phys. C 62 (1994) 99;  
B. Grzadkowski, J. Wudka, Phys. Lett. B 364 (1995) 49;  
G. Gounaris, J. Layssac, F.M. Renard, Z. Phys. C 65 (1995) 245;  
A. Skjold, P. Osland, Nuclear Phys. B 453 (1995) 3;  
J.P. Ma, B. McKellar, Phys. Rev. D 52 (1995) 22;  
G. Gounaris, F.M. Renard, N. Vlachos, Nuclear Phys. B 459 (1996) 51;  
W. Kilian, M. Krämer, P. Zerwas, Phys. Lett. B 381 (1996) 243;  
G. Mahlon, S.J. Parke, Phys. Rev. D 58 (1998) 054015;  
T. Han, J. Jiang, Phys. Rev. D 63 (2001) 096007;  
M. Dova, S. Ferrari, Phys. Lett. B 605 (2005) 376.
- [512] D.J. Miller, S.Y. Choi, B. Eberle, M. Muhlleitner, P. Zerwas, Phys. Lett. B 505 (2001) 149.
- [513] R.L. Kelly, T. Shimuda, Phys. Rev. D 23 (1981) 1940;  
R.M. Godbole, P. Roy, Phys. Rev. Lett. 50 (1983) 717;  
P. Kalyniak, J.N. Ng, P. Zakarauskas, Phys. Rev. D 29 (1984) 502;  
J.C. Romão, A. Barroso, Phys. Lett. B 185 (1987) 195;  
Z. Kunszt, J. Stirling, Phys. Lett. B 242 (1990) 507;  
N. Brown, Z. Phys. C 49 (1991) 657;  
V. Barger, K. Whisnant, Phys. Rev. D 43 (1991) 1443.
- [514] K. Hagiwara, S. Ishihara, J. Kamoshita, B. Kniehl, Eur. Phys. J. C 14 (2000) 457.
- [515] A. Djouadi, P.M. Zerwas, J. Zunft, Phys. Lett. B 259 (1991) 175.
- [516] B. Grzadkowski, J.F. Gunion, X. He, Phys. Rev. Lett. 77 (1996) 5172;  
J.F. Gunion, X. He. [hep-ph/9703330](#).
- [517] A. Djouadi, H.E. Haber, P.M. Zerwas, Phys. Lett. B 375 (1996) 203;  
P. Osland, P.N. Pandita, Phys. Rev. D 59 (1999) 055013;  
D.J. Miller, S. Moretti, Eur. Phys. J. C 13 (2000) 459;  
V. Barger, et al., Phys. Rev. D 67 (2003) 115001.
- [518] F. Boudjema, E. Chopin, Z. Phys. C 73 (1996) 85.
- [519] W. Kilian, LC-TOOL-2001-039;  
M. Moretti, T. Ohl, J. Reuter. [hep-ph/0102195](#).
- [520] V. Ilyin, A. Pukhov, Y. Kurihara, Y. Shimizu, T. Kaneko, Phys. Rev. D 54 (1996) 6717.
- [521] A. Pukhov, et al., CompHEP. [hep-ph/9908288](#).
- [522] A. Gutierrez-Rodriguez, M.A. Hernandez-Ruiz, O.A. Sampayo. [hep-ph/0302120](#).
- [523] M. Battaglia, E. Boos, W.M. Yao. [hep-ph/0111276](#) and in Ref. [460].
- [524] S. Moretti, HERWIG: An event generator for  $e^+e^-$  Linear Colliders. [hep-ph/0209209](#).
- [525] P. Janot, HZHA in Physics at LEP2, CERN 96-01, vol. 2, p. 309.
- [526] T. Ohl, CIRCE, Comput. Phys. Commun. 101 (1997) 269.
- [527] M. Pohl, H.J. Schreiber, SIMDET, LC-DET-2002-005.
- [528] T. Behnke, et al., BRAHMS, LC-TOOL-2001-005.
- [529] For a comparison of various event generators and fast detector simulation programs, see M. Ronan, Multi-Jet Higgsstrahlung Analysis, LC-PHSM-2003-048, 2003, in Ref. [457].
- [530] K. Desch, et al. Report of the Higgs Working Group for the Extended ECFA–DESY Study, Amsterdam 2003. [hep-ph/0311092](#).
- [531] See for instance the summary talks of the Higgs WG session given by S. Kanemura, [hep-ph/0410133](#) and T. Barklow, [hep-ph/0411221](#) at ILCW Paris, April 2004.
- [532] G. Weiglein, et al. (LHC–LC Study Group). [hep-ph/0410364](#).
- [533] A. Djouadi. <http://www.cern.ch/djouadi/programs.html>.
- [534] For discussions of backgrounds, see for instance: P. Grosse–Wiesmann, D. Haidt, H.J. Schreiber, Report DESY 92–123A in Ref. [493].  
P. Janot, Waikoloa Linear Collid (1993) 0192–217;  
E. Boos, M. Sachwitz, H.J. Schreiber, S. Shichanin, Z. Phys. C 64 (1994) 391;  
E. Boos, M. Sachwitz, H.J. Schreiber, S. Shichanin, Z. Phys. C 67 (1995) 613;  
G. Montagna, O. Nicrosini, F. Piccinini, Phys. Lett. B 348 (1995) 496;  
S. Moretti, Phys. Rev. D 52 (1995) 6316;  
S. Moretti, Z. Phys. C 71 (1996) 267;  
D. Apostolakis, P. Ditsas, S. Katsanevas, Z. Phys. C 76 (1997) 201.
- [535] V. Barger, K. Cheung, B. Kniehl, R. Phillips, Phys. Rev. D 46 (1992) 3725;  
A. Ballestrero, E. Maina, S. Moretti, Phys. Lett. B 333 (1994) 434; Phys. Lett. B 335 (1994) 460;  
S. Moretti, Phys. Rev. D 52 (1995) 6316.
- [536] R. van Kooten, Talk at LCWS, Baltimore, 2001; see also the Ph.D. Thesis of N. Meyer.
- [537] P. Garcia-Abia, W. Lohmann, Eur. Phys. J. direct C 2 (2000) 2.
- [538] P. Garcia-Abia, W. Lohmann, A. Resperaza, LC-PHSM-2000-62 in Ref. [457].
- [539] Recently, an analysis has shown that in the Higgs mass measurement using the recoil mass technique, systematical errors from the beam energy scale and differential luminosity distributions lead to an additional combined uncertainty of 30 MeV for  $M_H = 120$  GeV; see A. Resperaza in Ref. [531].



- [540] M. Dova, P. Garcia-Abia, W. Lohmann, LC-PHSM-2001-054.
- [541] M. Schumacher, LC-PHSM-2001-003.
- [542] K. Desch, N. Meyer, Eur. Phys. J. C 35 (2004) 171 and LC-PHSM-2001-025.
- [543] M. Hildreth, Preprint SLAC-PUB 6036;  
M.D. Hildreth, T.L. Barklow, D.L. Burke, Phys. Rev. D 49 (1994) 3441;  
I. Nakamura, K. Kawagoe, Phys. Rev. D 54 (1996) 3634;  
J. Kamoshita, Y. Okada, M. Tanaka, Phys. Lett. B 391 (1997) 124;  
G. Borisov, F. Richard, [hep-ph/9905413](#);  
Marco Battaglia, [hep-ph/9910271](#);  
E. Boos, V. Ilyin, A. Pukhov, M. Sachwitz, H.J. Schreiber, Eur. Phys. J. Direct C 2 (2000) 5.
- [544] C.T. Potter, J.E. Brau, M. Iwasaki, eConf C010630, 2001, P118 and Ref. [204].
- [545] Using an improved version of the TESLA detector simulation program SIMDET, it has been shown that the charm tagging capabilities have been overestimated in the analyses performed for the TESLA TDR and the precision on the  $b\bar{b}$ ,  $c\bar{c}$  and  $g\bar{g}$  are thus worse than those presented in Ref. [456]; see T. Kuhl in Ref. [531].
- [546] J.-C. Brient, Note ECFA - LC Workshop, LC-PHSM-2002-03.
- [547] T. Barklow, [hep-ph/0312268](#) and in Ref. [221].
- [548] E. Boos, et al., Eur. Phys. J. C 19 (2001) 455; Note LC-PHSM-2000-053.
- [549] J. Gunion, P.C. Martin, Phys. Rev. Lett. 78 (1997) 4541.
- [550] M. Dubinin, H.J. Schreiber, A. Vologdin, LC-PHSM-2003-004.
- [551] M. Battaglia, A. de Roeck, [hep-ph/0111307](#).
- [552] M. Battaglia, [hep-ph/0211461](#).
- [553] M. Schumacher, LC-PHSM-2003-096.
- [554] Most of the analyses with the tagging of heavy quarks use a realistic neural network algorithm based on D.J. Jackson, Nucl. Instrum. Meth. A 388 (1997) 247.
- [555] A. Gay, LC-Note 2004 and in Ref. [530].
- [556] A. Juste, G. Merino, [hep-ph/9910301](#);  
M. Martinez, R. Miquel, Eur. Phys. J. C 27 (2003) 49;  
K. Desch, M. Schmucher, in Ref. [536];  
S. Dawson, A. Juste, L. Reina, D. Wackerroth, in Ref. [536].
- [557] K. Hagiwara, H. Murayama, I. Watanabe, Nuclear Phys. B 367 (1991) 257.
- [558] For studies of  $H \rightarrow t\bar{t}$ , see also S. Bar-Shalom, D. Atwood, A. Soni, Phys. Lett. B 419 (1998) 340;  
B. Grzadkowski, J. Pliszka, Phys. Rev. D 60 (1999) 115018.
- [559] J. Alcaraz, E.R. Morales, [hep-ph/0012109](#).
- [560] C. Castanier, P. Gay, P. Lutz, J. Orloff, LC-PHSM-2000-061, [hep-ph/0101028](#).
- [561] U. Baur, T. Plehn, D. Rainwater in Ref. [532].
- [562] Y. Yasui, et al., in LCWS Fermilab, 2001, [hep-ph/0211047](#).
- [563] S. Kanemura, et al., Phys. Lett. B 558 (2003) 157, [hep-ph/0209326](#); [hep-ph/0410048](#).
- [564] N. Meyer, LC-PHSM-2003-066, [hep-ph/0308142](#).
- [565] K. Desch, M. Battaglia, LC-PHSM-2001-053.
- [566] A. Blondel, Phys. Lett. B 202 (1988) 145;  
K. Mönig, LC-PHSM-2000-059.
- [567] J. Erler, S. Heinemeyer, W. Hollik, G. Weiglein, P. Zerwas, Phys. Lett. B 486 (2000) 125.
- [568] I. Watanabe, et al. in Ref. [460];  
T. Ohgaki, T. Takahashi, I. Watanabe, T. Tauchi, Phys. Rev. D 56 (1997) 1723; Internat. J. Modern Phys. A 13 (1998) 2411;  
S. Soldner-Rembold, G. Jikia, Nucl. Phys. Proc. Suppl. 82 (2000) 373;  
M. Melles, [hep-ph/9906467](#); [hep-ph/0008125](#);  
P. Niezurawski, A.F. Zarniecki, M. Krawczyk, Acta Phys. Polon. B 34 (2003) 177;  
A. Rosca, K. Mönig, LC-PHSM-2003-084.
- [569] P. Niezurawski, A. Zarniecki, M. Krawczyk, [hep-ph/0307183](#).
- [570] G. Jikia, Phys. Lett. B 298 (1993) 224;  
G. Jikia, Nuclear Phys. B 405 (1993) 24;  
M.S. Berger, Phys. Rev. D 48 (1993) 5121;  
D.A. Dicus, C. Kao, Phys. Rev. D 49 (1994) 1265;  
G. Gounaris, J. Layssac, P. Porfyriadis, F.M. Renard, Eur. Phys. J. C 13 (2000) 79.
- [571] D. Morris, T. Truong, D. Zappala, Phys. Lett. B 323 (1994) 421;  
I. Ginzburg, I. Ivanov, Phys. Lett. B 408 (1997) 325;  
E. Boos, et al., Phys. Lett. B 427 (1998) 189.
- [572] P. Niezurawski, A.F. Zarniecki, M. Krawczyk, [hep-ph/0307175](#) and LC-PHSM-2003-088;  
P. Niezurawski, A.F. Zarniecki, M. Krawczyk, JHEP 0211 (2002) 034.
- [573] B. Grzadkowski, J.F. Gunion, Phys. Lett. B 294 (1992) 361;  
J.F. Gunion, J.G. Kelly, Phys. Lett. B 333 (1994) 110.
- [574] R. Godbole, S. Rindani, R. Singh, Phys. Rev. D 67 (2003) 095009.

- [575] E. Asakawa, K. Hagiwara, Eur. Phys. J. C 31 (2003) 351. [hep-ph/0409083](#).
- [576] E. Asagawa, J. Kamoshita, A. Sugamoto, I. Watanabe, Eur. Phys. J. C 14 (2000) 335;  
E. Asagawa, S.Y. Choi, K. Hagiwara, J.S. Lee, Phys. Rev. D 62 (2000) 115005.
- [577] For a recent work and for earlier references, see: B. Grzadkowski, Z. Hioki, K. Ohkuma, Nuclear Phys. B 689 (2004) 108.
- [578] J. Kuhn, E. Mirkes, J. Steegborn, Z. Phys. C 57 (1993) 615.
- [579] T. Barklow in Ref. [466];  
K. Ispirian, et al., Sov. J. Nucl. Phys. 11 (1970) 712.
- [580] M. Drees, et al., Phys. Lett. B 306 (1993) 371;  
D. Borden, et al., Phys. Rev. D 50 (1994) 4499;  
B. Kamal, Z. Merebashvili, A.P. Contogouris, Phys. Rev. D 51 (1995) 4808;  
G. Jikia, A. Tkabaldze, Phys. Rev. D 54 (1996) 2030.
- [581] V.S. Fadin, V.A. Khoze, A.D. Martin, Phys. Rev. D 56 (1997) 484;  
M. Melles, W.J. Stirling, Eur. Phys. J. C 9 (1999) 101;  
M. Melles, W.J. Stirling, Nuclear Phys. B 564 (1999) 325;  
M. Melles, W.J. Stirling, V.A. Khoze, Phys. Rev. D 61 (2000) 54015.
- [582] A. Denner, S. Dittmaier, M. Stöbel, Phys. Rev. D 51 (1996) 44.
- [583] M. Mühlleitner, M. Krämer, M. Spira, P. Zerwas, Phys. Lett. B 508 (2001) 31.
- [584] See for instance: M. Drees, R. Godbole, Z. Phys. C 59 (1993) 591.
- [585] For a review, see: M. Baillargeon, G. Bélanger, F. Boudjema. [hep-ph/9405359](#).
- [586] K. Cheung, Nuclear Phys. B 403 (1993) 19;  
G. Jikia, Nuclear Phys. B 494 (1997) 19.
- [587] R. Godbole, S. Kraml, R. Singh. [hep-ph/0409199](#).
- [588] G. Jikia, Nuclear Phys. B 412 (1994) 57.
- [589] R. Belusveic, G. Jikia, Phys. Rev. D 70 (2004) 073017.
- [590] M. Baillargeon, F. Boudjema, Phys. Lett. B 317 (1993) 371.
- [591] O. Eboli, M.C. Gonzalez-Garcia, S. Novaes, Phys. Rev. D 50 (1994) 3546;  
G. Gounaris, P. Porfyriadis, F.M. Renard, Eur. Phys. J. C 20 (2001) 659.
- [592] K. Cheung, Phys. Rev. D 47 (1993) 3750.
- [593] For additional discussions of this process, see: J.Y. Guo, Y. Liao, Y.P. Kuang, Phys. Rev. D 62 (2000) 035007;  
H. Chen, et al., Nuclear Phys. B 683 (2004) 196.
- [594] J.Y. Guo, et al., Phys. Rev. D 62 (2000) 035007;  
Y.J. Zhou, et al., Phys. Rev. D 68 (2003) 0903004.
- [595] K. Hagiwara, I. Watanabe, P. M. Zerwas, Phys. Lett. B 278 (1992) 187;  
E. Boos, et al., Phys. Lett. B 273 (1991) 173;  
K. Cheung, Phys. Rev. D 48 (1993) 1035.
- [596] E. Boos, A. Pukhov, M. Sachwitz, H.J. Schreiber, Z. Phys. C 75 (1997) 237.
- [597] S. Dittmaier, A. Kaiser, Phys. Rev. D 65 (2002) 113003.
- [598] W. Murray. [hep-ph/0104268](#) and in Ref. [473].
- [599] P. Janot in Ref. [473].
- [600] R. Casalbuoni, A. Deandrea, S. De Curtis, D. Dominici, R. Gatto, J.F. Gunion, Phys. Rev. Lett. 83 (1999);  
R. Casalbuoni, et al., JHEP 9908 (1999) 011.
- [601] V. Barger, T. Han, C.G. Zhou, Phys. Lett. B 480 (2000) 140.
- [602] B. Kamal, W.J. Marciano, Z. Parsa. [hep-ph/9712270](#).
- [603] D. Atwood, A. Soni, Phys. Rev. D 52 (1995) 6271;  
S.Y. Choi, J.S. Lee, Phys. Rev. D 61 (2000) 111702;  
E. Asakawa, S.Y. Choi, J.S. Lee, Phys. Rev. D 63 (2001) 015012.